

Pertanika Journal of

**SCIENCE &
TECHNOLOGY**

JST

VOL. 28 (1) JAN. 2020



A scientific journal published by Universiti Putra Malaysia Press

Journal of Science & Technology

About the Journal

Overview

Pertanika Journal of Science & Technology (JST) is the official journal of Universiti Putra Malaysia published by UPM Press. It is an open-access online scientific journal which is free of charge. It publishes the scientific outputs. It neither accepts nor commissions third party content.

Recognized internationally as the leading peer-reviewed interdisciplinary journal devoted to the publication of original papers, it serves as a forum for practical approaches to improving quality in issues pertaining to science and engineering and its related fields.

JST is a **quarterly** (January, April, July and October) periodical that considers for publication original articles as per its scope. The journal publishes in **English** and it is open to authors around the world regardless of the nationality.

The Journal is available world-wide.

Aims and scope

Pertanika Journal of Science and Technology aims to provide a forum for high quality research related to science and engineering research. Areas relevant to the scope of the journal include: bioinformatics, bioscience, biotechnology and bio-molecular sciences, chemistry, computer science, ecology, engineering, engineering design, environmental control and management, mathematics and statistics, medicine and health sciences, nanotechnology, physics, safety and emergency management, and related fields of study.

History

Pertanika was founded in 1978. A decision was made in 1992 to streamline Pertanika into three journals as Journal of Tropical Agricultural Science, Journal of Science & Technology, and Journal of Social Sciences & Humanities to meet the need for specialised journals in areas of study aligned with the interdisciplinary strengths of the university.

After almost 28 years, as an interdisciplinary Journal of Science & Technology, the revamped journal now focuses on research in science and engineering and its related fields.

Goal of *Pertanika*

Our goal is to bring the highest quality research to the widest possible audience.

Quality

We aim for excellence, sustained by a responsible and professional approach to journal publishing. Submissions are guaranteed to receive a decision within 14 weeks. The elapsed time from submission to publication for the articles averages 5-6 months.

Abstracting and indexing of *Pertanika*

The journal is indexed in SCOPUS (Elsevier), Clarivate-Emerging Sources Citation Index [ESCI (Web of Science)], BIOSIS, National Agricultural Science (NAL), Google Scholar, MyCite and ISC.

Future vision

We are continuously improving access to our journal archives, content, and research services. We have the drive to realise exciting new horizons that will benefit not only the academic community, but society itself.

Citing journal articles

The abbreviation for *Pertanika Journal of Science & Technology* is *Pertanika J. Sci. Technol.*

Publication policy

Pertanika policy prohibits an author from submitting the same manuscript for concurrent consideration by two or more publications. It prohibits as well publication of any manuscript that has already been published either in whole or substantial part elsewhere. It also does not permit publication of manuscript that has been published in full in Proceedings.

Code of Ethics

The *Pertanika* Journals and Universiti Putra Malaysia takes seriously the responsibility of all of its journal publications to reflect the highest in publication ethics. Thus all journals and journal editors are expected to abide by the Journal's codes of ethics. Refer to *Pertanika's Code of Ethics* for full details, or visit the Journal's web link at http://www.pertanika.upm.edu.my/code_of_ethics.php

International Standard Serial Number (ISSN)

An ISSN is an 8-digit code used to identify periodicals such as journals of all kinds and on all media—print and electronic. All *Pertanika* journals have ISSN as well as an e-ISSN.

Journal of Science & Technology: ISSN 0128-7680 (*Print*); ISSN 2231-8526 (*Online*).

Lag time

A decision on acceptance or rejection of a manuscript is reached in 3 to 4 months (average 14 weeks). The elapsed time from submission to publication for the articles averages 5-6 months.

Authorship

Authors are not permitted to add or remove any names from the authorship provided at the time of initial submission without the consent of the Journal's Chief Executive Editor.

Manuscript preparation

Refer to *Pertanika's INSTRUCTIONS TO AUTHORS* at the back of this journal.

Editorial process

Authors are notified with an acknowledgement containing a *Manuscript ID* on receipt of a manuscript, and upon the editorial decision regarding publication.

Pertanika follows a **double-blind peer-review** process. Manuscripts deemed suitable for publication are usually sent to reviewers. Authors are encouraged to suggest names of at least three potential reviewers at the time of submission of their manuscript to *Pertanika*, but the editors will make the final choice. The editors are not, however, bound by these suggestions.

Notification of the editorial decision is usually provided within ten to fourteen weeks from the receipt of manuscript. Publication of solicited manuscripts is not guaranteed. In most cases, manuscripts are accepted conditionally, pending an author's revision of the material.

The Journal's peer-review

In the peer-review process, three referees independently evaluate the scientific quality of the submitted manuscripts.

Peer reviewers are experts chosen by journal editors to provide written assessment of the **strengths** and **weaknesses** of written research, with the aim of improving the reporting of research and identifying the most appropriate and highest quality material for the journal.

Operating and review process

What happens to a manuscript once it is submitted to *Pertanika*? Typically, there are seven steps to the editorial review process:

1. The Journal's Chief Executive Editor (CEE) and the Editorial Board Members (EBMs) examine the paper to determine whether it is appropriate for the journal and should be reviewed. If not appropriate, the manuscript is rejected outright and the author is informed.
2. The CEE sends the article-identifying information having been removed, to three reviewers who are specialists in the subject matter represented by the article. The CEE requests them to complete the review in three weeks.

Comments to authors are about the appropriateness and adequacy of the theoretical or conceptual framework, literature review, method, results and discussion, and conclusions. Reviewers often include suggestions for strengthening of the manuscript. Comments to the editor are in the nature of the significance of the work and its potential contribution to the field.

3. The CEE, in consultation with the Editor-in-Chief (EiC), examines the reviews and decides whether to reject the manuscript, invites the author(s) to revise and resubmit the manuscript. The CEE may seek additional reviews. Final acceptance or rejection rests with the CEE and EiC, who reserve the right to refuse any material for publication. In rare instances, the manuscript is accepted with almost no revision. Almost without exception, reviewers' comments (to the author) are forwarded to the author. If a revision is indicated, the editor provides guidelines for attending to the reviewers' suggestions and perhaps additional advice about revising the manuscript.
4. The authors decide whether and how to address the reviewers' comments and criticisms and the editor's concerns. The authors return a revised version of the paper to the chief executive editor along with specific information describing how they have answered' the concerns of the reviewers and the editor, usually in a tabular form. The author(s) may also submit a rebuttal if there is a need especially when the author disagrees with certain comments provided by reviewer(s).
5. The CEE sends the revised paper out for re-review. Typically, at least one of the original reviewers will be asked to examine the article.
6. When the reviewers have completed their work, the CEE in consultation with the EiC and EBMs examine their comments and decide whether the paper is ready to be published, needs another round of revisions, or should be rejected.
7. If the decision is to accept, an acceptance letter is sent to all the author(s), the paper is sent to the Press. The article should appear online in approximately three months.

The Publisher ensures that the paper adheres to the correct style (in-text citations, the reference list, and tables are typical areas of concern, clarity, and grammar). The authors are asked to respond to any minor queries by the Publisher. Following these corrections, page proofs are mailed to the corresponding authors for their final approval. At this point, **only essential changes are accepted**. Finally, the article appears in the pages of the Journal and is posted online.

Pertanika Journal of
**SCIENCE
& TECHNOLOGY**

Vol. 28 (1) Jan. 2020



A scientific journal published by Universiti Putra Malaysia Press



EDITOR-IN-CHIEF

Mohd Adzir Mahdi

Physics, Optical Communications

CHIEF EXECUTIVE EDITOR

Abu Bakar Salleh

Biotechnology and Biomolecular Science

UNIVERSITY PUBLICATIONS COMMITTEE

Zulkifli Idrus, Chair

EDITORIAL STAFF

Journal Officers:

Kanagamalar Silvarajoo, *ScholarOne*

Siti Zuhaila Abd Wahid, *ScholarOne*

Tee Syin-Ying, *ScholarOne*

Ummi Fairuz Hanapi, *ScholarOne*

Editorial Assistants:

Rahimah Razali

Zulinaardawati Kamarudin

PRODUCTION STAFF

Pre-press Officers:

Nur Farrah Dila Ismail

Wong Lih Jiun

WEBMASTER

IT Officer:

Muhammad Zamiruddin Sahar

PUBLICITY & PRESS RELEASE

Magdalene Pokar (*ResearchSEA*)

EDITORIAL OFFICE

JOURNAL DIVISION

Office of the Deputy Vice Chancellor (R&I)

1st Floor, IDEA Tower II

UPM-MTDC Technology Centre

Universiti Putra Malaysia

43400 Serdang, Selangor Malaysia.

Gen Enq.: +603 9769 1622 | 1616

E-mail:

executive_editor.pertanika@upm.edu.my

URL: www.journals-ij.upm.edu.my

PUBLISHER

UPM Press

Universiti Putra Malaysia

43400 UPM, Serdang, Selangor, Malaysia.

Tel: +603 9769 8851

E-mail: penerbit@putra.upm.edu.my

URL: <http://penerbit.upm.edu.my>



EDITORIAL BOARD

2018-2020

Adem Kilicman

Mathematical Sciences
Universiti Putra Malaysia, Malaysia.

Ali A. Moosavi-Movahedi

Biophysical Chemistry
University of Tehran, Tehran, Iran.

Amu Therwath

Oncology, Molecular Biology,
Université Paris, France.

Angelina Chin

Mathematics, Group Theory and
Generalisations, Ring Theory,
University of Malaya, Malaysia.

Bassim H. Hameed

Chemical Engineering: Reaction
Engineering, Environmental Catalysis
& Adsorption,
Universiti Sains Malaysia, Malaysia.

Biswa Mohan Biswal

Medical, Clinical Oncology,
Radiotherapy
Universiti Sains Malaysia, Malaysia.

Christopher G. Jesudason

Mathematical Chemistry, Molecular
Dynamics Simulations, Thermodynamics
and General Physical Theory,
University of Malaya, Malaysia.

Hari M. Srivastava

Mathematics and Statistics,
University of Victoria, Canada.

Ivan D. Rukhlenko

Nonlinear Optics, Silicon Photonics,
Plasmonics and Nanotechnology
Monash University, Australia.

Kaniraj R. Shenbaga

Geotechnical Engineering,
India.

Kanury Rao

Senior Scientist & Head, Immunology
Group, International Center for Genetic
Engineering and Biotechnology,
Immunology, Infectious Disease Biology
and System Biology
International Centre for Genetic
Engineering & Biotechnology, New
Delhi, India.

INTERNATIONAL ADVISORY BOARD

2018-2021

Adarsh Sandhu

Editorial Consultant for Nature
Nanotechnology and Contributing
Writer for Nature Photonics, Physics,
Magneto-resistive Semiconducting
Magnetic Field Sensors, Nano-
Bio-Magnetism, Magnetic Particle
Colloids, Point of Care Diagnostics,
Medical Physics, Scanning Hall Probe
Microscopy, Synthesis and Application
of Graphene
Electronics-Inspired Interdisciplinary
Research Institute (EIIRIS), Toyohashi
University of Technology, Japan.

Graham Megson

Computer Science
The University of Westminster, U.K.

Kuan-Chong Ting

Agricultural and Biological Engineering
University of Illinois at Urbana-
Champaign, USA.

Ki-Hyung Kim

Computer and Wireless Sensor
Networks
AJOU University, Korea.

Kunnawee Kanitpong

Transportation Engineering-Road
Traffic Safety, Highway Materials and
Construction
Asian Institute of Technology, Thailand.

Megat Mohd Hamdan

Megat Ahmad
Mechanical and Manufacturing
Engineering
Universiti Pertahanan Nasional
Malaysia, Malaysia.

Mirnalini Kandiah

Public Health Nutrition, Nutritional
Epidemiology
UCSI University, Malaysia.

Mohamed Othman

Communication Technology and
Network, Scientific Computing
Universiti Putra Malaysia, Malaysia

Mohd. Ali Hassan

Bioprocess Engineering, Environmental
Biotechnology
Universiti Putra Malaysia, Malaysia.

Mohd Sapuan Salit

Concurrent Engineering and Composite
Materials
Universiti Putra Malaysia, Malaysia.

Narongrit Sombatsompop

Engineering & Technology: Materials
and Polymer Research
King Mongkut's University of
Technology Thonburi (KMUTT),
Thailand.

Prakash C. Sinha

Physical Oceanography, Mathematical
Modelling, Fluid Mechanics, Numerical
Techniques
Universiti Malaysia Terengganu,
Malaysia.

Rajinder Singh

Biotechnology, Biomolecular Sciences,
Molecular Markers/ Genetic Mapping
Malaysia Palm Oil Board, Kajang,
Malaysia.

Renuganth Varatharajoo

Engineering, Space System
Universiti Putra Malaysia, Malaysia.

Riyanto T. Bambang

Electrical Engineering, Control,
Intelligent Systems & Robotics
Bandung Institute of Technology,
Indonesia.

Roslani Abd-Shukur

Physics & Materials Physics,
Superconducting Materials
Universiti Kebangsaan Malaysia,
Malaysia.

Sabira Khatun

Engineering, Computer Systems
& Software Engineering, Applied
Mathematics
Universiti Malaysia Pahang, Malaysia.

Shiv Dutt Gupta

Director, IIHMR, Health Management,
Public Health, Epidemiology, Chronic
and Non-communicable Diseases
Indian Institute of Health Management
Research, India.

Suan-Choo Cheah

Biotechnology, Plant Molecular Biology
Asiatic Centre for Genome Technology
(ACGT), Kuala Lumpur, Malaysia.

Wagar Asrar

Engineering, Computational Fluid
Dynamics, Experimental Aerodynamics
International Islamic University,
Malaysia.

Wing Keong Ng

Aquaculture, Aquatic Animal Nutrition,
Aqua Feed Technology
Universiti Sains Malaysia, Malaysia.

Yudi Samudya

Chemical Engineering, Advanced
Process Engineering
Curtin University of Technology,
Malaysia.

Suhash Chandra Dutta Roy

Electrical Engineering
Indian Institute of Technology (IIT)
Delhi, India.

Vijay Arora

Quantum and Nano-Engineering
Processes
Wilkes University, USA.

Yi Li

Chemistry, Photochemical Studies,
Organic Compounds, Chemical
Engineering
Chinese Academy of Sciences, Beijing,
China.

ABSTRACTING AND INDEXING OF PERTANIKA JOURNALS

Pertanika has reached 40 years old; this accumulated knowledge has resulted in the journals being abstracted and indexed in SCOPUS (Elsevier), Clarivate-Emerging Sources Citation Index (ESCI (Web of Science)), BIOSIS, National Agricultural Science (NAL), Google Scholar, MyCite and ISC.

The publisher of *Pertanika* will not be responsible for the statements made by the authors in any articles published in the journal. Under no circumstances will the publisher of this publication be liable for any loss or damage caused by your reliance on the advice, opinion or information obtained either explicitly or implied through the contents of this publication.

All rights of reproduction are reserved in respect of all papers, articles, illustrations, etc., published in *Pertanika*. *Pertanika* provides free access to the full text of research articles for anyone, worldwide. It does not charge either its authors or author-institution for refereeing/publishing outgoing articles or user-institution for accessing incoming articles.

No material published in *Pertanika* may be reproduced or stored on microfilm or in electronic, optical or magnetic form without the written authorization of the Publisher.

Copyright © 2019 Universiti Putra Malaysia Press. All Rights Reserved.



Pertanika Journal of Science & Technology
Vol. 28 (1) Jan. 2020

Contents

Foreword

Abu Bakar Salleh

Engineering Sciences

Analysis of Velocity Profiles in Rectangular Straight Open Channel Flow 1
Abinash Sahoo, Sandeep Samantaray and Rosysmita Bikram Singh

Physical Characteristics of Structured Lipid Synthesized by Lipase 19
Catalyzed Interesterification of Coconut and Palm Oils
Siti Nurhasanah, S Joni Munarso, Nur Wulandari and Purwiyatno Hariyadi

Effect of DL-Methionine Concentration, Moisture Content and Bulk 33
Density of Animal Feed on the Light-Induced Fluorescence as a Process
Analytical Tool
*Mohammad Poozesh, Hamidreza Ghasemzadeh, Shamsollah
Abollahpour and Mitra Amoli Diva*

A Novel Approach for Automated Operational Modal Analysis Using 49
Image Clustering
*Muhammad Danial Bin Abu Hasan, Zair Asrar Bin Ahmad, Mohd
Salman Leong and Lim Meng Hee*

The Effect of Javanese Gamelan Music on the Growth of Chinese Broccoli 69
*Yusuf Hendrawan, Antonius Rizky, Bambang Susilo, Joko Prasetyo
and Retno Damayanti*

Information, Computer and Communication Technologies

A Genetic Algorithm Approach for Discovering Fuzzy Hierarchical 91
Censored Classification Rules (FHCCRs)
Renu Bala and Saroj Ratnoo

FLA-SLA Aware Cloud Collation Formation Using Fuzzy Preference 117
Relationship Multi-Decision Approach for Federated Cloud
*Pradeep Kumar Vadla, Bhanu Prakash Kolla and
Thinakaran Perumal*

Clustering with Modified Mutation Strategy in Differential Evolution 141
Seema Patil and Anandhi Rajamani Jayadharmarajan

DFRNets: Unsupervised Monocular Depth Estimation Using a Siamese Architecture for Disparity Refinement <i>John Paul Tan Yusiong and Prospero Clara Naval, Jr.</i>	163
Quantitative Assessment of Concept Maps for Conceptualizing Domain Ontologies: A Case of Quran <i>Rizwan Iqbal, Masrah Azrifah Azmi Murad and Adnan Ashraf</i>	179
Mathematical Sciences	
Efficient Model Selection of Collector Efficiency in Solar Dryer using Hybrid of LASSO and Robust Regression <i>Anam Javaid, Mohd. Tahir Ismail and Majid Khan Majahar Ali</i>	193
Logic Mining in League of Legends <i>Liew Ching Kho, Mohd Shareduwan Mohd Kasihmuddin, Mohd. Asyraf Mansor and Saratha Sathasivam</i>	211
Hybrid Discrete Hopfield Neural Network based Modified Clonal Selection Algorithm for VLSI Circuit Verification <i>Saratha Sathasivam, Mustafa Mamat, Mohd. Asyraf Mansor and Mohd Shareduwan Mohd Kasihmuddin</i>	227
Impacts of Asymmetric Biotic Interactions and Environmental Factors on the Presence-Absence of Multispecies <i>James Omaiye Ojonubah and Mohd Hafiz Mohd</i>	245
Medical and Health Sciences	
Aedestech Mosquito Home System Prevents the Hatch of <i>Aedes</i> Mosquito Eggs and Reduces its Population <i>Latifah Saiful Yazan, Kaveinesh Paskaran, Banulata Gopalsamy and Roslaini Abd Majid</i>	263
Acute Moderate and High-Intensity Endurance Exercise Suppresses <i>Ad-libitum</i> Energy Intake in Obese Males <i>Adam Linoby, Muhammad Alif Nazrin Jumat, Ahmad Safwanudin Nordin, Nur Hidayah Asilah Za'don, Jamiaton Kusrin and Sharifah Maimunah Syed Mud Puad</i>	279
Standardised Extracts of <i>Moringa Oleifera</i> and <i>Centella Asiatica</i> Enhanced the Antioxidant Activity, Learning and Memory Effects by Inhibiting Acetylcholinesterase Activity in D-Galactose Induced Ageing Rats <i>Hisyam Jamari, Mohd Salleh Rofiee, Richard James Johari, Mohd Zaki Salleh and Teh Lay Kek</i>	293

Toxicity Assessment of Gallic Acid Loaded Graphene Oxide (GAGO) Nano-Formulation in Zebrafish (<i>Danio Rerio</i>) Embryos <i>Ahmad Ashraful Hadi Abdul Ghafor, Nurhuda Elias, Suhaili Shamsi, Faizah Md Yasin and Seri Narti Edayu Sarchio</i>	311
Environmental Sciences	
<i>Review Article</i>	
Light Fishing Fleets Monitoring by GIS-Based Spatiotemporal Analysis in West Sumatera Waters <i>Nurholis, Jonson Lumban-Gaol and Fachrudin Syah Achmad</i>	327
Dye Removal by Membrane Technology for Wastewater Treatment using a Cationic Carrier <i>Huda Adil Sabbar, Wasan Omar Noori and Ahmed Samir Naje</i>	353
Applied Sciences and Technologies	
Comparative Study on Inhibitors Comprising Aromatic and Non-Aromatic Solvents towards Flow Assurance of Crude Oil <i>S M Anisuzzaman, Duduku Krishnaiah and Sharmini Nair Prathaban</i>	369
Earth Sciences	
An Integration Based Optimization Approach (ABC and PSO) for Parameter Estimation in BLRP Model for Disaggregating Daily Rainfall <i>Zulkarnain Hassan</i>	385
Material Sciences	
Study on Progressive Wear of Machine Reamer while Reaming Al6061/SiC Composite <i>Sandeep Nambiar, Raviraja Adhikari, Nagaraja Upadhya and Rajarama Hande</i>	403



Foreword

Welcome to the First Issue of 2020 for the Journal of Science and Technology (JST)!

JST is an open-access journal for studies in Science and Technology published by Universiti Putra Malaysia Press. It is independently owned and managed by the university for the benefit of the world-wide science community.

This issue contains 23 articles; one review article and the rest are regular articles. The authors of these articles come from different countries namely Malaysia, India, Indonesia, Iraq, Phillipines, Pakistan and Iran.

Adam Linoby and co-researchers from Universiti Teknologi MARA have investigated the acute effects of iso-caloric high intensity and moderate-intensity continuous exercise as well as high-intensity exercise on subsequent energy intake, appetite score and blood glucose for the obese adult population. They concluded that moderate intensity exercise and high-intensity exercise played an essential role in negative energy balance by induced suppression of appetite and calories intake. Details on this study are presented on page 279.

Huda Adil Sabbar and colleagues from Iraq investigated the removal efficiency of malachite green dye ions by using a bulk liquid membrane, which contained salicylic acid as carrier, sodium hydroxide as extractant and acetic acid as acceptor. The efficiency of the system was dependent upon the principal parameters, such as the acceptor phase pH, dye concentration and carrier concentration. They revealed that a relatively high percentage of removal of malachite green dye (98.4%) were achieved at pH 6 with 20 mg/L of dye concentration and 12mg/L of carrier concentration. Further details on the study can be found on page 353.

A regular article titled “Comparative study on inhibitors comprising aromatic and non-aromatic solvents towards flow assurance of crude oil” was published by S M Anisuzzaman, Duduku Krishnaiah and Sharmini Nair Prathaban from Universiti Malaysia Sabah. Their results showed that the most optimum ratio of inhibitor that gave the highest reduction in viscosity of the crude oil was 30% of ethylene vinyl acetate, 30% of methylcyclohexane and finally 40% ratio of solvent which was either toluene or butanol. Detailed information on this study can be found on page 369.

We anticipate that you will find the evidence presented in this issue to be intriguing, thought-provoking and useful in reaching new milestones in your own research. Please recommend the journal to your colleagues and students to make this endeavour meaningful.

All the papers published in this edition underwent Pertanika's stringent peer-review process involving a minimum of two reviewers comprising internal as well as external referees. This was to ensure that the quality of the papers justified the high ranking of the journal, which is renowned as a heavily-cited journal not only by authors and researchers in Malaysia but by those in other countries around the world as well.

We would also like to express our gratitude to all the contributors, namely the authors, reviewers, Editor-in-Chief and Editorial Board Members of JST, who have made this issue possible. JST is currently accepting manuscripts for upcoming issues based on original qualitative or quantitative research that opens new areas of inquiry and investigation.

Chief Executive Editor

Prof. Dato' Dr. Abu Bakar Salleh

executive_editor.pertanika@upm.edu.my

Analysis of Velocity Profiles in Rectangular Straight Open Channel Flow

Abinash Sahoo^{1*}, Sandeep Samantaray¹ and Rosysmita Bikram Singh²

¹Department of Civil Engineering, National Institute of Technology Silchar, Assam 788010, India

²Department of Civil Engineering, Veer Surendra Sai University of Technology Burla, Odisha 768018, India

ABSTRACT

This study aims at analysing the velocity profiles in a straight rectangular channel having a constant width and depth throughout the channel length. Experiment was conducted for five altered depths using the straight rectangular flume in hydraulic flow laboratory available at VSS University of Technology, Odisha, India. Furthermore, the distributions of stream wise velocity at the different flow depth were computed numerically using hydraulic software ANSYS FLUENT 18.1. The results of numerical simulation showed sensibly good agreement with experimental data, which was $\pm 10\%$ for both across and along the channel of rectangular flume. The Reynolds number in this study lay between 10,853 to 79,000. In case of channel flow, the velocity varied both in longitudinal and transverse direction. The isovel lines joining points of equal velocity normally curved upward due to the effect of turbulence. Peak velocity was found below the free surface of water. The law of logarithmic and power law was applied to study velocity distribution in terms of turbulent flow condition. The model could be validated by considering the various parameters of flow measurement such as the resultant velocity and the velocity at both horizontal and vertical direction. The inclusive idea of this study was to comprehend flow characteristic over a plane bed through experimental and numerical simulation methods.

Keywords: ANSYS, logarithmic law, power law, rectangular flume, velocity distribution, velocity profile

ARTICLE INFO

Article history:

Received: 13 January 2019

Accepted: 19 July 2019

Published: 13 January 2020

E-mail addresses:

bablushahoo1992@gmail.com (Abinash Sahoo)

samantaraysandeep963@gmail.com (Sandeep Samantaray)

puja003@gmail.com (Rosysmita Bikram Singh)

* Corresponding author

INTRODUCTION

The distribution of longitudinal component of velocity in a given cross-section is a significant parameter in the study of an open channel flow to find out various properties of flow. Diverse and complex behaviour of fluid flow which occurs at a particular period generates intricate structures that

have to be modelled or solved partially based on time and length scale. Hence a study of a consistent mathematical model of velocity distribution is frequently needed. Study of velocity distribution pattern indicates there is a rise in velocity consistently with vertical distance from bed of the channel. At lower depths of flow, magnitude of velocity is least at the bed because of no slip condition while velocity is found to be highest at some point below the free surface. When there is an increase in depth, the sequences of greater velocity occurs at free surface of the wall.

Bonakdari et al. (2014) developed a 3D Computational Fluid Dynamics (CFD) model using ANSYS software to examine flow patterns and the $k-\epsilon$ turbulence closure model was applied to resolve turbulence equations. Wake function is unable to detect the action of secondary currents and thus is not applicable to 3D flows, as it helps in predicting an increasing velocity with distance from the bed. Coles (1956) found that $k-\epsilon$ model took into account two equations for isotropic turbulence. Hence, model is inadequate to speculate the secondary currents and velocity-dip-phenomenon related to it. Nezu and Rodi (1986) and Cardoso et al. (1989) applied the classical log law to determine velocity profile for vertical flow in an open channel at a section $\xi < 0.2$ $\{\xi = y/h$, is ratio between distance from bed(y) to flow depth (h)}. Castro-Orgaz, and Dey (2011) proposed theory of power-law for velocity profile for flow under turbulent boundary layer. Naik et al. (2018) used ANSYS-Fluent software to simulate the model in two phases numerically in a converging compound channel. Welahettige et al. (2017) used ANSYS Fluent R16.2 for CFD simulations and outcomes were validated with experimental results done in an open Venturichannel. Naot et al. (1993) applied Log-wake and power law to narrate flows in two-dimensional open-channel. Kang and Choi (2006) gave additional advanced RANS equations based on anisotropic turbulence models and should be used for prediction of velocity-dip-phenomena. Sarma et al. (2000) described velocity distribution taking into consideration velocity dip for flow in open channel. They used binary version of velocity distribution, where inner section follows logarithmic law and outer section follows parabolic law. Afzal et al. (2007) used Velocity profile power law to cover the influence of friction in fully developing zone for turbulent pipe and open channel flows. Wilkerson and McGahan (2005) expanded two models which help in predicting depth-averaged velocity distributions. Guo and Julien (2006) derived modified-log-wake law to predict velocity-dip-phenomenon for flow in open channel. Absi (2011) modified this law and proposed another law for velocity profile called the full dip-modified-log-wake law and law was semi analytical.

The purpose of this study is to compute magnitude of velocity at various points longitudinally and laterally of the rectangular flume, which assists to draw the velocity flow profiles that help in studying the velocity distribution and its characteristics. The resulting velocity profiles are validated with the universal laws. The results found from this computational approach are hence contrasted with the experimental data for better

efficiency. The computational way is considerably being used globally due to competency and flow complexity, which helps in resolving and modelling instinctively in accordance to what the model requires.

METHODS

Theoretical Consideration

Study from literature suggested that in an open channel the magnitude of velocity is maximum at some point below top surface of water. For narrow channels where the aspect ratio $Ar < 5$, the occurrence of maximum velocity is below free surface of water. By assuming “shear stress is constant”, P-vK (Prandtl-von Karman) law is considered as general form of velocity distribution, applied near channel bed. The von Karman constant is modified and it can be applied in outer region of flow. P-vK law overlaps with log law at about 20% of flow depth and can be used for full flow depth. Log law is strictly applicable to the region below 20% of flow depth that may be attributed to the law of the wall (log-law) which is often applied to the entire depth. Log law is effective for inner region near the bed, but it will be deviated from the laboratory data on the outer layer:

$$\frac{u}{u_*} = \frac{1}{k} \left[\text{Ln} \left(\frac{y}{y_0} \right) \right] \quad (1)$$

Where, u = mean velocity in main flow direction

u_* = shear velocity

y = upright distance from bed

y_0 = distance where velocity is hypothetically zero

k denotes the von-Karman constant. For outer region of flow i.e. $\xi > 0.2$, there is a variance of log law from experimental data. So, for two-dimensional flows, this variance was adjusted by summing Coles wake function as

$$\frac{u}{u_*} = \frac{1}{k} \left[\text{Ln} \left(\frac{y}{y_0} \right) + 2\Pi \sin^2 \left(\frac{\pi y}{2h} \right) \right] \quad (2)$$

Where h = flow depth

Π = Coles' wake strength. The expression is called the log wake law, notation Π express the Coles parameter, denoting the wake function strength. General form of parabolic law given by:

$$\frac{u - u_{\max}}{u_*} = 6.3 \left(1 - \frac{\eta}{\eta_{\text{dip}}} \right)^2 \quad (3)$$

Where η = dimensionless distance from bed

η_{dip} = dimensionless distance of maximum velocity.

On basis of the intersection point, the parabolic law is valid to the free surface which ranges from 0.2 to 0.3 for flows in sediment-laden. Later, Coles proposed the limitations of the law and validity region for parabolic law. For a narrow channel where the aspect ratio $Ar < 5$, peak velocity occurs below free surface of water, resulting in phenomenon of velocity-dip-, which involves a variance from log-wake law. Using the laws proposed by Coles, velocity profile was validated in this present study.

Experimental Setup

Experiments were conducted utilizing the flume present in the Hydraulics Lab of VSSUT, Burla as shown in Figure 1. The experiments were performed in a straight simple rectangular flume described below in Figure 2 made of iron whose length is 2.5 m, width 0.3 m, and 0.3 m deep. The water supply was from a storage sump which was lifted by a number of parallel pumps to an overhead tank. From the overhead tank water was carried to the flume and discharge was controlled through a valve. The head gate was lifted fully to allow the water to enter the flume. Baffle walls were provided in series before the head gate so as to decrease the turbulence effect of the incoming water. The Point gauge was first checked for its smooth moving over the flume and its least count was noted. The tail-gate was responsible to maintain the uniformity of flow which was accumulated in a metal tank,

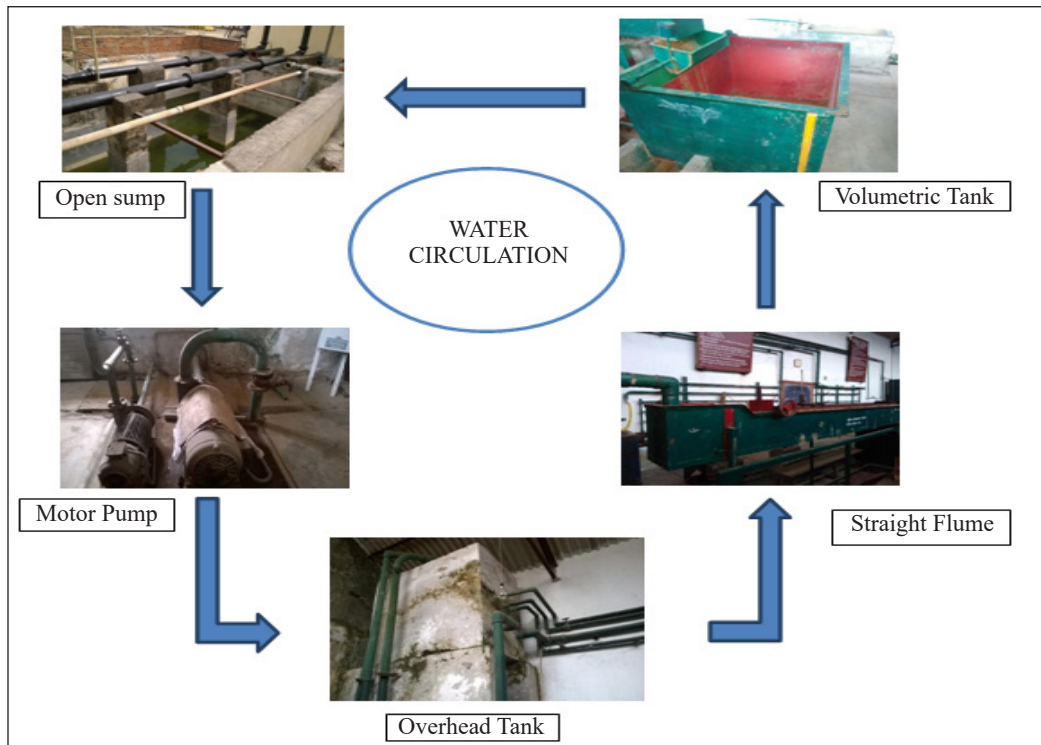


Figure 1. Experimental setup in the Lab

where the volumetric measurement could be taken. Further it can be redirected to the sump and from sump to overhead tank, with a help of a pump installed in the laboratory, thus setting a complete re-circulating water supply system to the flume. To attain a steady and uniform flow conditions every single experimental run of the flume was done by keeping the water surface gradient parallel to the bed slope.

The flow velocity in the experiment were measured at 9 mid-verticals ($x = 0.25, 0.5, 0.75, 1.0, 1.25, 1.5, 1.75, 2.0, 2.25$ m) alongside the flow developing region and 6 mid-horizontals ($y = 0.03, 0.06, 0.09, 0.12, 0.15$ and 0.18 m) across the flow developing zone across half width of the flow section revealed in Figure 2. This was for a single water flow depth. In this way, the same procedure was repeated for multiple flow depths starting from bed of the channel ($0.06, 0.1, 0.14, 0.18, 0.22$ m).

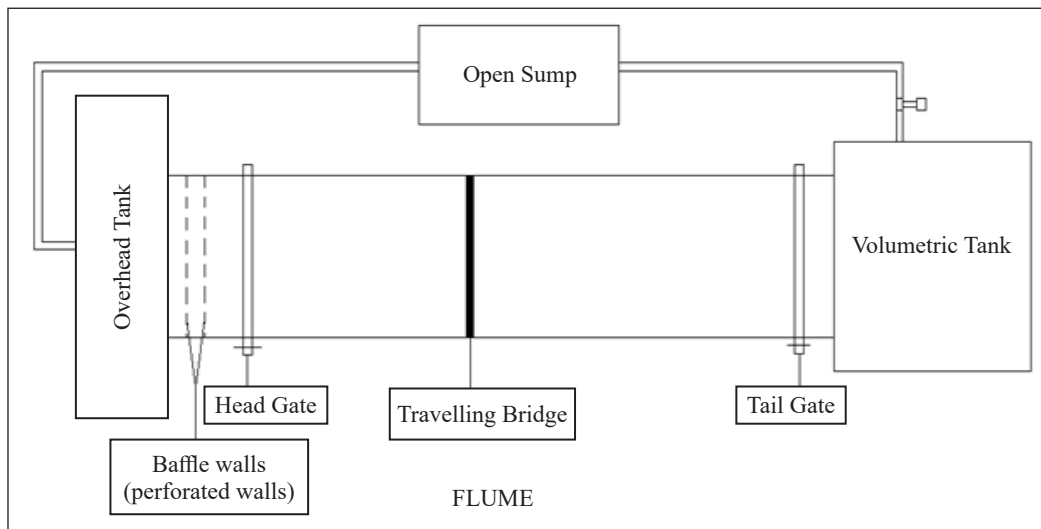


Figure 2. Plan view of the experimental flume

Table 1
Details of the experimental conditions

Test No.	Flow Discharge, Q (cm ³ /s)	Height, h (m)	Aspect Ratio, b/h	Froude number (F _r)	Reynolds number (R _c)
1	19.55	0.06	5	0.29	10,853
2	27.2	0.1	3	0.323	21,573
3	38.25	0.14	2.14	0.384	36,404
4	51	0.18	1.66	0.451	54,606
5	67.15	0.22	1.36	0.537	79,000

Table 1 indicates the different heights from channel bed where the velocity measurements have been conducted with different aspect ratio. F_r -Froude number = V/\sqrt{gh} , where V-average velocity, R_c -Reynolds number = VR/ν where R-hydraulic radius.

Depth of flow in rectangular channel was measured through piezometer which was static on the traveling bridge and manually functioned. We can note the height of water entering into the tank and with the help of a stopwatch we can calculate the time. Dividing height by time we obtained the velocity and then multiplying it with the base area of the tank we obtained the average discharge. The velocity of the flow was measured at various points using a Pitot tube connected to a manometer. While noting velocity readings using Pitot tube, Pitot was positioned facing towards the flow direction. After this setup it was again turned across flow direction. Along the longitudinal section of rectangular flume pitot was moved at 0.25 m intervals in horizontal direction and 0.2h, 0.4h, 0.6h, 0.8h (h-flow depth) just below free surface of the respective flow depth in vertical direction. Similarly, along lateral section of the flume pitot was moved at 0.03m intervals in horizontal direction and 0.2h, 0.4h, 0.6h, 0.8h below free surface in vertical direction as depicted in Figure 3. As the cross-section of channel was square in shape, velocity was measured from near side wall till mid interval of the channel because the magnitude of velocity remained same on the other half of the interval. The Pitot tube was fixed to primary scale which had least count of 0.1 mm with the Vernier scale. To the right limb of the Pitot the pipe was attached to the right limb of the manometer and the left limb of the pitot to the left limb. The velocity hence was calculated by formula:

$$V = \sqrt{2g\Delta H} \quad (4)$$

where g -force of gravity, ΔH -water elevation difference in the manometer.

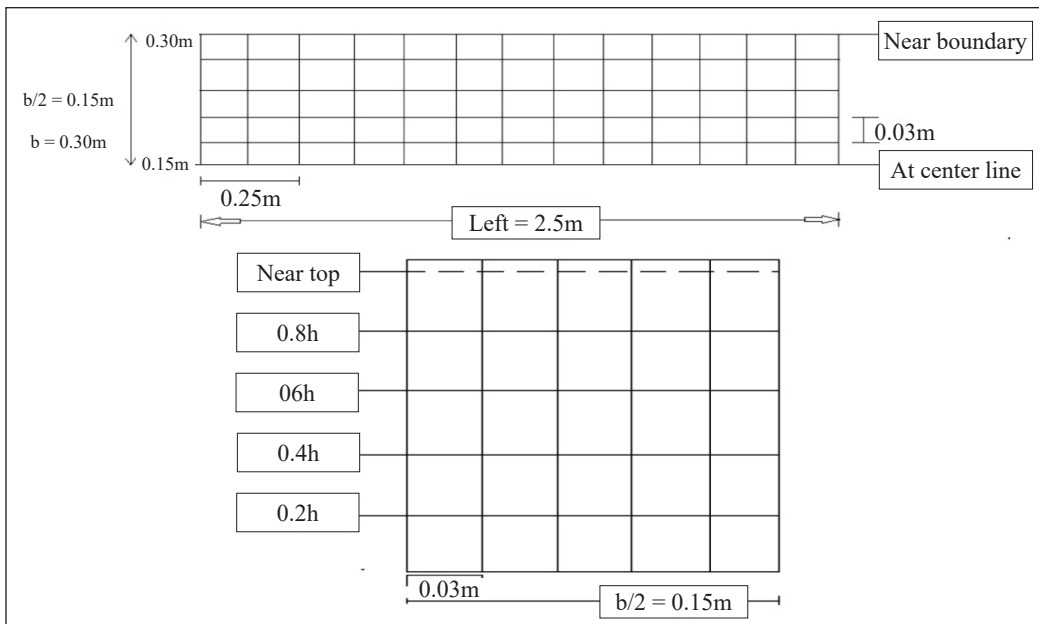


Figure 3. Detail plan (a) and cross-section (b) of experimental grid where velocity measured

NUMERICAL MODEL SETUP

A flow through the open channel is dependent on the various features such as bed properties, shear resistance and friction. k- ϵ model is highly adopted model in CFD to simulate characteristics of flow in turbulent flow condition. Larocque et al. (2013) proposed k- ϵ model which emphasised on mechanisms that impacted on turbulent kinetic energy. This kind of generality is lacking in the mixing length model. Assumptions made for the model is 'the average rate of distortions is alike in all directions'. It is a semi-empirical model which depends on model transport equations for turbulent-kinetic energy ' k ' and dissipation rate ' ϵ '. Simulation of flow model can be solved in an efficient manner with the help of ANSYS (Fluent). The cross-section of the rectangular flume used for the experimental purpose is drawn with the help of ANSYS software and is divided into different sections with plates placed both in horizontal and vertical directions as revealed in Figure 4 for numerical analysis. The fluid flow equation is governed by momentum equation and continuity equation. This method is fit for structured as well as unstructured mesh.

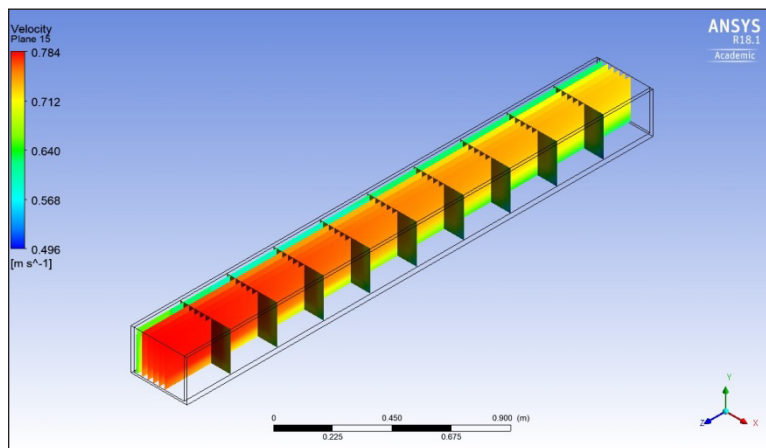


Figure 4. Cross-sectional plates along and across the flow direction

Boundary Conditions

Near wall and channel bed the components of velocity become zero due to effect of no slip condition. For the free surface, the boundary conditions are symmetric that is *no scalar flux takes place across the boundary*. The truncation error that arises by stepwise approximation can be controlled by providing a very fine Cartesian mesh. Nodes are required for the area near the wall and the wake regions. For this case study under consideration the flow domain was discretized by the use of structured grid and body-fitted coordinates. The meshing details of flume are indicated in Figure 5. Least size of the grid after meshing is 0.2527 mm and maximum size of the grid is found be 50.55 mm. The maximum face size of the flume is kept 25.27 mm. Grid size may vary depending on different model setup.

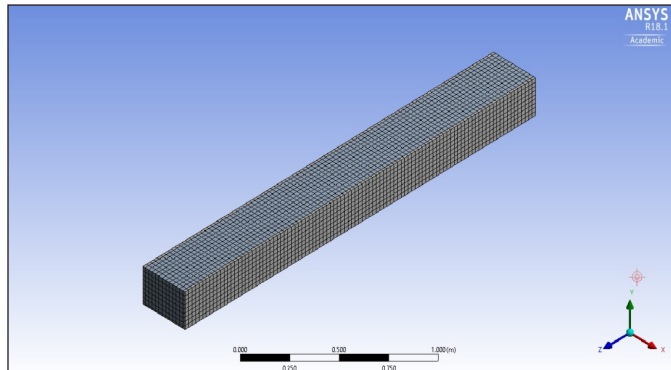


Figure 5. Meshing of the Flume in 3-D ANSYS

Application of Numerical Analysis

In present study, the coupling among velocity field and pressure field is complemented by PISO technique, which is pressure implicit splitting operator available in Fluent as proposed by (Issa, 1986). Figure 6, 7 and 8 show the velocity distribution in stream-wise, vertical, lateral direction and the resultant velocity distribution at 0.25, 1.25 and 2.25 m from the head gate for no load conditions as simulated in ANSYS. In the present work, it is observed that the results obtained from ANSYS were matching well with the experimental data and magnitude of maximum velocity and velocity distribution were virtually equal to the results derived experimentally.

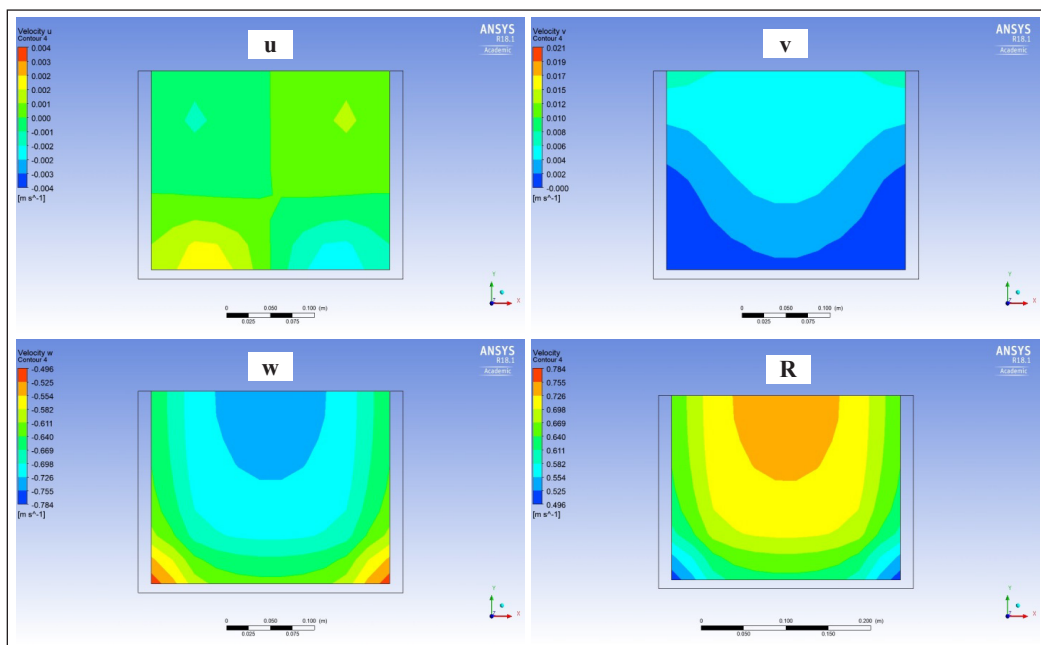


Figure 6. Contours for stream wise velocity (u), vertical velocity (v), lateral velocity (w), resultant velocity (R) at 0.25m from head

Analysis of Velocity Profiles in Rectangular Straight Open Channel Flow

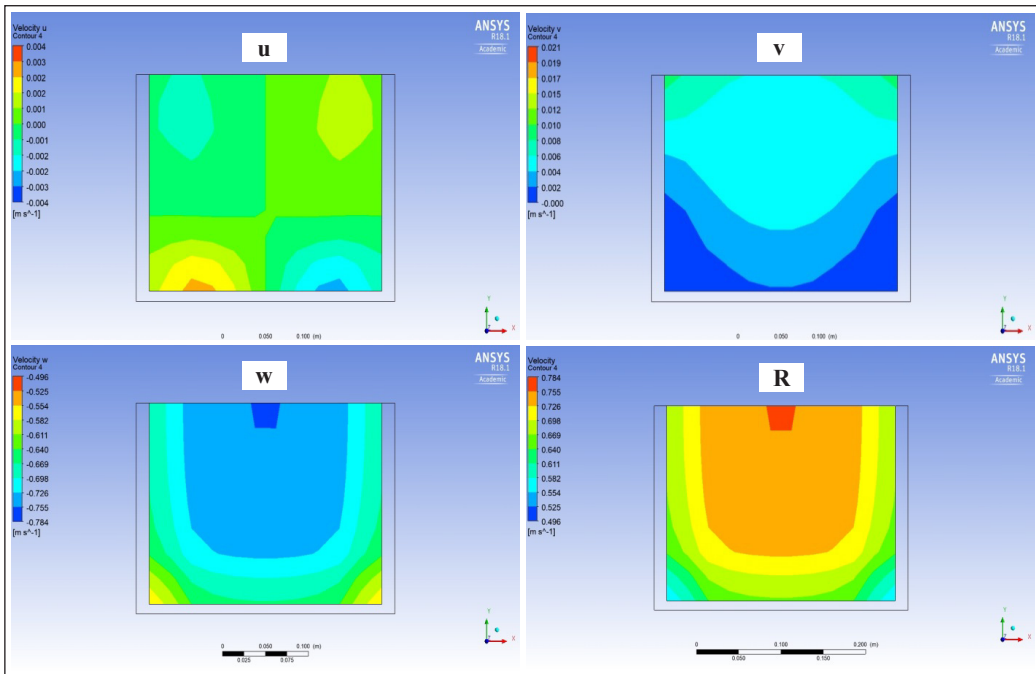


Figure 7. Contours for stream wise (u), velocity vertical velocity (v), lateral velocity (w), resultant velocity (R) at 1.5m from head

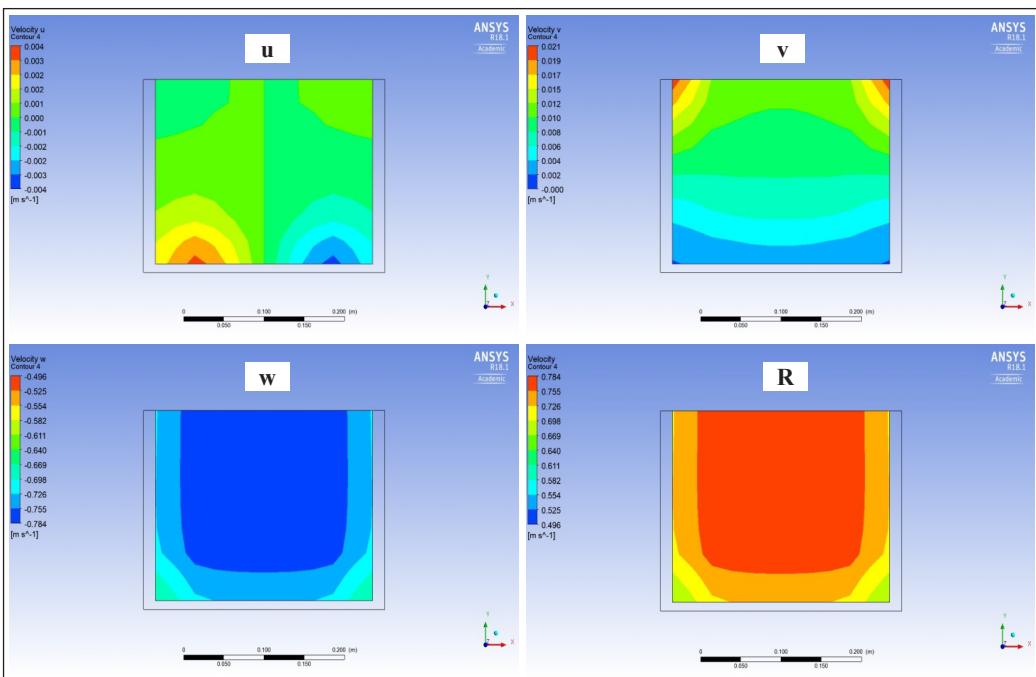
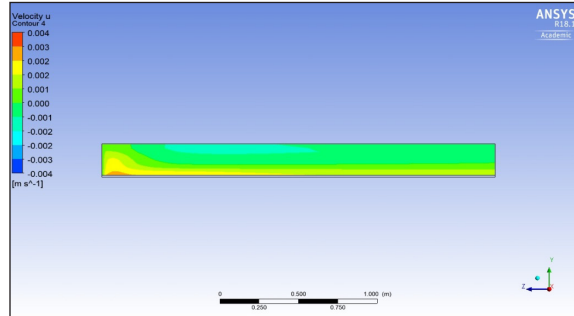
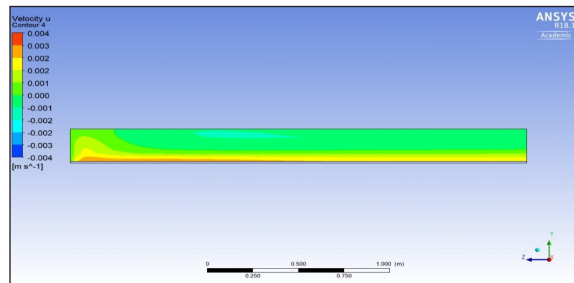


Figure 8. Contours for stream wise (u), velocity vertical velocity (v), lateral velocity (w), resultant velocity (R) at 2.25m from head

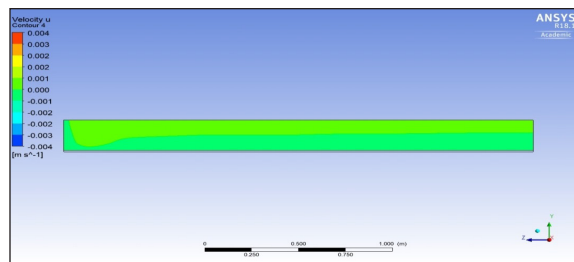
Figure 9 shows the velocity distribution contours across the flow cross-section at 0.03, 0.09, 0.15 m from the side walls simulated in ANSYS in no load condition.



(a)



(b)



(c)

Figure 9. Stream-wise velocity in lateral direction at (a) 0.03m, (b) 0.09m, (c) 0.15m from side wall

RESULTS AND ANALYSIS

Plot of stage vs discharge is represented with the data obtained from the experimental observations performed in the laboratory as shown below in Figure 10. In the Horizontal axis the value represents the discharge in cm^3/sec and the Stage of the flow in m is indicated in vertical axis in m (i.e. the height of flow).

The stream wise, vertical and lateral velocity components obtained from the experimental set up are revealed in Table 2. The results (the resultant velocity) generated from the experimental set up and the numerical analysis is indicated in Table 3. The overall

flow patterns of experimental runs for the rectangular flume are summarized in the graphs. In this paper the results for the test 5 i.e. at depth 0.22 m is shown. In similar way the results of all the other different depths were found out and put for validation.

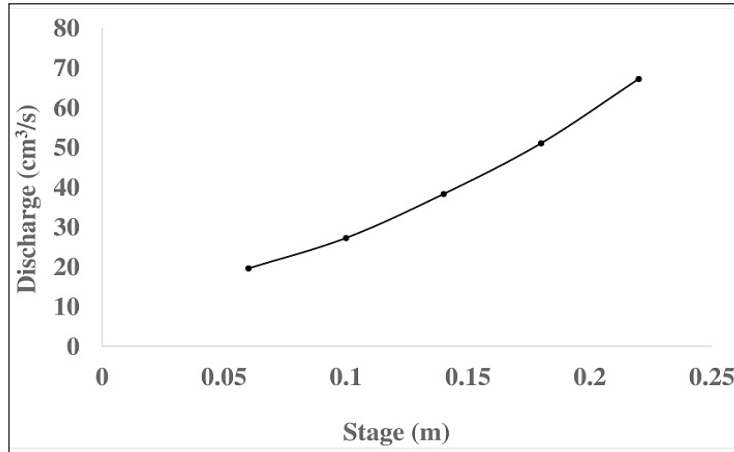


Figure 10. Plot of stage vs discharge

Table 2

Variation of stream wise velocity V_u , vertical velocity V_v , lateral velocity V_w

Height	Stream wise velocity		Vertical velocity	Lateral velocity
	Numerical	Experimental	Numerical	Numerical
0.01	0.000915	0.00086	-0.00021	-0.50673
0.03625	0.001122	0.001043	-0.0003	-0.5469
0.0625	0.001305	0.001226	-0.00036	-0.60262
0.115	0.001405	0.001321	-0.0004	-0.63509
0.14125	0.00148	0.001391	0.000105	-0.67234
0.1675	0.001553	0.001459	0.00016	-0.72495
0.19375	0.001494	0.001394	0.000252	-0.72651
0.22	0.001391	0.001294	0.00028	-0.72718

Table 3

Variation of resultant velocity (V_r)

Height	Numerical	Height	Numerical
0.005	0.1	0.05	0.585
0.015	0.2	0.0625	0.602618
0.022	0.281	0.08875	0.624936
0.027	0.37	0.115	0.666846
0.03	0.41	0.14125	0.711448
0.033	0.46	0.1675	0.730029
0.035	0.523	0.19375	0.712568
0.039	0.558	0.22	0.696472
0.044	0.57		

Graphs were plotted using the data extracted from ANSYS by placing plates at different intervals for purpose of velocity profile analysis. The numerical data obtained were compared to experimental data. Figure 11 shows the comparison of stream-wise velocity profile between experimental and numerical results. From the present study, it can be seen that magnitude of velocity is maximum at some point below free surface as in case of narrow channels which is true for both the experimental and numerical simulation. Variations of vertical velocity profile obtained from the numerical simulation are shown in Figure 12. It is seen that magnitude of velocity gives negative values to nearly mid height with respect to depth of flow and then changes to positive values of velocity (Song and Cox, 1993; Pittaluga & Imran, 2014). Figure 13 represents the variation of velocity in lateral direction. The flow characteristics give all negative magnitude of velocity.

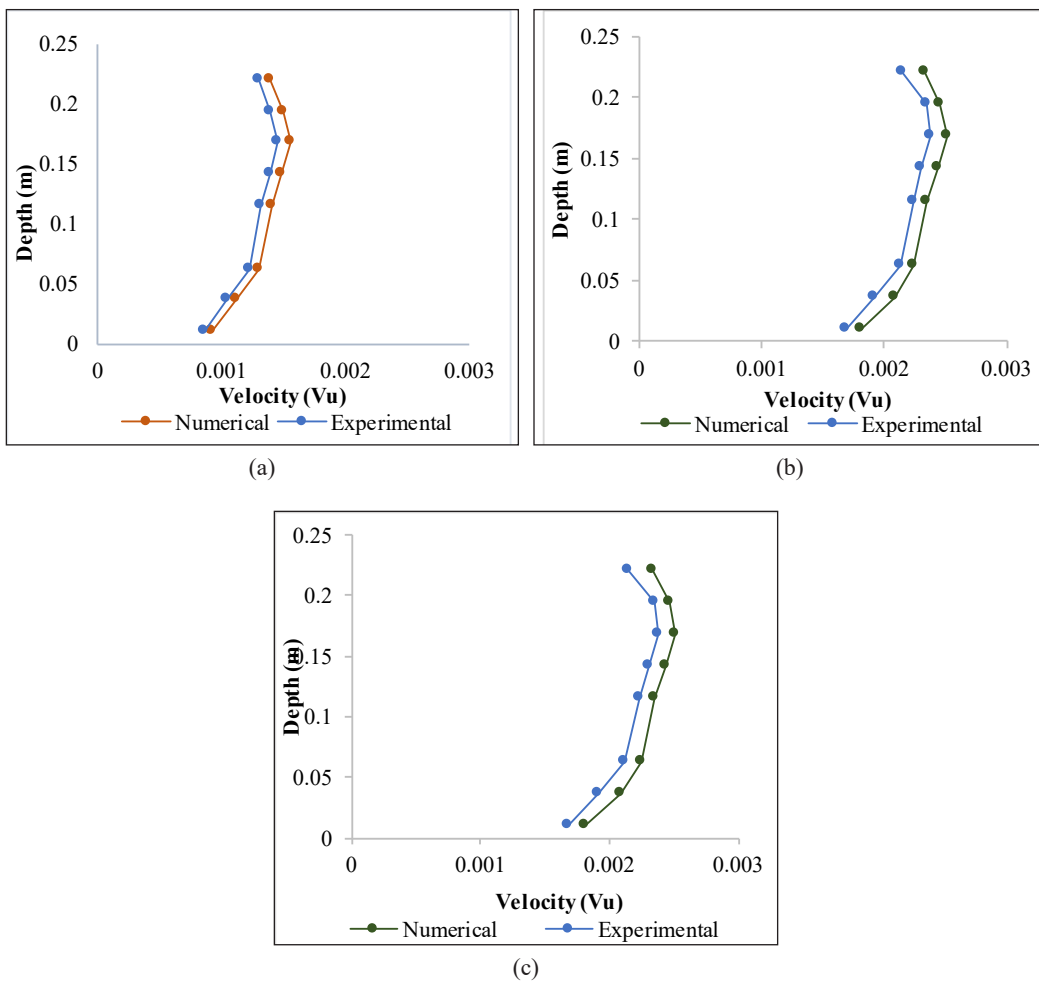
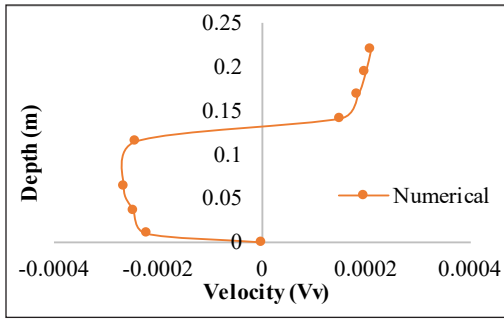
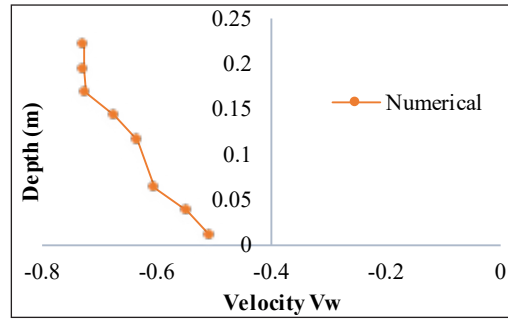


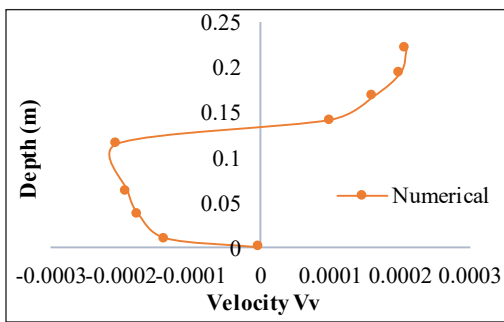
Figure 11. Variation of stream wise velocity comparison for numerical and experimental result at (a) 0.25 m, (b) 1.5m, (c) 2.25m from head gate



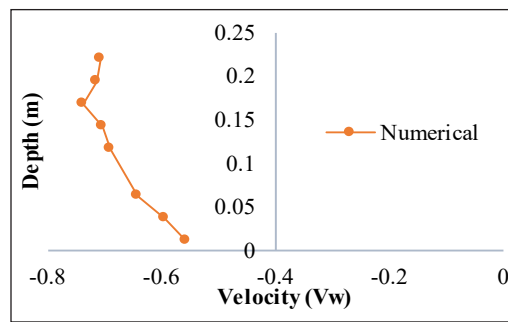
(a)



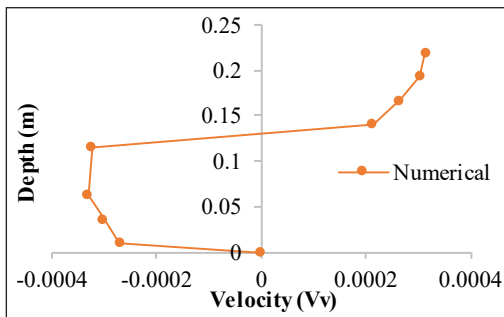
(a)



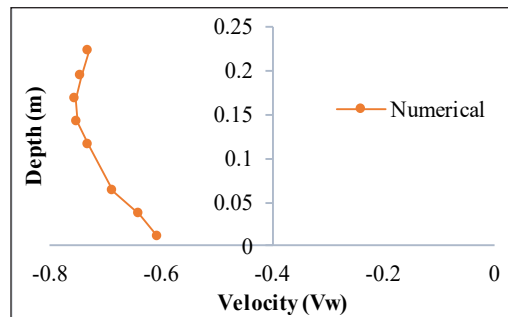
(b)



(b)



(c)



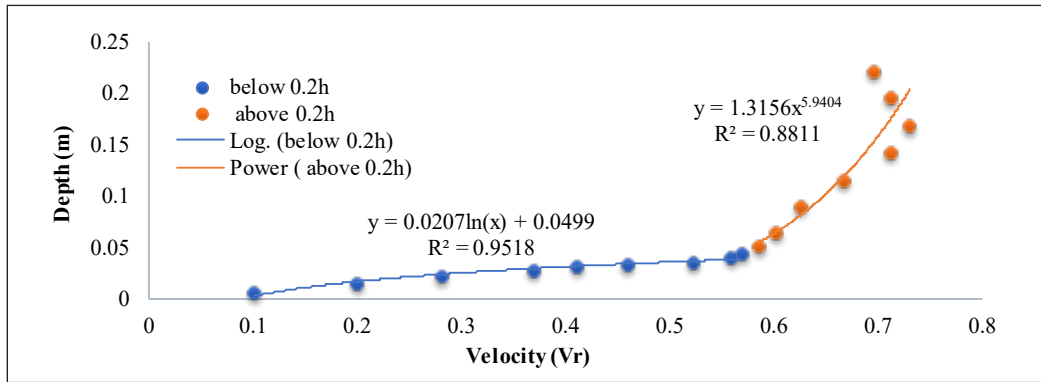
(c)

Figure 12. Variation of vertical velocity for numerical result at (a) 0.25 m, (b) 1.5m, (c) 2.25m from head gate

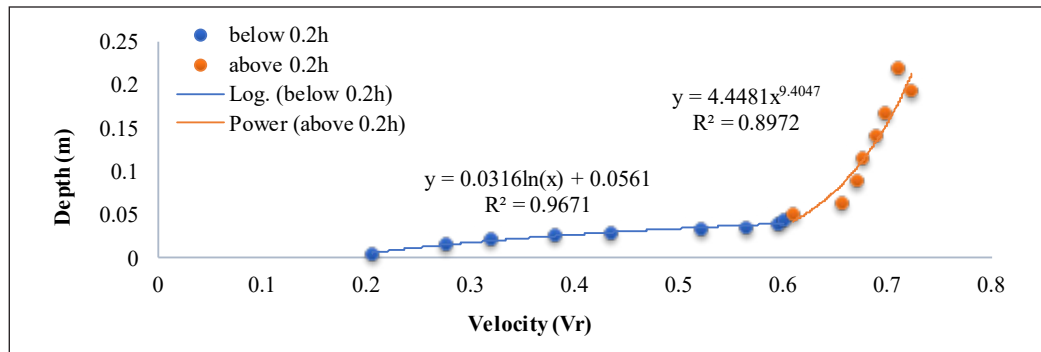
Figure 13. Variation of Lateral velocity for numerical result at (a) 0.25 m, (b) 1.5m, (c) 2.25m from head gate

The variation of resultant velocity profile found out by numerical simulation concerning universal laws (Log and Power Law) is shown in Figure 14. It is observed that the characteristics of flow profile below $0.2h$ (h -depth of flow) obeys Log law and above $0.2h$ follows the Power law (Sarma et al., 1983; Castro-orgaz & Dey, 2011). The R^2 values from the resulting trend line show that the magnitude of velocity obtained best fit to the universal laws. The equation of the two lines is given by 'y' which can be clearly indicated

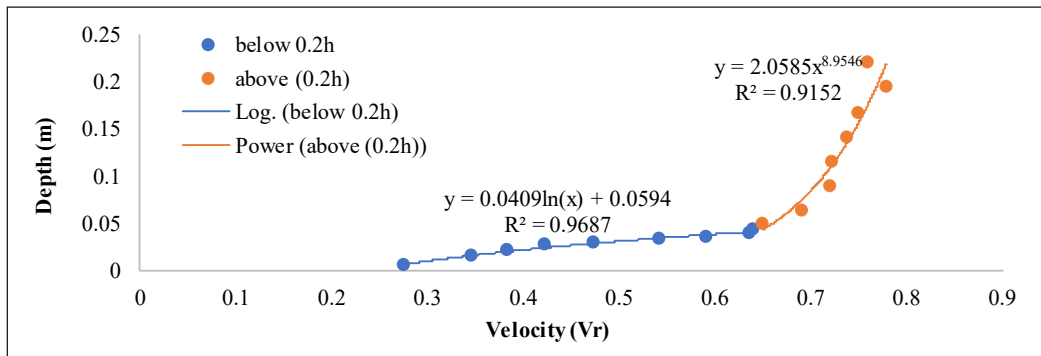
as the inner region follows a logarithmic path and the outer region follows an exponential path. Figure 15 represents the comparison of stream-wise velocity between experimental and numerical results at 0.03, 0.09 and 0.15m from side wall across the flow cross-section.



(a)

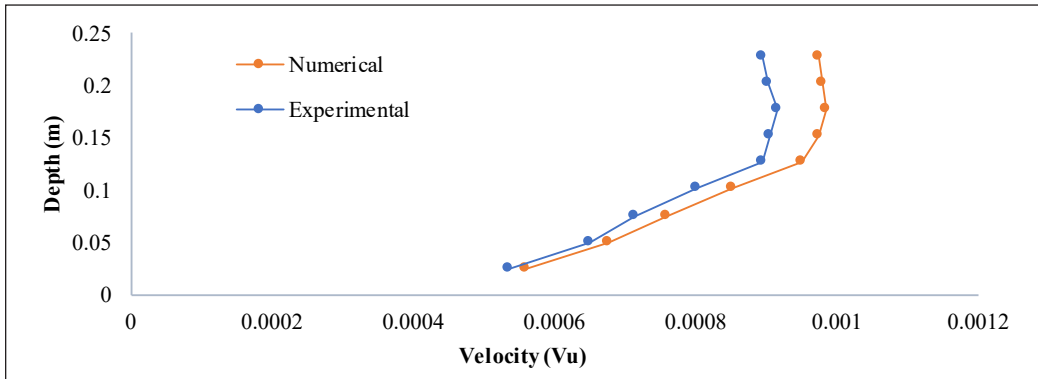


(b)

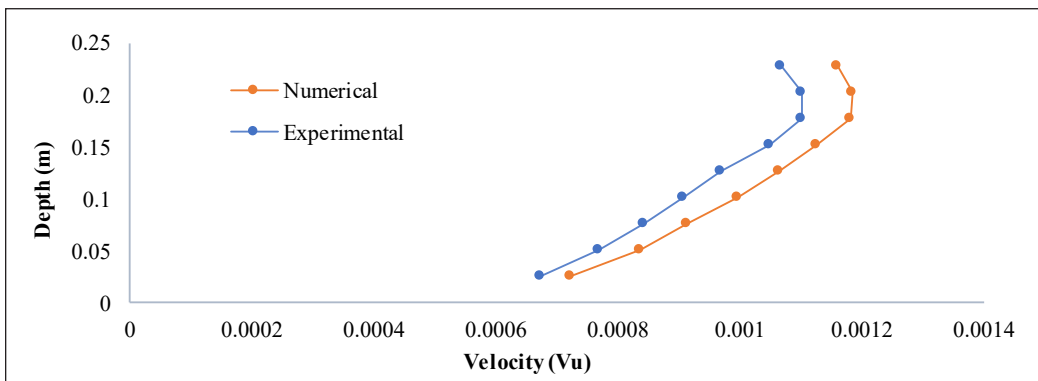


(c)

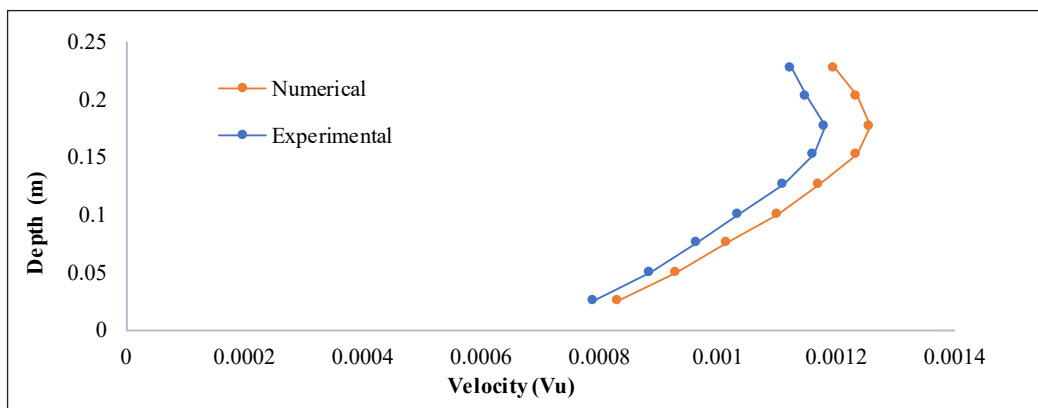
Figure 14. Resultant velocity concerning to Log Law and Power Law at (a) 0.25m, (b) 1.25m, (c) 2.25m from head gate



(a)



(b)



(c)

Figure 15. Stream wise velocity comparison for numerical and experimental result at (a) 0.03m, (b) 0.09m, (c) 0.15m from side wall

Analysis

The velocity profile can be broken into two regions such as the inner region, below $0.2h$ and the outer region, above $0.2h$ (where h =depth of flow). Velocity profile can be demonstrated by the law of logarithmic distribution and with the help of a power law distribution up to the point of maximum velocity. As per universal velocity profile laws, the region below $0.2h$ always follows logarithmic law and the region above $0.2h$ follows power law. The experimental data and the numerical data extracted show that the velocity profile drawn here fits well with the universal velocity profile laws.

CONCLUSION

In present scenario, the experimental and numerical investigation for prediction of velocity for *flow* over plain bed is shown. In the *primary* stage of the present study, a 3D turbulence model for flow over plain bed was simulated utilising $k-\epsilon$ closure model. With the help experimental and numerical results, deviation in values for velocity of *flow* was presented using contour mapping. The main distinguishing point between the velocity distribution in laminar and turbulent flow conditions is that in case of flow to be laminar, the peak velocity occurs at top surface of water while for most turbulent flow situations, the peak velocity is found to be at some point below the water surface which is in case of an open channel cross-section.

- It is examined that the peak velocity is not found at the water surface; rather it occurs at some point below the top surface of water because of effect of turbulence in the rectangular flume used for experiment during the fluid flow (Cardoso et al., 1989).
- The velocity dip is visible from the experimental results but in ANSYS inadequacy of numerical modelling is observed which is often reasonable as the source of computation are not worth to produce such *better* results.
- Additionally, at point when there is effect of sidewall, a lateral velocity component (w) is harmonized close from sidewall of the channel to centre of channel and a down *flow* (v) occurs from top water surface. The components of secondary *flow* give the magnitude of maximum velocity below the top water surface. This is observed for high depth of *flow*.
- Inner region of the flow depth is considered from bed of the channel to 0.2 of the height of flow which follows the Logarithmic law, whereas from above 0.2 of the flow height up to the top water surface is the outer region which follows the power law.
- From the Figure 9 it can be found out that the numerical results are showing error within 10% with respect to the experimental results. The best results are obtained

for highest flow depth. For lowest flow depth, maximum deviation is observed because of effect of boundary layer on the flow parameters.

- As it is observed from Figure 13, variation of velocity in vertical and lateral direction, the numerical results could only be found out using ANSYS, because of the use of Pitot tube which is usually a 1-D instrument and only measures the stream-wise velocity.

ACKNOWLEDGEMENT

We thank the anonymous reviewers and editors for their useful suggestion to develop this manuscript.

REFERENCE

- Absi, R. (2011). An ordinary differential equation for velocity distribution and dip-phenomenon in open channel flows. *Journal of Hydraulic Research*, 49(1), 82-89.
- Afzal, N., Seena, A., & Bushra, A. (2007). Power law velocity profile in fully developed turbulent pipe and channel flows. *Journal of Hydraulic Engineering*, 133(9), 1080-1086.
- Bonakdari, H., Baghalian, S., Nazari, F., & Fazli, M. (2014). Numerical analysis and prediction of the velocity field in curved open channel using artificial neural network and genetic algorithm. *Journal of Engineering Applications of Computational Fluid Mechanics*, 5(3), 384-396.
- Cardoso, A. H., Graf, W. H., & Gust, G. (1989). Uniform flow in a smooth open channel. *Journal of Hydraulic Research*, 27(5), 603-616.
- Castro-Orgaz, O., & Dey, S. (2011). Power-law velocity profile in turbulent boundary layers: An integral Reynolds-number dependent solution. *Acta Geophysica*, 59(5), 993-1012.
- Coles, D. (1956). The law of the wake in the turbulent boundary layer. *Journal of Fluid Mechanics*, 1(2), 191-226.
- Guo, J., & Julien, P. Y. (2006, May 21-25). Application of modified log-wake law in open-channels. In *World Environmental and Water Resource Congress 2006: Examining the Confluence of Environmental and Water Concerns* (pp. 1-9). Omaha, Nebraska, United States.
- Issa, R. I. (1986). Solution of the implicitly discretised fluid flow equations by operator-splitting. *Journal of Computational Physics*, 62(1), 40-65.
- Kang, H., & Choi, S. U. (2006). Reynolds stress modelling of rectangular open-channel flow. *International Journal for Numerical Methods in Fluids*, 51(11), 1319-1334.
- Larocque, L. A., Imran, J., & Chaudhry, M. H., (2013). 3D numerical simulation of partial breach dam break flow using the LES and k- ϵ turbulence models. *Journal of Hydraulic Research*, 51(2), 145-157.
- Naik, B., Khatua, K. K., Wright, N., Sleigh, A., & Singh, P. (2018). Numerical modeling of converging compound channel flow. *ISH Journal of Hydraulic Engineering*, 24(3), 285-297.
- Naot, D., Nezu, I., & Nakagawa, H. (1993). Hydrodynamic Behaviour of Compound Rectangular Open

- Channels. *ASCE Journal of Hydraulic Engineering*, 119(3), 390-408.
- Nezu, I., & Rodi, W. (1986). Open-channel flow measurements with a laser Doppler anemometer. *Journal of Hydraulic Engineering*, 112(5), 335-355.
- Pittaluga, M. B., & Imran, J. (2014). A simple model for vertical profiles of velocity and suspended sediment concentration in straight and curved submarine channels. *Journal of Geophysical Research: Earth Surface*, 119(3), 483-503.
- Sarma, K. V. N., Lakshminarayana, P., & Rao, N. S. L. (1983). Velocity distribution in smooth rectangular open channels. *Journal of Hydraulics Engineering*, 109(2), 270-289.
- Sarma, N. V. K., Prasad, R. V. B., & Sarma, K. A. (2000). Detailed study of binary law for open channel. *Journal of Hydraulics Engineering*, 126(3), 210-214.
- Song, R., & Cox, S. K. (1993, June 14-17). Vertical velocity in cirrus case obtained from wind profiler. In *Proceedings of a Conference on the FIRE Cirrus Science* (pp. 153-156). Breckenridge, Colorado, United States.
- Welahettige, P., Lie, B., & Vaagsaether, K. (2017). Flow regime changes at hydraulic jumps in an open Venturi channel for Newtonian fluid. *The Journal of Computational Multiphase Flows*, 9(4), 169-179.
- Wilkerson, V. G., & McGahan, J. L. (2005). Depth averaged velocity distribution in straight trapezoidal channel. *Journal of Hydraulics Engineering*, 131(6), 509-512.

Physical Characteristics of Structured Lipid Synthesized by Lipase Catalyzed Interesterification of Coconut and Palm Oils

Siti Nurhasanah^{1,2}, S Joni Munarso³, Nur Wulandari^{2,4} and Purwiyatno Hariyadi^{2,4*}

¹Department of Food and Industrial Technology, Faculty of Agro-Industrial Technology, Universitas Padjadjaran, Bandung 45363, Indonesia

²Department of Food Science and Technology, Faculty of Agricultural Engineering & Technology, IPB University, Bogor 16680, Indonesia

³Center for Agricultural Postharvest Research and Development, Ministry of Agriculture, Bogor 16124, Indonesia

⁴Southeast Asian Food and Agricultural Science and Technology (SEAFAST) Center, IPB University, Bogor 16680, Indonesia

ABSTRACT

The physical characteristics of lipids are important determining factors for appropriate food applications. The objective of this research is to study the physical characteristics, especially thermal (melting and crystallization) behavior, smoke point and solid fat content (SFC), of structured lipids (SLs) produced by interesterification of coconut and palm oils catalyzed by two commercial lipases (*Thermomyces lanuginosa* imobil/TLIM and Novozyme 435). The results showed that SLs produced by 5 hours of interesterification had physical characteristics differing from the original blended lipids. SLs obtained by

both enzyme systems exhibited a higher and wider range of melting temperature (higher enthalpy value, ΔH), lower and wider range of crystallization temperature (higher ΔH), lower smoke point, and lower SFC at 0°C and 10°C than those of their blended lipid counterpart. Furthermore, TLIM lipase produced SLs with a higher and wider range of melting temperature, lower and wider range of crystallization temperature, lower smoke point and SFC at 0°C and 10°C compared to those produced by Novozyme

ARTICLE INFO

Article history:

Received: 27 April 2019

Accepted: 27 November 2019

Published: 13 January 2020

E-mail addresses:

siti.nurhasanah@unpad.ac.id (Siti Nurhasanah)

jomunarso@gmail.com (S Joni Munarso)

wulandari_n@apps.ipb.ac.id (Nur Wulandari)

phariyadi@apps.ipb.ac.id (Purwiyatno Hariyadi)

*Corresponding author

435. The SLs produced have the potential to be used as an ingredient in refrigerated foodstuffs and more plastic than the original oil.

Keywords: Coconut oil, crystallization, enzymatic interesterification, palm oil, physical properties

INTRODUCTION

Coconut and palm are two important oil plants found in the tropical region. Both plants have become the source of leading vegetable oils for food and nonfood applications due to their unique qualities and properties. Coconut oil is rich in medium chain fatty acids and is suitable as a raw material for food, medical, or other functional products (McCarty & DiNicolantonio, 2016). Palm oil, especially from its olein fraction, has a high content of unsaturated fatty acids, such as oleic and linoleic acid, the specific functional properties of which are to increase high density lipoprotein (Mba et al., 2015). The use of these vegetable oils is increasing along with the development of the food processing industry. Furthermore, lipids application in food processing technology is also developing very rapidly. However, direct application of native lipids are not always suitable due to their limited properties. Therefore, there is a need to modify native lipids by synthesizing structured lipids (SLs) with specific properties (Rohm, 2018).

The enzymatic interesterification technique can be used to modify physicochemical properties of lipid substrates to produce a new type of lipid suitable for special food product applications. Enzymatic interesterification results in redistribution of fatty acids within the glycerol backbone, at which the position of fatty acids are interchanged (Norizzah et al., 2015; Smith, 2015). Consequently, interesterification of lipids may produce SLs having physical properties different from those of the original lipids due to rearrangement and/or redistribution of their fatty acids on the glycerol backbone (Farmani, 2015). However, this rearrangement does not change the degree of unsaturation or isomer configuration of the fatty acids (Pande & Akoh, 2013; Mba et al., 2015). SLs with different characteristics are expected to increase the added value of native lipids.

The use of lipase allows the reaction to have a specific affinity to produce a specific structured triacylglycerol (TAG). This allows the control of thermal properties and other physical characteristics of the SLs products. Many researchers have attempted to synthesize SLs by using lipases (Bornscheuer, 2014; Smith, 2015; Wirkowska-Wojdyła et al., 2016). The obtained SLs exhibit different physical properties compared to those of the original native lipids. Such physical properties include thermal properties (i.e., melting and crystallization behavior), smoke point, and solid fat content (SFC) (Danthine et al., 2014; Li et al., 2010; Sharma & Lokesh, 2012). Those physical properties are very unique and have a profound effect on certain plasticity behaviors of lipids, which are important for food product applications.

Thermal characteristics, an important aspect of oil and fat physical properties, can cause changes in the solid-liquid and liquid-solid phases, such as melting and crystallization behaviors. The thermal properties are determined based on the enthalpy profile during the crystallization and melting processes, and these properties can be analyzed by DSC (Saber et al., 2011; Menczel & Prime, 2014; Srivastava et al., 2017; Oliveira et al., 2017). Changing of crystallization conditions will affect the crystal type, crystal size, and crystal amount, which will influence the product's character (i.e. texture, consistency) (Zhang et al., 2013; Tan & Man, 2002; Azis et al., 2011). Meanwhile, smoke point is a vital analytical measurement for any lipid used for high temperature applications, such as the frying process in which a higher smoke point is desirable. Therefore, smoke point is an important consideration when selecting oil for this application. Another important physical property of oil is the SFC profile, which provides a complete melting profile of the lipid at various temperatures (Gunstone, 2011). The SFC profile provides information not only on the functional properties of lipids but also on controlling the crystal structure and polymorphism of a certain product, such as plasticity in bakery products (Xu et al., 2017; Mayamol et al., 2009). The SFC of lipids indicates product characteristics such as general appearance, simplicity of packing, organoleptic properties, and convenience of spreading. SFC can also be used to study fat compatibility by determining its changes in the percentage of solid phase against different fat proportions (Karabulut et al., 2004; Cheong et al., 2009). Time domain nuclear magnetic resonance (TD-NMR) is a tool used to determine SFC for the production and processing of fats and oils. Hindered diffusion is characterized by motion of molecules within the droplets phase of the emulsions (Cobo et al., 2017).

Through the interesterification process in a mixture of coconut oil and palm oil, it is expected that SLs can be produced with superior specific characteristics, both chemical and physical. In this study, the physical characteristics of SLs from a mixture of coconut oil and palm oil were examined. SLs were catalyzed by two commercial immobilized lipases with different specificity. *Thermomyces lanuginosa* imobil /TLIM is an sn-1 and sn-3 specific lipase and Novozyme 435 which is a nonspecific lipase. The physical characteristics were then analyzed, specifically thermal (melting and crystallization) behavior, smoke point and SFC.

MATERIALS AND METHODS

The main materials were coconut oil obtained from PT. Barco, olein fraction of palm oil with 60 iodine value obtained from PT. Salim Ivomas Pratama Tbk, immobilized lipases *Thermomyces lanuginosa* imobil (TLIM) and Novozyme 435 (Novozyme A/S, Bagsvaerd, Denmark), 4A molecular sieves, and chemical materials obtained for analysis purposes. The equipment used were an orbital shaker, differential scanning calorimetry (DSC-60

Shimadzu), and TD-NMR machine, Bruker. The research was conducted in Southeast Asian Food and Agricultural Science and Technology (SEAFAST) Center, Bogor Agricultural University, Indonesia; and Indonesian Oil Palm Research Institute (IOPRI) Medan, IPB, Sumatera, Indonesia.

Synthesis of SLs from Coconut and Palm Oils

SLs were synthesized using the enzymatic esterification method referred to by Yang et al. (2014) by mixing 10 g of coconut and 10 g of palm oils into a 50 mL Erlenmeyer flask in a free solvent system. The mixture was then combined with 6% (w/w) enzymes (TLIM lipase or Novozyme 435 lipase) and left to react for 5 hours using a rotary shaker (200 rpm, 55°C). At the end of the reaction time, the immobilized enzyme was removed from the mixture by vacuum filtration using Whatman® Grade 4.

Blending of Coconut and Palm Oils

Blending the coconut and palm oils was conducted by mixing coconut and palm oils in a ratio of 1:1 (w/w) to a total of 500 ml of oil, which was then homogenized using a magnetic stirrer for 15 minutes. The blended oil (without interesterification) was used as a reference to determine the effectiveness of interesterification, catalyzed by two types of lipases, in synthesizing SLs by comparing their respective physicochemical characteristics.

Analysis of Thermal Behavior

The thermal behavior of the oils was determined by using DSC as described by Saberi et al. (2011). As much as 10 mg of sample was added to an aluminum DSC sample pan. The exothermic curve was obtained by maintaining the sample at 80°C for 10 minutes, and continued with cooling until the temperature reached -50°C at a cooling rate of 5°C/minute. To obtain an endothermic curve, the sample was maintained at -50°C for 10 minutes, then gradually heated to 80°C at a rate of 5°C/minute. The crystallization process is indicated by peaks at the beginning of the cooling process stage, whereas the melting process is indicated by peaks produced at the end of the heating process stage.

Analysis of Smoke Point

The smoke point was determined by heating the oil sample using a Cleveland open-cup apparatus. The temperature at which smoke began to appear was taken as the smoke point (AOCS, 2011).

Analysis of Solid Fat Content (SFC)

The SFC was determined using NMR by the standard method of AOCS (Official method Cd 16b-93, AOCS, 1989). The melted oil sample was inserted into 12 tubes for SFC analysis

with a sample height of 4 ± 1 cm. Samples in sealed tubes were heated inside a water bath at 100°C for 15 minutes, then later moved to a 60°C water bath for 5 minutes. Six pairs of sample tubes were immersed in a water bath at 0, 10, 20, 30, 40, or 50°C for 30 minutes. The SFC of each sample at each temperature was measured by inserting the holder to the TD-NMR unit by using the Non Stab AOAC method.

RESULTS AND DISCUSSIONS

Lipase-catalyzed interesterification of coconut and palm oils produced SLs as a result of acyl exchange among the TAGs, with observed changes in physical characteristics, such as thermal (melting and crystallization) behavior, smoke point, and SFC.

Thermal Properties

The thermal properties were determined based on thermograms obtained by DSC analysis. Except DSC, other methods that can be used for thermal analysis are thermal gravimetric analysis and differential thermal analysis. DSC is a thermal analysis technique that has been applied in the characterization of thermal behaviors in lipids, especially melting and crystallization curves, and determining the melting temperature, crystallization temperature, and enthalpy value (ΔH). Furthermore, DSC also gives rapid, reproducible results without sample preparation and does not use dangerous solvents (Menczel & Prime, 2014; Chiavaro et al., 2008; Wetten et al., 2015). DSC can be used to determine cooling transition temperatures as well as monitor the extent of crystallization and various thermal parameters of the chemical reaction simultaneously (Tan & Man 2002; Musa & Wong 2013; Menczel & Prime, 2014; Lai et al., 2000; Indartono et al., 2011; Siregar et al., 2011). Figure 1 shows the thermograms of the blended oil and SLs produced from interesterification, whereas temperature and ΔH values are shown in Table 1.

Table 1

Thermal characteristics of blended oil and SLs from coconut and palm oils

Thermal characteristics		Temperature ($^{\circ}\text{C}$)			ΔH (J/g)
		onset	peak	offset	
Melting	B	11.28	16.17	20.55	-36.29
	N5	10.57	16.56	21.86	-66.43
	T5	10.54	17.50	28.30	-68.39
Crystallization	B	-7.83	-10.59	-13.87	4.71
	N5	-3.65	-9.00	-12.83	8.04
	T5	-4.88	-15.35	-27.85	8.32

Note: B = Blended oil, N5 = SL obtained using Novozym 435 for 5 hours, T5 = SL obtained using TLIM for 5 hours

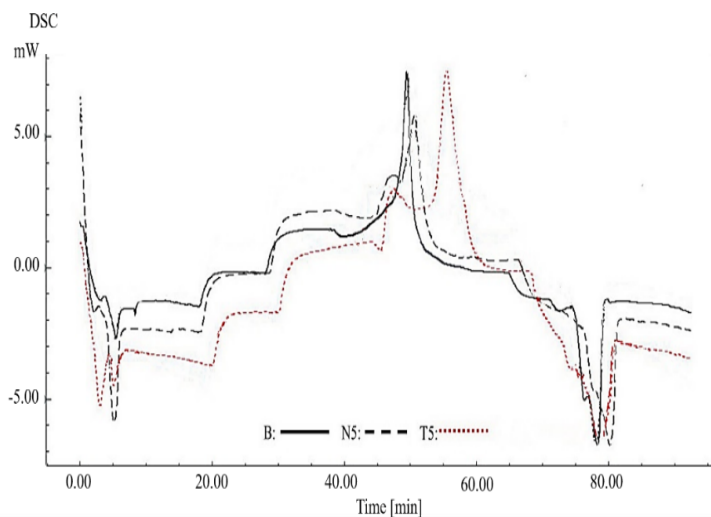


Figure 1. Thermograms of blended oil and SLs from coconut and palm oils

The obtained data was in the form of continuous thermogram representing melting and crystallization phenomena. According to research from Becker et al. (2015) the use of DSC can determine thermal behavior such as melting and recrystallization point, polymorphism, melting/recrystallizing fractions. The thermograms of the melting process of all samples show a negative curve, indicating that the process is endothermic (Chong et al., 2007). The thermograms of the crystallization process have a simpler shape than those of the melting process, attributed to the chemical composition of the oil, not by the crystallization status (Tan & Man, 2000). The crystallization process is marked by the beginning of fat crystal formation, related to the rearrangement of the molecule due to the presence of highly saturated TAG. The ending of crystallization is usually reflected by an aggregation and compaction of the molecule.

Melting point affects the plasticity and simplicity of the melting of fats at human body temperature. The TAG of oil that will first experience transformation into a solid during the cooling process is the one with the longest chain fatty acid (Timms, 2005). Several researchers have attempted to improve the melting properties of fats by the formation of SLs so that the melting profile is more suitable for a specific product application (Fauzi et al., 2013; Zhu et al., 2012).

Table 1 and Figure 1 show that SLs obtained using interesterification catalyzed by both enzymes exhibit a higher and wider range of melting temperature than that of blended oils. This result is in agreement with Oliveira et al. (2017), in which the chemical interesterification of palm stearin and patawa oil produced a lipid with an increased melting point. The melting point of fats is highly dependent on the properties of the materials,

especially the types of fatty acids comprising the fat (i.e., chain length and double bonds) (Marikkar et al., 2013; Knothe & Dunn, 2009). The difference in melting points results from the difference in the number of hydrogen bonds in the carboxyl group and the hydrophobic interactions along the hydrocarbon chain of each product.

SLs obtained by TLIM lipase-catalyzed interesterification have a higher melting peak and a longer melting process than those catalyzed by Novozyme 435 lipase. The increase in melting point is caused by the formation of high melting point TAGs and the occurrence of TAG hydrolysis during enzymatic interesterification. The formation of a new TAG species consisting of high melting fatty acids influences the melting point of the TAG itself, thus a high melting point TAG is produced. The TAG also changes to monoacylglycerol and diacylglycerol (Mardani et al., 2015).

Another important thermal property analyzed for SLs is the crystallization profile. The rates of crystal growth and nucleation determine parameters that are directly related to the consistency and characteristics of textures, such as crystal distribution, shape, and size (Saberli et al., 2011; Ribeiro, 2015). A crystallization profile starts with the formation of the fat crystal, which occurs upon the rearrangement of the molecule due to the presence of high saturated TAG and ends with aggregation and compaction of the fat molecule (Tan & Man, 2002). The crystallization peak was calculated based on the DSC crystallization curve. The results in Table 1 indicate that, in general, interesterification of coconut and palm oils produced SLs with a lower and wider range of crystallization temperature than that of their blended oils. SLs obtained by TLIM lipase interesterification had a lower and wider range of crystallization temperature compared to those catalyzed by Novozyme 435. The greater the range of onset and offset temperatures, the wider the range of crystallization temperature. Crystallization temperature may affect the kinetic and physical properties of the crystallization system significantly. Crystallization at lower temperatures is the driving force for the nucleation process and supports the formation of less stable polymorphs (Tran & Rousseau, 2016). Polymorphism characteristics of the end texture for food as complex systems can be determined by thermal treatment. Such characteristics consist of spreadability, microstructure, mouthfeel, and rheology (Rønholt et al., 2012; Rønholt et al., 2014).

The enthalpy value (ΔH) of melting can also be determined from the DSC thermogram, as presented in Table 1. ΔH of melting indicates the amount of energy absorbed by the sample when melting occurs, whereas ΔH of crystallization is the amount of energy released by the sample when crystallization occurs (Tan & Man, 2002). The controlled heating rate of the number of active nuclei and the time for growth affect the rate of crystallization. The crystallization enthalpy is a relative measure of the number of nuclei before the heating scan. Interactions between component TAGs and molecular structures is observable by kinetic crystallization. Increasing crystallization temperature causes the ΔH value to

decrease significantly (Tran & Rousseau 2016). SLs obtained using both enzymes show higher enthalpy values for both melting and crystallization processes, than those of their native blended lipids.

Smoke Point

During lipid heating in a smoke point analysis, the temperature is monitored and the smoke point is determined as the temperature of the lipid where a steady evolution of smoke emerges from the lipid in the cup (Eyres, 2015; Gunstone, 2011). This point indicates that the oil begins to break down to glycerol and free fatty acids, marking the beginning of both flavor and nutritional degradation. The smoke points of the SLs produced in this study are presented in Figure 2.

SLs produced by both enzymes had lower smoke points compared to their native blended lipids. The lower smoke point of the SLs obtained by lipase-catalyzed interesterification might be attributed to the exchange of fatty acid in the oil, which had a higher vapor pressure than TAG in blended oil (Willis & Marangoni, 2002).

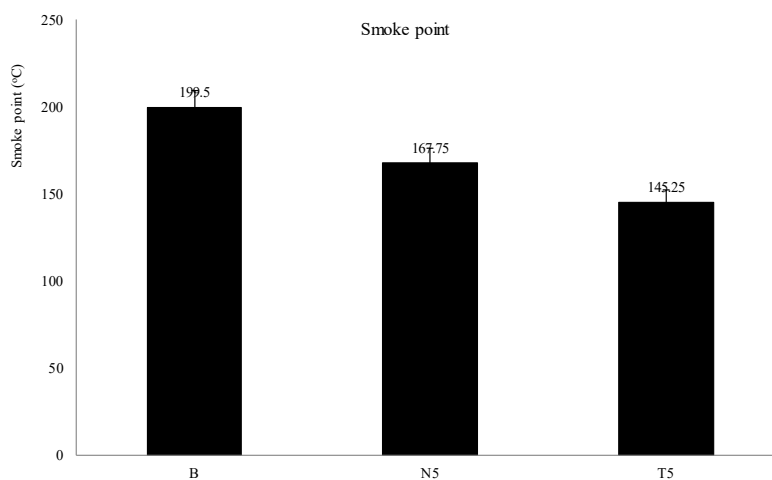


Figure 2. Smoke point of blended oil and SLs from coconut and palm oils

Note: B = Blended oil, N5 = SL obtained using Novozyme 435 for 5 hours, T5 = SL obtained using TLIM for 5 hours

Solid Fat Content (SFC)

Lipid consistency can be determined by SFC, which indicates the amount of solid TAG in the lipid at a certain temperature. The SFC profile of blended coconut and palm oils and the obtained SLs can be seen in Figure 3.

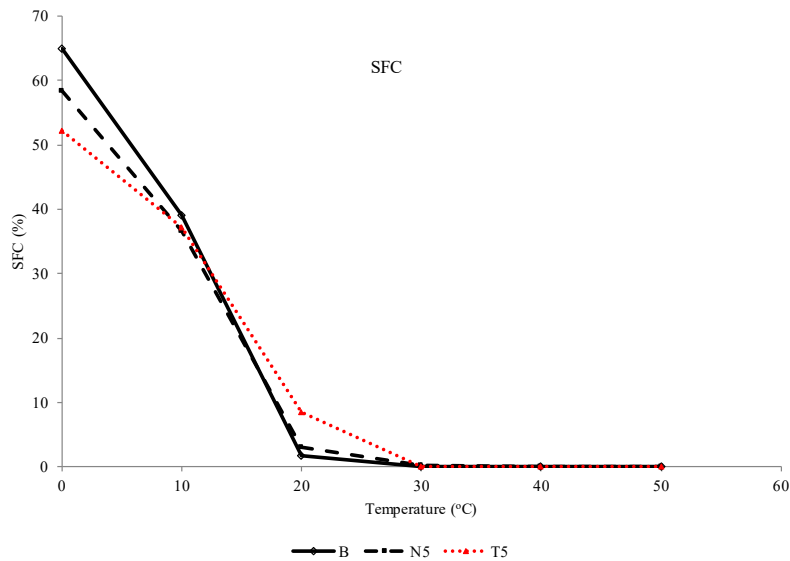


Figure 3. SFC of blended oil and SLs from coconut and palm oils

Note: B = Blended oil, N5 = SL obtained using Novozyme 435 for 5 hours, T5 = SL obtained using TLIM for 5 h

Figure 3 shows that the higher temperature produced lower SFC, because fat crystals would melt when the temperature rose to the fat melting point (Xu et al., 2017; Mayamol, et al. 2009). The SLs obtained by both enzymes had a lower SFC than the blended oil at 0°C and 10°C. The SLs catalyzed by TLIM lipase had a lower SFC at 0°C and 10°C, resulting in a more sloping curve compared to those catalyzed by Novozyme 435. SFC affects the hardness, melting rate, and flavor release in the mouth. A high SFC tends to give a waxy mouth feeling when the product is consumed. To ensure good melting properties and product temperature stability need a steep SFC profile is desired (Rousseau & Marangoni, 2002). Sloping SFC profiles (low SFC values at low temperatures) indicated more plastic lipids, suitable for spread product. The SFC test results are in line with the melting point test results using DSC. From the thermal and SFC characters, make lipids have plastic properties.

Based on the study of their physical properties, the SLs produced herein have higher melting temperature, lower crystallization temperature, lower smoke point, and lower SFC at 0°C and 10°C. Thus, it can be concluded that the structured lipids produced herein have the potential to be used as ingredients in refrigerated foodstuffs.

CONCLUSIONS

SLs obtained from interesterification of coconut and palm oils catalyzed by two lipases

exhibit different physical characteristics compared to their native oils. The SLs produced have a higher melting temperature and wider range of melting temperature, lower crystallization temperature and wider range of crystallization temperature, and higher enthalpy values for both melting and crystallization. The SLs also showed a decrease in smoke point and a lower SFC in the lower temperature region compared to their blended lipid counterpart. Based on the physical properties identified, the SLs produced have the potential to be used as an ingredient in refrigerated foodstuffs and more plastic than the original oil.

ACKNOWLEDGMENT

This study was sponsored by the Indonesian Agency for Agricultural Research and Development (IAARD) through KP4S program.

REFERENCES

- AOCS. (1989). *Official methods and recommended practices of the American oil chemists' society* (4th Ed.). Champaign, Illinois: American Oil Chemists' Society.
- AOCS. (2011). *Official methods and recommended practices of the American oil chemists' society* (6th Ed.). Champaign, Illinois: American Oil Chemists' Society.
- Azis, A. A., Mohamud, Y., Roselina, K., Boo, H. C., Nyuk, L. C., & Che Man, Y. B. (2011). Rheological, chemical and DSC thermal characteristics of different types of palm oil/palm stearin-based shortenings. *International Food Research Journal*, 18(1), 189-199.
- Becker, K., Salar-Behzadi, S., & Zimmer, A. (2015). Solvent-free melting techniques for the preparation of lipid-based solid oral formulations. *Pharmaceutical Research*, 32(5), 1519-1545.
- Bornscheuer, U. T. (2014). Enzymes in lipid modification: Past achievements and current trends. *European Journal of Lipid Science and Technology*, 116(10), 1322-1331.
- Cheong, L. Z., Tan, C. P., Long, K., Yusoff, M. S. A., & Lai, O. M. (2009). Physicochemical, textural and viscoelastic properties of palm diacylglycerol bakery margarine during storage. *Journal of the American Oil Chemists' Society*, 86(8), 723-731.
- Chiavaro, E., Rodriguez-Estrada, M. T., Barnaba, C., Vittadini, E., Cerretani, L., & Bendini, A. (2008). Differential scanning calorimetry: A potential tool for discrimination of olive oil commercial categories. *Analytica Chimica Acta*, 625(2), 215-226.
- Chong, C. L., Kamarudin, Z., Lesieur, P., Marangoni, A., Bourgaux, C., & Ollivon, M. (2007). Thermal and structural behaviour of crude palm oil: Crystallization at very slow cooling rate. *European Journal of Lipid Science and Technology*, 109(4), 410-421.
- Cobo, M. F., Deublein, E. J., Haber, A., Kwamen, R., Nimbalkar, M., & Decker, F. (2017). TD-NMR in quality control: Standard applications. In G. A. Webb (Ed.), *Modern magnetic resonance* (pp. 1-18). London, UK: Springer International Publishing.

- Danthine, S., De Clercq, N., Dewettinck, K., & Gibon, V. (2014). Monitoring batch lipase catalyzed interesterification of palm oil and fractions by differential scanning calorimetry. *Journal of Thermal Analysis and Calorimetry*, 115(3), 2219-2229.
- Eyres, L. (2015). Frying oils: Selection, smoke points and potential deleterious effects for health. *Food New Zealand*, 15(1), 30-31.
- Farmani, J. (2015). Modeling of solid fat content of chemically interesterified fully hydrogenated soybean oil and canola oil blends as a function of temperature and saturated fatty acids. *Journal of Food Measurement and Characterization*, 9(3), 281-289.
- Fauzi, S. H. M., Rashid, N. A., & Omar, Z. (2013). Effects of chemical interesterification on the physicochemical, microstructural and thermal properties of palm stearin, palm kernel oil and soybean oil blends. *Food Chemistry*, 137(1-4), 8-17.
- Gunstone, F. (Ed.). (2011). *Vegetable oils in food technology: composition, properties and uses*. Boca Raton, Florida: John Wiley & Sons.
- Indartono, Y. S., Suwono, A., Pasek, A. D., Mujahidin, D., & Rizal, I. (2011). Thermal characteristics evaluation of vegetables oil to be used as phase change material in air conditioning system. *Jurnal Teknik Mesin*, 12(2), 1019-1024.
- Karabulut, I., Turan, S., & Ergin, G. (2004). Effects of chemical interesterification on solid fat content and slip melting point of fat/oil blends. *European Food Research and Technology*, 218(3), 224-229.
- Knothe, G., & Dunn, R.O. (2009). A comprehensive evaluation of the melting points of fatty acids and esters determined by differential scanning calorimetry. *Journal of the American Oil Chemists' Society*, 86(9), 843-856.
- Lai, O. M., Ghazali, H. M., Cho, F., & Chong, C. L. (2000). Physical properties of lipase-catalyzed transesterified blends of palm stearin and anhydrous milk fat. *Food Chemistry*, 70(2), 215-219.
- Li, D., Adhikari, P., Shin, J. A., Lee, J. H., Kim, Y. J., Zhu, X. M., ... & Lee, K. T. (2010). Lipase-catalyzed interesterification of high oleic sunflower oil and fully hydrogenated soybean oil comparison of batch and continuous reactor for production of zero trans shortening fats. *LWT-Food Science and Technology*, 43(3), 458-464.
- Mardani, M., Farmani, J. A. M. S. H. I. D., & Esmailzadeh K. R. (2015). Efficacy of some commercial lipases in hydrolysis of palm olein for production of free fatty acids and diacylglycerol oil. *Journal of Oil Palm Research*, 27(3), 1-2.
- Marikkar, J. M. N., Saraf, D., & Dzulkifly, M. H. (2013). Effect of fractional crystallization on composition and thermal behavior of coconut oil. *International Journal of Food Properties*, 16(6), 1284-1292.
- Mayamol, P. N., Balachandran, C., Samuel, T., Sundaresan, A., & Arumugan, C. (2009). Zero trans shortening using rice bran oil, palm oil and palm stearin through interesterification at pilot scale. *International Journal of Food Science and Technology*, 44(1), 18-28.
- Mba, O. I., Dumont, M. J., & Ngadi, M. (2015). Palm oil: Processing, characterization and utilization in the food industry—A review. *Food Bioscience*, 10, 26-41.

- McCarty, M. F., & DiNicolantonio, J. J. (2016). Lauric acid-rich medium-chain triglycerides can substitute for other oils in cooking applications and may have limited pathogenicity. *Open Heart*, 3(2), 1-5.
- Menczel, J. D., & Prime, R. B. (Eds.). (2014). *Thermal analysis of polymers: Fundamentals and applications*. Boca Raton, Florida: John Wiley & Sons.
- Musa, N., & Wong, T. W. (2013). Fast-scan vs conventional differential scanning calorimetry (DSC) techniques in detection of crystallization events of tolbutamide–polyethylene glycol composite. *Journal of Thermal Analysis and Calorimetry*, 111(3), 2195-2202.
- Norizzah, A. R., Norsyamimi, M., Zaliha, O., Nurazimah, K., & Hazirah, S. M. F. (2015). Physicochemical properties of palm oil and palm kernel oil blend fractions after interesterification. *International Food Research Journal*, 22(4), 1390-1395.
- Oliveira, P. D., Rodrigues, A. M., Bezerra, C. V., & Silva, L. H. (2017). Chemical interesterification of blends with palm stearin and patawa oil. *Food Chemistry*, 215, 369-376.
- Pande, G., & Akoh, C. C. (2013). Enzymatic synthesis of trans-free structured margarine fat analogs with high stearate soybean oil and palm stearin and their characterization. *LWT-Food Science and Technology*, 50(1), 232-239.
- Ribeiro, A. P., Masuchi, M. H., Miyasaki, E. K., Domingues, M. A., Stroppa, V. L., de Oliveira, G. M., & Kieckbusch, T. G. (2015). Crystallization modifiers in lipid systems. *Food Science and Technology*, 52(7), 25-46.
- Rohm, H., Schäper, C., & Zahn, S. (2018). Interesterified fats in chocolate and bakery products: A concise review. *LWT-Food Science and Technology*, 87, 379-384.
- Rønholt, S., Kirkensgaard, J. J. K., Mortensen, K., & Knudsen, J. C. (2014). Effect of cream cooling rate and water content on butter microstructure during four weeks of storage. *Food Hydrocolloids*, 34, 169-176.
- Rønholt, S., Kirkensgaard, J. J. K., Pedersen, T. B., Mortensen, K., & Knudsen, J. C. (2012). Polymorphism, microstructure and rheology of butter: Effects of cream heat treatment. *Food Chemistry*, 135(3), 1730-1739.
- Rousseau, D., & Marangoni, A. G. (2002). The effects of interesterification on the physical properties of fats. In A. G. Marangoni & S. S. Narine (Eds.), *Physical properties of lipids* (pp. 479-527). New York, NY: Marcel Dekker, Inc.
- Saberi, A. H., Lai, O. M., & Toro-Vázquez, J. F. (2011). Crystallization kinetics of palm oil in blends with palm-based diacylglycerol. *Food Research International*, 44(1), 425-435.
- Sharma, M., & Lokesh, B. R. (2012). Effect of enzymatic trans-and interesterification on the thermal properties of groundnut and linseed oils and their blends. *Journal of the American Oil Chemists' Society*, 89(5), 805-813.
- Siregar, J. P., Salit, M. S., Rahman, M. Z. A., & Dahlan, K. Z. H. M. (2011). Thermogravimetric analysis (TGA) and differential scanning calorimetric (DSC) analysis of pineapple leaf fibre (PALF) reinforced high impact polystyrene (HIPS) composites. *Pertanika Journal of Science and Technology*, 19(1), 161-170.
- Smith, K. W. (2015). Structured triacylglycerols: Properties and processing for use in food. In G. Talbot (Ed.), *Specialty oils and fats in food and nutrition* (pp. 207-218). Cambridge, UK: Woodhead Publishing.

- Srivastava, Y., Semwal, A. D., Sajeevkumar, V. A., & Sharma, G. K. (2017). Melting, crystallization and storage stability of virgin coconut oil and its blends by differential scanning calorimetry (DSC) and Fourier transform infrared spectroscopy (FTIR). *Journal of Food Science and Technology*, *54*(1), 45-54.
- Tan, C. P., & Man, Y. B. C. (2002). Differential scanning calorimetric analysis of palm oil, palm oil based products and coconut oil: Effects of scanning rate variation. *Food Chemistry*, *76*, 89-102.
- Timms, R. E. (2005). Fractional crystallisation—the fat modification process for the 21st century. *European Journal of Lipid Science and Technology*, *107*(1), 48-57.
- Tran, T., & Rousseau, D. (2016). Influence of shear on fat crystallization. *Food Research International*, *81*, 157-162.
- Wetten, I. A., Herwaarden, A. W., Splinter, R., Boerrigter-Eenling, R., & Van Ruth, S. M. (2015). Detection of sunflower oil in extra virgin olive oil by fast differential scanning calorimetry. *Thermochimica Acta*, *603*, 237-243.
- Willis, W. M., & Marangoni, A. G. (2002). Enzymatic interesterification. In C. C. Akoh & D. B. Min (Ed.), *Food lipid: Chemistry, nutrition and biotechnology* (pp. 856-893). Boca Raton, Florida: CRC Press.
- Wirkowska-Wojdyła, M., Bryś, J., Górka, A., & Ostrowska-Ligeża, E. (2016). Effect of enzymatic interesterification on physiochemical and thermal properties of fat used in cookies. *LWT-Food Science and Technology*, *74*, 99-105.
- Xu, Y., Zhu, X., Ma, X., Xiong, H., Zeng, Z., Peng, H., & Hu J. (2017). Enzymatic production of trans-free shortening from coix seed oil, fully hydrogenated palm oil and *Cinnamomum camphora* seed oil. *Food Bioscience*, *22*, 1-8.
- Yang, H., Mu, Y., Chen, H., Su, C., Yang, T., & Xiu, Z. (2014). Sn-1, 3-specific interesterification of soybean oil with medium-chain triacylglycerol catalyzed by Lipozyme TL IM. *Chinese Journal of Chemical Engineering*, *22*(9), 1016-1020.
- Zhang, X., Li, L., Xie, H., Liang, Z., Su, J., Liu, G., & Li, B. (2013). Comparative analysis of thermal behavior, isothermal crystallization kinetics and polymorphism of palm oil fractions. *Molecules*, *18*(1), 1036-1052.
- Zhu, X., Hua, J., Xue, C., Lee, J., Schim, J., Hong, S., ... & Lee, K. (2012). Physiochemical and oxidative stability of interesterified structured lipid for soft margarine fat containing ω 5-UPIFAs. *Food Chemistry*, *131*, 533-540.



Effect of DL-Methionine Concentration, Moisture Content and Bulk Density of Animal Feed on the Light-Induced Fluorescence as a Process Analytical Tool

Mohammad Poozesh¹, Hamidreza Ghasemzadeh^{1*}, Shamsollah Ablollahpour¹ and Mitra Amoli Diva²

¹Department of Biosystems Engineering, University of Tabriz, Tabriz, Iran

²Department of Physics, Sharif University of Technology, Tehran, Iran

ABSTRACT

Mix uniformity is a critical quality control point in food manufacturing. Process analytical technology (PAT) provides new technological opportunities for fulfilling and perhaps replacing conventional sampling methods by proposing spectroscopic analyzers for measuring blend homogeneity. Many spectroscopic analyzers have been used in powder blending processes. Light-induced fluorescence (LIF) is the most rapid and consistent underutilized PAT. An experiment was conducted to evaluate the effects of DL-methionine concentration, moisture content (MC) and bulk density (BD) on LIF responses. Fluorescent responses to powder mixtures comprising 0.05–0.50% w/w fluorescent active pharmaceutical ingredient (API) were reported. Approximate density ranges of 6.5–20% w/w for MCs and 0.55–0.65 g/ml for animal food were also evaluated. Results indicated that DL-methionine concentration and MC were statistically significant factors affecting the LIF response, but the effect of BD was not statistically significant. DL-methionine

concentration from 0.05% to 0.50% caused a linear increase of LIF signals with $y = 41.04x + 715.8$, $R^2 = 0.990$ fitted to the data. Increasing MC from 6.5% to 20% w/w caused decreasing LIF although $y = -45.50x + 1037$ could not explain LIF variation versus MC because of low coefficient of determination ($R^2 = 0.851$).

ARTICLE INFO

Article history:

Received: 17 May 2019

Accepted: 13 September 2019

Published: 13 January 2020

E-mail addresses:

mpoozesh@gmail.com (Mohammad Poozesh)

ghasemzadeh@tabrizu.ac.ir (Hamidreza Ghasemzadeh)

shamstabriz@tabrizu.ac.ir (Shamsollah Ablollahpour)

mitraamoli@yahoo.com (Mitra Amoli Diva)

*Corresponding author

Keywords: ANVOA, LIF, moisture analyzer, PAT

INTRODUCTION

Today, process analytical technology (PAT) is increasingly being applied to better understand and control and monitor pharmaceutical units operation. Robust, reliable, accurate and fast, techniques that do not require sample preparation are essential for the in-line monitoring of blending. The Food and Drug Administration (FDA) has defined PAT as a system for controlling, analyzing and designing manufacturing by timely measuring the performance attributes and critical quality of in-process and raw materials and processes to ensure the quality of final product (U.S. Food and Drug Administration, 2014). Chanda et al. (2014) used an active pharmaceutical ingredients (API) process work-flow from the raw-material identification to the finished API to provide representative examples such as how and why the pharmaceutical industry used PAT tools in API development. Nutrient uniformity is crucial for proper nutrition when animals such as nursery pigs and baby chickens are on low daily intake of food (Ensminger et al., 1990; Clark et al., 2007). According to Beumer (1991), mix uniformity is a critical quality control point in food manufacturing. New technologies have the opportunity to fulfill and potentially replace conventional sampling methods by more consistent and rapid techniques of blend homogeneity measurement. Bakeev (2010) updated the application and implementation of spectroscopic process analyzers. Many spectroscopic analyzers have been utilized in powder blending process.

Near-infrared (NIR) spectroscopy has been widely accepted as a PAT tool for quantifying and identifying API and formulation excipients in the noninvasive monitoring of powder blends (Wargo and Drennen, 1996). NIR uses a complex reflectance spectrum specific to the analyzed substance and records the results of analyzing extensive data to reduce the spectra to a representative pattern for the mixture. This method can provide a foundation for the convergence and monitoring of the expected aggregate spectra and establish blend homogeneity. Given that the reflectance NIR is not usually a strong signal, except for water, the sensitivity of this method is limited for highly potent drug formulations in which drug contents are below 1% w/w in the mixture (Lai et al., 2001).

Raman spectroscopy has also been found to be a useful technique as a PAT tool in API and dosage form manufacturing and development, and for identifying pseudo-polymorphic, polymorphic and amorphous API forms (Jestel, 2010). Raman spectroscopy has also been applied to monitoring API crystallization, gel manufacturing processes, emulsion and wet granulation (Islam et al., 2004; Strachan et al., 2007).

Other PAT analyzers include process nuclear magnetic resonance spectroscopy (Edwards & Giammatteo, 2010), microwave resonance sensors (Corredor et al., 2011), acoustic emission (Tok et al., 2008), laser-induced breakdown spectroscopy (Madamba et al., 2007), acoustic resonance spectroscopy (Medendorp et al., 2006), far-infrared spectroscopy (Zeitler et al., 2007) and ultraviolet (UV) visible spectroscopy (Liau et al., 2010).

LIF is an underutilized PAT. In 2000, eight out of the top ten worldwide pharmaceutical products were reported to have fluorescent properties. Over sixty percent of the top 200 selling medicines were also found to have structural-associated fluorescent properties (Lai & Cooney, 2004). GlaxoSmithKline (GSK) found 50% out of more than 27 new medical compounds tested to have fluorescent properties (Ishan et al., 2015).

Numerous advantages of fluorescence over absorption spectroscopy include NIR and UV. The Stokes shift characterizes the fluorescence excitation and emission spectra and causes differences in the peak wavelength of emission and excitation. The fluorescent intensity equation used for low fluorophore concentrations offers another advantage:

$$I_f = P_0 \gamma \phi \epsilon b C = P_0 k C \quad (1)$$

in which k represents the proportionality constant, C the fluorophore concentration, b the optical path length, ϕ the molar absorption at the fluorophore excitation wavelength, ϕ the fluorophore quantum efficiency, the P_0 fluorescent collection efficiency, P_0 the incident irradiance or power per unit area and I_f the fluorescent intensity (Dickens, 2010; Brittain, 2006; Harris, 2010). According to Equation 1, a limited increase in the incident excitation irradiance proportionally increases the fluorescence intensity, which provides an advantage for LIF process analysis and higher detection flexibility. In absorption spectroscopy techniques, including UV and NIR, increasing the incident irradiance does not affect absorbance given that absorbance is a function of the $(P_0)/(I)$ ratio, in which I denotes the intensity of light emerging from the sample and absorbance equals $\log (P_0)/(I)$. Fluorescence is influenced by the matrix and environmental conditions, including temperature, pH, moisture, the presence of metal ions and viscosity. pH can influence the charge and resonance of fluorophore and change the fluorescence intensity. An increase in temperature increases the kinetic energy of molecules and the potential for collision deactivation through intermolecular energy transfer and thereby usually decreases the fluorescence intensity.

PAT studies have rarely been conducted on LIF so far, and the few key ones are presented as follows: LIF responses were used for the real-time monitoring of mini-scale dry powder blending. Lai et al. (2001) reported that an increase in powder bulk densities proportionally increased LIF signals at a single bulk powder concentration and an approximate density range of 0.45–0.80 g/cm³. Lai and Cooney (2004) developed a portable system using LIF as an analytical tool for on-line monitoring of various manufacturing process applications. Their LIF system was verified in several laboratory scale process applications specifically in noninvasive real-time observations of blend kinetics in tumbler blenders. They showed the actual blend characteristic behavior of powder mixtures such as homogeneity end point and blend stability and consistent blend homogeneity end point. A correlation between LIF signal and drug powder concentration was established with limits of detection below 0.02% w/w for the API, Triamterene. Dickens et al. (2011) described a

compact and portable LED array-based fluorescence sensor for rapid real-time monitoring. For the sensor configured for reflectance detection, the response sensitivity ranged from 100 to 60,000 and an estimated tryptophan detection limit was ~0.001% (w/w) in lactose. They discussed excitation parameter effects on the emission signal behavior, fundamental response functions, and standard analytical merits (sensitivity and detection limits) to highlight and benchmark the unique capabilities of their new sensor technology.

Brittain (2006) and Harris (2010) provided a nonlinear series expansion that described the measured fluorescent intensity as a function fluorophore concentration:

$$I_f = kP_o[C - C^2 / 2 + C^3 / 3! - \dots C^n / n!] \quad (2)$$

where I_f is the measured fluorescent intensity, k is the proportionality constant, P_o is the incident irradiance, and C is the concentration of the fluorophore. At low fluorophore concentrations, the higher-order terms can be dropped leaving the linear form of the equation (Eq. 1).

Karumanchi et al. (2011) reported curvilinear relationships between increasing fluorescent powder concentrations and LIF signals.

The present study was conducted to evaluate the impact of API concentration, moisture content (MC) and bulk density (BD) of animal food powder on LIF responses. Obtaining knowledge about these effects is crucial for the development of LIF as a PAT.

MATERIALS AND METHODS

Materials

The chicken feed powder was prepared in Kian chicken farm of Qom province in Iran with mean particle size of 700 μm . The inactive powder made from meal-based corn-soybean diet was first formulated for layer chickens (Corn 54.57%, Soybean Meal 27.73%, Calcium Carbonate 9.95%, Bran 2.61%, Wheat Flour 3.43%, Soybean Oil 1.40% and Salt 0.31%). Then, inactive diet was mixed using a vertical mixer (a 5-ton capacity) for the optimum blending time (20min). The inactive sample had no API so that no confounding effects on fluorescent signals. The feed grade MetAINO[®] (DL-methionine 99%; a necessary amino-acid in chicken diet manufactured by Evonik Antwerpen N.V. of Belgium having mean particle size 600 μm and Density 0.7 g/mL) was the API used in all the experiments.

LIF Sensor

According to Figure 1, LIF sensors use an LED light as the excitation source of light. LED beams were directed into a fiber-optic cable linked to a photo-sensor module including the detector photomultiplier tube and the lens. A dichroic mirror in the photo-sensor module reflected laser beams at ninety degrees to the sample. This lowered the scattered light reaching the detector and enhanced the signal to noise ratio. The fluorescent signal emitted

from the sample was collimated with the lens and passed through the dichroic mirror and an emission filter to the detector. The signals were converted to voltage and then recorded by a multi-meter interfaced through a hyper-terminal and RS-232 to a computer.

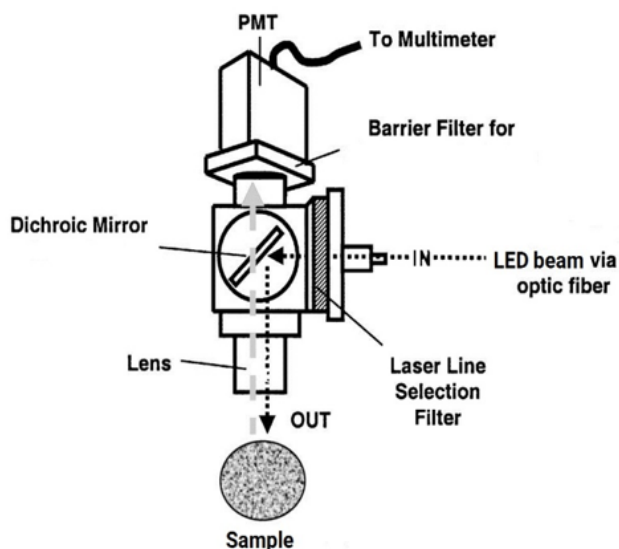


Figure 1. LIF Sensor; LED beam via optic fiber is directed to dichroic mirror. It enhances the beam and then reflects it 90° to the sample. Fluorescent API within sample is excited and emits fluorescent signal. Then, emitted light-induced fluorescence is collimated, filtered and converted to voltage and finally recorded to a computer.

Source: Lai et al. (2001)

An Avalight-LED[®] compact (Avantes Co., Netherlands) purchased for fluorescence applications produces pulsed or continuous spectral outputs at different wavelengths and with a spectral range of 530/590/780 (nm, an FWHM of 30 nm and an optical power of 25 μ W associated with a 600- μ m-fiber in the light source. Illumination in the probe was twelve 200- μ m UV/VIS fibers, wavelength range was 200-800 (nm) UV/VIS and detection was through a 600- μ m fiber. The AvaSpec-ULS3648 high-resolution spectrometer wavelength range was 200-1000 nm, its resolution 0.05-20nm, stray light 0.04-0.1%, signal to noise ratio 350:1 and sensitivity 160000 counts/ μ W per ms of integration time.

Calibration of the LIF Sensor

AvaSpec spectrometer has a standard wavelength calibration as well as coefficients for calculating wavelength based on the pixel number. These data were installed on the AvaSpec's EEPROM. Given the absence of moving elements inside the spectrometers, it did not require wavelength recalibration under normal conditions. Spectrometers could be recalibrated by the use of the auto-calibration software routine in AvaSoft-Full when a wavelength shift was measured in terms of the original wavelength calibration.

Preparing the Concentrations of Test Blends

The inactive blends of powder were prepared using the procedure discussed in materials. These blends were independently used in the experiments. The mass of 0.05–0.50% w/w API samples were obtained in two steps. First, inert powder diet was used to dilute a 10.00 % w/w fluorescent API achieving various equivalent concentrations of API. The inactive powder with a known weight was charged into a commercial mini-blender (Pars Khazar Co., Iran), and a pre-weighted amount (10.00% w/w) of diluted DL-methionine was layered on the top of the inactive powder to provide a total weight of 10 g of the mixture (Table 1). In order to provide a uniform material blending action for all the samples (0.05%, 0.10%, 0.15%, 0.20%, 0.25%, 0.30%, 0.40%, and 0.50% w/w), the mini-blender was rotated at 1000 rpm for five seconds 3 times.

Preparing the Test Blends for the MC Experiments

Moisturizing of samples was carried out in spectroscopy laboratory at the same time with moisture analyzing and LIF spectroscopy. First, samples were left in oven for 4 hours at 108°C. Four 5g samples with 6.57, 10.37, 12.39 and 21.52 % w/w MC were prepared through handy weighting and titration in laboratory conditions (35°C, 33% RH). Then, 5g of each moist sample was placed in moisture analyzer (MX-50 model by A&D Co., JAPAN), and simultaneously, another 5g was placed under LIF Aventus probe. Samples cooling within desiccator (from 108°C to 35°C) and transferring into moisture analyzer and LIF setup was done quickly to minimize any change in their moisture content. Analyzer determined powder moisture content after about 5 minutes but LIF signals was obtained very fast (about 1 minute).

Table 1
API and inactive diet for 0.05–0.50% w/w concentrations

% API (%w/w)	inactive diet (mg)	10% API (mg)	API Concentration (w/w)
0.05	9950	50	0.0005
0.10	9900	100	0.001
0.15	9850	150	0.0015
0.20	9800	200	0.002
0.25	9750	250	0.0025
0.30	9700	300	0.003
0.40	9600	400	0.004
0.50	9500	500	0.005

API concentrations were composed in two steps. First, inactive powder was mixed with 10% of API. Then, various weighted amounts of two materials were mixed that sum of two columns (10% API + inactive diet) of all samples will be 10000 g.

Preparing the Test Blends for BD Studies

Uniformly mixing the test API throughout the batch was important for determining the effect of material density on LIF responses. In order to break up the agglomerates potentially formed during the storage while avoiding the change in the nature of the material, an amount of the powder adequate for completing the test was passed through a sieve with 1.0 mm apertures. Fifty (50) g of the test sample (m) weighing with a 0.01 g accuracy was gradually introduced into a 100-ml (readable to 1 ml) dry graduated cylinder without compacting. The powder was then leveled carefully while avoiding compacting, and the unsettled apparent volume (V_0) was measured as the nearest graduated unit. BD was calculated in g/ml using the formula m/V_0 . These measurements were performed 3 times for each sample.

LIF Tests

The sensor uses AVALIGHT-LED as the excitation light source (Figure 2). DL-methionine generated a specific emission peak at 492 nm when was excited at 405 nm. The fluorescent counts were tested in powder mixtures including 0.05%–0.50% w/w of API. A BD range of approximately 0.55–0.65 g/mL and an MC of approximately 6.5%–20% w/w were also evaluated.

RESULTS AND DISCUSSION

The Impact of API Concentrations on LIF Responses

LED light excitation with wavelength 405 nm created a fluorescent emission wavelength with a peak in 492 nm. The difference in the wavelength of the excitation and emission peak maxima (87nm) is named as *Stokes shift*. This shift allows for a low detection limit to increase sensitivity while decreasing the background noise.



Figure 2. The LIF Test; AVALIGHT-LED® compact produces pulsed or continuous spectral outputs, when a sample is excited at 405 nm, generating a specific emission peak at 492 nm.

Figure 3 shows the impact of API concentrations on LIF responses. LIF peak was in 492 nm for all concentrations with 10% w/w moisture content and 0.65 g/mL bulk density. The lowest line peak (blue) was created with least API (0.05 %w/w) and it increased in the more concentrations in the first and second replication (r_1 , r_2). The third test of LIF test (r_3) showed inconsistent peaks for 0.3 and 4.0 % w/w

of API. This seems to be an experimental error. Therefore, it is derived that increasing API concentration increased LIF counts.

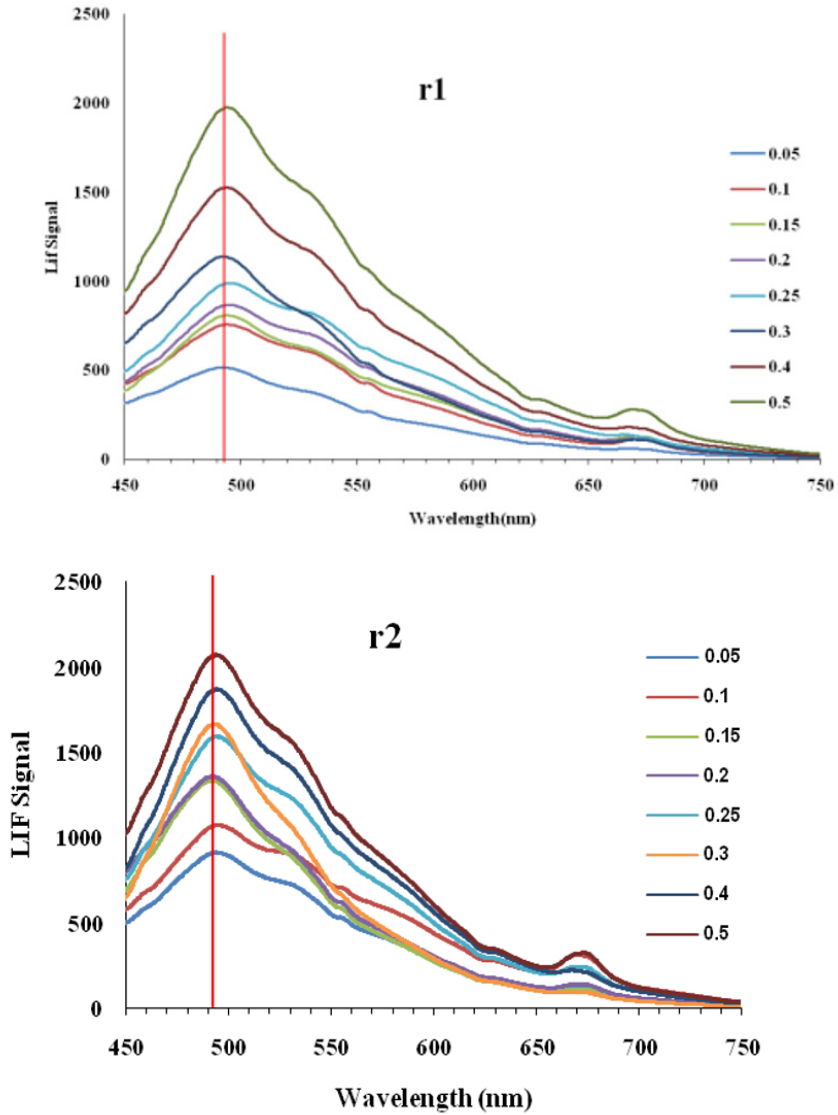


Figure 3. LIF peak was in 492 nm for all concentrations with 10% w/w moisture content and 0.65 g/mL bulk density in all three replications (r_1, r_2, r_3).

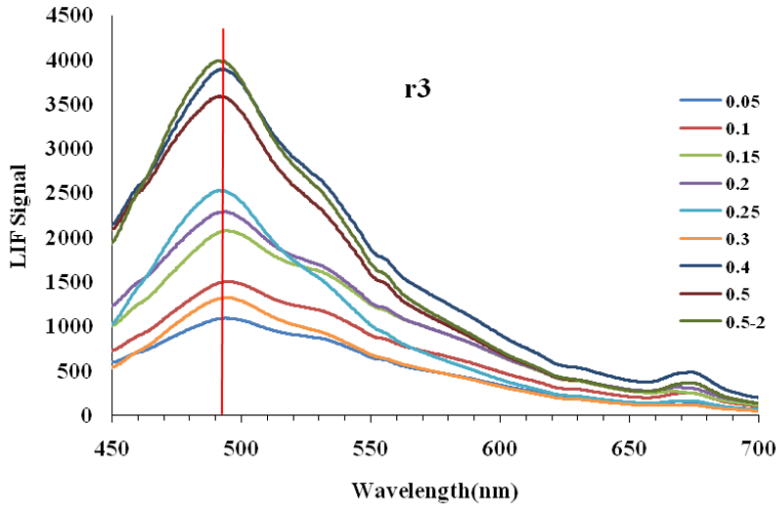


Figure 3. (Continued)

DL-methionine concentration from 0.05%–0.50% caused a linear increase of LIF signals (Figure 4). The model $y = 41.04x + 715.8$ was fitted to the data with $R^2 = 0.990$ where y was LIF counts and x was DL-methionine concentration weight to weight percentage. Methionine was the fluorophore (x) and it was straightly correlated with LIF counts (y). Whatever methionine concentration was increased consequently fluorescence intensity would be increased. Analysis of variance (ANOVA) was performed for LIF counts with eight API concentration and three replications plotted in Table 2.

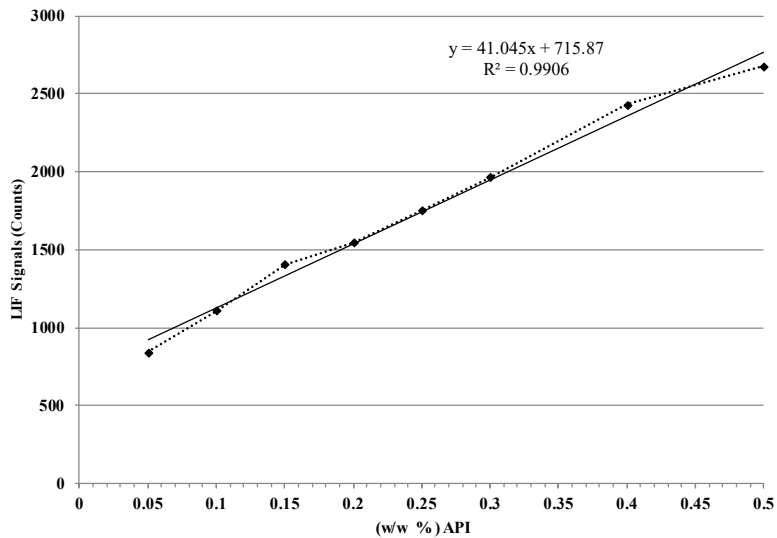


Figure 4. Linear variations in LIF with increasing API; increasing API caused a linear increase of fluorescence.

Table 2

ANOVA for LIF counts by API concentrations with replication

ANOVA	Some of Squares	D _f	Mean Squares	F _c	Significant
R	9089933	2	4544966	31.969	0.00**
LIF	8275918	7	1182274	8.316	0.00**
Error	1990374	14	142169		
Total	19356226	23			

** P<0.01 means the groups aren't statistically equivalent with a 99% confidence. In other words, at least difference of one pair of replications is significant. Also, the difference of fluorescence produced by API in various concentrations is significant.

Results show that at least one pair of group means was not statistically equivalent with 99% confidence. This was the same for between groups (Treatment) and within groups (Replication). Treatment group differences were supported by the Duncan's significant difference test (P<0.01). It compared all the mean pairs of the concentration groups. The Duncan test made up a more conservative alternative to ANOVA. All means were not statistically equivalent with 99% confidence as shown in Table 3. LIF signals in 0.15% and 0.20% w/w API were in one group. It means these were statistically equivalent.

Effect of BD on LIF Response

When corn-soybean meal-based diet was milled (in the range of 0.561- 0.649 g/mL), the volume of the materials was increased. Therefore, BD was decreased with having constant

Table 3

Duncan Compare means of LIF signals in API concentrations

SD	Mean	DL-methionine (w/w)
294	840 ^c	0.05%
374	1112 ^{de}	0.10%
636	1406 ^{cde}	0.15%
670	1546 ^{cde}	0.20%
712	1751 ^{bcd}	0.25%
1010	1964 ^{bc}	0.30%
1279	2430 ^{ab}	0.40%
1137	2679 ^a	0.50%

The group that has "a" index with 95% of confidence is different with other group (without "a" index). Therefore, mean LIF emitted by group 0.40% and 0.50% API have significant difference with group 0.25%, 0.20%, 0.15%, 0.10% and 0.05% API and so on and so forth.

mass. Decreasing density means API decreasing. Fluorescent experiments on bulk densities 0.561, 0.609 and 0.649 g/mL showed that LIF counts of 0.561 and 0.649 g/mL were more than 0.609 g/mL (Figure 5).

In all three replication LIF signals of powder with BD of 0.609 g/mL were least as shown in Figure 5. Therefore, in range of 0.561-0.649 g/mL BD had no increasing or decreasing trend. BD was analyzed through a three-replication randomized complete block design. Results showed that statistically there was no significant difference between BD groups. Whereas Lai et al. (2001) observed a proportional increase ($y = 9.29x + 16.86$, $R^2=0.975$) of LIF signal with increasing BD from 0.45-0.82 g/cc. However, Ishan et al. (2015) studying API in Lactose Monohydrate observed different results. Linear variation was observed in material densities of 0.6-1.4 g/cm³ at 0.25%, 0.50%, 1.00%, 2.00% and 2.50% w/w concentrations of API which contradicted the present findings shown in Figure 5.

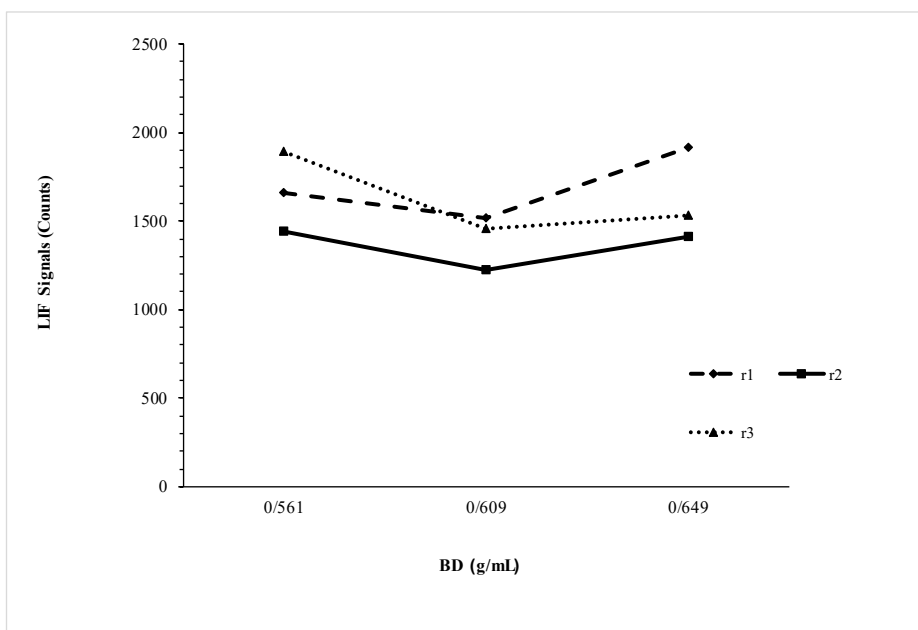


Figure 5. LIF signals in three bulk densities; the experiments was performed in three replications (r_1 , r_2 , r_3) that LIF falling of BD 0.609 g/mL was the same for all.

Effects of MCs on LIF Responses

Results showed that increasing MC caused decreasing of LIF signals. In all three replications MC from 6.57% w/w increasing to 20.83% w/w decreased LIF signals as shown in Figure 6. When moisture content was increased, really water content as a polar solvent was increased. Water using electrostatic interactions such as hydrogen bonding and influencing on electron shells was caused various deactivation phenomena such as

non-radiative deactivation. It caused reduction of fluorophore quantum efficiency (ϕ) mentioned in Equation 1.

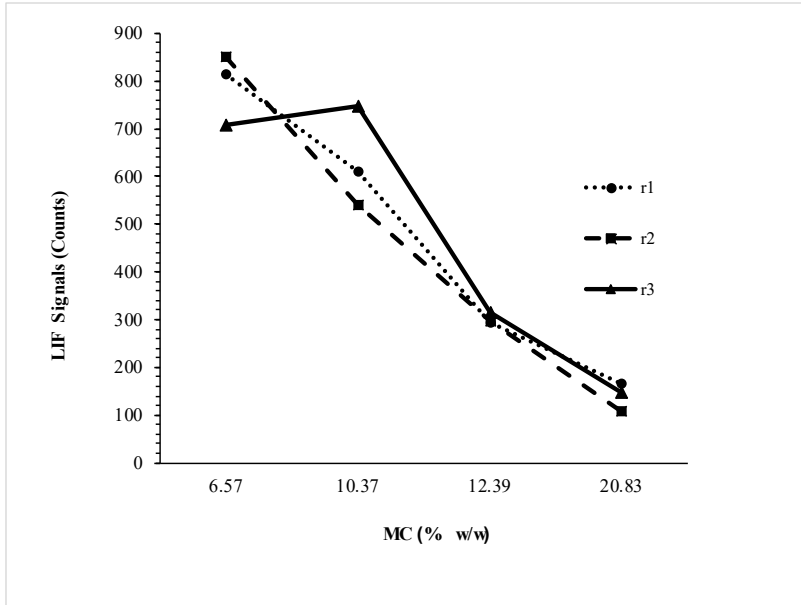


Figure 6. LIF signals in four MCs; in three replications (r_1, r_2, r_3) LIF decreases with MC increasing. The rising LIF of MC 10.37 in third replication (r_3) might be an outlier data.

There was an error signal in third replication that LIF in 10.37% w/w MC was more than 6.57% w/w. One-way ANOVA analyze was done for acceptance or rejection hypothesis of LIF signals equality on the various MCs (Table 4).

Table 4

ANOVA for LIF counts by MC

ANOVA	Some of Squares	D_f	Mean Squares	F_c	Significant
LIF	797414	3	265805	0.980	0.000**
Error	35452	8	4432		
Total	832866	11			

** If PValue<0.01 this means the groups are not statistically equivalent with 99% confidence

MC means were not statistically equivalent with 99% confidence as shown in Table 5.

The Duncan test supported results with significant difference ($p < 0.01$) comparing all group mean pairs. It was not any pair means statistically equivalent with 99% confidence

as shown in Table 5. Shah and Stagner (2015) used a Karl Fischer water titrator to make water measurements of granulations stored at 4.16, 4.51, 4.88, 5.89 and 6.53 % w/w MC. They found that increasing Lactose monohydrate MC caused a non-linear decrease in LIF responses. As shown in Figure 7, even though infrared moisture analyzer and handy titration used in this work but total trend of LIF signal variation with increasing MC was similar to their observation. Results of infrared moisture analyzer and handy titration used in this work were similar to Shah and Stagner (2015) who used a Karl Fischer water titrator to make water measurements. Total trend of LIF signal variation with increasing MC was the same.

Table 5

Duncan's multiple range test of LIF signals in MCs

SD	Mean	MC (w/w)
75	791 ^d	6.57%
105	633 ^c	10.37%
13	302 ^b	12.39%
30	142 ^a	20.83%

All groups with individual "a,b,c,d" indexes are different from the others.

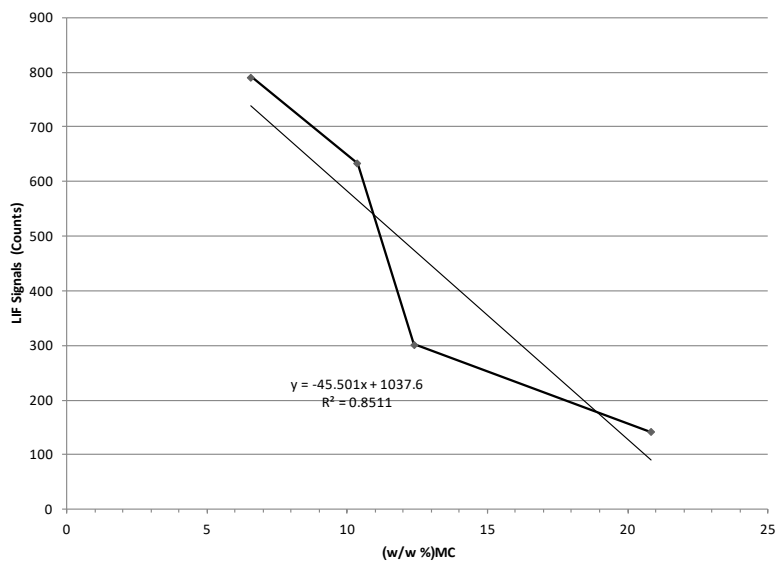


Figure 7. LIF variations with increasing MC; 85% of the moisture contents variations from 6.57% w/w increasing to 20.83% w/w can be explained by the linear model.

CONCLUSION

Nutrient uniformity is crucial for proper nutrition when animals are on low daily intake of food. An LED light excitation with wavelength 405 nm on corn-soybean meal-based diet created a fluorescent emission wavelength with a peak in 492 nm. LIF response increasingly affected by increasing API concentration from 0.05% to 0.50%. DL-methionine concentration caused a linear increase of LIF that fitted to $y = 41.04x + 715.8$ with $R^2 = 0.990$. This means that 99% of the experimental variation can be explained by the linear model and the relationship between LIF and API is statistically significant. Analyze of variance (ANOVA) showed that group means are not statistically equivalent with 99% confidence and also supported by the Duncan test. LIF counts of 0.561 and 0.649 g/mL were more than 0.609 g/mL BD. There was no increasing or decreasing trends in a range of 0.561-0.649 g/ml BD. ANOVA tests indicated that statistically there wasn't significant deference between BD groups. MCs in all three replications from 6.57% w/w increasing to 20.83% w/w decreased LIF Signals. One-way ANOVA analyze was done for acceptance or rejection hypothesis of LIF signals equality on the various MCs. The equality hypothesis (H_0) was rejected and MC means were not statistically equivalent with 99% confidence.

ACKNOWLEDGEMENT

We would like to thank Avantes for excellent LIF instrument and Evonik Antwerpen N.V. for fluorescent API. The authors also thank Mr. Shabani and Mr. Masoudi for their helpful suggestions.

REFERENCES

- Bakeev, K. A. (2010). *Process analytical technology* (2nd Ed.). Chichester, UK: John Wiley & Sons.
- Beumer, I. H. (1991). Quality assurance as a tool to reduce losses in animal feed production. *Advance Feed Technology*, 6, 6-23.
- Brittain, H. G. (2006). Luminescence spectroscopy. In H. G. Brittain (Ed.), *Spectroscopy of pharmaceutical solids* (pp. 155-157). New York, NY: Taylor & Francis Group.
- Chanda, A., Daly, A. M., Foley, D. A., LaPack, M. A., Mukherjee, S., Orr, J. D., ... & Ward, H. W. (2014). Industry perspectives on process analytical technology: Tools and applications in API development. *Organic Process Research and Development*, 19(1), 63-83.
- Clark, P. M., Behnke, K. C., & Poole, D. R. (2007). Effects of marker selection and mix time on the coefficient of variation (mix uniformity) of broiler feed. *Journal of Applied Poultry Research*, 16(3), 464-470.
- Corredor, C. C., Bu, D., & Both, D. (2011). Comparison of near infrared and microwave resonance for at-line moisture determination in powders and tablets. *Analytica Chimica Acta*, 696(1-2), 84-93.
- Dickens, J. E. (2010). Fluorescent sensing and process analytical applications. In K. Bakeev (Ed.), *Process analytical technology* (p. 343). Chichester, UK: John Wiley & Sons.

- Dickens, J. E., Vaughn, M. S., Taylor, M., & Ponsting, M. (2011). An LED array-based light induced fluorescence sensor for real-time process and field monitoring. *Sensors and Actuators B: Chemical*, 158(1), 35-42.
- Edwards, J. C., & Giammatteo, P. J. (2010). Process NMR spectroscopy: Technology and on-line applications. In K. Bakeev (Ed.), *Process analytical technology* (pp. 303-332). Chichester, UK: John Wiley & Sons.
- Ensminger, M. E., Oldfield, J. E., & Heinemann, W. W. (1990). *Feeds and Nutrition* (2nd Ed.). Clovis, California: Ensminger Publishing Company.
- Harris, D. C. (2010). *Quantitative chemical analysis*. New York, NY: WH Freeman and Company.
- Ishan, G. S., Kevin, J. E., & William, C. S. (2015). Effect of tapped density, compacted density, and drug concentration on light-induced fluorescence response as a process analytical tool. *Journal of Pharmaceutical Sciences*, 104(5), 1732-1740.
- Islam, M. T., Rodriguez-Hornedo, N., Ciotti, S., & Ackermann, C. (2004). The potential of Raman spectroscopy as a process analytical technique during formulations of topical gels and emulsions. *Pharmaceutical Research*, 21(10), 1844-1851.
- Jestel, N. L. (2010). Raman spectroscopy. In K. Bakeev (Ed.), *Process analytical technology* (pp. 195-231). Chichester, UK: John Wiley & Sons.
- Karumanchi V., Taylor, M. K., Ely, K. J., & Stagner, W. C. (2011). Monitoring powder blend homogeneity using light-induced fluorescence. *AAPS PharmSciTech*, 12(4), 1031-1037.
- Lai, C. K., Holt, D., Leung, J. C., & Cooney, C. L. (2001). Real time and noninvasive monitoring of dry powder blend homogeneity. *AIChE Journal*, 47(11), 2618-2622.
- Lai, C. K., & Cooney, C. L. (2004). Application of a fluorescence sensor for miniscale on-line monitoring of powder mixing kinetics. *Journal of Pharmaceutical Sciences*, 93(1), 60-70.
- Liau, M. A., Baylor, L. C., & O'Rourke, P. E. (2010). UV-visible spectroscopy for on-line analysis. In K. Bakeev (Ed.), *Process analytical technology* (pp. 81-104). Chichester, UK: John Wiley & Sons.
- Madamba, M. C., Mullett, W. M., Debnath, S., & Kwong, E. (2007). Characterization of tablet film coatings using laser-induced breakdown spectroscopy technique. *AAPS PharmSciTech*, 8(4), 184-190.
- Medendorp, J., Buice, R. G., & Lodder, R. A. (2006). Acoustic-resonance spectrometry as a process analytical technology for quantification of active pharmaceutical ingredient in semi-solids. *AAPS PharmSciTech*, 7(3), E22- E29.
- Shah, I. G., & Stagner, W. C. (2015). Effect of percent relative humidity, moisture content, and compression force on light-induced fluorescence (LIF) response as a process analytical tool. *AAPS PharmSciTech*, 4(17), 951-957.
- Strachan, C. J., Rades, T., Gordon, K. C., & Rantanen, J. (2007). Raman spectroscopy for quantitative analysis of pharmaceutical solids. *Journal of pharmacy and pharmacology*, 59(2), 179-192.
- Tok, A., Goh, X. P., Ng, W., & Tan, R. (2008). Monitoring granulation rate processes using three PAT tools in a pilot-scale fluidized bed. *AAPS PharmSciTech*, 9(4), 1083-1091.
- U.S. Food and Drug Administration. (2014). *Process analytical technology (PAT) initiative*. Retrieved October 10, 2015, from <http://www.fda.gov/aboutfda/centersoffices/officeofmedicalproductsandtobacco/cder/ucm088828.htm>

- Wargo, D., & Drennen, J. (1996). Near-Infrared spectroscopic characterization of pharmaceutical powder blends. *Journal of Pharmaceutical and Biomedical Analysis*, 14(11), 1415-1423.
- Zeitler, J. A., Taday, P. F., Newnham, D. A., Pepper, M., Gordon, K. C., & Rades, T. (2007). Terahertz pulsed spectroscopy and imaging in the pharmaceutical setting - a review. *Journal of Pharmacy and Pharmacology*, 59(2), 209-223.

A Novel Approach for Automated Operational Modal Analysis Using Image Clustering

Muhammad Danial Bin Abu Hasan^{1*}, Zair Asrar Bin Ahmad²,
Mohd Salman Leong¹ and Lim Meng Hee¹

¹*Institute of Noise and Vibration, Universiti Teknologi Malaysia, 54100 Kuala Lumpur, Malaysia*

²*School of Mechanical Engineering, Universiti Teknologi Malaysia, 81310 Skudai, Johor Bahru, Malaysia*

ABSTRACT

The present paper deals with the novel approach for clustering using the image feature of stabilization diagram for automated operational modal analysis in parametric model which is stochastic subspace identification (SSI)-COV. The evolution of automated operational modal analysis (OMA) is not an easy task, since traditional methods of modal analysis require a large amount of intervention by an expert user. The stabilization diagram and clustering tools are introduced to autonomously distinguish physical poles from noise (spurious) poles which can neglect any user interaction. However, the existing clustering algorithms require at least one user-defined parameter, the maximum within-cluster distance between representations of the same physical mode from different system orders and the supplementary adaptive approaches have to be employed to optimize the selection of cluster validation criteria which will lead to high demanding computational effort. The developed

image clustering process is based on the input image of the stabilization diagram that has been generated and displayed separately into a certain interval frequency. and standardized image features in MATLAB was applied to extract the image features of each generated image of stabilisation diagrams. Then, the generated image feature extraction of stabilization diagrams was used to plot image clustering diagram and fixed defined threshold was set for the physical modes classification. The application of

ARTICLE INFO

Article history:

Received: 1 June 2019

Accepted: 4 October 2019

Published: 13 January 2020

E-mail addresses:

muhd_danial200@yahoo.com (Muhammad Danial Abu Hasan)

zair@utm.my (Zair Asrar Ahmad)

salman.leong@gmail.com (Mohd Salman Leong)

limmenghee@gmail.com (Lim Meng Hee)

*Corresponding author

image clustering has proven to provide a reliable output results which can effectively identify physical modes in stabilization diagrams using image feature extraction even for closely spaced modes without the need of any calibration or user-defined parameter at start up and any supplementary adaptive approach for cluster validation criteria.

Keywords: Automated OMA (AOMA), automatization, clustering, operational modal analysis, stabilization diagram

INTRODUCTION

The advancement of automated operational modal analysis (OMA) has brought a recent trend in vibration-based monitoring and damage detection. Moreover, the mechanical and civil engineering appeal towards OMA is due to its ability to perform cost-effective and fast tests that depend solely on system responses.

The identification of modal parameters using nonparametric model involved direct estimation from frequency response or power spectral densities specifically peaks picking from the complex mode indicator function (CMIF) (Shih et al., 1988) or the averaged normalized power spectral density (Peeters, 2000), that are plotted as a function of frequency. The process to automate the peak selection have been recently introduced which heavily relied on the use MAC index and peak picking method (Brincker et al., 2007; Pioldi et al., 2017; Pioldi & Rizzi, 2017; Rainieri et al., 2007; Rainieri & Fabbrocino, 2010). In the frequency domain, the estimation of modal parameters is always overestimated particularly modal damping ratio due to the power of the signal 'leaking' out to neighboring frequencies, well known as spectral leakage and cause modal peaks of the spectral density functions will become wider (Brandt, 2011). Since simulation studies have confirmed that the identification modal parameters derived from the state space model of the parametric method are much more accurate than the non-parametric estimates (Peeters & De Roeck, 2001b; Reynders, 2009), most research effort has been spent in the automation of parametric techniques. Most research efforts have been heading towards automation engineering parametric techniques. Most research efforts have been directed towards parametric automation techniques.

In traditional modal identification using parametric method, the model order is often oversized in order to capture all physical modes in the frequency range of interest. Model oversizing is needed as models are often biased and do not include any noise modeling. The separation between physical and spurious modes involves a lot of interaction by a skilled analyst. Thus, a significant tool, such as a stabilization diagram, is needed to distinguish between physical and spurious modes. The selection of physical modes can be a complex task because it involved the setting of inconsistency thresholds for each modal parameter by the user (Piersol & Paez, 2010). The development of automated OMA procedures marked

a fundamental step toward the elimination of user intervention since traditional modal analysis requires a large amount of human intervention, particularly by an expert user.

Since a lot of human intervention is for monitoring purposes, early trials to automate modal identification focused on selection conditions and clustering tools to discriminate physical poles from others. The first attempts to automatically identify dynamic parameters were recorded during the last two decades based on the LSCF method performed using a number of deterministic and stochastic criteria and a fuzzy clustering approach. But it demanded high computational effort (Pappa et al., 1998; Peeters & De Roeck, 2001a; Vanlanduit et al., 2003). However, research efforts expanded after 2005, as demonstrated by the presence of numerous research papers over subsequent years. In recent years, research in automated OMA has become more systematic in term of analyses and arrangements (Andersen et al., 2007; Neu et al., 2017; Rainieri et al., 2011; Reynders et al., 2012).

A simple means for automated OMA was introduced by using the Stochastic Subspace Identification (SSI) technique and was utilized to perform structural health monitoring on the Z24 Bridge in Switzerland (Peeters & De Roeck, 2001a). This approach took advantage of the stabilization diagram on the choice of the poles that were at least five times stable and was able to trace the influences of varying environmental conditions on the modal parameters of Tamar bridge (Brownjohn & Carden, 2007). However, it had a drawback in terms of identifying physical poles. An enhancement of the SSI technique for automated OMA was introduced in subsequent years (Deraemaeker et al., 2008). Essentially, it was a tracking method because a number of modal parameters needed to be specified before beginning the procedure while using SSI and the stabilization diagram.

A fully automated OMA procedure by SSI was introduced in a similar period (Andersen et al., 2007). This multipatch subspace approach was applied to generate a clear stabilization diagram. Meanwhile, the selection for poles was implemented by the graph theory. It was a fast processing algorithm that was capable of being used as a monitoring routine, but additional enhancement was required to improve its robustness and reliability.

An improvised version of automated correlation-driven SSI, (COV-SSI) was accomplished several years later (Magalhaes et al., 2009). This algorithm was highly efficient in identifying closely spaced modes but was ineffective for weakly excited modes. The use of an advanced clustering algorithm permitted a reliable selection of physical modes with at least one user-defined parameter. However, several of these parameters needed to be specified at initial set up which could increase the time required for calibrations. A subsequent study proposed the use of an auto-generated parameter obtained from the real data using a fully automated with three-stage clustering approach. The three stages of the algorithm are related to the three stages in a manual analysis: setting stabilization thresholds for clearing out the diagram, detecting columns of stable modes, and selecting

a representative mode from each column (Reynders et al., 2012). However, this approach demands high computational time and effort.

An automated modal identification procedure using subspace identification techniques was proposed by tuning a few parameters and defining the clustering criterion for the random generation of the cluster seeds. This approach capable to deal with weakly excited and closely spaced modes (Ubertini et al., 2013). In 2015, a hybrid method for automated modal parameter identification (MPI) methods was introduced by combining analysis steps from different well-established OMA methods to simplify the interpretation of the stabilization diagrams, improving modal damping estimation and also neglecting the user-predefined parameter but demanded high computational efforts because the additional method like the standardized Euclidean distance and the single linkage method were used to compute the distance between pairs of poles and to construct hierarchical cluster tree respectively (Rainieri & Fabbrocino, 2015).

In subsequent year, an automated operational modal analysis was presented to reduce the number of user interactions to a single set of consistency thresholds by using agglomerative hierarchical clustering and a certain distance threshold. In this case, the sum of normalized pole distance and MAC were used to calculate inter-cluster distance between two nearest clusters (Neu et al., 2016). Then in the next year, automated operational modal analysis using parametric (SSI-COV) method with the construction of tri-dimensional stabilization diagrams and clustering (hierarchical clustering) tools able to efficiently obtain set of values for parametric method input parameters (Marrongelli et al., 2017). Then in the same year, a fully automated operational Modal analysis using parametric method (data-driven stochastic subspace identification (SSI) method) and multi-stage clustering was introduced to remove any user-provided thresholds and could be used for large system order ranges (Neu et al., 2017). The multi-stage clustering corresponds to hard validation criteria for remove certainly mathematical modes, k-means clustering to split modes into consistent and non-consistent sets, hierarchical clustering to divide the remaining modes into homogeneous sets and a threshold derived to remove mathematical modes. Additional steps were required in using hierarchical clustering. Besides that, Sun et al. (2017) introduced an automated operational modal analysis of a cable-stayed bridge by applying the proposed threshold for hierarchical clustering, two stages of k-means clustering were used to clear the stabilization diagram and identification of the final clusters and then density-based spatial clustering was applied to select the actual mode from each identified real cluster. In recent year, an automated procedure for covariance driven operational modal analysis (OMA) techniques was proposed to eliminate the need for a user interference for the selection of model order and size of the block-Hankel and block-Toeplitz matrices based on the reconstruction of the auto-correlation function from the cluster of complex poles (Bajrić et al., 2018). Then, the present study performed an

autonomous modal parameter estimation with three-dimensional space optimization by using non-iterative correlation-based method and fuzzy c-means for the clustering and bootstrap sampling (Yaghoubi et al., 2018). In the same year, an automated operational modal analysis methodology based on an eigensystem realization algorithm (ERA) and a two-stage clustering strategy was proposed (Yang et al., 2018). The proposed study using fuzzy C-means (FCM) clustering to separate stable modes from unstable ones. Also, in the presented study, the automated operational modal analysis (OMA) using stochastic subspace identification method and a three-stage clustering algorithm was proposed to automatically estimate the modal parameters (Marwitz et al., 2018). The most recent study introduced a novel multiscreening algorithm for the automated modal parameter identification based on the searching and averaging processes between clusters, and automatically identify the system poles on the basis of the numbers of their repetition in the spectral density via k-means clustering algorithms (Afshar & Khodaygan, 2019).

The above-mentioned literature demonstrates the current clustering tools require at least one user-defined parameter, the maximum within-cluster distance between representations of the same physical mode from different system orders and the supplementary adaptive approaches have to be employed to optimize the selection of cluster validation criteria which will lead to high demanding computational effort (Neu et al., 2017; Rainieri & Fabbrocino, 2014; Reynders et al., 2012; Yaghoubi et al., 2018). Thus, this paper will focus on developing a new clustering algorithm using image feature extraction that effectively identifies physical modes and neglect any calibration or user-defined parameter at start up and the need of any supplementary adaptive approach for cluster validation criteria.

MATERIALS AND METHODS

This analysis concerning a set of data from real structure, the Heritage Court Tower (HCT) building for verifying the theoretical framework which is using automatic versions of SSI-COV with the actual characteristics of realistic civil engineering structures. The structural dynamic testing on 15 stories of the Heritage Court Tower (HCT) building was carried out by researchers from the University of British Columbia (Bricker & Venture, 2015).

This building generally is characterised by representations of the closely spaced modes for the first three modes with the expectations of torsional and lateral vibration mode couplings, especially in the east-west direction, and corrupted with “noise modes” or spurious modes that originated from drilling and human activities close to the sensors during data acquisition.

The input natural excitation was based on wind and human activity as the construction of the building was about to be completed. The measurements were captured over a long period of time in order to ensure the loading on the structure is stochastic enough and behave according to white noise excitation for all modes to be adequately excited. The adopted

parameters in the processing were: length of time series, t (327.7s); the adopted time step (0.025s); sampling frequency (40 Hz) and adopted frequency resolution (0.0031Hz). Then, the input data was decimated to a Nyquist frequency of 5Hz which only concerning the dominant modes with representations of the three closely spaced modes from 1.2 to 1.5 Hz.

Automated Stochastic Subspace Identification (SSI)-COV

Automated OMA using Stochastic Subspace Identification (SSI)-COV comprises the subsequent steps as shown in Figure 1.

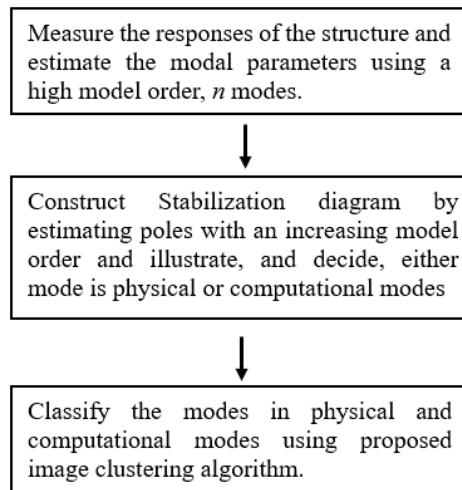


Figure 1. The following steps for automated OMA using parametric methods.

Stochastic Subspace Technique (SSI)

Stochastic Subspace Identification (SSI) has been a recognized approach since the previous decade, primarily because of its user-friendly execution (Bricker & Venture, 2015). This paper is only concerned with correlation-driven SSI (COV-SSI), one of SSI method. The COV-SSI analyze a stochastic state-space model from the response data of the structure (Rainieri & Fabbrocino, 2014) and working algorithm almost similar to Eigenvalue Realization Algorithm (ERA) (Peeters & De Roeck, 1999). The further details of its derivation are defined below.

The initial step was to compute the output correlations as shown in Equation (1). $[R_i]$ indicates the correlation matrix at time lag i based on discrete data as follows:

$$[R_i] = \frac{1}{N-i} [Y_{(1:N-i)}][Y_{(i:N)}]^T \quad (1)$$

Where $[Y_{(1:N-i)}]$ is the data matrix Y with the last block rows i removed and $[Y_{(i:N)}]^T$ is the transpose data matrix with the first block rows i removed. Hence each $[R_i]$ matrix got dimensions $l * l$. The computed correlations at different time lags were then stored in the

block Toeplitz matrix. The size of Toeplitz matrix became $n*n$ when estimating modal parameter with model order n . Thus, the subsequent Equation 3 should be correct for the number of block rows i :

$$li \geq n, \quad i_{min} = x \frac{n_{max}}{l} \tag{2}$$

The magnitude, x and maximum system order, n were set as 2 and 50 modes respectively. The next step was to calculate the singular value decomposition (SVD) of the block Toeplitz that could provide the unitary matrices $[U]$ and $[V]$. The positive singular values were ranked in descendant order of the diagonal matrix $[\Sigma]$ as fin Equation 4 (Wall et al., 2003).

$$[T_{1|i}] = [U_1][\Sigma_1][V_1]^T = [O_i][T_i] \tag{3}$$

To extract the dynamic response, the state matrix $[A]$ needs to be obtained. This was done for each order from 1 to n_{max} . The observability matrix $[O_i]$ and the reversed controllability matrix $[T_i]$ were found by the factorization of $[T_{1|i}]$. The result of SVD of $[T_{1|i}]$ computed in Equation 4 could be used to find $[O_i]$ and $[T_i]$ by separating the SVD into two parts and using the identity matrix $[I]$ as in Equation 8 and 9:

$$[O_i] = [U_1][\Sigma_1]^{1/2}[I]^T \tag{4}$$

$$[T_i] = [I]^{-1}[\Sigma_1]^{1/2}[V_1]^T \tag{5}$$

Now that $[O_i]$ and $[T_i]$ had been obtained, the output influence matrix $[C]$ and the state-output covariance matrix $[G]$ could be computed. Matrix $[C]$ was attained from the first l rows of $[O_i]$. Meanwhile, $[G]$ was obtained from the last l columns of $[T_i]$. The normal Toeplitz matrix produces Equation 10:

$$[T_{2|i+1}] = [O_i][A][T_i] \tag{6}$$

Resolving the eigenvalue problem for $[A]$ produces the diagonal matrix $[M]$ and the eigenvectors $[\Psi]$ as in Equation 12:

$$[A] = [\Psi][M][\Psi]^{-1} \tag{7}$$

The mode shapes of the system $[\Phi]$ were attained from $[\Psi]$ and $[C]$ and the other modal parameters were attained from the eigenvalues μ_m , which were found in the diagonal matrix $[M]$. The values were in discrete time and need to be transformed to continuous time as in Equation 14:

$$\lambda_m = \ln[\mu_m] / (\Delta t) \tag{8}$$

the complex λ_m comprised the continuous time eigenvalues of each mode for the current order which used to estimate the natural frequencies (ω_n), damped modal frequencies

(ω_d) and modal damping ratio (ζ). The step of identifying the state matrix and the modal parameters were repeated for each order up until n_{max} before plotted in a stabilization diagram.

Stabilization Diagram

The stabilization diagram is a typical means to distinguish physical poles from noise (spurious) poles, and once the model parameters are obtained, it was achieved by identifying poles with an increasing model order. Since the system model was frequently oversized, the plot would comprise noise modes which arose from physical reasons. Theoretically, the stabilize physical modes can be identified by the vertical alignment of stable poles, while noise modes are scattered. This is based on the poles comparability with respect to the order of the given model with the obtained from a lower order model (Rainieri & Fabbrocino, 2014).

The natural frequencies and damping ratio of poles from two orders were compared using Equation 18 and 19 (Schanke, 2015):

$$\frac{|f(n-1)-f(n)|}{f(n-1)} < x \tag{9}$$

$$\frac{|\zeta(n-1)-\zeta(n)|}{\zeta(n-1)} < y \tag{10}$$

Only poles that satisfy a stabilization criterion set by the user (x and y) were considered as stable. The following thresholds were set for variation between models of following orders: natural frequency variation < 1% (Magalhães, 2010) and modal damping ratio variation < 5%. These thresholds allow the clear dissimilarity of vertical alignments of stable modes. The stabilization diagram constructed from the first data sets obtained from the structural dynamic testing of HCT can be seen in Figure 2 and Figure 3.

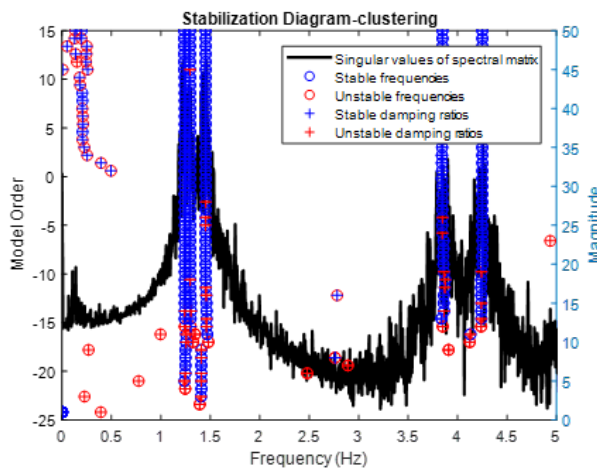


Figure 2. Singular values of the spectral matrix with stabilization diagram for first data sets of the HCT building.

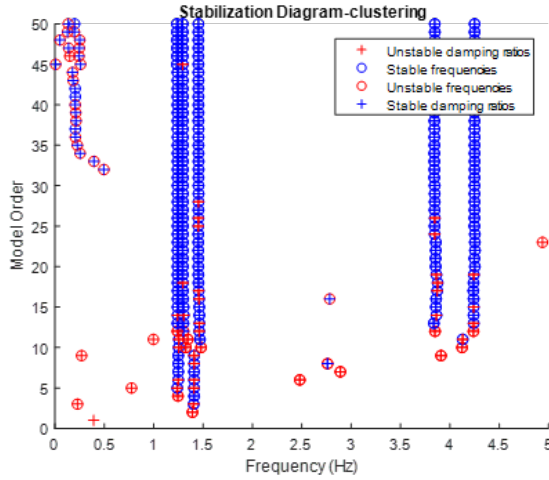


Figure 3. Stabilization diagram for first data sets of the HCT building.

Proposed Approach for Clustering. The procedure of using image clustering with respect to the similar physical pole of the stabilization diagrams is as follows:

Input Image

The process of image clustering requires the input image of the stabilization diagram that has been cut down into a certain interval frequency accordingly. In this case, the stabilization diagram was generated and displayed separately into every frequency according to 0.01 interval, (maximum frequency, 5Hz)/ 0.01 = 500 total images. Thus, every image represents the frequency of 0.01 Hz. The process of this procedure is shown in Figure 4 and Figure 5. In order to make image feature extraction more efficient, all axes and legend in the plot of these images had to be removed.

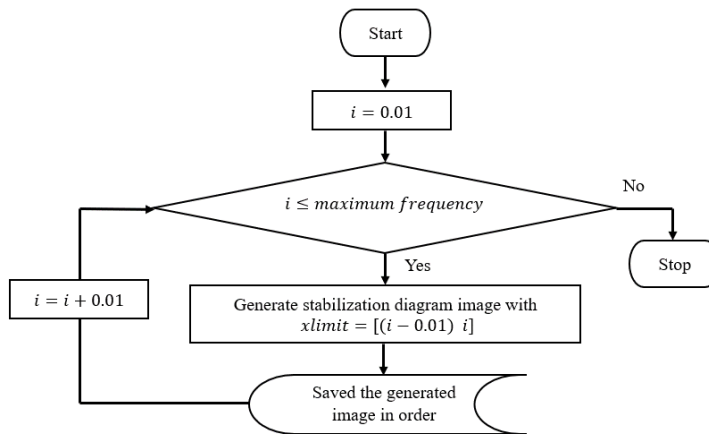


Figure 4. Flowchart process of generated input images from a stabilization diagram with a 0.1 Hz interval frequency

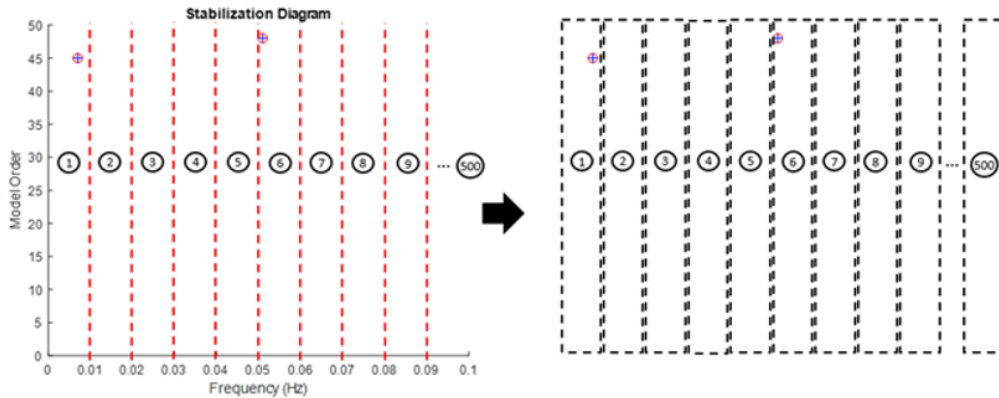


Figure 5. Illustration of generated input images from a stabilization diagram with a 0.1 Hz interval frequency for feature extraction

Image Feature Extraction

Then, the standardized image features from MATLAB was applied in this study to extract the image features of each image of stabilization diagrams that were previously generated. These features specifically represent the characteristics of each parameter (natural frequencies, damping ratios) for different conditions, either stable or unstable. Table 1 summarizes the features of the extracted images and their characteristic values. All the six standardized image features were used in this study in order to determine which image feature was the most appropriate to capture all the modes of interest particularly in term of computational mode appearance.

Table 1

Image features and their characteristic values

No	Feature	Characteristic value
1	Features from FAST	Corner Points
2	Minimum Eigenvalues	Corner Points
3	Harris Stephens	Corner Points
4	Speeded-Up Robust Features	Blob
5	Binary Robust Invariant Scalable Keypoints	Multiscale Corner
6	Maximally Stable External Regions	Regions

Generally, the image feature will provide a certain value based on its image characteristic. If the image is blank, the value will become zero, otherwise if the pole appears, the value will increase. The increasing value of image feature extraction depends on the number of poles appeared in that particular image. It works well with stabilization diagram because the stabilize physical modes consists of the vertical alignment of stable poles, while noise

modes are scattered. By generating the image of stabilization diagram according to 0.01 interval frequency (cut down vertically), the poles can be clustered accordingly. Therefore, the generated input image based on interval frequency of stabilization diagram play a key role for the performance of the image feature extraction. Details explanation about the process of this procedure was shown in Figure 6.

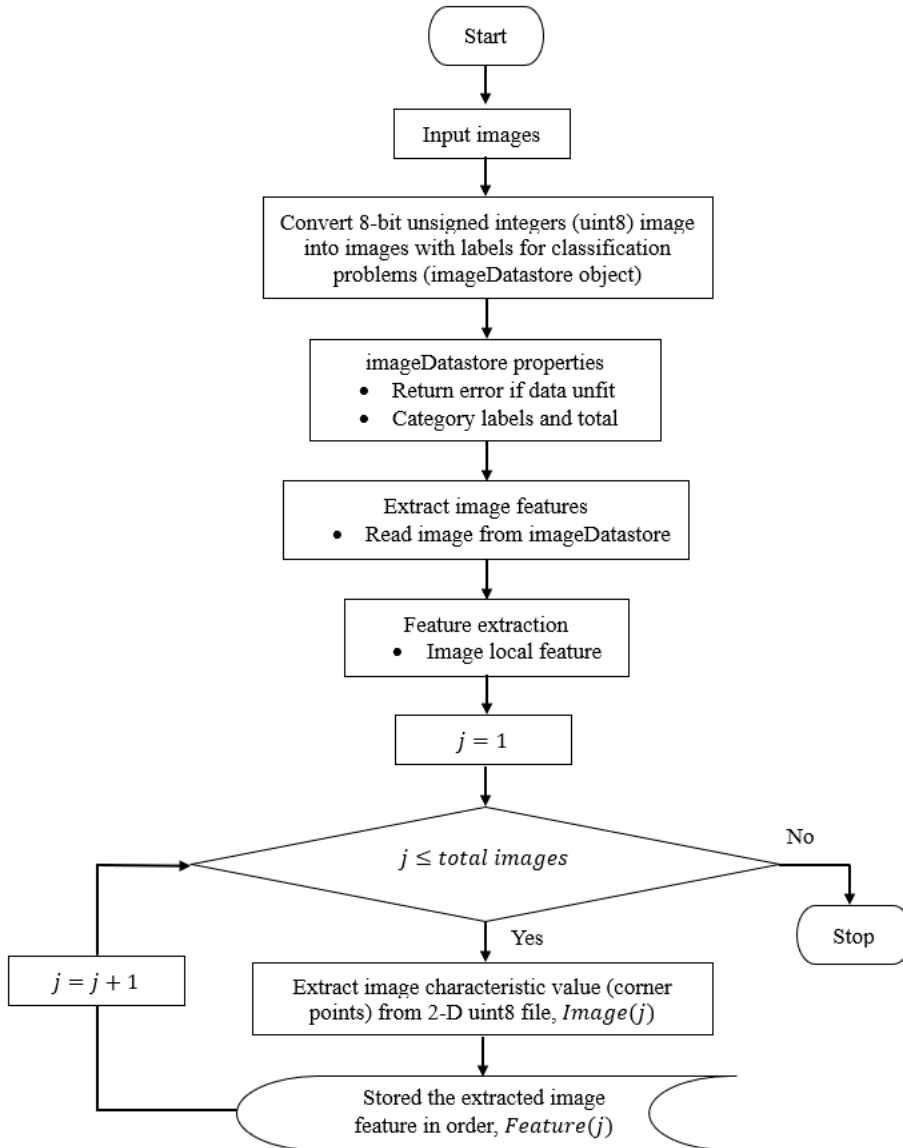


Figure 6. Flowchart process of image feature extraction

Selection of Physical Modes

The selection of the physical modes of the system that was autonomously implemented involved the MATLAB command – *find* – and the threshold in order to discriminate the unwanted mode and the actual modes. The threshold is determined by the half of the maximum peak in the image clustering plot. The selection of peaks in the image clustering plot are determine by using MATLAB command – *find* –. The value of image features extraction below than this threshold in image clustering plot represents the unwanted or computational mode, otherwise consider as dominant mode or physical mode.

RESULTS AND DISCUSSION

Image-based vibration measurement has brought a great attention to civil engineering communities and is increasingly being used in the area of structural dynamics, particularly for modal analysis and damage identification (Javh et al., 2018; Olaszek, 1999; Park et al., 2018; Peters & Ranson, 1982; Sarrafi et al., 2019). Optically-acquired data, usually from digital image correlation as an alternative method was introduced to reduce labor-intensive tasks during dynamic testing involving multiple number of accelerometers and handling the wiring and the connections (Chang et al., 2019; Sarrafi et al., 2019). Numerous image-processing techniques are being used to identify the displacements from image sequences. Among the most commonly used technique are: Gradient-Based Optical Flow (Horn & Schunck, 1981; Javh et al., 2017; Lucas & Kanade, 1981), Gradient-Based Digital Image Correlation (DIC) (Peters & Ranson, 1982), in fact the Lucas-Kanade method from (Lucas & Kanade, 1981) is the general form of DIC (Schreier et al., 2009), Point Tracking (Olaszek, 1999) and Phase-Based method (Fleet & Jepson, 1990; Sarrafi et al., 2019). Existing image-based applications are mostly used to detect movement of target objects and act as virtual sensors, but in contrast to this study the use of image-based applications involves image feature extraction as a new tool for clustering of actual modes and unwanted modes in the stabilization diagram.

The image clustering results plotted using image features extraction were displayed in Figure 7 with all the poles of the stabilization diagram that are presented in Figure 3. Moreover, the results of the estimated natural frequency using automated SSI- COV with image clustering in identification of physical modes are characterized in Table 2.

Based on the results of image clustering using six standardized image features in Figure 7, they show that all standardized image featured except for speeded-up robust features which was using blob as characteristic value capable to provide the clear illustration of image clustering plot with the appearance of all modes of interest particularly for computational or unwanted mode. A clear appearance of noise or unwanted mode was at a frequency of 0.21 Hz. Knowing the frequency that represents noise mode is essential because it can be used for the next step for removing the unwanted mode from original

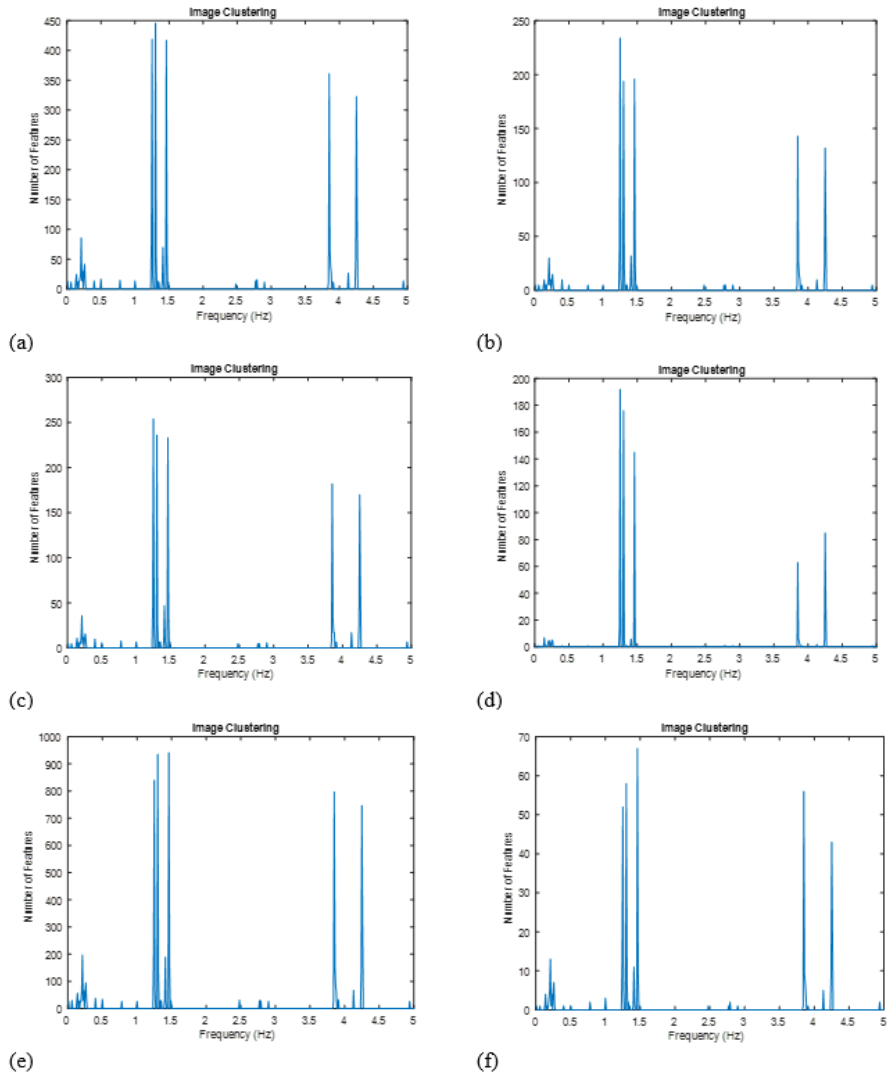


Figure 7. Image clustering plot by using image features extraction from (a) FAST, (b) Minimum Eigenvalues, (c) Harris Stephens, (d) Speeded-Up Robust Features, (e) Binary Robust Invariant Scalable Keypoints and (f) Maximally Stable External Regions respectively

Table 2

Identification results using image clustering on the stabilization diagram for the first data sets of the HCT building case. Modes determined to be physical are shown here

Mode	Feature	Frequency value
1	419	1.2500
2	446	1.3000
3	417	1.4600

Table 2 (Continued)

Mode	Feature	Frequency value
4	361	3.8500
5	323	4.2500

signal and reconstructed back to become a clean input time series signal. Moreover, this approach is also highly efficient in identifying and clearly separating closely spaced modes as seen in Figure 7 for the first three closely spaced modes of HCT from 1.2 to 1.5 Hz.

The outcomes of this study show that image clustering for the physical modes identification of stabilization diagrams is an effective method to identify modes without the need of any calibration or user-defined parameter at start up and any supplementary adaptive approach for cluster validation criteria that are summarized in Table 3 below. The comparative study with existing clustering is also well described in that table. Using standardized image features in MATLAB, image clustering provided a clear distinction of stable modes that signify structural modes. These standardized image features play a vital role in identifying which image represents the vertical alignment of stable modes.

In summary of Table 3 above, some common deficiencies have compromised the existing automated OMA methods (Hasan et al., 2019):

- The estimation of actual structural modes requires several predefined set parameters
- A time-demanding setting procedure for each analysis of the data set is compulsory at start-up
- The values for thresholds and parameters are inconsistent due to natural variations in modal properties of structures that come from damage or environmental influences.
- The existing clustering algorithms need supplementary adaptive approach for cluster validation criteria.

Table 3

Comparison of the proposed approach with existing clustering algorithms

	Proposed approach (image clustering)	Hierarchical	Non-hierarchical
Advantages	Effective identification of modes without the need of any supplementary adaptive approach for cluster validation criteria Does not require any parameters setup. Easy to implement and does not requires any expert user.	The more informative structure that allowing a good choice of the last number of clusters, depending on the previous construction of hierarchical tree.	Computationally faster than Hierarchical clustering for many variables. May produce tighter clusters than hierarchical clustering

Table 3 (Continued)

	Proposed approach (image clustering)	Hierarchical	Non-hierarchical
Disadvantages	Require plenty of images for reliable identification of structural modes.	Computationally demanding due the existence of many individuals, and the similarity of each individual must be calculated. Data order has an impact on the results. Highly sensitive to outliers.	The number of clusters must be specified, and cluster seeds need to be chosen. Seeds are chosen randomly which can cause inconsistent results.

CONCLUSIONS

This research demonstrates that the use of image clustering approach permits reliable identification of structural modes and unwanted modes without the need of any calibration or user-defined parameter at start up and any supplementary adaptive approach for cluster validation criteria. This prove by a clear appearance of noise or unwanted mode is at a frequency of 0.21 Hz. This approach is also user-friendly and does not require any expertise to conduct. Moreover, this approach is highly efficient in identifying and clearly separating closely spaced modes as seen in Figure 7 for the first three closely spaced modes of HCT from 1.2 to 1.5 Hz.

This research will be the basis for future research to improve automation technique as a modal information engine in vibration-based monitoring and damage detection by reducing some of the general shortcomings of the automated OMA methods.

ACKNOWLEDGMENTS

The authors would like to extend their greatest gratitude to the Institute of Noise and Vibration UTM for funding the current study under the Higher Institution Centre of Excellence (HICoE) Grant Scheme (R.K130000.7843.4J227). Additional funding for this research came from the UTM Research University Grant (Q.K130000.2543.11H36) and the Fundamental Research Grant Scheme (R.K130000.7840.4F653) from The Ministry of Higher Education, Malaysia.

REFERENCES

- Afshar, M., & Khodaygan, S. (2019). Enhanced stabilization diagram for automated modal parameter identification based on power spectral density transmissibility functions. *Structural Control and Health Monitoring*, 26(7), 1-24.

- Andersen, P., Brincker, R., Goursat, M., & Mevel, L. (2007, April 30 – May 2). Automated modal parameter estimation for operational modal analysis of large systems. In *Proceedings of the 2nd international operational modal analysis conference* (pp. 299-308). Copenhagen, Denmark.
- Bajrić, A., Høgsberg, J., & Rüdinger, F. (2018). Evaluation of damping estimates by automated operational modal analysis for offshore wind turbine tower vibrations. *Renewable Energy*, *116*, 153-163.
- Brandt, A. (2011). *Noise and vibration analysis: signal analysis and experimental procedures*. Chichester, UK: John Wiley and Sons.
- Bricker, R., & Venture, C. (2015). *Introduction to operational modal analysis*. Chichester, UK: John Wiley and Sons.
- Brincker, R., Andersen, P., & Jacobsen, N. J. (2007, February 19-22). Automated frequency domain decomposition for operational modal analysis. In *Proceedings of The 25th International Modal Analysis Conference (IMAC)*, (pp. 1-7). Orlando, Florida.
- Brownjohn, J. M., & Carden, E. P. (2007, November 14-16). Tracking the effects of changing environmental conditions on the modal parameters of Tamar Bridge. In *3rd International Conference on Structural Health Monitoring and Intelligent Infrastructure*. Vancouver, Canada.
- Chang, Y. H., Wang, W., Chang, J. Y., & Mottershead, J. E. (2019). Compressed sensing for OMA using full-field vibration images. *Mechanical Systems and Signal Processing*, *129*, 394-406.
- Deraemacker, A., Reynders, E., De Roeck, G., & Kullaa, J. (2008). Vibration-based structural health monitoring using output-only measurements under changing environment. *Mechanical Systems and Signal Processing*, *22*(1), 34-56.
- Fleet, D. J., & Jepson, A. D. (1990). Computation of component image velocity from local phase information. *International Journal of Computer Vision*, *5*(1), 77-104.
- Hasan, M. D. A., Ahmad, Z. A. B., Leong, M. S., Hee, L. M., & Haffizzi Md. Idris, M. (2019). Cluster Analysis for Automated Operational Modal Analysis: A Review. In *MATEC Web of Conferences* (Vol. 255, p. 1-5). Les Ulis, France: EDP Sciences.
- Horn, B. K. P., & Schunck, B. G. (1981). Determining optical flow. *Artificial Intelligence*, *17*(1-3), 185-203.
- Javh, J., Slavič, J., & Boltežar, M. (2017). The subpixel resolution of optical-flow-based modal analysis. *Mechanical Systems and Signal Processing*, *88*(August 2016), 89-99.
- Javh, J., Slavič, J., & Boltežar, M. (2018). Measuring full-field displacement spectral components using photographs taken with a DSLR camera via an analogue Fourier integral. *Mechanical Systems and Signal Processing*, *100*, 17-27.
- Lucas, B. D., & Kanade, T. (1981, August 24-28). An iterative image registration technique with an application to stereo vision. In *Proceeding 7th International Joint Conference on Artificial Intelligence* (pp. 674-679). Vancouver, British Columbia.
- Magalhães, F. (2010). *Operational modal analysis for testing and monitoring of bridges and special structures* (Doctorial Thesis). University of Porto, Portugal.

- Magalhaes, F., Cunha, A., & Caetano, E. (2009). Online automatic identification of the modal parameters of a long span arch bridge. *Mechanical Systems and Signal Processing*, 23(2), 316-329.
- Marrongelli, G., Magalhães, F., & Cunha, A. (2017). Automated operational modal analysis of an arch bridge considering the influence of the parametric methods inputs. *Procedia Engineering*, 199, 2172-2177.
- Marwitz, S., Zabel, V., & Könke, C. (2018). Modalanalyse von Monitoringdaten eines Sendeturms [Modal analysis of monitoring data of a transmission tower]. *Bautechnik*, 95(4), 288-295.
- Neu, E., Janser, F., Khatibi, A. A., & Orifici, A. C. (2016). Automated modal parameter-based anomaly detection under varying wind excitation. *Structural Health Monitoring*, 15(6), 730-749.
- Neu, E., Janser, F., Khatibi, A. A., & Orifici, A. C. (2017). Fully automated operational modal analysis using multi-stage clustering. *Mechanical Systems and Signal Processing*, 84, 308-323.
- Olaszek, P. (1999). Investigation of the dynamic characteristic of bridge structures using a computer vision method. *Measurement*, 25(3), 227-236.
- Pappa, R. S., James, G. H., & Zimmerman, D. C. (1998). Autonomous modal identification of the space shuttle tail rudder. *Journal of Spacecraft and Rockets*, 35(2), 163-169.
- Park, K. T., Torbol, M., & Kim, S. (2018). Vision-based natural frequency identification using laser speckle imaging and parallel computing. *Computer-Aided Civil and Infrastructure Engineering*, 33(1), 51-63.
- Peeters, B. (2000). System identification and damage detection in civil engineering (Doctoral Thesis). Katholieke Universiteit Leuven, Belgium.
- Peeters, B., & De Roeck, G. (1999). Reference-based stochastic subspace identification for output-only modal analysis. *Mechanical Systems and Signal Processing*, 13(6), 855-878.
- Peeters, B., & De Roeck, G. (2001a). One-year monitoring of the Z24-Bridge: environmental effects versus damage events. *Earthquake Engineering and Structural Dynamics*, 30(2), 149-171.
- Peeters, B., & De Roeck, G. (2001b). Stochastic system identification for operational modal analysis: A review. *Journal of Dynamic Systems, Measurement, and Control*, 123(4), 659-667.
- Peters, W. H., & Ranson, W. F. (1982). Digital imaging techniques in experimental stress analysis. *Optical Engineering*, 21(3), 427-431.
- Piersol, A. G., & Paez, T. L. (2010). *Harris' shock and vibration handbook* (6th ed.). New York, USA: McGraw-Hill.
- Pioldi, F., & Rizzi, E. (2017). A refined frequency domain decomposition tool for structural modal monitoring in earthquake engineering. *Earthquake Engineering and Engineering Vibration*, 16(3), 627-648.
- Pioldi, F., Ferrari, R., & Rizzi, E. (2017). Earthquake structural modal estimates of multi-storey frames by a refined Frequency Domain Decomposition algorithm. *JVC/Journal of Vibration and Control*, 23(13), 2037-2063.
- Rainieri, C., Fabbrocino, G., & Cosenza, E. (2007). Automated operational modal analysis as structural health monitoring tool: theoretical and applicative aspects. *Key Engineering Materials*, 347, 479-484.

- Rainieri, C., Fabbrocino, G., & Cosenza, E. (2011). Near real-time tracking of dynamic properties for standalone structural health monitoring systems. *Mechanical Systems and Signal Processing*, 25(8), 3010-3026.
- Rainieri, C., & Fabbrocino, G. (2010). Automated output-only dynamic identification of civil engineering structures. *Mechanical Systems and Signal Processing*, 24(3), 678-695.
- Rainieri, C., & Fabbrocino, G. (2014). *Operational modal analysis of civil engineering structures*. New York, NY: Springer.
- Rainieri, C., & Fabbrocino, G. (2015). Development and validation of an automated operational modal analysis algorithm for vibration-based monitoring and tensile load estimation. *Mechanical Systems and Signal Processing*, 60, 512-534.
- Reynders, E. (2009). *System identification and modal analysis in structural mechanics* (PhD thesis). Katholieke Universiteit Leuven, Belgium.
- Reynders, E., Houbrechts, J., & De Roeck, G. (2012). Fully automated (operational) modal analysis. *Mechanical Systems and Signal Processing*, 29, 228-250.
- Reynders, E., Houbrechts, J., & Roeck, G. De. (2012). Fully automated (operational) modal analysis. *Mechanical Systems and Signal Processing*, 29, 228-250.
- Sarrafi, A., Poozesh, P., Niezrecki, C., & Mao, Z. (2019). Detection of natural frequency and mode shape correspondence using phase-based video magnification in large-scale structures. In *Structural Health Monitoring, Photogrammetry & DIC* (Vol. 6, pp. 81-87). Cham, Switzerland: Springer
- Schanke, S. A. (2015). *Operational modal analysis of large bridges* (Master Thesis). Norwegian University of Science and Technology, Norway.
- Schreier, H., Orteu, J. J., & Sutton, M. A. (2009). *Image correlation for shape, motion and deformation measurements: Basic concepts, theory and applications* (Vol. 1). Boston, MA: Springer-Verlag.
- Shih, C. Y., Tsuei, Y. G., Allemang, R. J., & Brown, D. L. (1988). Complex mode indication function and its applications to spatial domain parameter estimation. *Mechanical Systems and Signal Processing*, 2(4), 367-377.
- Sun, M., Makki-Alamdari, M., & Kalthori, H. (2017). Automated operational modal analysis of a cable-stayed bridge. *Journal of Bridge Engineering*, 22(12), 1-26.
- Ubertini, F., Gentile, C., & Materazzi, A. L. (2013). Automated modal identification in operational conditions and its application to bridges. *Engineering Structures*, 46, 264-278.
- Vanlanduit, S., Verboven, P., Guillaume, P., & Schoukens, J. (2003). An automatic frequency domain modal parameter estimation algorithm. *Journal of Sound and Vibration*, 265(3), 647-661.
- Wall, M. E., Rechtsteiner, A., & Rocha, L. M. (2003). Singular value decomposition and principal component analysis. In D. P. Berrar, W. Dubitzky & M. Granzow (Eds.), *A practical approach to microarray data analysis* (pp. 91-109). Boston, MA: Springer.
- Yaghoubi, V., Vakilzadeh, M. K., & Abrahamsson, T. J. S. (2018). Automated modal parameter estimation using correlation analysis and bootstrap sampling. *Mechanical Systems and Signal Processing*, 100, 289-310.

Yang, X. M., Yi, T. H., Qu, C. X., Li, H. N., & Liu, H. (2018). Automated eigensystem realization algorithm for operational modal identification of bridge structures. *Journal of Aerospace Engineering*, 32(2), 1-24.



The Effect of Javanese Gamelan Music on the Growth of Chinese Broccoli

Yusuf Hendrawan*, Antonius Rizky, Bambang Susilo, Joko Prasetyo and Retno Damayanti

Department of Agricultural Engineering, Faculty of Agricultural Technology, Brawijaya University, Veteran St., Malang, East Java, ZIP 65145, Indonesia

ABSTRACT

Plant acoustic frequency technology (PAFT) is a technology that utilizes sound waves in the form of frequencies within the audiosonic threshold. The purpose of this study was to test PAFT by using Javanese gamelan music entitled puspawarna on the productivity of vegetative growth in Kailaan (*Brassica alboglabra*) plant. PAFT exposure time was given to plants during the morning and evening. The frequencies ranged in 3-5 kHz, 7-9 kHz and 11-13 kHz. In addition, sound exposure times were for 1 hour, 2 hours and 3 hours. Based on the statistical analysis, the results indicated that the frequency and sound exposure time had a significant effect on plant wet weight, plant length, and stomata openings. The best frequency for Kailaan plant growth was in 3-5 kHz with the best exposure time of 3 hours. The combination of frequency and sound exposure time resulted in the most optimal

stomata openings (stomata diameter at the top of the leaves of 89.19 ~ 93.45 μm and stomata diameter at the bottom of the leaves of 136.69 ~ 140.74 μm) with chlorophyll of 80.86 chlorophyll content index (cci), plant length of 47.33 cm, plant wet weight of 84 g, area of leaves of 207.06 cm^2 , plant height of 9.4 cm, and number of leaves of 11 strands.

ARTICLE INFO

Article history:

Received: 1 August 2019

Accepted: 15 November 2019

Published: 13 January 2020

E-mail addresses:

yusufhendrawan@gmail.com (Yusuf Hendrawan)

antoniousrizky@gmail.com (Antonius Rizky)

bmsusilo@gmail.com (Bambang Susilo)

jprasetyo2241@gmail.com (Joko Prasetyo)

just.ennox@gmail.com (Retno Damayanti)

*Corresponding author

Keywords: Frequency, kailaan, PAFT, sound exposure time

INTRODUCTION

Kailaan (*Brassica alboglabra*) is one of the green leafy brassicas which are widely grown for commercial production in East and Southeast Asia. Kailaan or Chinese broccoli is one of the most important leafy vegetables grown in Southeast Asia (Sagwansupyskorn, 1993). Plants can adapt to tropical lowland heat and humidity which can be planted throughout the year. Several benefits for tropical farmers include short harvest duration, low production costs compared to many other vegetable crops, ease of seed production, and Kailaan easy adaptation (Hanson et al., 2004). Commercial production of Kailaan is usually concentrated close to the city due to the characteristics of plants such as: fragile, easily damaged, and short shelf life that requires a production location adjacent to the market (Hanson et al., 2011). Kailaan has shiny blue-green leaves with thick crispy stems. This plant is harvested commercially when blossoming buds have been formed but are not yet open (Okuda, 2000).

In its growth, vegetable plants adjust to environmental factors including light, temperature, moisture, and mechanical perturbations such as: wind, rain, and touch. Several methods of vegetable cultivation have been developed to optimize productivity and quality of vegetable crops. One effective method is the manipulation of environmental factors in which vegetables are cultivated (Rouphael et al., 2018; Hendrawan et al., 2019; Umam et al., 2019). Modern greenhouses are designed and equipped with sensors and automatic control systems to adjust air temperature, root zone temperature, light intensity and quality, relative humidity and carbon dioxide (CO₂) concentration, according to plant needs and vegetative growth stages (Graamans et al., 2018). Scientific literature deals with the importance of temperature control for vegetable quality. Max et al. (2009) postulated the effect of temperature regulation on plant quality reporting that the air conditioning system in a polyethylene-covered greenhouse reduced the incidence of rot at small flower ends and fruit, and increased Ca content. Setting the temperature in the root zone is as important as in the room temperature, which provides effective effect on the growth of vegetable plants (Urrestarazu et al., 2008). Artificial lighting conditions in greenhouses play an important role for vegetable quality in terms of visual, organoleptic properties and chemical composition. According to Li and Kubota (2009) and Lin et al. (2013), the application of variable quality supplemental light (UV-A, blue, green, red and far red, and white LED diodes) causes significant differences in phytochemical content (anthocyanins, carotenoids, chlorophylls and flavonoids) from lettuce leaves, hence light additional can be a modulator of useful phytochemical content. Setting the intensity of light in a controlled environment is also essential which affects the photosynthetic activity and chemical composition in vegetables (Kyriacou et al., 2016; Ksas et al., 2015). Addition of CO₂ up to 1000-1200 µmol mol⁻¹ in the greenhouse also has a significant effect to increase vegetable productivity up to 30% and increase the quality of vegetable crops both in terms of chemical composition, antioxidant activity, fiber content, vitamin C, protein, organic acids,

fat, and sugar content (total, reducing, and non-reducing) (Chalabi et al., 2002; Becker & Klaring, 2016; Sgherri et al., 2017; Baslam et al., 2012; Khan et al., 2013). The regulation of environmental humidity (RH) of vegetable cultivation also has a significant effect on the productivity and quality of vegetable products (Vanhassel et al., 2015; Leyva et al., 2014). High RH results in heat damage due to reduced evapotranspiration rates, while at the same time reducing sap flow through phloem reduction and ion translocation in plant tissues, which produces symptoms of nutrient deficiencies. Among the environmental factors that have been mentioned (temperature, light and humidity), it is revealed that plants also respond to sound waves that can stimulate growth increasing productivity and immune systems in plants (Mishra et al., 2016; Chowdhury et al., 2014). Research on the effect of sound waves on plant growth has been unfortunately limited.

To date, there are still inadequate studies that focus on the use of plant acoustic frequency technology (PAFT) to increase the productivity and quality of Kailaan vegetables. PAFT aims to provide exposure to sound waves in plants under specific frequencies in accordance with the plant's meridian system to increase crop production and reduce fertilizer use (Meng et al., 2012; Collins & Foreman, 2001). Sound waves are roughly classified into three regimes by its frequency: infrasound (10^{-4} –20 Hz), audible sound (20×10^4 Hz) and ultrasound (2×10^4 – 10^{12} Hz). Several studies have proven that the application of audible PAFT is beneficial for plant growth, especially in vegetables (Hassanien et al., 2014; Jaramillo et al., 2018; Pujiwati & Djuhari, 2014; Ankur et al., 2016; Weiming et al., 2015). PAFT has been applied at various stages of plant physiological growth, such as: in seed germination, callus growth, endogenous hormones, photosynthetic mechanisms, and transcription of certain genes. Good stimulation can increase disease resistance and can reduce the use of chemical fertilizers and biocides (Zhao et al., 2002). The utilization of PAFT can also regulate the quality of plant products extending the shelf life (Kim et al., 2018). Plants can spontaneously produce sound waves at relatively low frequencies of 50-120 Hz. In addition, plants similar to humans and other animals have internal sound frequencies. Plants can also absorb and resonate with certain external sound frequencies (Hou et al., 1994; Hou & Li, 1997). Sound waves can change cell cycles (Wang et al., 1998). Sound waves vibrate the leaves of plants and accelerate protoplasmic movements in cells (Gagliano et al., 2012). Based on the facts about the advantages of PAFT, there is possibility that PAFT can improve the production of Kailaan as the most important vegetables in Southeast Asia. Furthermore, there has been no research which observe the effectiveness of PAFT for Kailaan growth.

The purpose of this study is to apply PAFT for the vegetative growth of Kailaan vegetables. The sound utilized as PAFT is derived from traditional Javanese music, with the Javanese Gamelan entitled Puspawarna. In previous studies, it has been proven the effectiveness of Javanese gamelan music compared to other types of music such as rock

and jazz (Hendrawan et al., 2018). The results showed that PAFT effectively increased vegetative growth of plants. The results for each type of music i.e. jazz, gamelan, and heavy metal were as follows: plant height of 14.84, 15.96, and 15.3 cm, respectively; leaf area of 13.9, 29.38, and 26.01 cm², respectively; plant root dry weight of 0.156, 0.244, and 0.238 g, respectively; plant length of 16.12, 18.74, and 19.5 cm, respectively; and plant wet weight of 1.94, 2.78, and 2.384 g, respectively.

MATERIAL AND METHODS

This research was conducted at the Agroindustry Tools and Machinery Mechatronics Laboratory, Department of Agricultural Engineering, Faculty of Agricultural Technology, Brawijaya University, Malang, Indonesia. The utilized tools in this study can be seen in Table 1.

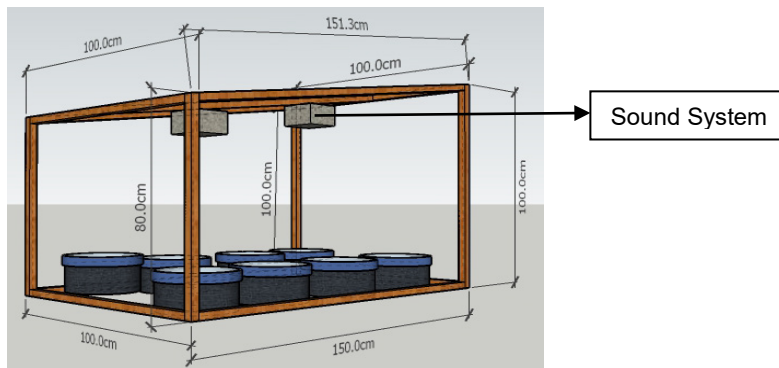
Table 1
The utilized tools in the study

Device	Specification	Function
Growth chambers	there were three growth chambers used, each chamber was coated with ultraviolet (UV) plastic with a thickness of 0.15 to 0.2 mm	as a place for Kailaan cultivation
Portable Speaker	Advance duo 050 speakers (3 watts, 4 ohms, 20 Hz ~ 20 kHz frequency response)	as a sound source
Digital timing module	DS3231 RTC	to control the timing of sound exposure
Relay	4-volt 4 channel relay	to turn on and off the speakers with digitally
Power Supply	AC to DC 12 V10 A Power Supply	as a power source
Microcontroller	Arduino uno atmega	as a microcontroller for control systems
Mono speaker	5-volt MP3 decoder	as a sound generator
Sound level meter	Extech Instruments	to measure sound noise levels
Chlorophyll Meter	SPAD-502Plus	to measure chlorophyll or green leaf index

Table 1 (Continued)

Device	Specification	Function
Digital Scales	(I-2000) and (Camry)	to measure leaf area and wet weight
Microscope	Olympus CX43 Binocular Microscope	to observe the diameter of the stomata opening

This study utilized the three chambers in a greenhouse measuring of 150 x 100 cm where each chamber had two speakers placed at the top center facing down towards the plant as shown in Figure 1. The treatment chamber was placed in a greenhouse that had been tested to be soundproof and was far from crowded. The distance of each chamber was



(a)

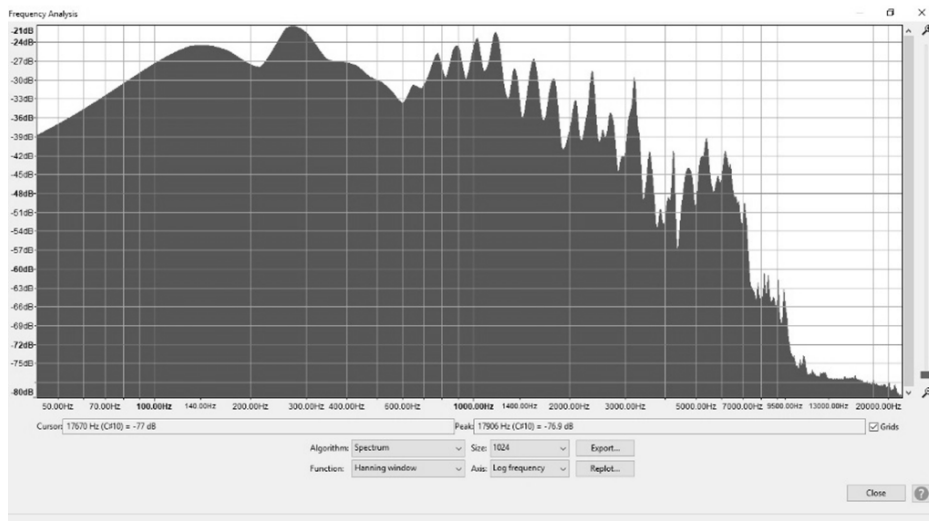


(b)

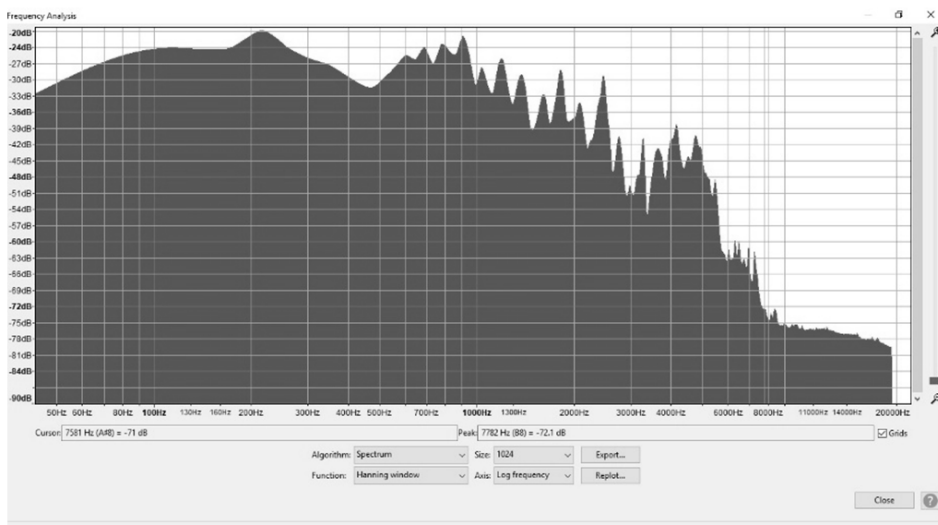
Figure 1(a) & (b). PAFT design in a cultivation chamber

set far enough from one another, so there was no noise inside the chamber. Before the study begin, each chamber was subjected to a soundproof test. Each chamber represented one frequency treatment. In the first hour treatment of PAFT exposure, all plants were in each growth chamber. At the second hour, a set of plants was removed away from each chamber. At the third hour, another set of plants was removed away from each chamber. After PAFT treatment was complete, all plants were returned to the chamber. Measurement result of environmental temperature both inside and outside the observation environment ranged from 28-32 °C and air humidity ranged from 40-50%. The measurements were conducted in the morning and evening when the plants were treated. Whereas, the sound intensity level from each treatment ranged from 68 to 76 db (Pujiwati et al., 2018; Hassanien et al., 2014). The utilized sample was Kailaan vegetable seedlings which had aged 20 days after seedling. PAFT treatment was performed for 24 days in the morning at 07.00-10.00 a.m and in the afternoon at 02.00-05.00 p.m. Based on previous research, the best stomata openings were in the morning and afternoon. Because during the daytime the evaporation rate was high, so the stomata would automatically close to reduce the rate of evaporation. At the end of the study, the Kailaan plant age was 44 day after seedling. Water and nutrition were given evenly and equally for all research treatments. Water was given to plants every morning (07.00 a.m) and in the afternoon (05.00 p.m) with a dose of 40-50 mL for each water supply. The nutrition provided was a mixture of vermicompost and soil in a ratio of 1:1. Plants that had been sown for 15 days were then transferred to a polybag with a mixture of vermicompost (25 kg) and soil (25 kg). Apart from giving vermicompost, nutrients were also given to plants in the form of organic liquid fertilizer 10 mL every 3 days at 07.00 a.m and 02.00 p.m. The sound applied as PAFT treatment was derived from Javanese Gamelan music entitled Puspawarna whose frequency had been set by using the Audacity application. The Javanese gamelan acoustic was taken directly from the recording process of a Javanese gamelan music. From the music data that had been taken, then the sound was corrected to eliminate noise and the frequency was adjusted to 3-5 kHz, 7-9 kHz, and 11-13 kHz using audacity software. The results of measurements in each level of frequency were illustrated in Figure 2. The frequency range shown in Figure 2 (3-5 kHz; 7-9 kHz; and 11-13 kHz) were applied in this study as frequency treatments. Determination of treatment was based on preliminary research (Hendrawan et al., 2018). From preliminary research, this study was recommended to apply the frequency level variation (Hassanien et al., 2014) ranging in 3-5 kHz, 7-9 kHz, and 11-13 kHz. The second treatment factors included sound exposure time (Pujiwati & Djuhari, 2014) for 1 hour, 2 hours, and 3 hours. The control plants as a comparison in this study were Kailaan plants without PAFT treatment. In this study, each treatment used five plants, so that the total plants used were 50 plant samples. However, from these samples only three samples were selected that were the best for each treatment. Environmental factors in the greenhouse had been optimally conditioned for the growth of

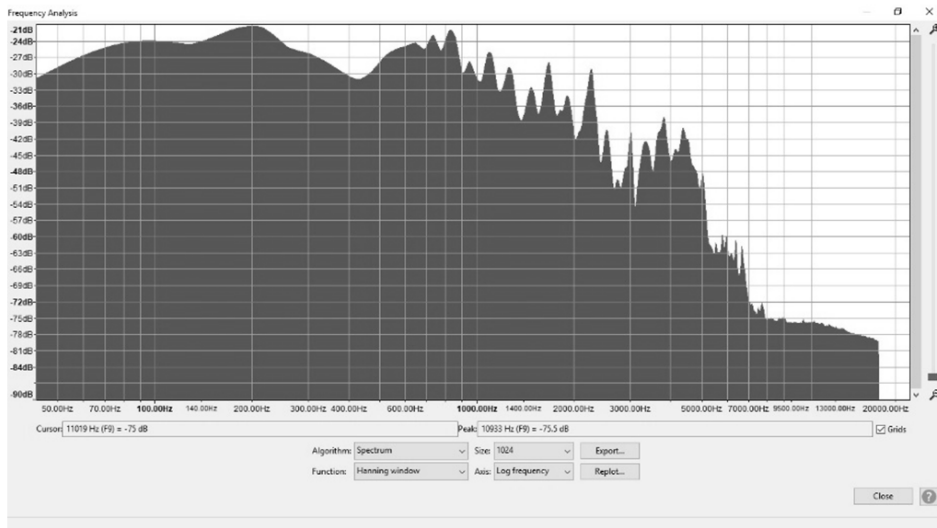
the Kailaan plant conveying: temperature control, air humidity, sound intensity, and light intensity. The PAFT test results were performed on several vegetative aspects of Kailaan plants, including: amount of chlorophyll / chlorophyll content index (cci), plant length (cm), plant wet weight (g), leaf area (cm²), plant height (cm), number of leaves (strands), and stomata opening diameter (μm) at the top of the leaf and at the bottom of the leaf. The measurement of plant height was performed by measuring plant height starting from the base of the stem which was parallel to the surface of the planting medium to the base of



(a)



(b)



(c)

Figure 2(a), (b) & (c). Analysis of frequency measurements by using Audacity

the plant stem. The measurement of plant height was conducted for every 3 days, starting from the 3rd day until the plants were 24 days old. The number of leaves was measured by selecting and counting each leaf of Kailaan plant. The selected leaves included the leaves that have begun to open until the leaves widely open; thus, leaves which were facedown were excluded. Calculation of the number of leaves in Kailaan plant was conducted for every 3 days until the plants are 24 days old. The measurement of leaf area was carried out when the plant was 24 days after planting, where the selected leaves were in the position of seven strands from the bottom of the stem for all observation samples. Measurement of wet weight was conducted when the plant was 24 days old after planting. Measuring the amount of leaf chlorophyll was performed when the plant was 24 days old after planting. Measurements were conducted before the plants were removed from the planting media. Measurements were conducted by using Chlorophyll meter from Konica Minolta SPAD 502. The selected leaves were six strands from the bottom of the base which were carried out in all treatment samples. Measurements were only carried out on the center of the leaf because the middle part contains the most chlorophyll by avoiding measurements on the leaf bone and mesophyll tissue. The measurement of plant length was performed after the plants were 24 days old after planting. The plants were placed on a flat medium to measure the length of Kailaan by using a ruler in a row, starting from the root to the top of the Kailaan stem. Stomata observation was conducted by using a digital microscope. The observation method for diameter of leaf stomata opening was conducted by selecting one of the three samples in each treatment, and later by applying transparent nail polish to the middle at the top and bottom of the leaves. In addition, after drying, transparent

nail paint was released from the leaves and observed by using a digital microscope of 40x magnification. Statistical analysis was conducted to test the significance of treatment in this study. Data from the study using two treatments i.e. different frequency levels and duration of time of exposure to sound in plants were analyzed using analysis of variance (ANOVA). After the ANOVA test was carried out and it was found that the results were significantly different then it was further tested using DMRT (Duncan's Multiple Range Test) (Kamal et al., 2018; Hossain et al., 2019).

RESULTS AND DISCUSSIONS

The results of Kailaan products after undertaking several treatment variations are depicted in Figure 3 and Figure 4. From the visual observations, Kailaan treated with PAFT demonstrated better result than the untreated Kailaan plants. Meanwhile, the quality of Kailaan plants among treatments was rather difficult to distinguish; thus, it was necessary to accurately measure vegetative parameters. Suwardi (2010) had also proven that there were significant differences between plants with PAFT and without PAFT. The results indicated that PAFT provided more optimal results in plant growth (Mishra et al., 2016; Chowdhury et al., 2014). Pujiwati et al. (2018) also explained the results of the research in which PAFT treatment on optimal frequency could improve the quality of vegetable crops including stomata openings, plant weight, harvest index, and leaf area with significant results.

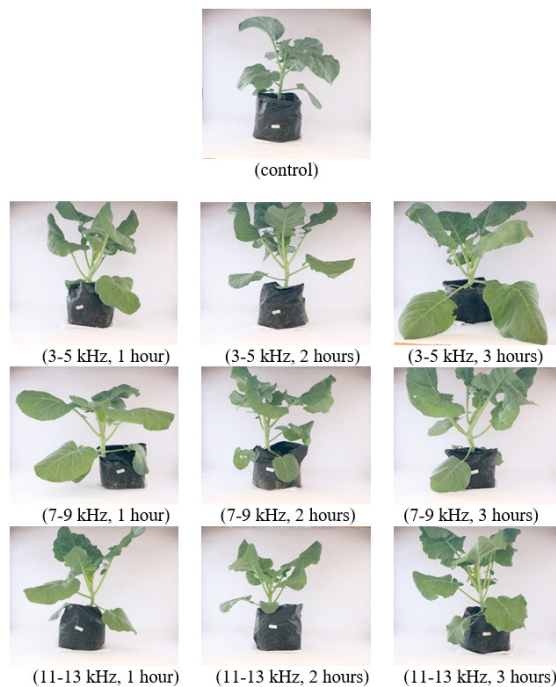


Figure 3. The results of Kailaan plant appearing side-by-side

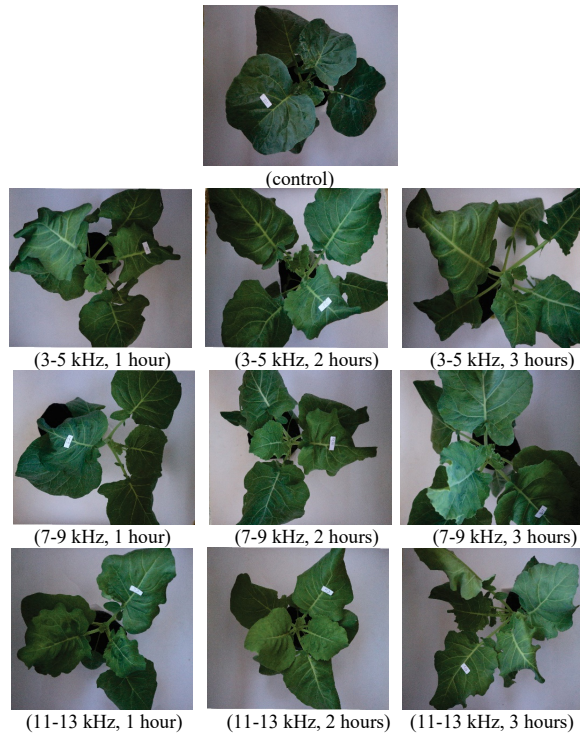


Figure 4. The results of Kailaan plant appearing above

From the data observed by the amount of leaf chlorophyll, it is apparent that the highest average value (80.86 cci) was found in the treatment frequency of 3-5 kHz and PAFT exposure time for 3 hours. Whereas, the lowest observation in the amount of leaf chlorophyll (48.96 cci) was found in the treatment frequency of 3-5 kHz and PAFT exposure time for 1 hour. The graph depicting the observation of the average number of chlorophyll leaves in each treatment is presented in Figure 5. The result of the PAFT test was able to increase the average of leaf chlorophyll by 61.5% than control treatment. From the ANOVA test results obtained that the treatment with the level of frequency and duration of exposure did not have a significant effect on the level of significance ($\alpha = 0.05$). However, PAFT in several studies has demonstrated to significantly increase the amount of leaf chlorophyll during growth. In several previous studies, it was proven that tomato, lettuce, and spinach plants which were given the PAFT treatment, significantly increased the amount of chlorophyll at a frequency of 0.08 ~ 2 kHz with an exposure time of 180 minutes compared to plants that did not apply PAFT (Hou & Mooneyham, 1999a; Hou & Mooneyham, 1999b). Whereas, the cucumber and sweet pepper plants are recognized to have the highest increase in the amount of chlorophyll at a frequency of 0.08 ~ 2 kHz with an exposure time of 180 minutes which is given once every day (Hassanien et al., 2014). Meng et al. (2012) in his research on the implementation of PAFT on strawberry

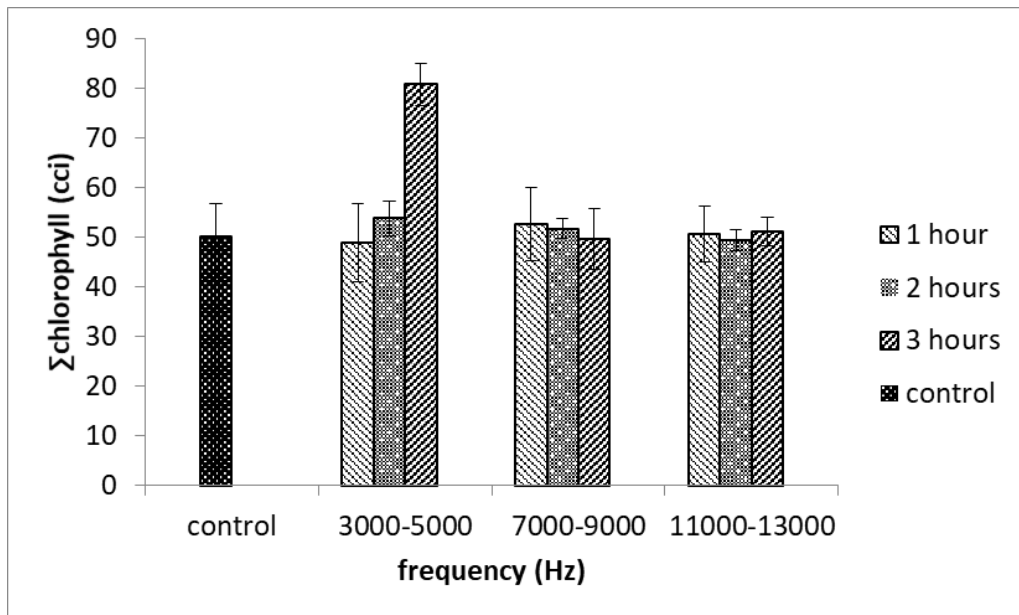


Figure 5. Relationship between variation in frequency and PAFT exposure time to the amount of chlorophyll of Kailaan leaves

plants, found that acoustic frequency treatments could optimally improve photosynthetic processes, which also affected the increase in the amount of leaf chlorophyll. Zakariya et al. (2017) tested PAFT on Mustard Pakcoy plants with significant results to increase total chlorophyll reaching 27.7%.

On the observation of Kailaan plant length, it is apparent that the highest average value (47.33 cm) was found in the treatment frequency of 3-5 kHz and the exposure time of PAFT for 3 hours. Meanwhile, the result from observations of the lowest plant length (30.00 cm) is found in the treatment frequency of 11-13 kHz and PAFT exposure time for 1 hour. Graphs of plant length observations are depicted in Figure 6. The result of PAFT test was able to increase the plant length by 35.2% than control plant. The statistical tests were conducted by using the real level ($\alpha = 0.05$) demonstrating that the treatment with various frequency and exposure time of PAFT, significantly affected the length of the Kailaan plant. From the results of Duncan’s multiple range test (DMRT) with 5% level, it was found that various frequency treatment with the most significant effect was at 3-5 kHz with an average plant length of 40.00 cm, while the treatment with PAFT exposure time for 3 hours, an average plant length was 43.33 cm. From this result, it is assumed that PAFT can have a significant effect on the length of the Kailaan plant, where the best treatment for plant length is reached at a frequency of 3-5 kHz and exposure time of 3 hours. PAFT is proven to significantly increase plant length. Wang et al. (2003) proved the success of PAFT in significantly increasing plant length in paddy rice seeds, compared to the untreated

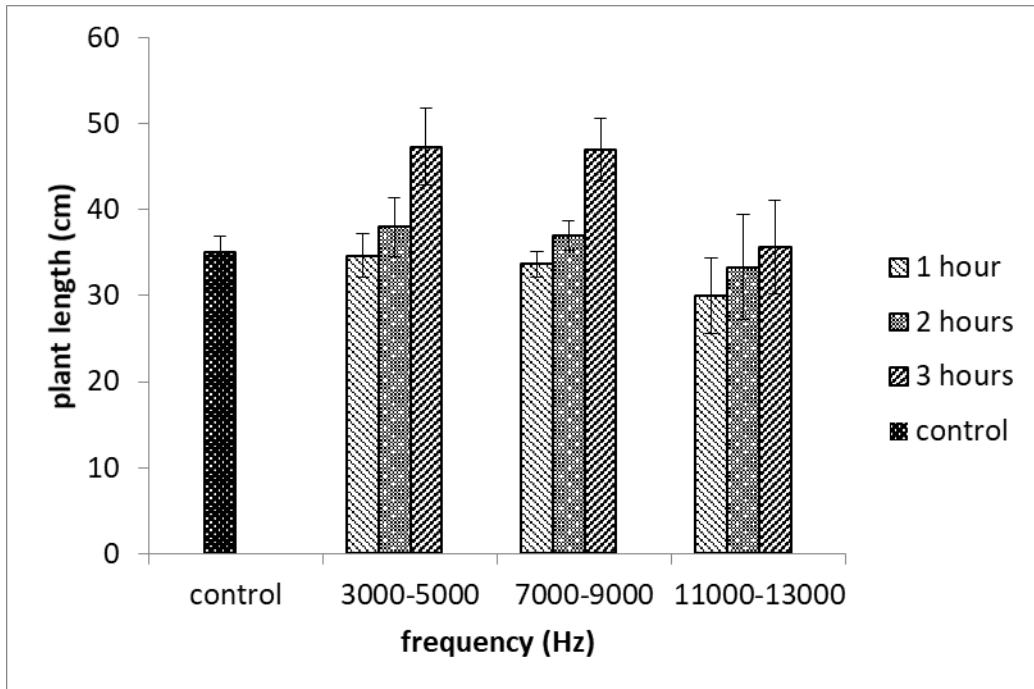


Figure 6. Relationship between variations in frequency and PAFT exposure time to Kailaan plant length

paddy rice seeds. In this study, the best results were obtained at the acoustical instrument frequency of 0.4 kHz. Cai et al. (2014) proved that PAFT could significantly increase the length of vegetable plants with the best frequency treatment at ± 2.5 kHz.

The results Kailaan plant wet weight indicated that the highest value of plant wet weight (84.00 g) was found in the treatment frequency of 3-5 kHz and the exposure time of PAFT for 3 hours. The lowest value of plant wet weight (34.66 g) was found in the treatment frequency 11-13 kHz and PAFT exposure time for 2 hours. Figure 7 illustrates the results of the average wet weight in each treatment. The result of PAFT test was able to increase the wet weight by 106.7% than control treatment. The results of the statistical analysis indicated that the treatment with variations in frequency and exposure time of PAFT significantly affected the wet weight of Kailaan plant. The results of DMRT demonstrated that the most significant frequency variation treatment was at a frequency of 3-5 kHz with an average wet plant weight of 64.33 g, while the treatment of PAFT exposure time with the most significant effect was at 3 hours with an average wet plant weight of 64.66 g. From the results of this statistical test, it is concluded that PAFT has a significant effect on Kailaan wet weight with the best treatment at a frequency of 3-5 kHz and PAFT exposure time for 3 hours. In several other studies, it was also proven that PAFT can significantly increase plant weight (dry weight and fresh weight). The 5 kHz frequency can increase the dry weight of wheat plants (Weinberger & Measures, 1979), while the 0.4 kHz frequency

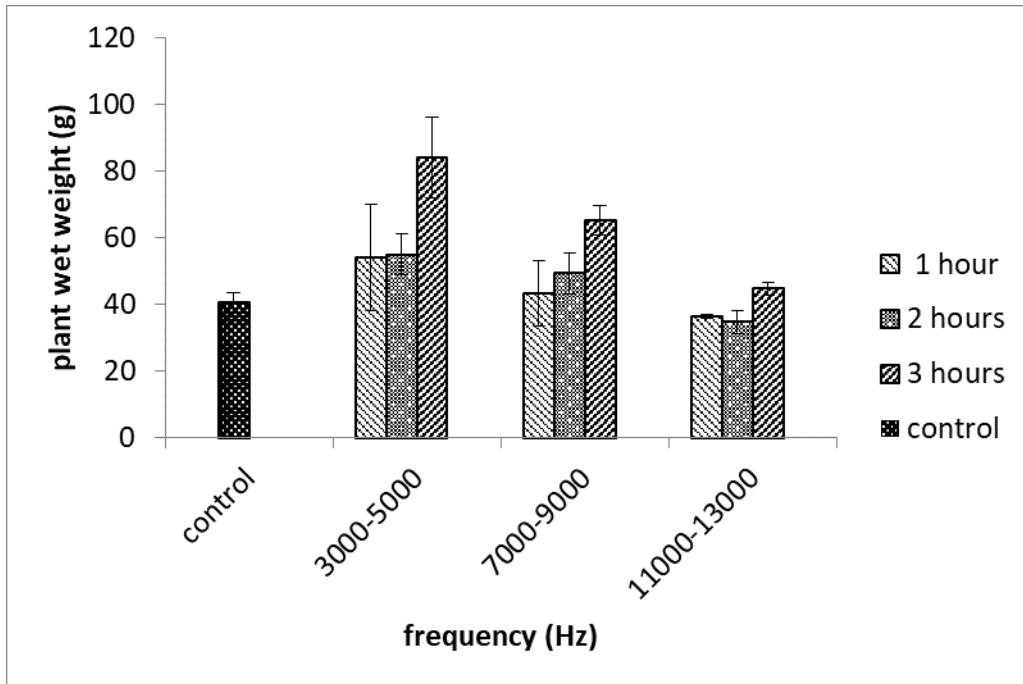


Figure 7. Relationship between variations in frequency and PAFT exposure time to Kailaan plant wet weight

can increase fresh weight on paddy rice seeds (Wang et al., 2003). Pujiwati and Djuhari (2014) also had proven that PAFT treatment with high-frequency could significantly increase fresh-weight of soybean plants. This result is also in accordance with the results of research conducted by Zakariya et al. (2017) with PAFT at a frequency of ± 2 kHz increasing the wet weight of vegetable plants by 25.6%. Cai et al. (2014) also examined the utilization of PAFT which could significantly increase the wet weight of vegetable plants with the best frequency treatment on ± 2.5 kHz.

The next parameter measured to observe Kailaan leaf area, in which the highest leaf area average value (207.06 cm²) was found in the treatment frequency of 3-5 kHz and PAFT exposure time for 3 hours. The lowest leaf area (98.58 cm²) was found in the treatment frequency of 11-13 kHz and PAFT exposure time for 2 hours. Figure 8 presents observations of leaf area for each treatment. The result showed that PAFT was able to increase the leaf area by 71.0% than control plant. The statistical analysis test indicated that the treatment with variations in frequency and exposure time of PAFT had a significant effect on Kailaan leaf area. This finding is evidenced, where the treatment with frequency variations has sig. ($\alpha = 0.002$) and treatment with variations in PAFT has sig. ($\alpha = 0.00$), indicating that both treatments have $< (\alpha = 0.05)$. Therefore, ANOVA test was conducted by using DMRT for both treatments. The result of DMRT advanced test with a real level of 5% indicated that the most significant frequency variation treatment was at a frequency of 7-9 kHz with

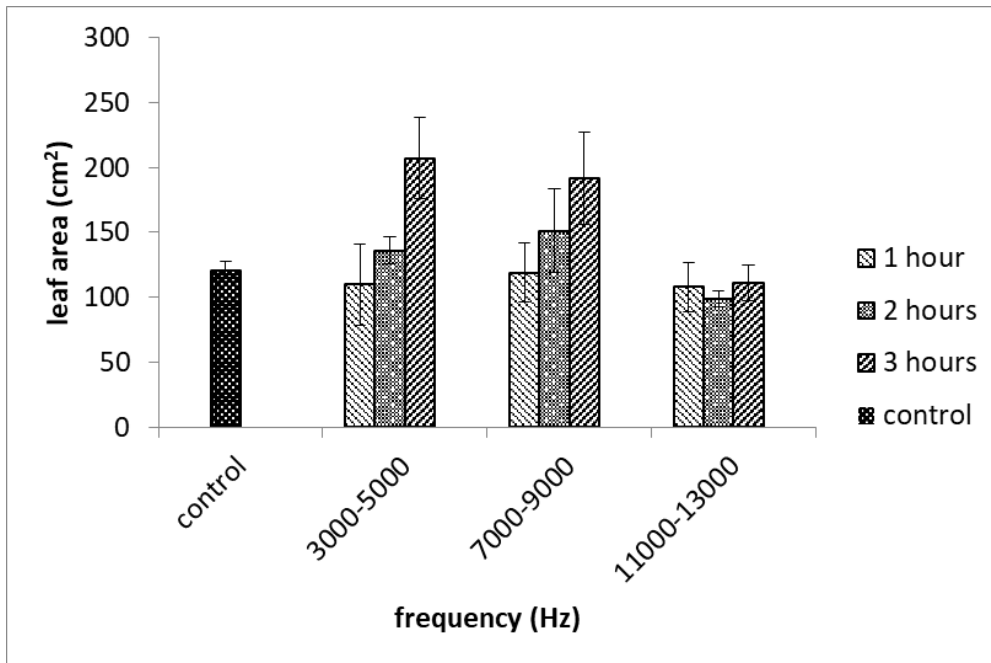


Figure 8. Relationship between variation in frequency and PAFT exposure time to Kailaan leaf area

an average leaf area of 153.92 cm², while the treatment with PAFT exposure time was the most significant at 3 hours with a leaf area average of 169.80 cm². From these results, it is assumed that the utilization of PAFT can have a significant effect on the area of Kailaan leaves where the best treatment is at a frequency of 7-9 kHz and the length of time exposed is 3 hours. The increase in leaf area due to PAFT treatment is also in line with the results of research conducted by Pujiwati and Djuhari (2014) where PAFT treatment with high frequency (± 10 kHz) could significantly increase the leaf area of soybean plants. This result is also in accordance with the study of Zakariya et al. (2017) who utilized PAFT for Pakcoy vegetable plants, presenting a significant increase in leaf area to reach 30.9%.

Observation of the height of the Kailaan plant has also been carried out, indicating that the highest average value (11.60 cm) was found in the treatment frequency of 3-5 kHz and PAFT exposure time for 2 hours. The lowest plant height (7.33 cm) was found in the frequency treatment 11-13 kHz and PAFT exposure time for 1 hour. Figure 9 provides observations of plant height for each treatment frequency and exposure time of PAFT. It shows that PAFT treatment was able to increase the plant height by 0.8% than control treatment. The results of the statistical analysis test indicated that the frequency variation treatment had a significant effect on the height of the Kailaan plant. The frequency treatment parameter has sig ($A = 0.005$) < ($\alpha = 0.05$). In DMRT test, it is concluded that the most significant frequency variation treatment was at a frequency of 3-5 kHz with an average

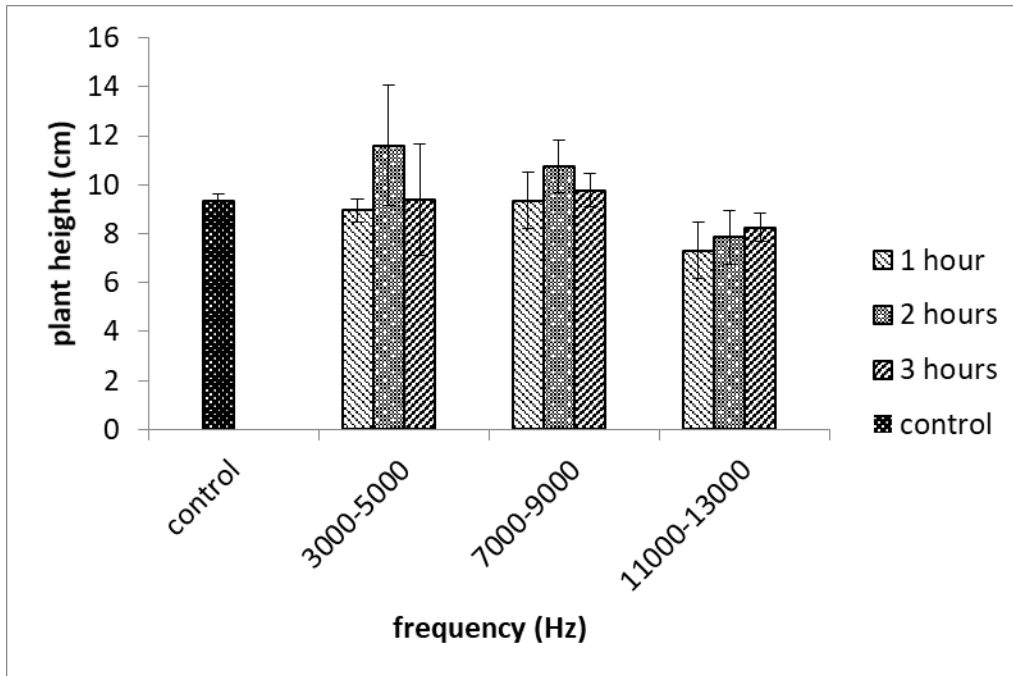


Figure 9. Relationship between variation in frequency and PAFT exposure time to Kailaan plant height

plant height of 9.98 cm. In a study conducted by Carlson (2013), it was proven that PAFT was able to increase plant height by using a 3-5 kHz frequency treatment given once a day for 180 minutes. In the study of Pujiwati and Djuhari (2014) high-frequency PAFT gave significant results to increase plant height. Whereas, in the study of Zakariya et al. (2017), it was proven that PAFT was able to increase vegetable height significantly until it reached 10.4%.

From the data observed, the number of Kailaan leaves with the highest average value was found in the treatment frequency of 3-5 kHz and 11-13 kHz with the exposure time of PAFT for 3 hours with 11 strands. Meanwhile, the smallest number of leaves was found at the 11-13 kHz frequency and PAFT exposure time for 1 hour with 9.33 strands. The results of observations on the number of leaves in each treatment are depicted in Figure 10. It shows that PAFT was able to increase the number of leaves by 13.9% than control plant. The results of the statistical analysis indicated that the exposure to PAFT significantly affected the number of leaves of the Kailaan plant. The time of exposure had sig. ($F = 0.032$) < ($\alpha = 0.05$). From the results of DMRT follow-up test with a real level of 5%, it was found that the best result of the treatment for PAFT exposure time was at 3 hours of treatment with 10.88 leaves. In a study conducted by Carlson (2013) and Hou et al. (1999a), it was proven that PAFT was able to increase the number of leaf plants by applying a 3-5 kHz frequency treatment given once a day for 180 minutes.

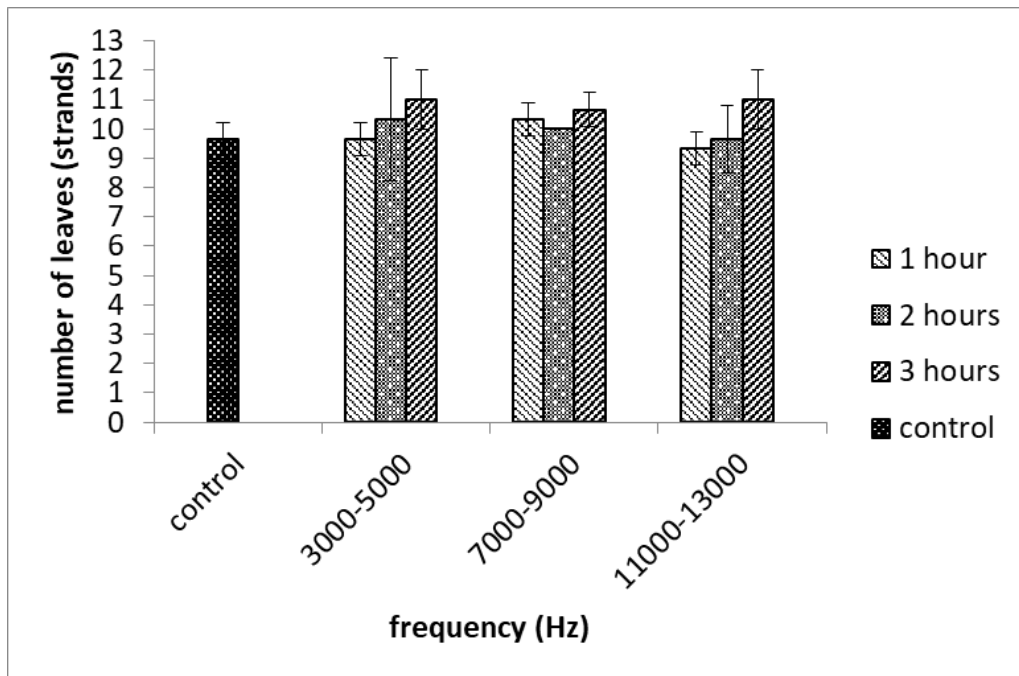


Figure 10. Relationship between variations in frequency and PAFT exposure time to number of Kailaan leaves

Stomata is the most important part of the plant due to its function as a place of respiration process. PAFT is a technology that utilizes the frequency of sound to stimulate the wider opening of leaf stomata. In Figure 11 and Figure 12, stomata openings are given PAFT exposure at frequencies of 3-5 kHz, 7-9 kHz, and 11-13 kHz as well as exposure times of 1 hour, 2 hours and 3 hours. From Figure 11 and Figure 12, it can be concluded that the total distribution of the widest stomata opening is in the lower stomata of the leaf. In addition, wider stomata openings are in the PAFT treatment with a frequency of 3-5 kHz compared to the treatment of 7-9 kHz, 11-13 kHz and control, where the PAFT treatment affects both stomata opening at the bottom and top of the leaf. At the best treatment, which is at a frequency of 3-5 kHz and exposure time of 3 hours, the most optimal stomata opening diameter at the top of the leaf was 89.19 - 93.45 μm and the stomata opening diameter at the bottom of the leaf was 136.69 - 140.74 μm . Thus, PAFT with a frequency scale and optimal exposure time can have a significant effect on the stomata openings of Kailaan plant. PAFT was able to increase the stomata opening at the top part of the leaf by 30.5%, and increase the stomata opening at the bottom part of the leaf by 79.4% than control treatment. Carlson (2013) had proven that frequency of 3-5 kHz had an effect on the optimal opening of the stomata to grasp free nutrients in the air including nitrogen and water. Pudjiwati and Djuhari (2014) suggested in a study that PAFT with high sound frequencies influenced stomata openings which ultimately increased the uptake of free nutrients in the air increasing plant productivity. This result is also in line with the study of

Javanese Gamelan Music on the Growth of Chinese Broccoli

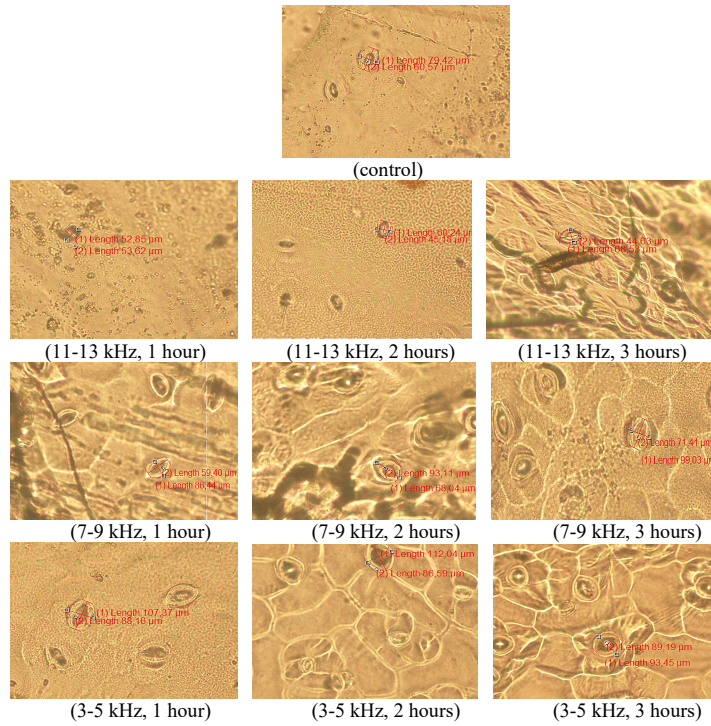


Figure 11. Enlargement image of stomata opening at the top part of the leaf

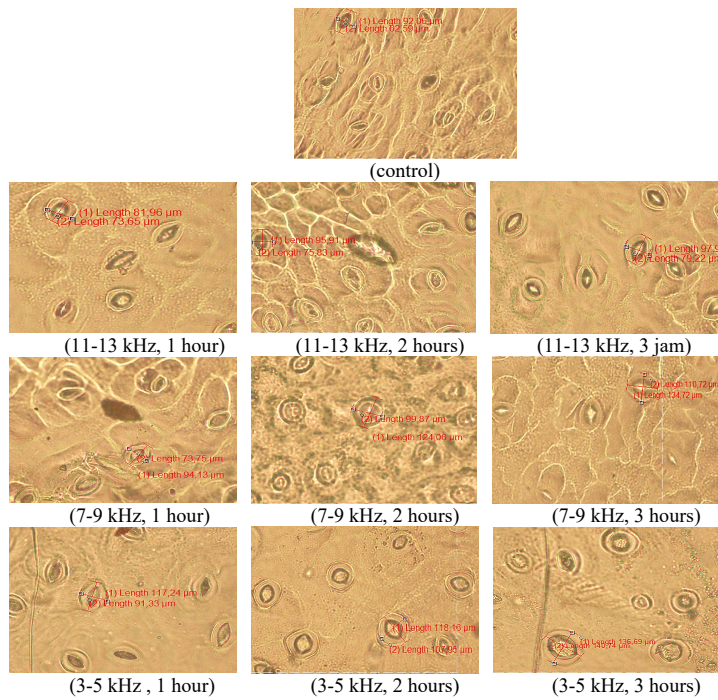


Figure 12. Enlargement image of stomata opening at the bottom part of the leaf

Zakariya et al. (2017) who applied PAFT to Mustard Pakcoy plants, in which leaf stomata openings increased to 28.4%.

CONCLUSIONS

Based on the results of the study, it can be concluded that the frequency of 3-5 kHz and exposure time of 3 hours are the best plant acoustic frequency technology (PAFT) treatment in Kailaan with the value of leaf chlorophyll, plant length, wet weight, leaf area, plant height, number of leaves, stomata opening width at the top of the leaf, and stomata opening width at the bottom of the leaf are 80.86 cci, 47.33 cm, 84.00 g, 207.06 cm², 11.60 cm, 11 strands, 89.19 ~ 93.45 μm, and 136.69 ~ 140.74 μm, respectively. The result of the PAFT test was able to increase the average of leaf chlorophyll by 61.5%, increase the plant length by 35.2%, increase the wet weight by 106.7%, increase the leaf area by 71.0%, increase the plant height by 0.8%, increase the number of leaves by 13.9%, increase the stomata opening at the top part of the leaf by 30.5%, and increase the stomata opening at the bottom part of the leaf by 79.4% than control treatment. It was found that the PAFT had a significant effect on the productivity and quality of Kailaan plants. For further development, PAFT using gamelan music can be combined with plant response-based sensing to improve the quality of vegetables in a closed bioproduction system.

ACKNOWLEDGEMENTS

The authors wish to acknowledge support from Department of Agricultural Engineering, Faculty of Agricultural Technology, University of Brawijaya, for assistance given during the research. This study was funded by Associate Professor Research Grant Program (Hibah Doktor Lektor Kepala 2019), University of Brawijaya, the Ministry of Research, Technology, and Higher Education of the Republic of Indonesia.

REFERENCES

- Ankur, P., Sangeetha, S., & Seema, N. (2016). Effect of sound on the growth of plant: plants pick up the vibration. *Asian Journal of Plant Science and Research*, 6(1), 6-9.
- Baslam, M., Garmendia, I., & Goicoechea, N. (2012). Elevated CO₂ may impair the beneficial effect of arbuscular mycorrhizal fungi on the mineral and phytochemical quality of lettuce. *Annals of Applied Biology*, 161, 180-191.
- Becker, C., & Kläring, H. (2016). CO₂ enrichment can produce high red leaf lettuce yield while increasing most flavonoid glycoside and some caffeic acid derivative concentrations. *Food Chemistry*, 199, 736-745.
- Cai, W., He, H., Zhu, S., & Wang, N. (2014). Biological effect of audible sound control on mug bean (*Vigna radiate*) sprout. *BioMed Research International*, 2014, 1-6.

- Carlson, D. (2013). *Sonic bloom organic farming made easy! The best organic fertilizer in the world*. Retrieved July 29, 2019, from http://www.relfe.com/sonic_bloom.html.
- Chalabi, Z. S., Biro, A., Bailey, B. J., Aikman, D. P., & Cockshull, K. E. (2002). Optimal control strategies for carbon dioxide enrichment in greenhouse tomato crops*Part 1: using pure carbon dioxide. *Biosystems Engineering*, *81*, 421-431.
- Chowdhury, M. E. K., Lim, H. S., & Bae, H. (2014). Update on the effects of sound wave on plants. *Research in Plant Disease*, *20*(1), 1-7.
- Collins, M., & Foreman, J. K. (2001). The effect of sound on the growth of plants. *Canadian Acoustic*, *29*(2), 3-8.
- Gagliano, M., Stefano, M., & Daniel, R. (2012). Towards understanding plant bioacoustics. *Trends in Plant Science*, *17*, 323-325.
- Graamans, L., Baeza, E., Dobbelsteen, A., & Tsafaras, I. (2018). Plant factories versus greenhouses: Comparison of resource use efficiency. *Agricultural Systems*, *160*, 31-43.
- Hanson, P. M., Yang, R. Y., Wu, J., Chen, J. T., Ledesma, D., Tsou, S. C. S., & Lee, T. C. (2004). Variation for antioxidant activity and antioxidants in tomato. *Journal of the American Society for Horticultural Science*, *29*, 704-711.
- Hanson, P., Yang, R., Chang, L., Ledesma, L., & Ledesma, D. (2011). Carotenoids, ascorbic acid, minerals, and total glucosinolates in choysum (*Brassica rapa* cvg. parachinensis) and kailaan (*B. oleraceae* Alboglabra group) as affected by variety and wet and dry season production. *Journal of Food Composition and Analysis*, *24*, 950-962.
- Hassanien, R. H. E., Hou, T. Z., Li, Y. F., & Li, B. M. (2014). Advances in effects of sound waves on plants. *Journal of Integrative Agriculture*, *13*(2), 335-348.
- Hendrawan, Y., Anta, D. K., Ahmad, A. M., & Sutan, S. M. (2019). Development of fuzzy control systems in portable cultivation chambers to improve the quality of oyster mushrooms. *IOP Conference Series: Materials Science and Engineering*, *546*(3), 1-7.
- Hendrawan, Y., Lazuardi, I. B., Umam, C., & Sutan, S. M. (2018, November 1-2). Effect of sonic bloom on vegetative growth of lettuce plants (*Lactuca sativa* L.). In *Proceedings of the 2nd International Seminar and Workshop of Plant Industry* (pp. 189-199). Jember, Indonesia.
- Hossain, M. A., Islam, M. A., Azad, M. A. K., Rahman, M. M., Shumi, W., & Shukor, N. A. A. (2019). Propagation of an endangered gymnosperm tree species (*Podocarpus neriifolius* D. Don.) by stem cutting in non-mist propagator. *Pertanika Journal of Tropical Agricultural Science*, *42*(1), 237-250.
- Hou, T. Z., & Li, M. D. (1997). Experimental evidence of a plant meridian system: IV. The effects of acupuncture on growth and metabolism of *Phaseolus vulgaris* L. beans. *The American Journal of Chinese Medicine*, *25*, 135-142.
- Hou, T. Z., Luan, J. Y., Wang, J. Y., & Li, M. D. (1994). Experimental evidence of a plant meridian system: III. The sound characteristics of Phylodendron (*Alocasia*) and effects of acupuncture on those properties. *The American Journal of Chinese Medicine*, *22*, 205-214.
- Hou, T. Z., & Mooneyham, R. E. (1999a). Applied studies of plant meridian system: I. The effect of agri-wave technology on yield and quality of tomato. *The American Journal of Chinese Medicine*, *27*, 1-10.

- Hou, T. Z., & Mooneyham, R. E. (1999b). Applied studies of the plant meridian system: II. Agri-wave technology increases the yield and quality of spinach and lettuce and enhances the disease resistant properties of spinach. *The American Journal of Chinese Medicine*, 27, 131-141.
- Jaramillo, A. A. F., Galvan, C. D., Mier, L. G., Garcia, S. N. J., & Medina, L. M. C. (2018). Effects of acoustic waves on plants: An agricultural, ecological, molecular and biochemical perspective. *Scientia Horticulturae*, 235, 340-348.
- Kamal, N. H. M., Aziz, M. A., Kadzimi, S., & Rashid, A. A. (2018). In vitro mass multiplication of *Artocarpus heterophyllus* Lam var. Tekam Yellow. *Pertanika Journal of Tropical Agricultural Science*, 41(3), 1289-1314.
- Khan, I., Azam, A., & Mahmood, A. (2013). The impact of enhanced atmospheric carbon dioxide on yield, proximate composition, elemental concentration, fatty acid and vitamin C contents of tomato (*Lycopersicon esculentum*). *Environmental Monitoring and Assessment*, 185, 205-214.
- Kim, J. Y., Lee, J. S., Kwon, T. R., Lee, S. I., Kim, J. A., Lee, G. M., ... & Jeong, M. J. (2018). Sound waves delay tomato fruit ripening by negatively regulating ethylene biosynthesis and signaling genes. *Postharvest Biology and Technology*, 110, 43-50.
- Ksas, B., Becuwe, N., Chevalier, A., & Havaux, M. (2015). Plant tolerance to excess light energy and photooxidative damage relies on plastoquinone biosynthesis. *Scientific Reports*, 5, 1-16.
- Kyriacou, M. C., Roupheal, Y., Di Gioia, F., Kyrtziz, A., Serio, F., Renna, M., ... & Santamaria, P. (2016). Micro-scale vegetable production and the rise of microgreens. *Trends in Food Science and Technology*, 57, 103-115.
- Leyva, R., Constán-Aguilar, C., Blasco, B., Sánchez-Rodríguez, E., Romero, L., Soriano, T., & Ruíz, J. M. (2014). Effects of climatic control on tomato yield and nutritional quality in Mediterranean screenhouse. *Journal of the Science of Food and Agriculture*, 94, 63-70.
- Li, Q., & Kubota, C. (2009). Effects of supplemental light quality on growth and phytochemicals of baby leaf lettuce. *Environmental and Experimental Botany*, 67, 59-64.
- Lin, K. H., Huang, M. Y., Huang, W. D., Hsu, M. H., Yang, Z. W., & Yang, C. M. (2013). The effects of red, blue, and white light-emitting diodes on the growth, development, and edible quality of hydroponically grown lettuce (*Lactuca sativa* L. var. *capitata*). *Scientia Horticulturae*, 150, 86-91.
- Max, J. F. J., Horst, W. J., & Mutwiwa, U. N. (2009). Effects of greenhouse cooling method on growth, fruit yield and quality of tomato (*Solanum lycopersicum* L.) in a tropical climate. *Scientia Horticulturae*, 122, 179-186.
- Meng, Q. W., Zhou, Q., Zheng, S. J., & Gao, Y. (2012). Responses on photosynthesis and variable chlorophyll fluorescence of *Fragaria ananassa* under sound wave. *Energy Procedia*, 16, 346-352.
- Mishra, R. C., Ghosh, R., & Bae, H. (2016). Plant acoustics: in the search of a sound mechanism for sound signaling in plants. *Journal of Experimental Botany*, 67(15), 4483-4494.
- Okuda, N., Fujime, Y., & Varanyanond, W. (2000). Earliness and self-compatibility of Chinese kale (*Brassicaoleracea* L. var. *albolabra* L. H. Bailey). *Acta Horticulturae*, 533, 89-97.

- Pujiwati, I., & Djuhari. (2014). The pattern of stomatal opening through the exposure of high-frequency sound wave with the different duration and age of soybeans (*Glycine mas (L.) Merrill*). *Agricultural Science*, 2(1), 69-77.
- Pujiwati, I., Aini, N., Sakti, S. P., & Guritno, B. (2018). The effect of harmonic frequency and sound intensity on the opening of stomata, growth, and yield of soybean (*Glycine max (L.) Merrill*). *Pertanika Journal of Tropical Agricultural Science*, 41(3), 963-974.
- Rouphael, Y., Kyriacou, M. C., Petropoulos, S. A., & Colla, S. G. (2018). Improving vegetable quality in controlled environments. *Scientia Horticulturae*, 234, 275-289.
- Sagwansupyskorn, C. (1993). Brassicaoleracea L. cv. group Chinese kale. In J. S. Siemonsma & K. Piluek (Eds.), *PROSEA Plant Resources Southeast Asia no. 8: Vegetables* (pp. 115-117). Wageningen, Netherland: Food and Agriculture Organization of the United Nations.
- Sgherri, C., Pérez-López, U., Micaelli, F., Miranda-Apodaca, J., Mena-Petite, A., Muñoz- Rueda, A., & Quartacci, M. F. (2017). Elevated CO₂ and salinity are responsible for phenolics-enrichment in two differently pigmented lettuces rez-L o. *Plant Physiology and Biochemistry*, 115, 269-278.
- Suardi. (2010). Study influence usage frequency sound waves on soybean seed growth. *Journal of Physics FLUX*, 7(2), 170-176.
- Umam, C., Sutan, S. M., & Hendrawan, Y. (2019). Fuzzy logic in determining the control temperature and humidity in plant factory for cultivation of pak choy (*Brassica chinensis L.*) hydroponics. *Indonesian Green Technology Journal*, 8(1), 9-14.
- Urrestarazu, M., Salas, C., Valera, D., Gómez, A., Mazuela, P. C., Urrestarazu, M., ... & Mazuela, P. C. (2008). Effects of heating nutrient solution on water and mineral uptake and early yield of two cucurbits under soilless culture. *Journal of Plant Nutrition*, 31, 527-538.
- Vanhassel, P., Bleyaert, P., Van Lommel, J., Vandevelde, I., Crappé, S., Van Hese, N., ... & Van Labeke, M.C. (2015). Rise of nightly air humidity as a measure for tipburn prevention in hydroponic cultivation of butterhead lettuce. *Acta Horticulturae*, 1107, 195-202.
- Wang, B. C., Yoshikoshi, A., & Sakanishi, A. (1998). Carrot cell growth response in a stimulated ultrasonic environment. *Colloids and Surfaces (B: Biointerfaces)*, 12, 89-95.
- Wang, B. C., Chen, X., Wang, Z., Fu, Q. Z., Zhou, H., & Ran, L. (2003). Biological effect of sound field stimulation on paddy rice seeds. *Colloids and Surfaces (B: Biointerfaces)*, 32, 29-34.
- Weiming, C., Songming, Z., Wang, N., Huinong, H., & Beihua, Y. (2015). Design of an experimental platform to investigate the effect of audible sounds on plant growth. *International Journal of Agricultural and Biological Engineering*, 8(5), 162-169.
- Weinberger, P., & Measures, M. (1979). Effects of the intensity of audible sound on the growth and development of Rideau winter wheat. *Canadian Journal of Botany*, 57, 1036- 1039.
- Zakariya, F. M., Rivai, M., & Aini, N. (2017, August 28-29). Effect of automatic plant acoustic frequency technology (PAFT) on mustard pakcoy (*Brassica rapa var. parachinensis*) plant using temperature and humidity parameters. In *IEEE Proceedings on 2017 International Seminar on Intelligent Technology and Its Applications* (pp. 334-339). Surabaya, Indonesia.

Zhao, H. C., Wu, J., Xi, B. S., & Wang, B. C. (2002). Effects of sound-wave stimulation on the secondary structure of plasma membrane protein of tobacco cells. *Colloids and Surfaces (B: Biointerfaces)*, 25, 29-32.

A Genetic Algorithm Approach for Discovering Fuzzy Hierarchical Censored Classification Rules (FHCCRs)

Renu Bala* and Saroj Ratnoo

Department of Computer Science & Engineering, Guru Jambheshwar University of Science & Technology, Hisar, India

ABSTRACT

Most of the classification algorithms discover flat Fuzzy Classification Rules (FCRs) in ‘If-Then’ form. The knowledge discovered in the form of FCRs allows us to deal with vague, inexact and incomplete premises, however, it ignores exceptions and hierarchies that may exist in data. The simple FCRs enlarge the size of Rule Bases (RBs) with the presence of duplicate clauses that can be removed by arranging the rules in a hierarchical fashion. Moreover, such rules infer incorrect conclusions in the presence of exceptional conditions. This paper proposes the discovery of accurate, interpretable and interesting rules in a novel form named as Fuzzy Hierarchical Censored Classification Rules (FHCCRs) using a Genetic Algorithm approach. The GA design for discovering FHCCRs includes designing of suitable encoding scheme, fitness function and genetic operators. The suggested approach works in three phases: i) fuzzifying a dataset in a pre-processing step, ii) applying a genetic algorithm for discovering FHCCRs and iii) merging FHCCRs into bigger hierarchies in a post-processing step. The proposed approach is applied to five benchmark datasets. It successfully discovers FHCCRs which contain exceptions (also referred as censors) as well as hierarchies. The knowledge discovered in the form of FHCCRs enriches rule bases in respect of interpretability and interestingness.

Keywords: Classification rule discovery, fuzzy censored classification rules (FCCRs), fuzzy hierarchical classification rules (FHCRs), fuzzy hierarchical censored classification rules (FHCCRs)

ARTICLE INFO

Article history:

Received: 28 June 2018

Accepted: 19 April 2019

Published: 13 January 2020

E-mail addresses:

renu0805@gmail.com (Renu Bala)

ratnoo.saroj@gmail.com (Saroj Ratnoo)

* Corresponding author

INTRODUCTION

In real world problem domains, a machine has to make predictions using inadequate, vague and uncertain information. Fuzzy

Rule Based Systems (FRBSs) are proficient systems for reasoning with ambiguous, imprecise and/or incomplete information (Zadeh, 1996). Most of the FRBSs consist of Fuzzy Classification Rules (FCRs) that ignore hierarchical relationships among the data/class labels. Such conventional FRBSs are not suitable for domains, where knowledge can be better expressed at various levels of abstraction. Therefore, researchers have suggested knowledge structures like Hierarchical Production Rules (HPRSs) (Al-Maqaleh & Bharadwaj, 2005; Bharadwaj & Saroj, 2009; Bharadwaj & Kandelwal, 2007), Hierarchical Censored Production Rules (HCPRs) (Bharadwaj & Saroj, 2010; Bharadwaj & Jain, 1992; Jain & Bharadwaj, 1998) and Fuzzy Hierarchical Censored Production Rules (FHCPs) (Neerja & Bharadwaj, 1996) to support the discovery of hierarchical fuzzy classification rules.

While designing hierarchical classification systems, we need to consider variable certainty and specificity as the two aspects of variable precision logic. A system that gives more certain answers given more time (resources) is called a variable certainty system and a system that gives more specific answers given more time (resources) is called variable specificity system (Michalski & Winston, 1986). Certainty refers to the degree of belief in a conclusion and specificity refers to the degree of details contained in a Rule Base (RB). The two aspects of variable precision logic (certainty and specificity) are associated with accuracy and interpretability - the two fundamental characteristics of classifiers/RBs in data mining. Accuracy is the capability of a RB to closely represent the real-world knowledge whereas interpretability of a RB is the power to state the behavior of a real system in an interpretable way (Gacto et al., 2011). In this context, accuracy provides a measure of certainty while specificity relates to interpretability.

Accuracy and interpretability are indeed important performance monitoring metrics but are not sufficient to measure the real interestingness of a RB. A RB is considered interesting if the knowledge represented by it is not only formerly unknown but it is also in contrast to the original beliefs of its users (Kontonasios et al., 2012). Although interestingness is a subjective term, yet unexpected and exceptional knowledge is considered interesting. Discovery of exceptions is interesting because exceptions are unusual conditions that contradict the prior knowledge about the domain, add curiosity and improve the quality of decision making in those rare circumstances when the default or generalized rules cease to work. Exceptions, also termed as censors in the literature (Bharadwaj & Al-Maqaleh, 2007a), have low support, and therefore, it is not possible to discover exceptions using the typical classification rule discovery methods. Most of the classification algorithms focus on the generality of the knowledge discovered, whereas exceptions make rules specific.

In this paper, we propose a genetic algorithm approach to discover Fuzzy Hierarchical Censored Classification Rules (FHCCRs) which are the integration of Fuzzy Censored

Classification Rules (FCCRs) and Fuzzy Hierarchical Classification Rules (FHCRs) (Bala & Ratnoo, 2018). The proposed system discovers accurate and interpretable fuzzy classification rules. In addition, these rules are interesting and have the ability to make predictions with variable certainty and specificity. We have employed two quantitative measures, the degree of subsumption and coefficient of similarity, to determine the hierarchical relationships in FHCCRs. The proposed approach is tested on benchmark data sets from the UCI machine learning repository. The approach initially generates FCRs which are, subsequently, converted into FHCCRs by appending exceptions/censors and hierarchies.

The rest of the paper has the following structure. Second part describes the supporting knowledge structures for discovering hierarchical rules with exceptions/censors and the related work to contextualize this research. Third part describes the proposed system to discover FHCCRs. It includes the fuzzification process, GA design, and a post-processing scheme to merge individual FHCCRs. It also explains the concepts of the degree of subsumption and degree of similarity. The suggested approach is employed in experimental design followed by the results obtained and lastly, conclusion and future scope of this research have been discussed.

RELATED WORK

Intelligent and reasoning based systems have to work in an environment of uncertainty and vagueness. Hence, the Rule Bases (RBs) of these systems consist of Fuzzy Classification Rules (FCRs). Researchers have been working to make these rule bases more concise and useful by accommodating exceptional clauses and hierarchies in these rule bases. This section describes novel rule structures and takes account of the research carried out for discovering knowledge in these various advanced rule forms to create RBs for intelligent systems.

Fuzzy Censored Classification Rules

Exceptions (also referred as Censors in this work) are the rare conditions which change the behavior of a default rule. Exceptions/ Censors pertain to limited instances in data and, hence, often get ignored as machine noise, if not tackled separately. An FCCR is a combination of an FCR and a Censor Production Rule (CPR) (Michalski & Winston, 1986). FCCRs have discussed in detail in Bala (2012).

FCCRs cover one aspect of variable precision, logic, i.e., variable certainty, but specificity remains constant here. Next Section describes FHCCRs which support variable specificity also in drawing conclusions.

Fuzzy Hierarchical Censored Classification Rules

Fuzzy Hierarchical Censored Classification Rules (FHCCRs) are the rules that contain censor conditions as well as hierarchical information. An FHCCR is represented as:

If P is X Then C_k Unless E is Y: C_k'

Generality [C_g]

Specificity [C_{s1} , C_{s2}]

Here, 'E' represents the censor conditions, C_k represents the rule class, C_g is the general class and C_{s1} , and C_{s2} are the specific classes. The rule class C_k may change to C_k' when the censor condition E is true. The general class represents the most general concept and specific classes show the more specific concepts in the hierarchies. The following real world example shows the illustration of FHCCRs.

/ Level 0*/*

If (S is household servant for family F) Then (S does household_work) Unless (S is Sick or S is on leave: S does not work) Generality [] // The Rule Class itself is the most General class

Specificity [S cooks for family F, S drives for family F]

/ Level 1*/*

*If (S has **good** cooking skills) Then (S cooks for family F) unless (Family F is outside: S does not cook for family F) Generality [S does household_work] Specificity [S cooks breakfast, S cooks lunch, S cooks dinner]*

*If (S has **good** driving skills) Then (S drives for family F) Unless (S is defaulter: S does not drive for family F)*

Generality [S does household_work] Specificity [S drives bike, S drives car]

/ Level 2*/*

*If (time is **morning**) Then (S cooks breakfast) Unless (Family F wakes up late on Sundays: S does not cook breakfast) Generality [S cooks for family F] Specificity[]*

*If (time is **noon**) Then (S cooks lunch) Unless (Family F eats out: S does not cook lunch)*

Generality [S cooks for family F] Specificity[]

*If (time is **night**) Then (S cooks dinner) Unless ()*

Generality [S cooks for family F] Specificity[]

*If (S travels **short** distance) Then (S drives bike) Unless ()*

Generality [S drives for family F] Specificity []

*If (S travels **long** distance) Then (S drives car) Unless ()*

Generality [S drives for family F] Specificity []

The above FHCCRs can further be merged into a single tree as shown in Figure 1. The root node in a FHCCR tree signifies the most general class and any child node is a specific case of its parent node. As we traverse towards the leaf nodes, the classes become more and more specific. Censors may be present at any level in the hierarchy.

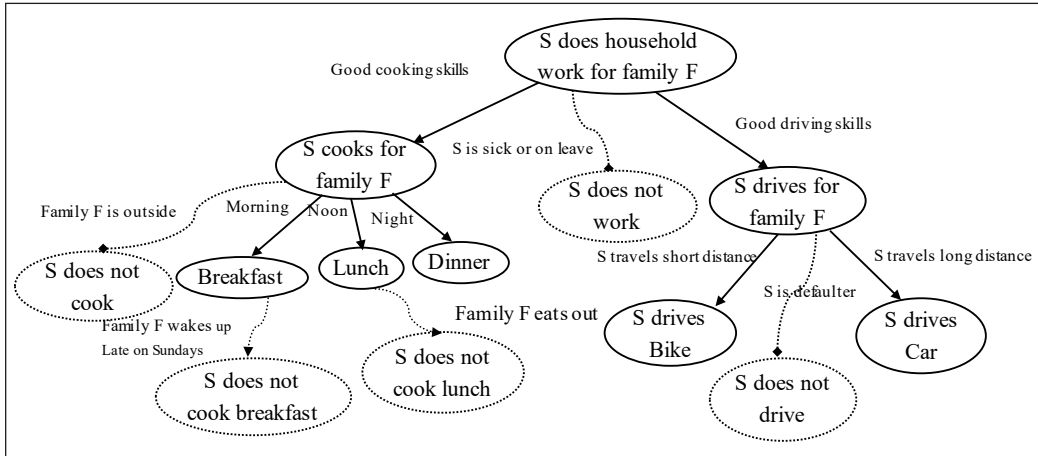


Figure 1. An example FHCCRs tree

Censors present at upper levels in the hierarchy are inherited at the lower levels as well. Since each rule in the hierarchy inherits all the properties of its parent FHCCR, it is not required to list all such properties repetitively. Hence, in the tree representation, redundancy is minimized in the listing of the properties. The solid circles represent the classes and solid arrows denote the properties. Censor conditions are represented along the dashed lines and dashed circles show the classes when censor/exception condition(s) is/are satisfied.

For discovering the best set of FHCCRs, one needs to search through all possible candidate FHCCRs for a dataset. In this context, it is an optimization problem that can be solved using a Genetic Algorithm. Applying an approach for discovering FHCCRs requires an evaluation/fitness function to guide the search towards an optimal solution. Therefore, we need to quantify the goodness of hierarchies. For this purpose, we have used degree of subsumption and coefficient of similarity- two quantitative measures- to decide about the levels of classes in the hierarchical framework (Al-Maqaleh & Bharadwaj, 2005; Bharadwaj & Saroj, 2010; Bharadwaj & Al-Maqaleh, 2007b). Degree of subsumption decides the hierarchical levels (Generality/ Specificity) among classes. If Class C_k subsumes class C_s then C_k is more general class than C_s , i.e. C_s is the specific class of C_k . Coefficient of similarity gives more comprehensible results if the degrees of subsumption between classes C_k and C_s are equal both ways. These measures are explained in detail in the proposed system.

Rule Mining using Genetic Algorithms

Genetic algorithms are random but guided search methods for solving complex optimization problems. These start with a random population of candidate solutions and apply genetic operators (selection, recombination and mutation) to form improved solutions from the better fit parents in successive generations by following Darwinian theory of evolution. The possible classification rules that can be learned from a dataset can be enormously large. Finding an optimal rule set that can perform effective classification is no less a challenging task. GAs, being global optimization tool, have been extensively used for classification rule mining (Freitas, 2002a; Freitas, 2002b). The block diagram for discovering classification rules is given in Figure 2.

Research for Discovering Knowledge in Various Rule Forms

FCRs have demonstrated their ability in a wide spectrum of applications in the domain of control (Palm et al., 1997), modeling (Pedrycz, 1996), and data mining problems (Ishibuchi et al., 2005b; Kuncheva, 2010). Therefore, there have been many attempts to discover FCRs from real-valued datasets (Cordón et al., 2000; Fernández et al., 2009; Herrera, 2008; Ishibuchi et al., 1995; Ishibuchi et al., 2005a; Ishibuchi et al., 2005b; Ishibuchi et al., 2011; Mendes et al., 2001). Most of these approaches discover the knowledge at a single conceptual level that results into RBs of large size. It may increase the accuracy of the RB but influences the interpretability adversely.

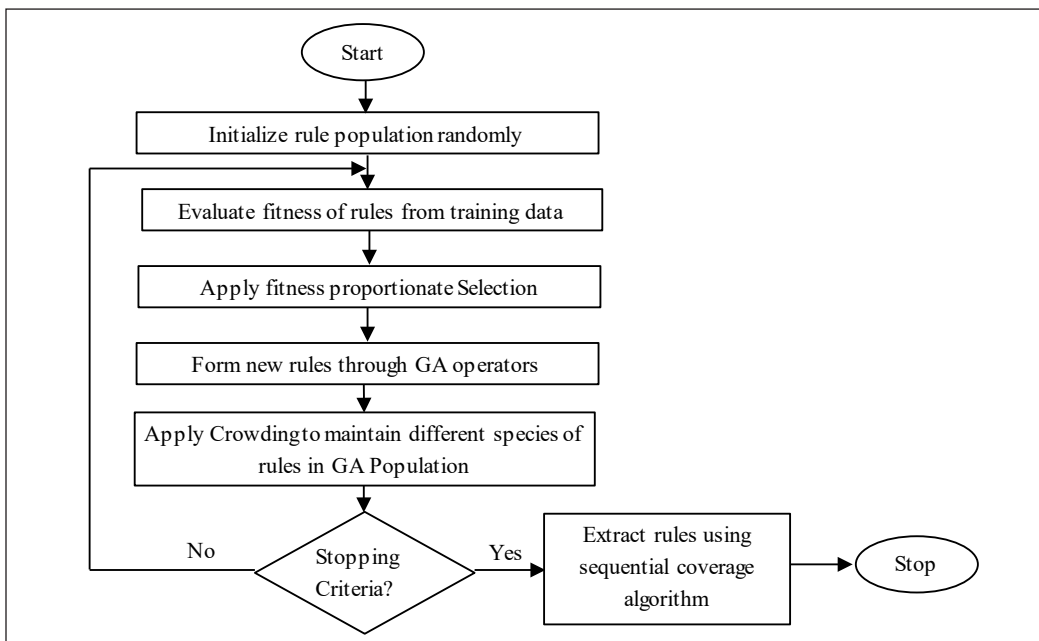


Figure 2. Block diagram of GA for discovering Classification Rules

Accuracy and interpretability are conflicting criteria; therefore, researchers depend on achieving the best trade-off between accuracy and interpretability. Several efforts have been made to reach an acceptable trade-off between accuracy and interpretability (Bala & Ratnoo, 2016; Gacto et al., 2011; Ishibuchi et al., 1997; Ishibuchi et al., 2001; Ishibuchi et al., 2011; Sanz et al., 2010). Ishibuchi and colleagues (1997, 2001, 2005a, 2005b & 2011) had proposed a GA for rule selection problem that tried to maximize accuracy and minimize the number of rules. In addition, multi-objective evolutionary algorithms have also been suggested for rule learning problems. These approaches discover non-dominated Pareto optimal solutions by considering accuracy and interpretability (in terms of the number of rules and the number of antecedent conditions per rule) as the optimization criteria (Ishibuchi et al., 1997; Ishibuchi et al., 2001). All these approaches discover knowledge in the form of FCRs which have the following shortcomings:

- FCRs severely fragment the knowledge, thereby, resulting in a large number of rules.
- FCRs, as an underlying rule structure for discovering classification rules, do not exhibit the two aspects of variable precision logic, i.e., variable certainty and variable specificity.
- FCRs simply ignore the exceptions as a noise and, hence, are unable to cope with exceptional/unusual conditions.

The problem of discovering flat classification rules has been extensively studied in the area of data mining and machine learning (Freitas, 2008). Hence, in the past few decades, discovery of the Hierarchical Classification Rules (HCRs) has become the priority of researchers in field of rule mining (Cerri et al., 2013; Cerri et al., 2012; Davies et al., 2007; Rousu et al., 2006; Secker et al., 2007; Secker et al., 2010; Sun et al., 2004; Sun & Lim, 2001; Tsumoto, 2003). A knowledge base organized in a hierarchical form is not only interpretable, it can also make predictions at multiple levels of abstractions, i.e., it can handle variable precision logic with respect to specificity. The most efficient and easy to understand underlying rule structures to support the discovery of the hierarchical classification rules are HPRs (Al-Maqaleh & Bharadwaj, 2005; Bharadwaj & Saroj, 2009; Bharadwaj & Kandelwal, 2007), HCPRs (Bharadwaj & Jain, 1992) and FHCPs (Neerja & Bharadwaj, 1996). Hierarchical multi-label classification is another complex challenging task that requires discovery of rules in hierarchical form. In hierarchical multi-label classification problems, an instance is assigned to more than one classes out of hundreds or thousands of the classes (Cerri et al., 2012). Popular examples of the hierarchical multi-label classification problems are the task of text classification (Rousu et al., 2006; Sun et al., 2004; Sun & Lim, 2001) and protein function prediction (Cerri et al., 2013; Sun et al., 2004).

Another important aspect of real world knowledge is interestingness which has been given considerably focus in the data mining literature. Silberschatz and Tuzhilin (Kontonasios et al., 2012; Silberschatz & Tuzhilin, 1996; Silberschatz & Tuzhilin, 1995) had dealt with the issue of interestingness. They had considered the exceptions as interesting pieces of knowledge that challenged the common beliefs. Suzuki and colleagues (Suzuki, 2002; Suzuki, 2004; Suzuki & Shimura, 1996; Suzuki & Zytchow, 2000) had done extensive work in the domain of exception discovery. They had classified exceptions in several categories and discovered exceptions in the form of rule pairs and rule triplets. They had addressed the task of dependence modeling, and their algorithm discovered a large number of exceptions, which made the discovered knowledge unsuitable for human insight and analysis. A classification algorithm based on the evolutionary approach for discovering comprehensible rules with exceptions in the form of Censored Production Rules (CPRs) is presented in (Bharadwaj & Al-Maqaleh, 2007a). A genetic algorithm approach has also been proposed to discover Fuzzy Censored Classification Rules in (Bala, 2012). A genetic programming-based intelligent miner has also been proposed to mine rules with fuzzy hierarchies with exceptions at every level (Bharadwaj & Saroj, 2010; Bharadwaj & Al-Maqaleh, 2007b). Vashishtha et al. (2013) had discovered classification rules with intra and inter-class exceptions. However, their algorithm was designed to work with datasets containing discretized /nominal attributes only. Another contribution for discovering exceptions has been made to discover tuned fuzzy classification rules with Intra and inter-class exceptions (Bala & Ratnoo, 2016). In this work, each attribute is fuzzified by finding an optimal combination of the type of MFs (triangular, trapezium) and the number of linguistic terms (varying from 1 to 5). In this research work, we take up the task of discovering knowledge in the form of FHCCRs using a genetic algorithm approach.

THE PROPOSED SYSTEM

This section describes the proposed approach for discovering FHCCRs in a step by step manner. It includes a pre-processing step to fuzzify the attributes, a genetic algorithm to discover FHCCRs and a post-processing step to merge FHCCRs into FHCCR trees. The overall flow chart of the proposed system is shown in Figure 3.

Fuzzification Process

The dataset is normalized by using the following formula in Equation 1.

$$A'_{ij} = \frac{A_{ij} - \min(A_j)}{\max(A_j) - \min(A_j)} \quad [1]$$

A'_{ij} is the normalized value of the j^{th} attribute of the i^{th} instance. After normalization the dataset is fuzzified by applying algorithm given by Bala and Ratnoo (2016). This algorithm

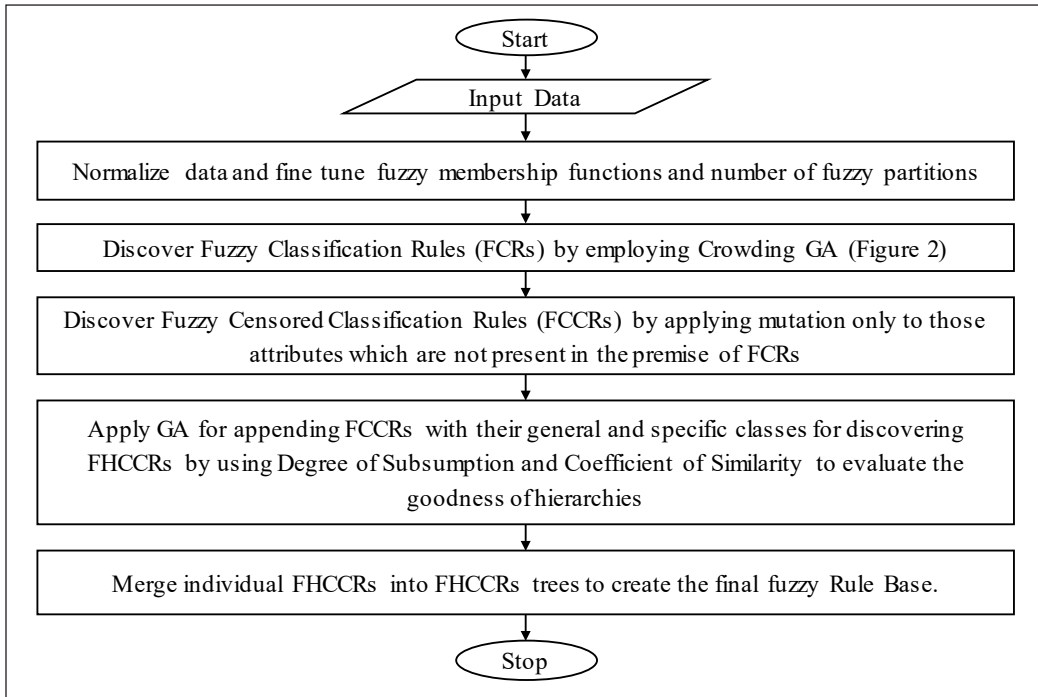


Figure 3. Flowchart for the overall process of the proposed system

produces optimal fuzzy partitions for attributes in relation to class labels. For each attribute, it selects an optimal combination of a Fuzzy Membership Function (FMF) and the number of linguistic partitions out of a given set of FMFs (i.e., Triangular and Trapezium) and a given set of linguistic partitions (i.e., 2:(small, medium), 3:(small, medium large), 4: (small medium, medium large), 5:(small, small medium, medium, medium Large, Large)). The algorithm computes the gain ratio for all the possible combinations of FMFs and number of linguistic partitions for an attribute using the following Equation 2:

$$GR(A^k) = \frac{IG(A^k)}{SplitInfo(A^k)} \quad [2]$$

Measuring Goodness of Hierarchies

This section explains the use of the degree of subsumption and the coefficient of similarity to quantify the goodness of hierarchies.

Degree of Subsumption. Degree of subsumption is a quantitative measure to decide the hierarchical relation of generality/specificity among the classes. To compute the degree of subsumption between two classes C_k and C_s , first, we need to spot their defining properties. The defining properties for the class C_k are the distinct linguistic labels (i.e., small, medium

and large), for the attributes of a given dataset, which have recalled more than a user-defined threshold value (θ_t) with respect to the class C_k (Bharadwaj & Saroj, 2009; Bharadwaj & Kandelwal, 2007). The values for recall, denoted by x and y , for the i^{th} property in the class C_k and j^{th} property in the class C_s are computed as below in equations 3 and 4:

$$x_i = \frac{|(\mu(P_i)_{\alpha} \wedge C_k)|}{|C_k|} \quad [3]$$

$$y_j = \frac{|(\mu(P_j)_{\alpha} \wedge C_s)|}{|C_s|} \quad [4]$$

The value of α needs to be greater than 0.51. This value has been chosen through experimental tuning. The set of defining properties $S(C_k)$ and $S(C_s)$ for the classes C_k and C_s are captured as Equation 5 and 6 below:

$$S(C_k) = \forall P_i \in U; x_i > \theta_t \quad [5]$$

$$S(C_s) = \forall P_j \in U; y_j > \theta_t \quad [6]$$

The subsumption between i^{th} and j^{th} properties of defining sets $S(C_k)$ and $S(C_s)$ is computed by using following Equation 7, 8 and 9.

$$\text{subsume}(S(C_k(i)), S(C_s(j))) = 1 \quad \text{if } (x \leq y) \text{ and } (i = j) \quad [7]$$

$$\text{subsume}(S(C_k(i)), S(C_s(j))) = y \quad \text{if } (x > y) \text{ and } (i = j) \quad [8]$$

$$\text{subsume}(S(C_k(i)), S(C_s(j))) = 0 \quad \text{if } (i \neq j) \quad [9]$$

The overall subsumption between the two classes is given by Equation 10:

$$\text{degree_subsumption}(C_k, C_s) = \sum_{i=1}^{|S(C_k)|} \sum_{j=1}^{|S(C_s)|} \frac{\text{subsume}(S(C_k(i)), S(C_s(j)))}{|S(C_k)|} \quad [10]$$

Here, we are calculating overall subsumption degree between every pair of the classes. Therefore, double summation is applied.

A subsumption matrix can be prepared using Equation 11. θ_s denotes the threshold value for the degree of subsumption which is kept at 0.6.

$$Subsumption_matrix[C_i, C_j] = \begin{cases} -1 & \text{if } i = j \\ 0 & \text{if } Subsumption(C_i, C_j) < \theta_{ts} \\ 0 & \text{if } Subsumption(C_j, C_i) > Subsumption(C_i, C_j) \\ Subsumption(C_i, C_j) & \text{otherwise} \end{cases}$$

[11]

Coefficient of Similarity

A coefficient of similarity is required to decide the hierarchy among those classes whose subsumption degree is same both ways. The coefficient of similarity (S) of attributes between two classes C_k and C_s is defined on the basis of a 2×2 contingency table (Table 1).

Table 1
Contingency table

$S(C_k)(C_l)$ ↓	$S(C_s)(C_2) \rightarrow$	
	Observed	Not observed
Observed	p	q
Not observed	r	s

$$\chi^2 = \frac{N(ps - qr)^2}{M}$$

[12]

$$N = p + q + r + s$$

[13]

$$M = (p + q)(r + s)(p + r)(q + s)$$

[14]

$$S = \sqrt{\frac{\chi^2}{N(k - 1)}}$$

[15]

In the above Equation 12, 13, 14 and 15, N is the total number of properties present; k is the degree of freedom. Degree of freedom is the number of independent quantities in the final calculation of a stastical distribution and it is calculated by $k = (Number\ of\ Rows - 1) \times (Number\ of\ Col - 1)$. For a two by two contingency table the degree of freedom is 1. The value of S shall always lie between 0 and 1. Higher the value of S, more is the similarity between the classes involved (Bharadwaj & Saroj, 2009; Bharadwaj & Kandelwal, 2007).

A similarity matrix can be prepared by using Equation 16. θ_{sim} , in Equation 16 represents the threshold for coefficient of similarity which is taken as 0.6.

$$Similarity_matrix[C_i, C_j] = \begin{cases} 1 & \text{if } i == j \\ 0 & \text{if } Similarity(C_i, C_j) < \theta_{tsim} \\ Similarity(C_i, C_j) & \text{otherwise} \end{cases} \quad [16]$$

The coefficient of similarity is helpful in deciding the hierarchy between the classes when a general class subsumes two classes with the same degree of subsumption.

The Genetic Algorithm Design

This section describes the proposed GA approach to discover FHCCRs. It illustrates encoding scheme, generation of the initial population, fitness function and genetic operators.

Individual’s Encoding. A set of four consequent blocks encodes the hierarchical chromosome with exceptions, as a candidate solution. The first block represents default rule, i.e., FCR. The second block captures the censor/exceptional condition(s) along with the class which gets predicted when censor conditions are satisfied. The third block contains the general class and the fourth block holds the specific classes. Two constraints that need to be enforced on individual FHCCRs are – 1) The properties present in the premise and exceptional parts are mutually exclusive and; 2) The rule class, the general class and the specific classes need to be all distinct.

Figure 4 shows the encoding of two chromosomes and their mapping to the corresponding FHCCRs. We have adopted the Michigan approach with a pure binary string for encoding the premise part of a chromosome. A block of n bits signifies n consecutive linguistic fuzzy variables in the order- ‘small’, ‘small-medium’, ‘medium’, ‘medium-large’ and ‘large’. Within a block, a ‘1’ bit marks the presence of the corresponding linguistic term, whereas a ‘0’ bit denotes its absence. A block with all bits set to 1 or 0 is treated as a ‘don’t care’ state which indicates the absence of an attribute from the rule. The consequent

Block 1						Block 2			Block 3	Block 4
A1	A2	A3	A4	A5	Class	A6	A7	Censor class	Generality	Specificity
10	010	0010	10	00000	2	00010	0100	7	1	4 5 0
A1	A2	A3	A4	A5	Class	A6	A7	Censor	Generality	Specificity
10	010	0010	01	00000	3	00001	1000	8	1	6 00

Genotype (Chromosomes)

If (A₁ is small) ∧ (A₂ is medium) ∧ (A₃ is medium-large) ∧ (A₄ is small) → C₂ ∩ (A₆ is medium-large) ∧ (A₇ is small-medium) : C₇; Generality[C₁] Specificity[C₄, C₅]

If (A₁ is small) ∧ (A₂ is medium) ∧ (A₃ is medium-large) ∧ (A₄ is large) → C₃ ∩ (A₆ is large) ∨ (A₇ is small) : C₈; Generality[C₁] Specificity [C₆]

Phenotype (FHCCR)

Figure 4. Encoding scheme

part contains the class label of the rule. The second block follows a similar strategy to represent exceptions and their corresponding classes. The attributes in block 1 and block 2 are mutually exclusive as per the first constraint. The Generality part contains the label for the general class of the rule. The next block consists of three bits – each for one of the specific classes - which indicates that there are at most three specific classes.

Initial Population. Initially, a set of FCRs is generated from data using the algorithms “Evolving FCRs” and “Crowding” given in Bala and Ratnoo (2016). This first phase of the design discovers a set of FCRs which occupies the first block of the FHCCRs. The second phase transforms the FCRs into a set of FCCRs based on the algorithm given in Saroj and Bharadwaj (2007) , and modified for discovery of fuzzy rules.

The third phase of the design creates an initial population of the FHCCRs by appending classes randomly to the generality and specificity parts of the pre-discovered FCCRs. The number of possible combinations in the generality and specificity parts increases with the rise in the number of classes present in the dataset. Hence, we have applied a genetic algorithm to fix the general and specific classes of FHCCRs in an optimal way.

Fitness Evaluation. Fitness function gives the quantitative measure to evaluate the quality of FHCCRs in the population. In the proposed approach, the degree of Subsumption and the similarity coefficient, already described in section of measuring goodness of hierarchies are used to evaluate the fitness of an individual. The fitness function is given below:

If (Generality = empty and Specificity= empty) then

$$Fitness = \frac{2 \times precision \times recall}{precision + recall}$$

Else

$$Fitness1 = \frac{2 \times precision \times recall}{precision + recall} // \text{Fitness of the first block of FHCCR}$$

$$Fitness2 = precision \times recall // \text{Fitness of the second block of FHCCR}$$

// Fitness of generality and specificity parts

$$Fitness3 = Subsumption(C_g, C_k) \times Similarity(C_g, C_k) + \sum_{i=1}^3 Subsumption(C_k, C_{si}) \times Similarity(C_k, C_{si})$$

$$Fitness = Fitness1 + Fitness2 + Fitness3$$

We have considered a maximum of three classes in the specificity part. The subsumption and similarity matrices are computed in advance from the set of FCCRs in the initial population to save the overhead of computation of these two measures again and again

for each FHCCR generated during the evolutionary process. Two FHCCRs that can be generated from the FCCRs given in the initial population are shown in the Figure 5. The fitness computations are also depicted in this Figure 5.

A1	A2	A3	A4	A5	Class	A6	A7	Censor Class	Generality	Specificity
10	010	0010	10	00000	2	00010	0100	7	1	4 5 0
Precision=0.36 Recall=0.66 Fitness1=0.465					Censor_precision=0.09 Censor_recall=1 Fitness2=0.09				Fitness3=1.9455 Total Fitness= 2.5005	
A1	A2	A3	A4	A5	Class	A6	A7	Censor Class	Generality	Specificity
10	010	0010	01	00000	3	00001	1000	8	1	6 0 0
Precision= 0.5 Recall=1 Fitness1=0.667					Censor_precision=0.083 Censor_recall=1 Fitness2=0.083				Fitness3=1.4613 Total Fitness=2.2113	

Figure 5. FHCCRs generated from initial FCCR and their fitness evaluation

Genetic Operators. Tournament selection is used as the selection operator. The selection is restricted to Intra-species (individuals of same class) individuals since inter-species (individuals of different classes) individuals create low fitness offspring after applying crossover. New offspring are created from the selected ones by employing one point crossover and flip mutation. Cross breeding is done on the generality and specificity parts of the individuals of the same species. The mutation operator generates a new offspring by mutating generality and specificity blocks of an individual. The algorithm uses pre-selection technique to maintain diversity, i.e., the better fit offspring replace their parents. Figure 6 shows the overall genetic algorithm approach for discovering FHCCRs.

Post-processing Scheme

The average number of defining properties in a rule is given by following Equation 17:

$$ADP = \frac{1}{N} \sum_{i=1}^N |prop(R_i)| \tag{17}$$

Where N is the number of rules and $prop (R_i)$ is the number of defining properties for the i^{th} rule.

Here, we are presenting a post processing scheme in which small and related hierarchies can be merged together to form bigger hierarchies in order to reduce redundancy and increase interpretability. The scheme is as follows:

1. If an FHCCR is already a part of a bigger hierarchy, then the bigger FHCCR is retained and the smaller one is dropped.

Algorithm: Discovering Fuzzy Hierarchical Censored Classification Rules (FHCCRs)
Input: Set of FCCRs, Population Size = 500; Mutation Rate = 0.1; Crossover Rate = 0
Output: A set of FHCCRs
Begin
 1. Evolve FCRs from data using Algorithms ‘Evolving FCR’ and ‘Crowding’..
 2. Discover FCCRs from the pre-discovered set of FCRs.
 3. Construct Subsumption and Similarity Matrices from the pre-discovered set of FCCRs
 4. Initialize random population P_0 of FHCCRs using set of FCCRs and generate random classes for generality and specificity parts
 5. Evaluate Fitness of the population P_0
 6. **While** stopping criteria not satisfied
 Begin
 6.1 Select two individuals i_1 and i_2 of same species
 6.2 Apply crossover and mutation to produce new individuals i'_1 and i'_2 //keeping the rule and censor parts fixed
 6.3 Compute fitness of i'_1 and i'_2
 6.4 **If** fitness of $i'_1 >$ fitness of i_1
 6.4.1 Replace i_1 in P_i with i'_1
 End if
 6.5 **If** fitness of $i'_2 >$ fitness of i_2
 Replace i_2 in P_i with i'_2
 End if
 End while
End.

Figure 6. The Genetic Algorithm to discover FHCCRs

2. If two FHCCRs have a common general class, but different specific classes, then these two FHCCRs are merged into a single hierarchy.
3. Two different hierarchies will be merged only and only if the threshold criteria for the degree of subsumption and coefficients of similarity are satisfied. These threshold values are kept at 0.6 for our experimentation.

After post processing step the related hierarchies are merged together and the redundant rules have been subsumed by the general rules.

The post processing scheme reduces the average number of defining properties significantly and hence the knowledge represented by the FHCCR tree is more compact and interpretable.

EXPERIMENTAL SETUP AND PERFORMANCE EVALUATION

The proposed approach was validated on five datasets. The Land-Transport dataset was taken from Bala and Ratnoo (2018), and it was further extended to include exceptions as well. Rests of the four datasets were from UCI machine learning repository. Table 2 shows the description of the datasets with respect to the number of attributes, number of classes and total instances. All the datasets had continuous attributes without any missing values.

Table 2
Description of datasets

Dataset	Attributes	Classes	Instances
Land-Transport	7	11	151
Hglass	9	6	214
E.coli	7	8	336
Yeast	8	10	1484
Vehicle	18	4	846

The datasets were normalized and fuzzified as described in the pre-processing step. Fuzzification of attributes had been carried out using the algorithm proposed in Bala & Ratnoo (2016). The resulting fuzzy partitions obtained for the attributes of different datasets are given in Table 3.

After fuzzifying the attributes, FHCCRs are discovered in three phases as described below:

1. In the first Phase, FCRs are discovered by using the algorithms ‘*Evolving_FCRs*’ and ‘*Crowding*’ proposed in (Bala & Ratnoo, 2016) as mentioned earlier. These FCRs occupy the first part of FHCCRs representation. We have compared the accuracy and number of rules discovered by the classifiers containing FCRs with those obtained from Decision table, JRIP, PART and J48 classifiers available in WEKA. (Witten et al., 2011). These classifiers are chosen since they produce rules in ‘*If-Then*’ form which are comparable with the rules discovered in the form of FCRs. All these classifiers are applied with their default settings provided in WEKA. The results have been taken with tenfold cross validation sampling method across all the datasets and classifiers. Table 4 compares the results averaged over ten folds.

The table shows that FCRs perform significantly better than the other classifiers on four datasets (*Land-Transport*, Hglass, E-coli and Yeast), but it fails to do better on one dataset (Vehicle). For Vehicle dataset, the PART algorithm obtains the highest accuracy, however, it discovers many rules (29) as compared to the number of rules (7) discovered by the classifier consisting of FCRs. This reflects the trade off between accuracy and number of rules discovered. Overall, JRip and the classifier containing FCRs discover lesser number of rules. As RBs with less number of rules are considered more interpretable (García et al., 2008), JRip and FCRs perform significantly better on this metric.

2. In the second phase of the design, FCRs have been converted to FCCRs based on algorithm given in (Saroj & Bharadwaj, 2007). The algorithm is modified for fuzzy rules. The exceptions/censors discovered in this phase are accommodated in the second part of the FHCCRs representation. We have compared the accuracy of

Table 3
Attribute-wise Fuzzy partitions for datasets

Attributes	FMF	Linguistic terms	Attributes	FMF	Linguistic terms
Dataset: Land_Transport					
1. Weight	\triangleleft	Low, Medium, High	5. Boot-Space	∇	Low, Low-medium, Medium-high, High
2. Mileage	\triangleleft	Low, Medium, High	5. Fuel-capacity	\triangleleft	Low, Medium, High
3. Width	\triangleleft	Low, Medium, High	6. Power	\triangleleft	Low, low-medium, Medium-high, High
4. Length	\triangleleft	Low, Medium, High			
Dataset: Hglass					
1. Refractive Index (RI)	\triangleleft	Low, High	6. Potassium (K)	\triangleleft	Low, High
2. Sodium(Na)	\triangleleft	Low, High	7. Calcium (Ca)	\triangleleft	Low, Low-medium, Medium-high, High
3. Magnesium (Mg)	∇	Low, High	8. Barium (Ba)	∇	Low, Low-medium, Medium-high, High
4. Aluminium (Al)	\triangleleft	Low, High	9. Iron (Fe)	\triangleleft	Low, High
5. Silicon (Si)	\triangleleft	Low, Medium, High			
Dataset:E-coli					
1. mcq	\triangleleft	Low, High	5. Vac	\triangleleft	Low, Medium, High
2. Gvh	\triangleleft	Low, High	6. Alm1	\triangleleft	Low, High
3. Lip	\triangleleft	Low, High	7. Alm2	\triangleleft	Low, High
4. Cb	\triangleleft	Low, High			
Dataset: Yeast					
1. Mcq	∇	Low, High	5. Eri	\triangleleft	Low, High
2. Gvh	\triangleleft	Low, High	6. Pox	\triangleleft	Low, High
3. Alm	\triangleleft	Low, Medium, High	7. Vac	\triangleleft	Low, Low-medium, Medium-high, High
4. Mit	\triangleleft	Low, High	8. Mv	\triangleleft	Low, Low-medium, Medium-high, High
Dataset: Vehicle					
1. Radius Ratio	\triangleleft	Low, Medium, High	7.Scaled Variance along major axis	\triangleleft	Low, High
2. PR Axis aspect Ratio	\triangleleft	Low, High	8. Scaled Variance along minor axis	\triangleleft	Low, Medium, High
3. Max length Aspect Ratio	\triangleleft	Low, Low-medium, Medium, Medium-high, High	9. Skewness about major axis	∇	Low, Medium, High
4. Scatter Ratio	\triangleleft	Low, Low-medium, Medium-high, High	10. Skewness about minor axis	\triangleleft	Low, High
5. Elongatedness	\triangleleft	Low, High	11. Kurtosis about minor axis	\triangleleft	Low, High
6. PR Axis Rectangularity	\triangleleft	Low, Medium, High			

FCRs and FCCRs (Fuzzy Classification Rules with Censors/Exceptions) in Table 5. The results illustrate that the accuracy slightly increases when exceptions/censors get appended to the default rules. This is so because exception/censor conditions decrease false positive (FP) rate and increase True Negative (TN) rate. The results in Table 5 show that exceptions have been discovered for all the datasets except E-coli. Discovering exceptions may not increase accuracy to a great extent, but their discovery is interesting because knowing exceptions gives us a chance to revise our decisions in those rare circumstances where the default rules become inapplicable.

3. FCCRs are converted into FHCCRs in the third phase by appending the respective general and specific information to the FCCRs. The Initial population of FHCCRs is generated by appending general and specific classes randomly among the FCCRs. The fitness of individuals in the population is calculated from the subsumption and similarity matrices. The crossover and mutation operators are applied only to the generality and specificity parts of the initial FHCCRs. Table 6 gives the GA parameters employed to discover FHCCRs.

The additional stopping criteria adopted was of no change in the fitness of individuals for last 10 generations. The FHCCRs discovered for the ‘Land transport’ dataset along with their fitness values are shown in Table 7.

Table 4
Comparison on the basis of accuracy and number of rules

Algorithm/ Dataset	Decision table		JRip		PART		J48		Classifier (FCR)	
	Acc.	No of Rules	Acc.	No of Rules	Acc.	No of Rules	Acc.	No of Rules	Acc.	No of Rules
Land-Transport	39.07	15	43.7	8	49.67	17	54.30	25	67.62	13.2
Hglass	68.22	38	69.62	8	68.22	14	66.82	30	83.59	7.5
E.coli	75.29	18	80.35	8	79.46	13	84.22	22	87.59	8.1
Yeast	53.77	109	57.82	15	53.5	132	55.86	185	72.57	10
Vehicle	61.82	62	63.71	16	68.68	29	68.20	61	60.58	7.1

Table 5
Comparison of accuracy of FCCRs with accuracy of FCRs

Dataset	Accuracy without Exceptions	Accuracy with Exceptions	No of Exceptions
Land-Transport	67.62	71.63	2
Hglass	83.59	84.25	1
E.coli	87.59	87.59	0
Yeast	72.57	73.45	1
Vehicle	60.58	60.70	1

In this table, the first column lists FHCCRs, the second column gives the fitness of the FCRs, the third column denotes the fitness of censor part and the fourth column gives the fitness of FHCRs. Finally, the fifth column provides the fitness of entire FHCCRs. The proposed algorithm has discovered 11 FHCCRs. The set of FHCCRs discovered are shown pictorially in Figure 7.

Table 6
GA parameters used for discovery of FHCCRs

Population Size	20*no. of FCCRs discovered
Crossover rate	0.6
Mutation rate	0.1
Maximum number of generations	50

Table 7
FHCCRs discovered for 'Land-transport' dataset

FHCCRs	Fitness1	Fitness2	Fitness3	Total Fitness
<i>If</i> (Weight is low) \wedge (Width is low) \wedge (Length is low) \wedge (Boot_space is low) \neg (Fuel_capacity is low) <i>Then</i> Two-wheeler \neg (Power is medium-high) : (Sports-bike); <i>Generality</i> [] <i>Specificity</i> [Scooter, Bike]	0.5	0.085	1.592	2.177
<i>If</i> (Weight is medium) \wedge (Mileage is low) \neg (Width is medium) <i>Then</i> Car \neg (Length is medium \vee power is high) : (Sports-car); <i>Generality</i> [] <i>Specificity</i> [Small-car, Big-car]	0.376	0.037	1.541	1.954
<i>If</i> (Weight is low) \wedge (Mileage is medium) \wedge (Width is low) \wedge (Length is low) \wedge (Boot_space is low) \wedge (Fuel_capacity is low) \wedge (Power is low) <i>Then</i> Scooter; <i>Generality</i> [Two-wheeler] <i>Specificity</i> []	0.733	0	0.796	1.530
<i>If</i> (Weight is low) \wedge (Mileage is high) \wedge (Width is low) \wedge (Length is low) \wedge (Boot_space is low) \wedge (Fuel_capacity is low) \wedge (Power is low) <i>Then</i> Bike; <i>Generality</i> [Two-wheeler] <i>Specificity</i> []	0.8	0	0.796	1.596
<i>If</i> (Weight is medium) \wedge (Mileage is low) \wedge (Width is medium) \neg (Length is medium) <i>Then</i> Small-car \neg (Power is high) : (Sports-car); <i>Generality</i> [Car] <i>Specificity</i> [Hatchback]	0.52	0.108	2.497	3.125
<i>If</i> (Weight is medium) \wedge (Mileage is low) \wedge (Width is medium) \wedge (Length is high) \wedge (Power is low-medium) <i>Then</i> Big-car; <i>Generality</i> [Car] <i>Specificity</i> [Sedan, SUV]	0.455	0	1.575	2.031
<i>If</i> (Weight is medium) \wedge (Mileage is low) \wedge (Width is medium) \wedge (Length is medium) \wedge (Fuel_capacity is low-medium) <i>Then</i> Hatchback; <i>Generality</i> [Small-car] <i>Specificity</i> []	0.733	0	0.820	1.553

Table 7 (continue)

<i>FHCCRs</i>	<i>Fitness1</i>	<i>Fitness2</i>	<i>Fitness3</i>	<i>Total Fitness</i>
<i>If</i> (Weight is medium) \wedge (Mileage is low) \wedge (Width is medium) \wedge (Length is high) \wedge (Boot_space is medium-high) \wedge (Power is low-medium) <i>Then</i> Sedan; <i>Generality</i> [Big-car] <i>Specificity</i> []	0.722	0	0.887	1.609
<i>If</i> (Weight is medium) \wedge (Mileage is low) \wedge (Width is medium) \wedge (Length is high) \wedge (Boot_space is Low-medium) \wedge (Power is low-medium) <i>Then</i> SUV <i>Generality</i> [Big-car] <i>Specificity</i> []	0.571	0	0.837	1.408
<i>If</i> (weight is low) \wedge (Mileage is low) \wedge (Width is low) \wedge (Length is low) \wedge (Boot-space is low) \wedge (Fuel-capacity is low) \wedge (Power is medium-high) <i>Then</i> Sports-bike; <i>Generality</i> [Two-wheeler] <i>Specificity</i> []	0.667	0	0.796	1.463
<i>If</i> (weight is medium) \wedge (Mileage is low) \wedge (Width is medium) \wedge (Length is medium) \wedge (Power is high) <i>Then</i> Sports-car; <i>Generality</i> [Car] <i>Specificity</i> []	0.5	0	0.870	1.370

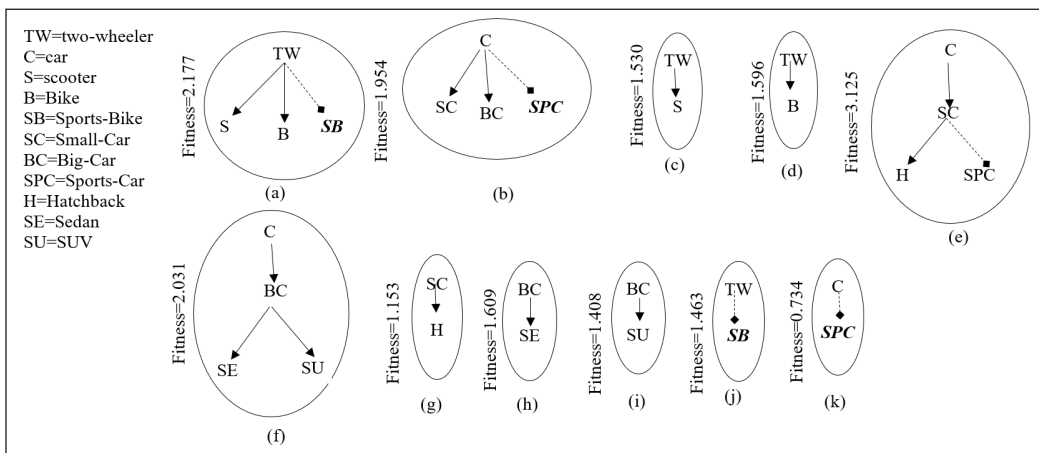


Figure 7. FHCCRs discovered for Land-Transport dataset

The post-processing step consolidates these FHCCRs into bigger hierarchies to further reduce the redundancy as described in post-processing scheme. Figure 8 shows the complete hierarchy for ‘Land-Transport’ dataset along with the defining properties. The bold dashed circle at the top level of the hierarchy represents the most abstract class which can be added by human intervention.

Table 8 gives the number of FHCCRs discovered, average number of defining properties before and after post-processing, size of hierarchy and number of exceptions discovered.

The fifth column of the table shows the size of hierarchies along with the number of classes encountered at each level. For ‘Land-transport’ dataset, two classes have been

encountered at first level, five classes at second level and four classes at third level. The last column shows the number of censors discovered at each level. The results show that merging of FHCCRs into bigger hierarchies reduces the average number of defining properties per rule significantly and hence reduces the redundancy in rule representation making them more interpretable. This reduction depends upon the size of hierarchies. Bigger a hierarchy is, more is the reduction in the average number of defining properties.

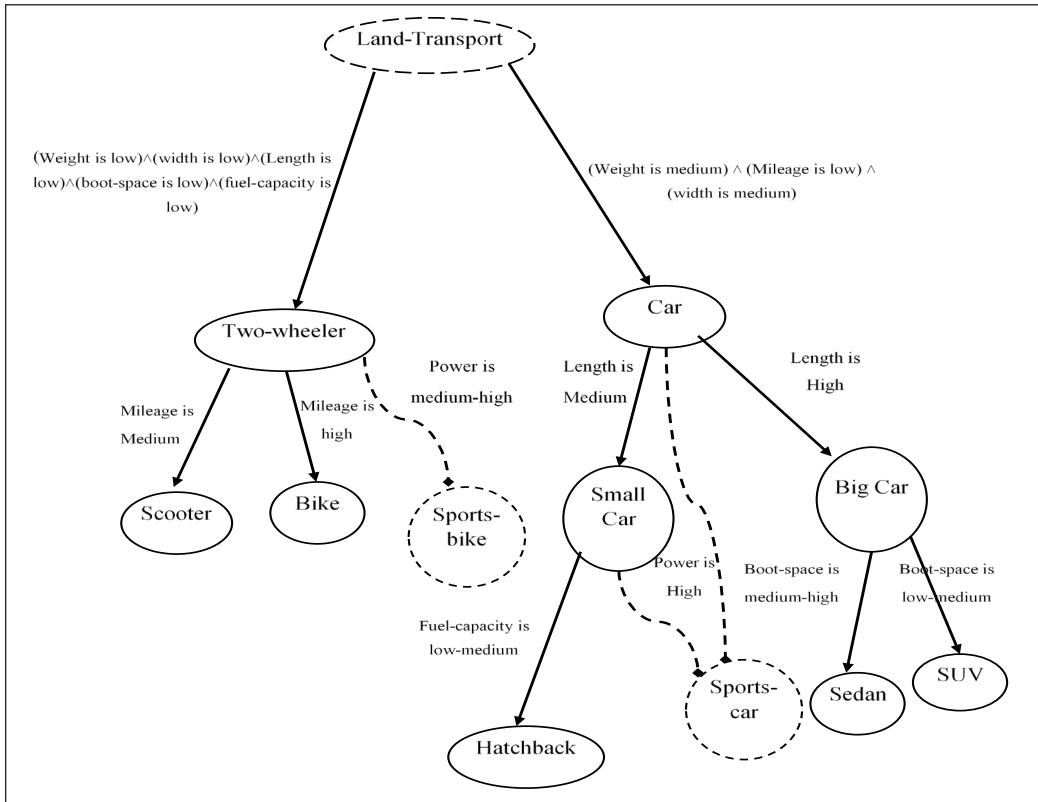


Figure 8. Complete hierarchical structure among classes of Land-transport dataset

Table 8
Properties of FHCCRs for different datasets

Dataset	No. of FHCCRs	Avg. Defining properties before Post-processing	Avg. Defining properties after Post-processing	Size of Hierarchy	No of censors/ Exceptions
Land-transport	11	5.8	1.8	3: (2, 5, 4)	0, 2, 1
Hglass	6	7.6	4.6	2: (3, 3)	1, 0
Ecoli	8	5.8	5.2	2: (7, 1)	0, 0, 0
Yeast	10	6.8	3.9	2: (5, 5)	2, 1
Vehicle	4	6.0	6.0	0	0

The proposed algorithm discovers concise, complete and interpretable rules in a hierarchical form for FRBs. It can classify objects at different levels of specificity. It also contains exceptions to the rules which enhance confidence in making decisions.

CONCLUSION AND FUTURE SCOPE

In this paper, we have proposed discovering Fuzzy Hierarchical Censored Classification Rules (FHCCRs) through genetic algorithm approach. The suggested approach has discovered FHCCRs in three phases. The first phase discovers FCRs which are, subsequently, converted into FCCRs and FHCCRs in the second and third phases respectively. The suggested approach has successfully captured the exceptions and hierarchical relationship in the class labels in the form of FHCCRs. Two measures- degree of subsumption and coefficient of similarity- have been used in the fitness function to measure the goodness of hierarchical relations. We have merged the individual FHCCRs to form larger hierarchies in a post processing step. This step has further organized the discovered knowledge in a more concise and non-redundant form because common properties among rules do not need to be repetitively represented and the specific classes inherit properties of the general classes.

Discovery of FHCCR trees is a contribution to form Fuzzy Rule Base Systems (FRBS) that are more accurate, interpretable and interesting. In addition, such FRBSs support variable certainty and specificity while drawing inference, i.e., these RBs are capable of taking corrective measures in the presence of censor/exceptional conditions, and classifying knowledge at multiple levels of abstraction. Since, FHCCRs have the capabilities to reason with incomplete and uncertain premises, to classify examples/objects at different levels of specificity and to take appropriate actions in exceptional circumstances; these have applications in the domains like robotics where human like adaptive decision making is required. This work can as well be extended to make multi-label classifications in the fields such as Bioinformatics and disease diagnosis where knowledge is commonly organized in a hierarchal manner.

ACKNOWLEDGEMENT

We sincerely thank Chairperson of the Department of the Computer Science and Engineering, Guru Jambheshwar University of Science and Technology, Hisar, who provided us an opportunity to join the department as JRFscholar, and who gave us access to the laboratory and research facilities. Our thanks also go to our friends and colleagues from the Department of Computer Science and Engineering, Guru Jambheshwar University of Science and Technology. Finally, We would like to gratefully acknowledge the financial support received from The UGC.

REFERENCES

- Al-Maqaleh, B. M., & Bharadwaj, K. K. (2005). Genetic programming approach to hierarchical production rule discovery. *Transactions on Engineering, Computing and Technology*, 6, 271-274.
- Bala, R. (2012). Discovering fuzzy censored classification rules (fcrs): A genetic algorithm approach. *International Journal of Artificial Intelligence and Applications*, 3(4), 175-188.
- Bala, R., & Ratnoo, S. (2016). A genetic algorithm approach for discovering tuned fuzzy classification rules with intra- and inter-class exceptions. *Journal of Intelligent Systems*, 25(2), 263-282.
- Bala, R., & Ratnoo, S. (2018). Discovery of fuzzy hierarchical classification rules (FHCRs): A genetic algorithm approach. In N. R. Shetty, L. M. Patnaik, N. H. Prasad, & N. Nalini (Eds.), *Emerging research in computing, information, communication and applications* (pp. 595-604). Basel, Swetzerland: Springer Nature.
- Bharadwaj, K. K., & Al-Maqaleh, B. M. (2007). Evolutionary approach for automated discovery of censored production rules. *International Journal of Computer, Electrical, Automation, Control and Information Engineering*, 10(1), 147-152.
- Bharadwaj, K. K., & Al-Maqaleh, B. M. (2007, March 21-23). Evolutionary approach for automated discovery of censored production rules with fuzzy hierarchy. In *International Multi-conference of Engineers and Computer Scientists* (pp. 716-721). Hong Kong.
- Bharadwaj, K. K., & Jain, N. K. (1992). Hierarchical censored production rules (HCPRs) system. *Data and Knowledge Engineering*, 8(1), 19-34.
- Bharadwaj, K. K., & Kandelwal, R. (2007). Cumulative learning based on dynamic clustering of hierarchical production rules (HPRs). *International Journal of Computer and Information Engineering*, 1(8), 2615-2620.
- Bharadwaj, K. K., & Saroj, S. (2009). Parallel genetic algorithm approach to automated discovery of hierarchical production rules. In J. Mehnen, M. Köppen, A. Saad, & A. Tiwari (Eds.), *Applications of Soft Computing* (pp. 327-336). Heidelberg, Germany: Springer.
- Bharadwaj, K. K., & Saroj, S. (2010). A parallel genetic programming based intelligent miner for discovery of censored production rules with fuzzy hierarchy. *Expert Systems with Applications*, 37(6), 4601-4610.
- Cerri, R., Barros, R. C., & de Carvalho, A. C. P. L. F. (2012, March 26-30). A genetic algorithm for hierarchical multi-label classification. In *Proceedings of the 27th Annual ACM Symposium on Applied Computing* (pp. 250-255). Trento, Italy.
- Cerri, R., Barros, R. C., de Carvalho, A. C., & Freitas, A. A. (2013, June 20-23). A grammatical evolution algorithm for generation of hierarchical multi-label classification rules. In *2013 IEEE Congress on Evolutionary Computation* (pp. 454-461). Cancun, Mexico.
- Cordón, O., Herrera, F., & Villar, P. (2000). Analysis and guidelines to obtain a good uniform fuzzy partition granularity for fuzzy rule-based systems using simulated annealing. *International Journal of Approximate Reasoning*, 25(3), 187-215.
- Davies, M. N., Secker, A., Freitas, A. A., Mendao, M., Timmis, J., & Flower, D. R. (2007). On the hierarchical classification of G protein-coupled receptors. *Bioinformatics*, 23(23), 3113-3118.

- Fernández, A., del Jesus, M. J., & Herrera, F. (2009). Hierarchical fuzzy rule based classification systems with genetic rule selection for imbalanced data-sets. *International Journal of Approximate Reasoning*, 50(3), 561-577.
- Freitas, A. A. (2002a). *Data mining and knowledge discovery with evolutionary algorithms*. Heidelberg, Germany: Springer-Verlag.
- Freitas, A. A. (2002b). Data mining tasks and concepts. In A. A. Freitas (Ed.), *Data mining and knowledge discovery with evolutionary algorithms* (pp. 13-43). Heidelberg, Germany: Springer.
- Freitas, A. A. (2008). A Review of evolutionary algorithms for data mining. In O. Maimon & L. Rokach (Eds.), *Soft Computing for Knowledge Discovery and Data Mining* (pp. 79-111). Boston, MA: Springer.
- Gacto, M. J., Alcalá, R., & Herrera, F. (2011). Interpretability of linguistic fuzzy rule-based systems: an overview of interpretability measures. *Information Sciences*, 181(20), 4340-4360.
- García, S., Fernández, A., Luengo, J., & Herrera, F. (2008). A study of statistical techniques and performance measures for genetics-based machine learning: accuracy and interpretability. *Soft Computing*, 13(10), 959-977.
- Herrera, F. (2008). Genetic fuzzy systems: taxonomy, current research trends and prospects. *Evolutionary Intelligence*, 1(1), 27-46.
- Ishibuchi, H., Murata, T., & Türkşen, I. B. (1997). Single-objective and two-objective genetic algorithms for selecting linguistic rules for pattern classification problems. *Fuzzy Sets and Systems*, 89(2), 135-150.
- Ishibuchi, H., Nakashima, T., & Murata, T. (2001). Three-objective genetics-based machine learning for linguistic rule extraction. *Information Sciences*, 136(1-4), 109-133.
- Ishibuchi, H., Nakashima, T., & Nii, M. (2005b). *Classification and modeling with linguistic information granules: Advanced approaches to linguistic data mining*. Heidelberg, Germany: Springer-Verlag.
- Ishibuchi, H., Nakashima, Y., & Nojima, Y. (2011). Performance evaluation of evolutionary multi-objective optimization algorithms for multi-objective fuzzy genetics-based machine learning. *Soft Computing*, 15(12), 2415-2434.
- Ishibuchi, H., Nozaki, K., Yamamoto, N., & Tanaka, H. (1995). Selecting fuzzy if-then rules for classification problems using genetic algorithms. *IEEE Transactions on Fuzzy Systems*, 3(3), 260-270.
- Ishibuchi, H., Yamamoto, T., & Nakashima, T. (2005a). Hybridization of fuzzy GBML approaches for pattern classification problems. *IEEE Transactions on Systems, Man, and Cybernetics, Part B (Cybernetics)*, 35(2), 359-365.
- Jain, N. K., & Bharadwaj, K. K. (1998). Some learning techniques in hierarchical censored production rules (HCPRs) system. *International Journal of Intelligent Systems*, 13(4), 319-344.
- Kontoniasos, K. N., Spyropoulou, E., & De Bie, T. (2012). Knowledge discovery interestingness measures based on unexpectedness. *Wiley Interdisciplinary Reviews: Data Mining and Knowledge Discovery*, 2(5), 386-399.
- Kuncheva, L. I. (2010). *Fuzzy Classifier Design* (1st Ed.). Heidelberg, Germany: Physica-Verlag HD.

- Mendes, R. R. F., Voznika, F. B., de Freitas, A. A., & Nievola, J. C. (2001). Discovering fuzzy classification rules with genetic programming and co-evolution. In L. D. Raedt & A. Siebes (Eds.), *Principles of Data Mining and Knowledge Discovery* (pp. 314-325). Heidelberg, Germany: Springer.
- Michalski, R. S., & Winston, P. H. (1986). Variable precision logic. *Artificial Intelligence*, 29(2), 121-146.
- Neerja, & Bharadwaj, K. K. (1996). Calculus of fuzzy hierarchical censored production rules (FHCCPRs). *International Journal of Intelligent Systems*, 11(1), 1-25.
- Palm, R., Driankov, D., & Hellendoorn, H. (1997). *Model based fuzzy control: Fuzzy gain schedulers and sliding mode fuzzy controllers*. Heidelberg, Germany: Springer.
- Pedrycz, W. (Ed.). (1996). *Fuzzy modelling* (Vol. 7). Boston, MA: Springer US.
- Rousu, J., Saunders, C., Szedmak, S., & Shawe-Taylor, J. (2006). Kernel-based learning of hierarchical multilabel classification models. *Journal of Machine Learning Research*, 7, 1601-1626.
- Sanz, J. A., Fernández, A., Bustince, H., & Herrera, F. (2010). Improving the performance of fuzzy rule-based classification systems with interval-valued fuzzy sets and genetic amplitude tuning. *Information Sciences*, 180(19), 3674-3685.
- Saroj, S., & Bharadwaj, K. K. (2007, February 12-14). A parallel genetic algorithm approach for automated discovery of censored production rules. In *Proceedings of the 25th Conference on Proceedings of the 25th IASTED International Multi-Conference: Artificial Intelligence and Applications* (pp. 435-441). Innsbruck, Austria.
- Secker, A. D., Davies, M. N., Freitas, A. A., Timmis, J., Mendao, M., & Flower, D. R. (2007). An experimental comparison of classification algorithms for hierarchical prediction of protein function. *Expert Update (Magazine of the British Computer Society's Specialist Group on AI)*, 9(3), 17-22.
- Secker, A., Davies, M. N., Freitas, A. A., Clark, E. B., Timmis, J., & Flower, D. R. (2010). Hierarchical classification of G-protein-coupled receptors with data-driven selection of attributes and classifiers. *International Journal of Data Mining and Bioinformatics*, 4(2), 191-210.
- Silberschatz, A., & Tuzhilin, A. (1995, August 20-21). On subjective measures of interestingness in knowledge discovery. In *Proceedings of the First International Conference on Knowledge Discovery and Data Mining* (pp. 275-281). Montréal, Québec, Canada.
- Silberschatz, A., & Tuzhilin, A. (1996). What makes patterns interesting in knowledge discovery systems. *IEEE Transactions on Knowledge and Data Engineering*, 8(6), 970-974.
- Sun, A., & Lim, E. P. (2001, November 29-December 2). Hierarchical text classification and evaluation. In *Proceedings of IEEE International Conference on Data Mining, ICDM 2001* (pp. 521-528). San Jose, CA, USA.
- Sun, A., Lim, E. P., Ng, W. K., & Srivastava, J. (2004). Blocking reduction strategies in hierarchical text classification. *IEEE Transactions on Knowledge and Data Engineering*, 16(10), 1305-1308.
- Suzuki, E. (2002). Undirected discovery of interesting exception rules. *International Journal of Pattern Recognition and Artificial Intelligence*, 16(08), 1065-1086.

- Suzuki, E. (2004, September 20-24). Discovering interesting exception rules with rule pair. In *Proceedings of the ECML/PKDD Workshop on Advances in Inductive Rule Learning* (pp. 163-178). Pisa, Italy.
- Suzuki, E., & Shimura, M. (1996, August 2-4). Exceptional knowledge discovery in databases based on information theory. In *Proceeding KDD'96 Proceedings of the Second International Conference on Knowledge Discovery and Data Mining* (pp. 275-278). Portland, Oregon.
- Suzuki, E., & Zytchow, J. M. (2000). Unified algorithm for undirected discovery of exception rules. In D. A. Zighed, J. Komorowski & J. Zytchow (Eds.), *Principles of data mining and knowledge discovery* (pp. 169-180). Heidelberg, Germany: Springer.
- Tsumoto, S. (2003). Automated extraction of hierarchical decision rules from clinical databases using rough set model. *Expert Systems with Applications*, 24(2), 189-197.
- Vashishtha, J., Kumar, D., & Ratnoo, S. (2013). An evolutionary approach to discover intra- and inter-class exceptions in databases. *International Journal of Intelligent Systems Technologies and Applications*, 12(3/4), 283-300.
- Witten, I. H., Frank, E., & Hall, M. A. (2011). *Data mining: practical machine learning tools and techniques* (3rd Ed.). Burlington, MA: Morgan Kaufmann.
- Zadeh, L. A. (1996). Fuzzy logic computing with words. *IEEE Transactions on Fuzzy Systems*, 4(2), 103-111.

FLA-SLA Aware Cloud Collation Formation Using Fuzzy Preference Relationship Multi-Decision Approach for Federated Cloud

Pradeep Kumar Vadla^{1*}, Bhanu Prakash Kolla¹ and Thinagaran Perumal²

¹Department of Computer Science and Engineering, Koneru Lakshmaiah Education Foundation, 520002 Vijayawada, Andhra Pradesh, India

²Faculty of Computer Science and Information Technology, Universiti Putra Malaysia, 43400 UPM, Serdang, Selangor, Malaysia

ABSTRACT

Cloud Computing provides a solution to enterprise applications in resolving their services at all level of Software, Platform, and Infrastructure. The current demand of resources for large enterprises and their specific requirement to solve critical issues of services to their clients like avoiding resources contention, vendor lock-in problems and achieving high QoS (Quality of Service) made them move towards the federated cloud. The reliability of the cloud has become a challenge for cloud providers to provide resources at an instance request satisfying all SLA (Service Level Agreement) requirements for different consumer applications. To have better collation among cloud providers, FLA (Federated Level Agreement) are given much importance to get consensus in terms of various KPI's (Key Performance Indicator's) of the individual cloud providers. This paper proposes an FLA-SLA Aware Cloud Collation Formation algorithm (FS-ACCF) considering both FLA and SLA as major features affecting the collation formation to satisfy consumer request instantly. In FS-ACCF algorithm, fuzzy preference relationship multi-decision approach was used to validate the preferences among cloud providers for forming collation and gaining maximum profit. Finally, the results of FS-ACCF were compared with S-ACCF (SLA Aware Collation Formation) algorithm for 6 to 10 consecutive requests of cloud consumers with varied VM configurations for different SLA parameters like response time, process time and availability.

ARTICLE INFO

Article history:

Received: 11 May 2019

Accepted: 13 September 2019

Published: 13 January 2020

E-mail addresses:

pradeepvadla@gmail.com (Pradeep Kumar Vadla)

drkbp@kluniversity.in (Bhanu Prakash Kolla)

thinaperug1@gmail.com (Thinagaran Perumal)

* Corresponding author

Keywords: Cloud federation, collation formation, federated level agreement, fuzzy preferences relationships, key performance indicators, service level agreement

INTRODUCTION

Cloud computing is a computing paradigm which provides the solution to all enterprise applications requirements. The virtual machine (VM) plays a key role in providing computational resources at different instances of the request made by cloud consumers (Mishra et al., 2012). Most of the cloud consumers can be any enterprises of ranging from small scale to large scale using VM instances dynamically. Due to cloud computing on-demand and high scalability nature it needs for enterprises to face some unique challenges in terms of meeting the consumer's requirements for high data-intensive applications which require low congestion of resources and less rejection rate.

The best possible way to attain the above challenge is either avoid over-provisioning of resources for particular VM, but it lacks the efficiency of underutilized physical resources during low demand of consumer's request. Another approach as used by Amazon EC2 is to give authenticated user's service level guarantee for best services. Even in this differentiated model, the privilege users are facing request's rejection, unpredicted delays and resources shortage (Chen et al., 2011). One solution is, Federated cloud, a type of flavored cloud computing model which forms alliances among different service providers and provides resources to customers satisfying their different SLA needs (Rochwerger et al., 2011). In this model cloud providers will collaborate to form collation and try to meet all possible requirements of cloud consumers and satisfy their large demand of resources requirements by maximizing their price by providing good user experience (Rochwerger et al., 2009).

In this paper, we propose an FLA-SLA based cloud collation formation approach. In our scheme, each cloud consumer request consists of the number and type of resources with specified SLA requirement. The KPI's (Key Performance Indicator's) of different cloud providers are considered in this paper to form a Federated Level Agreement (FLA) to have a fine measurement of SLA to form collation at a particular instance. The set of KPI's which have been agreed among cloud providers are used for computing the SLA parameters for collated providers during collaboration and can be considered as FLA's and used as a reference to check for meeting the SLA of a user request. These SLA's are calculated at different instances and checked against user request of resources for collation formation by different cloud providers and provide choice for cloud consumers to choose collated providers who satisfy their request within a specified SLA limit. The main objective considered in our approach was to maximize the total profit gained by the collated cloud providers and share the profit based on their contribution of resources to the collation without FLA and SLA violation.

The state of art of cloud collation formation solutions in federated clouds from Mashayekhy et al. (2014), Guazzone et al. (2014) and Hassan et al. (2011) is either highly computational with the mathematical approach or an iterative merge-split approach for collation formation. In Hadjres et al. (2018), SLA of cloud providers is given importance

for collation formation using Irvy's roommate algorithm which forms preferences for collation with not more than two cloud providers this leads to small collation size which needs next level of computation for collation formation (Irving, 1985). The previous collation formation models are either following high computational approaches or lagging in awareness of cloud providers KPI's specification which results in exhaustive search for forming collation among cloud providers. But our current approach uses concise method in solving the generation of preferences with KPI's parameters used in FLA agreement of cloud providers by using fuzzy preferences multi-decision approach for direct collation formation. Thus our scheme simultaneously analyzes SLA and FLA of cloud providers to solve the issue of collation formation and generate a differentiated model of collated providers which are ready to resolve any sort of resource provisioning issue in federated clouds.

Related Work

The concept of collation formation in the federated cloud is a result of collaboration made by cloud providers in providing resources meeting enterprise application requirements of cloud consumers. This concept offers benefits like dynamic resource provisioning, flexibility, maximized profits for different cloud providers, and improve the user experience. The purpose of creating federated clouds by cloud providers for different enterprise solutions was discussed by Rochwerger et al. (2009). In this work, the authors proposed a reservoir model which leveraged cloud providers in providing massive scale resources for meeting the infrastructure level agreements of different enterprise solutions. The proposed model highlights the need for federation for enabling cloud computing model to have features like service flexibility, controlled admission control, and optimized VM placements, cross-cloud VM allocation, monitoring, and migration. This work has not given any importance of collation formation which plays a critical role in the federation. Celesti et al. (2010) proposed cloud architecture for cross- cloud federation in which a home cloud did not fulfill the requests of its clients would forward these requests to other clouds for resolving their requirements. The cross-cloud federation formation was done by three simple steps like discovery, match making, and authentication. This work does not provide any profit maximization or sharing approach for foreign clouds. Goiri et al. (2012) proposed an economic model for federated cloud in which more public clouds were involved in federation formation given maximizing their profit. In this model, a federated provider module is developed to guide the cloud providers in taking decisions when to rent resources, get outsourced resources and turn of unused nodes. Similar to Celesti work, Giori's work does not consider profit sharing among collation formed cloud providers, nor it has given importance for heterogeneity of VM's while resource provisioning.

Different resource provisioning policies were proposed for cloud providers to maximize their profit and cloud consumers to maximize their resource utilization (Toosi et al., 2011). In this model, cloud providers were given the scope of terminating the VMs when the price for running them becomes negative. CloudSim toolkit was used to run their simulations for different workloads and check the impact of policies on effective resource management. Bittencourt and Madeira (2011) proposed a cost optimization algorithm for workflows of different applications involving high processing and storage cost on a hybrid cloud. In this work, their objective was to develop a recommended system to cloud consumers to have a decision of what amount resources to be leased from public cloud and got aggregated with a private cloud for further processing depending on his current demand. This model does not work on collation formation to maximize the profit of cloud providers and, it needs to be tested for multiple workflows.

Nordal et al. (2011) and Bin et al. (2011) proposed solutions for VM configurations in multiple clouds and cluster clouds with specific constraints like resource oriented, Performance, light-weight computations. The implementation in Nordal et al. (2011) was a new computation model named Balava to manage light-weight VM placement among multiple clouds but did not work on cloud collation formation. While the approach presented in Bin et al. (2011) highlighted on VM resilient systems to enable high availability property to perform with live migration and hardware predictive failure analysis to evacuate the VM before host system fails and provide continuous services to cloud consumers. In both approaches the cost of outsourcing was not considered. Chaisiri et al. (2012) proposed an optimal cloud provisioning algorithm to effectively manage price and demand among several cloud providers during the reservation period. In this algorithm, they used stochastic programming for maximizing profit of cloud providers. Yang et al. (2012) developed online real-time interactive applications for cloud federation architecture. This model focused on the concept of VM migration rather than resource provisioning on VM. In terms of cloud resource management, VM provisioning was proposed in several approaches. Kesavan et al. (2013) introduced a Cloud Capacity Manager to manage diverse workloads with variable demands. It failed to manage the reliability of VM for the low overhead of resources management. Rodriguez and Buyya (2014) proposed a meta-heuristic optimization technique which aimed to minimize overall workflow execution costs within deadline requirements. This algorithm was not successful in providing elasticity and heterogeneity of computing resources. Hassan et al. (2011) proposed a horizontal dynamic cloud federation (HDCF) platform which used game theory for solving distributed resource allocation problem. Game theory cooperative and non-cooperative approaches were used to analyze the criteria of interactions among collated cloud providers while allocating resources. Mihailescu and Teo (2010) proposed a strategy-proof dynamic scheme to achieve social welfare for users while getting priced for resource usage in federated clouds. While Zhang

et al. (2015) proposed COCA, an incentive-Compatible (truthful) Online Cloud Auction mechanism to manage different user demands and generate a new bidding language to buy and sell resources. Samaan (2014) proposed an economic model to regulate the resources sharing among cloud providers for maximum profit and to meet the uncertain needs of the workload of cloud consumers. None of these approaches stated about the collation formation in the federation cloud.

Cloud federation formation was proposed in several approaches. Niyato et al. (2011) implemented a hierarchical cooperation game model which initiated resources and revenue sharing among a group of CP's by forming resources pools to avoid any uncertainty in resolving internal user's request. Mashayekhy et al. (2014) proposed a cloud collation formation approach using game theory and optimizing the maximum profit for cloud providers. In this approach, hedonic game mechanism was used to evaluate fairness properties and the collation formation is computed using split and merge algorithm. Guazzone et al. (2014) extended Mashayekhy's work by using the same hedonic gaming mechanism approach for collation formation, for an energy-aware perspective. Hassan et al. (2016) also built on Mashayekhy's work by proposing two schemes. In Hassan et al. (2016), they proposed a trust-based cooperative game model on forming collation dynamically among trustworthy collated providers to fulfill the dynamic resources request for data-intensive applications on maximizing profits and minimizing penalty cost. In Hassan et al. (2015) they focused on energy-aware federation formation using capacity-sharing mechanism and highlighted on improving the social welfare among CP's while satisfying fairness and stability properties in federation. An overlapping collation framework has been proposed to reduce the security risk involved during the federation formation (Bairagi et al., 2016). This approach depended on the cooperative game to attain higher payoffs among collated CP's. All above schemes have good technical advantages, but most of them are implemented using split and merge approach for collation formation. This mechanism has limitations like lack of stability, higher request rejection rates and failed in handling complex scenarios of VM requests because of not considering collation formation with SLA or QoS parameters which are needed measurements playing a key role while deploying in cloud production environments.

The issue of SLA-driven cloud environments was well addressed in few works like in Stanik et al. (2014), in which the authors proposed the integration for Software Defined Network (SDN) into federated cloud environments, to provide SLA guarantee for cloud consumers. The proposed approach provided an API based software components and a three-layered architectural approach using "ProgNet" to manage the SLA aware negotiation measures for federated cloud networks. In this paper, the cloud federation formation was not addressed while enforcing SLA negotiation mechanisms in cloud environments. Harsh et al. (2011) proposed another framework named contrail to support SLA and Quality

of protection agreements support for federated clouds. Contrail also created a separate layer for SLA management between cloud providers and users. The SLA requirements consideration of cloud consumers was not given importance during federation formation.

Hadjres et al. (2018) proposed an approach in which SLA requirements of cloud users were taken into consideration of collation formation. Different test scenarios were used to analyze the execution time, total profit generation, and individual payoff during collation formation. In this approach, there is a need for KPIs of each cloud provider for forming federation level agreement (FLA) which is similar to SLA not taking into consideration during collation formation. These FLA's will have much impact in contributing resources among cloud providers to meet the SLA requirements of cloud consumers. Ray et al. (2018) proposed a federation formation approach among trusted cloud providers for maximizing satisfaction level of individual cloud providers on the basis of QoS and profit using broker based cloud federation architecture. This approach failed to identify fault and QoS violation during VM migration. Agmon et al. (2018) proposed a Vickrey-Clarke-Groves (VCG) auctions for maximizing social welfare among collated cloud providers by allocating resources efficiently. Sharing of profit among collated providers is not worked out in this approach and failed in providing collision among collated cloud providers which need to be avoided. The summary of the algorithms is listed in Table 1 highlighting the facts of not choosing KPI's of CP's as major factors while forming collation which favors our study of collation formation using both SLA and FLA with KPI's for generating maximum profit among collated cloud providers.

Table 1
Summary of algorithms/model approaches used for cloud collation formation

Author Reference	Algorithm/Model Approach	Pro's	Con's
(Rochwerger et al., 2009)	Reservoir Model	It analyzed primary requirements for creation of federation in cloud computing model.	Collation formation was not taken in to consideration with respect to SLA limitations.
(Celesti et al., 2010)	Cross- Cloud Federation	Basic steps like discovery, match making and authentication were considered during federation with foreign clouds.	Profit Sharing and maximization were not given importance during collation formation.
(Bittencourt, & Madeira, 2011)	Cost Optimization Algorithm	A recommended system was built to predict the usage of resources in hybrid clouds for workflows of specific applications.	It was not tested for multiple work flows and collation formation.
(Nordal et al., 2011)	Balava	VM placement for multi-cloud systems was managed in this model.	SLA Limitations were not given importance during VM placement.

Table 1 (continue)

Author Reference	Algorithm/Model Approach	Pro's	Con's
(Hassan et al., 2011)	Horizontal Dynamic Cloud Federation	It solved distributed resource allocation problem during collation formation.	Resource contentions are not dealt in meeting SLA requirements of cloud consumers.
(Niyato et al., 2011)	Hierarchical Cooperation Game Model	This model provided solution for resource pooling and revenue sharing among cloud providers.	SLA parameters were not taken in consideration while provisioning resources to cloud consumers.
(Chaisiri et al., 2012)	Optimal Cloud Provisioning Algorithm	It managed price and demand of resources during reservation period.	On demand and Spot requests of resources were not handled by cloud providers.
(Kesavan et al., 2013)	Cloud Capacity Manager	It analyzed diverse workloads with variable demands.	Failed in meeting reliability requirements of VM during resource management.
(Rodriguez & Buyya, 2014)	Meta-heuristic Optimization	It handled overall workflow execution costs within deadline requirements.	Elasticity and heterogeneity of resources were not managed.
(Mashayekhy et al., 2014)	Split and Merge Algorithm	Collation formation was achieved with fairness in profit share.	It was exhaustive in high computational time for forming collation.
(Hassan et al., 2015)	Energy- aware Federation Formation	Social welfare was achieved in profit sharing and stability was also attained in federation formation.	SLA parameters were not taken into consideration during federation formation.
(Bairagi et al., 2016)	Overlapping Collation Framework	It dealt with security risks while collation formation.	Lead to higher user request rejection rate.
(Hadjres et al., 2018)	SLA-Aware Collation Algorithm	SLA parameters with Irvy roommate algorithm was used to improve the collation formation.	High computational time in finding preferences and forming collation and KPI factors of CP's were not considered during collation formation.
(Ray et al., 2018)	Broker Based Cloud Federation Architecture	It dealt with satisfaction of individual cloud providers in maximizing profits during collation formation	SLA and KPI's were not dealt in this architecture model.
(Agmon et al., 2018)	Vickrey-Clarke-Groves (VCG) Auctions Model	It analyzed profit sharing effectively using social welfare.	Collision of CP's while sharing resources within SLA limitations was overlooked during collation formation

METHODS

An FLA-SLA Aware Cloud Coalition Formation Framework

This section presents the FLA-SLA Aware Cloud Coalition Formation (FS-ACCF) problem statement, details of the layered federated cloud model and architecture diagram of FS-ACCF model with mathematical formulation and describes the coalition formation algorithm.

Layered Federated Cloud Model

Figure 1 gives the layered federated cloud model which was considered to simulate the understanding of federated cloud approach. It consisted of the provider agent layer, Collated provider agent layer, Broker agent layer, Consumer agent layer. Each layer had set of agents which were involved in interaction to provide the idea of federation formation in cloud computing. The cloud consumer agents would request for resources with desired SLA requirements. In this model, the request of resources was done by considering the number of VMs of different types like small VMs, Medium VMs, Large VMs, and Extra large VMs. Table 2 shows VM instance characteristics of each VM type and these characteristics, prices were inspired by On-Demand instances of Amazon EC2. These requests were forwarded to cloud provider agents through broker agents and then collation formation process was started by having interaction among the set of provider agents and set of collated provider agent's layer was formed for serving the consumer request for a particular instance.

In this model set of KPI factors like (Uptime, Downtime, Reptimein, Reptimeout, Inbyte, Outbyte, Packsize, Availbandwidthin, Availbandwidthout, Packtimein, Packtimeout, Disksize) of cloud provider agents were considered for collation formation. The KPI's were provided by each cloud provider and FLA were computed based on these values.

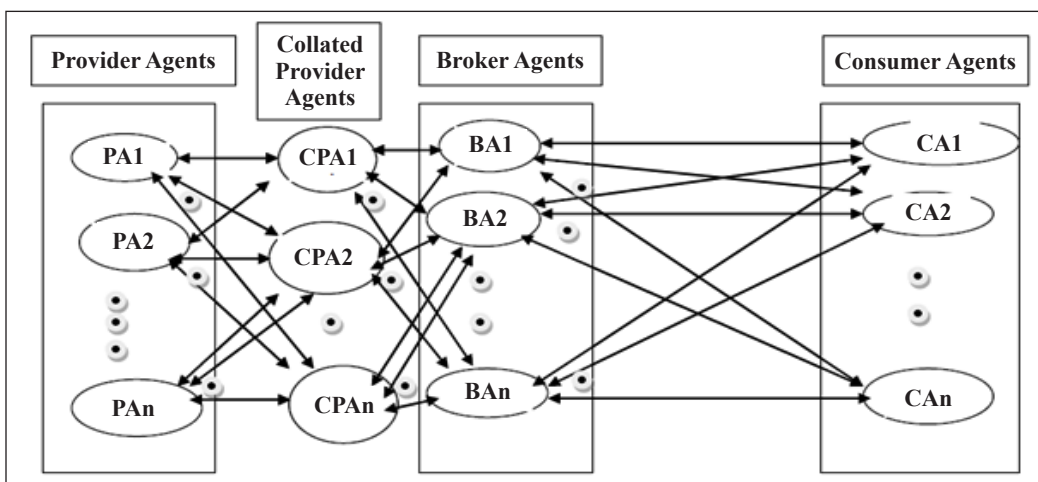


Figure 1. Layered federated cloud model

Architecture Diagram for FLA-SLA Aware Cloud Collation Formation Model

Figure 2 is a proposed architecture model in the above layered federated cloud model to analyze different KPI factors for FLA generation among different cloud providers and compute required SLA parameter values at various instances as the request made by cloud consumers. The cloud broker agent's forwards the request made by cloud consumers along with required SLA parameters. In this architecture model the user required SLA parameters were analyzed over cloud providers computed FLA values along with KPI factor.

Table 2
Example of VM configurations

Parameters	Small VM	Medium VM	Large VM	Extra Large VM
Number of Cores (1.6 GHz CPU)	1	2	4	8
Memory (GB)	1.7	3.75	7.5	15
Storage (TB)	22	48	98	199
Price	0.12	0.24	0.48	0.96

A set of collated provider's satisfying these consumers request at that instance were send for computing Fuzzy Relationship using multi-criteria decision approach for simultaneously analyzing collated providers collation formation for different SLA parameters. In this paper the different SLA Parameters were treated as X Parameters for FS-ACCF algorithm, where the X was used for Availability, Response time, and Process time.

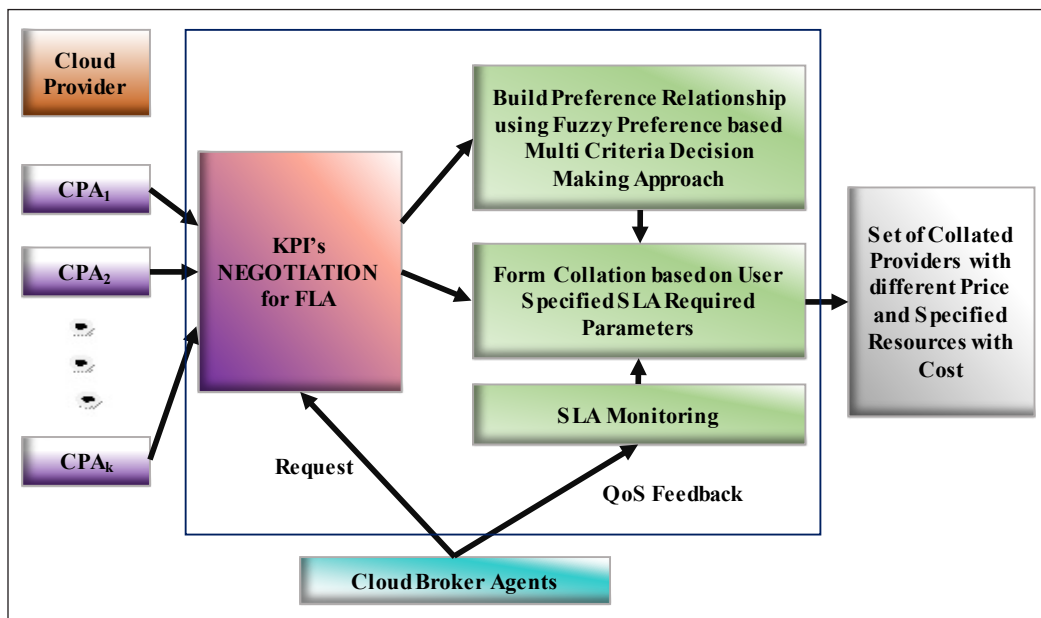


Figure 2. Architecture for FLA-SLA aware cloud collation formation model

Fuzzy preference relationship provides required collated providers list along with their cost at which they provide resources for cloud consumers. The list of collated providers was analyzed at different instances for providing resources. The cloud broker job was to provide this list of collated providers and their cost information to cloud consumers so that they can have a choice of service classes for their different SLA parameters request of resources. Fuzzy preference relationship provides required collated providers list along with their cost at which they provide resources for cloud consumers. The list of collated providers was analyzed at different instances for providing resources. The cloud broker job was to provide this list of collated providers and their cost information to cloud consumers so that they can have a choice of service classes for their different SLA parameters request of resources.

Notations. The set of Cloud providers specified by $CP = \{I/I=1, 2, \dots, N\}$ and User request vector $RV_k = \{rv_1, rv_2, \dots, rv_m\}$ rest of parameters and their descriptions are specified in Table 3 notations.

The best collation of provider agents that satisfied a user request along with their specified SLA parameters was found. The complex task was to analyze the KPIs of cloud

Table 3
Notations

Variables	Description
N	No of available CPs
CP	A set of Cloud Providers $CP = \{I/I=1, 2, \dots, N\}$
M	Number of types of VMs i.e. smallVM, mediumVM, LargeVM, ExtralargeVM for example (5,10,6,4)
VM_{ij}	VM of size j offered by provider i
RV_k	User Request Vector
$Cost_i$	A set of cost of VM's provided by i provider
rv_{kj}	No of VM 's of type j needed by user request
$AvailP_i$	Availability FLA parameter computed by a provider i using specified KPIs
PtP_i	Process time FLA parameter computed by a provider i using specified KPIs
RtP_i	Response time FLA parameter computed by a provider i using specified KPIs
X_{ij}	Decision variable that represents the no of VM's of allocated by provider i
F	Characteristic function that is used to obtain Total profit obtained by collation
CoIP	The set of all collations that can be formed from CPSs.
TotalProfitX	Total Profit earned by different collation formed on X parameters. Where X is Availability, Response time and Process time.
ShapelyValueX	Shapley Value computed for each cloud provider involved in collation formation on X parameters Where X is Availability, Response time and Process time
FXPrice	A set of prices proposed by the broker for each type of VM $FXPrice = \{price_1, price_2, \dots, price_m\}$

providers for computing FLA parameters and then the preferred combinations of cloud providers who satisfied the user request with required SLA parameters were found. In this system model the preference of cloud providers were computed using fuzzy preference relationship multi-decision approach for collation formation among cloud providers. Total profit was computed based on the price set by broker and cost computed by their preferred collation cloud providers to check for maximum profit earned by the collation formation. This maximum profit needed to be shared among collated providers based on their contribution of resources.

System Model and Mathematical Formulation

We modeled the FS-ACCF problem as a hedonic coalitional game (CP, V) with transferable utility (TU). A cooperative game as mentioned in Saad et al. (2009) and Álvarez-Mozos et al. (2013) is a set of players will cooperate to form collations and share profit among them based on their contribution in collation. A utility or characteristic function is used to measure the total profit of the possible collation by meeting specific requirements and condition in collation formation. In this system model the preference relation is established are computed based on the fuzzy preference relationship of multi-decision approach.

Collation Formation Model

In our case of hedonic game, the players were cloud providers among which their FLA parameters were computed using their specified KPIs and then performed fuzzy preference relationship to list the collated cloud providers who satisfied the cloud consumer request at that instance. In our system the SLA parameters between the cloud providers was considered as FLA and the values were computed by specified KPI's (i.e. Uptime, Downtime, Reptimein, Reptimeout, Inbyte, Outbyte, Packsize, Availbandwidthin, Availbandwidthout, Packtimein, Packtimeout, Disksize) of cloud providers by Equation [1], [2], [3], [4] and [5].

$$AvailP_i = 1 - \left(\frac{Downtime_i}{Uptime_i} \right), \text{ where } i \in CP \quad [1]$$

$$PtP_i = Reptimeout_i - Reptimein_i, \text{ where } i \in CP \quad [2]$$

$$RtP_i = RinP_i + RoutP_i, \text{ where } i \in CP \quad [3]$$

$$RinP_i = \frac{Packsize_i}{(Availbandwidthin_i - Inbyte_i)} \quad [4]$$

$$RoutP_i = \frac{Packsize_i}{(Availbandwidthout_i - Outbyte_i)} \quad [5]$$

Cloud provider computed their respective FLA parameters by above equations then each value of this compared with SLA parameter mentioned along with user request vector (RV_k). Initially the cloud providers whose FLA parameters not matching with the SLA values were eliminated from collation formation for that instance. The rest of cloud providers were considered for fuzzy preference relation multi-decision approach for checking preference relationship and forming collation preferences with respect to that FLA parameter values. The process of this fuzzy preference relation multi-decision approach was taken from Chang and Wang (2008), Tanino (1988), Hipel et al. (2011) and Mesiar (2007). In these approaches they had been applied this fuzzy preference computation for gathering preferences in different computation fields like WIMAX and System design decision.

The final lists of preferred collated providers were used for total profit computation. A characteristic function (i.e. F) was used to associate profit to a collation. Thus, total profit was a real valued function $F: ColP \rightarrow \mathbb{R}^+$ where $F(\emptyset) = 0$ and \emptyset is empty collation. A provider would get many choices of collated providers list generated because of fuzzy preferences relationship multi-decision approach. Now providers should choose which collation providers list would generate maximum total profit.

The best collation of cloud providers was analyzed by satisfying all requirements while maximizing total profit. This can be expressed as follows:

$$Max \sum_{CP_i \in C} \sum_{j=1}^M X_{ij} (Fprice_i - Cost_{ij} - \alpha_i PenaltyFunc(X)) \quad [6]$$

$$where \textit{PenaltyFunc}(X) = \sum_{j=1}^n \frac{\sum_{k=1, k \neq P}^{|C|} X_{kj} Cost_{kj}}{X_{ij} Cost_{ij}} \quad [7]$$

Subject to:

$$N, M \in \mathbb{N} \quad (\text{Cond1})$$

$$F \in \mathbb{R}^+ \quad (\text{Cond2})$$

$$X_{ij} \geq 0 \text{ for all } i=1 \dots N \text{ and } j=1..4 \quad (\text{Cond3})$$

$$\sum_i^j X_{ij} = r_{kj} \text{ for } j=1..4 \quad (\text{Cond4})$$

$$X_{ij} \leq VM_{ij} \text{ for } i=1..n \text{ and } j=1..4 \quad (\text{Cond5})$$

$$\alpha_i = \{ 0, 1 \} \quad (\text{Cond6})$$

The Equation (6) was used for computing maximum total profit for selected decision variable instances with fixed price; cost for required VM's allocated with penalty function. The penalty function of Equation (7) was applied by cloud providers CP_i to compute penalty cost for not supplying the resources with specified SLA values after collation formation. It was instantaneously computed for cost associated with those VMs of cloud providers which were not meeting their specified contribution among collated providers. Constraints (Cond1) and (Cond2) ensured the number of VMs and number of cloud providers to be set of Natural numbers and real positive numbers respectively. Constraints (Cond3) for the decision variable X_{ij} was a Positive Value. The constraint (Cond4) gives the request of that particular VM instance is meeting with their summated decision variable of all collated providers involved in collation formation. The constraint (Cond5) ensured that decision variable was not exceeding required VM instances. The final constraint (Cond6) was the decision parameter for penalty function existing or not while provisioning resources after forming collation.

Profit Sharing Model

Once the best collation formed, the total profit was obtained for particular instance of user request with specified SLA parameter. The total profit was distributed among those cloud providers who were contributing to the collation done based on normalized Shapley value computation. The Shapley value payoff was obtained by the product of collation profit by the normalized Shapley Value:

$$ShapleyPayoffX_i = \frac{ShapleyValueX_i}{\sum_{CP_j \in C} ShapleyValueX_j} * Profit \tag{8}$$

$$ShapleyValueX_i = \sum_{subC \subset comb(C \setminus \{CP_i\})} \frac{(S!(n_c - S - 1)!}{n_c!} (v(subC \cup \{CP_i\}) - v(subC)) \tag{9}$$

Where S is cardinal of the sub collation subC, n_c is the cardinal of C and Comb(C) to the set of all combinations of 1,2,..., n_c elements of C.

The Equation [8] was used for computing shapley payoff value for on a particular QoS parameter by normalizing shapley value for sharing profit among the collated cloud providers. The Equation [9] computed the Shapley value on each QoS parameter for sub-collation and collation set of cloud providers for sharing profit. The Figure 3 gives clear summary of integration of above both models.

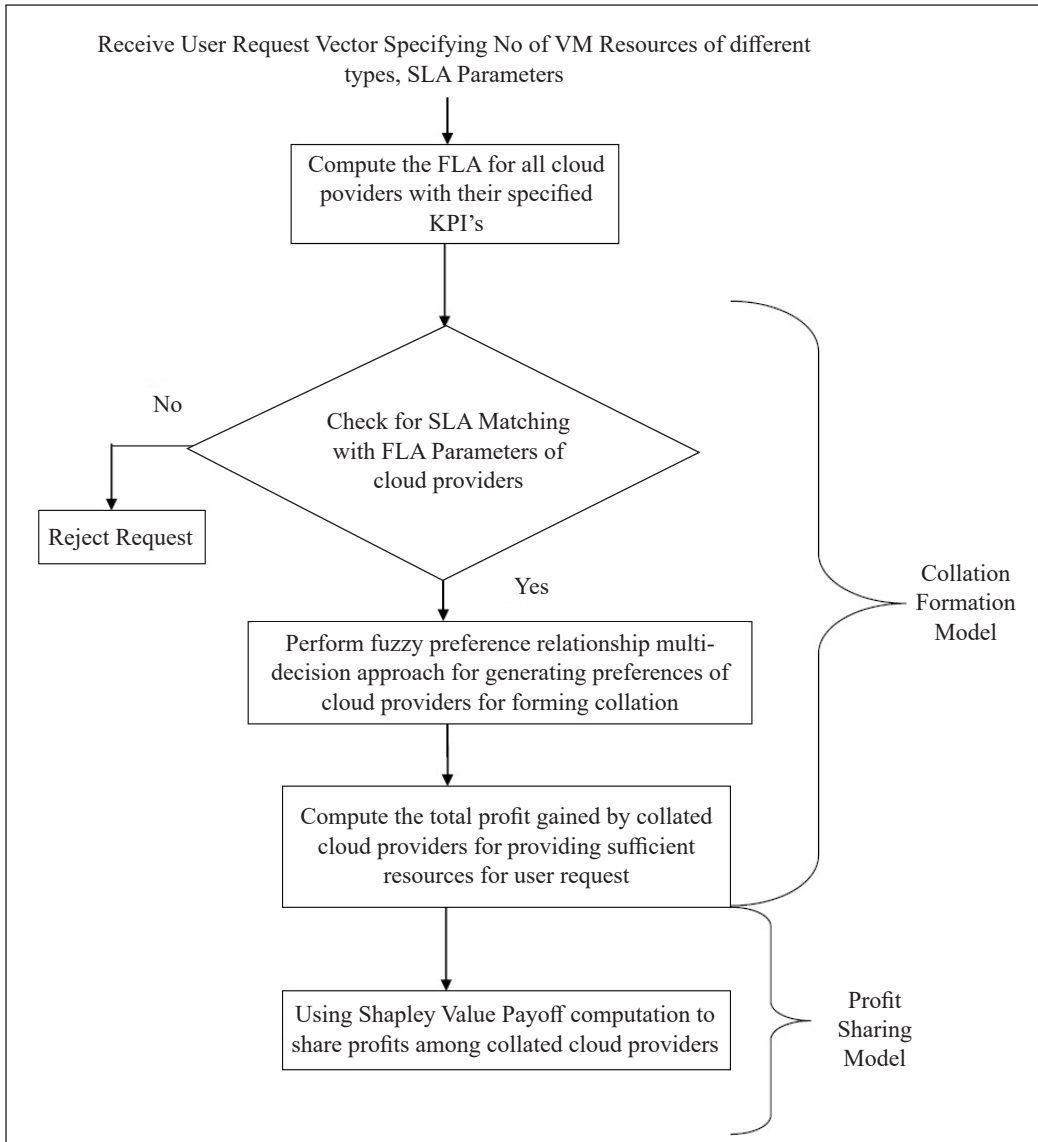


Figure 3. Dataflow diagram for FS-ACCF

FLA-SLA Aware Collation Formation Algorithm

Algorithm 1: FLA-SLA Aware Collation Formation Algorithm (FS_ACCF)

1. **Input:**the cloud providers set CP and their KPI's(Key Performance Indicator's the request R,SLA parameters
2. Calculate the FLA parameters from the specified KPI's of cloud providers
3. Eliminate from Set of CP all CP's that do not meet the required SLA parameters

4. $XCollatedPreferences = FuzzyPreferencesListX(NewCPList, XparametersofNewCP)$; (X will be Availability, Response time, Process time etc..)/ * Calculating Fuzzy Preference relation using multi criteria decision making approach */
5. $[TotalProfitX] = Find_CollationX(XCollatedPreferences, UserReq, CPRes, Cost)$; /* Calculated total profit earned by the collated providers during collation and providing resources without violation of SLA parameters.
6. $[ShapelyValueX] = CalShapelyValueX(XCollatedPreferneces, TotalProfitX, CPRes, Cost)$; /* calculate Share of profit among the collated provider using shapely value */
7. Validate the resource availability during collated providers providing resources.
8. If Current selected $XCollatedPreferences$ doesn't provide enough resources, then $UserReq$ will be checked for other $XCollatedPreferences$ and get allocated with different price.

The Algorithm 1 was used for processing the request made by cloud consumers along with their specified SLA parameters. Initially in step 2 of algorithm the set of KPI's were used for undertaking FLA agreement among cloud providers. In step 3 SLA parameters of cloud consumers were checked for FLA agreed values of cloud providers and selecting only those cloud providers matching with in SLA parameters limit. The step 4 is called the fuzzy preferences list Algorithm 2 by passing selected providers list with required X SLA parameters of those providers.

The Step 7 was used for calculating Total profit for those X SLA parameters with preferred Collated providers by checking their satisfaction of cloud consumer's request of resources within their SLA parameter limit. Step 9 was used for Shapley value calculation to share the profit among the collated providers. Step 11 and 12 were used if any of the selected collated providers fail to meet in providing required resources within their SLA limit.

Algorithm 2: Computing the Collated Preferences lists

Function $FuzzyPreferencesListX(NewCPList, Xparameter)$

1. $Count = Length(NewCPList)$
2. For $i=1:Count$ assign array $A(i) = Xparameter(NewCPList(i))$; end for
3. For $i=1:Count$ For $j=1:Count$ Intialize 2-dimensional matrix $CurrA$ for FAHP computation.
4. If $(i=j)$ $CurrA(i,j)=1$ else compute $m=A(i)-A(j)$ end if
If $(m < 0)$ $CurrA(i,j)=0$ else $CurrA(i,j)=m$ end if end for end for

5. For $i=1:\text{Count}$ For $j=1:\text{Count}$ $\text{fuzzyX}(i,j)=\max((\text{currA}(i,j)-\text{currA}(j,i)),0)$;
end for end for
 6. For $i=1:\text{Count}$ $\text{fuzzymaxX}(i)=1-\max(\text{fuzzyX}(:,i))$; end
 7. For $i=1:\text{Count}$ For $j=1:5$ if($\text{fuzzymaxX}(i)=\text{Xparameters}(j)$) $\text{finallist}(i)=j$;
end if end for end for
 8. for $i=1:\text{Count}$ For $j=1:\text{Count}$ if($\text{fuzzymaxX}(i)\leq\text{fuzzymaxX}(j)$)
 $\text{preferlistX}(i,j)=\text{finallist}(j)$; end if end for end for
 9. $\text{XCollatedpreferences}=\text{preferlistX}$;
 10. Return ($\text{XCollatedPreferences}$)
-

The Algorithm 2 Fuzzy Preferences List is purely a mathematical model multivariable decision approach used for calculating preferences among the cloud providers with their agreed FLA values of different X SLA parameters. It provides output as different collated providers list. At step 2 one dimensional matrix A(I) is initialized with new cloud providers SLA parameter values. At step 3 and 4 a two dimensional matrix CurrA (I,J) was initialized by comparing the A(i) values. At step 5 fuzzyX matrix was computed to get the maximum value of CurrA (I,J). At step 7 and 8 the finalist of preferred cloud providers for forming collation were listed by undergoing the fuzzy computation.

The Algorithm 3 was used for computing the total profit for different X Collated preferences simultaneously by collated cloud providers satisfying user requested and checked for their availability of resources and calculated the price which needed to be paid by cloud consumers for getting serviced by that collated providers.

Algorithm 3: Computing the total profit of XCollatedPreferences

Function Find_CollationX(XCollatedPreferences,UserReq,CPRes,Cost)

1. For each XCollatedPreferences list try to check for availability of resources and cost satisfy the UserReq and CPRes
 2. $\text{CPRes}(\text{XCollatedPreferences}) > \text{UserReq}(\text{Resources})$
 3. $\text{profiteachXCollated} = \text{Cost}(\text{XCollatedPreferences}) * \text{CPRes}(\text{XCollatedPreferences})$
 4. $\text{UserReq}(\text{Resources}) = \text{UserReq}(\text{Resources}) - \text{CPRes}(\text{XCollatedPreferences})$
 5. And repeat above steps for each XCollatedPreferences until UserReq(Resources) are satisfied.
 6. $\text{TotalProfitX} = \text{addall}(\text{profiteachXCollated})$
 7. Return(TotalProfitX)
-

Algorithm 4: Computing the ShapleyVal of XCollatedPreferences

Function CalShapelyValueX(XCollatedPreferences ,TotalProfitX, Cost, CPRes)

1. For each XCollatedPreferences TotalProfitX calculate
 2.
$$\text{ShapleyValX} = \frac{\text{Factorial}(n-1) * \text{Factorial}((n-(n-1)-1))}{\text{Factorial}(n)} * (\text{TotalProfitX}) - \text{Cost}(\text{XCollatedPreferences})$$
 3. List all ShapleyValX of each XCollatedPreferences
-

The Algorithm 4 was used for Shapley value calculation to share the total profit among the specified collated providers who collaboratively satisfied the consumer's request within his specified SLA limit.

RESULTS AND DISCUSSIONS

We implemented the FS-ACCF algorithm using MATLAB. The formulated computations were done through MATLAB code. The results were obtained by executing the FS-ACCF algorithm and compared with S-ACCF algorithm. The S-ACCF algorithm considered Irvy's roommate algorithm to pair the collated providers with minimum combination to achieve the collation with few SLA parameters and to attain total profit computations. But in the collation formation in FS-ACCF algorithm the KPI factors of cloud providers could be used for forming collation using fuzzy set approach of multi-decision criteria for different FLA parameters at particular instance and total profit are computed.

Simulation Environment and Evaluation Metrics

The simulation environment was carried through MATLAB for 6 to 10 consecutive requests for particular VM configurations as mentioned in Table 2, Table 4 gives the cloud providers with their SLA parameters and KPI's and Table 5 gives the resulted values of execution time and total profit during collation formation by both FS-ACCF and S-ACCF algorithms at different instances and tested for collation formation on Intel corei3 processor, 4GB RAM with Windows 7.

Evaluation Metrics. Five(5) metrics were used to evaluate the two approaches: 1) The execution time of the collation formation algorithms for different requests at different instances; 2) The total profit generated by collation; 3) The individual payoff for each provider in the collation for specific XFLA Parameter where X i.e. availability, response time and process time; 4) The no of providers in the generated collation; 5) The number of VMs per provider in the collation.

Performance Results and Analysis

The Figure 4 shows the execution time for different user requests and the comparison between S-ACCF algorithm and FS-ACCF algorithm for execution time with specific SLA parameters request made by them. It is clear from this graph that FS-ACCF using Fuzzy Preference Multi-decision approach resolved the collation formation much faster than S-ACCF Irvis rommmate algorithm. In Figure 4, the maximum difference between the execution time is because in S-ACCF algorithm the collation formation is checked only between pair of two cloud providers which take more time for forming collation where as in FS-ACCF algorithm many pair of collated cloud providers where simultaneously many QoS parameters are considered for collation formation with less execution time.

Table 4
List of SLA and KPI'S values of cloud providers participated in collation formation

Cloud Providers	SLA Parameters (Availability, Response Time ,Process Time)	KPI'S (Uptime, Downtime, Reqtimein, Reqtimeout, Inbyte, Outbyte, Packsize, Availbandwidthin, Availbandwidthout, Packtimein, Packtimeout, Disksize)
CP1	(0.989,0.36,0.23)	(5,10,0.253,0.415,5,6,1024,10,20,0.67,0.68,2)
CP2	(0.956,0.55,0.20)	(7,12,0.415,0.283,8,10,2048,23,45,0.54,0.87,4)
CP3	(0.975,0.43,0.26)	(2,8,0.645,0.923,3,4,512,21,56,0.23,0.45,1)
CP4	(0.968,0.67,0.45)	(4,10,0.93,0.283,4,7,4096,112,34,0.65,0.78,8)
CP5	(0.945,0.56,0.34)	(12,6,0.676,0.459,5,7,256,23,45,0.85,0.56,3)

Table 5
List of cloud consumers request vectors with resulted execution time and total profit gained during collation formation using FS-ACCF Algorithm and S-ACCF Algorithm

S.NO	Cloud Consumer Request Vector for Resources i.e No of (SmallVM, MediumVM, LargeVM, ExtralargeVM)	Execution Time taken for Collation Formation using FS-ACCF Algorithm	Execution Time taken for Collation Formation using S-ACCF Algorithm	Total Profit Gained by Forming Collation Using FS-ACCF Algorithm	Total Profit Gained by Forming Collation Using S-ACCF Algorithm
1	(3,5,8,9)	0.0014	0.0143	144.5	137.9
2	(13,15,18,19)	0.0029	0.0101	93.8	69.1
3	(10,5,18,19)	0.0042	0.0093	307.4	267.9
4	(20,5,18,19)	0.0015	0.0105	272.4	207.9
5	(2,6,8,9)	0.0022	0.011	310.4	198.6
6	(12,16,6,9)	0.0013	0.0088	92.7	69.23

Figure 5 shows the comparison of total profit for different user request specified response time SLA parameter between FS-ACCF algorithm and S-ACCF algorithm. The S-ACCF algorithm only considered one SLA parameter that is response time but in FS-

ACCF multiple SLA parameters are considered and analyzed simultaneously to check for resources by providing optimal choice for cloud consumers in selecting the collated providers within their price limit.

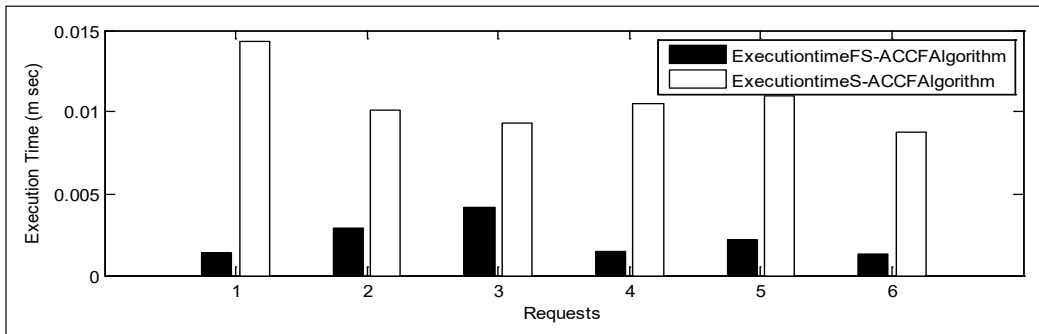


Figure 4. Execution time vs requests for FS-ACCF and S-ACCF algorithms

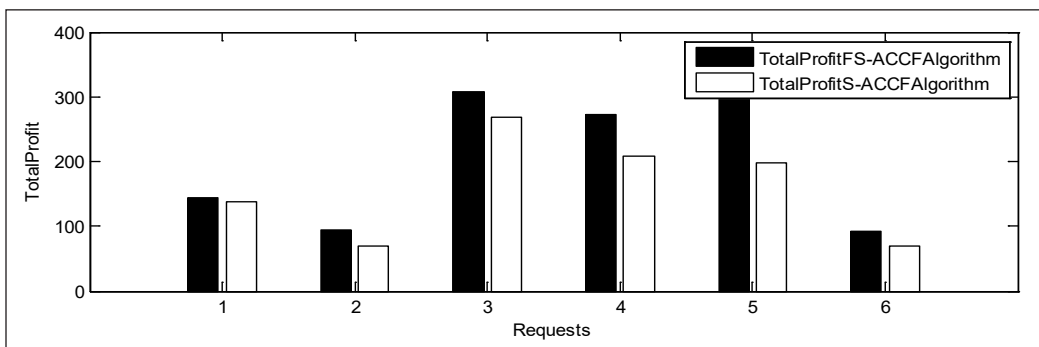


Figure 5. Total Profit vs requests of FS-ACCF and S-ACCF algorithms

Figure 6 gives the total profit for different XFLA parameters using FS-ACCF algorithm, here the X is Availability, Response time and Process Time which are the FLA parameters calculated based on FLA agreement among collated cloud providers with their specified KPI's. In the above graph X-axis Totalprofit(:,1) 1 is for total profit computed for Availability FLA Parameter Collated providers, Totalprofit(:,2) 2 for total profit computed for Response time FLA Parameter Collated providers and Totalprofit(:,3) 3 for total profit computed for Process time FLA Parameter Collated providers.

Figure 7 depicts the no of VM's (NoofVMs(:,1) Small, NoofVMs(:,2) Medium, NoofVMs(:,3) Large, NoofVMs(:,4) ExtraLarge) participated in collation formation for different FLA parameters on X-axis 1 for Availability, 2 for Response time, 3 for Process time using FS-ACCF algorithm. These are the results generated after running the fuzzy set approach of multi-decision criteria for different instance requests made by user for specified SLA parameter.

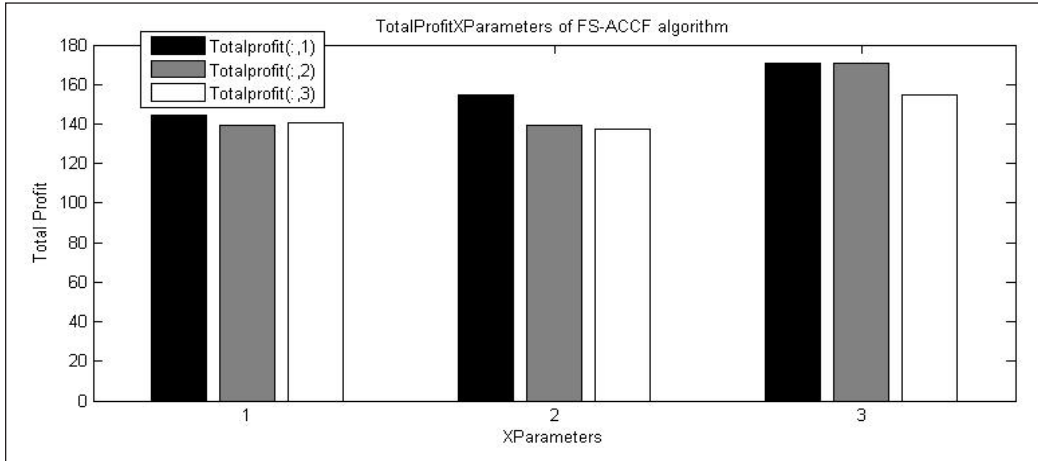


Figure 6. Total profit for different X parameters using FS-ACCF algorithm

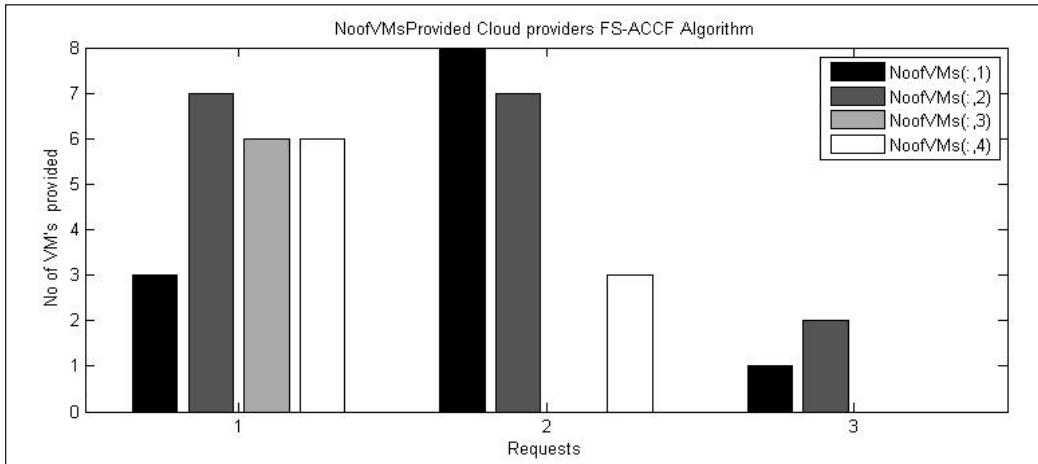


Figure 7. No of VM's participated in collation using FS-ACCF algorithm

Figure 8 gives the Shapley value for different collated providers sharing profit after forming collation on specific FLA parameter. The $ShapleyValue(:,1)$ is for Shapley value computation for availability, $ShapleyValue(:,2)$ is for shapley Value computation for response time, $ShapleyValue(:,3)$ for shapley value computation for process time by using FS-ACCF algorithm.

The Figure 8 only provides the sharing of total profit among the cloud providers who are involved in collation. The Figure 6 justifies the main objective of our paper which results in maximizing total profit for different SLA parameters and Figure 5 gives comparison of total profit generated for different consecutive requests for both FS-ACCF and S-ACCF algorithms.

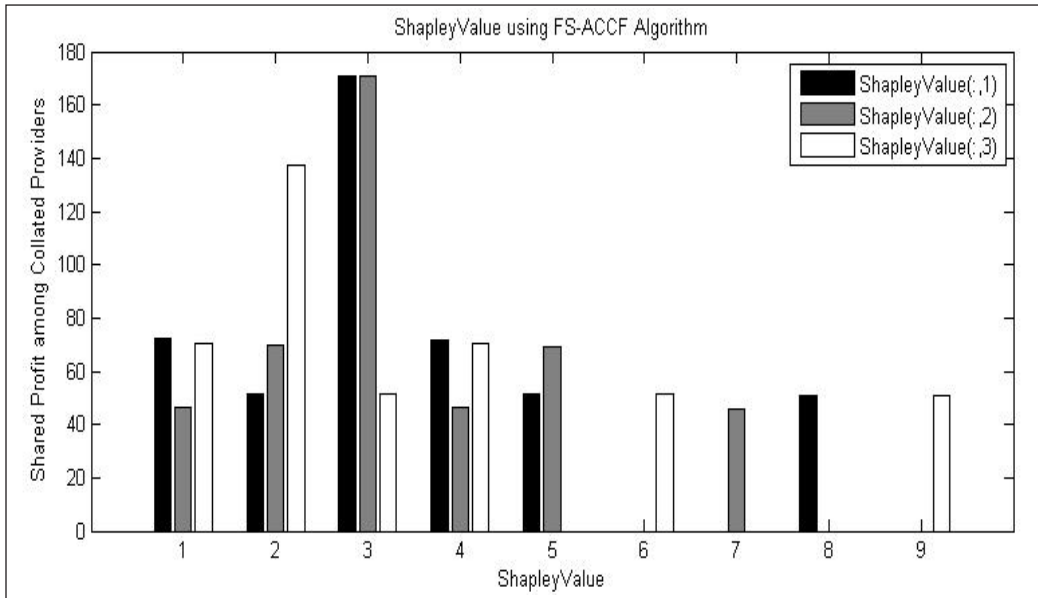


Figure 8. Shapley value of different XCollated providers using FS-ACCF algorithm

CONCLUSION

In this paper different flavor collation formation approach i.e. FS-ACCF algorithm was compared with S-ACCF algorithm in terms of total profit and sharing of profit among collated providers. The basic difference is in terms of generating preferences list from both approaches. In S-ACCF approach they used Irv's roommate algorithm for generating collation preferences which was having less time complexity in computation. Our approach is using fuzzy set multi-decision approach for preference relationship computation along with list of collated providers from whom the user's will have a perfect choice to choose a collated providers list who provides resources with maximum profit. Our current FLA-SLA collation formation was done on computing resources KPI factors for computing FLA values among cloud providers. The future work is to consider the storage KPI factors for computing FLA parameters and broadly try for all possible combinations of FLA parameters during collation formation for generating maximum profit and meeting all SLA parameter requirements of cloud consumers.

ACKNOWLEDGEMENT

We thank Dr. B. Thirumala Rao, Professor, K L University who provided insight and expertise that greatly assisted the research, although he might not agree with all the interpretations/conclusions of this paper. We also would like to show our gratitude to the Dr. Raj Kumar Buyya, Professor, University of Melbourne, for sharing his pearls of wisdom

with us during the course of this research, and we thank 3 “anonymous” reviewers for their so-called insights. We are also immensely grateful for their comments on an earlier version of the manuscript, although any errors are our own and should not tarnish the reputations of these esteemed persons.

REFERENCES

- Agmon, S., Ben-Yehuda, O. A., & Schuster, A. (2018). Preventing collusion in cloud computing auctions. In *International Conference on the Economics of Grids, Clouds, Systems, and Services* (pp. 24-38). Cham, Switzerland: Springer.
- Álvarez-Mozos, M., van den Brink, R., van der Laan, G., & Tejada, O. (2013). Share functions for cooperative games with levels structure of cooperation. *European Journal of Operational Research*, 224(1), 167-179.
- Bairagi, A. K., Alam, M. G. R., Talukder, A., Nguyen, T. H., & Hong, C. S. (2016, January 13-15). An overlapping coalition formation approach to maximize payoffs in cloud computing environment. In *2016 International Conference on Information Networking (ICOIN)* (pp. 324-329). Kota Kinabalu, Malaysia.
- Bin, E., Biran, O., Boni, O., Hadad, E., Kolodner, E. K., Moatti, Y., & Lorenz, D. H. (2011, June 20-24). Guaranteeing high availability goals for virtual machine placement. In *2011 31st International Conference on Distributed Computing Systems* (pp. 700-709). Minneapolis, MN, USA.
- Bittencourt, L. F., & Madeira, E. R. M. (2011). HCOC: a cost optimization algorithm for work flow scheduling in hybrid clouds. *Journal of Internet Services and Applications*, 2(3), 207-227.
- Celesti, A., Tusa, F., Villari, M., & Puliafito, A. (2010, July 5-10). How to enhance cloud architectures to enable cross-federation. In *2010 IEEE 3rd International Conference on Cloud Computing* (pp. 337-345). Miami, FL, USA.
- Chaisiri, S., Lee, B. S., & Niyato, D. (2012). Optimization of resource provisioning cost in cloud computing. *IEEE Transactions on Services Computing*, 5(2), 164-177.
- Chang, T. H., & Wang, T. C. (2008, June 1-6). Fuzzy preference relation based multi-criteria decision making approach for WiMAX license award. In *2008 IEEE International Conference on Fuzzy Systems (IEEE World Congress on Computational Intelligence)* (pp.37-42). Hong Kong, China.
- Chen, J., Wang, C., Zhou, B. B., Sun, L., Lee, Y. C., & Zomaya, A. Y. (2011, June 8-11). Tradeoffs between profit and customer satisfaction for service provisioning in the cloud. In *Proceedings of the 20th international symposium on High performance distributed computing* (pp. 229-238). San Jose, California, USA.
- Goiri, Í., Guitart, J., & Torres, J. (2012). Economic model of a cloud provider operating in a federated cloud. *Information Systems Frontiers*, 14(4), 827-843.
- Guazzone, M., Anglano, C., & Sereno, M. (2014, May 26-29). A game-theoretic approach to coalition formation in green cloud federations. In *2014 14th IEEE/ ACM International Symposium on Cluster, Cloud and Grid Computing* (pp. 618-625). Chicago, IL, USA.
- Hadjres, S., Kara, N., El Barachi, M., & Belqasmi, F. (In Press). An SLA-aware cloud coalition formation approach for virtualized networks. *IEEE Transactions on Cloud Computing*. doi: 10.1109/TCC.2018.2865737

- Harsh, P., Jegou, Y., Cascella, R. G., & Morin, C. (2011). Contrail virtual execution platform challenges in being part of a cloud federation. In W. Abramowicz, I. M. Llorente, M. SurrIDGE, A. Zisman & J. Vayssi ere (Eds.), *European Conference on a Service-Based Internet* (pp. 50-61). Heidelberg, Germany: Springer.
- Hassan, M. M., Al-Wadud, M. A., Almogren, A., Song, B., & Alamri, A. (2015). Energy-aware resource and revenue management in federated cloud: a game-theoretic approach. *IEEE Systems Journal*, 11(2), 951-961.
- Hassan, M. M., Al-Wadud, M. A., Almogren, A., Rahman, S. M. M., Alelaiwi, A., Alamri, A., & Hamid, M. A. (2016). QoS and trust-aware coalition formation game in data-intensive cloud federations. *Concurrency and Computation: Practice and Experience*, 28(10), 2889-2905.
- Hassan, M. M., Song, B., & Huh, E. N. (2011, September 2-4). Distributed resource allocation games in horizontal dynamic cloud federation platform. In *2011 IEEE International Conference on High Performance Computing and Communications* (pp. 822-827). Banff, AB, Canada.
- Hipel, K. W., Kilgour, D. M., & Bashar, M. A. (2011). Fuzzy preferences in multiple participant decision making. *Scientia Iranica*, 18(3), 627-638.
- Irving, R. W. (1985). An efficient algorithm for the "stable roommates" problem. *Journal of Algorithms*, 6(4), 577-595.
- Kesavan, M., Ahmad, I., Krieger, O., Soundararajan, R., Gavrilovska, A., & Schwan, K. (2013). Practical compute capacity management for virtualized datacenters. *IEEE Transactions on Cloud Computing*, 1(1), 1-1.
- Mashayekhy, L., Nejad, M. M., & Grosu, D. (2014). Cloud federations in the sky: Formation game and mechanism. *IEEE Transactions on Cloud Computing*, 3(1), 14-27.
- Mesiar, R. (2007). Fuzzy set approach to the utility, preference relations, and aggregation operators. *European Journal of Operational Research*, 176(1), 414-422.
- Mihailescu, M., & Teo, Y. M. (2010, May 17-20). Dynamic resource pricing on federated clouds. In *2010 10th IEEE/ACM International Conference on Cluster, Cloud and Grid Computing* (pp. 513-517). Melbourne, VIC, Australia.
- Mishra, A., Jain, R., & Durrezi, A. (2012). Cloud computing: Networking and communication challenges. *IEEE Communications Magazine*, 50(9), 24-25.
- Niyato, D., Vasilakos, A. V., & Kun, Z. (2011, May 23-26). Resource and revenue sharing with coalition formation of cloud providers: Game theoretic approach. In *2011 11th IEEE/ACM International Symposium on Cluster, Cloud and Grid Computing* (pp. 215-224). Newport Beach, CA, USA.
- Nordal, A., Kvalnes,  ., Hurley, J., & Johansen, D. (2011, July 4-9). Balava: Federating private and public clouds. In *2011 IEEE World Congress on Services* (pp. 569-577). Washington, DC, USA.
- Ray, B., Saha, A., Khatua, S., & Roy, S. (2018, In Press). Quality and profit assured trusted cloud federation formation: game theory based approach. *IEEE Transactions on Services Computing*. doi: 10.1109/TSC.2018.2833854
- Rochwerger, B., Breitgand, D., Epstein, A., Hadas, D., Loy, I., Nagin, K., & Levy, E. (2011). Reservoir-when one cloud is not enough. *Computer*, 44(3), 44-51.

- Rochwerger, B., Breitgand, D., Levy, E., Galis, A., Nagin, K., Llorente, I. M., ... & Ben-Yehuda, M. (2009). The reservoir model and architecture for open federated cloud computing. *IBM Journal of Research and Development*, 53(4), 4-11.
- Rodriguez, M. A., & Buyya, R. (2014). Deadline based resource provisioning and scheduling algorithm for scientific workflows on clouds. *IEEE Transactions on Cloud Computing*, 2(2), 222-235.
- Saad, W., Han, Z., Debbah, M., Hjørungnes, A., & Basar, T. (2009). Coalitional game theory for communication networks: A tutorial. *IEEE Signal Processing Magazine*, 26(5), 77-97.
- Samaan, N. (2014). A novel economic sharing model in a federation of selfish cloud providers. *IEEE Transactions on Parallel and Distributed Systems*, 25(1), 12-21.
- Stanik, A., Koerner, M., & Lymberopoulos, L. (2014). SLA-driven federated cloud networking: Quality of service for cloud-based software defined networks. *Procedia Computer Science*, 34, 655-660.
- Tanino, T. (1988). Fuzzy preference relations in group decision making. In J. Kacprzyk & M. Roubens (Eds.), *Non-conventional preference relations in decision making* (pp. 54-71). Heidelberg, Germany: Springer.
- Toosi, A. N., Calheiros, R. N., Thulasiram, R. K., & Buyya, R. (2011, September 2-4). Resource provisioning policies to increase iaas provider's profit in a federated cloud environment. In *2011 IEEE International Conference on High Performance Computing and Communications* (pp. 279-287). Banff, AB, Canada.
- Yang, X., Nasser, B., SurrIDGE, M., & Middleton, S. (2012). A business-oriented cloud federation model for real-time applications. *Future Generation Computer Systems*, 28(8), 1158-1167.
- Zhang, H., Jiang, H., Li, B., Liu, F., Vasilakos, A. V., & Liu, J. (2015). A framework for truthful online auctions in cloud computing with heterogeneous user demands. *IEEE Transactions on Computers*, 65(3), 805-818.

Clustering with Modified Mutation Strategy in Differential Evolution

Seema Patil^{1*} and Anandhi Rajamani Jayadharmarajan²

¹*Department of Computer Science and Engineering, The Oxford College of Engineering, Bangalore- 560068 and affiliated to Visvesvaraya Technological University, Belgavi, Karnataka, India*

²*Department of Information Science & Engineering, New Horizon College of Engineering, Bangalore-560103 and affiliated to Visvesvaraya Technological University, Belgavi, Karnataka, India*

ABSTRACT

This paper proposes a clustering approach based on Modified Mutation strategy in the Differential Evolution (MMDE). Differential evolution is an evolutionary computation technique used for optimization. Though DE is very efficient, it sometimes suffers from the issue of slow convergence and the difficulty of achieving a global solution. To overcome these issues, in this paper, a modified mutation method was developed, which maintained the balance between exploration and exploitation. The objectives of modification were to achieve a higher rate of convergence and to obtain better cluster efficiency. The proposed form of modification had been applied on probabilistic environment to define the differential vector through randomly selected members and to obtain the best solution. Over the number of benchmark dataset, clustering efficiency had been estimated and compared with Conventional Differential Evolution (CDE) as well as Particle Swarm Optimization. The proposed method had been tested on a number of benchmark datasets. Experimental

results had shown that MMDE had better and consistent clustering efficiency when compared to Conventional Differential Evolution (CDE) and Dynamic Weighted Particle Swarm Optimization (DWPSO).

ARTICLE INFO

Article history:

Received: 11 July 2019

Accepted: 27 November 2019

Published: 13 January 2020

E-mail addresses:

theseema@gmail.com (Seema Patil)

rjanandhi@hotmail.com (Anandhi Rajamani Jayadharmarajan)

*Corresponding author

Keywords: Clustering, convergence, differential evolution, mutation, particle swarm optimization

INTRODUCTION

Data based knowledge offer numerous opportunities in various practical applications like bioinformatics, engineering, biology, healthcare, medicine, prediction analysis, crime forecasting and computing techniques. The tremendous growth of data-based knowledge in scientific studies has presented a lot of challenges before the researchers to extract useful information using traditional database techniques. Hence effective mining methods are essential to discover the implicit knowledge from huge database.

This knowledge extraction is done with the help of data mining techniques such as classification and clustering. Clustering is an important task of combining various population or data points into clusters. Clustering performs grouping of similar points. It is iterative process to discover the knowledge which involves major trial and failure. The clustering process does not require any kind of feedback to perform similarity of data points, it is self-organized. Clustering using PSO defines a new Swarm Intelligence (SI) for partitioning any datasets into an optimal number of groups through a single run of optimization. SI is an innovative distributed intelligent paradigm for solving optimization problems that originally took its inspiration from biological examples such as swarming, flocking and herding behavior in vertebrates.

Data clustering is a popular approach of automatically finding classes, concepts, or groups of patterns. Particle Swarm Optimization (PSO) incorporates swarming behaviors observed in flocks of birds, schools of fish, and swarms of bees, and even in human social behavior. Data clustering using PSO can be used to find the centroids of user specified number of clusters. DE is one of the most powerful algorithms available in the community and it is being used for various practical purposes. DE works on the steps of defining differential vector, mutation vector, crossover, selection and finally with termination step, any further enhancement in the fundamental structure of DE will help to improve the quality of performance.

This work proposes the method for clustering based on differential evolution. Even though DE is very efficient, sometimes it suffers from the issue of slow convergence and the difficulties in achieving a global solution. To overcome these, balance between exploration and exploitation has been maintained by adding the two modules in the conventional DE. To increase the level of exploitation, under the probabilistic mode, selection between best and randomly selected member takes place. The Differential vector made by best solution, delivers fast change in the solution and results in a faster convergence. The multi-culture approach helps in exploration of new and efficient solutions. Gathering and selection of solutions from different environments will maintain the diversity in the population.

Related Work

Das et al. (2008) used Differential Evolution for automatic clustering of large unlabeled data sets. Gupta and Saini (2018) proposed a new efficient clustering approach which was applied on k harmonic means (KHM) by using PSO. The local optimum problem of KHM was overcome by PSO. Also, fuzzy logic was used to control the various parameters of PSO. Nerurkar et al. (2018) had achieved the global optima on clustering by making use of two validation indices criteria. These indices were simple and robust against other outliers and showed best clustering that had lower computation cost and parallel execution and faster convergence.

Wang et al. (2018) combined PSO and DE approach by taking velocity update of PSO and mutation parameter of DE to generate the new population. The DE re-mutation, crossover and selection were performed throughout the optimization process to get good results. This approach gave the best result when compared with inertia weight PSO and comprehensive learning PSO and basic DE. Zhu et al. (2018) discussed complications associated with K-means clustering algorithm and proposed the concept of centroid all rank distance. Liu et al. (2018) presented an efficient and intelligent DDC algorithm that helped to overcome the difficulties associated with density and delta distance clustering (DDC) when data derived from the two indicators were large.

Yi et al. (2018) had presented a robust recommendation algorithm based on kernel principal component analysis and fuzzy c-means clustering. Kuo and Zulvia (2019) presented a variation of differential evolution (DE) algorithm to solve an automatic clustering problem. Tran et al. (2015) described the new improved approach of PSO by improving the diversity mechanism and mutation operator to employ new neighborhood search strategy. These new approaches were tested on well-defined benchmark data sets. Jiau et al. (2006) presented a hierarchical clustering algorithm based on matrix partitioning.

MATERIALS AND METHODS

Modified Mutated DE (MMDE)

DE is one of the most powerful algorithms in which the formation of Differential vector is the central part that defines the quality of final solution. The existing method of DE based on random member selection slows down the convergence and results in a suboptimal solution.

To increase the convergence speed of DE, a new approach in mutation operation has been presented. It has two possibilities of differential change under the probabilistic environment. In the first case, differential change is defined through best member and random selected member. While in second case, three random members are selected to define the differential change. A threshold value is defined to determine the selection of differential change type. Best member based differential change generates faster change,

while the random member-based selection prevents from suboptimal convergence. The pseudo code for applied mutation strategy is shown below:

```

1. Define the parameter value for:
   Popsz ← population size,  Mf ← mutation rate,  Cf ← cross-over rate,
   K ← No. of Clusters,  Thr ← Define a Threshold value
   Dm ← problem dimension (k *No. of data attributes)

2. Initialize the population:
   For i=1:Popsz
     POP (i, :) ← [Select 'K' Random sample of data from data set and convert into an array];
   End

3. While termination doesn't occur, {do
   For i=1: Popsz
     X ← POP(i,:);
     r ← U [0, 1]; a random number generated through uniform distribution in range of [0, 1];

     if r < Thr
       • Select two members' m1 & m2 randomly from population
       • Select best member BM from population
       • Mutation vector defined as: Mv = m1+ Mf* [ BM- m2];
     Else
       • Select three members m1, m2 & m3 randomly from population
       • Mutation vector defined as: Mv= m1+ Mf*[m2-m3]
     End

     rv ← generate a random vector of size [1 1] by U [0, 1];

     For j=1: dm

       if rv(j) < Cr
         Ox(j) ← Mv(j);
       Else
         Ox(j) ← X(j);
       End

     End

     Select the better one among parent and offspring
     If  $f_{fitness}(Ox) > f_{fitness}(X)$ 
       NPOP(i,:) ← Ox;
     Else
       NPOP(i,:) ← X;
     End;

   End
   Bs ← Best solution from NPOP
   If (termination doesn't occur)
     Go to step 3
   Else
     Final solution ← Bs;
   End

```

In this proposed work Thr is considered as 0.2. Threshold value should not be high otherwise population will lose the diversity soon.

Multi-domain-based DE

A multi-culture concept called “Multi-culture modified mutation Differential Evolution” has been developed to evolve the individual population independently and later to exploit the population to form a better community, which allows an efficient search of the solution space. This approach finds its inspiration from the present human society, where two things can happen at the fundamental level (i) the independent existence of a number of separate populations, each progressing under the same environment up to a certain period of time, (ii) a number of selected individuals belonging to different population, forms a new population to achieve desired objectives.

Rather than working under a monoculture formed by one population as in the conventional PSO, in this paper a multicultural environment has been considered, where a number of different environments are independently created by a different set of population. This study considered population samples that had undergone independent social evolution and among all from the diverse population samples the best individual were selected to finish the task. This was a dual stage process where first stage found some potential solution discovered from different regions of solution space, and later in the second phase, each individual contributed more efficiently to find a global solution. Even with the small size of the population, the proposed method had achieved better quality solution with a very high degree of consistency.

In the working principle of MMDE, population (POP) represents the initial random population, that evolves through the DE process, individually and independently, undergoing fewer iterations, and creates the multi-culture new population (NPOP). Even though the process of creating the NPOP is same for all POP, because of difference in leadership and different community environment, each NPOP has different characteristics. Through the fitness-based selection process, among all members of NPOP, better members were selected to form a new population (SPOP), which had the same size as initial POP. In SPOP, there are a number of good candidates, which are different and have higher fitness value, hence high level of diversity exists in the SPOP. Finally, to obtain the Final Population (FPOP), MMDE applied over SPOP, till the terminating criteria are met.

Datasets Used for Experiment

Experiment was conducted on the three benchmark data sets of UCI repository (Dua & Graff, 2019). Wine, Iris, and Glass datasets had been considered to analyze and compare the performance of proposed method with the evolutionary methods. Table 1 shows the details of Wine, Iris, and Glass datasets.

Table 1

Description of datasets

Data set	No of attributes	No of instances	Type of data
Wine	13	178	Multivariate
Iris	4	150	Multivariate
Glass	10	214	Multivariate

RESULTS AND DISCUSSION

This section discusses the results obtained from various evolutionary methods. Parameters under discussion are size of population, mutation, crossover rate, and number of iterations. Lower population size will have lesser diversity and low exploration rate, which may result in convergence with suboptimal solution. Higher population size may lead to very slow convergence. So practically, depending upon the kind of application, a population size of 50 to 150 is generally considered.

In practical applications, it was observed that low value of mutation and crossover rate caused slower convergence, while high mutation rate led to travelling the same area of search landscape. It also observed that high crossover rate caused loss of diversity and led to less exploration. It was also observed that very high value of crossover would cause loss of diversity and exploration. Therefore, a moderate value in the range of 0.3 to 0.7 was preferred for both mutation and crossover rate and the mutation rate value must be lesser than the crossover rate value.

In the algorithm design process, instead of opting for self-termination it is better to give enough opportunity to the algorithm to come up with optimum results; this helps in evaluating the strength of the algorithm. During the process, more diversion characteristics had been observed from 100 to 200 iterations, while stability was observed from 300 to 400 iterations and which was maintained up to 600 iterations, which could be clearly observed in the figures shown below. Hence, 600 iterations were good enough to define the stability of algorithm performance.

Therefore, in this experiment, the size of population had been considered as 100, mutation rate and crossover rate as 0.4 and 0.5 respectively and the allowed number of iterations as 600.

The performances of all three approaches (DWPSO, CDE, MMDE) have been represented in a tabular format in terms of no of trials, correctly placed data samples in the clusters, number of data samples placed wrongly, cluster efficiency and total intra cluster distance value.

In the first part, only the MMDE had been applied and performances had been obtained for 5 independent trials for 'Wine', 'Iris' and 'Glass' datasets. Comparison had been made with Conventional DE (CDE) and Dynamic Weighted PSO (DWPSO).

In second part, multidomain based experiment had been included with MMDE and performances had been estimated over “Glass” data set. Experimental process had been developed in the MATLAB version 7.1 environment.

Dataset: Wine Data

There are total 178 set of data carrying 3 clusters. Each data contains 13 attributes.

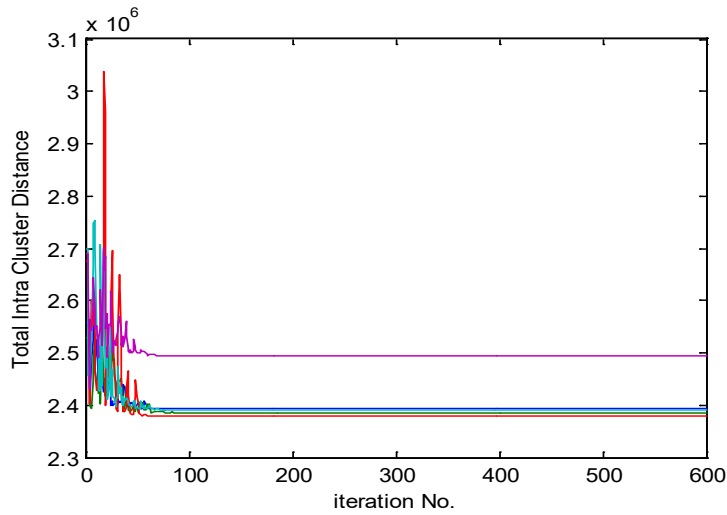


Figure 1. DWPSO based convergence in 5 trials for wine data set

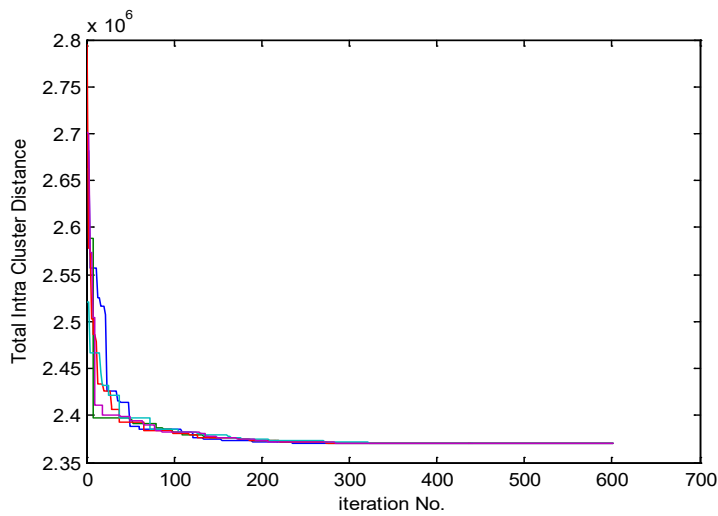


Figure 2. CDE based convergence in 5 trials for wine data set

Table 2

Mean Performance over 5 trials by different algorithm over wine data set

	Correctly clustered data samples	Wrongly clustered data samples	Clustered efficiency	Total Intra Cluster Distance value $1.0e+006$ *
DWPSO	125	53	70.22	2.4088e+006
CDV	125	53	70.22	2.3707e+006
MMDV	125	53	70.22	2.3707e+006

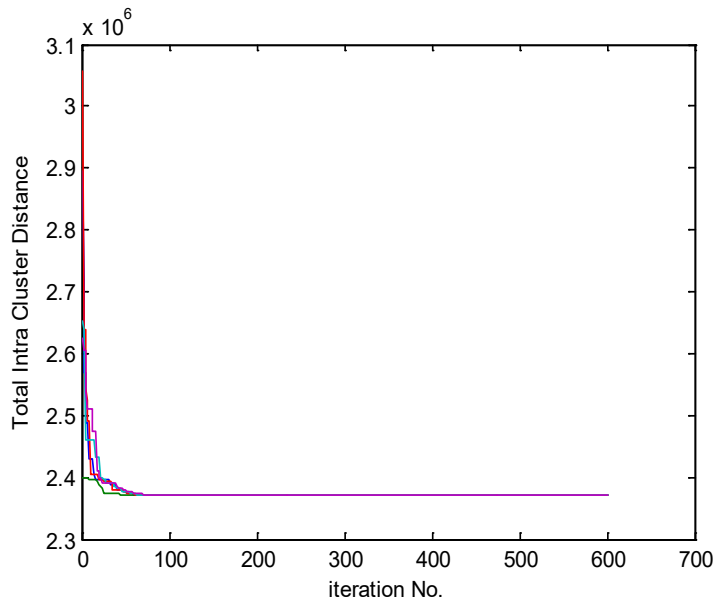


Figure 3. MMDE based convergence in 5 trials for wine data set

Table 3

Centroid position for wine data

Centroids of Wine data set									
C1	3.0351	3.0067	3.0065	3.0541	3.2816	3.0057	3.0043	3.0108	3.0041
C2	3.0375	3.0051	3.0065	3.0462	3.2867	3.0078	3.0081	3.0008	3.0051
C3	3.0339	3.0067	3.0062	3.0565	3.2508	3.0057	3.0048	3.0010	3.0040

Centroids of Wine data set				
C1	3.0154	3.0024	3.0067	4.9797
C2	3.0154	3.0029	3.0084	6.2486
C3	3.0111	3.0024	3.0067	4.2455

The performances obtained under 5 independent trials by different algorithms are shown in Table 2. It can be observed that all the three algorithms have nearly the same performances; while the distance value is marginally greater for DWPSO. The obtained centroid values by MMDE for the 1st trial are shown in Table 3.

The convergence characteristics for DWPSO over wine data in 5 independent trials have been shown in Figure 1. It can be observed that, good amount of diversity existed in their convergence characteristics and mean convergence value obtained was around $2.4088e+006$, which is shown in Table 2. Over the same data set, CDE had been applied for 5 independent trials and obtained convergence characteristics are shown in Figure 2.

It can be observed that, nearly same convergence path had appeared over different trials and the obtained final convergence value for total intra cluster distance was around $2.3707e+006$ which was substantially less compared to the value obtained by DWPSO. To get clarity on advantages of proposed MMDE, the experiment has been repeated over wine data with MMDE and obtained convergence characteristics have been shown in Figure 3.

It can be observed that faster convergence, with excellent reliability feature, has been achieved compared to both DWPSO and CDE. To demonstrate the relative comparison between DWPSO, CDE and MMDE, their mean performances over 5 trials have been plotted on a graph as shown in Figure 4. It is observed from Table 2 that, the mean intra cluster distance for DWPSO and MMDE were nearly same. However, convergence of MMDE occurred around 100th iteration, while DWPSO took more than 200 iterations to converge.

Dataset: IRIS Data

Iris dataset contains a total of 150 data sets and each data has 4 attributes. Three different global clusters exist in the dataset. The performances over Iris data by different algorithms for a number of trials have been analyzed. Figure 5 depicts the performance of DWPSO in 5 trials for Iris dataset.

It can be observed that, there was a consistency in performance in all the trials. While initially more uncertainty to explore the optimal solution has been observed, later after around the 80th iteration, optimal solution has been explored smoothly. The performance by DWPSO and MMDE on Iris dataset are shown in Figure 6 and in Figure 7 respectively.

Diverse convergence has been observed in the beginning, later smooth convergence has been observed. CDV is the vector used by CDE and MMDV is the vector used by MMDE. The mean convergence characteristics comparison of DWPSO, CDE and MMDE has been shown in Figure 8. Intra cluster distance obtained for DWPSO, CDE and MMDE has been shown in Table 4, 5 and 6 respectively. The obtained centroid values have been shown in Table 7. It is observed that mean distance obtained by MMDE is less compared to distance obtained by CDE and DWPSO.

Table 4

DWPSO performance over Iris data

Trial No.	Correctly clustered data samples	Wrongly clustered data samples	Clustered efficiency	Total Intra Cluster Distance value
1	134	16	89.33	79.3157
2	134	16	89.33	80.2949
3	133	17	88.67	79.4755
4	136	14	90.67	83.2333
5	133	17	88.67	79.7068
Mean	134	16	89.33	80.4052

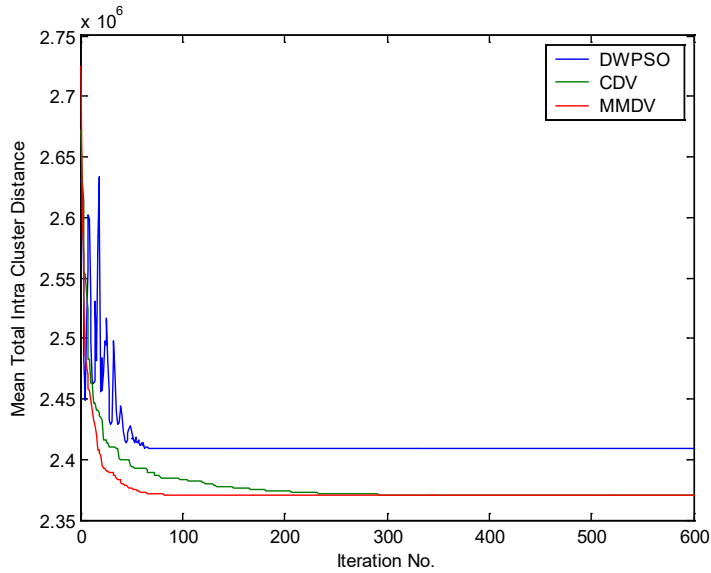


Figure 4. Mean convergence comparison for wine data set

Table 5

CDE performance over Iris data

Trial No.	Correctly clustered data samples	Wrongly clustered data samples	Clustered efficiency	Total Intra Cluster Distance value
1	134	16	89.33	79.2028
2	134	16	89.33	78.9563
3	133	17	88.67	79.1462
4	134	16	89.33	79.2389
5	134	16	89.33	78.9430
Mean	133.8	16.2	89.2	79.0974

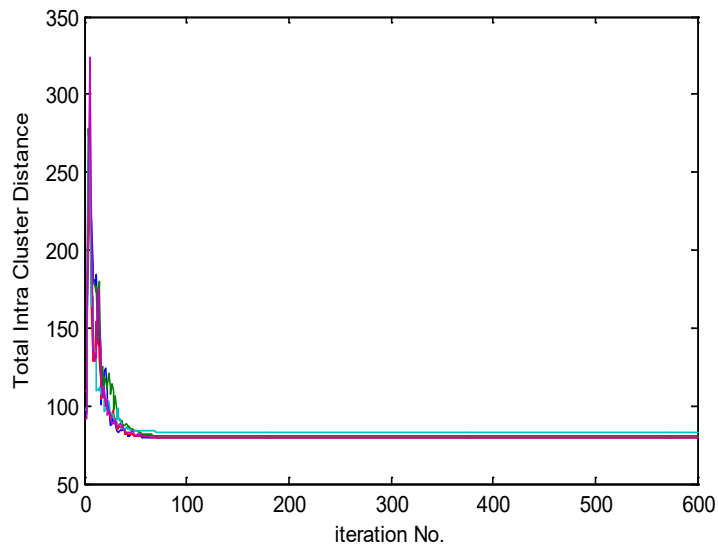


Figure 5. DWPSO based convergence in 5 trials for Iris data set

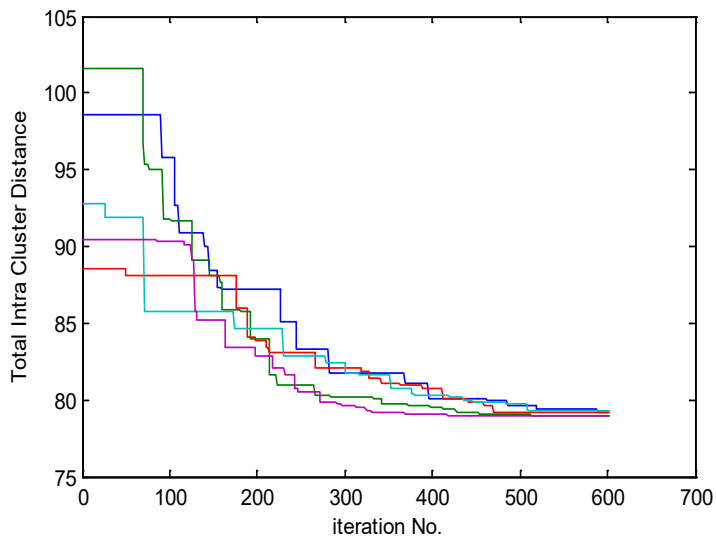


Figure 6. CDE based convergence in 5 trials for Iris data set

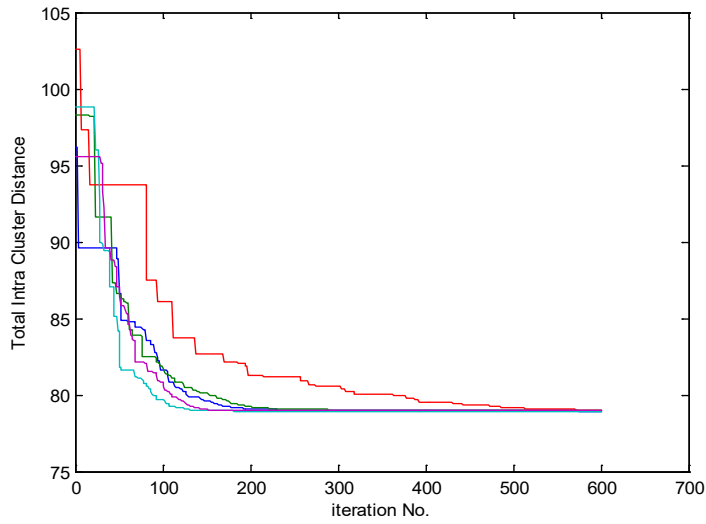


Figure 7. MMDE based convergence in 5 trials for Iris data set

Table 6

MMDE performance over Iris data

Trial No.	Correctly clustered data samples	Wrongly clustered data samples	Clustered efficiency	Total Intra Cluster Distance value
1	134	16	89.33	78.9471
2	134	16	89.33	78.9631
3	134	16	89.33	79.0133
4	134	16	89.33	78.9454
5	134	16	89.33	78.9494
Mean	134	16	89.33	78.9637

Table 7

Centroids value for Iris data set

Centroids of IRIS Dataset				
C1	5.8863	2.7456	4.3731	1.4115
C2	5.0173	3.4385	1.4452	0.2704
C3	6.8326	3.1128	5.7640	2.0469

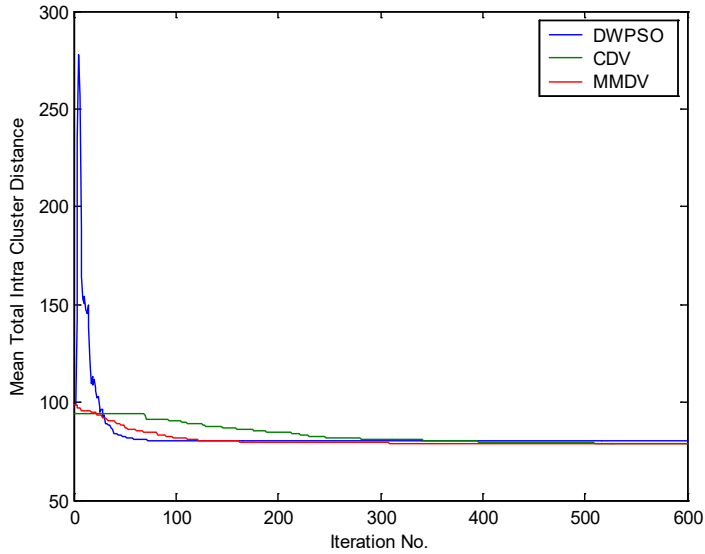


Figure 8. Mean convergence comparison for Iris data set

Dataset: Glass Data

This data set contains total 214 data set. Each data set carried 10 attributes and 6 clusters exists.

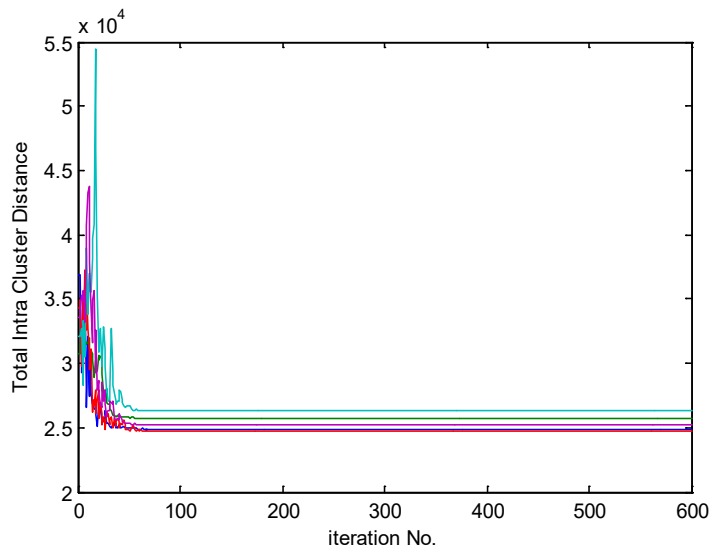


Figure 9. DWPSO based convergence in 5 trials for Glass data set

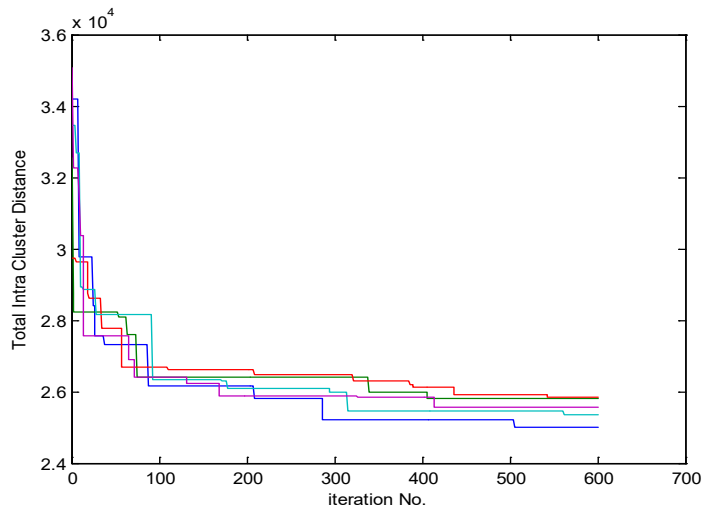


Figure 10. CDE based convergence in 5 trials for Glass data set

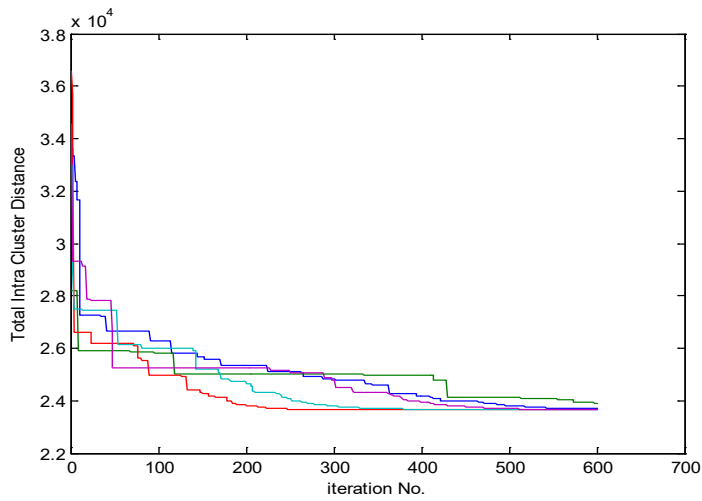


Figure 11. MMDE based convergence in 5 trials for Glass dataset

Table 8

DWPSO performance over Glass data

Trial No.	Correctly clustered data samples	Wrongly clustered data samples	Clustered efficiency	Total Intra Cluster Distance value
1	183	31	85.51	2.4897 e+004
2	189	25	88.32	2.5737 e+004
3	178	36	83.18	2.4721 e+004

Table 8 (Continued)

Trial No.	Correctly clustered data samples	Wrongly clustered data samples	Clustered efficiency	Total Intra Cluster Distance value
4	184	30	85.98	2.6271 e+004
5	188	26	87.85	2.5209 e+004
Mean	184.4	29.6	86.17	2.5367e+004

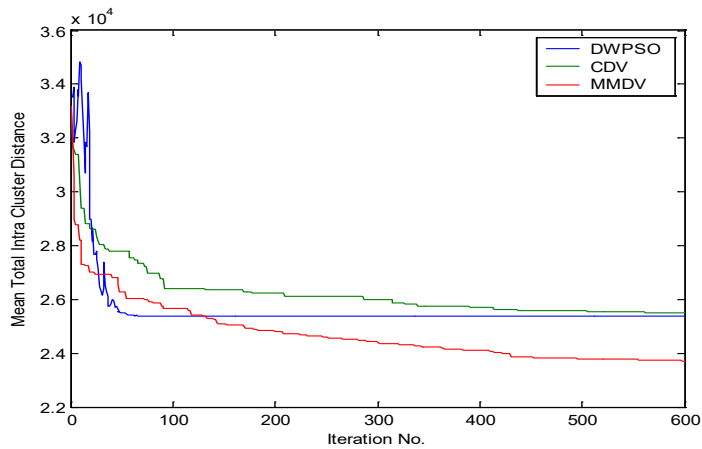


Figure 12. Mean convergence comparison for Glass data set

Table 9

CDE performance over Glass data

Trial No.	Correctly clustered data samples	Wrongly clustered data samples	Clustered efficiency	Total Intra Cluster Distance value
1	187	27	87.38	2.4990 e+004
2	187	27	87.38	2.5797 e+004
3	187	27	87.38	2.5850 e+004
4	189	25	88.32	2.5368 e+004
5	184	30	85.98	2.5546 e+004
Mean	186.8	27.2	87.29	2.5510e+004

Table 10

MMDE performance over Glass data

Trial No.	Correctly clustered data samples	Wrongly clustered data samples	Clustered efficiency	Total Intra Cluster Distance value
1	183	31	85.51	2.2950 e+004
2	189	25	88.32	2.3174 e+004
3	178	36	83.18	2.3401e+004
4	184	30	85.98	2.4461 e+004
5	188	26	87.85	2.3604 e+004
Mean	184.4000	29.6000	86.17	2.3518e+004

Table 11

Centroids value for Glass data set

Centroids of Glass data set							
C1	166.0782	2.4471	13.7061	3.5266	2.2563	73.3031	2.4611
C2	198.4844	2.5638	16.2827	3.2212	2.7751	73.5565	1.7972
C3	54.2369	2.1344	14.2542	4.4666	1.9043	72.6730	1.0457
C4	18.5031	2.1863	13.2582	4.4278	1.5191	74.4194	1.3567
C5	129.9205	0.8875	13.9521	4.3390	2.7228	75.5818	0.9168
C6	91.0957	2.8459	14.1901	3.6017	2.9122	72.2789	0.9257

Centroids of Glass data set			
C1	10.7421	-0.1976	0.5747
C2	9.9803	1.6024	-0.1853
C3	9.7003	1.4352	0.2335
C4	10.2181	0.4565	10.1096
C5	8.7067	1.4468	1.4522
C6	10.0617	0.7071	1.1787

Convergence characteristics obtained for DWPSO, CDE and MMDE on glass dataset over 5 independent trials have been shown in Figures 9, 10 and 11 respectively. It is observed that DWPSO converges faster than CDE. For DWPSO variation is observed in all the trials at the beginning, after 500 iterations, smooth convergence is obtained. Comparative mean convergence for DWPSO, CDE and MMDE is shown in Figure 12. Intra cluster distance obtained for DWPSO, CDE and MMDE is shown in Table 8, 9 and 10 respectively. The obtained best centroid value has also been shown in Table 11. It is

observed that mean distance obtained by MMDE is less compared to distance obtained by CDE and DWPSO. MMDE has shown improved tendency of convergence with iteration when compared to DWPSO and CDE.

Multidomain Based MMDE

For the first stage, 10 independent population were considered to maintain the diversity. It can be observed that within 50 iterations each population has evolved in different manner. With this diversity, intra cluster distance of 720 to 775 was obtained. All the evolved population was combined to form the 2nd stage population. The diversity introduced has resulted in achieving minimal value of intra cluster distance.

For the 5 independent trials, the obtained convergence in 1st stage and 2nd stage is shown in Figure 13 and Figure 14 respectively. It can be observed that multidomain MMDE has shown remarkable improvement and mean intra cluster distance value of 702.0192 MMDE has been obtained. Also, better cluster efficiency of 87.48% has been obtained as displayed in Table 12. The corresponding centroid values obtained by multidomain MMDE has been presented in Table 13.

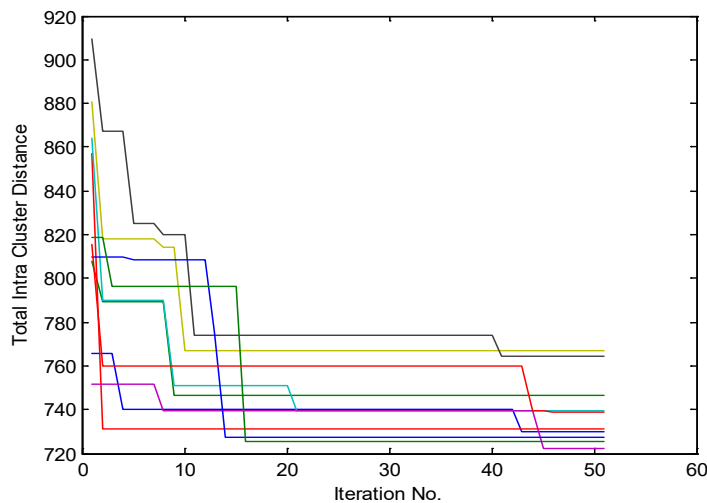


Figure 13. Convergence characteristics in 1st Stage for multidomain MMDE

Table 12

Multidomain MMDE performance over Glass data

Trial No.	Correctly clustered data samples	Wrongly clustered data samples	Clustered efficiency	Total Intra Cluster Distance value
1	188	26	87.85	695.5811
2	188	26	87.85	694.0454

Table 12 (Continued)

Trial No.	Correctly clustered data samples	Wrongly clustered data samples	Clustered efficiency	Total Intra Cluster Distance value
3	189	25	88.32	707.4350
4	190	24	88.79	697.8723
5	181	33	84.58	715.1624
Mean (Std.Dev)	187.2 (3.5637)	26.8 (3.5637)	87.48 (0.1252)	702.0192 (9.042)

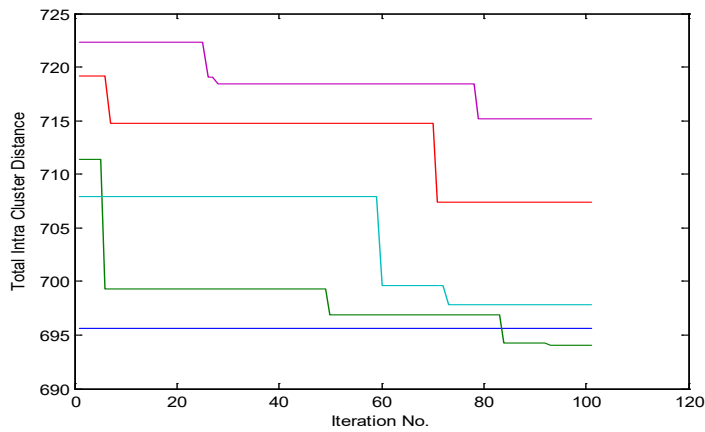


Figure 14. Convergence characteristics in 2nd stage for multidomain MMDE

Table 13

Centroid values by Multidomain MMDE

Centroids of MMDE							
C1	16.0000	1.5165	13.4754	3.3530	2.4072	74.6342	0.0100
C2	201.3622	1.5122	14.7074	0.1029	1.2528	72.3216	0.1859
C3	165.4855	1.5189	12.7370	2.3479	2.1774	71.8032	0.7419
C4	48.0214	1.5246	11.9324	4.4900	1.1781	72.9279	0.7290
C5	88.8809	1.5116	13.4721	3.3903	1.0875	72.9210	0.3255
C6	127.1936	1.5134	13.9751	3.8544	1.4775	73.6876	0.2323

Table 13 (Continued)

Centroids of MMDE			
C1	8.7993	0.0894	0.2050
C2	8.6580	1.3473	0.0031
C3	7.7070	0.2396	0.0068
C4	9.8281	0.0987	0.0876
C5	7.9812	0.0100	0.1157
C6	9.0625	0.0100	0.1454

Comparative Study of MMDE with K-Means

In practice it has been observed that K-means algorithm is very effective and useful along with having the dominance in the utilization. In fact it is one of the best algorithms in terms of computational cost and efficiency.

Comparative performance between Multi-Domain MMDE and K-Means over all the three different data sets are shown in Table 14 to Table 16. For each data set 5 independent trials had been applied. It can be understood from the outcomes that the problems with K-Means algorithm are twofold.

First it may not deliver the optimal performances, second, there is high level of variations in the performances over trials which is a really serious issue from the practical point of view. This happens because of sensitivity of K-Means algorithm towards initialization. Whereas the proposed method Multi-domain MMDE has delivered not only better performance because of exploration but also the variation level is marginal.

Table 14

Comparative Performance of MMDE and K-means for Wine Data

WineData	Multi-Domain		K-Means	
	MMDE Samples		K means Samples	
Trial	Correctly clustered	Wrongly Clustered	Correctly clustered	Wrongly Clustered
1	125	53	125	53
2	125	53	120	58
3	125	53	120	58
4	125	53	120	58
5	125	53	120	58
Mean	125	53	123.75	54.28
Efficiency	70.22		67.98	

Table 15
Comparative Performance of MMDE and K-means for Iris Data

Iris Data	Multi-Domain		K-Means	
	MMDE Samples		K means Samples	
Trial	Correctly clustered	Wrongly Clustered	Correctly clustered	Wrongly Clustered
1	135	15	134	16
2	134	16	134	16
3	137	13	100	50
4	133	17	134	16
5	134	16	100	50
Mean	134.6	15.4	120.4	29.6
Efficiency	89.73		80.27	

Table 16
Comparative Performance of MMDE and K-means for Glass Data

Glass Data	Multi-Domain		K-Means	
	MMDE Samples		K means Samples	
Trial	Correctly clustered	Wrongly Clustered	Correctly clustered	Wrongly Clustered
1	188	26	187	27
2	188	26	187	27
3	189	25	187	27
4	190	24	187	26
5	191	33	187	27
Mean	187.2	26.8	187	26.8
Efficiency	87.48		87.38	

CONCLUSION

In this paper, a Modified Mutation Strategy for Differential Evolution (MMDE) has been proposed to facilitate the clustering requirement of data. This modification increases the convergence rate and delivers satisfactory cluster efficiency. To increase the level of exploration, two stage based a multimodal structure has also been proposed. With this structure, the bias variation sensitivity of cluster activity decreases. Number of benchmarks had been tested that had the number of clusters from 2 to 6 to ensure the algorithms generalized capability. Proposed solution has outperformed the Conventional form of DE

as well as Dynamic weighted form of PSO. Proposed work had been evaluated only using datasets of UCI Repository, further it could be applied on application oriented dataset to evaluate performance.

ACKNOWLEDGEMENT

SP would like to offer my special thanks to Dr. Anandhi Rajamani Jayadharmarajan, Professor and Head, Department of Information Science and Engineering, New Horizon College of Engineering, Bengaluru, my research supervisor, for her patient guidance, enthusiastic encouragement and useful critiques of this research work. SP would also like to thank the Principal, The Oxford College of Engineering, Bengaluru, for his advice and assistance in keeping my progress on schedule. SP would like to thank UCI machine learning repository for providing datasets. Finally, SP wishes to thank her husband and parents for their support and encouragement throughout her research work. We gratefully thank the Visvesvaraya Technological University, Jnana Sangama, Belgavi for providing opportunity to conduct this research work.

REFERENCES

- Das, S., Abraham, A., & Konar, A. (2008). Automatic clustering using an improved differential evolution algorithm. *IEEE Transactions on Systems, Man, and Cybernetics - Part A: Systems and Humans*, 38(1), 218-237.
- Dua, D., & Graff, C. (2019). *UCI machine learning repository*. Irvine, California: University of California, School of Information and Computer Science.
- Gupta, Y., & Saini, A. (2018). A new swarm-based efficient data clustering approach using KHM and fuzzy logic. *Soft Computing*, 23(1), 145-162.
- Jiau, H. C., Su, Y. J., Lin, Y. M., & Tsai, S. R. (2006). MPM: A hierarchical clustering algorithm using matrix partitioning method for non-numeric data. *Journal of Intelligent Information Systems*, 26(2), 185-207.
- Kuo, R. J., & Zulvia, F. E. (2019). An improved differential evolution with cluster decomposition algorithm for automatic clustering. *Soft Computing*, 23(18), 8957-8973.
- Liu, X., Yuan, J., & Zhao, H. (2018). Efficient and intelligent density and delta-distance clustering algorithm. *Arabian Journal for Science and Engineering*, 43(12), 7177-7187.
- Nerurkar, P., Pavate, A., Shah, M., & Jacob, S. (2018). Performance of internal cluster validations measures for evolutionary clustering. *Computing, Communication and Signal Processing*, 810, 305-312.
- Tran, D. C., Wu, Z., & Deng, C. (2015). An improved approach of particle swarm optimization and application in data clustering. *Intelligent Data Analysis*, 19(5), 1049-1070.
- Wang, H., Zuo, L. L., Liu, J., Yi, W. J., & Niu, B. (2018). Ensemble particle swarm optimization and differential evolution with alternative mutation method. *Natural Computing*, 18(71), 1-14.

- Yi, H., Niu, Z., Zhang, F., Li, X., & Wang, Y. (2018). Robust recommendation algorithm based on kernel principal component analysis and fuzzy C-means clustering. *Wuhan University Journal of Natural Sciences*, 23(2), 111-119.
- Zhu, Y., Zhang, M., & Shi, F. (2018). Application of algorithm CARDBK in document clustering. *Wuhan University Journal of Natural Sciences*, 23(6), 514-524.

DFRNets: Unsupervised Monocular Depth Estimation Using a Siamese Architecture for Disparity Refinement

John Paul Tan Yusiong^{1,2*} and Prospero Clara Naval, Jr.¹

¹Computer Vision and Machine Intelligence Group, Department of Computer Science, College of Engineering, University of the Philippines, Diliman, Quezon City, Philippines

²Division of Natural Sciences and Mathematics, University of the Philippines Visayas Tacloban College, Tacloban City, Leyte, Philippines

ABSTRACT

Monocular depth estimation is gaining much interest in the computer vision community because it has broad applications in autonomous driving systems, robotics, and scene understanding. Significant progress has been made in solving the monocular depth estimation problem using deep learning techniques. Unsupervised learning methods are particularly appealing since the problem can be treated as an image reconstruction task, thereby forgoing the need for ground-truth depths. This paper presents an unsupervised approach to training convolutional neural networks for monocular depth estimation by introducing a novel architecture called DFRNets. DFRNets shares weight parameters

between the image reconstruction sub-network and the disparity refinement sub-network and adopts a multi-scale structure for disparity predictions. The proposed method computes dense disparity maps directly from monocular images and refines them in an end-to-end fashion to reduce visual artifacts and blurred boundaries, thereby improving the method's overall performance. Experiment results using the KITTI test set showed that the proposed method outperformed many state-of-the-art methods, since it achieved the best performance on the two distance ranges: 0–80 meters and 1–50 meters. Moreover, the

ARTICLE INFO

Article history:

Received: 27 July 2019

Accepted: 15 November 2019

Published: 13 January 2020

E-mail addresses:

jtyusiong@up.edu.ph (John Paul Tan Yusiong)

penaval@dcs.upd.edu.ph (Prospero Clara Naval, Jr.)

*Corresponding author

qualitative results revealed that the method generated more detailed and accurate depth maps of the scenes, with no border artifacts around the image boundary.

Keywords: Disparity refinement, monocular depth estimation, siamese architecture, unsupervised learning methods

INTRODUCTION

Depth estimation is a fundamental problem in computer vision, with various applications in autonomous driving systems, robotics, and scene understanding. The problem of estimating depth from a single image is ill-posed and inherently ambiguous, and as a result, a variety of methods to solve it have been proposed (Cadena et al., 2016; Liu et al., 2014; Saxena et al., 2005; Saxena et al., 2008). With the rapid development of deep learning methods and the availability of large training datasets, the performance of depth estimation models has improved significantly. Recently, there has been a growing interest in solving the monocular depth estimation problem using deep learning methods (Eigen et al., 2014; Garg et al., 2016; Godard et al., 2017; Yusiong & Naval, 2019; Zhou et al., 2017) since these methods combine local and global contexts to automatically infer a depth map from a single image.

Existing monocular depth estimation methods can be divided into two categories: supervised and unsupervised. Supervised learning methods require many training data with ground-truth depths since models must be trained using these ground-truth depths (Eigen et al., 2014). However, such training data may not always be available since it is quite challenging and expensive to collect numerous and diverse training data with ground-truth depths from different real-world scenarios; these ground-truth depths must also be carefully aligned and calibrated. Unsupervised learning methods overcome this limitation by training models to infer depth; this is accomplished by minimizing the photometric loss using a warping-based view synthesis procedure, thereby forgoing the need for ground-truth depths. The unsupervised methods can be further sub-divided into two groups based on the training data used: methods that employ monocular video sequences (Zhou et al., 2017) and methods that use only rectified stereo images (Garg et al., 2016; Godard et al., 2017; Yusiong & Naval, 2019).

Unsupervised learning methods also have certain limitations. As shown in the work of Zhou et al. (2017), training a model from monocular video sequences lowers the quality of depth predictions at test time. Also, in addition to estimating depth, the model requires a separate pose network to determine the ego-motion between temporal image pairs. It also requires the intrinsic camera parameters and the video frames as inputs during training. Moreover, models trained on monocular video sequences must address a scene's motion or depth-speed ambiguity and occluded regions. For the latter, occlusion masks must be

integrated into the loss function to indicate the valid pixel coordinates when computing the training loss (Mahjourian et al., 2018; Zhou et al., 2017). In contrast to training on monocular video sequences, with rectified stereo images (Garg et al., 2016; Godard et al., 2017; Yusiong & Naval, 2019), the model requires only the images as inputs during training, and it can achieve promising results even though the predicted depth maps have visual artifacts and blurred boundaries. These visual artifacts and blurred boundaries are due to occlusions, since some parts of the scene are not visible given a fixed camera baseline. To resolve these issues and improve the model's overall accuracy, mechanisms to handle occlusions are necessary. One such mechanism is the introduction of a post-processing step to refine the predicted disparity maps, but this decouples the final disparity maps from the training (Godard et al., 2017).

This research is another step toward solving the monocular depth estimation problem using the unsupervised learning method. First, this paper addresses the issue of decoupling depth estimation from disparity refinement by presenting a deep network that is trained using only rectified stereo images but can predict and refine a disparity map from a single image simultaneously and in an end-to-end manner. The proposed approach transforms the idea of a post-processing step into a trainable component of the model presented here so that it can perform depth estimation and refinement simultaneously, unlike in previous models (Garg et al., 2016; Godard et al., 2017; Yusiong & Naval, 2019), which can only perform depth estimation. The proposed method employs a novel Siamese architecture called DFRNets that has two autoencoders. These autoencoders generate high-quality disparity maps by sharing weight parameters between the image reconstruction sub-network and the disparity refinement sub-network, and they adopt a multi-scale structure for disparity predictions. In essence, training a model with this method requires performing a forward pass using the proposed Siamese architecture and inputting the original images to the image reconstruction sub-network and the horizontally flipped images to the disparity refinement sub-network. The predicted disparity maps are fused with a pixel-wise mean operation, while image boundaries are handled in a manner similar to that used by Godard et al. (2017). Next, the DFRNets is trained to jointly perform learning and refinement of depth maps in an end-to-end manner by reformulating an existing training loss function that was initially designed for depth estimation only. This paper presents a comprehensive evaluation of the proposed method using the challenging KITTI 2015 driving dataset, and experiment results show that, with the proposed Siamese architecture, the model achieves state-of-the-art results in an unsupervised setting, both quantitatively and qualitatively. The proposed unsupervised framework generates better disparity maps than other frameworks by converting the post-processing step into a trainable component of the model. It does this by training the model to simultaneously perform depth estimation and disparity refinement in an end-to-end manner using rectified stereo images only. This work is the first of its kind

to use a Siamese network consisting of two autoencoders that share weight parameters to handle the unsupervised monocular depth estimation problem by training the model to learn two related tasks jointly. The sample predictions in Figure 1 reveal that the proposed method effectively recovers scene structures such as street symbols. The main contributions of this work are the following:

1. It introduces an unsupervised learning framework that can jointly perform learning and refinement of depth maps in an end-to-end manner, thereby transforming the idea of a post-processing step into a trainable component of the model. This framework deviates from the usual approach, which involves training a model for depth estimation only.
2. It employs a novel Siamese architecture called DFRNets to simultaneously perform depth estimation and refinement of depth maps. This architecture consists of two autoencoders and shares weight parameters between the image reconstruction sub-network and the disparity refinement sub-network.
3. It reformulates an existing training loss function for joint learning and refinement of depth maps even though it was originally designed for depth estimation only.
4. It demonstrates the effectiveness of the proposed method using the KITTI 2015 driving dataset and compares the results against existing state-of-the-art methods in unsupervised monocular depth estimation, both quantitatively and qualitatively.

METHODOLOGY

This section describes the proposed method in detail. Essentially, the proposed method involves learning to simultaneously predict and refine disparity maps in an unsupervised manner, that is, in an end-to-end manner with only rectified stereo images as inputs. Figure 2 provides an overview of the framework and its components. At the core of this method is a Siamese network architecture called DFRNets, which consists of two autoencoders

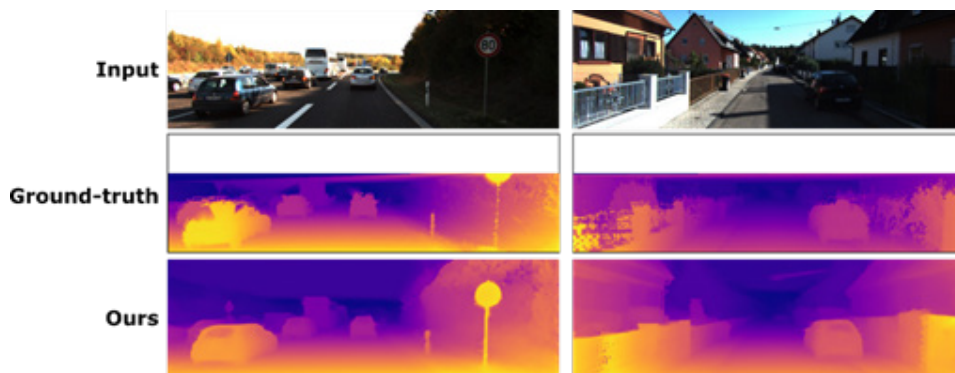


Figure 1. Example predictions generated by the proposed method using the KITTI 2015 test set. Top to bottom: input left image, ground-truth depth map, and the proposed method's prediction.

that share weight parameters. More precisely, each sub-network of the DFRNets is an autoencoder; one handles the image reconstruction task while the other handles the visual artifacts and blurred boundaries to refine the predicted disparity maps.

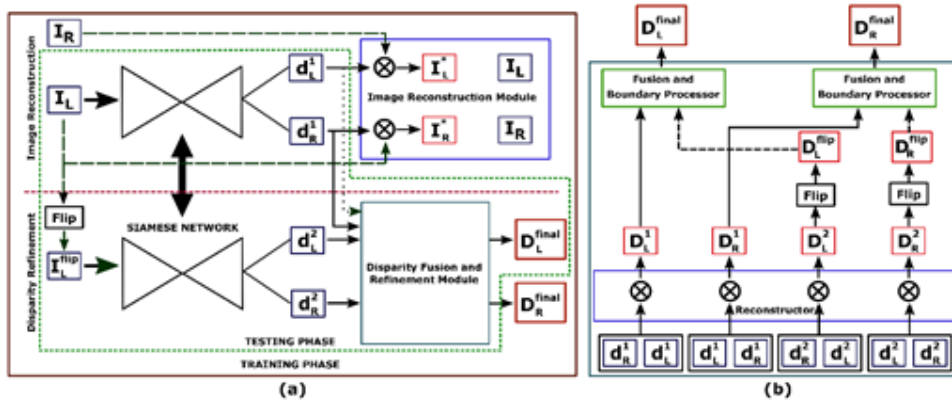


Figure 2. Network architecture: (a) DFRNets, (b) disparity fusion and refinement module

Network Architecture

The proposed framework adopts a Siamese network using the AsiANet model (Yusiong & Naval, 2019) as the autoencoder, but the autoencoder can be any architecture that can produce a disparity map. The Siamese architecture consists of two sub-networks: the image reconstruction sub-network and the disparity refinement sub-network. These two sub-networks share weight parameters to perform two different tasks simultaneously: predicting disparity maps and refining the predicted disparity maps. The image reconstruction sub-network receives the original left images I_L as inputs, while the disparity refinement sub-network receives the horizontally flipped left input images I_{flip} . The sub-networks produce two pairs of disparity maps (d_{L1}, d_{R1}) and (d_{L2}, d_{R2}) for each scale, respectively.

Image Reconstruction Module. The main objective of training the Siamese network is to minimize image reconstruction errors between the input image I and the reconstructed image I^* ; therefore, the image reconstruction sub-network contains a module that transforms the disparity maps d_{L1} and d_{R1} and the images I_R and I_L to reconstruct I_L^* and I_R^* at each scale using the sampler from the spatial transformer network (Jaderberg et al., 2015) that performs bilinear interpolation. Essentially, the module accepts two pairs of inputs (I_L, d_{R1}) and (I_R, d_{L1}) to reconstruct I_R^* and I_L^* at each scale, respectively.

Disparity Fusion and Refinement Module. As shown in Figure 2(a), the disparity refinement sub-network contains a disparity fusion and refinement module that processes the disparity maps (d_{L1}, d_{R1}) and (d_{L2}, d_{R2}) and outputs a pair of refined disparity maps (D_{finalL}, D_{finalR}) .

D_{finalR}) at each scale. This module is one of the main features of the DFRNets; it processes the inputted pairs of disparity maps by performing fusion and refinement to generate a pair of refined disparity maps, (D_{finalL}, D_{finalR}) . Although DFRNets generates (D_{finalL}, D_{finalR}) from the left image I_L at four different scales, only the left disparity map D_{finalL} with scale equal to 1 is relevant at test time. This module has three key components: the left–right disparity reconstructor, the disparity flip operator, and the disparity fusion and boundary processor. The left–right disparity reconstructor, which is based on the left–right consistency term from Godard et al. (2017), enforces coherence when generating two pairs of refined disparity maps (D_{L1}, D_{R1}) and (D_{L2}, D_{R2}) , which are given in Equation 1, 2, 3 and 4.

$$\begin{aligned} D_{L1}(x, y) &= d_{R1}(x - d_{L1}(x, y), y), & [1] \\ D_{R1}(x, y) &= d_{L1}(x + d_{R1}(x, y), y), & [2] \\ D_{L2}(x, y) &= d_{R2}(x - d_{L2}(x, y), y), & [3] \\ D_{R2}(x, y) &= d_{L2}(x + d_{R2}(x, y), y). & [4] \end{aligned}$$

In designing this module, the authors expanded the left–right consistency principle of Godard et al. (2017) instead of merely using it as a term in the training loss function. Specifically, extending this principle required creating a left–right disparity reconstructor that generates two pairs of refined disparity maps from the Siamese network. Conversely, the disparity flip operator performs the horizontal flip operation on the disparity maps (D_{L2}, D_{R2}) to produce (D_{flipL}, D_{flipR}) . To generate the final left disparity map D_{finalL} , the disparity fusion and boundary processor fuses (D_{L1}, D_{flipL}) by performing a pixel-wise mean operation and then removing the disparity ramps on the boundary pixels using the same technique as described in Godard et al. (2017). Essentially, removing the disparity ramps on the boundary pixels of the final left disparity map entails assigning the first 5% of D_{flipL} to the left of the final left disparity map and the last 5% of D_{L1} to the right of D_{finalL} . A similar step is taken to fuse (D_{R1}, D_{flipR}) and produce the final right disparity map D_{finalR} . Integrating this module as a trainable component of the model improves the model’s performance significantly because it enables it to more effectively address the visual artifacts and blurred boundaries while performing depth estimation.

Loss Function

The model is designed to adopt an existing training loss function by reformulating it for joint depth estimation and refinement using a Siamese architecture, even though the original function was designed for depth estimation only and did not consider disparity refinement as a trainable component. As shown in Equation (5), the training loss at each scale s is a combination of three terms – appearance dissimilarity, disparity smoothness,

and left–right consistency – and is aggregated through four different scales for a total loss of $\mathcal{L} = \sum_{s=1}^4 \mathcal{L}_s$, given in Equation 5, 6, 7 and 8.

$$\mathcal{L}_s = \alpha \mathcal{L}_{app} + \beta \mathcal{L}_{smooth} + \gamma \mathcal{L}_{lr}, \quad [5]$$

$$\mathcal{L}_{app} = \mathcal{L}_{app}^{left} + \mathcal{L}_{app}^{right}, \quad [6]$$

$$\mathcal{L}_{smooth} = \mathcal{L}_{smooth}^{left} + \mathcal{L}_{smooth}^{right}, \quad [7]$$

$$\mathcal{L}_{lr} = \mathcal{L}_{lr}^{left} + \mathcal{L}_{lr}^{right}, \quad [8]$$

where \mathcal{L}_{app} measures the quality of the reconstructed images, \mathcal{L}_{smooth} encourages the predicted disparities to be locally smooth, \mathcal{L}_{lr} enforces consistency between the left and right disparities, and α, β, γ are the loss weightings for each term. This section provides details only for the left components \mathcal{L}^{left} of the loss function since the right components \mathcal{L}^{right} are defined symmetrically.

Appearance Dissimilarity Term. The appearance dissimilarity term measures the quality of the reconstructed image and usually involves minimizing the dissimilarity of pixel-wise correspondence between a target image and a reconstructed image. This term is a linear combination of the single-scale structural similarity (SSIM) term (Wang et al., 2004) and the L_1 photometric term, as defined in Equation (9). It is used in several studies to evaluate the quality of a reconstructed image (Godard et al., 2017; Li et al., 2018; Mahjourian et al., 2018; Wang et al., 2018; Yin & Shi, 2018; Yusiong & Naval, 2019). This term is given in Equation 9.

$$\mathcal{L}_{app}^{left} = \frac{1}{N} \sum_{x,y} \omega \frac{1 - SSIM(I_L(x,y), I_L^*(x,y))}{2} + (1 - \omega) \|I_L(x,y) - I_L^*(x,y)\| \quad [9]$$

with a 3-by-3 box filter for the SSIM term, and ω is set to 0.85.

Disparity Smoothness Term. The disparity smoothness term is used to regularize the predicted disparities in textureless, low-gradient, and occluded regions to enforce the assumption that the predicted disparities must be locally smooth. As shown in Equation (10) and described in Godard et al. (2017) and Mahjourian et al. (2018), this term considers the gradient of the corresponding input image to allow for sharp changes in depth at pixel locations where there are sharp changes in the image. However, to train the DFRNets, this term is modified to include the final left disparity map D_{finalL} in the training loss. This term is given in Equation 10.

$$\mathcal{L}_{smooth}^{left} = \frac{1}{N} \sum_{x,y} \left| \partial_x D_{finalL}(x,y) e^{-|\partial_x I_L(x,y)|} + \partial_y D_{finalL}(x,y) e^{-|\partial_y I_L(x,y)|} \right|. \quad [10]$$

Left–Right Consistency Term. As described in Godard et al. (2017), Li et al. (2018), and

Yusiong and Naval (2019), the left–right consistency term enforces consistency between the left and right disparities and is crucial when generating the refined disparity maps. This modified term considers the final left disparity map D_{finalL} . This term is given in Equation 11.

$$\mathcal{L}_{lr}^{left} = \frac{1}{N} \sum_{x,y} |D_{finalL}(x, y) - D_{L1}(x, y)|. \quad [11]$$

Enabling the model to handle visual artifacts and blurred boundaries requires a simple modification to the disparity smoothness term and the left–right consistency term to incorporate the refined disparity maps, D_{finalL} and D_{finalR} , in the training loss computation. Reformulating the existing loss function is necessary to allowing the training algorithm to optimize all the outputs of the network by minimizing training loss, which enables the model to generate depth maps of the scenes with no border artifacts around the image boundary.

Implementation Details

This research utilized TensorFlow (Abadi et al., 2016) to implement DFRNets and trained the model from scratch using a single GTX 1080 Ti (11GB) GPU. The Adam optimizer (Kingma & Ba, 2015) with $\beta_1 = 0.9$, $\beta_2 = 0.999$, and $\varepsilon = 10^{-8}$ trained the model for 50 epochs with a batch size of 2 by optimizing the training loss. The learning rate was initially set to $\lambda = 10^{-4}$ for the first 30 epochs and halved every 10 epochs afterward until the training was completed. The weightings of the different terms of the loss function were $\alpha = 1.0$, $\beta = \frac{0.1}{2^s}$, and $\gamma = 1.0$, where s is the output scale. The dimensions of the stereo image pairs were reduced to 256 by 512 for training, but at testing time, the network could predict disparity maps for single images of varying dimensions. The weight parameters were initialized randomly using the Xavier initialization procedure (Glorot & Bengio, 2010). To prevent overfitting, L_2 regularization was applied to all the weight parameters by adding a small constant, 0.00001. Furthermore, DFRNets was trained using the same train/test split as used in Eigen et al. (2014); this split is often referred to as the Eigen split. The dataset consisted of 22,600 stereo image pairs for training and 697 for testing. Training involved data augmentation, as in Godard et al. (2017).

RESULTS AND DISCUSSION

This section presents the results of the experiments conducted to evaluate the proposed framework, DFRNets, for monocular depth estimation in an unsupervised manner. The model was evaluated using the publicly available KITTI 2015 driving dataset (Gieger et al., 2012). Training the model entailed the use of rectified stereo image pairs, while testing required the left image to generate a depth map; the corresponding Velodyne data served as the ground-truth depth for benchmarking. Furthermore, the proposed model’s performance was compared both quantitatively and qualitatively with that of existing state-of-the-art methods. An ablation study was also conducted to show the versatility of the proposed

framework and the advantages of integrating a disparity refinement component into the depth estimation model.

Specifically, the performance of DFRNets in monocular depth estimation was evaluated using the Velodyne ground-truth data of the test images. The experiment results were compared with various state-of-the-art methods by directly using the results reported in the original papers. As in the previous studies, an experiment was performed that involved pre-training the network on the Cityscapes dataset and then fine-tuning it on KITTI. Table 1 and Table 2 show the quantitative comparisons between the proposed model and other state-of-the-art methods in unsupervised monocular depth estimation using the depth evaluation metrics introduced in Eigen et al. (2014). For the training dataset, *K* means trained on the KITTI dataset, and *CS + K* means pre-trained on the Cityscapes dataset and fine-tuned on the KITTI dataset. For the training protocol, *depth* means the methods used ground-truth depths at training time, *mono* means the methods used monocular sequences for training, and *stereo* means the methods used rectified stereo images for training. The evaluation results using the KITTI test set reveal that the proposed model achieved the best performance on the two distance ranges: 0–80 meters and 1–50 meters, since it obtained the lowest errors and achieved the highest accuracy compared to the previous methods.

In addition to the quantitative results, qualitative comparisons to certain related methods using the KITTI test set, as shown in Figure 3, reveal that the proposed method generated depth maps that are visually more accurate than those produced by other methods, since these predicted depth maps have no border artifacts around the image boundary. Also, these results show that the proposed method significantly reduced the ghosting and shadow artifacts around the boundaries of the objects, thereby enabling the model to capture the underlying geometry of distant objects and objects in areas with thin structures and homogeneous regions. Moreover, the model can successfully reconstruct various objects that are difficult to recover, such as poles, tree trunks, and street symbols, and recover scene structures with more explicit object boundaries. These results demonstrate that simultaneously generating depth maps from the monocular images and refining the predicted depth maps in an end-to-end manner lead to better performance.

Architectural Analysis

The ablation study introduced three more variants by using ResNet50 (He et al., 2016), the modified DispNet with skip connections (Godard et al., 2017), and U-Net (Ronneberger et al., 2015) to better illustrate the effectiveness of jointly performing depth estimation and refinement instead of using a post-processing heuristic that is decoupled from the training process. Some modifications to the different network architectures were performed to incorporate a multi-scale structure for disparity predictions into the decoder section of the network. Experiments involved using the KITTI 2015 driving dataset to train the different

Table 1

Error metrics. Monocular depth estimation results using the KITTI test set and the Eigen split. The bold values indicate the best results

Method	Training Dataset	Train	Error Metric (Lower Is Better)			
			ARD	SRD	RMSE (Linear)	RMSE (Log)
<i>Depth range: 0–80 meters</i>						
Eigen et al. (2014) Coarse	K	Depth	0.194	1.531	7.216	0.273
Eigen et al. (2014) Coarse + Fine	K	Depth	0.190	1.515	7.156	0.270
DDVO (Wang et al., 2018)	K	Mono	0.151	1.257	5.583	0.228
	CS + K	Mono	0.148	1.187	5.496	0.226
GeoNet (Yin & Shi, 2018)	K	Mono	0.155	1.296	5.857	0.233
	CS + K	Mono	0.153	1.328	5.737	0.232
Mahjourian et al. (2018)	K	Mono	0.163	1.240	6.220	0.250
	CS + K	Mono	0.159	1.231	5.912	0.243
Zhou et al. (2017)	K	Mono	0.208	1.768	6.856	0.283
	CS + K	Mono	0.198	1.836	6.565	0.275
Godard et al. (2017)	K	Stereo	0.148	1.344	5.927	0.247
	CS + K	Stereo	0.124	1.076	5.311	0.219
AsiANet (Yusiong & Naval, 2019)	K	Stereo	0.145	1.349	5.909	0.230
	CS + K	Stereo	0.128	1.161	5.470	0.213
Ours (DFRNets)	K	Stereo	0.133	1.137	5.332	0.212
	CS + K	Stereo	0.114	0.927	4.885	0.194
<i>Depth range: 1–50 meters</i>						
GeoNet (Yin & Shi, 2018)	K	Mono	0.147	0.936	4.348	0.218
Mahjourian et al. (2018)	K	Mono	0.155	0.927	4.549	0.231
	CS + K	Mono	0.151	0.949	4.383	0.227
Zhou et al. (2017)	K	Mono	0.201	1.391	5.181	0.264
	CS + K	Mono	0.190	1.436	4.975	0.258
Garg et al. (2016) L12 Aug. 8x	K	Stereo	0.169	1.080	5.104	0.273
Godard et al. (2017)	K	Stereo	0.140	0.976	4.471	0.232
	CS + K	Stereo	0.117	0.762	3.972	0.206
AsiANet (Yusiong & Naval, 2019)	K	Stereo	0.122	0.786	4.014	0.198
	CS + K	Stereo	0.107	0.663	3.717	0.184
Ours (DFRNets)	K	Stereo	0.111	0.679	3.675	0.183
	CS + K	Stereo	0.096	0.539	3.325	0.168

Table 2

Accuracy metrics. Monocular depth estimation results using the KITTI test set and the Eigen split. The bold values indicate the best results

Method	Training Dataset	Train	Accuracy Metric (Higher Is Better)		
			$\delta < 1.25$	$\delta < 1.25^2$	$\delta < 1.25^3$
Depth range: 0–80 meters					
Eigen et al. (2014) Coarse	K	Depth	0.679	0.897	0.967
Eigen et al. (2014) Coarse + Fine	K	Depth	0.692	0.899	0.967
DDVO (Wang et al., 2018)	K	Mono	0.810	0.936	0.974
	CS + K	Mono	0.812	0.938	0.975
GeoNet (Yin & Shi, 2018)	K	Mono	0.793	0.931	0.973
	CS + K	Mono	0.802	0.934	0.972
Mahjourian et al. (2018)	K	Mono	0.762	0.916	0.968
	CS + K	Mono	0.784	0.923	0.970
Zhou et al. (2017)	K	Mono	0.678	0.885	0.957
	CS + K	Mono	0.718	0.901	0.960
Godard et al. (2017)	K	Stereo	0.803	0.922	0.964
	CS + K	Stereo	0.847	0.942	0.973
AsiANet (Yusiong & Naval, 2019)	K	Stereo	0.824	0.936	0.970
	CS + K	Stereo	0.858	0.947	0.974
Ours (DFRNets)	K	Stereo	0.848	0.947	0.976
	CS + K	Stereo	0.878	0.958	0.979
Depth range: 1–50 meters					
GeoNet (Yin & Shi, 2018)	K	Mono	0.810	0.941	0.977
Mahjourian et al. (2018)	K	Mono	0.781	0.931	0.975
	CS + K	Mono	0.802	0.935	0.974
Zhou et al. (2017)	K	Mono	0.696	0.900	0.966
	CS + K	Mono	0.735	0.915	0.968
Garg et al. (2016) L12 Aug. 8x	K	Stereo	0.740	0.904	0.962
Godard et al. (2017)	K	Stereo	0.818	0.931	0.969
	CS + K	Stereo	0.860	0.948	0.976
AsiANet (Yusiong & Naval, 2019)	K	Stereo	0.864	0.953	0.978
	CS + K	Stereo	0.893	0.960	0.981
Ours (DFRNets)	K	Stereo	0.885	0.962	0.982
	CS + K	Stereo	0.909	0.969	0.985

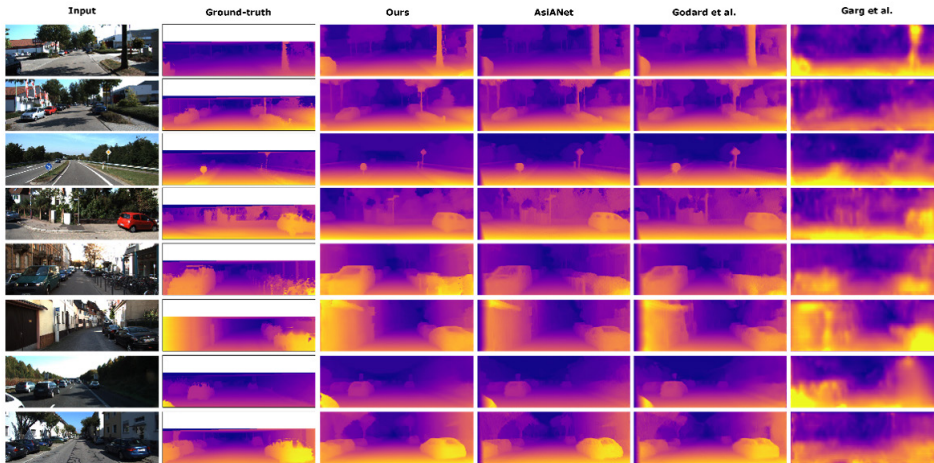


Figure 3. Qualitative results using the KITTI test set. A visual comparison of the results generated by the proposed method and with the results of Garg et al. (2016), Godard et al. (2017), and AsiANet (Yusiong & Naval, 2019). The ground-truth depth maps are interpolated for visualization purposes only. Best viewed in color.

non-Siamese networks and then applying the post-processing step as in Godard et al. (2017). Table 3 shows that the models based on the proposed framework perform much better than the other models. In Table 3, *K* means the network was trained on the KITTI dataset without the post-processing step, similar to Godard et al. (2017); *pp* means a post-processing step was performed on the output of the model, as in Godard et al. (2017); and *Ours* means DFRNets was implemented with the specified network architecture as the autoencoder. The results also demonstrate the versatility of the proposed framework, since it may use any network architecture that can generate disparity maps. Most importantly, the results clearly show the advantages of integrating a disparity refinement component into the depth estimation model.

Table 3

Architectural analysis. Results using the KITTI test set with a depth range of 0–80 meters. The bold values indicate the best results

Architecture	Method	Error Metric (Lower Is Better)			
		ARD	SRD	RMSE (Linear)	RMSE (Log)
DispNet	K	0.163	1.620	6.265	0.247
	pp	0.153	1.360	5.884	0.235
	Ours	0.149	1.316	5.788	0.229

Table 3 (Continued)

Architecture	Method	Error Metric (Lower Is Better)			
		ARD	SRD	RMSE (Linear)	RMSE (Log)
ResNet	K	0.148	1.344	5.839	0.233
	pp	0.140	1.181	5.557	0.223
	Ours	0.137	1.149	5.449	0.217
U-Net	K	0.151	1.466	5.980	0.237
	pp	0.141	1.223	5.585	0.224
	Ours	0.138	1.210	5.543	0.219
AsiaNet	K	0.145	1.349	5.909	0.230
	pp	0.135	1.132	5.475	0.217
	Ours	0.133	1.137	5.332	0.212

CONCLUSIONS

This work has presented an unsupervised learning framework, DFRNets, for jointly performing depth estimation and depth refinement using rectified stereo images during training. In essence, the model can be trained to simultaneously predict and refine disparity maps using a Siamese network architecture consisting of two autoencoders and a novel DFRM that performs disparity refinement as a trainable component of the model. The DFRM enables the model to more effectively handle visual artifacts and blurred boundaries, resulting in better performance. Moreover, this paper has shown that an existing training loss function can be reformulated for the joint learning and refinement of depth maps even though the original purpose was for depth estimation only. Experiment results using the KITTI 2015 driving dataset reveal that the proposed method achieved superior quantitative and qualitative performance compared to previous unsupervised state-of-the-art methods. In addition, the ablation study confirmed that the proposed framework is versatile, since it can use any encoder–decoder network architecture. Also, the results have revealed the advantages of performing these two tasks simultaneously and in an end-to-end manner rather than introducing a post-processing heuristic as a separate component of the model.

ACKNOWLEDGEMENT

This research work has been supported by the Department of Science and Technology-Engineering Research and Development for Technology Program. We also wish to express our appreciation to the editor and anonymous reviewers for their valuable comments and suggestions.

REFERENCES

- Abadi, M., Agarwal, A., Barham, P., Brevdo, E., Chen, Z., Citro, C., Corrado, G., Davis, A., Dean, J., Devin, M., ... Zheng, X. (2016). Tensorflow: Large-scale machine learning on heterogeneous distributed systems. In *Computer science – Distributed, parallel and cluster computing* (pp. 1-19). Ithaca, New York: Cornell University.
- Cadena, C., Latif, Y., & Reid, I. D. (2016, October 9-14). Measuring the performance of single image depth estimation methods. In *Proceedings of the IEEE/RSJ International Conference on Intelligent Robots and Systems* (pp. 4150-4157). Daejeon, South Korea.
- Eigen, D., Puhrsch, C., & Fergus, R. (2014, December 8-13). Depth map prediction from a single image using a multi-scale deep network. In *Proceedings of the 27th International Conference on Neural Information Processing Systems* (pp. 2366-2374). Palais des Congrès de Montréal, Montréal, Canada.
- Garg, R., Kumar, V., Carneiro, G., & Reid, I. (2016). Unsupervised CNN for single view depth estimation: Geometry to the rescue. In B. Leibe, J. Matas, N. Sebe & M. Welling (Eds.), *European Conference on Computer Vision* (pp. 740-756). Cham, Switzerland: Springer.
- Geiger, A., Lenz, P., & Urtasun, R. (2012, June 16-21). Are we ready for autonomous driving? The KITTI vision benchmark suite. In *Proceedings of the IEEE Conference on Computer Vision and Pattern Recognition* (pp. 3354-3361). Providence, RI, USA.
- Glorot, X., & Bengio, Y. (2010, May 13-15). Understanding the difficulty of training deep feedforward neural networks. In *Proceedings of the Artificial Intelligence and Statistics Conference* (pp. 249-256). Sardinia, Italy.
- Godard, C., Aodha, O. M., & Brostow, G. J. (2017, July 21-26). Unsupervised monocular depth estimation with left-right consistency. In *Proceedings of the IEEE Conference on Computer Vision and Pattern Recognition* (pp. 270-279). Honolulu, Hawaii.
- He, K., Zhang, X., Ren, S., & Sun, J. (2016, June 27-30). Deep residual learning for image recognition. In *Proceedings of the IEEE Conference on Computer Vision and Pattern Recognition* (pp. 770-778). Las Vegas, NV, USA.
- Jaderberg, M., Simonyan, K., Zisserman, A., & Kavukcuoglu, K. (2015, December 7-12). Spatial transformer networks. In *Proceedings of the 28th International Conference on Neural Information Processing Systems* (pp. 2017-2025). Montreal, Canada.
- Kingma, D., & Ba, J. (2015, May 7-9). Adam: A method for stochastic optimization. In *Proceedings of the International Conference on Learning Representations* (pp. 1-15). San Diego, CA, USA.
- Li, R., Wang, S., Long, Z., & Gu, D. (2018, May 21-25). UnDeepVO: Monocular visual odometry through unsupervised deep learning. In *Proceedings of the IEEE International Conference on Robotics and Automation* (pp. 7286-7291). Brisbane, QLD, Australia.
- Liu, M., Salzmann, M., & He, X. (2014, June 23-28). Discrete-continuous depth estimation from a single image. In *Proceedings of the IEEE Conference on Computer Vision and Pattern Recognition* (pp. 716-723). Columbus, OH, USA.

- Mahjourian, R., Wicke, M., & Angelova, A. (2018, June 18-22). Unsupervised learning of depth and ego-motion from monocular video using 3d geometric constraints. In *Proceedings of the IEEE Conference on Computer Vision and Pattern Recognition* (pp. 5667-5675). Salt Lake City, Utah.
- Ronneberger, O., Fischer, P., & Brox, T. (2015, October 5-9). U-Net: Convolutional networks for biomedical image segmentation. In *Proceedings of the International Conference on Medical Image Computing and Computer-Assisted Intervention* (pp. 234-241). Munich, Germany.
- Saxena, A., Chung, S. H., & Ng, A. Y. (2005, December 5-8). Learning depth from single monocular images. In *Proceedings of the 18th International Conference on Neural Information Processing Systems* (pp. 1161-1168). British Columbia, Canada.
- Saxena, A., Chung, S. H., & Ng, A. Y. (2008). 3-d depth reconstruction from a single still image. *International Journal of Computer Vision*, 76(1), 53-69.
- Wang, C., Buenaposada, J., Zhu, R., & Lucey, S. (2018, June 18-22). Learning depth from monocular videos using direct methods. In *Proceedings of the IEEE/CVF Conference on Computer Vision and Pattern Recognition* (pp. 2022-2030). Salt Lake City, Utah.
- Wang, Z., Bovik, A. C., Sheikh, H. R., & Simoncelli, E. P. (2004). Image quality assessment: From error measurement to structural similarity. *IEEE Transactions on Image Processing*, 13(4), 600-612.
- Yin, Z., & Shi, J. (2018, June 18-22). GeoNet: Unsupervised learning of dense, optical flow and camera pose. In *Proceedings of the IEEE/CVF Conference on Computer Vision and Pattern Recognition* (pp. 1983-1992). Salt Lake City, Utah.
- Yusiong, J. P. T., & Naval, P. C. Jr. (2019, January 7-11). AsiANet: Autoencoders in autoencoder for unsupervised monocular depth estimation. In *Proceedings of the IEEE Winter Conference of Applications on Computer Vision* (pp. 443-451). Waikoloa Village, USA.
- Zhou, T., Brown, M., Snavely, N., & Lowe, G. (2017, July 21-26). Unsupervised learning of depth and ego-motion from video. In *Proceedings of the IEEE Conference on Computer Vision and Pattern Recognition* (pp. 6612-6619). Honolulu, Hawaii.



Quantitative Assessment of Concept Maps for Conceptualizing Domain Ontologies: A Case of Quran

Rizwan Iqbal^{1*}, Masrah Azrifah Azmi Murad² and Adnan Ashraf³

¹Department of Computer Engineering, Bahria University, Karachi Campus, Karachi, Pakistan

²Faculty of Computer Science and Information Technology, Universiti Putra Malaysia, 43400 UPM, Serdang, Selangor, Malaysia

³Department of Computer Systems Engineering, Mehran University of Engineering and Technology, Jamshoro, Pakistan

ABSTRACT

The use of graphical knowledge representation formalisms with a representational vocabulary agreement of terms of conceptualization of the universe of discourse is a new high potential approach in the ontology engineering and knowledge management context. Initially, concept maps were used in the fields of education and learning. After that, it became popular in other areas due to its flexible and intuitive nature. It was also proven as a useful tool to improve communication in corporate environment. In the field of ontologies, concept maps were explored to be used to facilitate different aspects of ontology development. An essential reason behind this motivation is the structural resemblance of concept maps with the hierarchical structure of ontologies. This research aims to demonstrate quantitative evaluation of 4 different hypotheses related to the effectiveness of using concept maps for ontology conceptualization. The domain of Quran was selected for the purpose of this

study and it was conducted in collaboration with the experts from the Centre of Quranic Research, Universiti Malaya, Kuala Lumpur, Malaysia. The results of the hypotheses demonstrated that concept mapping was easy to learn and implement for the majority of the participants. Most of them experienced improvement in domain knowledge regarding the vocabularies used to refer to the structure of organization of the Quran, namely Juz, Surah, Ayats, tafsir,

ARTICLE INFO

Article history:

Received: 18 November 2018

Accepted: 02 August 2019

Published: 13 January 2020

E-mail addresses:

mail.rizwaniqbal@yahoo.com (Rizwan Iqbal)

masrah.azrifah@gmail.com (Masrah Azrifah Azmi Murad)

adnan.arain@faculty.muett.edu.pk (Adnan Ashraf)

* Corresponding author

Malay translation, English translation, and relationships among these entities. Therefore, concept maps instilled the element of learning through the conceptualization process and provided a platform for participants to resolve conflicting opinions and ambiguities of terms used immediately.

Keywords: Binomial test, concept maps, domain conceptualization, ontology

INTRODUCTION

Ontologies have been discussed for centuries in philosophy. It describes ontology as “the study of being or existence” (Cahn, 2012; Simperl, 2009). In computer science, ontologies are extensively used in the fields of knowledge management, information retrieval, natural language processing, e-Commerce, information integration, e-learning, database design, geographical information systems and many other areas. They are the essential parts of intelligent information systems where they are utilized by knowledge engineers to come up with problem-solving and reasoning mechanisms.

According to Lassila & McGuinness (2001), “An explicit specification of a conceptualization or ontology has the following properties: (1) a finite controlled vocabulary, (2) an unambiguous interpretation of classes and term relationships and, (3) strict hierarchical subclass relationships between classes”. There may be many definitions for ontology depending on the purpose of creation and utilization. Therefore, there is no one definite definition of ontology. It depends on the context that it is being referred to.

Similarly, there is no one definite methodology for engineering ontologies. There have been several feasible solutions and methodologies for engineering ontologies proposed to date. Instead of using a particular methodology, the notion of merging different methodologies and techniques is supported by the practitioners from the field of ontology engineering (Brusa et al., 2008; Spyns et al., 2008).

CONCEPT MAPS FOR ONTOLOGY DEVELOPMENT

There have been different techniques for conceptualizing ontologies presented over the years. Conceptualization comprises a simplified version of objects, concepts and other entities that are assumed to exist in some area of interest and the relationships among them. The use of graphical knowledge representation formalisms with a representational vocabulary agreement of terms of conceptualization of the universe of discourse is a new high potential approach in the ontology engineering and knowledge management context (Soares & Sousa, 2008).

A concept map is a kind of graphical knowledge representation formalisms that can be used for the purpose of ontology development. Concept maps present meaningful relationships between concepts linked by words from a semantic unit (Novak & Cañas,

2008). The concepts are included in circles or boxes while the links that connect the boxes represent relations among the concepts.

In the field of ontologies, concept maps were explored to use to facilitate different aspects of ontology development. Concept maps are effective, intuitive and adaptive in nature. They can be used to visualize any domain and can serve as a mechanism for domain experts to present the primary elements of their knowledge (Castro et al., 2006).

Tools were also proposed to convert concept maps into OWL ontologies. The tool proposed by Brillhante et al. (2006) which converted concept maps into OWL ontologies. The experts created the concept maps and a knowledge engineer used the tool to perform the conversion of maps into ontologies. Similarly, Dimitrova et al. (2008) came up with the notion of using controlled natural language to guide experts for ontology development. The system facilitated the users to develop ontologies by different ways. For instance, prompts errors when using controlled language and allows tracking classes that have been mentioned. There was another method proposed by Starr and De Oliveira (2013) to cater the need of a knowledge engineer to perform the conversion of concept maps into ontologies by using concept maps as a mean of defining domain knowledge by the experts followed by an application to analyze the concept maps using a set of questions.

Over the years, concept maps have been applied to develop ontologies for many different domains using different methods and techniques due to the structural resemblance of concept maps with the hierarchical structure of ontologies which makes them desirable to be used as a knowledge acquisition tool, and also as an intermediate representation to visualize any domain of knowledge. Some of the recent works on developing and conceptualizing ontologies using concept maps in different domains are discussed below.

The study conducted by Qi and Sugumaran (2018) semi-automatically created detailed level of concepts as a keyword list by applying natural language processing techniques. The list was then used to extract concepts for the domain of automotive safety. The study reported that this method helped to enrich the existing ontology and at the same time closed the gap between ontology and real-world organization ontology-based knowledge management systems.

The study conducted by Hedayati et al. (2017) explored to enhance curriculum development in the domain of ICT vocational education by using concept maps for collaborative ontology maintenance. The results of the study reported that the proposed method enabled to evaluate the external validity of the ontology developed for the domain of ICT vocational education effectively.

Similarly, study conducted by Verbeek and Bothma (2019) reported that the use of concept maps and ontologies were used in the field of civil engineering design in order to analyze and record specific experience by the engineers. The study discussed on how knowledge theories could be coupled with knowledge acquisition techniques to come

up with solutions by creating new knowledge that can be linked to both existing and new ontologies. This will facilitate the thinking process and systematic organization of knowledge.

Another study conducted by Rousseau et al. (2018) placed the foundation to develop an ontology for the domain of Systemology. The study argued that by drawing (concept maps) system thinking principles improvement could be made in the standard methods for ontology development. The study reported four examples of how these could be applied for both domain-specific and upper ontologies. Therefore, the study came up with a systematic framework for selecting and organizing knowledge in order to develop an ontology for Systemology.

CONCEPTS IN QURAN

The conceptualization emphasizes on the structure of organization of the Quran. The concepts in the Quran include Juz, Surah, Ayats, tafsir, translations and relationships among these concepts. The key concepts are explained as follows:

A Juz is one of thirty parts of which the Quran is divided. Of note, the division of the Quran into Juz has no relevance to the meaning of the Quran and anyone can start reading from anywhere in the Quran. The most commonly memorized juz is Juz Amma, which is the 30th juz and contains chapters (Surah) 78 through 114.

A Surah is a chapter of the Quran. There are 114 chapters of the Quran and each chapter is divided into verses. The chapters or Surahs are of unequal length where the shortest chapter (Al-Kawthar) has only three ayat (verses) while the longest chapter (Al-Baqara) contains 286 verses. Out of 114 chapters in the Quran, 86 of them are classified as Meccan while 28 of them are classified as Medinan. This classification is based on the locations of revelation.

Ayat means “evidence” or “sign”. In the context of Quran, ayat means “verse”, namely each statement or paragraph marked by a number. Sometimes an ayat contains more than one sentence or may even have many sentences within it. A sentence may also be divided by a break in the ayat and one would have to read from the next ayat to complete the subject or topic. Tafsir is a body of commentary to explain the meaning of verses (Ayats) in the Quran. It is a lengthy explanation which spans over a few sentences to explain a particular ayat.

ONTOLOGY CONCEPTUALIZATION IN A COLLABORATIVE ENVIRONMENT

This research presents an experiment of ontology conceptualization in a collaborative environment using concept maps. There were a total of 30 participants and it was in line with the size of samples used in the similar studies exploiting concept maps (Dimitrova et

al., 2008; Milton et al., 2006; Starr & De Oliveira, 2013). All the participants engaged in the study were split into groups and domain experts were invited to facilitate the discussion among the participants. The domain experts were from the Centre of Quranic Research, Universiti Malaya, Kuala Lumpur, Malaysia who specialized in the areas of Quran, hadith and Fiqh (Islamic jurisprudence). On the other hand, the participants (non-domain experts) engaged in the study were between the ages of 25 to 45. The minimum qualification of the participants in the study was Bachelor's Degree. In respect of knowledge of the Quran, majority of the participants were having little knowledge about the domain of Quran and its concepts. The experiment was to perform ontology conceptualization for the domain of Quran. The conceptualization emphasis on the structure of organization of the Quran, namely, Juz, Surah, Ayats, tafsir, Malay translation, English translation and relationships among these entities. A sample concept map for the domain of Quran is shown in Figure 1. It shows that Quran is divided into Juz and each Juz has its given name which comprises different Surahs. Furthermore, each Surah has its given name which has its revelation place and there are a number of verses associated with each of the Surah. Each verse has its translation and there is tafsir associated with it. The following sets of instructions were given to the participants:

1. Every two members should construct one concept map and share it with others in the team.
2. Participants should not hesitate to share any thoughts regarding any term used in the concept maps. Participants are encouraged to interact actively with each other as well as with the domain experts. They should feel free to suggest exclusion of any existing terms or inclusion of any new terms. The reason should be taken down for every suggestion.
3. Whenever the domain knowledge of the participants increases as a result of interaction and discussion, the participants are advised to make changes to their maps. They are advised to keep all copies of their maps from the beginning till the end.
4. A detailed discussion should be carried out until a consensus is reached on the agreed terms used in the map at the intra-team level.
5. After this, every team should share the final agreed maps with the other teams and send a representative from their team for inter-team interaction. In the event there is any conflicting opinion among the teams, instruction 3 and 4 should be followed but it is at inter-team level for this round.

The interactive nature of such an activity reduced the ambiguity level of terms used and enhanced the understanding of the design and scope of ontology of the team members. Furthermore, it assured homogeneity and coherence in the way the team members perceived

of how the domain was being modeled.

The reduction of ambiguities and growth or change of knowledge of participants was tracked and incorporated into subsequent versions of their maps over the time as highlighted by (Novak, 2003). The output of this activity is that the team develops a shared, homogeneous, coherent and unambiguous understanding of the ontology design through the concept mapping platform. All the participants engaged in the experiment were required to fill up the questionnaire after the completion of the experiment.

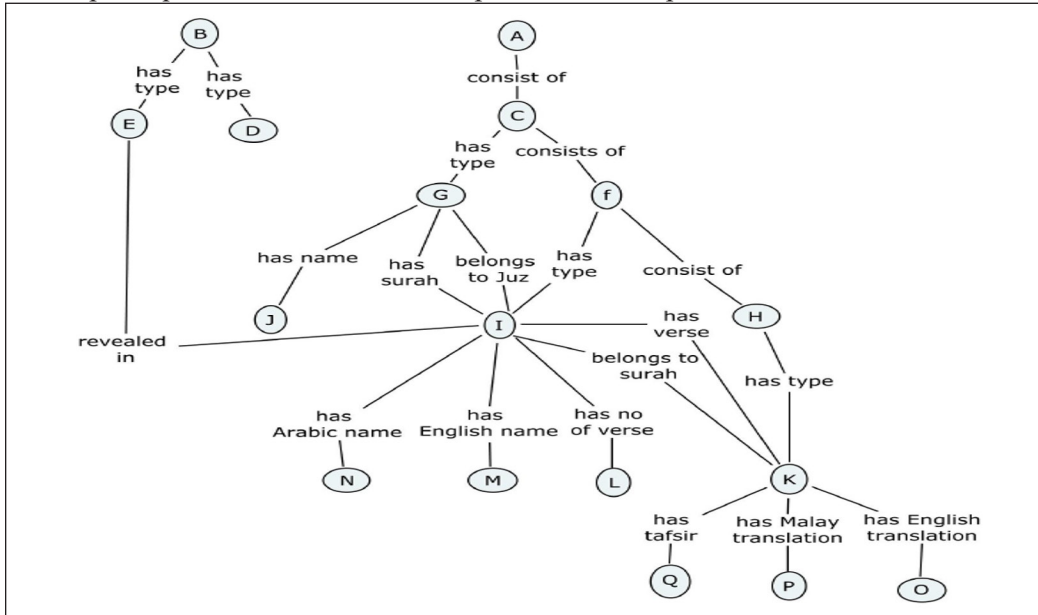


Figure 1. Concept map for the domain of Quran

QUANTITATIVE EVALUATION

The details of the quantitative evaluation of the effectiveness of using concept maps for ontology conceptualization are covered in this section.

Questionnaire

The questionnaire used in this research consisted of 21 closed-ended questions including the demographic questions. The questions of the questionnaire are shown in Table 1. The reason of using questionnaire of close-ended questions is because it provides faster response. Besides that, it provides the respondents a set of answers (explaining their response) for them to select of which is more reliable and consistent as compared to open-ended questions. There were some important factors being considered when formulating the questionnaire (Kumar, 2011):

- (a) Using simple and everyday language
- (b) Avoid asking ambiguous questions

- (c) Avoid asking double-barreled questions
- (d) Avoid asking leading questions
- (e) Avoid asking questions based on presumptions

Table 1
Questions in the questionnaire

1. Age
2. Gender
3. Highest Qualification
4. Years of working experience
5. Are you a domain expert
6. If yes, which category describes you best
7. Do you understand the term “ontology”?
8. Was it easy to learn concept mapping?
9. Did you feel comfortable creating the maps?
10. Were motivation scenarios and competency questions are effective way to represent ontology requirements & scope?
11. Was the term extraction engine (TEE) effective in reducing development time & efforts?
12. Was conceptualization process useful in resolving conflict in opinions & ambiguities related to terms used in the ontology on immediate basis?
13. Do you think that participants experience any improvement or enhancement in their knowledge while performing concept mapping activities?
14. Did you get a chance to input your feedback during the evolution of ontology design?
15. Was the expert map a true and clear representation of the domain?
16. Did the “correct-incorrect discrimination task” provide you an opportunity to test your knowledge about the ontology design?
17. Was the understanding about the ontology design clear before it was implemented?
18. Were the tabular outputs and the expert map helpful in getting a quick insight about the ontology design details?
19. Was the ontology evaluation process effective in assessing compliance of the implemented ontology with its requirements specification?
20. Do you think that all the participants experience homogeneity & coherence in the way each one of them perceives the domain being modeled?
21. Do you feel confident in recommending the developed ontology for reuse?

The questions in the questionnaire are based on the Likert scale as it provides a reliable and direct mechanism for assessing any phenomenon when a definite answer is required. The answers in the questionnaire are based on 4 levels of Likert scale, denoted by L(4). The scale ranges from “strongly agree” to “strongly disagree.” An even number of options is chosen for the Likert scale in order to ensure that the respondents take a side where the middle option of “Neither agree nor disagree” is not available. The respondents have to either agree or disagree. It is sometimes called the “forced choice” method since the neutral option is removed (Allen & Seaman, 2007). The neutral option can be an easy option for a respondent who is unsure, and as such it is questionable whether it is a true neutral option (Armstrong, 1987). It was also taken into account that the sequence of the questions appearing in the questionnaire should follow a logical progression based on the

objectives of the study. This is to help to retain the interest of the respondents and keep them motivated to answer the questions.

Method of Analysis: Non-parametric Statistics

In this research, each individual participant of the study is deemed as a unit of analysis. This research employed nonparametric statistics which was not based on parameterized families of probability distributions. They included both descriptive and inferential statistics. The typical parameters included mean and variance. Unlike parametric statistics, nonparametric statistics do not make any assumptions on the probability distributions of the variables being assessed. Non-parametric models differ from parametric models in that the model structure is not specified a priori but is instead determined from data (Wasserman, 2006). The term nonparametric is not meant to imply that such models are completely lack of parameters but that the number and nature of the parameters are flexible and not fixed in advance. Therefore, nonparametric models are also known as distribution-free (Wasserman, 2006). Non-parametric (or distribution-free) inferential statistical methods are analytical procedures for statistical hypothesis testing which, unlike parametric statistics, do not make any assumptions on the frequency distributions of the variables being assessed (Gibbons & Chakraborti, 2003; Hollander et al., 2013). In this research, statistical hypothesis testing was performed, which is a method of inferential statistics. The binomial test was used, which is a non-parametric test of statistical significance and is an integral part of confirmatory data analysis (Wagner-Menghin, 2005). This binomial test was selected due to the dichotomous nature of the data where all the answers of the participants based on the questionnaire can be grouped into two categories: positive (agree) and negative (disagree) (Wagner-Menghin, 2005). The standard binomial test was applied to the data considering the p-value to be always less than 5% ($p < 0.05$). All the hypotheses referred to a proportion of the population. In the given scenario, the test was used to investigate the minimum population's proportion with respect to the p-value due to the fact that there was no prior expected value for the population's proportion. The following formula was used to calculate inference of the proportion of the population which at least agreed with the hypothesis (Fields, 2005). In the formula, \hat{p} in Equation (1) presents the success proportion of a sample size where *positive responses* refer to those responses which are categorized as positive and *total response (n)* refer to the total number of responses. Similarly, \hat{q} in Equation (2) presents the failure proportion of a sample size of which is calculated by subtracting \hat{p} (success proportion in the sample) by 1, considering p-value to be $p < 0.05$. A small p-value indicates strong evidence which is against the null hypothesis. The margin of error is presented as $\hat{p} \pm 1.96 (se)$. As such, 1.96 is the z-score for 95% confidence that is commonly used in statistics.

$$\hat{p} = \frac{\text{positive responses}}{\text{total response } (n)} \quad (1)$$

$$\hat{q} = 1 - \hat{p} \quad (2)$$

$$se = \sqrt{\frac{\hat{p}\hat{q}}{\text{total responses } (n)}}$$

$$\hat{p} \pm 1.96 (se)$$

Hypotheses to be Tested

This research intended to investigate 4 hypotheses that were related to the effectiveness of employing concept maps for ontology conceptualization in a collaborative environment. The hypotheses are as follows:

Hypothesis 1. Concept mapping is easy to learn.

Hypothesis 2. Concept maps are comfortable to create.

Hypothesis 3. During conceptualization, learning is experienced by the participants.

Hypothesis 4. During conceptualization conflict of opinions are resolved on an immediate basis.

The quantitative hypothesis testing results for questions 8, 9, 12, and 13 of the questionnaire are reported in order to test the above hypotheses.

RESULTS AND DISCUSSION

Hypothesis 1 which is related with the ease of learning of concept maps is tested by the quantitative hypothesis testing result of question 8 of the questionnaire. The answers “Agree” and “Strongly Agree” were considered as the positive answer where 27 out of 30 participants were on the positive side with a $p < 0.05$. This infers that at least 79% of the population agreed that concept mapping was easy to learn. The statistical output of the binomial test is shown in Table 2.

Table 2
Binomial Output for Hypothesis 1

	Category	N	Observed Prop.	Test Prop.	Exact Sig. (2-tailed)
<i>Group 1</i>	<i>Positive</i>	27	0.90	0.50	0.00
<i>Group 2</i>	<i>Negative</i>	3	0.10		
<i>Total</i>		30	1.00		

Hypothesis 2 which is related with the comfort in developing concept maps is tested by the quantitative hypothesis testing result of question 9 of the questionnaire. The answers “Agree” and “Strongly Agree” were considered as the positive answer where 26 out of 30 participants were on the positive side with a $p < 0.05$. This infers that at least 74% of the population agreed that concept maps were comfortable to develop. The statistical output of the binomial test is shown in Table 3.

Table 3
Binomial Output for Hypothesis 2

	Category	N	Observed Prop.	Test Prop.	Exact Sig. (2-tailed)
<i>Group 1</i>	<i>Positive</i>	26	0.87	0.50	0.00
<i>Group 2</i>	<i>Negative</i>	4	0.13		
<i>Total</i>		30	1.00		

The quantitative results of hypotheses 1 and 2 are in line with the recommendation found in the existing literature that a down to earth method must be devised for conceptualization because the domain experts (as well as other participants including project stakeholders and users) have primarily practical skills with no experience whatsoever in modeling (Spyns et al., 2008). Some of the interviewees manifested their thoughts on the concept mapping as follows:

- “Concept mapping was easy to understand and implement.”
- “Concept mapping provided an easy way for us to model the concepts and relationships together in a way which enable us to visualize how will the final ontology design look like.”
- “It helped us to see how the structure of the final ontology will look.”

In addition, some critical characteristics of the concept mapping were identified through the responses of the interviewees during the interview sessions. These characteristics are the potential reason for the participants to agree on the fact that concept mapping was easy to learn and implement. These characteristics are as follows:

- Easy for the brain to comprehend and straight forward.
- It aligns with the daily categorization of entities, how things are related in the physical world.
- It enables the ideas to flow freely and enables to link up things in a natural order.
- It is simple, intuitive and expressive.
- It is self-explanatory, and all the elements in it are logically connected.
- It enables to sort vast and complex information and see connections in between different elements.
- It is an effective way to visualize data and its connections.
- It enables to understand the key terms in a domain quickly.

- The users do not face any difficulty in learning it.
- It is close to the way how the human mind thinks and perceives any phenomena.
- It had a learning element in itself. It increased knowledge and understanding gradually.
- It does not require any prior technical knowledge or expertise for learning and implementing it.
- Provides smooth transition of ontology design to its implementation.

Hypothesis 3 which is related to the existence of learning element during the experiment is tested by the quantitative hypothesis testing result of question 12 of the questionnaire. The answers “Agree” and “Strongly Agree” were considered as the positive answer where 28 out of 30 participants were on the positive side with a $p < 0.05$. This infers that at least 84% of the population agreed that they were learning through the process. The statistical output of the binomial test is shown in Table 4.

Table 4
Binomial Output for Hypothesis 3

	Category	N	Observed Prop.	Test Prop.	Exact Sig. (2-tailed)
<i>Group 1</i>	<i>Positive</i>	28	0.93	0.50	0.00
<i>Group 2</i>	<i>Negative</i>	2	0.07		
<i>Total</i>		30	1.00		

The above result is also found to be consistent with the existing literature on concept maps which emphasize on their usage in different ways to enhance learning process where they can be exploited as a teaching, learning and assessment tool (Darmofal et al., 2002).

Hypothesis 4 which is related with the resolution of conflict of opinions on immediate basis during the experiment is tested by the quantitative hypothesis testing result of question 13 of the questionnaire. The answers “Agree” and “Strongly Agree” were considered as the positive answer where 27 out of 30 participants were on the positive side with value of $p < 0.05$. This infers that at least 79% of the population agreed that the decisive mechanism enables to resolve the conflict of opinions experienced during conceptualization on an immediate basis. For instance, in the domain of Quran, different participants know of the other name of the same concept (i.e., Juz and Para refer to the same concept in the domain of Quran). The statistical output of the binomial test is shown in Table 5.

Table 5
Binomial Output for Hypothesis 4

	Category	N	Observed Prop.	Test Prop.	Exact Sig. (2-tailed)
<i>Group 1</i>	<i>Positive</i>	27	0.90	0.50	0.00
<i>Group 2</i>	<i>Negative</i>	3	0.10		
<i>Total</i>		30	1.00		

Some of the participants also expressed their views during the interview sessions conducted after the experiment. Some statements of the interviewees supporting hypothesis 4 are as follows:

- “We had differences in opinions in a few matters, but we were able to resolve it via group interaction, we knew that we have limited time and have to reach a consensus within the given time frame.”
- “We got the opportunity to give our idea and suggestions supported with reasons. However, the final decisions were made based on the strength of the reason supporting the argument.”
- “The agreement of users based on two-step decision-making mechanism helped to foster communication amongst all the people in an organized and timely manner.”

Furthermore, some observations of the participants which signifies the effectiveness of concept maps while conceptualization are as follows:

- (a) The team members openly discussed their opinions, conflicts, and suggestions with each other and settled them on an immediate basis.
- (b) The team members continuously revised their concept maps.
- (c) The participants experienced improvement and enhancement in their domain knowledge.
- (d) All the participant groups actively contributed during the sessions.

As highlighted above, the domain knowledge of the participants was improved and they were able to clear ambiguities and resolve conflicting opinions immediately. It differs from most of the existing approaches which result in delayed argumentation and decisive mechanisms.

CONCLUSIONS

The results of hypotheses 1 and 2 show that 79% of the participants at least found that concept maps were easy to learn and 74% of the participants at least agreed that concept maps were comfortable to develop. The results of hypothesis 3 show that majority of the participants who participated the experiment of ontology conceptualization in a collaborative environment for the domain of Quran were learning through the experiment. Statistical inference shows that at least 84% of the population agreed that they were learning through the experiment and it is in line with the findings of an earlier study (Borgo et al., 2012). Moreover, it was shown that there was continuous enhancement in the domain knowledge of most of the participants evidenced by the series of artifacts (concept maps) drawn by the participants especially in the last maps drawn by them. As for hypothesis 4, the results manifest that participants who participated the experiment of ontology conceptualization had the opportunity to resolve conflicts and ambiguities. Statistical inference manifests that

at least 79% of the population agreed that the decisive mechanism enables to resolve the conflicts of opinions and ambiguities related to the terms used during conceptualization on an immediate basis.

Therefore, the overall results and observations from the experiment strongly support the existence of discourse and learning through ontology conceptualization process. Moreover, it also provides a platform for the participants to resolve conflicting opinions and ambiguities of terms used immediately.

ACKNOWLEDGEMENT

The authors would like to acknowledge financial assistance provided by Universiti Putra Malaysia for supporting the fee for professional proof reading of the manuscript.

REFERENCES

- Allen, I. E., & Seaman, C. A. (2007). Likert scales and data analyses. *Quality Progress*, 40(7), 64-65.
- Armstrong, R. L. (1987). The midpoint on a five-point Likert-type scale. *Perceptual and Motor Skills*, 64(2), 359-362.
- Borgo, R., Abdul-Rahman, A., Mohamed, F., Grant, P. W., Reppa, I., Floridi, L., & Chen, M. (2012). An empirical study on using visual embellishments in visualization. *IEEE Transactions on Visualization and Computer Graphics*, 18(12), 2759-2768.
- Brilhante, V., Macedo, G., & Macedo, S. (2006, October 23-27). Heuristic transformation of well-constructed conceptual maps into owl preliminary domain ontologies. In *Proceedings of the Workshop on 2nd Workshop on Ontologies and their Applications co-located with the International Joint Conference IBERAMIA-SBIA-SBRN'06* (pp. 1-12). Ribeirao Preto, SP, Brazil.
- Brusa, G., Caliusco, M. L., & Chiotti, O. (2008). Towards ontological engineering: a process for building a domain ontology from scratch in public administration. *Expert Systems*, 25(5), 484-503.
- Cahn, S. M. (2012). *Classics of western philosophy*. Indianapolis, Indiana: Hackett Publishing.
- Castro, A. G., Rocca-Serra, P., Stevens, R., Taylor, C., Nashar, K., Ragan, M. A., & Sansone, S. A. (2006). The use of concept maps during knowledge elicitation in ontology development processes-the nutrigenomics use case. *BMC Bioinformatics*, 7(1), 1-14.
- Darmofal, D. L., Soderholm, D. H., & Brodeur, D. R. (2002, November 6-9). Using concept maps and concept questions to enhance conceptual understanding. In *32nd Annual Frontiers in Education* (Vol. 1, pp. T3A-T3A). Boston, MA, USA.
- Dimitrova, V., Denaux, R., Hart, G., Dolbear, C., Holt, I., & Cohn, A. G. (2008, October). Involving domain experts in authoring OWL ontologies. In *International Semantic Web Conference* (pp. 1-16). Heidelberg, Germany: Springer.
- Fields, A. (2005). *Discovering statistics using SPSS*. Beverly Hills, California: Sage Publications.

- Gibbons, J. D., & Chakraborti, S. (2003). *Nonparametric statistical inference* (Vol. 168). New York, NY: Marcel Dekker.
- Hedayati, M. H., Laanpere, M., & Ammar, M. A. (2017). Collaborative ontology maintenance with concept maps and Semantic MediaWiki. *International Journal of Information Technology*, 9(3), 251-259.
- Hollander, M., Wolfe, D. A., & Chicken, E. (2013). *Nonparametric statistical methods* (Vol. 751). Hoboken, New Jersey: John Wiley & Sons.
- Kumar, R. (2011). *Research methodology: a step-by-step guide for beginners* (3rd Ed.). Los Angeles, California: SAGE Publications Ltd.
- Lassila, O., & McGuinness, D. (2001). The role of frame-based representation on the semantic web. *Linköping Electronic Articles in Computer and Information Science*, 6(5), 1-10.
- Milton, N., Clarke, D., & Shadbolt, N. (2006). Knowledge engineering and psychology: Towards a closer relationship. *International Journal of Human Computer Studies*, 64(12), 1214-1229.
- Novak, J. D. (2003). The promise of new ideas and new technology for improving teaching and learning. *Cell Biology Education*, 2(2), 122-132.
- Novak, J., & Cañas, A. (2008). *The theory underlying concept maps and how to construct and use them* (Technical Report). Retrieved July 17, 2018, from <http://eprint.ihmc.us/5/2/TheoryUnderlyingConceptMaps.pdf>
- Qi, Z., & Sugumaran, V. (2018). Ontology development through concept map and text analytics: the case of automotive safety ontology. In *International Conference on Applications of Natural Language to Information Systems* (pp. 155-166). Cham, Switzerland: Springer.
- Rousseau, D., Billingham, J., & Calvo-Amodio, J. (2018). Systemic semantics: A systems approach to building ontologies and concept maps. *Systems*, 6(3), 1-24.
- Simperl, E. (2009). Reusing ontologies on the semantic web: a feasibility study. *Data and Knowledge Engineering*, 68(10), 905-925.
- Soares, A., & Sousa, C. (2008). Using concept maps for ontology development: a case in the work organization domain. *Innovation in Manufacturing Networks*, 266, 177-186.
- Spyns, P., Tang, Y., & Meersman, R. (2008). An ontology engineering methodology for DOGMA. *Applied Ontology*, 2(3), 13-39.
- Starr, R. R., & De Oliveira, J. M. (2013). Concept maps as the first step in an ontology construction method. *Information Systems*, 38(5), 771-783.
- Verbeek, T., & Bothma, T. J. D. (2019). The application of restructuring of knowledge in civil engineering. *Journal of the South African Institution of Civil Engineering*, 61(1), 52-66.
- Wagner-Menghin, M. M. (2005). Binomial Test. In B. S. Everitt & D. Howell (Eds.), *Encyclopedia of statistics in behavioral science* (pp. 158-162). Hoboken, New Jersey: John Wiley & Sons, Ltd.
- Wasserman, L. (2006). *All of nonparametric statistics*. New York, NY: Springer Science & Business Media.

Efficient Model Selection of Collector Efficiency in Solar Dryer using Hybrid of LASSO and Robust Regression

Anam Javaid^{1,2*}, Mohd. Tahir Ismail¹ and Majid Khan Majahar Ali¹

¹*School of Mathematical Sciences, Universiti Sains Malaysia, 11800 USM, Penang, Malaysia*

²*Department of Statistics, The Women University Multan, Pakistan*

ABSTRACT

There are many variables involved in the real life problem so it is difficult to choose an efficient model out of all possible models relating to analytical factors. Interaction terms affecting the model also need to be addressed because of its vital role in the actual dataset. The current study focused on efficient model selection for collector efficiency of solar dryer. For this purpose, collector efficiency of solar dryer was used as a dependent variable with time, inlet temperature, collector average temperature and solar radiation as independent variables. Hybrid of the least absolute shrinkage and selection operator (LASSO) and robust regression were proposed for the identification of efficient model selection. The comparison was made with the ordinary least square (OLS) after performing a multicollinearity and coefficient test and with a ridge regression analysis. The final selected model was obtained using eight selection criteria (8SC). To forecast the efficient model, the mean absolute percentage error (MAPE) was used. As compared to other methods, the proposed method provides a more efficient model with minimum MAPE.

Keywords: model selection, ordinary least square, robust regression, selection criteria, sparse regression

ARTICLE INFO

Article history:

Received: 28 January 2019

Accepted: 04 November 2019

Published: 13 January 2020

E-mail addresses:

anamjavaid0786@yahoo.com (Anam Javaid)

m.tahir@usm.my (Mohd. Tahir Ismail)

majidkhanmajaharali@usm.my (Majid Khan Majahar Ali)

* Corresponding author

INTRODUCTION

Food insecurity is considered to be a major problem in the agricultural sector (Ahmed et al., 2017). It is therefore necessary to produce more food due to the food insecurity problems (Rockstrom et al., 2009). There are many stages of crop management, such as nutrient supply, water, crop production environment, in the process of seeding to harvesting (Yan, 2011). Drying

is one of the key processes in agriculture or aquaculture. Air drying is the most commonly used dehydration operation in food and chemical industries (Ali et al., 2014). The global population has been growing over the years, and there are many variables with interactions needed to solve food insecurity in agriculture or aquaculture, so the main problem is to find the key variables amongst them so that the complexity of the model can be reduced and the model can be used to predict the supply demand for food using a more efficient model (Taylor & Adelman, 2003).

Many models only emphasise a single term without considering terms of interaction (Chen, 2012). Seaweed is one of the most common products used in agriculture and aquaculture. It is currently used mostly in food manufacturing, medical and manufacturing industries. Seaweed is regarded as a potential source for renewable energy. It also can be transformed into energy such as gas and biofuel oil. Dissa et al. (2011) claimed that carrageenan was a major cause of seaweed extraction. Ali et al. (2015) conducted the study to find out that carrageenan was also used in food and non-food products for humans, cosmetics, animal foods, meat binder and they developed a mathematical model for drying method and for smoothing drying rate. Many models have been proposed using analytical or empirical solutions in the aquacultural field (Neitsch et al., 2011). Different simple techniques such as ordinary least square (OLS) and other simple methods such as analysis of variance, principle component analysis was used to address problems related to agriculture and aquaculture, but these simple techniques have many constraints (Zuur et al., 2009).

Multicollinearity is one of the problems, particularly in the case of large-scale data analysis. Rischbeck et al. (2016) used multiple linear regression models for midly drought-stressed field trials that were impacted by multicollinearity problems. In the case of multicollinearity, OLS estimates have large variances and covariances that make it difficult to calculate precisely estimates (Gujarati, 2004). The OLS model was also used to predict grain yield (Montesinos-Lopez et al., 2017). Linear regression was also used for the development of the dengue forecast model (Guo et al., 2017). The regression analysis was used to explore the interaction between climate, water and agriculture by adding linear and quadratic terms (Mendelsohn & Dinar, 2003). Linear regression was used to estimate the structural economic model to increase productivity in agriculture (Pender et al., 2004). Some research has been performed on multicollinearity, as Giacalone et al. (2018) launched the regularizaton methods (L norm) for the compaction of the multicollinearity problem. Other work was done by Wouldiams et al. (2012) as they used the analysis of variance to examine the yield-related factors.

Variable selection is another issue with regression analysis as OLS does not cope with variable selection. Sparse regressions are implemented for this type of problem by adding a penalty term. This penalty term is introduced in the function of minimisation so it is necessary to work with sparse regression analysis for variable selection. Xu and Ying (2010)

used median regression with least absolute shrinkage and selection operator (LASSO) type penalty regression to select variables afterwards Zhao et al. (2012) investigated wavelet-based LASSO methodology to regress function scalars. They also explored its asymptotic convergence as well as its finite-sample performance by using both simulation and actual data examples. Zhang et al. (2016) implemented LASSO, adaptive LASSO, adaptive LASSO II, multitask LASSO, reweighted LASSO on quantitative trait loci analysis that offered helpful insights in the research of human cancer. Zou (2006) used adaptive weights to penalize distinct coefficients in terms of the absolute value of magnitude of coefficients (L1 penalty). In order to understand the contribution of individual observations and robustness outcome for evaluated values of the model parameters (Jang & Anderson-Cook, 2017) examined the influence plot of LASSO.

The presence of outliers is also a major problem in the dataset. The removal of the outlier is not always a good option for analysis, so robust methods are necessary in order to detect and remove outlier as (Gad & Qura, 2016) have reviewed a wide variety of robust outliers methods. Midi et al. (2011) proposed some practical lower bound (LB) and upper bound (UB) for high leverage collinearity influential measure (HLCIM) that was an essential measure for the detection of multicollinearity degree. Ridge regression is also used in cases of multicollinearity but is considered to be affected in the presence of outliers (Shariff & Ferdaos, 2017). Gusnanto and Pawitan (2015) had compared various methods including sparse regression in case of number of variables were greater than number of observations ($p > n$) and had preferred sparse methods for high multicollinearity.

The method named two-step robust weighted least squares (TSRWLS) method was studied in Midi et al. (2014). Beath (2018) worked on robustness method for linear models but the disadvantage was that it could only deal with group logistics, not binary logistics, as binary logistics could not exactly fit observation. It had been evident, that LASSO was mostly applied to medical fields and gene data since in this area, there was a large number of variables to deal with, but little research was done in relation to LASSO as a wavelet-based LASSO technique was done by Zhao et al. (2012). Gusnanto and Pawitan (2015) compared ridge, cauchy, LASSO, mixture of Normals and adaptive LASSO on near infrared (NIR) instruments. Similarly, in terms of robust or ridge regression analysis, not much research has been performed on agriculture. Many types of estimators were used in robust regression analysis as Susanti et al. (2014) presented maximum likelihood type estimators (M estimators), modified M estimates (MM) and estimators of scale (S) estimates on maize production data while mostly researchers preferred M estimates as Sinova and Van Aelst (2018) showed advantages for Tukey bisquare-based M estimates by comparing them with the hampel loss function for fuzzy number value calculation. Shariff and Ferdaos (2017) provided a robust ridge method of regression model for multi-collinearity and outlier problems. Model selection was also made by different reserachers, as Abdullah et al. (2011)

used eight selection criteria (8SC) to obtain the best model among all possible models. Similarly Zainodin et al. (2011) used 8SC in model selection problem.

It is clear that the work was done separately on LASSO and robust, but there is no such model that uses 8SC to combine Robust and LASSO. In this study, therefore, this gap is addressed in the development of a robust and LASSO models and the objective is to select the best model by using 8SC that can be used to efficient prediction. In this study, collector efficiency factors are observed for solar drier using a hybrid model of LASSO and Huber M estimator, and comparisons are made with OLS and ridge regression analysis.

MATERIAL AND METHODS

OLS, Tikhonov regularisation (Ridge), LASSO and robust regression would be used for dataset assessment. The flow chart used in this research can be found in Figure 1.

The following phases were performed for the application of the flow chart referred to in Figure 1.

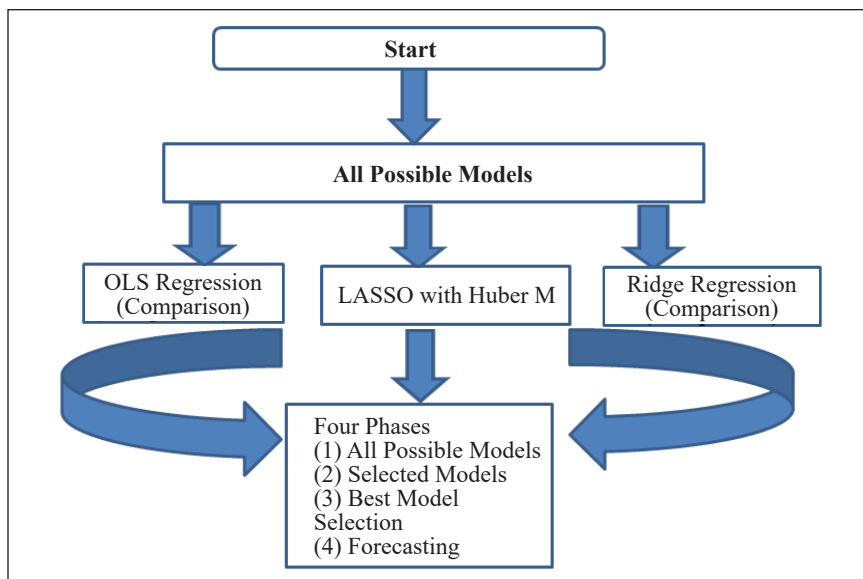


Figure 1. Flow Chart for best selected model

Phase 1– All Possible Models

According to Khuneswari et al. (2008), all possible models are the prerequisite for determination of the best model and can be derived by using Equation 1

$$N = \sum_{j=1}^k j \binom{k}{j} \tag{1}$$

Where N is the number of all Possible models, k is total number of independent variables and $j=1,2,\dots,k$

These all possible models would be used by OLS, LASSO and ridge after that the procedure would be moved on to the next phase.

No observation was missing in the dataset. Thus, approximately 16.67% of data reserved for the mean absolute percentage error (MAPE) would be used to predict the best model in Phase 3 later.

Phase 2- Selected Variables

For this phase, two tests were performed for OLS, *i.e.* the multicollinearity test and the coefficient test. After performing these two tests, selected models would be obtained in the OLS regression analysis while the significant variables would be selected for the ridge and LASSO regression because LASSO is a sparse regression to perform an automatic selection of variables. The coefficients were compared to the 0.05 level of significance for ridge regression.

Multicollinearity Test. Multicollinearity occurs in the case of a correlation of independent variables and is considered to be a problem in multiple regression analysis as a problem arises in the model validity of the investigation (Gujarati, 2004).

The following steps were taken to address the problem of multicollinearity.

- i. In the first step, the correlation coefficient is calculated for all variables in each model and the verification is performed between independent variables with a high value (coefficient > 0.95).
- ii. Following this, most common high correlation coefficient variable was removed and the correlation coefficient recalculated.
- iii. Steps (i) and (ii) are repeated until there is no variable left with a high multicollinearity problem, if any, the variable with a lower value of the absolute correlation coefficient with the dependent variable is removed.
- iv. The correlation coefficient between the dependent variable and the entire multicollinearity source was checked for the existence or non-existence of multicollinearity between the dependent and the other variables.

Coefficient Test. According to Ramanathan (2002), the coefficient test is considered to be a test for each independent variable whether or not it differs significantly from zero. *i.e.* it can be tested under the following hypothesis.

$$H_0: \beta_j = 0$$

$$H_1: \beta_j \neq 0$$

Where is the coefficient of variable in the model for $j = 1, 2, \dots, k$ and the t test would be performed at a 5% level of significance for the test. The best model would undergo a fitness test that includes a normality test and a randomness test on residuals for the model (Abdullah et al., 2011).

For LASSO regression analysis, robust regression was conducted as a coefficient test on each model. Tibshirani (1996) first introduced LASSO that could select coefficients β to minimise (Equation 2).

$$\begin{aligned} & (y - X\beta)(y - X\beta)' + \lambda \sum_{j=1}^p |\beta_j| \\ & = (y - X\beta)(y - X\beta)' \quad \text{s.t.} \quad \sum_{j=1}^p |\beta_j| \leq s \end{aligned} \quad (2)$$

Where s and λ are considered to be non-negative regularisation parameters. LASSO used the $L1$ norm that explains the coordinates vertices and the edge polotype where some coordinate values are zero. A solution for LASSO is commonly found on polotype vertex or polotype edges. LASSO can therefore be called a variable selection method where coefficient shrinkage to zero can eliminate variables from the model. Hoerl and Kennard (1970) introduced ridge regression with a bias parameter $b(d)$ obtained by using all variables as follows (Equation 3).

$$b(d) = (X'X + dI)^{-1}X'y \quad (3)$$

Where d is the bias parameter. If $d=0$, the ridge parameter is equal to the OLS parameter.

There are many types of estimators available in the case of robust regression analysis, but the most common types are the M estimators where Huber, Hampel and bisquares were mostly used. Stuart (2011) defined the typical tuning constant for Huber as $a= 1.345$ for 95% relative efficiency, For Hampel the typical tuning constants are $a = 2, b = 4$ and $c = 8$ and for Tukey's Bisquare the typical tuning constant is $a= 4.685$ results in 95% relative efficiency with the weight functions defined in Table 1

Phase 3 - The Best Model

Once the selected models have been obtained, the best model can be obtained among selected models. Ali et al. (2017) stated the 8SC that could be used to choose the best model from the list of selected models. For best model selection, 8SC would be used in this research. The formulae are outlined in Table 2.

Table 1
Weight function used for different Regression methods

	Objective Function $\rho(u)$	Score function	Weight Function $w(u) = \frac{\psi(u)}{u}$
a) Least Squares	$\frac{1}{2}u^2 \quad -\infty \leq u \leq \infty$	u	1
b) Huber M $a > 0$	$\begin{cases} \frac{1}{2}u^2 & \text{if } u < a \\ a u - \frac{1}{2}a^2 & \text{if } u \geq a \end{cases}$	$\begin{cases} u & \text{if } u < a \\ a \operatorname{sign} u & \text{if } u \geq a \end{cases}$	$\begin{cases} 1 & \text{if } u < a \\ \frac{a}{ u } & \text{if } u \geq a \end{cases}$
c) Hampel M $a, b, c > 0$	$\begin{cases} \frac{1}{2}u^2 & \text{if } u < a \\ a u - \frac{1}{2}a^2 & \text{if } a \leq u < b \\ a \frac{c u - \frac{1}{2}u^2 - \frac{7a^2}{6}}{c-b} & \text{if } b \leq u \leq c \\ a(b+c-a) & \text{Otherwise} \end{cases}$	$\begin{cases} u & \text{if } u < a \\ a \operatorname{sign} u & \text{if } a \leq u < b \\ a \frac{c \operatorname{sign} u - u}{c-b} & \text{if } b \leq u \leq c \\ 0 & \text{Otherwise} \end{cases}$	$\begin{cases} 1 & \text{if } u < a \\ \frac{a}{ u } & \text{if } a \leq u < b \\ 0 & \text{Otherwise} \end{cases}$
d) Tukey Bisquare M $a > 0$	$\begin{cases} \frac{a^2}{6} \left(1 - \left(1 - \left(\frac{u}{a} \right)^2 \right)^3 \right) & \text{if } u \leq a \\ \frac{1}{6}a^2 & \text{if } u > a \end{cases}$	$\begin{cases} u \left(1 - \left(\frac{u}{a} \right)^2 \right) & \text{if } u < a \\ 0 & \text{if } u > a \end{cases}$	$\begin{cases} \left(1 - \left(\frac{u}{a} \right)^2 \right)^2 & \text{if } u \leq a \\ 0 & \text{if } u > a \end{cases}$

Table 2
Formula used for eight selection criteria

Selection criteria	Formula	Reference
<i>AIC</i>	$\left(\frac{SSE}{n}\right)(e)^{2(k+1)/n}$	Akaike, 1969
<i>RICE</i>	$\left(\frac{SSE}{n}\right)\left[1 - \left(\frac{2(k+1)}{n}\right)\right]^{-1}$	Rice, 1984
<i>FPE</i>	$\left(\frac{SSE^2}{n}\right)\frac{n + (k + 1)}{n - (k + 1)}$	Akaike, 1974
<i>SCHWARZ</i>	$\left(\frac{SSE}{n}\right)n^{(k+1)/n}$	Schwarz, 1978
<i>GCV</i>	$\left(\frac{SSE}{n}\right)\left[1 - \left(\frac{k + 1}{n}\right)\right]^{-2}$	Golub et al., 1979
<i>SGMASQ</i>	$\left(\frac{SSE}{n}\right)\left[1 - \left(\frac{k + 1}{n}\right)\right]^{-1}$	Ramanathan, 2002
<i>HQ</i>	$\left(\frac{SSE}{n}\right)(\ln n)^{2(k+1)/n}$	Hannan and Quinn, 1979
<i>SHIBATA</i>	$\left(\frac{SSE}{n}\right)\frac{n + 2(k + 1)}{n}$	Shibata, 1981

where

n = total number of observations

$k + 1$ = estimated parameters numbers (including constant)

SSE = sum of square error

By using formula in Table 2, Akaike information criterion (*AIC*), RICE, Final prediction error (FPE), SCHWARZ(SBC), generalized cross validation (GCV), sigma square(SGMASQ), Hannan-Quinn information criterion (HQ) and SHIBATA were calculated for the purpose of efficient model selection.

Phase 4 - Goodness of Fit

Gujarati (2004) had described some assumptions concerning the least square estimators, such as that there should be no ideal multicollinearity and that the model should be completely identified. Ramanathan (2002) stated that the goodness of the fitness test ensured that the model fitted well into the data. In this phase, 16.67% of Phase 1 datasets were used for the calculation of the MAPE value, in order to determine model efficiency. Residual data would be gathered by taking into account the difference in real and expected value for the best model in Phase 3. Ali et al. (2017) used the MAPE Formula as in Equation 4.

$$MAPE = \frac{100}{N} \left(\frac{\sum_{i=1}^j |A_i - E_i|}{A_i} \right) \quad i=1, 2, \dots, j \quad (4)$$

Where

A = actual value of dependent variable (y)

E = expected value (\hat{y})

N = number of observations points

A non-parametric test such as a randomness test would be performed to check the random pattern of observations. For normality assumptions, the Shapiro Wilk test and the Kolmogorov Smirnov test would be used with the sporting documents of the scatter plot, the histogram and the box plot of the residues obtained from the efficient selected models.

RESULT AND DISCUSSION

Data Collection and Procedure

The information used in this research was drawn from Sabah. In Sabah, solar dryer is used for the drying method and various variables influence on the effectiveness of the collector. In this research, four factors, such as time, inlet temperature, collector average temperature and solar radiation, were taken as independent variables while the collector efficiency was maintained as dependent variables. For analysis purposes, 66 observations were taken. Data were collected for every second and then converted into hour to analyse the behaviour of different variables during the given time frame. Dataset was collected for four days in which solar radiation was at the peak during this time period, from 8:00 a.m. to 5:00 p.m. The purpose of this study was to monitor each factor behaviour on collector efficiency of solar dryer in which Y was used to indicate the efficiency of the collector as a dependant variable whereas x_1, x_2, x_3 and x_4 represented independent variables such as time, inlet temperature, collector average temperature and solar radiation, respectively, where x_{12} represented the interaction between x_1 and x_2 and was used to observe the combined behaviour of x_1 and x_2 on the collector effectiveness. Inlet temperature was observed to be between 27.9°C and 58.3°C in the complete data procedure, while the collector average temperature was found to be between 33.0°C and 87.7°C. Solar radiation was observed to be between 104.3 W/m² and 819.8 W/m² at 8:00 a.m. to 5:00 p.m. in four days.

For four independent variables, 32 possible models were available until the third order interaction term. All possible models consisting of four independent variables could be observed as shown in Table 3.

All possible models were calculated as indicated in Table 3 and, following a multicollinearity test and a coefficient test, a list of selected models was obtained. The list of selected models was achieved by the sum of square of error (SSE) and the number of variables left in the selected model (k) can be seen in Table 4.

From Table 4, the original model demonstrated that Model M32 had to go through two phases. The multicollinearity test was applied to this original model and, as a result,

Table 3
All possible models

No of variables	single	Interact			Total
		1 st Order	2 nd Order	3 rd Order	
1	4	-	-	-	4
2	6	6	-	-	12
3	4	4	4	-	12
4	1	1	1	1	4
Total Models	15	5	5	1	32
Model ID	M1-M15	M16-M26	M27-M31	M32	

Table 4
Selected models by using ordinary least square method

Sr. NO	Selected models using OLS	k	SSE
1	M1.0.0=M5.0.1	1	2810.25
2	M2.0.2	1	3021.1
3	M3.0.0= M6.0.1	1	2090
4	M4.0.0 = M7.0.1	1	1210.8
5	M8.0.0=M19.1.0	2	1547.1
6	M9.0.0=M12.0.1=M25.4.0	2	948.53
7	M10.0.0=M13.0.1=M14.0.1=M15.0.2=M21.1.0	2	824.86
8	M11.0.0	3	1361.23
9	M16.0.1	2	2588.28
10	M17.0.1	2	1566.93
11	M18.0.1	2	915.71
12	M20.1.0	2	1341.24
13	M22.2.0=M27.2.1	4	990.71
14	M23.1.1	4	650.97
15	M24.2.0	4	742.16
16	M26.5.1	4	585.31
17	M28.2.1	4	650.97
18	M29.2.0	5	562.59
19	M30.4.1	2	619.59
20	M31.8.4	3	544.92
21	M32.7.2	6	444.07

seven variables were removed from the model. So it became as M32.7.0. Coefficient test was performed and two variables were removed from the model so that the best selected model obtained as M32.7.2. With all significant variables in the model, the resulting model was now free of multicollinearity. The best model selected using the formula for the 8SC set out in Table 2 can be found in Table 5.

Table 5
Eight selection criteria for OLS selected models

Selected models from OLS	AIC	FPE	GCV	HQ	RICE	SCHWARZ	SGMASQ	SHIBATA
<i>M1.0.0=M5.0.1</i>	54.94	54.95	55.02	56.52	55.10	59.11	53.0	54.81
<i>M2.0.2</i>	59.07	59.07	59.15	60.764	59.237	63.55	57.001	58.92
<i>M3.0.0= M6.0.1</i>	40.86	40.86	40.9	42.0	40.98	43.96	39.43	40.76
<i>M4.0.0 = M7.0.1</i>	23.67	23.67	23.70	24.35	23.74	25.46	22.84	23.61
<i>M8.0.0=M19.1.0</i>	31.37	31.37	31.46	32.72	31.57	35.00	29.75	31.19
<i>M9.0.0=M12.0.1=M25.4.0</i>	19.23	19.23	19.293	20.06	19.35	21.45	18.24	19.12
<i>M10.0.0=M13.0.1=M14.0.1=M15.0.2=M21.1.0</i>	16.7	16.72	16.77	17.44	16.83	18.66	15.86	16.63
<i>M11.0.0</i>	27.60	27.60	27.68	28.79	27.78	30.79	26.17	27.44
<i>M16.0.1</i>	52.48	52.48	52.64	54.7	52.82	58.5	49.77	52.19
<i>M17.0.1</i>	31.7	31.77	31.87	33.14	31.9	35.44	30.1	31.59
<i>M18.0.1</i>	18.56	18.57	18.62	19.3	18.68	20.7	17.60	18.46
<i>M20.1.0</i>	27.19	27.19	27.28	28.3	27.3	30.34	25.79	27.04
<i>M22.2.0=M27.2.1</i>	21.60	21.6	21.79	23.18	22.01	25.92	19.81	21.28
<i>M23.1.1</i>	14.19	14.202	14.32	15.23	14.4	17.03	13.01	13.98
<i>M24.2.0</i>	16.18	16.19	16.32	17.36	16.49	19.42	14.84	15.94
<i>M26.5.1</i>	12.76	12.77	12.87	13.69	13.00	15.31	11.70	12.57
<i>M28.2.1</i>	14.19	14.20	14.32	15.23	14.46	17.03	13.01	13.98
<i>M29.2.0</i>	12.7	12.73	12.88	13.84	13.08	15.83	11.48	12.46
<i>M30.4.1</i>	12.56	12.56	12.60	13.10	12.64	14.01	11.91	12.49
<i>M31.8.4</i>	11.45	11.46	11.52	12.12	11.59	13.25	10.68	11.34
<i>M32.7.2</i>	10.41	10.42	10.60	11.49	10.83	13.44	9.251	10.12

From Table 5, it is clear that the minimum selection criterion value for model $M32.7.2$ was obtained from all the best possible models by using formulae for each selection criterion, thus the final selected model $M32.7.2$ can be observed with its coefficient values in Equation 5 using R software.

$$M32.7.2 = Y = 32.12 + 1.58x_1 - 0.0548x_4 - 0.0274x_{12} - 0.002x_{14} + 0.005x_{23} + 0.0000058x_{1234} \quad (5)$$

For the purpose of analysis, coefficients were observed in the final selection of models for each variable. After multicollinearity and coefficient testing of 15 variables, there were 6 variables left in the model including interaction terms in it. From the selected model in Equation 4, the significant variables were time, solar radiation, interaction of time and inlet temperature, interaction of time and solar radiation, interaction of inlet temperature and collector average temperature, interaction of time, inlet temperature, collector average temperature and solar radiation. The interaction terms between variables could be seen to be crucial for model selection so that we could not ignore them. From the coefficient, as the time increased, dryer collector efficiencies were increased by 1.58 units. Similar to the increase in solar radiation, there would be a 0.05 unit decrease in collector dryer efficiency, as solar radiation would mostly be effective from 11:00 a.m. to 1:00 p.m. Time and inlet temperature interactions would cause collector efficiency to decrease by 0.0274 units as inlet temperature can not be controlled. Solar radiation would cause collector efficiency to decrease by 0.002 units. Interaction between the inlet temperature and the average collector temperature had a positive effect on the collector's efficiency.

For this selected model, the MAPE value was calculated using a specific formula as defined in Equation 4. SSE with the number of variables left in the model (k) was used to obtain MAPE value. The MAPE value for the dataset was found to be MAPE = 29.2198.

The MAPE value is not so high that the selected model can be used for forecasting. The standardised residuals for the selected model were calculated after MAPE calculation. The standardised residual for this final selected model can be viewed as in Figure 2.

In Figure 2, the pattern for an effective chosen model is random and suggests a good fit for a linear model. Outliers can be seen outside the 2 sigma boundaries. The randomness test and the normality test were also conducted for proof. Stuart (2011) explained that the performance of the least square estimators was not good in the case of outliers or in the case of deviations from normal assumptions, so that Ridge regression was considered as an alternative method in the case of highly collinear predictors. The ridge regression estimates are biased, but the mean square error of the ridge estimator is smaller than the OLS estimators of Hoerl and Kennard (1970). Since the data used in this study also has multicollinearity problem, for comparison purposes ridge regression is performed on all

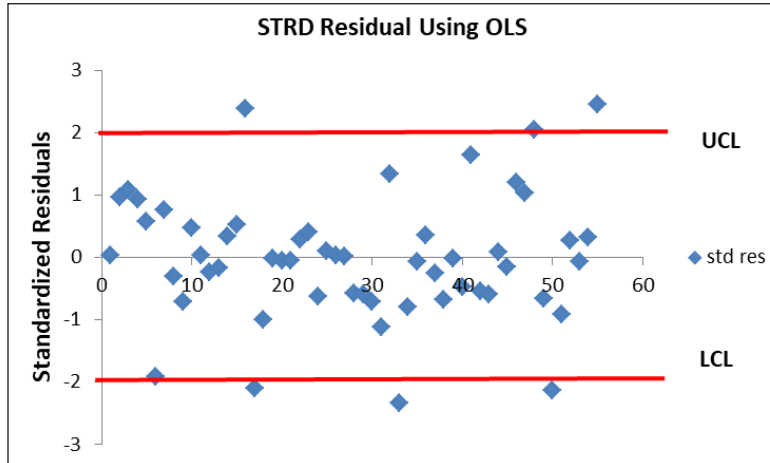


Figure 2. Standardized residual for OLS

possible models and the selected models are obtained. In these selected models, 8SC is performed in the same way as in OLS and the best model is selected. *M24* was observed as the best model with a minimum SSE value of 8SC. The coefficients are obtained using the library *glmnet* in R software (Equation 6).

$$\begin{aligned}
 M24 = & 31.938 + 0.3144 x_1 + 0.0604 x_3 - 0.0218x_4 + \\
 & 0.0022x_{13} + 0.00082x_{14} - 0.000032x_{34}
 \end{aligned}
 \tag{6}$$

The best model in Equation 6 can be observed with the key variables. Since ridge regression and OLS contained all the variables in the model as they did not have the ability to select the model, so for the purpose of a sparse regression analysis, the modified LASSO was performed using the Huber M estimation method. LASSO was performed on all possible models for a sparse regression analysis. Significant variables were observed in LASSO with 17 models after grouping a model consisting of the same variables, while Huber M was used for efficient model selection. After the performance of Huber M, 12 models were left at a 0.05% significance level in the modified LASSO. 8SC for efficient model selection were performed on these 12 models and *M29.1.1* was observed to describe the efficient model with minimum SSE as in Equation 7.

With 239.48 SSE and significant variables for collector efficiency can be seen from the above selected models. Using R software (*glmnet* library), other models with their coefficients were selected the same way. *M29.1.1* represented that from model 29, one variable was removed in LASSO and one variable was removed using Huber M as non-significant variables. The resulting model notation became as *M29.1.1*.

Table 6
MAPE for final selected models of all methods

Selected Model	Technique used	Variables in the Model	SSE	MAPE
M32.7.2	OLS	$Y = \beta_0 + \beta_1x_1+ \beta_4x_4+ \beta_{12}x_{12}+ \beta_{14}x_{14}+ \beta_{23}x_{23}+\beta_{1234}x_{1234}$	444.07	29.21
M24	Ridge Regression	$Y= \beta_0+ \beta_1x_1+ \beta_3x_3+ \beta_4x_4+ \beta_{13}x_{13}+\beta_{14}x_{14}+ \beta_{34}x_{34}$	740.801	33.89
M29.1.1	LASSO with Huber M	$Y= \beta_0+ \beta_1x_1+ \beta_3x_3+ \beta_4x_4+ \beta_{14}x_{14}+ \beta_{134}x_{134}$	239.48	28.28

From Table 6, it is clear that LASSO used the Huber M estimator to provide a good forecasting fit as compared to other methods because the MAPE value was smaller than the Huber M estimator compared to other methods. While the weight function for OLS is $1/n$, it means that all observations including outliers are given equal weight as well as ridge regression MAPE is high as compared to others because ridge regression is capable of dealing with multicollinearity but has an effect in the presence of outliers.

As a consequence, five variables remain in the efficient model chosen from LASSO with Huber M with 28.28% MAPE. There are 6 variables in the final model in OLS and ridge regression analysis, but MAPE is greater than the suggested method with a enormous difference in SSE.

By comparing all methods with OLS, it is evident that there is a 46.07% reduction in SSE for Huber M compared to OLS. For all methods used in the analysis, a standardised residual graph is noted as in Figure 3 and Figure 4.

The box plot for an effective model is also observed for all three methods used in the analysis

From box plots in Figure 5, 6 and 7, it is possible to see the outlier detection for each method. It is clear that OLS shows three observations as outlier but there is one observation as outlier for the ridge regression and for Huber’s M method.

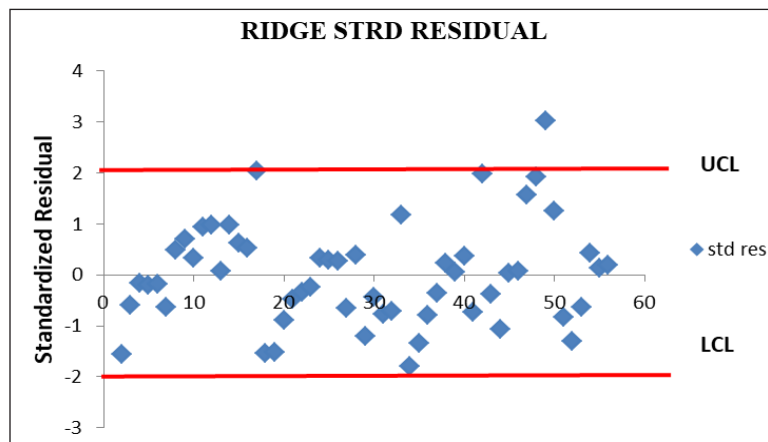


Figure 3. Standardized residual by using ridge regression

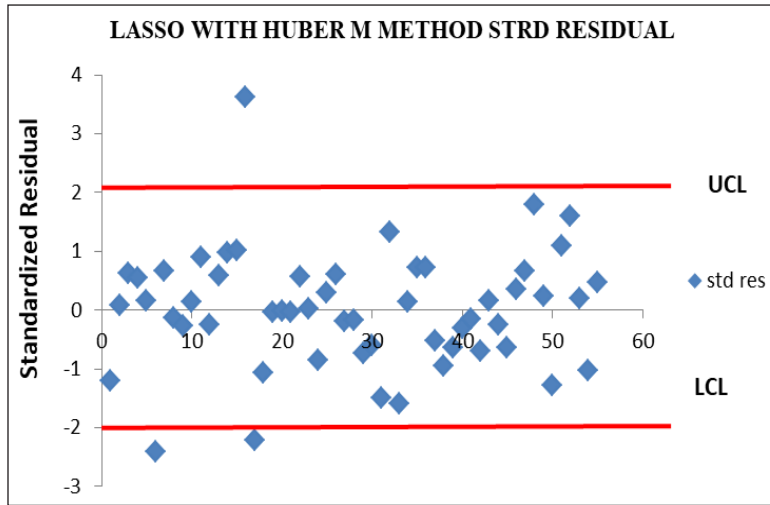


Figure 4. Standardized residual using Huber M after LASSO

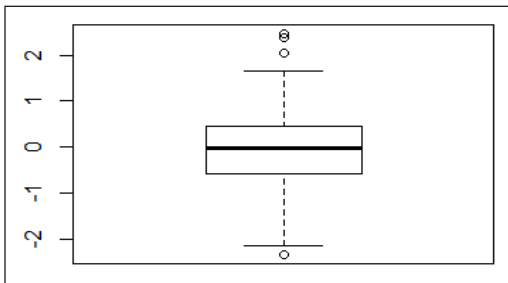


Figure 5. Box plot for OLS

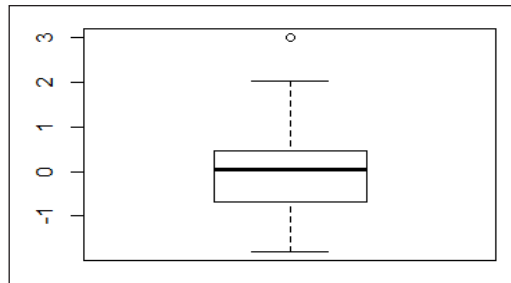


Figure 6. Box Plot for Ridge Regression

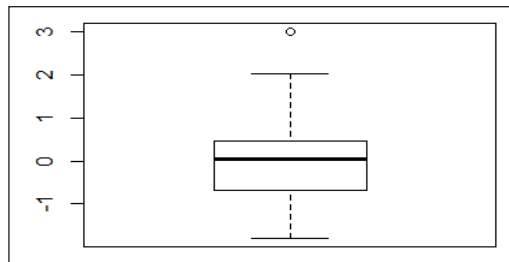


Figure 7. Box plot for Huber M method after LASSO

CONCLUSION

From the above results, it can be concluded that LASSO with the Huber M estimator provides the most efficient model compared to other methods with minimum MAPE. Thus, the best model for forecasting can be chosen by using the significant variables as time, collector average temperature, solar radiation, interaction of time and solar radiation,

interaction of time, collector average temperature and solar radiation. The model is ready to predict the collector efficiency of solar drier. By using 8SC for different types of data, this developed model may also be used in big data analyses.

ACKNOWLEDGEMENT

The authors would like to thank the Women University Multan Pakistan and University Sains Malaysia for the support in this research project.

REFERENCES

- Abdullah, N., Jubok, Z., & Ahmed, A. (2011). Improved stem volume estimation using P-value approach in polynomial regression models. *Research Journal of Forestry*, 5(2), 50- 65.
- Ahmed, U. I., Ying, L., Bashir, M. K., Abid, M., & Zulfiqar, F. (2017). Status and determinants of small farming households' food security and role of market access in enhancing food security in rural Pakistan. *PLoS ONE*, 12(10), 1-15.
- Akaike, H. (1969). Fitting autoregressive models for prediction. *Annals of the Institute of Statistical Mathematics*, 21(1), 243-247.
- Akaike, H. (1974). A new look at the statistical model identification. *IEEE Trans Auto Control*, 19, 716-723.
- Ali, M. K. M., Sulaiman, J., Yasir, S. M., & Ruslan, M. (2015). The effectiveness of sauna technique on the drying period and kinetics of seaweed *Kappaphycus alvarezii* using solar drier. *Advances in Environmental and Agricultural Science*, 1, 86-95.
- Ali, M. K. M., Ruslan, M. H., Muthuvalu, M. S., Wong, J., Sulaiman, J., & Yasir, S. M. (2014). Mathematical modelling for the drying method and smoothing drying rate using cubic spline for seaweed *Kappaphycus Striatum* variety Durian in a solar dryer. *AIP Conference Proceedings*, 1602(1), 113-120.
- Ali M. K. M., Fudholi, M., Muthuvalu, S., Sulaiman, J., & Yasir, S. M. (2017). Implications of drying temperature and humidity on the drying kinetics of seaweed. *AIP Conference Proceedings*, 1905(1), 1-7.
- Beath, K. J. (2018). A mixture-based approach to robust analysis of generalised linear models. *Journal of Applied Statistics*, 45(12), 2256-2268.
- Chen, G. J. (2012). A simple way to deal with multicollinearity. *Journal of Applied Statistics*, 39(9), 1893-1909.
- Dissa, A. O., Bathiebo, D. J., Desmorieux, H., Coulibaly, O., & Koulidiati, J. (2011). Experimental characterisation and modelling of thin layer direct solar drying of Amelie and Brooks mangoes. *Energy*, 36(5), 2517-252
- Gad, A. M., & Qura, M. E. (2016). Regression estimation in the presence of outliers: A comparative study. *International Journal of Probability and Statistics*, 5(3), 65-72
- Giacalone, M., Panarello, D., & Mattera, R. (2018). Multicollinearity in regression: an efficiency comparison between L p-norm and least squares estimators. *Quality and Quantity*, 52(4), 1831-1859.
- Golub, G. H., Heath, M., & Wahba, G. (1979). Generalized cross-validation as a method for choosing a good ridge parameter. *Technometrics*, 21, 215-223.

- Gujarati, D. N. (2004). *Basic econometrics* (4th Ed.). New York, USA: The McGraw-Hill Companies.
- Guo, P., Liu, T., Zhang, Q., Wang, L., Xiao, J., Zhang, Q., ... & Ma, W. (2017). Developing a dengue forecast model using machine learning: A case study in China. *PLoS Neglected Tropical Diseases*, *11*(10), 1-22.
- Gusnanto, A., & Pawitan, Y. (2015). Sparse alternatives to ridge regression: A random effects approach. *Journal of Applied Statistics*, *42*(1), 12-26.
- Hannan, E. J., & Quinn, B. (1979). The determination of the order of an autoregression. *Journal of the Royal Statistical Society: Series B (Methodological)*, *41*, 190-195.
- Hoerl, A. E., & Kennard, R. W. (1970). Ridge regression: Biased estimation for nonorthogonal problems. *Technometrics*, *12*(1), 55-67.
- Jang, D. H., & Anderson-Cook, C. M. (2017). Influence plots for LASSO. *Quality and Reliability Engineering International*, *33*(7), 1317-1326.
- Khuneswari, G., Zainodin, H. J., Darmesah, G., & Sim, S. H. (2008). An alternative approach in getting a representative model in a multiple regression analysis. *The 3rd international Conference on Mathematics and Statistics (ICoMS-3)*, *23*(1), 47-64.
- Mendelsohn, R., & Dinar, A. (2003). Climate, water, and agriculture. *Land Economics*, *79*(3), 328-341.
- Midi, H., Bagheri, A., & Imon, A. H. M. R. (2011). A Monte Carlo simulation study on high leverage collinearity-enhancing observation and its effect on multicollinearity pattern. *Sains Malaysiana*, *40*(12), 1437-1447.
- Midi, H., Rana, S., & Imon, A. H. M. R. (2014). Two-step robust estimator in heteroscedastic regression model in the presence of outliers. *Economic Computation and Economic Cybernetics Studies and Research*, *48*(3), 3-8.
- Montesinos-Lopez, O. A., Montesinos-Lopez, A., Crossa, J., de los Campos, G., Alvarado, G., Suchismita, M., ... & Burgueno, J. (2017). Predicting grain yield using canopy hyperspectral reflectance in wheat breeding data. *Plant Methods*, *13*(1), 1-23.
- Neitsch, S. L., Arnold, J. G., Kiniry, J. R., & Wouldiams, J. R. (2011). *Soil and water assessment tool theoretical documentation version 2009*. Berlin, Germany: Springer.
- Pender, J., Nkonya, E., Jagger, P., Sserunkuuma, D., & Ssali, H. (2004). Strategies to increase agricultural productivity and reduce land degradation: evidence from Uganda. *Agricultural Economics*, *31*(2-3), 181-195.
- Ramanathan, R. (2002). *Introductory econometrics with application* (5th Ed.). Ohio, USA: Thomson Learning.
- Rice, J. (1984). Bandwidth choice for nonparametric regression. *Annals of Statistics*, *12*, 1215-1230.
- Rischbeck, P., Elsayed, S., Mistele, B., Barmerier, G., Heil, K., & Schmidhalter, U. (2016). Data fusion of spectral, thermal and canopy height parameters for improved yield prediction of drought stressed spring barley. *European Journal of Agronomy*, *78*, 44-59.
- Rockström, J., Falkenmark, M., Karlberg, L., Hoff, H., Rost, S., & Gerten, D. (2009). Future water availability for global food production: the potential of green water for increasing resilience to global change. *Water Resources Research*, *45*(7), 1-16.

- Schwarz, G. (1978). Estimating the dimension of a model. *Annals of Statistics*, 6, 461-464.
- Shariff, N. S. M., & Ferdaos, N. A. (2017). An application of robust ridge regression model in the presence of outliers to real data problem. *Journal of Physics: Conference Series Paper*, 890(1), 1-6.
- Shibata, R. (1981). An optimal selection of regression variables. *Biometrika*, 68(1), 45-54.
- Sinova, B., & Van Aelst, S. (2018). Advantages of M-estimators of location for fuzzy numbers based on Tukey's biweight loss function. *International Journal of Approximate Reasoning*, 93, 219-237.
- Stuart, C. (2011). *Robust regression*. Durham, England: Durham University.
- Susanti, Y., Pratiwi, H., Sulistijowati H., S., & Liana, T. (2014). M estimation, S estimation, and MM estimation in robust regression. *International Journal of Pure and Applied Mathematics*, 91(3), 349-360.
- Taylor, J. E., & Adelman, I. (2003). Agricultural household models: Genesis, evolution and extensions. *Review of Economic Households*, 1(1), 1-44.
- Tibshirani, R. (1996). Regression shrinkage and selection via the LASSO. *Journal of the Royal Statistical Society*, 58(1), 267-288.
- Wouldiams, R., Borges, L. F., Lacoste, M., Andersen, R., Nesbitt, H., & Johansen, C. (2012). On-farm evaluation of introduced maize varieties and their yield determining factors in East Timor. *Field Crops Research*, 137, 170-177.
- Xu, J., & Ying, Z. (2010). Simultaneous estimation and variable selection in median regression using lasso-type penalty. *Annals of the Institute of Statistical Mathematics*, 62(3), 487-514.
- Yan, E. D. (2011, March 28-29). Design of intelligent agriculture management information system based on IoT. In *4th International Conference on Intelligent Computation Technology and Automation* (pp. 1045-1049). Shenzhen, Guangdong, China.
- Zainodin, H. J., Noraini, A., & Yap, S. J. (2011). An alternative multicollinearity approach in solving multiple regression problem. *Trends in Applied Sciences Research*, 6(11), 1241-1255.
- Zhang, K., Zhe, S., Cheng, C., Wei, Z., Chen, Z., Chen, H., ... & Ye, J. (2016, August 13-17). Annealed sparsity via adaptive and dynamic shrinking. In *22nd ACM SIGKDD International Conference on Knowledge Discovery and Data Mining* (pp. 1325-1334). San Francisco, California, USA.
- Zhao, Y., Ogden, R. T., & Reiss, P. T., (2012). Wavelet-based LASSO in functional linear regression. *Journal of Computational and Graphical Statistics*, 21(3), 600-617.
- Zou, H., (2006). The adaptive LASSO and its oracle properties. *Journal of the American Statistical Association*, 101(476), 1418-1429.
- Zuur, A. F., Ieno, E. N., Walker, N. J., Saveliev, A. A., & Smith, G. M., (2009). Limitations of linear regression applied on ecological data. In A. F. Zuur, E. N. Ieno, N. J. Walker, A. A. Saveliev & G. M. Smith (Eds.), *Mixed effects models and extensions in ecology with R* (pp. 11-33). New York, USA: Springer.

Logic Mining in League of Legends

Liew Ching Kho¹, Mohd Shareduwan Mohd Kasihmuiddin^{1*}, Mohd. Asyraf Mansor² and Saratha Sathasivam¹

¹*School of Mathematical Sciences, Universiti Sains Malaysia, 11800 USM, Minden, Pulau Pinang, Malaysia*

²*School of Distance Education, Universiti Sains Malaysia, 11800 USM, Pulau Pinang, Malaysia*

ABSTRACT

Since its debut in 2009, League of Legends (LoL) has been on a rise in becoming an extremely favoured multiplayer online battle arena (MOBA) game. This paper presented a logic mining technique to model the results (Win / Lose) of the LoL games played in 3 regions, namely South Korea, North America and Europe. In this research, a method named *k* satisfiability based reverse analysis method (*k*SATRA) was brought forward to obtain the logical relationship among the gameplays and objectives in the game. The logical rule obtained from the LoL games was used to categorize the results of future games. *k*SATRA made use of the advantages of Hopfield Neural Network and *k* Satisfiability representation. The data set used in this study included the data of all 10 teams from each region, which composed of all games from Spring Season 2018. The effectiveness of *k*SATRA in obtaining logical rule in LoL games was tested based on root mean square error (RMSE), mean absolute error (MAE), mean absolute percentage error (MAPE) and CPU time. Results acquired from the computer simulation showed the robustness of *k*SATRA in exhibiting the performance of the LoL teams.

Keywords: 2 satisfiability, 2 satisfiability reverse analysis method, hopfield neural network, league of legends, logic mining

ARTICLE INFO

Article history:

Received: 09 May 2019

Accepted: 12 September 2019

Published: 13 January 2020

E-mail addresses:

cindyklc90@gmail.com (Liew Ching Kho)

shareduwan@usm.my (Mohd Shareduwan Mohd Kasihmuiddin)

asyrafman@usm.my (Mohd. Asyraf Mansor)

saratha@usm.my (Saratha Sathasivam)

* Corresponding author

INTRODUCTION

In these past few years, eSports has started to attain more fans and recognition from all over the globe. It is difficult to define eSports since the industry is comparatively new. Hence, several authors have written on what defines a sport and why eSports should be recognized as sports (Kane and Spradley, 2017; Jenny et al., 2017). While there is

a vast number of studies on data mining for sports, such as, football (Nunes & Sousa, 2006; Baio & Blangiardo, 2010), swimming (Chen et al., 2007; Johnson et al., 2009) and basketball (Bhandari et al., 1997; Lamb et al., 2010), there is still an inadequate amount of researches exploring data mining in eSports.

League of Legends (LoL) is a multiplayer online battle arena (MOBA) game developed and published by Riot Games. LoL is a competitive eSports played in teams of five. In LoL, each player takes control of one “champion” and compete with another team of players. The aim is to knock down the opposing team’s “nexus”, a structure in the middle of the base. Reitman (2018) gave a complete introduction of gameplay for LoL for those unfamiliar with its distinct quirks and features. LoL has a global competitive scene. Major regional competition exist in North America (NA LCS), Europe (EU LCS), China (LPL), South Korea (LCK), Taiwan/Hong Kong/Macau (LMS) and various other regions. Teams that won in their respective regions will get the chance to compete in the annual World Championship. The 2018 World Championship had 99.6 million unique viewers and a total prize pool of over 6.45 million USD (Riot Games, 2018). As the eSports scene advances forward, the need to analyse game strategies arises. At present, most professional gaming teams recruit analysts to analyse their opponents, work out their strategies and come up with counterstrategies. Shout casters and analysts report their analyses during tournaments and matches. Nowadays, eSports players are lodged together with their team coaches, managers and strategists. With the fast growing level of competition, the need for strategies to enhance players’ performance also increases.

Kim et al. (2017) used collective intelligence to anticipate team performance in LoL. They showed that collective intelligence was able to anticipate the team performance based on the players’ tacit coordination. Nascimento Jr et al. (2017) divided teams’ performance into several groups. They evaluated the features in each group to find out how these features affected the results in LoL by applying machine learning and statistical analysis. Yang et al. (2014) modelled combat tactics in graphs and extracted features from the graphs to construct a decision tree that predicted the results of MOBA game. Lan et al. (2018) proposed a player behaviour model that allowed to predict the result of a MOBA game once enough data on the behaviour of the players were collected. They used recurrent neural network to process the interaction among the features of player behaviour variation and predict the outcome of a game. Johansson and Wikström (2015) showed that partial game data collected as the game progressed could be used to accurately predict the results of an ongoing game of Defense of the Ancients 2 (DotA 2) in real-time with the application of machine learning techniques. Wang (2016) used multi-layer feedforward neural networks to predict DotA 2 game outcome based on hero draft data. All these studies did not take gameplays or objectives in game into consideration while the main purpose of the game was to take down the objectives such as the turrets in order to win. Hence, we would like

to propose a new method to determine the relationship among the gameplays or objectives and how they affect the outcome of the game.

Rojas (1996) mentioned that artificial neural network (ANN) learnt how the brain of human beings process information. One of the popular network used to solve several optimization problems is Hopfield Neural Network (HNN) (Hopfield & Tank, 1985). HNN shows outstanding learning behaviour. For example, productive learning and retrieval operation. Traditional HNN is susceptible to a few deficiencies (Gee et al., 1993), so HNN is embedded with logic programming to work as a single intelligent unit (Abdullah, 1992). HNN was proven to be effective in data mining (classification) with incomplete survey data (Wang, 2005). Gaber et al. (2000) presented an algorithm to solve data mining problems (association rule mining) using HNN. Logic mining in HNN was proposed by Sathasivam (2006) by applying Reverse Analysis method. This method could obtain the logical rule among neurons. Mean field theory applied to perform logic programming in HNN had proven to be fruitful in accelerating the computational ability of neuro symbolic integration by Velavan et al. (2015). Maknickas (2015) showed that 2 Satisfiability (2SAT) could further improve the representation of general SAT. Hence, it is appropriate to select 2SAT as the logical rules in HNN. It also lowers the logical complexity in learning the relationship between the variables in real life problems since only 2 literals per clause are taken into consideration. By hybridizing HNN, Reverse Analysis and 2SAT, a new method, 2 Satisfiability based Reverse Analysis method (2SATRA) will be utilized to obtain the logical rule of LoL games. In this paper, we will employ the 2 Satisfiability based Reverse Analysis method (2SATRA) to induce the best logical rule that shows how gameplays or objectives in game can affect the outcome of a game in 3 different regions, namely NA LCS, EU LCS and LCK.

The remaining of this paper is organized as follows. In Materials and methods section, 2SAT representation and logic programming in HNN will be discussed in detail. The implementation of 2SATRA in doing LoL data sets from 3 different regions is illustrated. Results and discussion section demonstrated the performance analysis of the data sets such as root mean square error, mean absolute error, mean absolute percentage error and computation time. Key findings from induced logic are summarized. Conclusion section concluded the research work with summary of findings and future works.

MATERIALS AND METHODS

2 Satisfiability Representation

Logical rule that is made up of 2 literals per clause is called 2 Satisfiability (2SAT). 2SAT is composed of a few elements (Kasihmuddin, 2017):

- (a) A set of x variables, $v_1, v_2, v_3, \dots, v_x$.
- (b) A set of literals. A literal can be any variable or a negation of any variable.

(c) A set of y definite clauses, $C_1, C_2, C_3, \dots, C_y$ linked by logical AND (\wedge). Each clause contains only 2 literals connected by logical OR (\vee).

Each variable can take bipolar value of 1 or -1 only. It represents true or false respectively. Definition of the 2SAT formula P_{2SAT} is as follows

$$P_{2SAT} = \bigwedge_{i=1}^y C_i \quad [1]$$

where C_i is a list of clause with 2 variables each,

$$C_i = \bigvee_{i=1}^y (m_i, n_i) \quad [2]$$

The primary aim of 2SAT representation is to discover the consistent interpretation that makes formula P_{2SAT} become satisfied (Kasihmuddin et al., 2017). The focal point of the logic programming in this paper is to make sure in every execution, the program only considers 2 literals per clause. It has been proven that a great number of combinatorial problem can be directly or indirectly formulated by using 2SAT logical rule (Even et al., 1975; Miyashiro & Matsui, 2005; Mukherjee & Roy, 2015). In this paper, 2SAT logic will be embedded to HNN as a proposed logical rule.

Logic Programming in Hopfield Neural Network

Neural network is able to model complex relationships between inputs and outputs also look for patterns in data. Pattern recognition and function estimation are the reasons why neural networks are utilized in data mining (Singh & Chauhan, 2009). Hopfield Neural Network (HNN) is a widely used recurrent neural network model. Muezzinoglu et al. (2003) mentioned that HNN saved patterns as content addressable memory (CAM). HNN was chosen for logic mining because recurrent neural networks were able to learn the patterns of the data inputted to them, and used the pattern at one instant to assist in making prediction for the next instance (Craven & Shavlik, 1997). In HNN, each neuron's output and input are connected. The connection weight from neuron i to j is denoted by $w_{ij} = w_{ji}$. In HNN, $w_{ij} = w_{ji}$ (symmetric networks) and $w_{ii} = w_{jj} = 0$ (no self-feedback connections). Let θ be the state or output of the i th unit, θ is the pre-defined threshold of unit i . In an asynchronous network such as HNN, each neuron was "excited" at random time and changes its state to 1 or -1 independently according to the total excitation. For bipolar networks, S_i is either +1 or -1. HNN assumed that the individual units preserved their individual states until they were selected for a new update. General updating rule in HNN is given by:

$$S_i = \begin{cases} 1 & \text{if } \sum_j w_{ij} S_j > \theta_i \\ -1 & \text{Otherwise} \end{cases} \quad [3]$$

The local field of the network is given by:

$$h_i(t) = \sum_j w_{ij}^{(2)} S_j + w_i^{(1)} \quad [4]$$

The updating rule of $h_i(t)$ is given by:

$$S_i(t + 1) = \text{sgn}[h_i(t)] \quad [5]$$

where “sgn” represent the signum function. Signum function offers an output squashing mechanism to HNN.

The final state of neurons was examined by using Lyapunov energy function:

$$H_{P_{2SAT}} = -\frac{1}{2} \sum_i \sum_j w_{ij}^{(2)} S_i S_j - \sum_i w_i^{(1)} S_i \quad [6]$$

Final energy of HNN will without exception decrease with the dynamics. Minimum values from the energy function correspond to the stable state of the neurons. The aim of the HNN model is to ensure the solution move towards the lowest point. Lowest point (global minimum energy) corresponds to the optimal solution produced by HNN model. Learning phase of HNN model advanced by embedding the correct synaptic weight of 2SAT logic in HNN. 2SAT in HNN is abbreviated as HNN-2SAT model. Figure 1 shows the algorithm of implementation of HNN-2SAT models.

2 Satisfiability Based Reverse Analysis Method (2SATRA) in League of Legends

Logic mining will execute efficiently if the most favourable HNN-2SAT model is used. The neurons are represented in bipolar form $\{-1,1\}$. By acquiring the synaptic weight between 2 neurons, 2SATRA might be able to reveal the level of their connectedness. Therefore, Wan Abdullah’s method was utilized in the learning phase of 2SATRA to figure out the accurate synaptic weight between the two neurons (Abdullah, 1992). By considering both neurons C and D where $S_D \in \{-1,1\}$ and $S_C \in \{-1,1\}$, Table 1 summarizes the feasible synaptic weight corresponding to the 2SAT clause.

As an example, given that neuron C and D exhibits 1 and -1, P_3 is going to be selected as the clause representation for the data set. In accordance with the nature of the neuron, 2SATRA will convert the data sets into 2SAT logic. Figure 2 shows the implementation of 2SATRA.

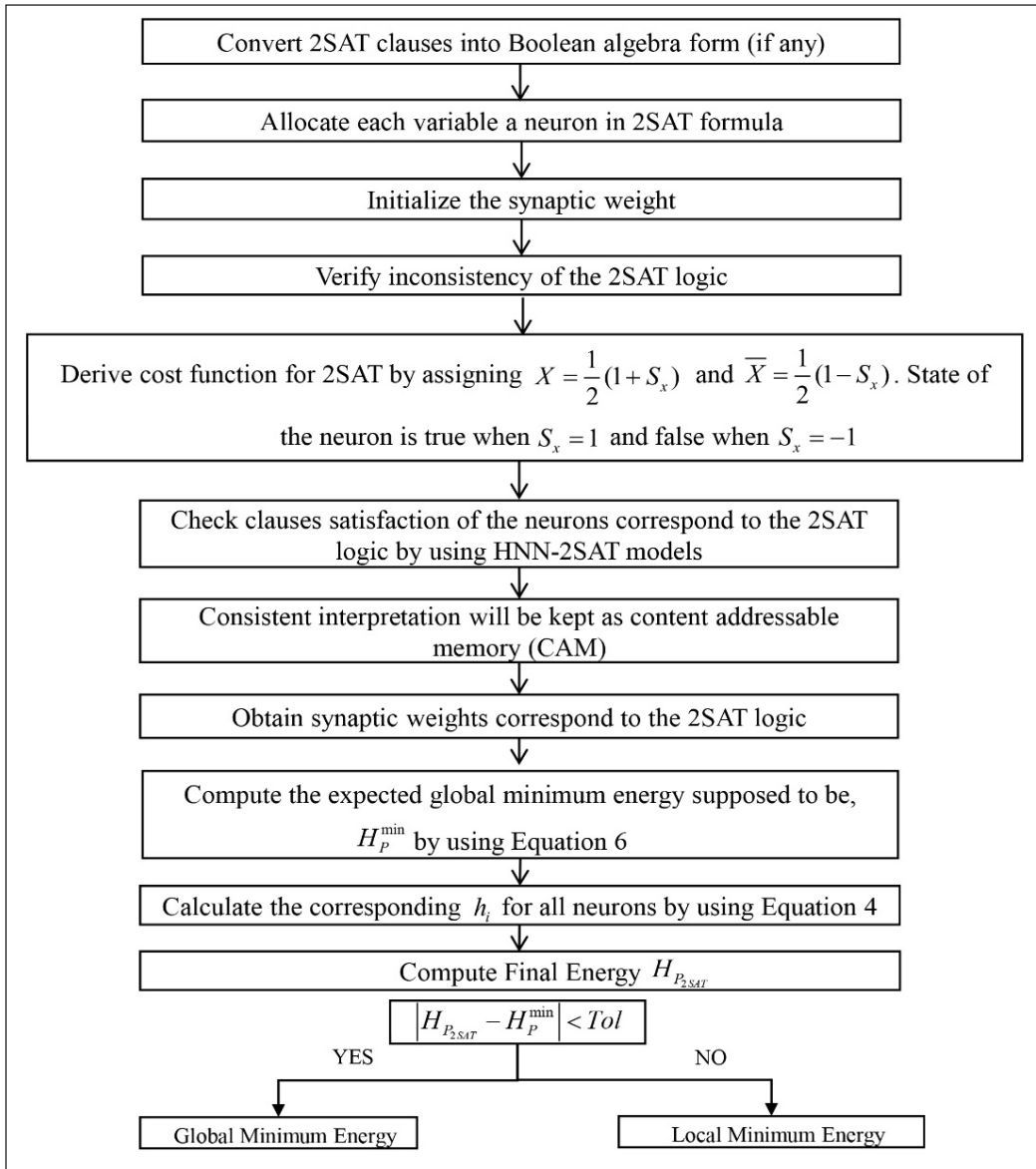


Figure 1. Algorithm of implementation of HNN-2SAT models

Table 1
Feasible synaptic weight corresponding to 2SAT logic

Synaptic Weight	$P_1 = C \vee D$	$P_2 = \neg C \vee D$	$P_3 = C \vee \neg D$	$P_4 = \neg C \vee \neg D$
W_C	0.25	-0.25	0.25	-0.25
W_D	0.25	0.25	0.25	-0.25
W_{CD}	-0.25	0.25	-0.25	-0.25

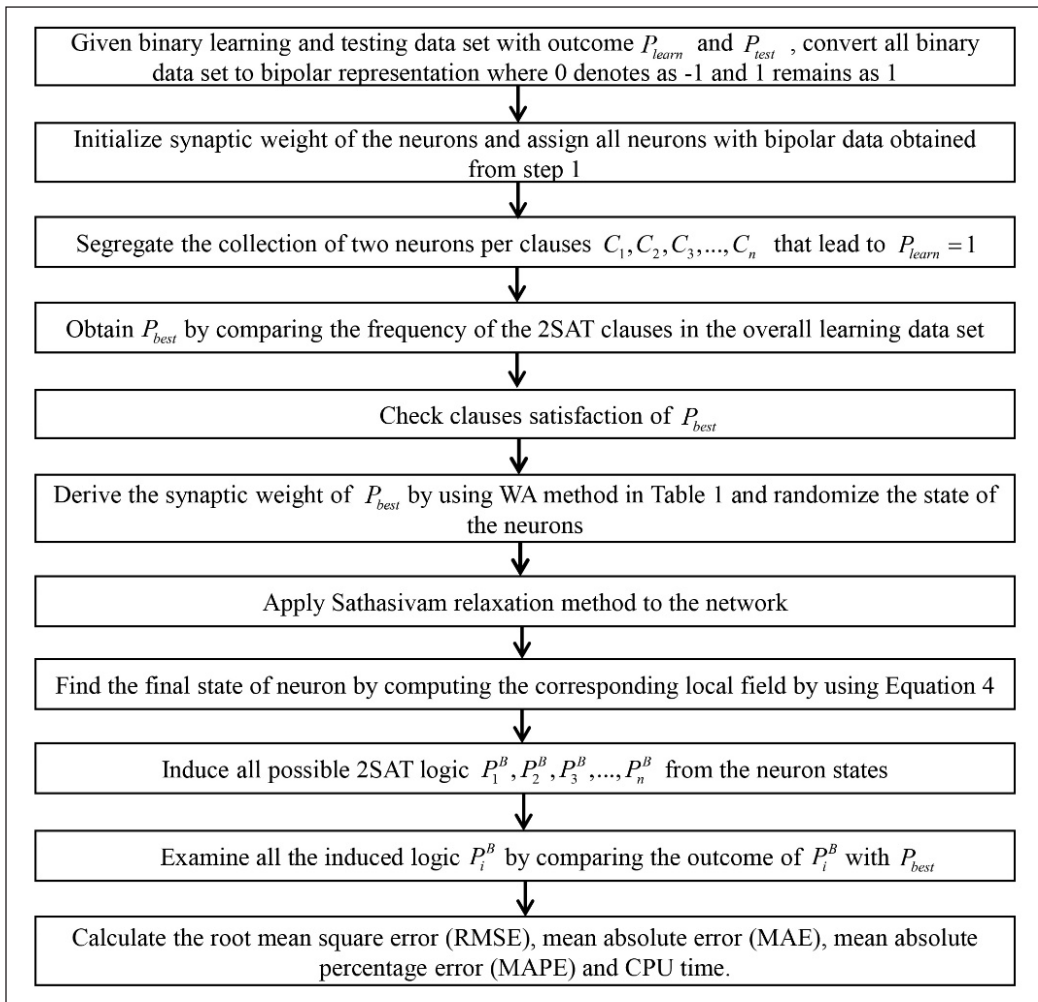


Figure 2. Algorithm of implementation of 2SATRA

In LoL, a split second decision or one team fight could turn the results of the game around. Hence, the coaches and players should be extra cautious when coming up with game strategies and their decisions in game. Logic mining is used in LoL to help the coaches and strategists in analysing the important gameplay or objectives in game. In this paper, 2SATRA is used to extract the logical relationship among the gameplay or objectives in game.

Experimental Setup

Every region has their own read on the game and hence there will be slight difference in the way they approach the game. Therefore, it is important to figure out the playing pattern

of every region in order to win games. By using 2SATRA, it is possible to determine the relationship among the gameplay or objectives in game. In learning data set, {Win, Lose} would be converted into bipolar representation {1,-1} respectively. Each gameplay or objective taken would be represented in terms of neuron in 2SATRA. Hence, there would be a total of six neurons being considered in this data set. The respective gameplay or objective taken and neuron are summarized in Table 2. Explanation of the gameplay or objective is summarized in Table 3.

Table 2
Respective gameplay/objective and neuron

Neuron	Gameplay/Objective
A	First Blood (<i>FB</i>)
B	First Turret (<i>FT</i>)
C	First Dragon (<i>FD</i>)
D	Rift Herald (<i>RH</i>)
E	Gold Ahead at 20 Minutes (<i>GA</i>)
F	First Baron Nashor (<i>FN</i>)

Table 3
Explanation for gameplay/objective

Gameplay/Objective	Explanation
First Blood	The first kill in the game.
First Turret	The first tower to fall in the game.
First Dragon	The first elemental drake secured in the game.
Rift Herald	Rift Herald secured in the game.
Gold Ahead at 20 Minutes	Gold lead exists at the 20 th minute mark of the game.
First Baron Nashor	The first Baron Nashor secured in the game.

The threshold CPU time was 24 hours and outputs that exceeded the time were all excluded. Dev C++ Version 5.11 was used to implement the HNN-2SAT model. Computer used was equipped with Intel Core i7 2.5GHz processor, 8GB RAM and Windows 8.1. In order to decrease the statistical error, the program ran 100 trials with 100 combination of neurons. (Sathasivam & Abdullah, 2011).

Performance Evaluation

In order to determine the efficiency of the HNN-2SAT model in doing 2SATRA, four performance evaluation metrics namely root mean square error, mean absolute error, mean absolute percentage error and computational time were analysed.

Root Mean Square Error

Root mean square error (RMSE) showed the differences between observed value and target value of a model. RMSE is defined as follows (Schwenker et al., 2001; Willmott et al., 1985)

$$RMSE = \sum_{i=1}^n \sqrt{\frac{1}{n} (f_{NC} - f_i)^2} \quad [7]$$

where f_i is the fitness of the solution in HNN-2SAT model, $f_i = f_{NC}$ is the total number of 2SAT clauses, and n is the number of iteration before $f_i = f_{NC}$. Lowest value of $RMSE$ indicates the best HNN-2SAT model.

Mean Absolute Error

Mean absolute error (MAE) is derived from each difference of $f_{NC} - f_i$. MAE is defined by (Mansor et al., 2018).

$$MAE = \sum_{i=1}^n \frac{1}{n} |f_{NC} - f_i| \quad [8]$$

The best HNN-2SAT model has the least value of MAE .

Mean Absolute Percentage Error

Mean absolute percentage error (MAPE) is a measure of accuracy in percentage form. MAPE can be expressed as (Tayman & Swanson, 1999)

$$MAPE = \sum_{i=1}^n \frac{100}{n} \frac{|f_{NC} - f_i|}{|f_i|} \quad [9]$$

However, $MAPE$ cannot be used if the observed value is zero as it will lead to division by zero. Lowest percentage of $MAPE$ shows the best HNN-2SAT model.

Computational Time

CPU time is the time required by a HNN-2SAT model to finish one execution. CPU time implies the capability and stability of the HNN-2SAT model. Equation of CPU time is as follows (Sathasivam, 2010)

$$CPU_Time = Learning_Time + Retrieval_Time \quad [10]$$

The best HNN-2SAT model would have the shortest CPU time since a good HNN-2SAT model is capable of reducing the computation time in learning phase of HNN.

RESULTS AND DISCUSSION

A total of 4 performance evaluation namely RMSE, MAE, MAPE and CPU time were analysed to determine the effectiveness, precision and steadiness of HNN-2SAT in doing 2SATRA. NC was the total number of clause and 1 clause had 2 neurons. Figure 3, Figure 4, Figure 5 and Figure 6 show the results of RMSE, MAE, MAPE and CPU time for all 3 regions. In this execution, 214 data points for LCK, 95 data points for NA LCS and 91 data points for EU LCS had been embedded to 2SATRA. The data points for LCK, NA LCS and EU LCS were obtained from the Riot Games website <https://matchhistory.na.leagueoflegends.com>. 60% were used as learning data and 40% used as testing data.

Based on Figure 3, Figure 4 and Figure 5, it can be observed that at $NC=1$, the HNN-2SAT model had the best results in terms of RMSE, MAE and MAPE. The reason behind this was when the number of clauses got larger, learning phase of 2SATRA got more complicated as HNN-2SAT had to discover the consistent interpretation for P_{best} . Conjointly, the learning error for 2SATRA increased as the number of neurons increased. 2SATRA achieved maximum value of RMSE, MAE and MAPE when $NC=10$. In this case,

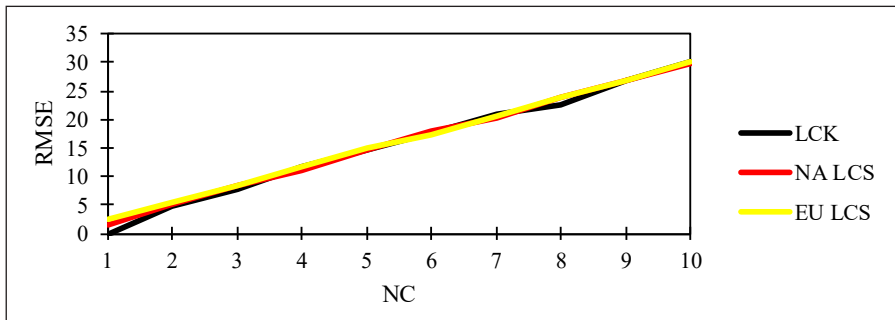


Figure 3. RMSE for HNN-2SAT model

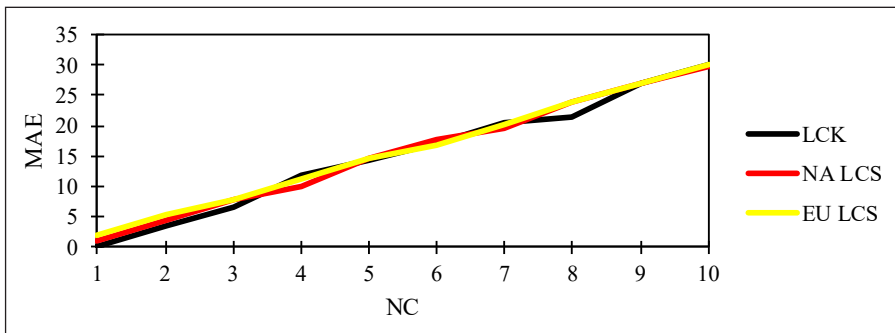


Figure 4. MAE for HNN-2SAT model

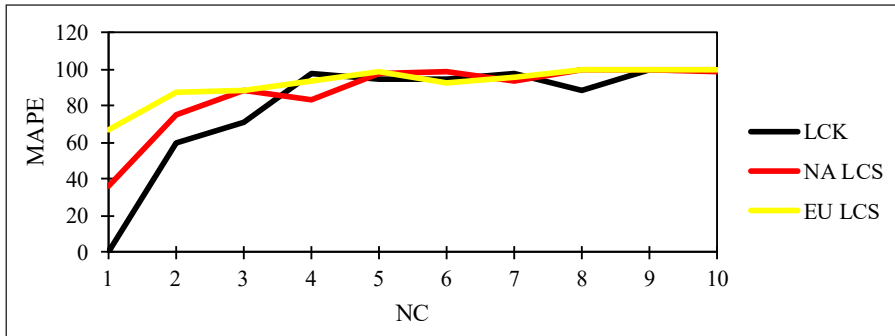


Figure 5. MAPE for HNN-2SAT model

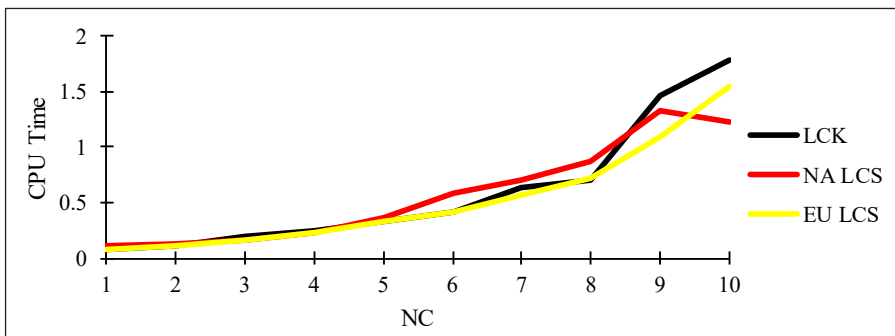


Figure 6. CPU Time for HNN-2SAT model

learning phase of HNN in 2SATRA reached a trial and error state. This phenomenon had a good agreement with the study by Sathasivam (2010). Figure 6 demonstrated the stability of 2SATRA in logic mining. 2SATRA was capable of inducing optimal P_i^B in moderate CPU time. At $NC=4$, 2SATRA was capable of inducing optimal P_i^B in 0.2 seconds. P_i^B induced by 2SATRA during the learning phase managed to accomplish an accuracy of 72% (LCK), 75% (NA LCS) and 73% (EU LCS). This is because the character of neuron in HNN, rather than oscillating, the neurons have always converged to minimum energy. Limitation of this model was the proposed gameplay or objective in game might not be the ones that will come out with the highest accuracy in 2SATRA. This was because in a LoL game, a lot of different factors will affect the outcome of the game. In this paper, we were only considering 6 of them. The results in this paper was not being compared to other existing methods because the approaches were different and incomparable. For example, Wang (2016) managed to achieve an accuracy of 61.04%. However, the research was done based on hero draft data while this paper was considering the gameplay or objectives in game. The best induced logic, $P_{inconsistent}$ and inconsistent interpretation, $P_{inconsistent}$ for each region are summarized in Table 4.

Table 4
Best induced logic and inconsistent interpretation

Region	Best induced logic, P_{best}	Inconsistent interpretation, $P_{inconsistent}$
LCK	$(\neg FB \vee FT) \wedge (FD \vee RH) \wedge (GA \vee FN)$	$(FB \wedge \neg FT) \vee (\neg FD \wedge \neg RH) \vee (\neg GA \wedge \neg FN)$
NA LCS	$(FB \vee FT) \wedge (FD \vee \neg RH) \wedge (GA \vee FN)$	$(FB \vee FT) \wedge (FD \vee RH) \wedge (GA \vee \neg FN)$
EU LCS	$(FB \vee FT) \wedge (FD \vee RH) \wedge (GA \vee \neg FN)$	$(\neg FB \wedge \neg FT) \vee (\neg FD \wedge \neg RH) \vee (\neg GA \wedge FN)$

According to Table 4, the relationship among the gameplays and objectives taken in game is shown. A list of key findings are summarized in Table 5.

Table 5
Key findings from induced logic

Region	Key Findings
LCK	In LCK, first blood is the least deciding factor of the game. Players should focus on contesting other objectives on the map such as first turret, first dragon, rift herald and first baron nashor. They should also maintain a gold lead at 20 minutes to increase their chances of winning the game.
NA LCS	For games in NA LCS, rift herald does not have much impact on the outcome of the game. Hence, teams should give priority on getting first blood, first turret, first dragon and first baron nashor. It is also important to maintain a gold lead at 20 minutes.
EU LCS	The winning rate is higher when a team gets first blood, first turret, first dragon, rift herald and gold lead at 20 minutes. The impact of first baron nashor in the game is not huge. Therefore, teams should not give away free kills or objectives to contest the first baron nashor of the game.

Every different regions have their own playstyle and hence the best induced logic, P_{best} for all 3 regions, LCK, NA LCS and EU LCS are different. The results have shown that 2SATRA has decent potential to obtain the logical rule that classifies the results of win or lose for a LoL game. It is extremely important to understand the playstyle of each region especially during the LoL World Championships. This is because the teams are not only competing with another team from their own region, they are also competing with top teams from other regions. The induced logic can help the coaches, managers and strategists in deciding the strategies in game. Game casters could also use the induced logic to provide expert discussion during a LoL game.

CONCLUSION

In this research, 2SATRA is shown to be a decent relationship extraction system to model the results of LoL games. The effectiveness of 2SATRA in doing logic mining is examined by using 3 data sets from 3 different regions. The results acquired showed that 2SATRA has decent potential to obtain optimal logic from learned data set. Future research could be done by using other gameplays such as first buff stolen, first success gank, numbers of turret plating fallen, first inhibitor taken and vision score at 20 minutes. Another logical

rule such as randomized k SAT where $k > 2$ could also be utilized. Metaheuristic algorithm such as Ant Colony Optimization, Artificial Bee Colony and Artificial Immune System could also be utilized to accelerate the process of learning phase of 2SATRA.

ACKNOWLEDGEMENT

This research is supported by Short Term Grant (304/PMATHS/6315226) by Universiti Sains Malaysia (USM).

REFERENCES

- Abdullah, W. A. T. W. (1992). Logic programming on a neural network. *International Journal of Intelligent Systems*, 7(6), 513-519.
- Baio, G., & Blangiardo, M. (2010). Bayesian hierarchical model for the prediction of football results. *Journal of Applied Statistics*, 37(2), 253-264.
- Bhandari, I., Colet, E., Parker, J., Pines, Z., Pratap, R., & Ramanujam, K. (1997). Advanced scout: data mining and knowledge discovery in NBA data. *Data Mining and Knowledge Discovery*, 1, 121-125.
- Chen, I., Homma, H., Jin, C., & Yan, H. H. (2007). Identification of elite swimmers' race patterns using cluster analysis. *International Journal of Sports Science and Coaching*, 2, 293-303.
- Craven, M. W., & Shavlik, J. W. (1997). Using neural networks for data mining. *Future Generation Computer Systems*, 13(2-3), 211-229.
- Even, S., Itai, A., & Shamir, A. (1975, October 13-15). On the complexity of time table and multi-commodity flow problems. In *16th Annual Symposium of Foundations of Computer Science* (pp. 184-193). Washington, DC, USA.
- Gaber, K., Bahi, M. J., & El-Ghazawi, T. (2000, November 15). Parallel mining of association rules with a Hopfield type neural network. In *Proceedings of 12th IEEE International Conference on Tools with Artificial Intelligence* (pp. 90-93). Vancouver, BC, Canada.
- Gee, A. H., Aiyer, S. V., & Prager, R. W. (1993). An analytical framework for optimizing neural networks. *Neural Networks*, 6(1), 79-97.
- Hopfield, J. J., & Tank, D. W. (1985). "Neural" computation of decisions in optimization problems. *Biological Cybernetics*, 52(3), 141-152.
- Jenny, S. E., Manning, R. D., Keiper, M. C., & Olrich, T. W. (2017). Virtual(ly) athletes: where eSports fit within the definition of "Sport". *Quest*, 69(1), 1-18.
- Johansson, F., & Wikström, J. (2015). *Result prediction by mining replays in dota 2* (Master Thesis). Blekinge Institute of Technology, Sweden.
- Johnson, M. B., Edmonds, W. A., Jain, S., & Cavados, J. J. (2009). Analysis of elite swimming performances and their respective between-gender differences over time. *Journal of Quantitative Analysis in Sports*, 5(4), 1-18.

- Kane, D., & Spradley, B. D. (2017). Recognizing eSports as a sport. *The Sport Journal*, 21, 1-9.
- Kasihmuddin, M. S. M. (2017). *Satisfiability logic programming incorporating metaheuristics in Hopfield neural networks* (PhD Thesis). Universiti Sains Malaysia, Malaysia.
- Kasihmuddin, M. S. M., Mansor, M. A., & Sathasivam, S. (2017). Hybrid genetic algorithm in the Hopfield network for logic satisfiability problem. *Pertanika Journal of Science and Technology*, 25(1), 139-152.
- Kim, Y. J., Engel, D., Woolley, A. W., Lin, J. Y. T., McArthur, N., & Malone, T. W. (2017, February 25 - March 01). What makes a strong team?: Using collective intelligence to predict team performance in League of Legends. In *Proceedings of 2017 ACM Conference on Computer Supported Cooperative Work and Social Computing* (pp. 2316-2329). Portland, Oregon, USA.
- Lamb, P., Bartlett, R., & Robins, A. (2010). Self-organising maps: An objective method for clustering complex human movement. *International Journal of Computer Science in Sport*, 9, 20-29.
- Lan, X., Duan, L., Chen, W., Qin, R., Nummenmaa, T., & Nummenmaa, J. (2018). A player behavior model for predicting win-loss outcome in MOBA games. In *International Conference on Advanced Data Mining and Applications* (pp. 474-488). Cham, Switzerland: Springer.
- Maknickas, A. A. (2015). How to solve kSAT in polynomial time. *International Journal of Operational Research*, 23(3), 257-267.
- Mansor, M. A., Sathasivam, S., & Kasihmuddin, M. S. M. (2018). 3 satisfiability logic programming approach for cardiovascular diseases diagnosis. *AIP Conference Proceedings*, 1974(1), 020022.
- Miyashiro, R., & Matsui, T. (2005). A polynomial-time algorithm to find an equitable home-away assignment. *Operations Research Letters*, 33(3), 235-241.
- Muezzinoglu, M. K., Guzelis, C., & Zurada, J. M. (2003). A new design method for the complex-valued multistate Hopfield associative memory. *IEEE Transactions on Neural Networks*, 14(4), 891-899.
- Mukherjee, S., & Roy, S. (2015, June 26-29). Multi terminal net routing for island style FPGAS using nearly-2-sat computation. In *19th International Symposium on VLSI Design and Test (VDATE)* (pp. 1-6). Ahmedabad, India.
- Nascimento Jr, F. F. D., Melo, A. S. D. C., da Costa, I. B., & Marinho, L. B. (2017, October 17-20). Profiling Successful Team Behaviors in League of Legends. In *Proceedings of the 23rd Brazilian Symposium on Multimedia and the Web* (pp. 261-268). Gramado, RS, Brazil.
- Nunes, S., & Sousa, M. (2006, January 9). Applying data mining techniques to football data from European championships. In *Actas da 1ª Conferência de Metodologias de Investigação Científica (CoMIC'06)* (pp. 4-16). University of Porto, Portugal.
- Reitman, J. G. (2018). Distributed cognition and temporal knowledge in league of legends. *International Journal of Gaming and Computer-Mediated Simulations (IJGCMS)*, 10(1), 23-41.
- Riot Games. (2018). *2018 events by the numbers*. Retrieved April 27, 2019 from <https://nexus.leagueoflegends.com/en-us/2018/12/2018-events-by-the-numbers/>
- Rojas, R. (1996). *Neural networks: a systematic introduction*. Berlin, Germany: Springer.
- Sathasivam, S. (2006). *Logic Mining in Neural Networks* (PhD Thesis). Universiti Malaya, Malaysia.

- Sathasivam, S. (2010). Upgrading logic programming in Hopfield network. *Sains Malaysiana*, 39(1), 115-118.
- Sathasivam, S., & Abdullah, W. A. T. W. (2011). Logic mining in neural network: reverse analysis method. *Computing*, 91(2), 119-133.
- Schwenker, F., Kestler, H. A., & Palm, G. (2001). Three learning phases for radial-basis-function networks. *Neural Networks*, 14(4-5), 439-458.
- Singh, Y., & Chauhan, A. S. (2009). Neural networks in data mining. *Journal of Theoretical and Applied Information Technology*, 5(1), 37-42.
- Tayman, J., & Swanson, D. A. (1999). On the validity of mape as a measure of population forecast accuracy. *Population Research and Policy Review*, 18(4), 299-322.
- Velavan, M., Yahya, Z. R., Halif, M. N. A., & Sathasivam, S. (2015). Mean field theory in doing logic programming using Hopfield network. *Modern Applied Science*, 10(1), 154-160.
- Wang, S. (2005). Classification with incomplete survey data: a Hopfield neural network approach. *Computers and Operations Research*, 32(10), 2583-2594.
- Wang, W. (2016). *Predicting multiplayer online battle arena (MOBA) game outcome based on hero draft data* (PhD Thesis). National College of Ireland, Dublin.
- Willmott, C. J., Ackleson, S. G., Davis, R. E., Feddema, J. J., Klink, K. M., Legates, D. R., ... & Rowe, C. M. (1985). Statistics for the evaluation and comparison of models. *Journal of Geophysical Research: Oceans*, 90(C5), 8995-9005.
- Yang, P., Harrison, B. E., & Roberts, D. L. (2014, April 3-7). Identifying patterns in combat that are predictive of success in MOBA games. In *9th International Conference on the Foundations of Digital Games* (pp. 1-8). Liberty of the Seas, Caribbean.



Hybrid Discrete Hopfield Neural Network based Modified Clonal Selection Algorithm for VLSI Circuit Verification

Saratha Sathasivam¹, Mustafa Mamat², Mohd. Asyraf Mansor^{3*} and Mohd Shareduwan Mohd Kasihmuddin¹

¹*School of Mathematical Sciences, Universiti Sains Malaysia, 11800 USM, Penang, Malaysia*

²*Faculty of Informatics and Computing, Universiti Sultan Zainal Abidin, 21300 UniSZA, Kuala Terengganu, Terengganu, Malaysia*

³*School of Distance Education, Universiti Sains Malaysia, 11800 USM, Penang, Malaysia*

ABSTRACT

Clonal selection algorithm and discrete Hopfield neural network are extensively employed for solving higher-order optimization problems ranging from the constraint satisfaction problem to complex pattern recognition. The modified clonal selection algorithm is a comprehensive and less iterative immune-inspired searching algorithm, utilized to search for the correct combination of instances for Very large-scale integrated (VLSI) circuit structure. In this research, the VLSI circuit framework consists of Boolean 3-Satisfiability instances with the different complexities and number of transistors are considered. Hence, a hybrid modified clonal selection algorithm with discrete Hopfield neural network is well developed to optimize the configuration of VLSI circuits with different number of electronic components such as transistors as the instances. Therefore, the performance of the developed hybrid model was assessed experimentally with the standard models, HNNVLSI-3SATES and HNNVLSI-3SATGA in term of circuit accuracy, sensitivity, robustness and runtime to complete the verification process. The results have demonstrated the developed model, HNNVLSI-3SATCSA produced a minimum error (consistently approaching 0), better accuracy (more than 80%) and faster computational time (less than 125 seconds) against changes in the complexity in term of the number of transistors.

Furthermore, the developed hybrid model is able to minimize the computational burden and configurational noises for the variant of VLSI circuits.

Keywords: 3-Satisfiability problem, clonal selection algorithm, genetic algorithm; Hopfield neural network; VLSI circuit

ARTICLE INFO

Article history:

Received: 09 May 2019

Accepted: 19 July 2019

Published: 13 January 2020

E-mail addresses:

saratha@usm.my (Saratha Sathasivam)

must@unisza.edu.my (Mustafa Mamat)

asyrafman@usm.my (Mohd. Asyraf Mansor)

shareduwan@usm.my (Mohd Shareduwan Mohd Kasihmuddin)

* Corresponding author

INTRODUCTION

The unprecedented growth of hybrid computational approach combining neural network and the nature-inspired algorithm has benefited various applications such as in the circuit verification, face recognition, path optimization and many more (Erdener & Ozoguz, 2016; Jain et al., 2018; Elhoseny et al., 2018). The bombardments of hybrid verification model are fueled by the complexities of the problem as the industrial demand is challenging in this era. The conventional production of binary transistor units in Very Large-Scale Integration (VLSI) circuit requires an effective hybrid model to verify for any early fault due to power dissipation during the production (Constantinescu, 2003). Hence, the VLSI design with early verification will improve the performance of the VLSI configuration itself as the complexities are dependent on the number of transistors embedded in the system. We will propose a VLSI verification model by hybridizing the modified clonal selection algorithm (CSA) and Hopfield neural network (HNN) with the different number of bipolar transistors combination. The VLSI verification process tends to be tedious, due to the extensive searching process in the response to complexities (Kumar et al., 2018).

According to Mansor et al. (2016), the VLSI circuit can be configured into Boolean 2-Satisfiability (2-SAT) and its higher order counterpart, 3-Satisfiability (3-SAT) logic form by representing the literals as a single unit of bipolar transistors. The results were encouraging with the circuit accuracy above 90 % for the different number of transistors. However, according to Global VLSI circuit perspective, it was observed that the method proposed by Mansor et al. (2016) required modification in terms of training algorithm to obtain a better result. The work of Zaruba et al. (2016) utilizing the nature-inspired algorithm which was an artificial bee colony (ABC) in optimizing VLSI design has been the motivation to venture the robust nature-inspired algorithm. In addition, Kumar et al. (2018) had successfully applied the adaptive particle swarm optimization in improving VLSI optimization. The 3-Satisfiability was chosen for this work due to the reducibility feature especially for the higher-order combinatorial problem. The work of Rai et al. (2018) discussed the reduction in polynomial 3-SAT for solving the Sudoku puzzle.

Recently, a renowned immune-inspired algorithm, called clonal selection algorithm (CSA) has been utilized in various optimization problems ranging from the social media metrics, routing problem and pattern recognition. Basically, the CSA serves as other meta-heuristic or searching approach, probably effective than the standard standalone evolutionary algorithm such as a genetic algorithm (GA). Nevertheless, CSA is apparently different than GA, with the normalization and hypermutation will take place. The pioneer work of CSA has been coined by Layeb et al. (2010). Therefore, the modified clonal selection is selected due to the capability to work in tandem with discrete Hopfield neural network to tackle the logic programming such as Maximum k-Satisfiability problem (Mansor et al., 2017). The recent work by Zhang et al. (2019) had highlighted the ability of CSA with modified combinatorial recombinant in solving the various numerical

optimization problem. The results obtained were acceptable to support the effectiveness of CSA in solving the optimization problem. Since the VLSI circuit verification can be regarded as an optimization problem, this work motivates us to venture this approach. Then, Avatefipour and Nafisian (2018) proposed the modified CSA as a feature selection paradigm to predict the load consumption with minimum error and iterations. The work has demonstrated better performance metrics when CSA is deployed as a feature selection approach. The effectiveness of CSA has been a motivation in modeling cell formation and verification problems (Karoum & Elbenani, 2017). Pursuing that, Schmidt et al. (2017) had applied CSA in internet traffic classification, which was a common problem in computer sciences. Cai et al. (2015) utilized CSA in order to detect the community in a complex network. In addition, CSA is applied widely in higher scale hydrothermal scheduling problem (Swain et al., 2011). Since most of the work focus on the implementation of CSA in solving optimization directly, there is limited work on combining CSA with a neural network as a single model. The effectiveness of CSA will be able to boost the capability of HNN during training and retrieval stage. Thus, we will combine CSA with HNN in verifying VLSI circuit in 3-SAT form.

In order to test the capability of CSA with HNN, we compare with the standard genetic algorithm (GA) and exhaustive search (ES). The genetic algorithm is a standard nature inspired searching algorithm, inspired by the Darwin theory. The standard algorithm of GA being used in this work is based on the studies done by Aiman and Asrar (2015) and Kasihmuddin et al. (2016). The effectiveness of GA in optimizing the weight in Multi-Criteria recommender system. This work has been coined by Kaur and Ratnoo (2019). Additionally, the exhaustive search is a primitive searching algorithm by deploying “enumerate and test” procedure in attaining the solution. In this work, the basis of exhaustive search is based on Mansor et al. (2016) and Kasihmuddin et al. (2017a). The ability of Hopfield neural network as a dynamic network especially to store the important information is the motivation of this research. Theoretically, Hopfield Neural Network is a class of recurrent neural network with sturdy capability in learning, acceptable memory, storage and mimics our biological brain system (Rojas, 2013). HNN was proposed by Hopfield (1982) to be utilized as a tool to solve notable combinatorial optimization problem and constraint satisfaction problem. In fact, HNN is an approach in artificial intelligence that demonstrates high-level learning behavior such as effective learning and retrieval mechanism. Since traditional HNN is prone to a few drawbacks (Gee et al., 1993), logic programming was embedded in HNN as a single intelligent unit (Abdullah, 1992). The effectiveness of HNN in VLSI verification has been demonstrated in the work of Mansor et al. (2016). The results were generally good, but the modifications need to be made to make it better. The main weaknesses of the work are the training method should be effective to truncate any circuit miss and errors especially if the number of transistors gets higher. In order to overwhelm the problem in complex VLSI circuit verification, the effectiveness

of the proposed hybrid model will be simulated by using VLSI circuit with a different combination of transistors.

The work is organized as follows. The materials and method discuss about VLSI circuit, Boolean 3 Satisfiability representation, 3SAT Programming in Hopfield Neural Network, Clonal Selection Algorithm in VLSI Configuration and Implementation. In the following section, the results and discussions are enclosed briefly. In the final section, the concluding remarks are included to summarize the output of the work.

MATERIALS AND METHOD

Very Large-Scale Integration (VLSI) Circuit

The Boolean logic is the building block of the Boolean circuit units, utilized in various electronic components in the market. In theory, Very Large-Scale Integration (VLSI) can be defined as an amalgamation of an array of bipolar transistors to form an integrated circuit (IC) to be utilized in various devices (Kumar et al., 2018). The transistor plays an integral role as an automatic switch or controller for a specific IC. Due to the complexities of the devices, the VLSI circuit verification became tedious as the circuit structural configuration loss and defect might occur without any early alarm.

According to Mansor et al. (2016), the conventional paradigm to configure the VLSI circuit by translating then circuit structure (transistors configuration) into a Conjunctive Normal Form (CNF) instances. The weakness of this method is the circuit structural configuration loss, specifically if the circuit components are getting higher in number. Therefore, a VLSI circuit inspired by the Boolean circuit is suggested by considering the 3-SAT instances. The HNNVLSI-3SATCSA model shall magnify the early error or fault in the VLSI circuit.

According to Figure 1, the configuration of the bipolar transistor was constructed by representing its Boolean 3-SAT representation. The single clauses of 3-SAT logic are

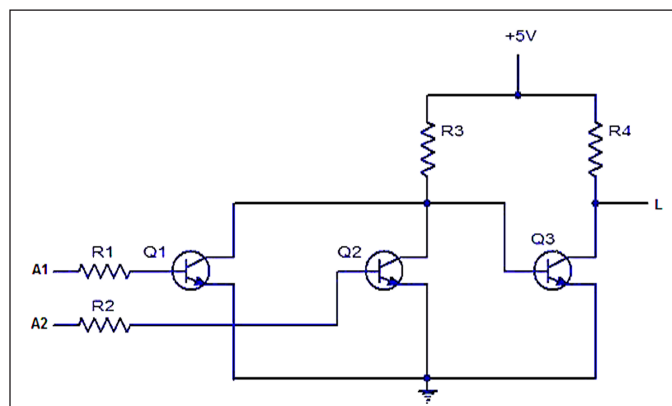


Figure 1. Schematic diagram of VLSI circuit (Mansor et al., 2016)

represented by a unit consisting of 3 bipolar transistors. Hence, the task of verifying the correct output is basically dependent on the number of transistors. The full implementation has been coined by Mansor et al. (2016). However, we verified the capability of CSA algorithm during the training phase to speed up the process per execution especially when dealing with more transistors.

Boolean 3 Satisfiability Representation

Implicit knowledge is hard to be represented in standard mathematical formulation (Sun et al., 2007). The conversion from implicit information to explicit representation can be done efficiently by formulating Boolean Satisfiability (SAT). SAT has been applied in different areas of electronic automation and functional verification (Kanj et al., 2017). With respect to VLSI application, any abstract circuit can be represented in terms of SAT formulation for which the output value needs to be validated. The resulting formulation will be mapped onto an instance of SAT. Given a set of assignment that represents the state of each component, the aim is to find the assignment of the component that satisfy the output circuit. Boolean Satisfiability (SAT) is a problem of deciding if there is a truth assignment that makes the Boolean function to be true. Any n-SAT problem with $n > 2$ where n is the number of variable, the problem can be reduced to 3-SAT (Shazli & Tahoori, 2010). In this paper, the systematic form of SAT will be formulated. The properties of SAT that ensembles 3-SAT logical rule are as follows:

The SAT formula comprises of an array of n variables, $z_1, z_2, \dots, z_n, z \in \{-1, 1\}$ inside each clause. Since $n = 2$, any SAT clauses will strictly consist of 3 variable/clause.

A set of k clauses connected by AND (\wedge) in a 3-SAT formula as follows:
 $\exists k: F = c_1 \wedge c_2 \wedge \dots \wedge c_k$.

A set of $l_{k,i}$ literals and each clause $c_k, \forall 1 \leq k \leq m, c_k = (l_{k,1} \vee l_{k,2} \vee l_{k,3})$ which consists of only literals combined by the logic operator OR (\vee).

The literals can be the variable itself or the negation of the variable.
 $\forall 1 \leq k \leq m, \leq i \leq 3: l_{k,i} = z_p$ or $l_{k,i} = \neg z_p$ for $1 \leq p \leq n$.

The 3-SAT formula is usually specified in product of sums or conjunctive normal form or CNF. Typical example of 3-SAT formula are as follows:

$$P = (\neg A \vee B \vee C) \wedge (\neg D \vee E \vee F) (\neg G \vee H \vee I) \quad (1)$$

If the state of each variable reads $A = D = E = F = 1, B = C = -1, P$ becomes unsatisfiable. Several studies formulated (Prasad et al., 2005) various methods to find the consistent assignment that makes P became satisfiable. The problem with the proposed method is the complexity of the backtracking algorithm. This algorithm demands more conflict analysis towards the SAT formulation before the correct assignment can be

generated. Thus, the complexity of the algorithm increases with the number of 3-SAT variables. These limitation motivates researchers (Martinez-Rios, 2017, Kasihmuddin et al., 2017b & Layeb, 2012) to explore intelligent metaheuristic method to find the correct assignments. In this paper, the clonal selection metaheuristics is proposed to find consistent interpretation of 3-SAT formulaton.

3SAT Programming in Hopfield Neural Network

There is a number of ways of organizing bipolar input data. Generally, the element will be arranged in a single layer of N neurons that influence each other with external bias. One of the most powerful single layer neural network is Hopfield Neural Network (HNN). In HNN, each neuron represents the solution of the constraint optimization problem and the quality of the solution increase with the decrease of the energy function. In this case, if the energy function of HNN decreased to absolute minima, HNN reached optimal solution. Several studies implemented (Wang & Hong, 2019) Hebbian learning during the learning phase of HNN. Ideally, this learning rule produced optimal synaptic weight that asynchronously update the state of the neurons. In reality, conventional HNN prone to several weaknesses such as low storage capacity (Agliari et al., 2013) and easy to be trapped in local minima solution (Yang et al., 2016). Several studies indicated that the usage of logical rule during learning phase of HNN could increase the accuracy of the models (Sathasivam, 2010). In this paper, transistor configuration is tranformed to 3SAT logical rule.

$$(T_1, T_2, T_3, T_4, \dots, T_N) \rightarrow P_{3SAT}, T_i \in \{-1, 1\} \tag{2}$$

$T_i \in \{-1, 1\}$ signifies “off” and “on” of the transistor. The cost function $E_{P_{Circuit}}$ of the logical rule in HNN is given by

$$E_{P_{Circuit}} = \sum_{i=1}^{NC} \prod_{j=1}^k M_{ij}, k = 3 \tag{3}$$

where NC is denoted by the number of clause containing transistors and M_{ij} is the inconsistency of the clause C_i given by

$$M_{ij} = \begin{cases} \frac{1}{2}(1 - T_x), \text{if } \neg x \\ \frac{1}{2}(1 + T_x), \text{Otherwise} \end{cases} \tag{4}$$

where $\neg x$ is the negation of literal in 3SAT clause. Generally, the local field of the HNN-3SAT is given as follows

$$T_i = \begin{cases} 1, & \sum_{k=1, l \neq j \neq k}^N Q_{ijk}^{(3)} T_j T_k + \sum_{j=1, l \neq j}^N Q_{ij}^{(2)} T_j + Q_i^{(1)} \geq \xi \\ -1, & \sum_{k=1, l \neq j \neq k}^N Q_{ijk}^{(3)} T_j T_k + \sum_{j=1, l \neq j}^N Q_{ij}^{(2)} T_j + Q_i^{(1)} < \xi \end{cases} \quad (5)$$

where Q_{ij} is the synaptic weight from unit j to i . $Q_i^{(1)}$, $Q_{ij}^{(2)}$, $Q_{ijk}^{(3)}$ are the first, second and third order neuron connection. T_j is the state of unit j and ξ is the threshold of unit i . The connection in HNN-3SAT has no connection with itself $Q_{ii} = Q_{jj} = Q_{kk} = Q_{iii} = Q_{jjj} = Q_{kkk} = 0$. It is necessary to examine the quality of the neuron state produced in equation (5). The Lyapunov energy function for the $P_{Circuit}$ is given as follows

$$H_{P_{Circuit}} = -\frac{1}{3} \sum_{i=0, l \neq j \neq k}^N \sum_{j=0, j \neq i \neq k}^N \sum_{k=0, k \neq i \neq j}^N Q_{ijk}^{(3)} T_i T_j T_k - \frac{1}{2} \sum_{i=0, l \neq j}^N \sum_{j=0, j \neq i}^N Q_{ij}^{(2)} T_i T_j - \sum_{i=0}^N Q_i^{(1)} T_i \quad (6)$$

Synaptic weight of HNN-3SAT will be obtained by comparing equation (3) and (6). Due to the symmetrical property of HNN, Lyapunov energy function always converge to minimum energy. Since the energy value of each clause in 3SAT is always constant, the separation of global and local minimum energy is defined with energy threshold ψ .

$$|H_{P_{Circuit}}^{min} - H_{P_{Circuit}}| \leq \psi \quad (7)$$

Plotting the final state of neuron in HNN-3SAT as heights on a 2D state-space plane creates a landscape of hills and valleys. Lyapunov energy function will develop a neuron state that are locally stable. In this case, global solution corresponds to the correct transistor configuration.

Clonal Selection Algorithm in VLSI Configuration

Creating a functional VLSI model is important before it can be physically manufactured. Thousands of transistors will be simulated inside a single circuit board before it is ready for experimentation. Due to mathematical complexity in deciding the valid VLSI model such as Castañeda et al. (2018), the usage of metaheuristics will find the optimal solution in acceptable time range. Unfortunately, the inherent problems of VLSI configuration simulation are exacerbated in an exponential manner as the number of transistors increases linearly. Only a few works has attempted to simulate the VLSI configuration by using

evolutionary metaheuristics algorithm (Laudis et al., 2018 & Kumar et al., 2018). These metaheuristics have been converted to binary representation. Pursuing that, the most popular evolutionary algorithm used is binary genetic algorithm. Although binary GA has a successful theoretical a practical history that arguably stretches further back compared to recent metaheuristics, binary GA prone to limitation such as initial solution convergence. Kasihmuddin et al. (2017b) argued that during the first few hundreds generation of crossover, only mutation would reduce the similarity of the candidate solution. This finding shows that the solution quality of GA (during the first few generation) is almost similar to conventional exhaustive search method.

This poses an important question, what if we could fully utilize the directional mutation behavior of the GA? Artificial Immune System (AIS) algorithm has evolved as a prolific metaheuristic technique that improve the main weaknesses in binary GA. AIS was introduced by Farmer et al. (1986) by systematically model the solution search according to Jerne's Immune network theory. Due to the nature of the immune system, AIS can be described as a distributed solution network which consist of functional B-Cell. Any massive and diverse population in B-Cells represent a massive space search of solutions that tends to global solutions. In this paper, each B-Cell is represented with a bipolar string which is a possible configuration of transistors. Bipolar string of 1 and -1 will be represented as "on" and "off" respectively. Our approach is to create a functional VLSI model that has the following objective function:

$$E_{P_{Circuit}} = 0 \quad (8)$$

The following steps represent the algorithm of AIS embedded to HNN:

Step 1: B-cells Initialization. 100 B-cells, B_{ij} are initialized. Each B-cell contains bipolar value that represent the configuration of transistors in VLSI. The formulation of initialization is as follows

$$B_{ij} = \begin{cases} 1, & \text{rand}(0,1) \geq 0.5 \\ -1, & \text{otherwise} \end{cases}, 1 \leq i \leq N, 1 \leq j \leq 100 \quad (9)$$

Step 2: B-cell Affinity Computation. The affinity of every B-cells would be computed. The affinity measures the sum of satisfied $P_{Circuit}$ that contains set of transistors.

$$aff_i = \sum_{i=1, j=1}^{NC} C_{ij} \quad (10)$$

$$C_{ij} = \begin{cases} 1, & E_{B_{i,j} \wedge B_2 \wedge B_3} = 0 \\ -1, & E_{B_{i,j} \wedge B_2 \wedge B_3} \geq 0 \end{cases} \quad (11)$$

where $E_{B_{i,j} \wedge B_2 \wedge B_3}$ is the cost function of clause C_{ij} .

Step 3: Cloning of B-cells. Based on step 2, top 5 B-cells with the (highest affinity value) were chosen. Roulette wheel selection (Goldberg & Deb, 1991) would identify B-cell with the most affinity value in order to proceed with the cloning phase.

$$N_{B_i} = \frac{aff_i}{\sum aff_i} \times \beta \quad (12)$$

where N_{B_i} is a number of newly produced B-cells population and β is the predefined number of clone population.

Step 4: Normalization of B-Cells. The antibodies exist in a memory response achieve a higher average affinity than those of the initial primary response (maturation of the immune response). Hence the normalized affinity of each B-cell, aff_{B_i} will be calculated based on the following:

$$aff_{B_i} = \frac{aff_{B_i} - \min aff_{B_i}}{\max aff_{B_i} - \min aff_{B_i}} \quad (13)$$

where $\max aff_{B_i} \neq \min aff_{B_i}$ because B-cell that achieved $aff_{B_i} = \max aff_{B_i}$ will automatically exit the algorithm via step 2. Normalization of B-Cell is crucial in AIS because it defines the rigorousness of mutation during the next step.

Step 5: Somatic Hypermutation. Local maxima (non-improving B-cell) is potentially disrupted the local search process. In this step, somatic hypermutation is implemented by flipping the state of B-Cell based on the following formula

$$NB_i = \left(\frac{1}{\eta}\right)(aff N_i) + (1 - aff N_i)(0.01) \quad (14)$$

where NB_i denotes the number of mutation in B-cell i and η refers to the number of variables. The affinity of the B-cells was calculated by using equation (10). The best B-cells were selected as the candidate cell and stored into the memory cell. In this case, this memory cell would be retrieved to combat pathogenic attacks. This step is required to reduce the similarity index among the antibodies. In our context, any satisfied VLSI configuration would be stored in CAM to be recalled by the network.

Implementation

The implementation of hybrid models in VLSI reconfiguration are:

Step 1. The 3-SAT clauses were translated and transformed into Boolean algebra. Basically, the clauses would form a formula that would determine the overall satisfiability. In VLSI circuits, the clauses denote the different set of bipolar transistors.

Step 2. Identify a neuron to each ground neuron.

Step 3. Initialize the entire synaptic weights to zero.

Step 4. Derive a cost function that is related with negation of all 3-SAT clauses. For instance, $X = \frac{1}{2}(1 + S_x)$ and $\bar{X} = \frac{1}{2}(1 - S_x)$. $S_x = 1$ (True) and $S_x = -1$ (False). Multiplication represents CNF and addition represents DNF.

Step 5. Compare the cost function with energy function to attain the values of synaptic weight. (Abdullah, 1992).

Step 6. Check clauses satisfaction by using ES (Mansor et al., 2016), GA (Kasihmuddin et al, 2017a) and the modified CSA. Hence, the satisfied clauses will be stored. In VLSI circuits, the satisfied transistors configuration will be stored as content addressable memory.

Step 7. Randomize the states of the neurons. The network undergoes sequences of network relaxation via Sathasivam method (Sathasivam, 2010).

Step 8. Find the corresponding local field of the state. If the final state is stable for 5 runs, we consider it as final state.

Step 9. Compute the corresponding final energy of the final state by using Lypunov equation. Validate whether the final energy obtained is a global minimum energy or local minima. In VLSI circuit, the final energy will determine correct configuration of the circuit.

Step 10. The RMSE, MAE, SSE, circuit accuracy and circuit runtime are calculated the VLSI circuit with different number of transistors per execution.

The implementation of VLSI verification models, HNNVLSI-3SATCSA, HNNVLSI-3SATES and HNNVLSI-3SATGA was carried out via Microsoft Visual Basic C++ 2013 for Windows 10. Similar processing system and CPU would be used in every execution to avoid possible bad sector. In addition, it would make the comparison to be fair and square.

RESULTS AND DISCUSSIONS

As compared to the previous VLSI verification method by utilizing HNN as coined by Mansor et al. (2016), this simulation had been developed by using modified clonal selection

algorithm (CSA) as the training algorithm. The comparison would be made with the other algorithms such as exhaustive search (ES) and genetic algorithm (GA). The hybrid VLSI verification model proposed is HNNVLSIA-3SATCSA and would be compared with HNNVLSI-3SATES and HNNVLSI-3SATGA. The simulation had been restricted until the number of transistors was 108 for simplicity.

The root mean square error (RMSE) and mean absolute error (MAE) recorded by the developed model, HNNVLSI-3SATCSA are presented in Figure 2 and Figure 3 to

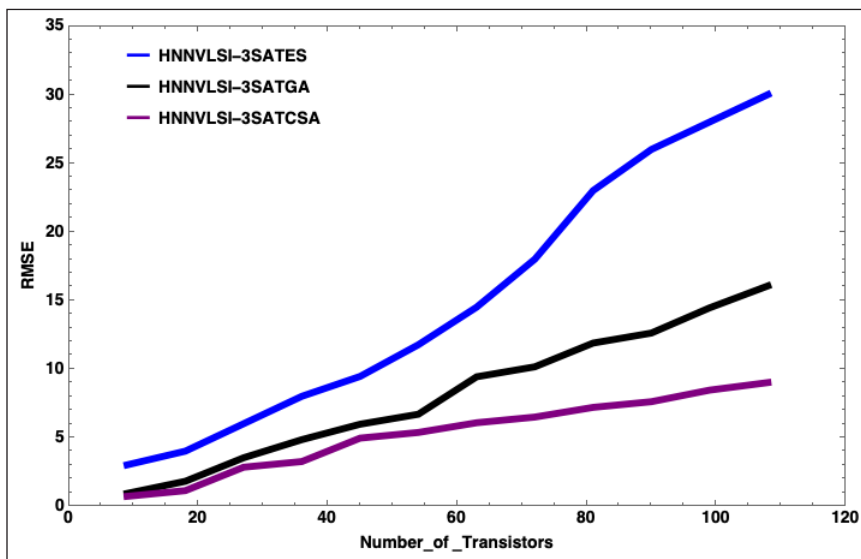


Figure 2. RMSE for the HNNVLSI-3SAT models

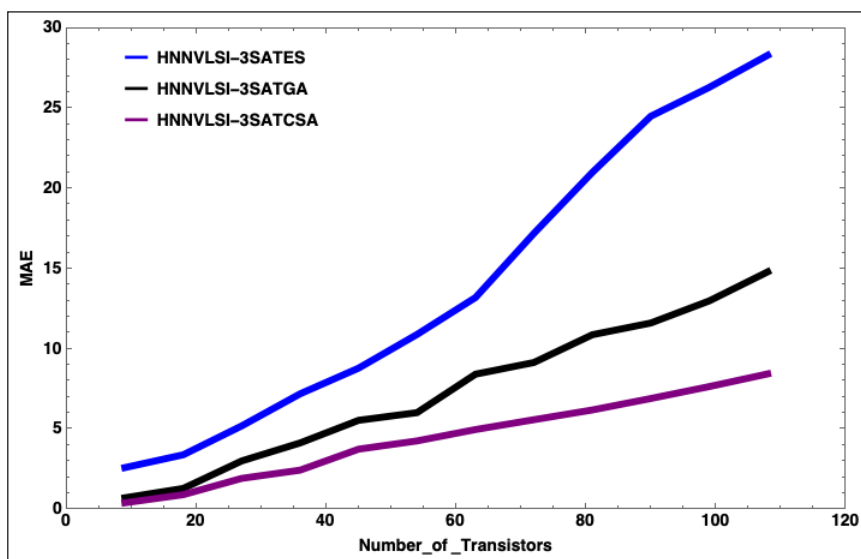


Figure 3. MAE for the HNNVLSI-3SAT models

be compared to other two counterparts, HNNVLSI-3SATES and HNNVLSI-3SATGA. Figure 2 and Figure 3 demonstrate the ability of our proposed model in verifying the circuit configuration during training phase without consuming the additional iterations and errors in generating fit strings as VLSI combinations. Thus, this emphasizes the supremacy of the somatic hypermutation operator in CSA that allows the VLSI circuits to be verified accurately without undergoing multiple unnecessary iterations and processes. The solutions will be improved directly via the effective flipping mechanism (Layeb, 2012) to obtain the feasible VLSI circuit combinations. Hence, fewer iterations will allow the model to attain faster convergence, resulting in minimum RSME and MAE obtained by HNNVLSIA-3SATCSA. HNNVLSI-3SATES is performed apparently poor due to the “trial and enumerate” procedure in attaining the correct VLSI circuit combinations. Additionally, HNNVLSI-3SATGA is still acceptable for the lower number of transistors as the non-fit strings need to be improved before undergoing the mutation operator (Aiman & Asrar, 2015).

Figure 4 shows the sum of squared error (SSE) recorded by the models in VLSI verification. Generally, it can be deduced that as the number of transistors increases, the accumulation of errors also increases. The accumulation of the errors can be magnified by observing the SSE for different execution. The significant differences can be seen when the number of transistors is between 63 to 108. From that point, the developed model, HNNVLSI-3SATCSA outperforms HNNVLSI-3SATES and HNNVLSI-3SATGA in term of sensitivity towards any incoming errors. Thus, the error during the training phase of the VLSI verification can be reduced by the optimization operators employed by CSA such as normalization of affinity and somatic hypermutation. In fact, the effectiveness of somatic hypermutation in improving the solutions has been coined by Layeb (2012) and Mansor et al. (2017). On the contrary, the ES algorithm deploys the tedious iteration processes before attaining the feasible solutions. Then, GA worked well but required early fitness and undergoing crossover and mutation.

Figure 5 manifests the circuit accuracy when the simulation is carried out by using different models. The circuit accuracy is calculated by the number of correct configurations of VLSI circuit after the retrieval phase. The proposed model, HNNVLSI-3SATCSA has recorded the accuracy between 95%-100% for the different number of transistors. The results delineate the performance of the developed model as compared with HNNVLSI03SATES and HNN-3SATGA in generating the correct VLSI circuits at the end of every execution. The reason lies in the efficiency of CSA in modeling and verifying the VLSI circuits without the interferences of massive errors and iterations. Apart from that, the proposed model is apparently worked well when the number of transistors was 108 compared to the other counterparts. Relatively high circuit accuracy demonstrates that HNNVLSI-3SATCSA has a greater stability when more transistors are introduced. In addition, better accuracy

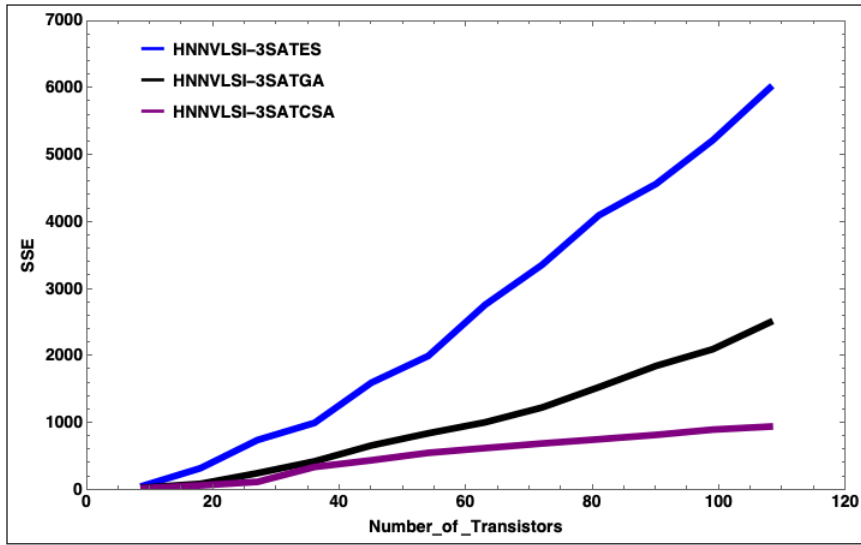


Figure 4. SSE for the HNNVLSI-3SAT models

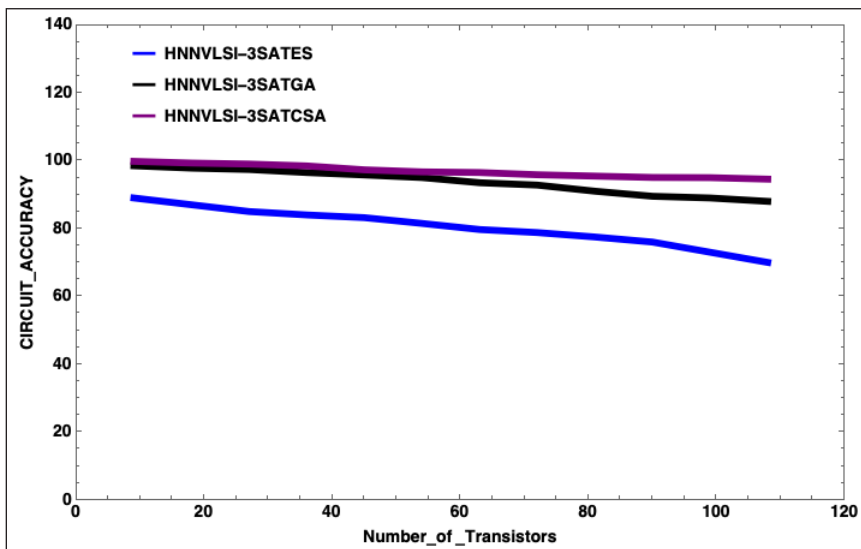


Figure 5. Circuit accuracy (%) for the HNNVLSI-3SAT models

will improve the functionality of normal VLSI circuit as the complexity increases. The robust training algorithm will exponentially lower the complexity of the whole VLSI verification processes. The conventional approach, HNNVLSI-3SATES has recorded the lowest accuracy due to the ineffectiveness of generating the fit VLSI combinations and reduced the number of correct VLSI configurations generated at the end of the execution.

Figure 6 demonstrates the circuit runtime recorded by HNNVLSI-3SATCSA, HNNVLSI-3SATGA, and HNNVLSI-3SATES by using different combinations of the

transistor. Based on the circuit runtime, HNNVLSI-3SATCSA completes the VLSI verification faster than HNNVLSI-3SATGA and HNNVLSI-3SATES. Theoretically, the training process by ES requires extra training time due to the trial and error process in attaining the correct VLSI configurations. Therefore, the entire non-fit strings that resemble the VLSI combinations will collapse if any one of the clauses is not satisfied. On the contrary, the GA will enhance the training process but require early population adjustment together with crossover and mutation. The procedure will reduce the time taken to check the VLSI circuit as compared to ES. However, when compared with CSA, the correct non-fit VLSI circuit can be improved with the robust hypermutation operator without the need to reset the whole combinations. Thus, HNNVLSI-3SATCSA experienced less computation burden during the training processes as compared to the other two approaches. Thus, the developed model is more robust than the other two counterparts. The faster circuit runtime together with better accuracy is essentially needed in VLSI circuit verification in order to avoid any miss and power dissipation. The results have improved the VLSI verification paradigm done by Mansor et al. (2016) and Kumar et al. (2018).

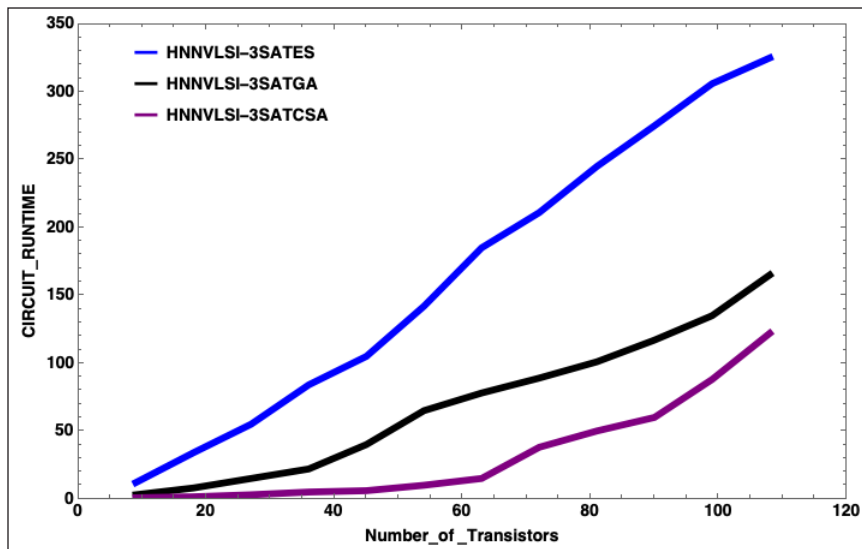


Figure 6. Circuit runtime for the HNNVLSI-3SAT models

CONCLUSION

This work was largely motivated from industrial application point of view where we clearly identified a need for model verification by using neural network ensembles as decision support system. We have presented our proposed algorithms, namely HNNVLSI-3SATCSA model and the conventional models, HNNVLSI-3SATGA and HNNVLSI-3SATES to check the VLSI circuit accuracy if the number of transistors gets higher. It had been shown by the

computer simulations that both models that incorporated with HNN were able to retrieve the desired output as the traditional VLSI models did. However, it was identified that HNNVLSI-3SATCSA outperformed the other models in terms of accuracy and robustness of the techniques in VLSI configuration. Hence, the proposed models are supported by the solid agreement of RMSE, MAE, SSE, circuit accuracy and circuit runtime obtained. Thus, our hybrid paradigm can be further integrated to solve and model more complicated electronics problem. Future research topics are to deal with other variant of HNN such as Mutation HNN (Hu et al., 2011), memristor HNN (Liu et al., 2018) and genetic optimized HNN (Jayashree & Kumar, 2019).

ACKNOWLEDGEMENT

This research is supported by Universiti Sains Malaysia and Fundamental Research Grant Scheme (FRGS) (203/PMATHS/6711689) by Ministry of Higher Education Malaysia.

REFERENCES

- Abdullah, W. A. T. W. (1992). Logic programming on a neural network. *International Journal of Intelligent Systems*, 7(6), 513-519.
- Agliari, E., Barra, A., De Antoni, A., & Galluzzi, A. (2013). Parallel retrieval of correlated patterns: From Hopfield networks to Boltzmann machines. *Neural Networks*, 38, 52-63.
- Aiman, U., & Asrar, N. (2015). Genetic algorithm based solution to SAT-3 problem. *Journal of Computer Sciences and Applications*, 3(2), 33-39.
- Avatefipour, O., & Nafisian, A. (2018). A novel electric load consumption prediction and feature selection model based on modified clonal selection algorithm. *Journal of Intelligent and Fuzzy Systems*, 34(4), 2261-2272.
- Cai, Q., Gong, M., Ma, L., & Jiao, L. (2015). A novel clonal selection algorithm for community detection in complex networks. *Computational Intelligence*, 31(3), 442-464.
- Castañeda, O., Goldstein, T., & Studer, C. (2018). VLSI designs for joint channel estimation and data detection in large SIMO wireless systems. *IEEE Transactions on Circuits and Systems I: Regular Papers*, 65(3), 1120-1132.
- Constantinescu, C. (2003). Trends and challenges in VLSI circuit reliability. *IEEE Micro*, 23(4), 14-19.
- Elhoseny, M., Tharwat, A., & Hassanien, A. E. (2018). Bezier curve based path planning in a dynamic field using modified genetic algorithm. *Journal of Computational Science*, 25, 339-350.
- Erdener, Ö., & Ozoguz, S. (2016). A new neuron and synapse model suitable for low power VLSI implementation. *Analog Integrated Circuits and Signal Processing*, 89(3), 749-770.
- Farmer, J. D., Packard, N. H., & Perelson, A. S. (1986). The immune system, adaptation, and machine learning. *Physica D: Nonlinear Phenomena*, 22(1-3), 187-204.
- Gee, A. H., Aiyer, S. V., & Prager, R. W. (1993). An analytical framework for optimizing neural networks. *Neural Networks*, 6(1), 79-97.

- Goldberg, D. E., & Deb, K. (1991). A comparative analysis of selection schemes used in genetic algorithms. In G. J. E. Rawlins (Ed.), *Foundations of genetic algorithms* (Vol. 1, pp. 69-93). San Mateo, CA: Morgan Kaufmann Publishers, Inc.
- Hopfield, J. J. (1982). Neural networks and physical systems with emergent collective computational abilities. *Proceedings of the National Academy of Sciences*, 79(8), 2554-2558.
- Hu, L., Sun, F., Xu, H., Liu, H., & Zhang, X. (2011). Mutation Hopfield neural network and its applications. *Information Sciences*, 181(1), 92-105.
- Jain, N., Kumar, S., Kumar, A., Shamsolmoali, P., & Zareapoor, M. (2018). Hybrid deep neural networks for face emotion recognition. *Pattern Recognition Letters*, 115, 101-106.
- Jayashree, J., & Kumar, S. A. (2019). Evolutionary correlated gravitational search algorithm (ECGS) with genetic optimized hopfield neural network (GHNN)—A hybrid expert system for diagnosis of diabetes. *Measurement*, 145, 551-558.
- Kanj, I., Thilikos, D. M., & Xia, G. (2017). On the parameterized complexity of monotone and antimonotone weighted circuit satisfiability. *Information and Computation*, 257, 139-156.
- Karoum, B., & Elbenani, Y. B. (2017). A clonal selection algorithm for the generalized cell formation problem considering machine reliability and alternative routings. *Production Engineering*, 11(4-5), 545-556.
- Kasihmuddin, B. M., Shareduwan, M., Mansor, B., Asyraf, M., & Sathasivam, S. (2016). Genetic Algorithm for Restricted Maximum k-Satisfiability in the Hopfield Network. *International Journal of Interactive Multimedia and Artificial Intelligence*, 4(2), 52-60.
- Kasihmuddin, M. S. M., Mansor, M. A., & Sathasivam, S. (2017a). Hybrid Genetic Algorithm in the Hopfield Network for Logic Satisfiability Problem. *Pertanika Journal of Science and Technology*, 25(1), 139-152.
- Kasihmuddin, M. S. M., Sathasivam, S., & Mansor, M. A. (2017b). Hybrid genetic algorithm in the Hopfield network for maximum 2-satisfiability problem. In U. Wagenknecht, P. Potschke, S. Wiessner & M. Gehde (Eds.), *AIP Conference Proceedings* (Vol. 1870, No. 1, p. 050001). Melville, NY: AIP Publishing.
- Kaur, G., & Ratnoo, S. (2019). Adaptive genetic algorithm for feature weighting in multi-criteria recommender systems. *Pertanika Journal of Science & Technology*, 27(1), 123-141.
- Kumar, S. V., Rao, P. V., Sharath, H. A., Sachin, B. M., Ravi, U. S., & Monica, B. V. (2018, In Press). Review on VLSI design using optimization and self-adaptive particle swarm optimization. *Journal of King Saud University-Computer and Information Sciences*.
- Laudis, L. L., Shyam, S., Jemila, C., & Suresh, V. (2018). MOBA: multi objective bat algorithm for combinatorial optimization in VLSI. *Procedia Computer Science*, 125, 840-846.
- Layeb, A. (2012). A clonal selection algorithm based tabu search for satisfiability problems. *Journal of Advances in Information Technology*, 3(2), 138-146.
- Layeb, A., Deneche, A. H., & Meshoul, S. (2010). A new artificial immune system for solving the maximum satisfiability problem. In N. García-Pedrajas, F. Herrera, C. Fyfe, J. M. Benítez & M. Ali (Eds.), *Trends in Applied Intelligent Systems* (pp. 136-142). Berlin, Heidelberg: Springer.

- Liu, S., Yu, Y., Zhang, S., & Zhang, Y. (2018). Robust stability of fractional-order memristor-based Hopfield neural networks with parameter disturbances. *Physica A: Statistical Mechanics and its Applications*, 509, 845-854.
- Mansor, M. A. B., Kasihmuddin, M. S. B. M., & Sathasivam, S. (2017). Robust Artificial Immune System in the Hopfield network for Maximum k-Satisfiability. *International Journal of Interactive Multimedia and Artificial Intelligence*, 4(4), 63-71.
- Mansor, M. A., Kasihmuddin, M. S. M., & Sathasivam, S. (2016). VLSI circuit configuration using satisfiability logic in Hopfield network. *International Journal of Intelligent Systems and Applications (IJISA)*, 8(9), 22-29.
- Martinez-Rios, F. (2017). A new hybridized algorithm based on population-based simulated annealing with an experimental study of phase transition in 3-SAT. *Procedia Computer Science*, 116, 427-434.
- Prasad, M. R., Biere, A., & Gupta, A. (2005). A survey of recent advances in SAT-based formal verification. *International Journal on Software Tools for Technology Transfer*, 7(2), 156-173.
- Rai, D., Chaudhari, N. S., & Ingle, M. (2018). Polynomial 3-SAT Reduction of Sudoku Puzzle. *International Journal of Advanced Research in Computer Science*, 9(3), 194-197.
- Rojas, R. (2013). *Neural networks: A systematic introduction*. Heidelberg, Germany: Springer-Verlag.
- Sathasivam, S. (2010). Upgrading logic programming in Hopfield network. *Sains Malaysiana*, 39(1), 115-118.
- Schmidt, B., Al-Fuqaha, A., Gupta, A., & Kountanis, D. (2017). Optimizing an artificial immune system algorithm in support of flow-Based internet traffic classification. *Applied Soft Computing*, 54, 1-22.
- Shazli, S. Z., & Tahoori, M. B. (2010). Using boolean satisfiability for computing soft error rates in early design stages. *Microelectronics Reliability*, 50(1), 149-159.
- Sun, R., Zhang, X., Slusarz, P., & Mathews, R. (2007). The interaction of implicit learning, explicit hypothesis testing learning and implicit-to-explicit knowledge extraction. *Neural networks*, 20(1), 34-47.
- Swain, R. K., Barisal, A. K., Hota, P. K., & Chakrabarti, R. (2011). Short-term hydrothermal scheduling using clonal selection algorithm. *International Journal of Electrical Power and Energy Systems*, 33(3), 647-656.
- Wang, H., & Hong, M. (2019). Supervised Hebb rule based feature selection for text classification. *Information Processing and Management*, 56(1), 167-191.
- Yang, G., Wu, S., Jin, Q., & Xu, J. (2016). A hybrid approach based on stochastic competitive Hopfield neural network and efficient genetic algorithm for frequency assignment problem. *Applied Soft Computing*, 39, 104-116.
- Zaruba, D., Zaporozhets, D., & Kureichik, V. (2016). Artificial bee colony algorithm-a novel tool for VLSI placement. In A. Abraham, S. Kovalev, V. Tarassov, & V. Snášel (Eds.), *Proceedings of the First International Scientific Conference "Intelligent Information Technologies for Industry" (IITI'16)* (pp. 433-442). Cham, Switzerland: Springer.
- Zhang, W., Gao, K., Zhang, W., Wang, X., Zhang, Q., & Wang, H. (2019). A hybrid clonal selection algorithm with modified combinatorial recombination and success-history based adaptive mutation for numerical optimization. *Applied Intelligence*, 49(2), 819-836.



Impacts of Asymmetric Biotic Interactions and Environmental Factors on the Presence-Absence of Multispecies

James Omaiye Ojonubah* and Mohd Hafiz Mohd

School of Mathematical Sciences, Universiti Sains Malaysia, 11800 USM, Georgetown, Penang, Malaysia

ABSTRACT

Interactions between multispecies are usual incidence in their habitats. Such interactions among the species are thought to be asymmetric in nature, which combine with environmental factors can determine the distributions and abundances of the species. Most often, each species responds differentially to biotic interactions and environmental factors. Therefore, predicting the presence-absence of species is a major challenge in ecology. In this paper, we used mathematical modelling to study the combined effects of biotic interactions (i.e. asymmetric competition) and environmental factors on the presence-absence of the species across a geographical region. To gain better insight on this problem, we performed invasion and numerical simulation analyses of the model of multispecies competitive dynamics. Different threshold values of competition coefficients were observed, which result in different phenomena; such as coexistence of species and priority effects. Consequently, we propose that asymmetric biotic interactions, combined with environmental factors can allow coexistence of relatively weak and strong species at the same location x .

Keywords: Coexistence, competition, invasion point, priority effects, threshold values

ARTICLE INFO

Article history:

Received: 21 June 2019

Accepted: 15 November 2019

Published: 13 January 2020

E-mail addresses:

ojonubahjames@gmail.com (James Omaiye Ojonubah)

mohdhafizmohd@usm.my (Mohd Hafiz Mohd)

*Corresponding author

INTRODUCTION

Generally, all species have natural geographic range margins (i.e. the geographic boundary of species presence-absence). Most often, the range margins of the species can be shifted due to biotic interactions (e.g.

competitions) and environmental factors (e.g. climate change) (Freeman et al., 2018). These factors, are recognized as part of ecological forces that have significant impacts on the distributions and range margins of species (Godsoe et al., 2015). Climate change may persist and biotic interactions in a multispecies habitat, usually, is unavoidable due to limited resources. Consequently, the prediction of the presence-absence of the species in a geographical region is still one of the challenges in ecology (Amundrud, & Srivastava, 2019). Therefore, a research study which focuses on the influence of these factors on the species distribution, will continue to fascinate the ecologists.

Environmental factors often act as a limiting factor on species distributions and its range margins (Hill & Preston, 2015) and can lead to the presence-absence of the species across a geographical region (Kearney & Porter, 2009; Wiens, 2011). Environmental factors have been demonstrated to determine the distributions of species in a habitat. For example, species in intertidal communities are shown to have altered their range margins due to shore temperature changes (Barry et al., 1995). Also, Perry et al. (2005) illustrated that fish species distributions had shifted in mean depth (or latitude) due to temperature increase. In a similar way, Rowe et al. (2015) demonstrated that extreme cold spells had strong impacts on the distributions and abundances of tropical species.

Similar to environmental factors, biotic interactions in the form of competition among the species, have significant effects on the distributions and range shifts of the species (Gause, 1932). Empirical studies have shown that biotic interactions is a key factor affecting species distributions (Wisz et al., 2013). Also, there are suggestions which also acknowledged that competitive interactions can regulate species range margins in geographic environments (Mohd et al., 2017). They observed that, weak biotic interactions lead to coexistence of species, while strong biotic interactions result in exclusion of species; i.e. multiple coexistence of these interacting species is impossible. Consequently, only single-species can be observed at a particular location. In this case, initial abundance of the species determines the competitive outcomes of the species (Hiscox et al., 2015) and the phenomenon is known as priority effects. However, the occurrence of priority effects can be influenced by environment factors. Empirical study on *Daphnia* species has shown how environmental factors (e.g. temperature, salinity and humidity) altered priority effects outcomes (Loureiro et al., 2013). Other experimental evidences exist which used initial abundance to illustrate the occurrence of priority effects (Park et al., 1965).

Also, species distributions can be influenced by the combined effects of biotic interactions and abiotic environments (Alexander et al., 2016). This is because the effects of climate change on species can strongly be influenced by species' interactions (Gilman et al., 2010). Similarly, environmental components can also influence the nature of biotic interactions (Meier et al., 2011). Experimental studies conducted on fruit fly species distributions, confirmed that competitive interactions could lead to different responses

of species to environmental perturbations (Davis et al., 1998a; Davis et al., 1998b). Connell (1961) also, demonstrated empirically the combined effects of biotic interactions and environmental factors in shaping community assembly. Similarly, Park (1954) in experimental study illustrated the importance of interactions between biotic and abiotic factors in species distributions. It was also confirmed that the roles of both biotic and abiotic factors were significant in shaping range margins of species (Darwell et al., 2017).

However, there are few theoretical researches which investigate the interplay of biotic interactions and environmental factors on species range margins, using mathematical modelling. One obvious limitation of the existing models is the assumptions that species competitive strength is symmetrical (Godsoe et al., 2014; Mohd et al., 2017), which may not be true. The strength of competition among species is often asymmetrical (Lawton & Hassell, 1981). These differences may modify the outcomes of species interactions and then, the presence-absence of species across a geographical region. On this basis, Mohd et al. (2017) suggested that the analysis of multispecies competition could be extended to asymmetric competition, which was the main thrust of this paper.

To gain insight on the presence-absence of interacting multispecies across a heterogeneous geographical region, we used mathematical model which incorporated biotic and environmental factors. Hence, we performed analytical and numerical simulations analyses of the model, to observe the range margins of multispecies communities. To further illustrate the presence-absence of the species across the geographical locations, we constructed summary plots and then bifurcation analyses of the model as a parameter value varies.

Thus, this paper is organized as follows. After this section, is another section with the presentation and description of the model. This is followed by derivations of our analytical results on the range margins of species using invasion analysis. Then, we illustrate our results on the range margins of species using numerical simulations. We then, present the results of our summary plots and bifurcation analyses to show the presence-absence of the species across a geographical location as a model's parameter varies. Based on our results, we highlight our observations and then discuss the ecological implications of the results.

MATERIALS AND METHODS

The Models

In the 1920s and 1930s, Lotka (1925) and Volterra (1926) developed competition model between two-species, which is popularly referred to as Lotka-Volterra competition (LVC) model. The well-known LVC, which becomes the framework for studying competition in ecology (Gavina et al., 2018), is spatially implicit, and does not explicitly incorporate environmental changes. However, the analysis of the LVC have revealed fundamental predictions. These include coexistence of two species when competition is weak and

bi-stability of single-species, which converges to one species and the other excluded when competition is strong. The existence of bi-stability gave rise to the question of what additional ecological forces lead to convergence to one single-species. To answer this question, resulting in several possibilities of studies, which include the effects of environmental heterogeneity (Godsoe et al., 2017; Birand & Barany, 2014). Therefore, we extended LVC model to study the distributions of n -species with densities $N_i(x, t)$ across heterogeneous environments. The competition model is a system of ordinary differential equations (ODEs) in one-dimensional domain with $0 \leq x \leq 1$, which is written as Equation 1:

$$\frac{dN_i}{dt} = \frac{r_i N_i}{k_i(x)} \left(k_i(x) - \sum_{j=1}^n \alpha_{ij} N_j \right), \quad (i = 1, 2, \dots, n) \quad [1]$$

where r_i is the intrinsic growth rate, $k_i(x)$ is the carrying capacity at location, α_{ij} is the coefficient of the competition of species j on species i , α_{ii} is the intraspecific coefficients and N_i is the densities of species i at time t . For simplifying the model, α_{ii} is rescaled to equal 1 and $\alpha_{ij} \neq \alpha_{ji}$ implies asymmetric competition strengths between the interacting species. Subsequently, we would simply denote α_{ij} as α_j ; such that for a system of four species interactions (i.e. $n = 4$), $\alpha_1, \alpha_2, \alpha_3$, and α_4 represent species 1, 2, 3 and 4 interspecific competition coefficients respectively.

The suitability of the environments is modelled into the carrying capacity of each species, such that the effects of environmental factors on the species, depend on $k_i(x)$. The term x represents a geographical location and it is used as a proxy for abiotic components like temperature, humidity and salinity. Thus, we modeled $k_i(x)$ to vary linearly with x ; such that in Equation 2:

$$k_i(x) = m_i x + b_i \quad [2]$$

Here, m_i is the slope of species i 's carrying capacity and it serves as a measure of the environmental suitability with respect to x , b_i is the intercept of species i carrying capacity when $x = 0$.

To understand the dynamics of the system, we solved numerically for the steady states of Equation [1] by setting $\frac{dN_i}{dt}$ to zeros. The stability analysis of the steady states was then performed using MAPLE $\frac{dN_i}{dt}$ package. Thus, at a location x , the steady state who's all the real parts of the eigenvalues are negative is considered stable. Based on the steady states, we used the techniques of invasion analysis to derive analytical results on the species' range margins. Numerical simulation results on the range margins of the species were obtained by employing MATLAB ode15s solver (Higham & Higham, 2016) for $t = 1000$ to solve Equation [1] until steady states were achieved. We also generated summary plots using MATLAB ode15s solver and then computed bifurcation analyses of the Equation [1] using XPPAUT package, as the model parameter (α_1) varies. The numerical simulations were carried out separately at categorized levels of species coefficients of competition. The

values of α_j were determined from Table 1 of Ayala et al. (1973), when they conducted empirical study using pairs of *Drosophila species* in eight experiment to determine the abundances of the species at equilibrium. α_j was estimated between 0.33 and 5.32; except one outrageous value which was 12.37 (Ayala et al., 1973). In this study, we assumed that competition strengths of the species were asymmetrical and because of the uncertainty of competition coefficients, our model's behavior was analyzed for a range of α_j . However, modifying the values of α_j used this study, could alter the range margins of the species. Also, the parameter values b_i and m_i of the carrying capacities of the species in Table 1, were determined from the linear regression analysis of Figure 3 of Davis et al. (1998b) by Godsoe et al. (2014). Similarly, the intrinsic growth rate, r_i of the species was obtained. The parameters values used in the analyses are shown in Table 1 and parameter values not presented in Table 1 are written below the Figures.

Table 1

Symbols with the descriptions and parameter values used for the computation of the figures

Symbol	Items description	Parameter value
r_i	The intrinsic growth rates of species i	1
m_1	Gradient of k_1	1
m_2	Gradient of k_2	0.8
m_3	Gradient of k_3	0
m_4	Gradient of k_4	0
b_1	Carrying capacity of species 1 at $x = 0$	0
b_2	Carrying capacity of species 2 at $x = 0$	0
b_3	Carrying capacity of species 3 at $x = 0$	0.5
b_4	Carrying capacity of species 4 at $x = 0$	0.4

RESULTS

This section consists both analytical and numerical simulation results of the Equation [1]. The analytical results are based on numerical simulation results on the species' range margins illustrated in Figure 1A and both results broadly agreed with each other.

Analytical Results on the Range Margins of Species

Here, we used the method of invasion analysis to derive analytical results of the Equation [1]. The invasion analysis method was based on the derivation of species' range margins using the criterion that a species that could invade at a location must be rare at that point and its growth rate had to be greater than zero (i.e. $\frac{dN_i}{dt} > 0$) (Hastings & Gross, 2012).

Godsoe et al. (2014) analyzed the invasion points (denoted by x_i) of Equation [1] with $n = 2$. The technique is by setting the right-hand side of Equation [1] greater than

zero; then, substitute the steady states and the values of the carrying capacities in it. We extended their method to derive the invasion points for four-species. The method of our analysis was based on tracking the species that are present in the numerical result, and the species that can invade when rare at a location x . Based on Figure 1A, only species 3 and 4 were present at the locations where species 1 and 2 were rare. In this case, either species 1 or 2 could invade in the presence of species 3 and 4; depending on the magnitude of the carrying capacities of species 1 and 2. From Table 1, $k_1 > k_2$; so that species 1 had higher potentials to invade in the presence of species 3 and 4 than species 2. Thus, for species 1 to invade it required that the right-hand side of $\frac{dN_1}{dt}$ in Equation [1] be greater than zero. Species 1 was considered rare at its invasion point and so, its density (i.e. N_1) was set to zero. Similarly, the density of species 2 (i.e. N_2) was also considered to be zero, since at the invasion point of species 1 only species 3 and 4 were present. Thus, species 1 could invade if $k_1(x) = \alpha_3 N_3^* + \alpha_4 N_4^* k_1(x)$. Therefore, the point x satisfying $k_1(x) = \alpha_3 N_3^* + \alpha_4 N_4^*$ corresponds to species 1 invasion point which is denoted as x_1 . But $k_1(x) = m_1 x$ and for stable steady state $(0, 0, N_3^*, N_4^*)$, with $k_3 = b_3$ and $k_4 = b_4$, we have the invasion point of species 1 given as in Equation 3:

$$x_1 = \frac{\alpha_3 \alpha_4 (b_3 + b_4) - (\alpha_3 b_3 + \alpha_4 b_4)}{m_1 (\alpha_3 \alpha_4 - 1)} \quad [3]$$

Moving along the environmental gradient x to the right of x_1 (see Figure 1A), we observed the presence of species 1, 3 and 4 with species 2 absent. Thus, we can derive species 2 invasion point in a similar manner to species 1. In this case, $\frac{dN_2}{dt}$ in Equation [1] must be greater than zero for species 2 to invade. Also, at the invasion point of species 2, its density (i.e. N_2) was zero, so that $k_2(x) > \alpha_1 N_1^* + \alpha_3 N_3^* + \alpha_4 N_4^*$. Thus, invasion point of species 2 satisfies $k_2(x) = \alpha_1 N_1^* + \alpha_3 N_3^* + \alpha_4 N_4^*$ and for stable steady state $(N_1^*, 0, N_3^*, N_4^*)$ where $k_2(x) = m_2 x$, $k_3 = b_3$ and $k_4 = b_4$, the invasion point of species 2 becomes Equation 4:

$$x_2 = \frac{\alpha_1 \alpha_3 \alpha_4 (b_3 + b_4) + \alpha_3 b_3 (1 - \alpha_1 - \alpha_4) + \alpha_4 b_4 (1 - \alpha_1 - \alpha_3)}{m_2 (2\alpha_1 \alpha_3 \alpha_4 - \alpha_1 \alpha_3 - \alpha_1 \alpha_4 - \alpha_3 \alpha_4 + 1) - \alpha_1 m_1 (\alpha_3 \alpha_4 - \alpha_3 - \alpha_4 + 1)} \quad [4]$$

In this case, the scenarios by which species 2 range margin can increase depends on strong interspecific competition from species 1, 3 and 4 at the boundary of species 2 fundamental niche. For instance, increase in $\alpha_3 b_3$ or $\alpha_4 b_4$ or both can shift species 2 from its fundamental niche and increase the range of x for which species 2 can be present or absent. However, since species 2 is ecologically different from species 3 and 4 due to their carrying capacities vary differently as the environmental gradient changes; so, we expect a modest change in species 1, 3 and 4 to bring about a modest change in the range margin of species 2 (Godsoe et al., 2014). Also, species 2 range margin can also increase when the denominator in Equation [4] becomes rather small. As the denominator tends to zero,

the range margin of species 2 also tends to infinity. This second mechanism is associated with two species (e.g. species 1 and 2) that are ecologically similar (i.e. their carrying capacities vary directly as the environmental gradient changes).

In a similar way, species 4 invasion point can be computed in the presence of species 1, 2 and 3. Thus, invasion point of species 4 is given as in Equation 5.

$$x_4 = \frac{b_4(2\alpha_1\alpha_2\alpha_3 - \alpha_1\alpha_2 - \alpha_1\alpha_3 - \alpha_2\alpha_3 + 1) - \alpha_3b_3(\alpha_1\alpha_2 - \alpha_1 - \alpha_2 + 1)}{\alpha_1m_1(\alpha_2\alpha_3 - \alpha_2 - \alpha_3 + 1) + \alpha_2m_2(\alpha_1\alpha_3 - \alpha_1 - \alpha_3 + 1)} \quad [5]$$

Similarly, we have the invasion point of species 3 computed to give in Equation 6:

$$x_3 = \frac{b_3(\alpha_1\alpha_2 - 1)}{\alpha_1m_1(\alpha_2 - 1) + \alpha_2m_2(\alpha_1 - 1)} \quad [6]$$

Numerical Results on the Range Margins of Species

Numerical results are presented to illustrate the influence of biotic interactions and environmental gradients on the range margins of species across locations x . To show the impacts of asymmetrical competition strengths on multispecies community structures, the numerical results were obtained separately for different competitive strengths of the species. A detection threshold value of 0.5% was employed for these results, such that a species was considered absent if its density was below the expected value (Gaston, 2003).

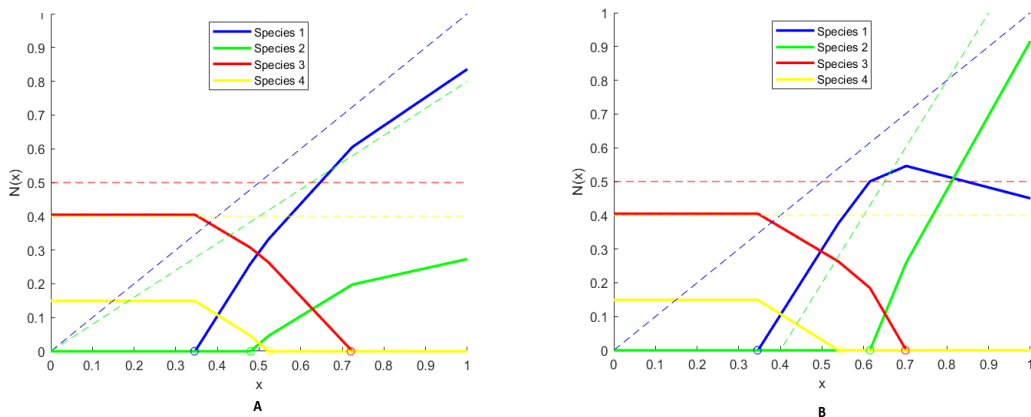


Figure 1. The steady states of species i due to weak interactions ($\alpha_j < 1$). Solid lines indicate steady states and the dotted lines represent the carrying capacities of species i . Circles on the horizontal axis of the Figures, represent the invasion points (x_i) of the species. Figures 1A and B are computed with $\alpha_1 = 0.63$, $\alpha_2 = 0.60$, $\alpha_3 = 0.62$, $\alpha_4 = 0.64$; $k_1(x) = x$, $k_2(x) = 0.8x$, $k_3(x) = 0.5$, $k_4(x) = 0.4$ and initial abundance: $N_1(x) = 0.1k_1(x)$, $N_2(x) = 0.9k_2(x)$, $N_3(x) = 0.1k_3(x)$, $N_4(x) = 0.9k_4(x)$. In Figure 1B, $k_2(x) = 2x - 0.8$

Multispecies Range Margins due to Weak Interactions ($\alpha_j < 1$)

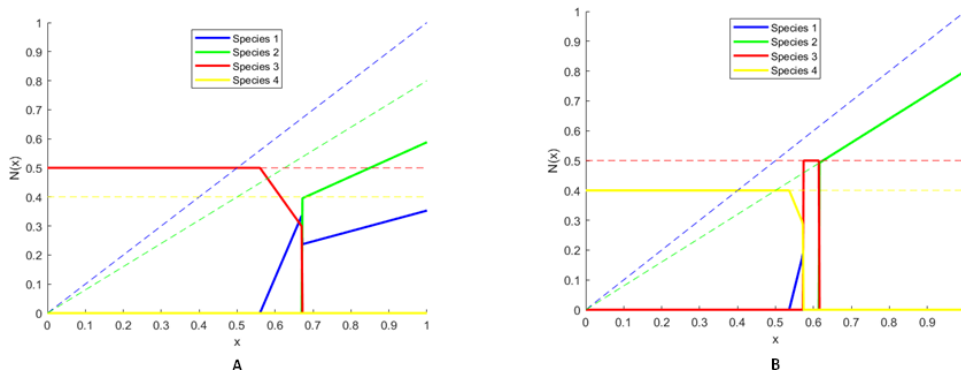
Figures 1A and B illustrate interactions outcomes of multispecies with relatively weak interaction strengths (i.e. $\alpha_j < 1$) of all the species. The same carrying capacities (dotted

lines) and initial abundances are used for the two Figures except in Figure 1B where $k_2(x) = 2x - 0.8$. We observed multispecies coexistence and the range margins of the species depended on the interaction strengths and carrying capacities of the species. For instance, in Figure 1A, two or more species coexisted at the same locations x , with multiple species coexistence was possible near the central location. However, due to impacts of competition interactions, the region of coexistence between the four-species was rather very small. This observation is also illustrated in Figure 4A, where the region of four-species (i.e. red colored region) also decreased as α_1 varies from 0.3 – 1.4. The range margins of the species are indicated as circles, according to the colors of the species on the horizontal axis and they correspond to the invasion points of our analytical results.

To illustrate the influence of environmental components on the community assembly, we compute Figure 1B. In this case, the community structures differ from that observed in Figure 1A. Due to changes in the environmental gradient, only two and three species coexistence are possible. However, in both cases illustrated, species 1 and 2 occupied the right-hand side of the locations x ; while species 3 and 4 occupied the left-hand side. This community structures are possible because, species 1 and 2 are both warm tolerant species and so, they are regarded as similar species. Also, species 3 and 4 are also another set of similar species with homogenous distributions throughout the locations x . Thus, they can easily be displaced from the upper locations by species 1 and 2. This also, accounts for species 1 and 2 being rare at the lower part of the locations and multispecies coexistence at the centre, where the environment is most suitable for all the species. Generally, competing species coexist for relatively weak (i.e $\alpha_j < 1$) biotic interactions.

Multispecies Range Margins due to Weak ($\alpha_1 < 1$) and Strong ($\alpha_j > 1$) Biotic Interactions

Figure 2 is computed to illustrate competition outcomes between relatively weaker ($\alpha_1 < 1$) species 1 and other relatively stronger ($\alpha_j > 1$) species. Thus, Figures 2A and C and Figures 2B and D, are computed with $\alpha_1 = 0.60, \alpha_2 = 1.10, \alpha_3 = 1.12, \alpha_4 = 1.14$ and $\alpha_1 = 0.60, \alpha_2 = 1.30, \alpha_3 = 1.32, \alpha_4 = 1.34$ respectively. The same carrying capacities are used for the figures



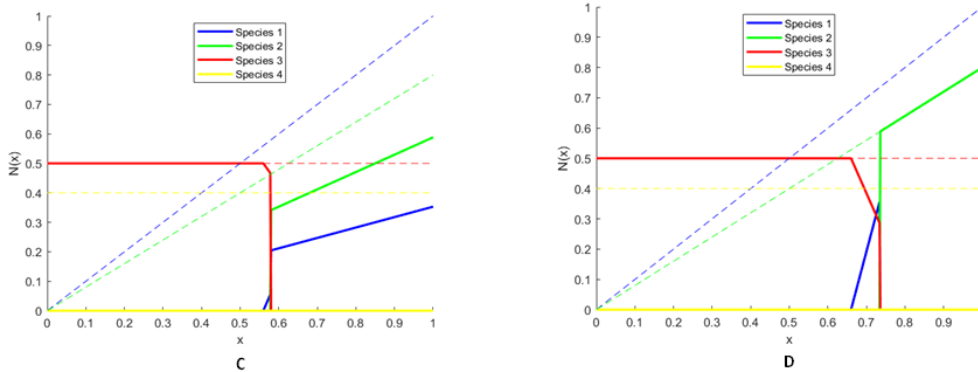
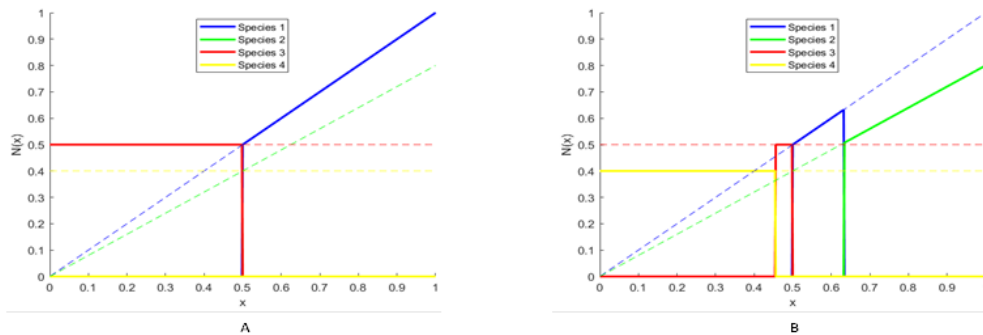


Figure 2. The steady states of species i due to weak ($\alpha_i < 1$) and strong ($\alpha_j > 1$) interactions. Solid lines indicate steady states and the dotted lines represent the carrying capacities of species i . Figures 2A and C are computed with $\alpha_1 = 0.60$, $\alpha_2 = 1.10$, $\alpha_3 = 1.12$, $\alpha_4 = 1.14$ and Figures 2B and D are computed with $\alpha_1 = 0.60$, $\alpha_2 = 1.30$, $\alpha_3 = 1.32$, $\alpha_4 = 1.34$. The Figures are computed with the same carrying capacities: $k_1(x) = x$, $k_2(x) = 0.8x$, $k_3(x) = 0.5$, $k_4(x) = 0.4$ and varied initial abundance.

with varying initial abundance to show the range margins where a species may be present or absent. In both cases, we observed exclusion of species and coexistence of competitively weaker species 1 with other stronger species at the same location x . For instance, Figures 2A and C show *bistable* coexistence of species 1 with species 2 and 3 (i.e. $(N_1, 0, N_3, 0)$ and $(N_1, N_2, 0, 0)$) at the same location x (e.g. see location $x = 0.6$). To further illustrate these results, we computed Figures 2B and D which also show coexistence of relatively weaker species 1 with other stronger species at the same location x . However, due to high priority effects (see Figures 2B and D), the weaker species 1 lost its coexistence with the similar stronger species 2 and maintained its coexistence with the dissimilar stronger species 3 and 4. These observations illustrate that, ecologically similar species (e.g. 1 versus 2 and 3 versus 4) competitively affect each other more than the dissimilar species.



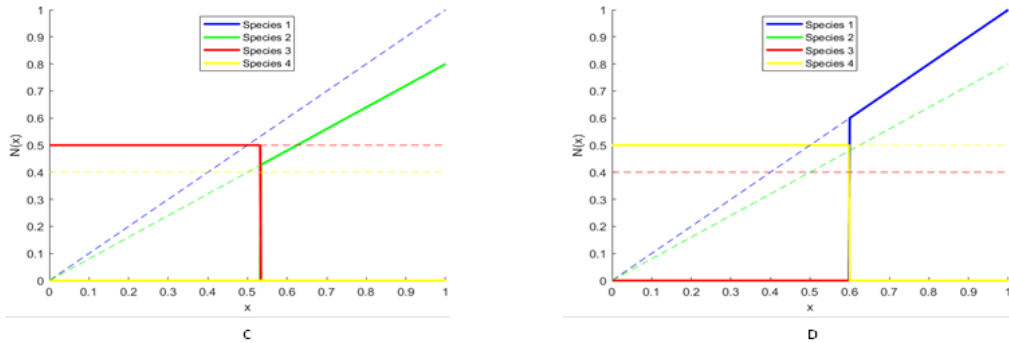


Figure 3. The steady states of species i due to intense biotic interactions ($\alpha_j > 1$). Solid lines indicate steady states and the dotted lines represent the carrying capacities of the species i . Figure 3A is computed with $\alpha_1 = 1.33, \alpha_2 = 1.30, \alpha_3 = 1.32, \alpha_4 = 1.34; k_1(x) = x, k_2(x) = 0.8x, k_3(x) = 0.5, k_4(x) = 0.4$ and initial abundance: $N_1(x) = 0.1k_1(x), N_2(x) = 0.9k_2(x), N_3(x) = 0.1k_3(x), N_4(x) = 0.9k_4(x)$. Figure 3B is computed with $\alpha_1 = 1.43, \alpha_2 = 1.40, \alpha_3 = 1.42, \alpha_4 = 1.44; k_1(x) = x, k_2(x) = 0.8x, k_3(x) = 0.5, k_4(x) = 0.4$ and initial abundance: $N_1(x) = 0.1k_1(x), N_2(x) = 0.9k_2(x), N_3(x) = 0.1k_3(x), N_4(x) = 0.9k_4(x)$. Figure 3C is computed with $\alpha_1 = 1.33, \alpha_2 = 1.30, \alpha_3 = 1.32, \alpha_4 = 1.34; k_1(x) = x, k_2(x) = 0.8x, k_3(x) = 0.5, k_4(x) = 0.4$ and initial abundance: $N_1(x) = 0.001k_1(x), N_2(x) = 0.9k_2(x), N_3(x) = 0.1k_3(x), N_4(x) = 0.9k_4(x)$. Figure 1D is computed with $\alpha_1 = 1.33, \alpha_2 = 1.30, \alpha_3 = 1.32, \alpha_4 = 1.34; k_1(x) = x, k_2(x) = 0.8x, k_3(x) = 0.4, k_4(x) = 0.5$ and initial abundance: $N_1(x) = 0.1k_1(x), N_2(x) = 0.9k_2(x), N_3(x) = 0.1k_3(x), N_4(x) = 0.9k_4(x)$.

Multispecies Range Margins due to Intense Biotic Interactions ($\alpha_j > 1$)

We observed that when competitive strengths of species are relatively intense, $\alpha_j > 1$, coexistence of species is impossible, and the dynamical outcomes of the model depend on initial abundances, interaction strengths and carrying capacities of the species. For instance, Figure 3A illustrate interactions outcomes of the multispecies, where species 1 and 3 occupied the geographical region as single-species; each to its carrying capacity and exclude species 2 and 4. To illustrate the effects of interaction strengths on competition outcomes, we compute Figure 3B with different competition coefficients, $\alpha_1 = 1.43, \alpha_2 = 1.40, \alpha_3 = 1.42, \alpha_4 = 1.44$ but with the same carrying capacities and initial abundances as in Figure 3A. Due to increase in the competition coefficients, we observe the presence of the four single-species. However, species 2 with higher initial abundance dominated the larger part of the right region and then shifted species 1 with smaller initial abundance towards a smaller right center. Similarly, species 4 with higher initial abundance than species 3 occupied a larger region on the left.

To further illustrate the importance of initial abundance, we compute Figure 3C with the same competition coefficients and carrying capacities as in Figure 3A but with different initial abundances: $N_1(x) = 0.001k_1(x), N_2(x) = 0.9k_2(x), N_3(x) = 0.1k_3(x), N_4(x) = 0.9k_4(x)$. We observed the presence of species 2 in the place of species 1 (compare Figure 3A with Figure 3C). The result demonstrates the influence of initial abundance in the presence-absence of species. This situation where the dynamical behavior of the model depends

on initial abundance is known as alternative stable states; ecologically refer to as priority effects (Gilman et al., 2010). Lastly, Figure 3D was computed to illustrate the influence of the environmental gradients on the presence-absence of the species. Thus, we computed the Figure with the same parameters as in Figure 3A except that, the carrying capacities of species 3 and 4 were interchanged with each other. Species 4 now with the advantage of the carrying capacity and initial abundance, excluded species 3 and occupied the region as a single-species (compare Figure 3A and Figure 3D). Generally, ecologically similar species have more impacts on one another than the reverse.

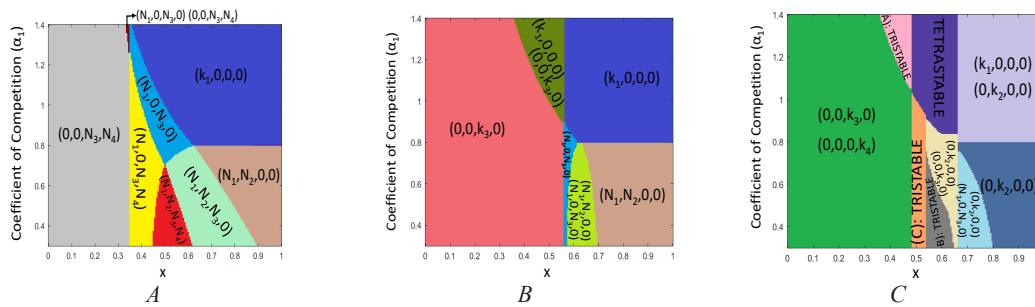


Figure 4. The summary plots of the presence-absence of the species as competitive strength of species 1 (i.e. α_1) varies with respect to environmental gradients x . Different colors are used to represent different combinations of species present and the change in color represent a change in stability of one combination of species for another one. Figure 4A is computed with $\alpha_1 = 0.3 - 1.4$, $\alpha_2 = 0.60$, $\alpha_3 = 0.62$, $\alpha_4 = 0.64$; Figure 4B is computed with $\alpha_1 = 0.3 - 1.4$, $\alpha_2 = 1.10$, $\alpha_3 = 1.12$, $\alpha_4 = 1.14$ and Figure 4C is computed with $\alpha_1 = 0.3 - 1.4$, $\alpha_2 = 1.30$, $\alpha_3 = 1.32$, $\alpha_4 = 1.34$

Presence-Absence of Species Across Geographical Locations as Competition Strength (α_1) Varies

Figures 4A-C are summary plots of the Equation [1] generated to show the presence-absence of species as competition strength of species 1 (i.e. α_1) changes with respect to environmental locations x . The plots are generated using four sets of initial abundances, each favoring one of the four species. Changes in colors illustrate different combinations of species present across the geographical region. Each color represents the range margins of species present at a given location x . Also, the boundary where one-color changes to another correspond to the critical value of the competitive strength of species 1 (i.e. α_1); where one stable combination of species lost its stability for another stable combination of species. In Figures 4A-C, α_1 varies from 0.3 - 1.4 with competitive strengths of other species kept constant at $\alpha_2 = 0.60$, $\alpha_3 = 0.62$, $\alpha_4 = 0.64$ in Figure 4A, $\alpha_2 = 1.10$, $\alpha_3 = 1.12$, $\alpha_4 = 1.14$ in Figure 4B and $\alpha_2 = 1.30$, $\alpha_3 = 1.32$, $\alpha_4 = 1.34$ in Figure 4C. The regions label (A):, (B): and (C): *tristable* in Figure 4C respectively correspond to the presence of three stable combinations of species at the same location x .

When $\alpha_1 < 1$ in Figure 4A, we observed multispecies coexistence especially near the central location x . However, as competition strength α_1 increases, species 2 and 4 are simultaneously exclude, such that only species 1 and 3 coexistence can be observed. As earlier observed in our numerical simulations in Figure 2, coexistence of relatively weaker species with stronger species is also evident in Figure 4. For instance, Figure 4A illustrates *bistable* coexistence of species (i.e. $(N_1, 0, N_3, 0)$ and $(0, 0, N_3, N_4)$) where species 1 is a stronger competitor at that location relative to other species. The same *bistable* coexistence of species (i.e. $(N_1, 0, N_3, 0)$ and $(N_1, N_2, 0, 0)$) is also observed in Figure 4B, where species 1 is a weaker competitor at that location compared to other competitors. These results show the leading roles of asymmetric interactions among multispecies; through which the coexistence of weaker species with stronger species is illustrated. Further, as other species competition strengths become stronger relative to species 1 as in Figure 4C, we observed higher priority effects which result to more species diversity. Thus, we observe single- and multiple- species and two or three single species co-occurrences at the same location x when $\alpha_1 < 0.8$. However, as $\alpha_1 > 0.8$ (see Figure 4C), co-occurrence of multiple species and single- and multiple- species (e.g. $(0, k_2, 0, 0)$, $(N_1, 0, N_3, 0)$) is impossible due to higher priority effects. This situation leads to existence of *bistable*, *tristable* and *tetratable* single-species steady states. These results show the persistence of priority effects throughout the range of $\alpha_1 = 0.3 - 1.4$ except in Figure 4A where evidence of priority effects is observed only at $\alpha_1 > 1.24$. This means that priority effects can occur if at least, the coefficient of competition of one of the competing multispecies is greater than 1.

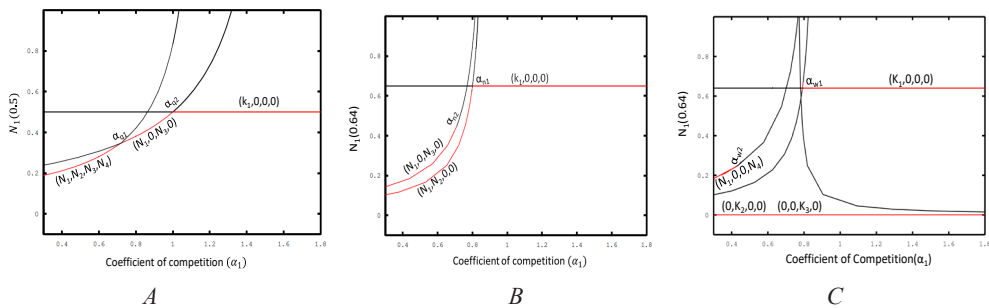


Figure 5. The density plot at a location x of focal species (i.e. species 1) as competitive strength of species 1 (i.e. α_1) varies. Figure 5A represents the density of the species 1 at the location $x = 0.5$. Figures 5B and C represent the density of the species 1 at the location $x = 0.64$. Red and black solid curves indicate stable and unstable steady states respectively. The threshold values correspond to transcritical bifurcation points (i.e. α_{q1} , α_{q2} , ..., α_{w2}). Figure 5A is computed with $\alpha_1 = 0.3 - 1.8$, $\alpha_2 = 0.60$, $\alpha_3 = 0.62$, $\alpha_4 = 0.64$; Figure 5B is computed with $\alpha_1 = 0.3 - 1.8$, $\alpha_2 = 1.10$, $\alpha_3 = 1.12$, $\alpha_4 = 1.14$ and Figure 5C is computed with $\alpha_1 = 0.3 - 1.8$, $\alpha_2 = 1.30$, $\alpha_3 = 1.32$, $\alpha_4 = 1.34$

Presence-Absence of Species at a Location as Competition Strength (α_1) Varies

To improve the understanding of different species presence-absence as α_1 varies, we performed bifurcation analysis (Figure 5) to track the stable and unstable steady states of the species at a location x . Figure 5A and Figures 5B-C illustrate the stable steady states densities of species 1 at locations $x = 0.5$ and $x = 0.64$ respectively. The same results are expected if any of the species, other than species 1 is used for the plots. The red and black curves represent stable and unstable steady states respectively.

The results show threshold values which correspond to the critical values in the summary plots in Figure 4 and transcritical bifurcation points (i.e. α_{q1} , α_{q2} , ... α_{w2}) that illustrate different species presence-absence. Thus, we have the region of four species coexistence as illustrated in Figure 5A for $\alpha_1 < \alpha_{q1}$. This region is followed by another region (i.e. $\alpha_{q1} < \alpha_1 < \alpha_{q2}$) where we have simultaneous exclusion of species 2 and 4 with only species 1 and 3 coexisting as competition gets stronger. Beyond the region, $\alpha_1 > \alpha_{q2}$ is the region of stable steady states of single species ($k_1, 0, 0, 0$). We also observe (Figure 5B) that at the location $x = 0.64$, the model exhibits *bistable* coexistence of species (i.e. $(N_1, 0, N_3, 0)$ and $(N_1, N_2, 0, 0)$) which undergoes transcritical bifurcation at $\alpha_1 > \alpha_{n1}$ to show one stable single-species ($k_1, 0, 0, 0$). Also, Figure 5C illustrate co-occurrence of *bistable* single-species and coexisting species (i.e. $(0, k_2, 0, 0)$, $(0, 0, k_3, 0)$ and $(N_1, 0, 0, N_4)$) at the same location $x = 0.64$. The presence of *bistable* and *tristable* species respectively in Figures 5B and C further illustrate evidence of priority effects for $\alpha_1 < 1$.

DISCUSSIONS

We studied multispecies competition in an environmentally changing habitat with asymmetrical competitive strengths of the species. The numerical simulation results generated provide an easier and accurate predictions of species distributions; and the results are found to be consistent with previous studies (Connell, 1961). Our findings are significant as they improve the understanding on the combined effects of biotic interactions and environmental factors, in determining multispecies community structures. For instance, environmental components alone can determine the range margins and then, defines the fundamental niche of the species (Geijzendorffer et al., 2011). The inclusion of competition interactions can shift the range margins of the species to a realized niche. Therefore, the presence-absence of species depends on the competitive intensity on one another and the response of species to environmental changes.

Our results show that different values of the competition coefficients can lead to different dynamical behavior of the model. For instance, when $\alpha_j < 1$, we observe coexistence of multispecies near the central region with the exclusion of some species at the peripheral regions. This form of community structure has earlier been observed in empirical study of small mammal species along elevational gradients (McCain, 2004;

McCain, 2005). The implication is that, diversity of species will be at its peak where the environment is moderately suitability with low competition intensity on the species. Thus, exclusion of the species at the lower and upper environments of the locations is expected due to unfavorable environments on some species, couple with competition interactions from the environmentally favored species. Connell (1961) reported in his empirical research that, competitive interactions and environmental factors could combine to determine the presence-absence of species. Consequently, the conservation of biodiversity can be maintained at relatively weak biotic interactions and moderate environmental components. In this way, both species can favorably compete for space and resources without anyone being eliminated from the community.

However, with strong competition interactions among the species, exclusion of the species from the locations are observed and coexistence is impossible. Consequently, initial abundances determine the presence-absence of the species. However, environmental suitability of the species has also been illustrated in our results to influence priority effects outcomes. This observation agreed with empirical research using *Daphnia* species (Loureiro et al., 2013) who observed that the outcomes of priority effects and community dynamics can be altered by environmental factors. Also, the coexistence of weaker competitor with other stronger (i.e. $\alpha_j > 1$) competitors as indicated in our result, implies that species whose ecological needs are not very similar can afford to coexist, in-respective of their competition strengths.

Also, our numerical continuation results which illustrate both stable and unstable steady states and bifurcation points of the models, proffer detail explanation on the differences in the presence-absence of species observed in our numerical simulation results. The threshold values of the competitive strengths α_1 , correspond to the critical points of gradual exchange of one stable combination of species for another stable one. The bifurcation points therefore, give rise to different dynamical behaviors of the models such as coexistence, simultaneous exclusion of species and priority effects.

CONCLUSIONS

We studied competition interactions dynamics in multispecies using a system of ordinary differential equations to illustrate the competition outcomes in a varying environment. The model analyses revealed different dynamical outcomes such as coexistence of species and priority effects. Our result is significant as it further improved understanding on multispecies community dynamics. Most intuitively, is the coexistence of both weak and strong species at the same location, especially if the species are less ecologically similar. Generally, the findings of our research illustrate how biotic interactions and environmental factors can combined to strongly shape the range margins of multispecies in a habitat (Little & Altermatt, 2018). A previous study (Mittelbach, 2012) had shown that, without

biotic interactions, environmental factor alone determined the fundamental niche of the species. Thus, in this research, we have shown that competition interactions can exclude interacting multispecies from some locations in their habitat and then, determine their realized range margins.

However, other ecological factors such as dispersal may change the dynamics of the competitions. Therefore, inclusion of dispersal in our model will be an interesting extension of this paper. Since species response to environmental changes is not always linear, as claimed in this paper, model that expresses the carrying capacities of the species as Gaussian equations, is also a possible extension of our model for future studies.

ACKNOWLEDGEMENT

Thanks to the School of Mathematical Sciences and the Universiti Sains Malaysia for the facilities and support. Mohd Hafiz Mohd is supported by the USM Fundamental Research Grant Scheme (FRGS) No. 203/PMATHS/6711645 and USM Short-Term Research Grant No. 304/PMATHS/6315083.

REFERENCES

- Alexander, J. M., Diez, J. M., Hart, S. P., & Levine, J. M. (2016). When climate reshuffles competitors: A call for experimental macroecology. *Trends in Ecology and Evolution*, *31*, 831-841.
- Amundrud, S. L., & Srivastava, D. S. (2019). Disentangling how climate change can affect an aquatic food web by combining multiple experimental approaches. *Global Change Biology*, *25*(10), 3528-3538.
- Ayala, F. J., Gilpin, M. E., & Ehrenfeld, J. G. (1973). Competition between species: Theoretical models and experimental tests. *Theoretical Population Biology*, *4*, 331-356.
- Barry, J. P., Baxter, C. H., Sagarin, R. D., & Gilman, S. E. (1995). Climate-related, long-term faunal changes in a California rocky intertidal community. *Science(Washington)*, *267*(5198), 672-675.
- Birand, A., & Barany, E. (2014). Evolutionary dynamics through multispecies competition. *Theoretical Ecology*, *7*, 367-379.
- Connell, J. H. (1961). The influence of interspecific competition and other factors on the distribution of the barnacle *Chthamalus stellatus*. *Ecology*, *42*(4), 710-723.
- Darwell, C. T., Segraves, K. A., & Althoff, D. M. (2017). The role of abiotic and biotic factors in determining coexistence of multiple pollinators in the yucca–yucca moth mutualism. *Ecography*, *40*(4), 511-520.
- Davis, A. J., Jenkinson, L. S., Lawton, J. H., Shorrocks, B., & Wood, S. (1998). Making mistakes when predicting shifts in species range in response to global warming. *Nature*, *391*(6669), 783-786.
- Davis, A. J., Lawton, J. H., Shorrocks, B., & Jenkinson, L. S. (1998). Individualistic species responses invalidate simple physiological models of community dynamics under global environmental change. *Journal of Animal Ecology*, *67*(4), 600-612.

- Freeman, B. G., Lee-Yaw, J. A., Sunday, J. M., & Hargreaves, A. L. (2018). Expanding, shifting and shrinking: The impact of global warming on species' elevational distributions. *Global Ecology and Biogeography*, 27, 1268-1276.
- Gaston, K. J. (2003). *The structure and dynamics of geographic ranges*. Oxford, UK: Oxford University Press.
- Gause, G. F. (1932). Experimental studies on the struggle for existence. *Journal of Experimental Biology*, 9(4), 389-402.
- Gavina, M. K. A., Tahara, T., Tainaka, K. I., Ito, H., Morita, S., Ichinose, G., ... & Yoshimura, J. (2018). Multi-species coexistence in Lotka-Volterra competitive systems with crowding effects. *Scientific Reports*, 8(1), 1198-1205.
- Gejzendorffer, I., Van der Werf, W., Bianchi, F., & Schulte, R. (2011). Sustained dynamic transience in a Lotka-Volterra competition model system for grassland species. *Ecological Modelling*, 222(15), 2817-2824.
- Gilman, S. E., Urban, M. C., Tewksbury, J., Gilchrist, G. W., & Holt, R. D. (2010). A framework for community interactions under climate change. *Trends in Ecology and Evolution*, 25(6), 325-331.
- Godsoe, W., Murray, R., & Plank, M. J. (2014). Information on biotic interactions improves transferability of distribution models. *The American Naturalist*, 185(2), 281-290.
- Godsoe, W., Murray, R., & Plank, M. J. (2015). The effect of competition on species' distributions depends on coexistence, rather than scale alone. *Ecography*, 38(11), 1071-1079.
- Godsoe, W., Franklin, J., & Blanchet, F. G. (2017). Effects of biotic interactions on modeled species' distribution can be masked by environmental gradients. *Ecology and Evolution*, 7, 654-664.
- Hastings, A., & Gross, L. (2012). *Encyclopedia of theoretical ecology*. Berkeley, California, USA: University of California Press.
- Higham, D. J. & Higham, N. J. (2016). *MATLAB guide*. Massachusetts, USA: Society for Industrial and Applied Mathematics Philadelphia.
- Hill, M. O., & Preston, C. D. (2015). Disappearance of boreal plants in southern Britain: habitat loss or climate change? *Biological Journal of the Linnean Society*, 115(3), 598-610.
- Hiscox, J., Savoury, M., Müller, C. T., Lindahl, B. D., Rogers, H. J., & Boddy, L. (2015). Priority effects during fungal community establishment in beech wood. *The ISME Journal*, 9(10), 2246-2260.
- Kearney, M., & Porter, W. (2009). Mechanistic niche modelling: Combining physiological and spatial data to predict species' ranges. *Ecology Letters*, 12(4), 334-350.
- Lawton, J., & Hassell, M. (1981). Asymmetrical competition in insects. *Nature*, 289(5800), 793-795.
- Little, C. J., & Altermatt, F. (2018). Do priority effects outweigh environmental filtering in a guild of dominant freshwater macroinvertebrates? *Proceedings of the Royal Society B: Biological Sciences*, 285(1876), 1-9.
- Lotka, A. J. (1925). *Elements of physical biology*. Baltimore, Maryland: Williams and Wilkins.
- Loureiro, C., Pereira, J. L., Pedrosa, M. A., Gonçalves, F., & Castro, B. B. (2013). Competitive outcome of *Daphnia-Simocephalus* experimental microcosms: salinity versus priority effects. *PloS one*, 8(8), 1-7.
- McCain, C. M. (2004). The mid-domain effect applied to elevational gradients: species richness of small mammals in Costa Rica. *Journal of Biogeography*, 31(1), 19-31.
- McCain, C. M. (2005). Elevational gradients in diversity of small mammals. *Ecology*, 86(2), 366-372.

- Meier, E. S., Edwards Jr, T. C., Kienast, F., Dobbertin, M., & Zimmermann, N. E. (2011). Co-occurrence patterns of trees along macro-climatic gradients and their potential influence on the present and future distribution of *Fagus sylvatica* L. *Journal of Biogeography*, 38(2), 371-382.
- Mittelbach, G. G. (2012). *Community ecology*. Massachusetts, USA: Sinauer Associates Inc.
- Mohd, M. H., Murray, R., Plank, M. J., & Godsoe, W. (2017). Effects of biotic interactions and dispersal on the presence-absence of multiple species. *Chaos, Solitons and Fractals*, 99, 185-194.
- Park, T. (1954). Experimental studies of interspecies competition II. Temperature, humidity, and competition in two species of *Tribolium*. *Physiological Zoology*, 27(3), 177-238.
- Park, T., Mertz, D. B., Grodzinski, W., & Prus, T. (1965). Cannibalistic predation in populations of flour beetles. *Physiological Zoology*, 38(3), 289-321.
- Perry, A. L., Low, P. J., Ellis, J. R., & Reynolds, J. D. (2005). Climate change and distribution shifts in marine fishes. *Science*, 308(5730), 1912-1915.
- Rowe, K. C., Rowe, K. M., Tingley, M. W., Koo, M. S., Patton, J. L., Conroy, C. J., ... & Moritz, C. (2015). Spatially heterogeneous impact of climate change on small mammals of montane California. *Proceedings of the Royal Society of London B: Biological Sciences*, 282(1799), 1-10.
- Volterra, V. (1926). Flunctuations in the abundance of a species considered mathematically. *Nature*, 118, 558-560.
- Wiens, J. J. (2011). The niche, biogeography and species interactions. *Philosophical Transactions of the Royal Society of London B: Biological Sciences*, 366(1576), 2336-2350.
- Wisn, M. S., Pottier, J., Kissling, W. D., Pellissier, L., Lenoir, J., Damgaard, C. F., ... & Guisan, A. (2013). The role of biotic interactions in shaping distributions and realised assemblages of species: implications for species distribution modelling. *Biological Reviews*, 88(1), 15-30.



Aedestech Mosquito Home System Prevents the Hatch of *Aedes* Mosquito Eggs and Reduces its Population

Latifah Saiful Yazan¹, Kaveinesh Paskaran¹, Banulata Gopalsamy¹ and Roslaini Abd Majid^{2*}

¹Department of Biomedical Sciences, Faculty of Medicine and Health Sciences, Universiti Putra Malaysia, 43400 UPM, Serdang, Selangor, Malaysia

²Department of Medical Parasitology and Entomology, Faculty of Medicine and Health Sciences, Universiti Putra Malaysia, 43400 UPM, Serdang, Selangor, Malaysia

ABSTRACT

Dengue fever (DF) is a global health problem and considered to be endemic in Malaysia. Conventional mosquito traps currently applied as vector control do not effectively reduce *Aedes* mosquito population. AedesTech Mosquito Home System (AMHS) is an autocidal ovitraps for *Aedes* mosquitoes that uses the 'lure and kill' concept and is expected to be able to reduce *Aedes* mosquito population. The effectiveness of AMHS in reducing *Aedes* mosquito population was investigated in Block A, B and D (control) of the 17th College, Universiti Putra Malaysia (UPM). For the first two weeks (pre-intervention), the conventional ovitraps were used to obtain the initial abundance of mosquito population in Block A, B and D. Subsequently, AMHS was used for the next three months and again followed by the conventional ovitrap for the final two weeks (post-intervention). Ovitrap Index, Hatching Index and percentage of emergence of adult mosquitoes were calculated once every two weeks. Data were analysed using Paired Sample T-test. Values

were considered significant at $p \leq 0.05$. The Ovitrap Index that indicates the mosquito population at Block A and B was significantly higher ($p \leq 0.05$) than of Block D. Hatching Index of AMHS was significantly lower ($p \leq 0.05$) than conventional ovitraps. All mosquito eggs collected in AMHS did not develop into adult mosquitoes. There was a significant reduction ($p \leq 0.05$) in the mosquito population between the pre- and post-intervention. In conclusion, AMHS

ARTICLE INFO

Article history:

Received: 08 February 2019

Accepted: 27 November 2019

Published: 13 January 2020

E-mail addresses:

latifahsy@upm.edu.my (Latifah Saiful Yazan)

neshjoel@gmail.com (Kaveinesh Paskaran)

banulatagopalsamy@gmail.com (Banulata Gopalsamy)

roslaini@upm.edu.my (Roslaini Abd Majid)

* Corresponding author

was effective in reducing the mosquito population in 17th College, UPM. Therefore, it is believed to be a very promising vector management option to control the incidence of DF.

Keywords: *Aedes*, dengue fever, hatching index, ovitrap index, ovitraps, vector management

INTRODUCTION

Dengue fever (DF) or commonly known as dengue, is caused by dengue virus (DENV), which is a single-stranded RNA virus. DENV is a flavivirus from the family of Flaviviridae that is transmitted to an individual by a mosquito from an infected person. The mosquito acts as a vector for the virus. According to the World Health Organization (WHO), DENV causes a wide range of diseases in humans, from a self-limited DF to life-threatening syndromes called dengue hemorrhagic fever (DHF) and dengue shock syndrome (DSS) (WHO, 2017).

There are four DENV serotypes that can cause DF, which are DENV1, DENV2, DENV3 and DENV4. The presence of more than one serotype of DENV in a person's blood circulation indicates repeated infection of the virus leading to DHF and even DSS (CDC, 2017). The vectors that transmit DENV are mosquitoes specifically *Aedes* mosquitoes namely *Aedes albopictus* (Skuse) and *Ae. aegypti* (Linnaeus) (Rosen et al., 1983).

According to the Centre for Disease Control and Prevention, about 40% of the total population in the world live in areas with high risk of DENV transmission (CDC, 2017). An estimation of 50 to 100 million of the infection was deduced by the WHO in 2017. The fatality rate of DF was almost 25% of the reported cases (WHO, 2016). In Malaysia, the number of DF cases remains increasing. The total DF cases reported in 2018 was 80615, with 147 dengue-related deaths. The state of Selangor with 45349 DF cases recorded the highest number among all states in Malaysia. The first three months of the year 2019 recorded 37027 DF cases with 59 dengue-related deaths (iDengue, 2019).

The symptoms of DF can vary from a normal fever to a very serious convulsion. The general symptoms of DF include high fever, headache, vomiting, rashes, and joint and muscle pain (Tiga et al., 2016). There are also several warning signs, for instances, persistent diarrhoea, mucosal bleeding and serious decrease in platelet count. Immediate treatment is needed once diagnosed with DF as it could be fatal if there are severe plasma leakage, severe haemorrhage and severe organ impairment (WHO, 2009).

There are several approaches to prevent and control the DENV transmission including physical, biological and chemical control, and integrated vector management. Nevertheless, the number of DF cases is still increasing in Malaysia and globally although preventive and control measures are taken into action (Rajapakse et al., 2012). This is because the actions are not fully effective and infeasible to be applied everywhere.

The drawback of currently available ovitraps are that they are mostly unable to prevent the hatching of the eggs. Close and constant monitoring is required to avoid the development

of adult mosquito from the eggs (WHO, 2009). This in turn can be very laborious and costly. Other vector control measure such as fogging or space-spraying with insecticide is only able to eliminate adult mosquitoes and not mosquito eggs (Chua et al., 2005). Recently, a vaccine for DF, Dengvaxia, has been developed. Nevertheless, it causes side effects to who have not been previously infected with DENV (Halstead, 2017). On that note, a more effective solution to curb the spread of DENV is crucial.

AedesTech Mosquito Home System (AMHS) is a commercial *Aedes* trap manufactured by One Team Network Sdn. Bhd. This invention emerged as the sole winner of Prevention-Vector Control group in the Dengue Tech Challenge 2016 funded by Newton-Ungku Omar Fund and British Council. AHMS works in the concept of “lure and kill”, as it contains mosquito attractant which attracts adult female *Aedes* mosquitoes to lay eggs inside the trap (Lim Chee Hwa, personal communication April 29, 2018).

The attractant also contains an insect growth regulator (IGR), pyriproxyfen that effects the development of mosquitoes at various phases of its life cycles. The high ovicidal activity of pyriproxyfen at a dose as low as 1 ppm of multiple *Aedes* species has been documented (Suman et al., 2013). Due to the higher permeability of chorionic membranes of newly deposited eggs, pyriproxyfen has better ovicidal effects on those eggs than fully embryonated eggs of non-diapausing eggs. Pyriproxyfen on the other hand terminates egg diapause and are able to chemically induce the hatching of eggs from *Ae. albopictus* under diapausing conditions (Suman et al., 2015). Pyriproxyfen is also species specific as the ovicidal effect was effective against *Ae. albopictus* and *Ae. aegypti* but had no effect on *Ae. atropalpus*. Pyriproxyfen inhibits juvenile hormones and ecdysteroid titres of insects inhibiting embryogenesis and adult formation. Pyriproxyfen causes lowered fertility and fecundity in adults that develop from larva that has been exposed at sublethal levels of this IGR (Loh & Yap, 1989). Even though the pyriproxyfen is an effective larvicide and pupacide, it is not an adulticide.

On the basis that this trap is able to attract the deposition of eggs and prevents the development of eggs, this new intervention could be an effective method in vector management. This study investigated the effectiveness of AHMS in reducing the mosquito population in 17th College, Universiti Putra Malaysia (UPM).

MATERIALS AND METHODS

Study Site

Seventeenth College (17th College), one of the hostels in Universiti Putra Malaysia, UPM, was selected as the study area. The study area covers an area of 92, 015.75 m² with a population of approximately 1800 people. The hostel consists of four wings with five levels in each wing. Several student utilities are located within the block such as store, recreational room and study room. Forest and lakes can be found at the surrounding

campus. There was abundance of breeding sites for *Aedes* mosquitoes found in this area especially around the big trees, fish pond, various types of artificial containers, drains and toilets. Block A and B were used for the intervention, whereas Block D was chosen as the experimental control for this study.

Conventional Ovitrap

Conventional ovitraps are dark containers that were prepared by using plastic drinking cups (opening diameter 7.8 cm, base diameter 6.5 cm and height 9.0 cm) painted in black. One oviposition substrate (10 cm x 2.5 cm x 0.3 cm) was placed in each ovitraps. The containers were filled with water and substrate to a height of 5.5 cm. The ovitraps mimics the dark breeding site of the mosquito, whereas the substrate is the surface for the mosquito to lay eggs. The traps were labelled according to the block, wing, and level they were placed.

AedesTech Mosquito Home System

The commercial *Aedes* trap (AMHS), was kindly supplied by One Team Network Sdn. Bhd. C-fold white paper towels (20 cm x 7.5 cm, Brand: Scott, Philadelphia) placed in AMHS, served as the surface for the mosquitoes to lay eggs. The traps were labelled according to the block, wing, and level they were placed.

Pre-Intervention Study

For the pre-intervention study, a total of 120 conventional ovitraps were placed at the corridors and along the staircases of Block A, B and D for the first two weeks. Two conventional ovitraps were placed at each level with a distance of less than five meters from each other and left there for four days. Wet substrates from the conventional ovitraps were collected (hereafter referred as sample collection 1) into a dry container and were replaced with new substrates. The wet substrates collected were brought back to the lab and dried, and the mosquito eggs attached to them were counted. The Ovitrap Index was calculated using the following Equation 1.

$$Ovitrap\ Index = \frac{No.\ of\ positive\ ovitraps\ (with\ eggs)}{No.\ of\ ovitraps\ deployed} \times 100\% \quad [1]$$

The substrates were then submerged in dechlorinated water for the eggs to hatch. The Hatching Index was then calculated using the following Equation 2.

$$Hatching\ Index = \frac{No.\ of\ eggs\ hatched}{Total\ no.\ egg\ counted} \times 100\% \quad [2]$$

The species of larvae was then identified and killed using Dettol.

Intervention Study

For the intervention study, a total of 80 AMHS were placed at the corridors and along the staircases of Block A and B for the following three months. Two AMHS were placed at each level with a distance of less than five meters from each other. Wet tissues from the AMHS were collected by placing them into a dry container and replaced with new tissues for the next collection. The wet tissues collected were brought back to the lab and dried, and the mosquito eggs attached to them were counted. The Ovitrap Index and Hatching Index were then calculated.

Mid-Intervention Study

For the mid-intervention study, a total of 120 conventional ovitraps were placed at the corridors and along the staircases of Block A, B and D, after the first four weeks of the intervention study (hereafter referred as collection 2, 3, 4 and 5) alongside AMHS. The Ovitrap Index and Hatching Index were then calculated.

Post-Intervention Study

For the post-intervention study a total of 120 conventional ovitraps were placed at the corridors and along the staircases of Block A, B and D after the intervention study for two weeks (hereafter referred as collection 6). The Ovitrap Index and Hatching Index were then calculated.

Mosquito Eggs Counting

The wet substrates in the conventional ovitraps or tissues in the AMHS were removed from the container. They were then dried using an oven at 50°C for one day. The substrate was sectioned into several parts to ease the counting of the eggs. The eggs were laid singly and black in colour (Figure 1). Next, the eggs attached on the substrate or tissue were manually counted under a dissecting microscope at $\times 20$ magnification (Leica EZ4 Stereo Microscope, USA) and recorded.



Figure 1. Eggs of the *Aedes* mosquitoes attached on the tissue collected from AMHS as observed under a stereo-microscope

Species Identification

The dried substrates in the conventional ovitraps or tissues in the AMHS with the eggs attached were submerged in a container containing dechlorinated water or tap water, and left for four days. The number of larvae found in the container was counted starting from Day 5. The larvae were then collected one by one, placed onto a glass slide, covered with a cover slip, and observed under a compound microscope under the magnification of 400X (Leica, Germany). Species of the larva was identified based on the comb teeth structure in the larvae with reference to Farajollahi and Price (2013). The comb teeth of *Ae. albopictus* is thorn like (Figure 2a), while the one of *Ae. aegypti* is pitch-fork like (Figure 2b).

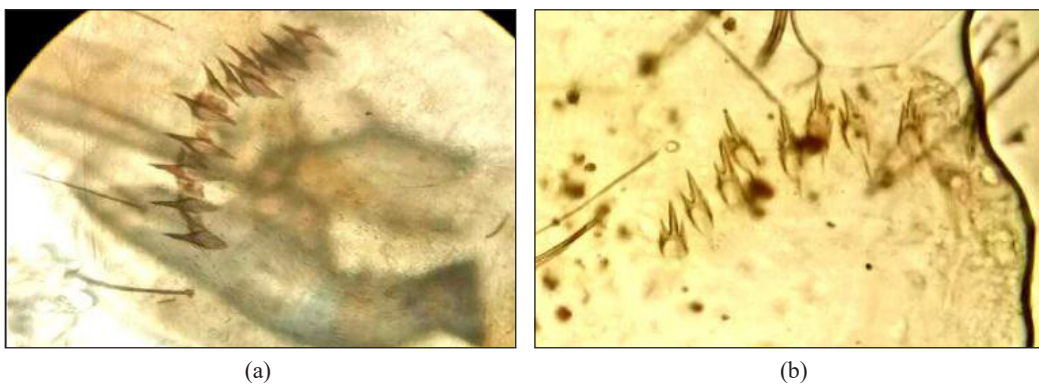


Figure 2. Larva of (a) *A. albopictus* and (b) *A. aegypti* observed under a light microscope (400× magnification)

Data Analysis

Data were analysed using SPSS version 11.5. The difference between the pre- and post-intervention data was compared among Block A, B and D using the Paired Sample T-test. A value was considered significant at $p \leq 0.05$.

RESULTS

The presence of *Aedes* mosquito and its dominant species were screened using conventional ovitraps whereby the population of *Ae. albopictus* was significantly higher than *Ae. aegypti* (Figure 3). The effectiveness of AMHS in attracting *Aedes* mosquitoes to deposit the eggs were evaluated against conventional ovitrap. AMHS recorded significantly higher ($p \leq 0.05$) Ovitrap Index compared to conventional ovitrap (Figure 4). Furthermore, all the eggs present in AMHS did not hatch recording a hatching index of $0.00 \pm 0.00\%$.

This value is significantly lower ($p \leq 0.05$) than the hatching index of the conventional ovitrap as shown in Figure 5. The hatched eggs from the conventional trap were allowed to develop into adult mosquitoes (Figure 6) recording a value of 93.13% and 92.85% in Block A and B, respectively. Since none of the eggs in AMHS hatched, the emergence of

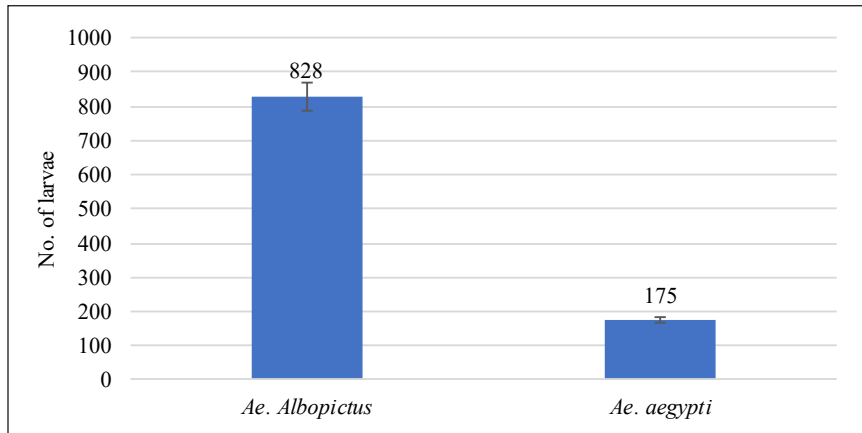


Figure 3. Number of larvae of *Ae. albopictus* and *Ae. aegypti* collected in the conventional ovitraps placed in Block A, B and D of 17th College, UPM

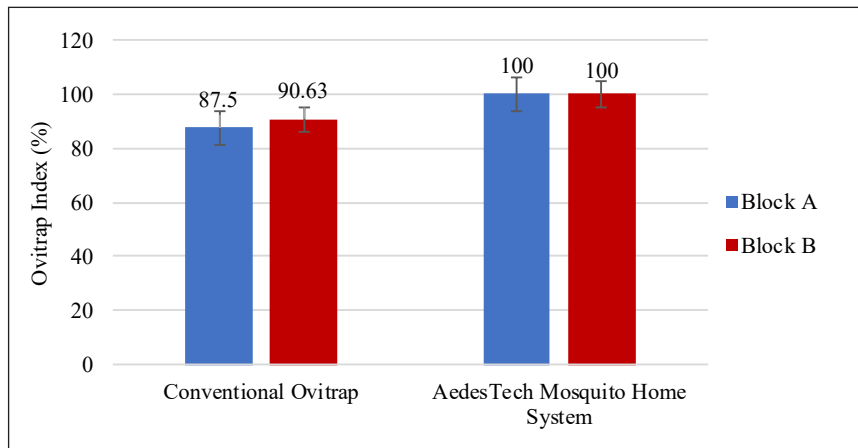


Figure 4. Ovitrap Index of the conventional ovitrap and AMHS in Block A and B of 17th College, UPM, during the pre-intervention study

adult mosquito was also 0% in both the blocks. The number of mosquito eggs collected in AMHS from each sample collection, as displayed in Figure 7, shows a general decreasing trend with drastic reduction between the first and second sample collections compared to the following collections. The reduction in the eggs count was significant ($p \leq 0.05$) after the three months of intervention using AMHS. The number of mosquito eggs in the three blocks where the study was carried out is represented in Figure 8. Prior to the intervention the mosquito population were almost similar among the three blocks. However, Block A and B installed with AMHS recorded a reduction during their mid- and post-intervention studies. Block D that served as the control remains with high eggs counts until the end of the study. Figure 9 depicts the OI in Blocks A, B and D during the pre-, mid- and post- intervention study. The blocks installed with AMHS show a decreasing trend in the

number of traps positive with eggs but Block D shows and increase from 75 to 81.25% during the mid-intervention study before decreasing to 75% during the post-intervention study. The OI in the different levels of the 17th College building (Figure 10) shows the ground level and level 1 recorded the highest (83.33%) and lowest (66.66%) percentage of OI, respectively. No significant difference ($p < 0.05$) in the OI was observed between the different levels of the building.

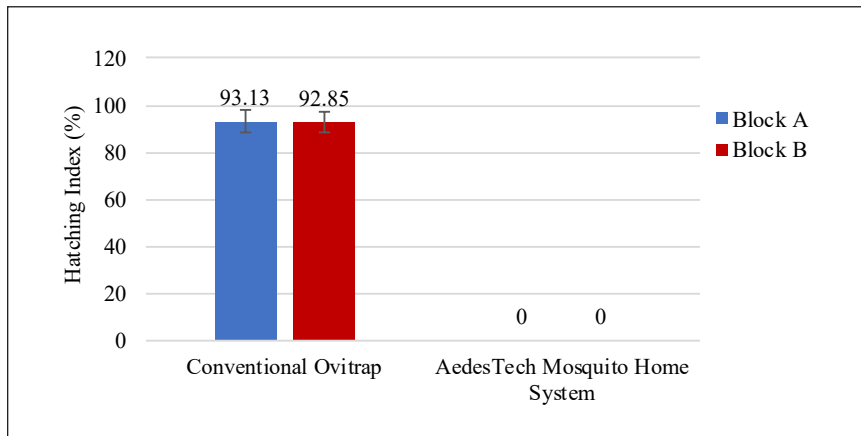


Figure 5. Hatching Index of the conventional ovitrap and AMHS in Block A and B of 17th College, UPM, during the intervention study

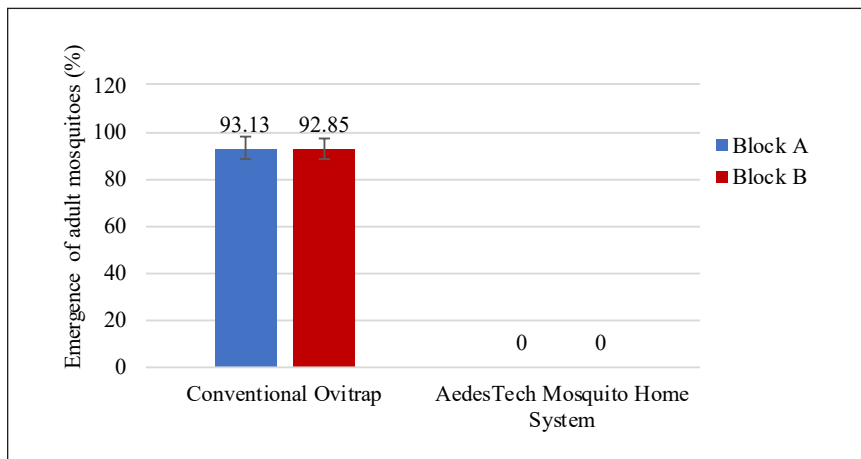
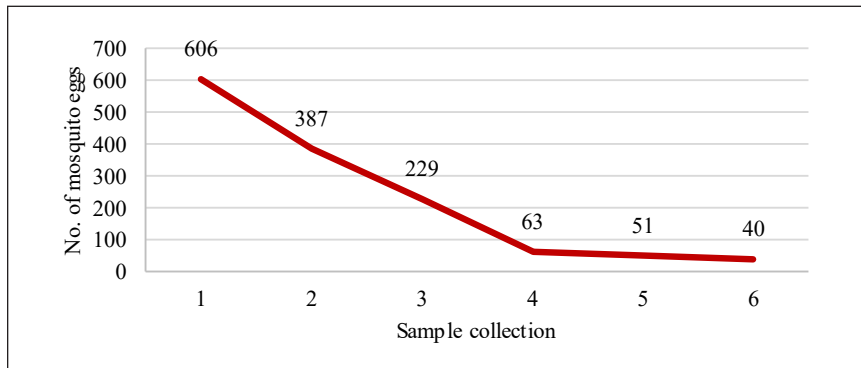
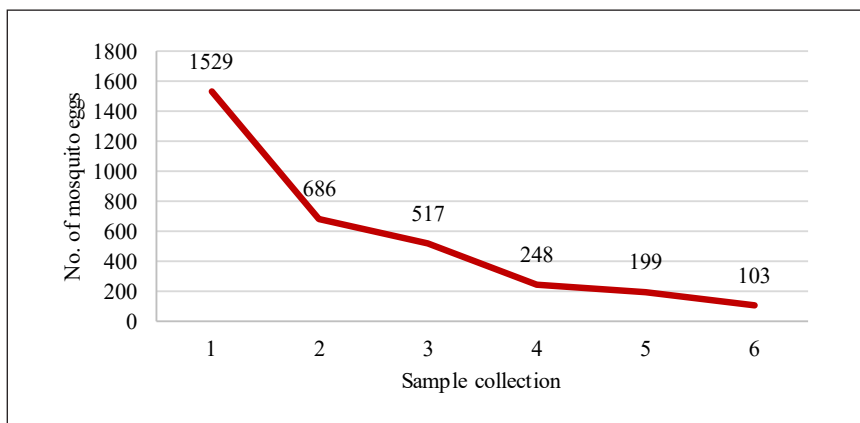


Figure 6. Emergence of adult mosquitoes from the hatched eggs of the conventional ovitrap and AMHS in Block A and B of 17th College, UPM, during the intervention study



(a)



(b)

Figure 7. Number of *Aedes* mosquito eggs in Block A (a) and Block B (b) of 17th College, UPM, in the intervention study

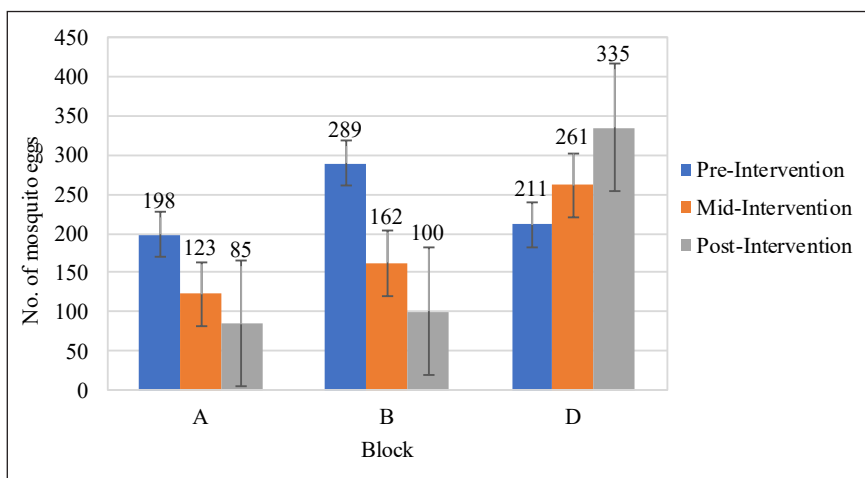


Figure 8. Number of *Aedes* mosquito eggs during pre-, mid- and post-intervention study in Block A, B and D of 17th College, UPM

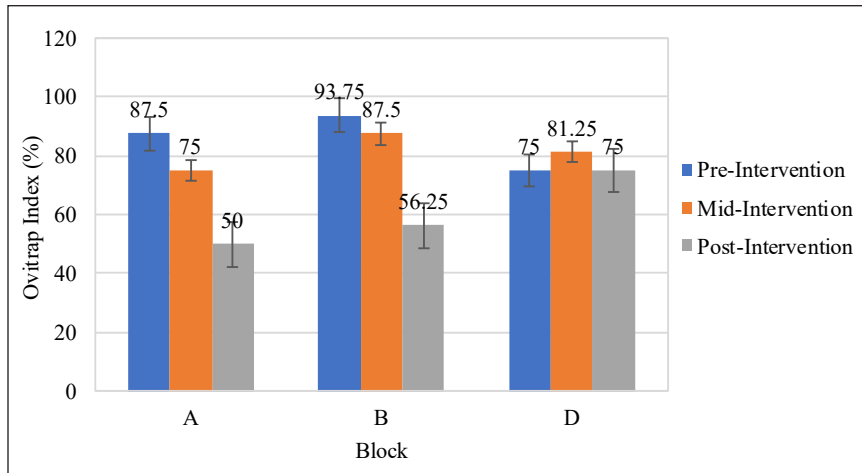


Figure 9. Ovitrap index during pre-, mid- and post-intervention study in Block A, B and D of 17th College, UPM

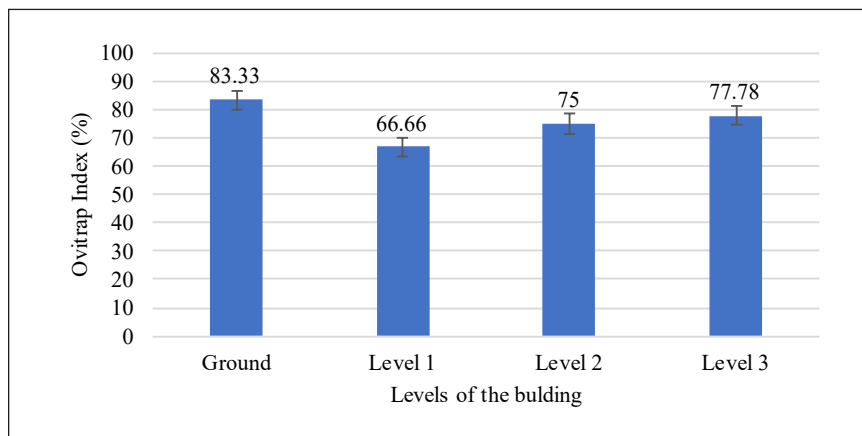


Figure 10. Ovitrap index in the different levels of the building in 17th College, UPM

DISCUSSION

There were many approaches studied in addressing the problems faced to reduce the DF cases (Achee et al., 2015; Bowman et al., 2016) but none is yet deemed effective. AMHS is a promising integrated vector management that attracts adult female *Aedes* mosquitoes to lay eggs in the trap and prevents the development of larvae from the hatched eggs. In this study, the effectiveness of AMHS to reduce the mosquito population was investigated in 17th College, UPM.

It was discovered in this study that *Ae. albopictus* and *Ae. aegypti* were the only *Aedes* mosquito species found in 17th College, UPM. The eggs were laid singly (University of Nebraska-Lincoln, 2018) and the uniqueness of *Aedes* larvae is that the comb scale structure

is arranged in a single row (Barraud, 1934; Bar & Andrew 2013; Rueda, 2004). The college is surrounded with trees and lakes. *Ae. albopictus* and *Ae. aegypti* are commonly found and breed outdoor (in the forest and adapting itself to suburban and human environment) and indoor, respectively (MOH, 2017). *Ae. albopictus* was more dominant in number compared to *Ae. aegypti*. *Ae. albopictus* is associated with the term container breeder where it breeds in small containers found outdoor (Rozilawati et al., 2015) while adults of *Ae. aegypti* typically resides inside houses. Since this study was carried out by placing the ovitraps outdoor, that might be the reason that *Ae. albopictus* outnumbered *Ae. aegypti* in this area.

In this study, the eggs collected from the ovitraps hatched into larvae gradually starting from Day 4 (~10%) upon submerging in dechlorinated water, which was used to support bacterial growth that serves as food for the developing larvae. The presence of chlorine in water can kill the bacteria, hence, the developing larvae (Barrera et al., 2004). Most of the eggs (~75%) hatched in between Day 8 and Day 10. The average Hatching Index reached 82.83% to 93.13% from Day 10 to Day 14 (unpublished data). Similar findings were reported by the Centre for Disease Control and Prevention (CDC, 2017).

The effectiveness of AMHS to attract *Aedes* mosquitoes in comparison to the conventional ovitrap was evaluated based on the Ovitrap Index. Based on the higher Ovitrap Index of AMHS (100%) compared to the conventional ovitraps (90.63%), the concept of “lure” of the former worked in this study. AMHS contains attractant that attracts the female *Aedes* mosquitoes to lay eggs inside the trap (Lim Chee Hwa, personal communication April 29, 2018).

The Hatching Index was determined based on the number of larvae being hatched from the eggs, which is possible to be performed in the ovitrap because the larvae can be counted. AMHS contains pyriproxyfen that mimics a natural hormone that functions as an insect growth regulator, which inhibits development of adult mosquitoes from the hatched eggs (Hallman et al., 2015) by suppressing embryogenesis (Ishaaya & Horowitz, 1995). Similar finding was reported by Unlu et al. (2017), stating that the usage of pyriproxyfen showed significant reduction of larval population and also eggs count.

During the mid-intervention, the conventional ovitrap was used alongside with AMHS. There was no larvae development from the hatched eggs, hence, zero emergence of adult mosquitoes from the conventional ovitrap where the larvae are supposed to develop. It is postulated that the mosquitoes that laid eggs inside AMHS transfer pyriproxyfen in the solution via horizontal transfer to the conventional ovitrap, preventing the development of the larvae from the hatched eggs and later to adult mosquitoes. The tarsal and legs of ovipositing mosquitoes are exposed to the pyriproxyfen from the solution. The toxicant is able to attach and retain on the contaminated female and when the mosquitoes fly to another oviposition site, larvicide on their bodies may be transferred at a lethal concentration into the water killing existing larvae (Ohba et al., 2013; Wang et al., 2014).

There was a significant reduction in the number of mosquito eggs between collection 2, 3 and 4 performed for 6 weeks (mid-intervention) using both conventional ovitrap and AMHS. Drastic reduction (by ~50%) was noted between the first and the second collection. The reduction was less drastic between the second and the third collection (by ~20%). It is postulated that AMHS has prevented the emergence of adult mosquitoes in the second collection that the mosquito population is reduced following the third and fourth collection. Hence, the mosquito population kept on reducing as the weeks went by for three months.

The control group, which was Block D, showed an increase in the *Aedes* mosquito eggs count in contrast to the reduction of eggs in both Block A and B. This shows that it is the use of AMHS which has reduced the mosquito population, not the external interference or environmental factors such as fogging and the change in weather that might have caused the reduction of mosquito population in Block A and B. Furthermore, the outcome of OI also support this claim whereby Block D with no intervention showed no reduction in the number of ovitraps positive with eggs but was clearly observed in Block A and B. The possible risk of an outbreak to occur in a particular area is indicated by OI value of more than 10% (Braks et al., 2003; MOH, 1997). We recorded above 50% of OI even in Blocks A and B indicating that even though AMHS was able to reduce the mosquito population, it is insufficient to fully eliminate the risk of possible outbreak in the vicinity of 17th College, UPM. Moving forward, efforts to improvise the intervention or increase the number of traps could be carried out to reduce the mosquito population more effectively.

Ovitraps were deployed in all the four levels (ground level, level 1, level 2 and level 3) of the hostel building and OI was not affected by the different elevation of the building. This outcome is similar to the reports by Lau et al. (2013) in a study carried out in multiple storey buildings in four residential areas located in Selangor and Roslan et al. (2013) who conducted the experiment in apartments in Kuala Lumpur, Malaysia. However, the study by Wan-Norafikah et al. (2010) reported that lower *Aedes* sp populations was found at higher levels of high-rise apartments. That outcome was different to ours probably due to the different structure of the buildings where both these experiments were carried out. High-rise buildings are buildings with more than five stories while buildings fewer than five stories and landed properties are considered low-rise buildings (Mahmud et al., 2018). Since the building in our study area falls within the category of low-rise building, the mosquito population was not affected by the elevation.

Data from this current study are in concordance with previous report whereby, researchers have correlated the density of adult mosquitoes with the number of eggs being collected in the ovitrap. Higher number of eggs indicates higher density of adult mosquitoes. The reduction of the eggs count reflects the reduction of the mosquito population (Reiter et al., 1991).

CONCLUSION

The 17th College, Universiti Putra Malaysia, has high population of both species of *Aedes* mosquitoes namely *Ae. albopictus* and *Ae. aegypti* with the former being more dominant. The commercial *Aedes* trap, AedesTech Mosquito Home System, was effective in reducing the mosquito population in the college.

ACKNOWLEDGEMENTS

The authors thank Mr. Lim Chee Hwa from One Team Network Sdn. Bhd. for his kind contribution in providing financial assistance and necessary materials for this project. The formulation of the attractant is the company's trade secret and therefore is not disclosed. However, the presence of some chemicals has been revealed to the researcher for discussion of the outcome and is cited as (Lim Chee Hwa, personal communication April 29, 2018). However, the complete formulation and amount present in the attractant remains unknown to the researchers. The authors also thank Faculty of Medicine and Health Sciences, Universiti Putra Malaysia for providing the facilities.

REFERENCES

- Achee, N. L., Gould, F., Perkins, T. A., Reiner, R. C., Morrison, A. C., Ritchie, S. A., ... & Scott, T. W. (2015). A critical assessment of vector control for dengue prevention. *PLoS Neglected Tropical Diseases*, 9(5), 1-19.
- Bar, A., & Andrew, J. (2013). Morphology and morphometry of *Aedes aegypti* larvae. *Annual Review and Research in Biology*, 3(1), 1-21.
- Barrera, R., Amador, M., & Clark, G. G. (2004). The use of household bleach to control *Aedes aegypti*. *Journal of the American Mosquito Control Association*, 4, 444-448.
- Barraud, P. J. (1934). *The fauna of British India Diptera* (Vol. 4). London, UK: Taylor and Francis.
- Bowman, L. R., Donegan, S., & McCall, P. J. (2016). Is dengue vector control deficient in effectiveness or evidence? Systematic review and meta-analysis. *PLoS Neglected Tropical Diseases*, 10(3), 1-24.
- Braks, M. A. H., Honorio, N. A., Lourenco-de-Oliveira, R., Juliano, S. A., & Lounibos, L. P. (2003). Convergent habitat segregation of *Aedes aegypti* and *Aedes albopictus* (Diptera: Culicidae) in South-eastern Brazil and Florida. *Journal of Medical Entomology*, 40(6), 785-794.
- CDC. (2017). *Dengue CD*. Retrieved July 22, 2017, from <https://www.cdc.gov/dengue/>
- Chua, K.B., Chua, I. L., Chua, I. E., & Chua, K. H. (2005). Effect of chemical fogging on immature *Aedes* mosquitoes in natural field conditions. *Singapore Medical Journal*, 46(11), 639-644.
- Farajollahi, A., & Price, D. C. (2013). A rapid identification guide for larvae of the most common North American container-inhabiting *Aedes* species of medical importance. *Journal of the American Mosquito Control Association*, 29(3), 203-221.

- Hallman, A., Bond, C., Buhl, K., & Stone, D. (2015). *Pyriproxyfen general fact sheet*. National Pesticide Information Center, Oregon State University Extension Services. Retrieved July 4, 2017, from <http://npic.orst.edu/factsheets/pyriprogen.html>.
- Halstead, S. B. (2017). Dengvaxia sensitizes seronegatives to vaccine enhanced disease regardless of age. *Vaccine*, 35(47), 6355-6358.
- iDengue. (2019). *iDengue untuk komuniti* [iDengue for Community] Retrieved April 1, 2019, from idengue.remotesensing.gov.my
- Ishaaya, I., & Horowitz, A. R. (1995). Pyriproxyfen, a novel insect growth regulator for controlling whiteflies: Mechanisms and resistance management. *Pesticide Science*, 43, 227-232.
- Lau, K. W., Chen, C. D., Lee, H. L., Izzul, A. A., Asri-Isa, M., Zulfadli, M., & Sofian-Azirun, M. (2013). Vertical distribution of *Aedes* mosquitoes in multiple storey buildings in Selangor and Kuala Lumpur, Malaysia. *Tropical Biomedicine*, 30(1), 36-45.
- Loh, P. Y., & Yap, H. H. (1989). Laboratory studies on the efficacy and sublethal effects of an insect growth regulator, pyriproxyfen (S-31183) against *Aedes aegypti* (Linnaeus). *Tropical Biomedicine*, 6, 7-12.
- Mahmud, M. A. F., Mutalip, M. H., Lodz, N. A., & Shahar, H. (2018). Study on key *Aedes* spp breeding containers in dengue outbreak localities in Cheras district, Kuala Lumpur. *International Journal of Mosquito Research*, 5(2), 23-30.
- MOH. (1997). *Guidelines on the use of ovitrap for Aedes surveillance*. Vector Control Unit, Vector Borne Disease Section, Malaysia Ministry of Health. Retrieved June 16, 2017, from <http://www.moh.gov.my/moh/attachments/5502.pdf>
- MOH. (2017). *Denggi*. Retrieved March 23, 2017, from <http://denggi.myhealth.gov.my/?lang=en>.
- Ohba, S. Y., Ohashi, K., Pujiyati, E., Higa, Y., Kawada, H., Mito, N., & Takagi, M. (2013). The effect of pyriproxyfen as a "population growth regulator" against *Aedes albopictus* under semi-field conditions. *PLoS ONE*, 8(7), 1-10.
- Rajapakse, S., Rodrigo, C., & Rajapakse, A. (2012). Treatment of dengue fever. *Infect Drug Resistance*, 5, 103-112.
- Reiter, P., Amador, M. A., & Colon, N. (1991). Enhancement of the CDC ovitrap with hay infusions for daily monitoring of *Aedes aegypti* populations. *Journal of the American Mosquito Control Association*, 7(1), 52-55.
- Rosen, L., Shroyer, D. A., Tesh, R. B., Freier, J. E., & Lien, J. C. (1983). Transovarial transmission of dengue virus by mosquitoes: *Aedes albopictus* and *Aedes aegypti*. *American Journal of Tropical Medicine and Hygiene*, 32, 1108-1119.
- Roslan, M. A., Shafie, A., Ngui, R., Lim, Y. A. L., & Sulaiman, W. Y. W. (2013). Vertical infestation of the dengue vectors *Aedes aegypti* and *Aedes albopictus* in apartments in Kuala Lumpur, Malaysia. *Journal of the American Mosquito Control Association*, 29(4), 328-36.
- Rozilawati, H., Tanaselvi, K., Nazni, W. A., Mohd Masri, S., Zairi, J., Adanan, C. R., & Lee, H. L. (2015). Surveillance of *Aedes albopictus* breeding preference in selected dengue outbreak localities, Peninsular Malaysia. *Tropical Biomedicine*, 32(1), 49-64.

- Rueda, L. M. (2004). *Pictorial keys for the identification of mosquitoes (Diptera: Culicidae) associated with dengue virus transmission*. Auckland, New Zealand: Magnolia Press.
- Suman, D. S., Wang, Y., Bilgrami, A. L., & Gaugler, R. (2013). Ovicidal activity of three insect growth regulators against *Aedes* and *Culex* mosquitoes. *Acta Tropica*, *128*, 103-109.
- Suman, D. S., Wang, Y., & Gaugler, R. (2015). The insect growth regulator pyriproxyfen terminates egg diapause in the asian tiger mosquito, *Aedes albopictus*. *PLoS ONE*, *10*(6), 1-12.
- Tiga, D., Shepard, D., Ramos-Castañeda, J., Martínez-Vega, R., Undurraga, E., & Tschampl, C. (2016). Persistent symptoms of dengue: Estimates of the incremental disease and economic burden in Mexico. *American Journal of Tropical Medicine and Hygiene*, *94*(5), 1085-1089.
- University of Nebraska-Lincoln. (2018). *Urban entomology - Mosquito update*. Retrieved June 16, 2017, from <https://entomology.unl.edu/urbanent/mosquito.shtml>.
- Unlu, I., Suman, D. S., Wang, Y., Klingler, K., Faraji, A., & Gaugler, R. (2017). Effectiveness of autodissemination stations containing pyriproxyfen in reducing immature *Aedes albopictus* populations. *Parasites and Vectors*, *10*(1), 1-10.
- Wang, Y., Suman, D. S., Bertrand, J., Dong, L., & Gaugler, R. (2014). Dual-treatment autodissemination station with enhanced transfer of an insect growth regulator to mosquito oviposition sites. *Pest Management Science*, *70*(8), 1299-1304.
- Wan-Norafikah, O., Nazni, W. A., Noramiza, S., Shafa'ar-Ko'ohar, S., Azirol-Hisham, A., Nor-Hafizah, R., ... & Lee, H. L. (2010). Vertical dispersal of *Aedes* (*Stegomyia*) spp. in high-rise apartments in Putrajaya, Malaysia. *Tropical Biomedicine*, *27*(3), 662-667.
- WHO. (2009). *Dengue guidelines for diagnosis, treatment, prevention and control*. Retrieved October 22, 2017, from https://apps.who.int/iris/bitstream/handle/10665/44188/9789241547871_eng.pdf?sequence=1&isAllowed=y
- WHO. (2016). *Dengue situation update number 500: Update on the dengue situation in the Western Pacific Region (Northern Hemisphere)*. Retrieved June 4, 2017, from http://www.wpro.who.int/emerging_diseases/dengue_biweekly_20160920.pdf?ua=1
- WHO. (2017). *Dengue fact sheet*. SEARO. Retrieved June 3, 2017, from http://www.searo.who.int/entity/vector_borne_tropical_diseases/data/data_factsheet/en/



Acute Moderate and High-Intensity Endurance Exercise Suppresses *Ad-libitum* Energy Intake in Obese Males

Adam Linoby^{1*}, Muhammad Alif Nazrin Jumat¹, Ahmad Safwanudin Nordin¹, Nur Hidayah Asilah Za'don¹, Jamiaton Kusrin² and Sharifah Maimunah Syed Mud Puad¹

¹ Faculty of Sports Science and Recreation, Universiti Teknologi MARA, Negeri Sembilan Branch, Seremban Campus, 70300 Seremban, Negeri Sembilan, Malaysia

² Faculty of Sports Science and Recreation, Universiti Teknologi MARA, 40460 Shah Alam, Selangor, Malaysia

ABSTRACT

High-intensity exercise acutely improves suppression of appetite in populations with normal body mass index (BMI). However, whether moderate intensity exercise (MIE) and high-intensity exercise (HIE) can elicit similar (or greater) appetite suppression effects for obese populations are still relatively unknown. The main aim is to investigate the acute effects of MIE and HIE on the appetite score, eating behaviour and blood glucose regulation among the obese population. Twelve obese participants (age: 20.8 ± 1 yr, BMI: 34.1 ± 3 kg·m⁻², $\dot{V}O_{2\max}$: 30.7 ± 3 ml·kg·min⁻¹) were randomly allocated, in a crossover manner, with a 7-day interval in between (1) MIE (cycling at 60-75% HR_{max}), (2) HIE (cycling at

80-95% HR_{max}, 8-sec sprint x 12 sec rest) and (3) control (CON) condition after a 10-hr overnight fast. Physiological (fasting blood [glucose] and 24-hr calorie intake) and psychological responses (Three Factor Eating Questionnaire-R18, TFEQ-R18, and appetite score using Visual Analog Scale, VAS) were recorded prior to and after exercise interventions. Both MIE and HIE significantly reduced the calorie intake compared to CON ($P < 0.05$), despite no changes in psychological measures were related to appetite (i.e. TFEQ-R18 and

ARTICLE INFO

Article history:

Received: 20 July 2019

Accepted: 4 October 2019

Published: 13 January 2020

E-mail addresses:

linoby@uitm.edu.my (Adam Linoby)

alifnazrinn@gmail.com (Muhammad Alif Nazrin Jumat)

safwanrjn23@gmail.com (Ahmad Safwanudin Nordin)

hidayahasilahzadon@gmail.com (Hidayah Asilah Za'don)

jamiaton@salam.uitm.edu.my (Jamiaton Kusrin)

shari0971@ns.uitm.edu.my (Sharifah Maimunah Syed Mud Puad)

*Corresponding author

VAS) between the groups ($P > 0.05$). A difference was found in fasting blood [glucose] level between trials in MIE ($P < 0.05$), but not following the HIE condition ($P > 0.05$). In response to acute intervention, both MIE and HIE improved some psychological appetite score and attenuated daily energy consumption; these positive effects could benefit obese and diabetic populations.

Keywords: Appetite, endurance, energy intake, high intensity exercise, moderate intensity exercise, obese

INTRODUCTION

The World Health Organization (WHO) cautions of the rising risk of chronic diseases since overweight and obesity rates are dramatically increasing every year. Statistics worldwide recorded a staggering population of 1.6 billion overweight and approximately 400 million obese (World Health Organization, 2017). Obesity can negatively impact the quality of life and increase the risk of cardiovascular diseases, diabetes and several types of cancers. It is currently recognised that overweight and obesity are the top 5 and top 10 risk factors for mortality and morbidity, respectively (Oreopoulos et al., 2008). It is clear that overweight and obesity impose various health-related problems, and the current global trend requires a practical strategy for weight management to expeditiously address the issue. It is recommended that weight loss intervention programs should combine the progressive reduction in energy intake (EI) with increases in energy expenditure (Alkahtani et al., 2014). Physical exercise is intimately related to energy intake and energy expenditure. It is widely believed that when exercise is performed regularly, it can elevate body energy turnover which then leads to an increase in energy expenditure, followed by a subsequent decline in body weight. Nevertheless, exercise-induced energy deficit may disturb the energy demand homeostasis, and this may affect body appetite regulation (Beaulieu et al., 2018). Accordingly, in the last few decades, there has been a surge in interest regarding the effects of exercise on appetite-related measures and hormones.

Physical activity has a prominent role in stimulating the negative energy balance by elevating energy expenditure. However, the magnitude of weight reduction is mainly dependent on calorie intake succeeding the activity; an increase in appetite to compensate the energy deficit will likely impose psychological difficulty towards any weight loss efforts. The relevance of this issue was discussed in articles from renowned media which highlighted the possibility of exercise hampering weight loss (Sailer et al., 2016) which may, in turn, promote fat accumulation (Leow et al., 2018). This is mainly a result of the increased desire for food intake following physical activity. The articles were primarily derived from evidence which indicated that energy consumption significantly increased a few minutes to hours after bouts of acute exercise (Martins et al., 2008a; Pomerleau et

al., 2004; Shorten et al., 2009). In contrast, some evidences suggested that appetite and energy consumption are relatively unchanged (Balaguera-Cortes et al., 2011; King et al., 2010). Several other studies claimed a higher rise in satiety hormone and weight reduction following acute bouts of exercise (Dorling et al., 2018; Ueda et al., 2009). These conflicting conclusions could be associated with the intensity and type of exercise used in previous studies. In support of this, clear justification is present which indicates that high-intensity exercise stimulates the circulating concentration of several appetite-related hormones, promoting weight reduction. Interestingly, the same study observed a lesser magnitude of changes in appetite-related measures and hormones with moderate intensity exercise (Bailey et al., 2015; Douglas et al., 2015; Martins et al., 2015).

Investigations on the impact of exercise concerning appetite-related measures and energy intake have mostly been restricted to limited comparisons of a single variation of type and intensity of exercise. Martins et al. (2015) reported that insulin levels and glucagon-like peptide (satiety hormones) were reduced and elevated, respectively, following isocaloric bouts of high and moderate intensity continuous cycling. However, this study mainly measured physiological data. The influence of these biomarkers on psychological indices related to appetite was not presented. Therefore, there is a notable lack of research investigating the impact of physiological and psychological measures of appetite following different exercise intensities (i.e. moderate-intensity exercise, MIE, and high-intensity exercise, HIE) and types of exercise (i.e. aerobic and resistance exercises) in the obese population. Therefore, the objective of this study is to investigate the acute effects of iso-caloric high intensity and moderate-intensity continuous exercise as well as high-intensity exercise on subsequent energy intake, appetite score and blood glucose for the obese adult population.

METHODS

Participants

Participants were screened for inclusion criteria, which includes participants that are: 1) healthy but sedentary obese individuals (body mass index of $30.0 \text{ kg}\cdot\text{m}^{-2}$ or greater) and 2) aged between 18 to 30 years old. A set of exclusion criteria were also used to determine participants' eligibility which includes: (1) current or history of cardiovascular, metabolic, gastrointestinal, renal or pulmonary disease; (2) significant change in body weight ($\geq 5\%$); (3) pregnancy within the previous 12 months; (4) user of dietary supplements (excluding macronutrients) or illicit drug use; and (5) receiver of any investigational research agent within the previous 3 months. The sample size was calculated using previous studies (Maria et al., 2015). A minimum of 11 participants were required for the current study. This was on the basis of a sample size calculation of 95% confidence interval using the changes in calorie intake detected in a previous study (Sim et al., 2014). All experimental trials

were conducted at approximately the same time of day (± 1 hr). The subjects recorded the calorie intake within 24 hrs before the commencement of the first intervention protocol and were asked to perform activities as well as have similar meals in the subsequent trial. The subjects were thoroughly informed of the protocol and the possible risks and benefits of participation before a written informed consent was obtained. This study was registered, prior to its commencement, in the University hospital Medical Information Network Clinical Trials Registry (UMIN-CTR) with registration identification number: UMIN000016335. The study was approved by the Research Ethics Committee (FSR/SR243/038/2018) and conforms to the code of ethics of the Declaration of Helsinki.

Study Design

During the first visit, subjects underwent the familiarisation session and a baseline data collection. Subjects were then randomly assigned into a group of three intervention conditions in a crossover manner: (1) MIE (cycling at 60-75% HR_{max}), (2) HIE (cycling at 80-95% HR_{max}, 8-sec sprint x 12-sec rest) and (3) control (CON). MIE and HIE interventions were designed to induce approximately 250-kcal energy deficit. The trials were performed on different days with at least 7-day interval periods between each condition. Primary outcome measures included pre and post-exercises *ad-libitum* energy intake, changes in appetite score (using visual analogue scale, VAS), the food intake-behaviour analysis (using Three-Factor Eating Questionnaire-Revised 18-items, TFEQ-R18) and changes in fasting blood [glucose] level.

Pre-experimental Assessment

The preliminary examination on the subjects consisted of BMI and body composition, which were assessed using Bioelectrical Impedance Analyser (Omron BF-508, Omron Healthcare, Kyoto, Japan). Before the experimental trial, estimation of aerobic capacity was performed using a 20-m multilevel shuttle run. Results of the test were then converted to $\dot{V}O_{2max}$ based on a formula by Bammann et al. (2019). Subsequently, subjects were familiarised with the experimental protocols; on similar cycle ergometer throughout the current study and similar breakfast test meal (see *Experimental trials*).

Experimental Trials

In the 24-h before each experimental trial, subjects were required to record all food and drink consumptions in the form provided. On the morning of each experimental trial, subjects arrived at 0800 hours, having fasted for 10-hr (water was permitted during this time). Subjects then completed VAS, TFEQ-R18 and blood [glucose] for baseline (PRE) assessment. All subjects subsequently performed one of the exercise protocols (i.e. MIE

or HIE) or resting control protocol. The duration of each exercise session was individually designed (on the basis of the $\dot{V}O_{2\max}$) to induce a 250-kcal (MIE and HIE) energy deficit. The exercise intensities were confirmed by monitoring HR. One hour after the exercises (i.e. MIE and HIE) or CON, each subject was provided with a standardised breakfast consisting of bread, milo drink and snacks (~442 kcal) after fasting blood [glucose] was taken. Next, subjects were instructed to fill the TFEQ-R18 and rate their Visual Analogue Scale before each trial. After each trial, VAS was immediately measured for rated hunger and followed with fasting blood [glucose]. A fingerprick-based blood glucose was conducted by trained personnel using standard protocol outlined in Rothberg et al. (2016). Additionally, subjects were provided with a standardised lunch and instructed to fill in the TFEQ-R18 immediately after consuming the lunch, 3 hours after each experimental trial. The lunch test meal consisted of fried rice, fruit drinks and snacks (~800 kcal). Subjects were then instructed to record all food and drink consumed 24-h prior to each trial.

Data Analysis Procedures

Appetite score was assessed using 100 mm Visual Analogue Scale immediately at pre and post exercise (Flint et al., 2000). The visual analogue scale took the form of five straight lines (100mm), each accompanied by a question anchored with words representing opposing extreme states of fullness, hunger, satiation, desire to eat and prospective food consumption at either end. 100 mm Visual Analogue Scale (Flint et al., 2000) was used in present study to measure the rate of hunger among the subjects, in terms of their subjective measurement such as determination to eat (DTE), hunger, fullness, and prospective food consumption (PFC) (Kawano et al., 2013; Martins et al., 2015). Scoring were calculated using the following formula: Average appetite score (mm) = [DTE + hunger + (100 - fullness) + PFC] / 4. Three factors eating questionnaire-revised 18 items (TFEQ-R18) were used to assess food intake-behaviour of subjects at (i) PRE and (ii) immediately post a standardised lunch meal. Consists of cognitive restraints (6 items), uncontrolled eating (9 items), and emotional eating (3 items). Energy intake (24-h) was assessed using a self-recorded food diary. Subjects were instructed to write everything they ate and drank (breakfast, lunch, dinner), consisted details such as time of the meals, food or beverages consumed and portion or serving of the food or beverages. The dietary macronutrient and overall energy intake were estimated (by accredited dietitians) using nutritional analysis software (Nutritics Ltd., Co. Dublin, Ireland) with calorie guidelines reference from the Ministry of Health (Malaysia) was used to insert the food information that was missing from the software database (Ministry of Health, n.d.). In each condition, fasting blood [glucose] at before and after exercise intervention were measured. The blood sample was analysed using the glucometer (One Touch model Ultra, LifeScan, Milpitas, California. Within-run precisions on the One Touch glucometer, as determined by coefficient of variation, was < 6%) .

Statistical Analysis

Descriptive statistics were used to characterise and compare the baseline characteristics of the subjects. Changes in energy intake, fasting blood [glucose], appetite score, and eating behaviour across all experimental conditions and time (i.e., pre and post) were assessed using repeated measures ANOVA. Post-hoc pairwise comparisons (Bonferroni adjustment method) were used to probe for specific differences. Where any differences were identified, 95% confidence intervals (95% CI) were used to display the likely range of the actual value in the sample population. Furthermore, effect size using partial eta squared (η^2_p) and Cohen's d (d_z) were calculated, which were defined as trivial (0–0.19), small (0.20–0.49), moderate (0.50–0.79), or large (> 0.80) (*ref; Cohen 1992). Analysis of data was conducted using the SPSS version 20 (SPSS Inc., Chicago, IL), with statistical significance accepted at $P < 0.05$.

Results

Twelve obese male university students (mean \pm SD: age 21 ± 1 yr, body weight 99 ± 1 kg, height 170 ± 6 m, BMI 34.1 ± 3 kg·m⁻², total body fat 33 ± 3 %, maximal oxygen uptake ($\dot{V}O_{2max}$) 30.7 ± 2.8 ml·kg·min⁻¹) voluntarily participated in this study.

Psychological Factors of Appetite

Baseline cognitive restraint, uncontrolled eating, emotional eating and appetite score were not significantly different between conditions ($P > 0.05$), and no significant alteration in all of these parameters between pre and post CON trial ($P > 0.05$). Cognitive restraint post MIE was significantly lower from the post CON condition (mean difference: 32; $P = 0.002$; 95% CI=15 to 49) and corresponding pre-trial (mean difference: 15; $P = 0.049$; 95% CI=0.07 to 30) value. Emotional eating post CON was significantly higher post MIE (mean difference: 30; $P = 0.006$; 95% CI=50 to 11) and post HIE (mean difference: 25; $P = 0.003$; 95% CI=40 to 11) value, respectively. However, there were no significant changes in appetite score observed between the experimental condition ($P > 0.05$) (Table 1).

Calorie Consumption

The group daily calorie intake in the MIE, HIE, and CON conditions are shown in Figure 1. Baseline calorie intake was not significantly different between conditions ($P > 0.05$), and no significant alteration in calorie intake was found between pre and post CON trial ($P > 0.05$). A trivial interaction effect ($F_{(1,8,20)} = 7.6$, $P = 0.004$, $\eta^2_p = 0.41$) and a large time effect ($F_{(1,0,11)} = 39$, $P < 0.001$, $\eta^2_p = 0.78$) of calorie intake was discovered throughout the intervention, but no effect on exercise intervention condition ($P > 0.05$) were identified. Post hoc analysis revealed that calorie intake following CON (2163 ± 478 kcal) was significantly higher than

Table 1
Appetite score (VAS) and food intake-behavior (TFEQ-R18)

	CON		MIE		HIE	
	Pre	Post	Pre	Post	Pre	Post
TFEQ-R18						
Cognitive Restraint	45.0 ± 28.4	63.6 ± 21.8	46.3 ± 28.9	31.4 ± 22.5†*	44.3 ± 23.0	45.3 ± 26.6
Uncontrolled Eating	49.4 ± 20.5	54.4 ± 12.7	52.2 ± 23.3	45.8 ± 35.8	55.8 ± 20.7	41.7 ± 18.0
Emotional Eating	51.3 ± 29.2	24.8 ± 14.9	56.3 ± 26.4	55.0 ± 23.9†	46.7 ± 24.6	50.1 ± 17.5†
Appetite score	48.8 ± 4.33	48.1 ± 3.86	46.0 ± 6.07	48.5 ± 9.38	48.8 ± 9.91	45.4 ± 7.37

Values are presented as mean ± SD

†Significantly different from the corresponding baseline (Pre) value ($P<0.05$);

*Significantly different from the corresponding CON value ($P<0.05$)

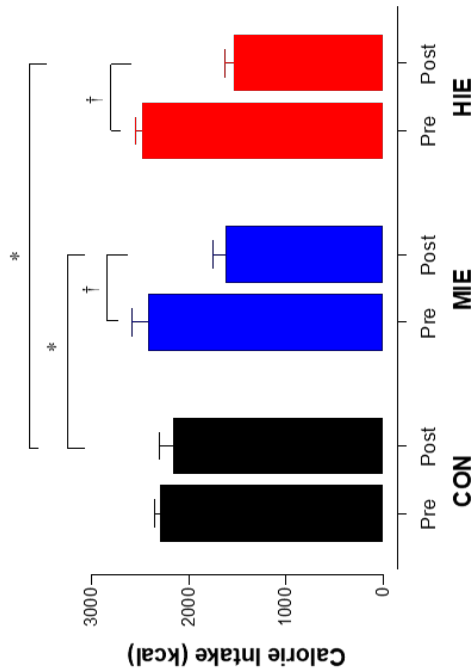


Figure 1. Mean ± SE total calorie intake at pre and post control (CON), moderate intensity exercise (MIE) and high-intensity exercise (HIE). †Significantly different from the corresponding baseline (pre) value ($P<0.05$); *Significantly different from CON condition ($P<0.05$).

post HIE (1622 ±460 kcal; $P=0.005$, $d_z=1.01$; 95% CI=233 to 1026) and post MIE (1533 ±339 kcal; $P=0.004$, $d_z=0.74$; 95% CI=206 to 875). Post calorie intake following MIE (mean difference: 795 kcal; $P<0.001$; 95% CI=403 to 1187) and HIE (mean difference: 943 kcal; $P<0.001$; 95% CI=4611 to 1276) was significantly lower from the corresponding pre-trial.

Fasting Blood [Glucose]

The group mean fasting blood [glucose] responses in the MIE, HIE, and CON conditions are illustrated in Figure 2. Baseline fasting blood [glucose] was not significantly different between conditions ($P>0.05$), and no significant change in fasting blood [glucose] was observed between pre and post CON trial ($P>0.05$). A trivial interaction effect of fasting blood [glucose] was observed throughout the intervention ($F_{(1.8, 20)}=4.2$, $P=0.03$, $\eta^2_p=0.13$), but no main effect of fasting blood [glucose] ($P>0.05$) were detected. Post hoc analysis revealed that fasting blood [glucose] following MIE (4.7 ±0.36 mmol) was significantly lower than post HIE (5.1 ±0.34 mmol; $P=0.03$, $d_z=0.74$; 95% CI=0.06 to 0.74) and post CON (5.0 ±0.36 mmol; $P=0.006$, $d_z=0.84$; 95% CI=-0.58 to -0.12).

Discussion

Reports of several previous investigations had shown that exercise (and exercise intensity) played a vital role in negative energy balance by exerting a suppression of energy intake in normal-weight adults. The present study aims to investigate the acute effects of MIE and HIE on the appetite score, eating behaviour and blood glucose regulation in obese men. Appetite score assessment was unaltered after a bout of MIE and HIE, compared to the CON condition. Our results contradict the belief that acute exercise might hamper weight loss efforts due to an acute change in hunger, fullness and satiety (King et al., 1996;

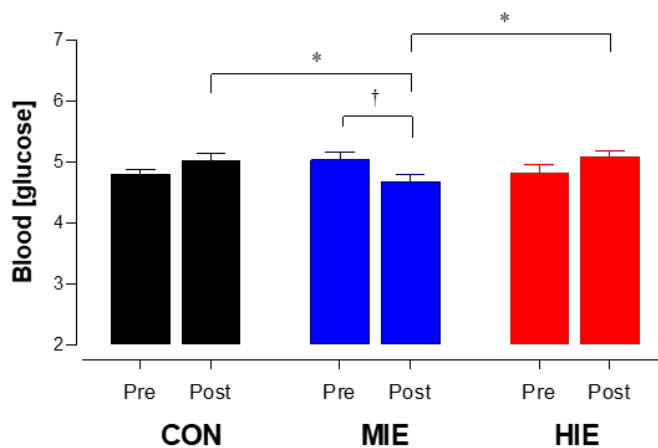


Figure 2. Mean ± SE fasting plasma [glucose] at pre and post control (CON), moderate intensity exercise (MIE) and high-intensity exercise (HIE). †Significantly different from the corresponding baseline (pre) value ($P<0.05$); *Significantly different from CON condition ($P<0.05$).

Pomerleau et al., 2004). Although the appetite score was not suppressed after an acute bout of exercise, as previously reported by Chanoine et al. (2008), we found that the total energy intake along with cognitive restraint levels were lowered in both modes of exercise intervention used in the current study. Unlike the usual dietary restriction methods which commonly result in a compensatory increase in energy intake (Taylor et al., 2018), the current investigation demonstrates that acute bout of exercise could induce energy deficit for at least ~180 min post-exercise. Overall, this finding suggests that both HIE and MIE can lower the total daily energy consumption. However, whether this improvement in energy deficit observed in obese adults could be preserved beyond the time point measured in the current study still remains unknown.

Over the past decade, the focus has been on investigating the intensity component of exercise as a way of facilitating the regulation of energy balance. Indeed, increasing exercise intensity enhances energy cost and promotes higher post-exercise energy expenditure. Fat oxidation increases the potential of skeletal muscles to utilise lipids and favours a decrease in energy intake. The central hypothesis of this study is that MIE and HIE would exert appetite suppression (as reflected by the acute decrease in energy intake), with higher intensity exercise eliciting a more significant suppression effect (Deighton et al., 2013). Although both exercise interventions attenuated the calorie intake post-exercise, the current study found no difference in the consumption of calories between both intensities of the exercises. It is worth noting that lowering of calorie intake observed in current study can be considered clinically significant, as indicated by considerable reduction in acute calories intake by 795 kcal and 943 kcal, post HIE and MIE, respectively. The US National Institutes of Health recommend that overweight or class I obese individual to reduce energy intake by 500 kcal·day⁻¹. It is estimated that overweight or class I obese to benefit a reduction of weekly body weight by 0.5 kg with daily calories deficit of 500 kcal (Fock & Khoo, 2013). Likewise, it has been suggested that, in diabetic population, a 1 mmol reduction in fasting glucose might reduce the risk of total stroke by 21% and ischemic heart disease by 23%. However, it is not known whether similar (or greater) reduction can be expected in overweight and obese population (Rodgers, 2004). Several past studies had shown that acylated ghrelin, which increases the desire to eat, was reduced and peptide YY concentration (PYY: a hormonal response which suppresses appetite desire) increased after moderate continuous exercise and high-intensity exercise (Martins et al., 2015; Ueda et al., 2009). Accordingly, Ueda et al. (2009) observed attenuation in psychological indices of appetite and total calorie intake in normal-weight subjects (Dorling et al., 2018). It was further discovered that suppression of appetite following exercise was corroborated with the finding of elevated biomarker related to the enhancement of satiety (i.e. GLP-1), which is speculated to result in reduced calorie intake of their obese subjects (Dorling et al., 2018; Ueda et al., 2009).

The food intake-behaviour was assessed using TFEQ, and the scale was selected due to its robust measure of cognitive restraint, uncontrolled eating and emotional eating (Chambers & Yeomans, 2008; Chanoine et al., 2008; Karlsson et al., 2000). Cognitive restraint is characterised by the restriction of food intake when conscious in order to influence and control body weight. As for uncontrolled eating, it represents the tendency to eat more than the regular intake because of loss of control over intake. Emotional eating characterises overeating or the inability to control eating due to a negative emotional mood, state or cues such as stress and loneliness (de Lauzon-Guillain et al., 2009). A model was proposed on how body mass, eating behaviour and physical activity could influence energy balance (Hill et al., 1995). This model proposes that one's susceptibility to physiologic cues of appetite (i.e. hunger, satiety and fullness) would be dependent on the individual's eating behaviours (i.e. cognitive restraint, uncontrolled eating and emotional eating). Using this model, it can be speculated that any changes in physical activity would individually (based on body weight and dietary behaviour) and directly affect a person's energy compensation.

Results of the current study did not reveal changes in uncontrolled eating behaviour in response to exercise. The results negate those of Hill et al. (1995) which found that being overweight with uncontrolled dietary behaviour lowered the energy intake with increased physical activity, resulting in overall negative energy balance. The current study observed higher emotional eating scores in the PRE and CON compared to the MIE and HIE conditions. Accordingly, previous studies had found a link between negative emotional eating behaviour as probed by TFEQ (Chambers & Yeomans, 2008; Chanoine et al., 2008; de Lauzon-Guillain et al., 2009). However, this is in contrast with the externality theory which asserts that the unresponsiveness of internal states found in obese individuals means that the population would unlikely be affected by emotional eating behaviour. In the current study, we observed that MIE lowered scores for cognitive dietary restraint. This study supports the evidence from previous observations in which overweight sedentary male subjects differed in terms of dietary restraints in response to an acute bout of moderate intensity exercise (Martins et al., 2008b). Contrary to expectations, this study did not find a significant change in cognitive restraint in response to HIE exercise. Logically, a more intense exercise is expected to enhance the awareness of food consumption, and thus, dietary restraint is expected for an individual who is actively monitoring to limit food intake.

Doucet et al. (2003) found no significant differences in the ratings of appetite sensations (hunger and satiety) in overweight participants before access to an *ad libitum* lunch (Doucet et al., 2003). The result of the present study revealed that there was no significant difference in VAS appetite score between and within groups. However, high-intensity exercise had shown a positive main effect. Despite no statistical differences observed within the experimental session, high-intensity exercise showed a trend of improvement in appetite suppression. According to Mattes and Cowart (1994), there is a lack of strong

influence between exercise and appetite because in some studies, VAS may not have been sensitive to detect specific minor changes after exercise due to small sample sizes. In contrast, a study on different modes and exercise intensities in healthy young men showed a correlation between appetite-regulating hormones and visual analogue scale. The study demonstrated acylated ghrelin and the ratings of VAS were suppressed while PYY increased during and immediately after the exercises (Kawano et al., 2013). Additionally, other studies further stated that ratings perceived from hunger, satiation and satiety were aligned with appetite-regulating hormones in suppressing the appetite (Martins et al., 2015; Stensel, 2011; Thackray et al., 2016; Ueda et al., 2009). The current study found significant reduction in blood [glucose] levels in response to MIE, but not for HIE and CON. However, it was noted that the reduction in blood [glucose] following MIE was clinically trivial. A possible explanation for this could be that a higher elevation of blood [lactate] (found in the previous study) may contribute to retarding the lowering of blood [glucose] during HIE (Guelfi et al., 2007; Júnior et al., 2001). However, this is only an extrapolation as this study did not measure the lactate level. The interference in the release of insulin and its response to skeletal muscle glucose uptake can be expected with vigorous activity, which may explain the higher blood [glucose] during post HIE compared to MIE. The gain in catecholamine levels in response to HIE found in the previous study may heighten renal glucose synthesis and simultaneously suppress the insulin-glucose uptake. It is suggested that portable glucometers may lack validity and reliability in comparison to laboratory glucose analysers, which provide more accurate results; similar to the industry reference standards (Salacinski et al., 2014). However, portable glucometers used in the current study seemingly produced valid and reliable results, as observed in previous studies (Chan et al., 1997; Naito et al., 1993). This demonstrates that the glucometer presently utilised was amply sensitive and appropriate for the blood glucose measurement.

CONCLUSION

In conclusion, this study has identified that MIE and HIE plays an essential role in negative energy balance by induced suppression of appetite and calories intake. These findings suggest that exercise (i.e. MIE and HIE) can reduce calories intake within 24-h post-intervention but may not be accounted for by changes in appetite score and eating behaviour.

ACKNOWLEDGEMENT

This research was funded by the Fundamental Research Grant Scheme (FRGS/1/2018/WAB13/UITM/03/1), Ministry of Higher Education, Malaysia. All authors read and approved the final manuscript. We thank the participants for their time and effort.

REFERENCES

- Alkahtani, S. A., Byrne, N. M., Hills, A. P., & King, N. A. (2014). Acute interval exercise intensity does not affect appetite and nutrient preferences in overweight and obese males. *Asia Pacific Journal of Clinical Nutrition*, 23(2), 232-238.
- Bailey, D. P., Smith, L. R., Christmas, B. C., Taylor, L., Stensel, D. J., Deighton, K., ... & Kerr, C. J. (2015). Appetite and gut hormone responses to moderate-intensity continuous exercise versus high-intensity interval exercise, in normoxic and hypoxic conditions. *Appetite*, 89, 237-245.
- Balaguera-Cortes, L., Wallman, K. E., Fairchild, T. J., & Guelfi, K. J. (2011). Energy intake and appetite-related hormones following acute aerobic and resistance exercise. *Applied Physiology, Nutrition, and Metabolism*, 36, 958-966.
- Bammann, K., Lissner, L., Pigeot, I., & Ahrens, W. (Eds.). (2019). *Instruments for Health Surveys in Children and Adolescents*. Cham, Switzerland: Springer International Publishing.
- Beaulieu, K., Hopkins, M., Blundell, J., & Finlayson, G. (2018). Homeostatic and non-homeostatic appetite control along the spectrum of physical activity levels: An updated perspective. *Physiology and Behavior*, 192, 23-29.
- Chambers, L., & Yeomans, M. R. (2008). Appetitive behaviours and the three factor eating questionnaire. *Appetite*, 50(2-3), 555-567.
- Chan, J. C. N., Wong, R. Y. M., Cheung, C. K., Lam, P., Chow, C. C., Yeung, V. T. F., ... Cockram, C. S. (1997). Accuracy, precision and user-acceptability of self blood glucose monitoring machines. *Diabetes Research and Clinical Practice*, 36(2), 91-104.
- Chanoine, J. P., MacKelvie, K. J., Barr, S. I., Wong, A. C. K., Meneilly, G. S., & Elahi, D. H. (2008). GLP-1 and appetite responses to a meal in lean and overweight adolescents following exercise. *Obesity*, 16, 202-204.
- de Lauzon-Guillain, B., Romon, M., Musher-Eizenman, D., Heude, B., Basdevant, A., & Charles, M. A. (2009). Cognitive restraint, uncontrolled eating and emotional eating: Correlations between parent and adolescent. *Maternal and Child Nutrition*, 5, 171-178.
- Deighton, K., Barry, R., Connon, C. E., & Stensel, D. J. (2013). Appetite, gut hormone and energy intake responses to low volume sprint interval and traditional endurance exercise. *European Journal of Applied Physiology*, 113(5), 1147-1156.
- Dorling, J., Broom, D., Burns, S., Clayton, D., Deighton, K., James, L., ... & Stensel, D. (2018). Acute and Chronic Effects of Exercise on Appetite, Energy Intake, and Appetite-Related Hormones: The Modulating Effect of Adiposity, Sex, and Habitual Physical Activity. *Nutrients*, 10(9), 1140-1160.
- Doucet, E., St-Pierre, S., Alm eras, N., & Tremblay, A. (2003). Relation between appetite ratings before and after a standard meal and estimates of daily energy intake in obese and reduced obese individuals. *Appetite*, 40, 137-143.
- Douglas, J. A., King, J. A., McFarlane, E., Baker, L., Bradley, C., Crouch, N., ... & Stensel, D. J. (2015). Appetite, appetite hormone and energy intake responses to two consecutive days of aerobic exercise in healthy young men. *Appetite*, 92, 57-65.

- Flint, A., Raben, A., Blundell, J. E., & Astrup, A. (2000). Reproducibility, power and validity of visual analogue scales in assessment of appetite sensations in single test meal studies. *International Journal of Obesity*, 24, 38-48.
- Fock, K. M., & Khoo, J. (2013). Diet and exercise in management of obesity and overweight. *Journal of Gastroenterology and Hepatology*, 28, 59-63.
- Guelfi, K. J., Ratnam, N., Smythe, G. A., Jones, T. W., & Fournier, P. A. (2007). Effect of intermittent high-intensity compared with continuous moderate exercise on glucose production and utilization in individuals with type 1 diabetes. *American Journal of Physiology-Endocrinology and Metabolism*, 292, E865-E870.
- Hill, J. O., Melby, C., Johnson, S. L., & Peters, J. C. (1995). Physical activity and energy requirements. *The American Journal of Clinical Nutrition*, 62(5), 1059S-1066S.
- Júnior, P. B., Neiva, C. M., & Denadai, B. S. (2001). Effect of an acute β -adrenergic blockade on the blood glucose response during lactate minimum test. *Journal of Science and Medicine in Sport*, 4(3), 257-265.
- Karlsson, J., Persson, L. O., Sjöström, L., & Sullivan, M. (2000). Psychometric properties and factor structure of the Three-Factor Eating Questionnaire (TFEQ) in obese men and women. Results from the Swedish Obese Subjects (SOS) study. *International Journal of Obesity*, 24, 1715-1725.
- Kawano, H., Mineta, M., Asaka, M., Miyashita, M., Numao, S., Gando, Y., ... & Higuchi, M. (2013). Effects of different modes of exercise on appetite and appetite-regulating hormones. *Appetite*, 66, 26-33.
- King, J. A., Miyashita, M., Wasse, L. K., & Stensel, D. J. (2010). Influence of prolonged treadmill running on appetite, energy intake and circulating concentrations of acylated ghrelin. *Appetite*, 54, 492-498.
- King, N. A., Snell, L., Smith, R. D., & Blundell, J. E. (1996). Effects of short-term exercise on appetite responses in unrestrained females. *European Journal of Clinical Nutrition*, 50(10), 663-667.
- Leow, S., Jackson, B., Alderson, J. A., Guelfi, K. J., & Dimmock, J. A. (2018). A role for exercise in attenuating unhealthy food consumption in response to stress. *Nutrients*, 10(2), 176-195.
- Martins, C., Morgan, L., & Truby, H. (2008a). A review of the effects of exercise on appetite regulation: an obesity perspective. *International Journal of Obesity*, 32, 1337-1347.
- Martins, C., Robertson, M. D., & Morgan, L. M. (2008b). Effects of exercise and restrained eating behaviour on appetite control. *Proceedings of the Nutrition Society*, 67(1), 28-41.
- Martins, C., Stensvold, D., Finlayson, G., Holst, J., Wisloff, U., Kulseng, B., ... & King, N. (2015). Effect of Moderate- and High-Intensity Acute Exercise on Appetite in Obese Individuals. *Medicine and Science in Sports & Exercise*, 47, 40-48.
- Mattes, R. D., & Cowart, B. J. (1994). Dietary assessment of patients with chemosensory disorders. *Journal of the American Dietetic Association*, 94, 50-56.
- Ministry of Health, N. D. (n.d.). *Panduan nilai kalori 200 jenis makanan* [Guideline of Calorie Value of 200 types of food]. Ministry of Health Malaysia. Retrieved July 9, 2018, from <http://www.moh.gov.my/english.php/pages/view/198>
- Naito, H. K., Kwak, Y. S., & Cottingham, C. (1993). Accuracy of the One Touch II whole blood glucose analyzer when used by analysts with diverse technical backgrounds. *Journal of Family Practice*, 37(2), 153-158.

- Oreopoulos, A., Padwal, R., Kalantar-Zadeh, K., Fonarow, G. C., Norris, C. M., & McAlister, F. A. (2008). Body mass index and mortality in heart failure: a meta-analysis. *American Heart Journal*, *156*, 13-22.
- Pomerleau, M., Imbeault, P., Parker, T., & Doucet, E. (2004). Effects of exercise intensity on food intake and appetite in women. *American Journal of Clinical Nutrition*, *80*, 1230-1236.
- Rodgers, A. (2004). Blood glucose and risk of cardiovascular disease in the Asia Pacific region. *Diabetes Care*, *27*(12), 2836-2842.
- Rothberg, L. J., Lees, T., Clifton-Bligh, R., & Lal, S. (2016). Association between heart rate variability measures and blood glucose levels: implications for noninvasive glucose monitoring for diabetes. *Diabetes Technology and Therapeutics*, *18*(6), 366-376.
- Sailer, C., Schmid, V., Fritsche, L., Gerter, T., Machicao, F., Niess, A., ... & Heni, M. (2016). FTO genotype interacts with improvement in aerobic fitness on body weight loss during lifestyle intervention. *Obesity Facts*, *9*, 174-181.
- Salacinski, A. J., Alford, M., Drevets, K., Hart, S., & Hunt, B. E. (2014). Validity and reliability of a glucometer against industry reference standards. *Journal of Diabetes Science and Technology*, *8*(1), 95-99.
- Shorten, A. L., Wallman, K. E., & Guelfi, K. J. (2009). Acute effect of environmental temperature during exercise on subsequent energy intake in active men. *American Journal of Clinical Nutrition*, *90*, 1215-1221.
- Sim, A. Y., Wallman, K. E., Fairchild, T. J., & Guelfi, K. J. (2014). High-intensity intermittent exercise attenuates ad-libitum energy intake. *International Journal of Obesity*, *38*(3), 417-422.
- Stensel, D. (2011). Exercise, appetite and appetite-regulating hormones: Implications for food intake and weight control. *Annals of Nutrition and Metabolism*, *57*(Suppl. 2), 36-42.
- Taylor, J., Keating, S. E., Holland, D. J., Coombes, J. S., & Leveritt, M. D. (2018). The Chronic Effect of Interval Training on Energy Intake: A Systematic Review and Meta-Analysis. *Journal of Obesity*, *2018*, 1-13.
- Thackray, A. E., Deighton, K., King, J. A., & Stensel, D. J. (2016). Exercise, appetite and weight control: Are there differences between men and women? *Nutrients*, *8*(9), 583-601.
- Ueda, S. Y., Yoshikawa, T., Katsura, Y., Usui, T., & Fujimoto, S. (2009). Comparable effects of moderate intensity exercise on changes in anorectic gut hormone levels and energy intake to high intensity exercise. *Journal of Endocrinology*, *203*, 357-364.
- World Health Organization. (2017). *WHO: Obesity and overweight*. Retrieved February 16, 2018, from <https://www.who.int/news-room/fact-sheets/detail/obesity-and-overweight>

Standardised Extracts of *Moringa Oleifera* and *Centella Asiatica* Enhanced the Antioxidant Activity, Learning and Memory Effects by Inhibiting Acetylcholinesterase Activity in D-Galactose Induced Ageing Rats

Hisyam Jamari¹, Mohd Salleh Rofiee¹, Richard James Johari^{1,2},
Mohd Zaki Salleh^{1,2} and Teh Lay Kek^{1,2*}

¹Integrative Pharmacogenomics Institute (iPROMISE), Universiti Teknologi MARA Selangor, 42300 Puncak Alam, Malaysia

²Faculty of Pharmacy, Universiti Teknologi MARA Selangor, 42300 Puncak Alam, Malaysia

ABSTRACT

The potential of *Moringa oleifera* Lam. (Moringaceae) and *Centella asiatica* (L.) Urban (Apiaceae) extracts (TGT-PRIMAAGE) in slowing the decline of memory and learning activity was investigated using D-galactose-induced ageing rat model. The extracts were profiled and standardised based on markers identified using LC/MS-QTOF. Toxicity study of the extract was done, and the rat did not show any sign of toxicity. The extract was orally administered to the rat and dose dependent (100, 500 and 1000 mg/kg) efficacy were investigated. The rats were subjected to Morris Water Maze whereby 3 parameters were studied (number of entry to platform, latency and novel object recognition).

Plasma was collected for the determination of catalase (CAT) activity and levels of malondialdehyde (MDA) and advanced glycation end products (AGEs). The activity of acetylcholinesterase (AChE), level of acetylcholine (ACh) and lipid peroxidation (LPO) were measured using the brain lysates. Significant improvement ($p < 0.05$) was seen in the memory and learning abilities in the aged rats that received medium and high dose of TGT-PRIMAAGE, and tocotrienol.

ARTICLE INFO

Article history:

Received: 3 August 2019

Accepted: 15 November 2019

Published: 13 January 2020

E-mail addresses:

hisyamjamari.ipromise@gmail.com (Hisyam Jamari)

bio_salleh82@yahoo.com (Mohd Salleh Rofiee)

ritchjj@yahoo.fr (Richard James Johari)

zakisalleh.ipromise@gmail.com (Mohd Zaki Salleh)

tehlakek@uitm.edu.my/ tehlakek2016@gmail.com

(Teh Lay Kek)

*Corresponding author

Rats treated with TGT-PRIMAAGE had also shown improved CAT activity and resulted in reduced LPO. The level of ACh was found increased in parallel with the reduced AChE activity. The capabilities of learning and memory of the TGT-PRIMAAGE treated rats were enhanced via inhibition of AChE activity and subsequently increased level of ACh.

Keywords: Anti-ageing, antioxidant, *Centella asiatica*, D-galactose, *Moringa oleifera*

INTRODUCTION

Globally, the life expectancy of a human is on the rise with the number of more than 65-year-old elderly is expected to double between 2000 and 2050 (Jin et al., 2015). With the advancement in the health care system, the life span is increased; this should be accompanied by an increased in health span by slowing or limiting the speed of the ageing process. As a natural phenomenon, ageing however, has been associated with chronic diseases which include Alzheimer's, diabetes mellitus and cancers (Prasad et al., 2011). There are several theories underlying the mechanism of ageing such as increased reactive oxygen species (ROS) or oxidative stress caused by the uncontrolled production of free radicals and decreased antioxidant defences as one ages (Davalli et al., 2016). Oxidative stress had been claimed to cause ageing via accumulated damages of the macromolecules within the cell leading to cellular dysfunction and eventually death (Harman, 1956; Harman, 1972; Sohal & Weindruch, 1996). Therefore, therapy that limits the excessive or uncontrolled oxidative stress will aid in slowing ageing.

A high dose of exogenous D-gal-induced ageing rat model which was used in this study had been adopted by many studies as a useful animal ageing model. High dose D-galactose was shown to accelerate ageing in rodents due to the production of superoxide anions and oxygen-derived free radicals (Li et al., 2005; Chen et al., 2006; Parameshwaran et al., 2010; Haidar et al., 2015; Budni et al., 2017). In addition, D-gal changes the structures of peptides and proteins and caused the accumulation of advanced glycation end (AGE) products through non-enzymatic glycation (Wu et al., 2008).

The search for antioxidant resources which reduces the oxidative stress slows the aging process is an on-going interest of the scientific community. The continuous efforts include the discovery of natural products with antioxidative potentials. The *Moringa oleifera* Lam. leaves has been reported to possess high phenolic content and potent antioxidant properties which act via direct trapping of free radicals and metal chelation (Verma et al., 2009). The leaves of several cultivars of *Moringa* are valuable sources of polyphenols and are potential functional food and nutraceuticals (Nouman et al., 2016). On the other hand, the leaf of *C. asiatica* also possesses important phytochemicals that have an antioxidant

activity such as carotenoids and phenolic compounds (Singh et al., 2014). *C. asiatica* extract was reported to have abilities in reducing α -glucosidase activity and scavenge free radical (Dewi & Maryani, 2015).

In this study, we investigated the potential of a combination extract of *Moringa oleifera* Lam. and *Centella asiatica* Urb. in arresting the oxidative stress due to high dose D-galactose injected peritoneally to the rats. The effects in enhancing the capabilities of memory and learning were also studied.

MATERIALS AND METHODS

Sources and Identification of Plant materials

The leaves extracts of both the *Moringa oleifera* and *Centella asiatica* were obtained from The Borneo Moringa Sdn. Bhd. (Malaysia) in Tenom, Sabah, Malaysia. The leaves carried the voucher identification number of Bm_mo_191012_1 and Mtt_ca_150113_1 for *Moringa oleifera* and *Centella asiatica*, respectively. The identification was done by Sandakan Herbarium Sabah Forestry Department, Sabah, Malaysia. The combination of the leave extracts of *M. oleifera* leaves and *C. asiatica* leaves is referred to as TGT-PRIMAAGE and was prepared by The MitoMasa Sdn. Bhd. Malaysia.

LCMS-based Profiles of TGT-PRIMAAGE

The active ingredients in each batch of the extracts of TGT-PRIMAAGE were profiled using LC/MS-QTOF for the purpose of standardising the extracts produced. The dried form of TGT-PRIMAAGE extract (1 mg/mL) were reconstituted in the mobile phase before being injected into LC-MS/QTOF (model 6520 Agilent Technologies, SA, USA) using a ZORBAX Eclipse Plus C18 column (100 mm x 2.1 mm x 1.8 μ m, Agilent Technologies, SA, USA) maintained at 40°C. The flow rate used was 0.25 mL/min with a linear gradient comprising solvent A (water with 0.1% formic acid) and solvent B (acetonitrile with 0.1% formic acid) over 36 minutes from 5% to 95% of mobile phase (B). The total run time was 48 minutes for each analysis. Electrospray ionization (ESI) source were set with V Cap 4000 V, skimmer 65 V and fragmentor 125 V. The nebulizer was set at 45 psig and the flow rate of nitrogen drying gas was set at 12 L/min. The drying gas temperature was maintained at 350°C. The range of data collected in positive ESI mode was from 100 to 1000 m/z . Two reference masses were continuously injected; i.e. 121.0509 m/z ($C_5H_4N_4$) and 922.0098 m/z ($C_{18}H_{18}O_6N_3P_3F_{24}$) to monitor and ensure detection of the accurate mass of the compounds. Agilent Mass Hunter Qualitative Analysis B.05.00 software (Agilent Technologies, Santa Clara, CA, USA) was used for the processing and analysis of the MS data. The chromatographic profiles of TGT-PRIMAAGE was analysed based on the accurate mass data identified and the possible chemical formula for compounds were

annotated using METLIN databased year 2012. The widely accepted accuracy threshold for confirmation was established at 5 ppm with score more than 90.

Acute Toxicity Study

An acute toxicity test was carried out according to the stepwise procedure by Organization of Economic Cooperation and Development (OECD) guideline 423 for testing of chemical.

Experimental Study Using the D-Galactose-Induced Ageing Rats

The protocol of the study was reviewed and approved by the Research Committee on the Ethical Use of Animal UiTM (UiTM CARE: 91/2015). Adult male Sprague Dawley rats (200-360 gram) were caged separately (one rat per cage) with access to a standard rodent diet. They were fed with 400 gm of pellets and tap water *ad libitum* with 12-hour light and dark cycle in a room at controlled temperature and humidity. The standard rodent diet comprised crude protein, fibre and fat, moisture, ash, calcium and phosphorus at 21, 5, 3, 13, 8, 0.8, 0.4%, respectively. The rats were exposed to the procedure of acclimatization for 1 week to minimize the psychological pressure of the environment and handling stress.

The D-galactose induced ageing rat model was developed according to Haider et al. (2015). The rats (n=21) were assigned into 7 groups (each group comprised of 3 rats):

- i. Normal control
- ii. D-GAL: ageing rats administered with 300 mg/kg of D-Galactose
- iii. TE: D-GAL rats treated with 200 mg/kg of Tocotrienol
- iv. P-100: D-GAL rats served with low dose (100 mg/kg) of TGT-PRIMAAGE
- v. P-500: D-GAL rats served with medium dose (500 mg/kg) of TGT-PRIMAAGE
- vi. P-1000: D-GAL rats served with high dose (1000 mg/kg) of TGT-PRIMAAGE

All the rats (except the normal controls) were intraperitoneally injected with D-galactose (300 mg/kg) for 7 days to induce ageing and three groups were orally administered with TGT-PRIMAAGE at different doses. Tocotrienol (TE) were used as the positive control. The physical states of the rats were observed every day to check for abnormalities with respect to behaviours and death. The rats were then subjected to memory and learning test 24 hours after the last injection on day 7.

Memory and Learning Test

The rats were subjected to Morris Water Maze (MWM) for the evaluation on spatial memory performance of the rats. A circular pool with an appropriate size was used (diameter of 1.8 metre top, 1.4-metre bottom, 1.4-metre height). The temperature of the water was kept at 25±1°C. In this experiment, the time taken by the rats to find the hidden platform

(latency) and the numbers of entry to the platform zone were recorded and analyzed using Any-Maze (Version 8, USA).

Object recognition memory was assessed using a white painted open-field maze box with the size of (52 cm x 52 cm x 52 cm). The novel object preference ratio was determined as the ratio of the amount of time spent exploring novel object over the total time exploring both novel & familiar objects. All the rats were sacrificed using an overdose of ketamine, and the rats were incinerated at the end of the study.

Measurement of Catalase (CAT) Activity in Plasma

Fifty (50) μ l of plasma samples were incubated with 1.0 ml of substrate (65 μ mol per ml H_2O_2 in 60 mmol/l phosphate buffer, pH 7.4) at 37°C for 60 seconds. The enzymatic reaction was stopped with 1.0 ml of 32.4 mmol/l ammonium molybdate ($(NH_4)_6Mo_7O_{24} \cdot 4H_2O$) and the yellow complex of molybdate and hydrogen peroxide was measured at 405 nm (Microplate Reader, POLARstar Omega, BMG LabTech, Germany) against blank. Three measurements were done for each sample. Serum CAT activity was calculated following the equation below:

$$\text{Serum CAT activity (kU/L)} = \frac{[A(\text{Blank 1}) - A(\text{Sample})]}{[A(\text{Blank 2}) - A(\text{Blank 3})]} \times 271$$

Where:

Blank 1 = Control, Blank 2 = Standard, Blank 3 = Reagent Blank, and 271 = Constant.

Measurement of Advanced Glycation End Products (AGEs) in Plasma

AGEs was measured using the quantitative sandwich enzyme immunoassay technique with an antibody specific for AGEs which had been pre-coated onto a microplate (Cusabio Biotech Co., Ltd, China). A concentration curve over the range from 3.9 μ g/ml to 250 μ g/ml was calibrated using the standards provided by the manufacturer. Plasma samples were diluted 20-fold with sample diluent provided. AGEs present in the samples were bound by the immobilized antibody while the unbound substances were removed and biotin-conjugated antibody specific for AGEs was added to the wells. Avidin conjugated Horseradish Peroxidase (HRP) and its substrates were added to the wells subsequent to removal of unbound avidin-enzyme. The optimal density of the colour developed was determined within 5 minutes by the use of microplate reader that was set to 450 nm (Microplate Reader, POLARstar Omega, BMG LabTech, Germany).

Lipid Peroxidation in Plasma

Thiobarbituric acid reactive substances (TBARS) which are the by-products of lipid peroxidation were measured according to the protocol provided by the supplier (Cayman's TBARS Assay, Cayman Chemical, Ann Arbor, MI). Briefly, 100 μ L of each of the plasma

sample was mixed with sodium dodecyl sulphate (SDS) solution and 4 mL of colour reagent. The colour reagent contains TBA, acetic acid and sodium hydroxide. The mixture was boiled for 1 hour and the reaction was stopped by leaving the mixture on ice for 10 min. The mixture was centrifuged at 2000 x g at 4°C for 10 min. The supernatant was subjected to spectrometry measurement at 530 nm using the Microplate Reader (POLARstar Omega, BMG LabTech, Germany).

Acetylcholine (ACh) Abundance in Brain Lysates

The level of acetylcholine (ACh) in the brain tissues of the rats were measured using EnzyChrom™ Acetylcholine Assay (BioAssay System, CA) in accordance with the manufacturer's instruction. ACh was hydrolyzed by acetylcholinesterase to choline which was oxidized by choline oxidase to betaine and H₂O₂. The resulting H₂O₂ reacted with a specific dye to form a pink coloured product. Twenty (20) µL of the supernatant from brain tissue lysates was mixed with 80 µL of working reagent and the intensity of colour change proportional to the acetylcholine concentration was measured at 570 nm (Microplate Reader, POLARstar Omega, BMG LabTech, Germany).

Acetylcholinesterase (AChE) in Brain Lysates

QuantiChrom™ Acetylcholinesterase Assay (BioAssay System, CA) was used to measure the concentration of AChE. Briefly, 200 µL of the reaction mixture containing 10 µL of the supernatant from the brain homogenate of each rat and 190 µL of the working reagent in the 96-well plate was prepared. The intensity of the colour change was measured at 412 nm at 2 time points; after 1 minute and after 9 minutes using microplate reader (POLARstar Omega, BMG LabTech, Germany). The activity of AChE was the difference of absorbance values between the samples and the standard.

Lipid Peroxidation in Brain Lysates

The procedure was the same as described in 2.4.1.3. In this assay, 100 µL of the supernatant from brain tissue lysates was used instead of plasma.

Statistical Analysis

The data collected were tabulated and analyzed using IBM SPSS ver. 22.0 (IBM Co., Armonk, NY, USA). The study parameters were presented as mean ± standard error and compared between different experimental groups using one-way analysis of variance (ANOVA), followed by post-hoc Tukey's test. The data was considered as statistically significant with p-value of less than 0.05.

RESULTS AND DISCUSSION

Standardised Compounds Profiled in TGTPRIMAAGE

The LCMS profile of the extract starting from retention time 7.5 to 13.5 minutes revealed the presence of 10 phenolic compounds (Figure 1; Table 1). The top ten most abundantly identified compounds were phenolic compounds, one of the compounds (brucine) belonged to alkaloids groups; two compounds (2'-Hydroxygenistein 7-(6''-malonylglucoside) and Iriflogenin 4'-O-glucoside) were isoflavonoids and the rest were flavonoids. These compounds were used as markers for standardisation of the batches of TGT-PRIMAAGE.

Most of the compounds found in the extract were flavonoid which belonged to the family of flavonoids glycosides. The compounds have been associated with a broad spectrum of health-promoting effects and are an indispensable component in a variety of medicinal applications including enhancing memory function by regulating proteins such as the cAMP response element-binding protein (CREB), involved in the expression of important gene related to memory (Krishnaveni, 2012). Standardisation of the extraction procedure are fundamentally important to produce batches of extracts with similar profiles of compounds and therefore ensure more consistent efficacy for routine use either as supplement or for alternative health promoting and maintenance therapy.

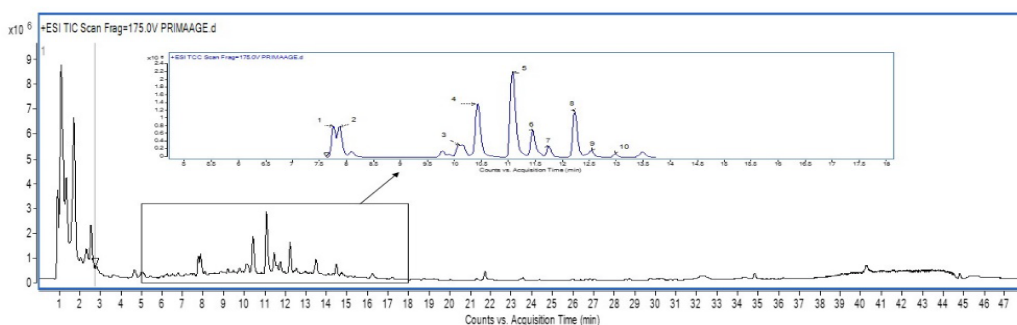


Figure 1. LC/MS Q-TOF total ion chromatogram (TIC) of TGT-PRIMAAGE extract

Acute Toxicity Study

Administration of the extract up to the maximum dose did not result in mortality or change in the behaviour of the animals. Thus, there is no evidence of acute toxicity of TGT-PRIMAAGE in rats.

Memory and Learning Tests

The number of platform entries achieved by the rats treated with medium dose (P-500) and high dose (P-1000) of TGT-PRIMAAGE was 3.89 ± 0.29 and 4.22 ± 0.40 , respectively

Table 1
Ten most abundantly identified phenolic compounds identified in TGT-PRIMAAGE

Peak number	Retention Time (min)	(M+H) ⁺ m/z	Error (ppm)	Score	Molecular Formula	Predicted LC-MS/MS Fragmentation – 10V	Predicted compound	Class
1	7.753	395.1965	-1.1	95.14	C23 H26 N2 O4	115.0393, 163.0576, 259.0799, 295.1021, 356.1156	Brucine	Alkaloid
2	7.868	595.1676	-3	94.12	C27 H30 O15	107.0494, 131.0536, 252.1118, 345.1078, 412.1453, 523.6995	Kaempferol 3-O-glucosyl-(1->2)-rhamnoside	Flavonoids
3	10.084	611.1611	-0.32	97.67	C27 H30 O16	107.0492, 213.1163, 262.0930, 386.0628, 480.0304, 577.1481	Isorhamnetin 3-O-[b-D-xylopyranosyl-(1->6)-b-D-glucopyranoside]	Flavonoids
4	10.427	465.1027	-0.06	98.75	C21 H20 O12	153.1252, 189.0756, 315.1791, 382.7752, 433.1265	Myricitrin	Flavonoids
5	11.068	551.1047	-2.99	94.45	C24 H22 O15	103.0423, 207.1605, 303.0478, 417.1183, 477.2124, 519.0181	Quercetin 3-O-(6-O-malonyl-β-D-glucoside)	Flavonoids
6	11.445	449.1088	-1.69	94.38	C21 H20 O11	107.0478, 208.1529, 287.0570, 356.9702	astragalin	Flavonoids
7	11.727	507.1133	-0.37	96.56	C23 H22 O13	107.0500, 163.0398, 211.1667, 287.0737, 341.1373, 428.4636, 499.1238	Quercetin 3-(6"-acetylglucoside)	Flavonoids

Table 1 (Continued)

Peak number	Retention Time (min)	(M+H) ⁺ m/z	Error (ppm)	Score	Molecular Formula	Predicted LC-MS/MS Fragmentation – 10V	Predicted compound	Class
8	12.222	535.1087	-1.3	96.72	C ₂₄ H ₂₂ O ₁₄	137.0596, 201.0952, 303.0526, 338.2431, 386.1955, 435.9733, 508.7124	2'-Hydroxygenistein 7-(6"-malonylglucoside)	Isoflavonoids
9	12.525	565.1188	-0.3	98.07	C ₂₅ H ₂₄ O ₁₅	127.0379, 239.1246, 287.0555, 329.0668, 400.9877, 448.9877, 503.0624	Isorhamnetin 3-(6"-malonylglucoside)	Flavonoids
10	12.913	491.1184	0.72	94.44	C ₂₃ H ₂₂ O ₁₂	107.0480, 129.0552, 205.0949, 248.1645, 355.1419, 394.2155, 463.3346	Iriflogenin 4'-O-glucoside	Isoflavonoids

(Figure 2). There was no significant difference in the number of platform entries achieved by these 2 groups of rats when compared with the rats that received tocotrienol (3.45 ± 0.40 ; Tukey HSD, $p > 0.05$). However, a significant difference was observed for the behaviour of the rats treated with low dose versus medium and high doses of TGT-PRIMAAGE (1.56 ± 0.11 ; Tukey HSD, $p < 0.05$).

For the escape platform (latency), rats induced with the D-galactose group took the longest time (30.84 ± 2.38 seconds) to reach the platform while the rats that received high dose TGT-PRIMAAGE took a shorter time (7.71 ± 0.61 seconds); which was significantly different (Tukey HSD, $p < 0.05$). There were also no significant difference in the latencies compared between the rats treated with high dose TGT-PRIMAAGE with (i) the normal control (6.30 ± 1.00 seconds; Tukey HSD, $p < 0.05$) and (ii) the rats that received tocotrienol (11.10 ± 3.30 seconds; Tukey HSD, $p < 0.05$). Rats treated with a low dose of TGT-PRIMAAGE had similar latency with the D-galactose induced ageing rats without treatment (30.73 ± 7.02 vs. 30.84 ± 2.38 , Tukey HSD, $p > 0.05$).

The differences in the ability to recognize novel object between the D-galactose induced ageing and the normal rats were statistically significant (Figure 2; 28.34 ± 1.87 vs 62.64 ± 5.86 ; Tukey HSD, $p < 0.05$). The rats treated with medium (72.41 ± 1.45) and a high dose of TGT-PRIMAAGE (83.62 ± 1.13) had a significant improvement (Tukey HSD test, $p < 0.05$) in the ability to recognize novel object compared to the D-Galactose group (28.34 ± 1.87). The improved ability was similar for the rats treated with medium and high dose of TGT-PRIMAAGE and tocotrienol (57.17 ± 11.93 ; Tukey HSD, $p > 0.05$). Interestingly, the rats treated with high dose TGT-PRIMAAGE had a higher percentage of time spent near the novel object, which indicates enhanced memory and learning ability as compared to the normal group (83.62 ± 1.13 vs. 62.64 ± 5.86 ; Tukey HSD test, $p < 0.05$).

The Morris water maze (MWM) is one of the most frequently used platforms to investigate spatial learning and memory in laboratory rats. The MWM had been used in the validation of rodent models for neurocognitive disorders and the evaluation of possible neurocognitive treatments (D'Hooge and De Deyn, 2001). MWM was used to test for spatial learning that relied on distal cues to navigate from the start locations around the perimeter of an open swimming arena to locate a submerged escape platform. Spatial learning is assessed across repeated trials and reference memory is determined by a preference for the platform area when the platform is absent (Vorhees and Williams, 2006). In addition, non-spatial object recognition memory task tests were conducted to study the memory for previously explored objects (Clark et al., 2000). The task, which requires no deprivation or punishment, is based on the rats' innate tendency to preferentially explore novel versus familiar objects. Task performance depends on an intact hippocampal function (Clark et al., 2000). Ageing tends to cause an impairment in the visual object recognition memory (Pilotti et al., 2003). Based on the tests conducted, rats treated with a medium and a high

dose of TGT-PRIMAAGE had gained better learning and memory abilities compared to the rats that were not treated. In fact, the rats treated with high dose TGT-PRIMAAGE showed significantly higher improvement in the latency and novel object recognition tests compared to the rats treated with tocotrienol.

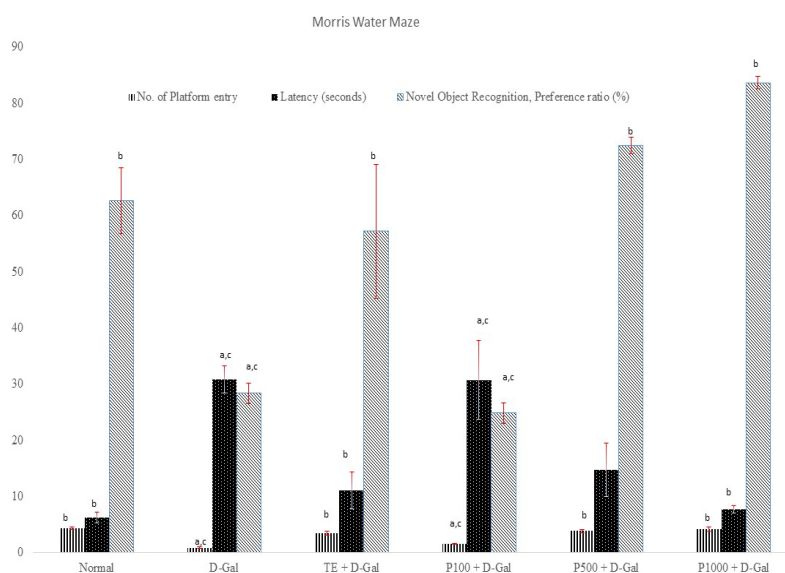


Figure 2. Cognitive activity of normal rats, untreated and pre-treated rats induced with D-galactose. * **Mean number of platform entries in Morris Water Maze test** with S.E.M in different group. a, $p < 0.05$: significantly different when compared to normal group (Tukey HSD test). b, $p < 0.05$: significantly different when compared to D-galactose (Tukey HSD test). c, $p < 0.05$: significantly different when compared to TE (Tukey HSD test). * **Mean latency to reach platform in Morris Water Maze test** with S.E.M in different group. a, $p < 0.05$: significantly different when compared to Normal group (Tukey HSD test). b, $p < 0.05$: significantly different when compared to D-Galactose group (Tukey HSD test). c, $p < 0.05$: significantly different when compared to TE (Tukey HSD test). * **Novel object preference ratio in novel object recognition test** with S.E.M in different group. a, $p < 0.05$: significantly different when compared to normal group (Tukey HSD test). b, $p < 0.05$: significantly different when compared to D-galactose group (Tukey HSD test). c, $p < 0.05$: significantly different when compared to TE (Tukey HSD test)

Catalase (CAT) Activity in Plasma

D-galactose induced a significant decrease of CAT activity in the rats as compared to the rats in the normal control (Figure 2, 57.28 ± 6.80 vs. 78.32 ± 4.26 kU/L; Tukey HSD, $p < 0.05$). Interestingly, CAT activities in all the three groups of rats treated with TGT-PRIMAAGE (low dose, 75.89 ± 2.91 kU/L; medium dose, 90.79 ± 0.95 kU/L; high dose, 94.44 ± 3.69 kU/L) were found to be elevated with significant differences compared to the D-Galactose group (Figure 3). The CAT activities increased as the doses of TGT-PRIMAAGE were increased. Furthermore, the catalase activity of the rats that received medium and high dose TGT-PRIMAAGE had significantly higher CAT activities compared to the rats that received tocotrienol (63.39 ± 1.90 kU/L; Tukey HSD, $p > 0.05$).

Catalase (CAT) is an enzyme involved in antioxidant defence by neutralising radicals produced by D-galactose (Bolzán et al., 1997). Current study showed that ageing rats had the lowest catalase activity while ageing rats supplemented with TGT-PRIMAAGE higher catalase activity. This is a useful indicator that TGT-PRIMAAGE is beneficial in slowing down the ageing processes by reducing the free radicals induced by D-Galactose.

Advanced Glycation End Products (AGEs) in Plasma

In the anti-glycation assay, the AGEs levels in the D-galactose induced rats were significantly elevated compared to the normal control (Figure 3, $294.97 \pm 16.67 \mu\text{g/mL}$ vs. $212.77 \pm 3.35 \mu\text{g/mL}$; Tukey HSD, $p < 0.05$). D-galactose induced ageing rats that received a medium ($248.67 \pm 2.98 \mu\text{g/mL}$) and high dose ($236.17 \pm 1.71 \mu\text{g/mL}$) of TGT-PRIMAAGE and tocotrienol showed significantly lower levels of AGEs compared with the ageing rats without treatment (Figure 3). Interestingly, rats that received tocotrienol ($233.18 \pm 2.99 \mu\text{g/mL}$) and high dose TGT-PRIMAAGE ($236.17 \pm 1.71 \mu\text{g/mL}$) had AGEs level similar with the normal control ($212.77 \pm 3.35 \mu\text{g/mL}$).

AGEs are the end results of a chain of chemical reactions involving an initial glycation reaction. AGEs originate from the non-enzymatic glycation reaction between sugars and protein, nucleic acids or lipid. AGEs were therefore higher in D-galactose induced ageing rats due to the higher glucose concentrations injected to the rats. High level of AGEs in serum is recognized as an ageing-related biomarker (Ramasamy et al., 2005). TGT-PRIMAAGE was found to reduce the level of AGEs. The high dose of TGT-PRIMAAGE and tocotrienol showed a similar reduction in the level of AGEs. Ascorbic acid and vitamins had been demonstrated previously to blocks glycation of erythrocyte haemoglobin by inhibiting *in vitro* lipid peroxidation and being regarded as both a glycation and AGE inhibitor (Vinson et al., 1996). In this study, TGT-PRIMAAGE had shown the ability to inhibit lipid peroxidation and reduced the levels of AGEs.

Lipid Peroxidation (MDA) in Plasma

MDA level was significantly higher in the D-galactose induced rats compared to the normal control (Figure 3, 627.90 ± 98.95 vs. $438.70 \pm 36.04 \text{ nmol/mL}$; Tukey HSD, $p < 0.05$). The effect of high dose TGT-PRIMAAGE was slightly higher than tocotrienol (507.16 ± 56.44 vs. $571.70 \pm 84.58 \text{ nmol/mL}$, Tukey HSD, $p > 0.05$) but no significant difference was observed. The results suggested dose-dependent reduction of the levels of MDA by TGT-PRIMAAGE (Figure 3).

MDA is a sensitive index for the lipid peroxidation induced by free radicals which may lead to oxidative deterioration of polyunsaturated lipids. Under the normal physiological conditions, only low levels of lipid peroxidation occur in the tissue of the body; while

excessive generation of free radicals leads to peroxidative changes that result in an increase in lipid peroxidation (Niki et al., 1993; Rikans & Hornbrook, 1997).

Ageing is associated with increased disruption of membrane lipids which leads to the formation of peroxide radicals. Lipids are a major component of living organisms and probably the first easy target of free radicals thus lipid peroxidation might play an important role in initiating and/or mediating some aspects of the ageing process (Praticò, 2002). In this study, the level of MDA was significantly higher (Tukey HSD, $p < 0.05$) in the D-galactose group as compared with the normal and the tocotrienol and TGT-PRIMAAGE treated groups. Interestingly, the medium and high dose of TGT-PRIMAAGE showed a better potential in arresting lipid peroxidation in both the blood and brain samples. A dose-dependent effect was observed, the higher the dose of TGT-PRIMAAGE the lower the MDA levels. TGT-PRIMAAGE had protected the cells against oxidative stress by reducing lipid peroxidation products as measured systemically and in the brain.

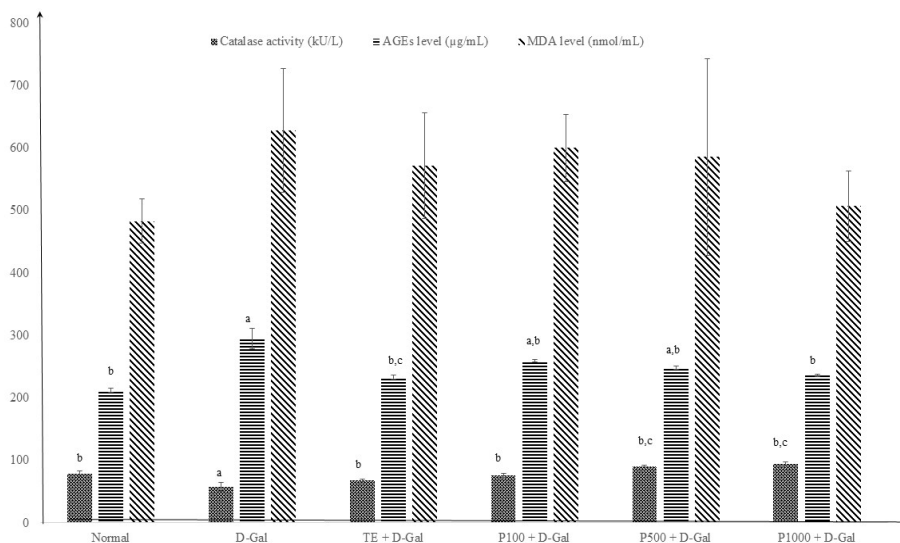


Figure 3. Catalase activity, AGEs and MDA levels in the plasma samples of the rats with different treatment. ***Mean value of assay.** a, $p < 0.05$ significantly different when compared to Normal group (Tukey HSD test). b, $p < 0.05$ significantly different when compared to D-Galactose group (Tukey HSD test) c, $p < 0.05$ significantly different when compared to TE (Tukey HSD test).

Lipid Peroxidation (MDA) in Brain Lysates

Similar to the trend observed for MDA level in the plasma samples, the MDA levels in the brain lysate was higher in the D-galactose induced rats compared to the normal control (Table 2, 12.64 ± 0.67 vs. 7.05 ± 0.34 nmol/mL; Tukey HSD, $p < 0.05$). The MDA levels

in the rats which received treatment of tocotrienol and 100 mg/kg of TGT-PRIMAGES were higher than those measured in the D-galactose induced ageing rats. Rats treated with medium (7.75 ± 0.56 nmol/mL) and high dose (7.52 ± 0.28 nmol/mL) of TGT-PRIMAAGE achieved significantly lower levels of MDA in the brain lysates compared to non-treatment group. The data is presented in Table 2.

Acetylcholinesterase Activity and Acetylcholine Levels in Brain Lysates

Non treated rats induced with D-galactose showed the highest level of acetylcholinesterase activity compared to the control and treatment groups (236.23 ± 6.85 U/L). There is a dose-dependent effect in a decreasing trend of the level of acetylcholinesterase activity in groups of rats treated with TGT-PRIMAAGE. The higher the dose of TGT-PRIMAAGE, the lower the level of acetylcholinesterase activity. Rats treated with the medium (141.44 ± 11.81 U/L) and high dose (138.63 ± 8.1 U/L) of TGT-PRIMAAGE had levels which are lower than the normal control (170.39 ± 5.33 U/L) and tocotrienol (148.88 ± 3.75 U/L) treated rats. The data is presented in Table 2.

The level of acetylcholine was the highest in the normal control, not induced with D-galactose (269.52 ± 22.32 μ M); while the level was the lowest in the non-treated D-galactose ageing rats (85.71 ± 6.23 μ M). The acetylcholine levels were similar among the rats treated with tocotrienol (151.43 ± 11.55 μ M), medium dose TGT-PRIMAAGE (142.38 ± 9.67 μ M) and high dose TGT-PRIMAAGE (152.86 ± 3.78 μ M). The data is presented in Table 2.

ACh is a cholinergic neurotransmitter that plays important role in regulating the cognitive functions of the brain. AChE hydrolyzes ACh into acetate and choline, resulting in the termination of synaptic transmission (Zugno et al., 2014). Anwar et al. (2012) reported that phenolic compounds decreased AChE activity in the cerebral cortex and striatum of adult Wistar rats resulting in higher ACh in the rats and better cognitive function. In this study, the memory-enhancing effect of TGT-PRIMAAGE was found to be accompanied by increasing cholinergic activity in the brain of the rats. The present study found that TGT-PRIMAAGE inhibited AChE activity and at the same time enhanced ACh in treated rats. AChE activity was inhibited in a dose-dependent manner for the rats that were treated with TGT-PRIMAAGE in comparison with the rats without treatment. AChE activity was also inhibited in the rats that received tocotrienol in comparison with rats induced by D-galactose. There were no significant differences in the inhibitory effect of AChE in the normal control and tocotrienol treated group on the AChE. The level of ACh was reduced in the D-galactose induced rats compared to the normal control rats. The levels of ACh increased as the doses of TGT-PRIMAAGE were increased.

Table 2
Lipid peroxidation (MDA), acetylcholinesterase activity and the level of acetylcholine in the brain lysates of the rats

	Normal	D-Gal	TE + D-Gal	P100 + D-Gal	P500 + D-Gal	P1000 + D-Gal
MDA (nmol/mL)	7.05±0.34 ^{b,c}	12.64±0.67 ^{a,b,c}	15.86±0.65 ^{a,b,c}	18.96±0.21 ^{a,b,c}	7.75±0.56 ^{b,c}	7.52±0.28 ^{b,c}
Acetylcholinesterase (U/L)	170.39±5.33 ^b	236.23±6.85 ^{a,c}	148.88±3.75 ^b	158.48±3.87 ^b	141.44±11.81 ^b	138.63±8.10 ^b
Acetylcholine (µM)	269.52±22.32 ^{b,c}	85.71±6.23 ^{a,c}	151.43±11.55 ^{a,b}	104.29±3.60 ^a	142.38±9.67 ^{a,b}	152.86±3.78 ^{a,b}

***Mean value of assay.** a, p<0.05 significantly different when compared to Normal group (Tukey HSD test), b, p<0.05 significantly different when compared to D-Galactose group (Tukey HSD test) c, p<0.05 significantly different when compared to TE (Tukey HSD test).

CONCLUSION

TGT-PRIMAAGE increased the antioxidant capacity by increasing CAT activity. With reduced oxidative stress, the levels of MDA and AGEs were reduced. The supplementation of TGT-PRIMAAGE to the ageing rats also showed improvement in memory and learning abilities by inhibiting acetylcholinesterase activity and increasing the level of acetylcholine.

ABBREVIATIONS

CAT – Catalase

D-gal – D-galactose

AGEs – Advanced glycation end products

MDA – Malondialdehyde

TE – Tocotrienol

ACKNOWLEDGEMENTS

This study was conducted at the Integrative Pharmacogenomics Institute (iPROMISE) and Laboratory Animal Facility and Management (LAFAM), Faculty of Pharmacy, Universiti Teknologi MARA (UiTM), Malaysia. This study was funded by the Ministry of Agriculture & Agro-Based Industry Malaysia (KP/HDO/S/34-9), The Mitomasa Sdn. Bhd. and Bestari Grant UiTM (600-IRMI/DANA 5/3/BESTARI (066/2017)).

ETHICS STATEMENT

All the protocol was approved by the Research Committee on the Ethical Use of Animal UiTM (UiTM CARE: 91/2015 dated 1 July 2015).

REFERENCES

- Anwar, J., Spanevello, R. M., Thome, G., Stefanello, N., Schmatz, R., Gutierrez, J., ... & Rubin, M. A. (2012). Effects of caffeic acid on behavioral parameters and on the activity of acetylcholinesterase in different tissues from adult rats. *Pharmacology Biochemistry and Behavior*, *103*(2), 386-394.
- Bolzán, A. D., Bianchi, M. S., & Bianchi, N. O. (1997). Superoxide dismutase, catalase and glutathione peroxidase activities in human blood: influence of sex, age and cigarette smoking. *Clinical Biochemistry*, *30*(6), 449-454.
- Budni, J., Garcez, M. L., Mina, F., Bellettini-Santos, T., Da Silva, S., Da Luz, A. P., ... & Quevedo, J. (2017). The oral administration of D-galactose induces abnormalities within the mitochondrial respiratory chain in the brain of rats. *Metabolic Brain Disease*, *32*(3), 811-817.
- Chen, C. F., Lang, S. Y., Zuo, P. P., Yang, N., Wang, X. Q., & Xia, C. (2006). Effects of D-galactose on the expression of hippocampal peripheral-type benzodiazepine receptor and spatial memory performances in rats. *Psychoneuroendocrinology*, *31*, 805-811.

- Clark, R. E., Zola, S. M., & Squire, L. R. (2000). Impaired recognition memory in rats after damage to the hippocampus. *The Journal of Neuroscience*, *20*(23), 8853-8860.
- Davalli, P., Mitic, T., Caporali, A., Lauriola, A., & D'Arca, D. (2016). ROS, cell senescence, and novel molecular mechanisms in aging and age-related diseases. *Oxidative Medicine and Cellular Longevity*, *2016*, 1-18.
- D'Hooge, R., & De Deyn, P. P. (2001). Applications of the Morris water maze in the study of learning and memory. *Brain Research Reviews*, *36*(1), 60-90.
- Dewi, R. T., & Maryani, F. (2015). Antioxidant and α -Glucosidase inhibitory compounds of *Centella Asiatica*. *Procedia Chemistry*, *17*, 147-152.
- Haider, S., Liaquat, L., Shahzad, S., Sadir, S., Madiha, S., Batool, Z., ... & Perveen, T. (2015). A high dose of short term exogenous D-galactose administration in young male rats produces symptoms simulating the natural aging process. *Life Sciences*, *124*, 110-119.
- Harman, D. (1956). Aging: a theory based on free radical and radiation chemistry. *Journal of Gerontology*, *11*(3), 298-300.
- Harman, D. (1972). The biologic clock: the mitochondria? *Journal of the American Geriatrics Society*, *20*(4), 145-147.
- Jin, K., Simpkins, J. W., Ji, X., Leis, M., & Stambler, I. (2015). The critical need to promote research of aging and aging-related diseases to improve health and longevity of the elderly population. *Aging Disease*, *6*(1), 1-5.
- Krishnaveni, M. (2012). Flavonoid in enhancing memory function. *Journal of Pharmacy Research*, *5*(7), 3870-3874.
- Li, L., Ng, T. B., Gao, W., Li, W., Fu, M., Niu, S. M., ... & Liu, F. (2005). Antioxidant activity of gallic acid from rose flowers in senescence accelerated mice. *Life Sciences*, *77*(2), 230-240.
- Niki, E., Noguchi, N., & Gotoh, N. (1993). Dynamics of lipid peroxidation and its inhibition by antioxidants. *Biochemical Society Transactions*, *21*(2), 313-317.
- Nouman, W., Anwar, F., Gull, T., Newton, A., Rosa, E., & Domínguez-Perles, R. (2016). Profiling of polyphenolics, nutrients and antioxidant potential of germplasm's leaves from seven cultivars of *Moringa oleifera* Lam. *Industrial Crops and Products*, *83*, 166-176.
- Parameshwaran, K., Irwin, M. H., Steliou, K., & Pinkert, C. A. (2010). D-Galactose effectiveness in modeling aging and therapeutic antioxidant treatment in mice. *Rejuvenation Research*, *13*(6), 729-735.
- Pilotti, M., Meade, M. L., & Gallo, D. A. (2003). Implicit and explicit measures of memory for perceptual information in young adults, healthy older adults, and patients with Alzheimer's disease. *Experimental Ageing Research*, *29*(1), 15-32.
- Prasad, S., Sung, B., & Aggarwal, B. B. (2011). Age-associated chronic diseases require age-old medicine: role of chronic inflammation. *Preventive Medicine*, *54*(Suppl), S29-S37.
- Praticò, D. (2002). Lipid peroxidation and the aging process. *Science of Aging Knowledge Environment*, *2002*(50), 1-4.

- Ramasamy, R., Vannucci, S. J., Yan, S. S. D., Herold, K., Yan, S. F., & Schmidt, A. M. (2005). Advanced glycation end products and RAGE: a common thread in aging, diabetes, neurodegeneration, and inflammation. *Glycobiology*, *15*(7), 16R-28R.
- Rikans, L. E., & Hornbrook, K. R. (1997). Lipid peroxidation, antioxidant protection and aging. *Biochimica et Biophysica Acta (BBA)-Molecular Basis of Disease*, *1362*(2), 116-127.
- Singh, S., Singh, D. R., Banu, V. S., & Avinash, N. (2014). Functional constituents (micronutrients and phytochemicals) and antioxidant activity of *Centella asiatica* (L.) Urban leaves. *Industrial Crops and Products*, *61*, 115-119.
- Sohal, R. S., & Weindruch, R. (1996). Oxidative stress, caloric restriction, and aging. *Science*, *273*, 59-63.
- Verma, A. R., Vijayakumar, M., Mathela, C. S., & Rao, C. V. (2009). In vitro and in vivo antioxidant properties of different fractions of *Moringa oleifera* leaves. *Food and Chemical Toxicology*, *47*(9), 2196-2201.
- Vinson, J. A., & Howard, T. B. (1996). Inhibition of protein glycation and advanced glycation end products by ascorbic acid and other vitamins and nutrients. *The Journal of Nutritional Biochemistry*, *7*(12), 659-663.
- Vorhees, C. V., & Williams, M. T. (2006). Morris water maze: procedures for assessing spatial and related forms of learning and memory. *Nature Protocols*, *1*(2), 848-858.
- Wu, D. M., Lu, J., Zheng, Y. L., Zhou, Z., Shan, Q., & Ma, D. F. (2008). Purple sweet potato color repairs d-galactose-induced spatial learning and memory impairment by regulating the expression of synaptic proteins. *Neurobiology of Learning and Memory*, *90*(1), 19-27.
- Zugno, A. I., Matos, M. P., Canever, L., Fraga, D. B., De Luca, R. D., Ghedim, F. V., ... & Volpato, A. M. (2014). Evaluation of acetylcholinesterase activity and behavioural alterations induced by ketamine in an animal model of schizophrenia. *Acta Neuropsychiatrica*, *26*(1), 43-50.

Toxicity Assessment of Gallic Acid Loaded Graphene Oxide (GAGO) Nano-Formulation in Zebrafish (*Danio Rerio*) Embryos

Ahmad Ashrafu Hadi Abdul Ghafor¹, Nurhuda Elias², Suhaili Shamsi²,
Faizah Md Yasin³ and Seri Narti Edayu Sarchio^{1*}

¹Department of Biomedical Science, Faculty of Medicine and Health Sciences, Universiti Putra Malaysia, 43400 UPM, Serdang, Selangor, Malaysia

²Department of Biochemistry, Faculty of Biotechnology and Biomolecular, Universiti Putra Malaysia, 43400 UPM, Serdang, Selangor, Malaysia

³Institute of Advanced Technology, Universiti Putra Malaysia, 43400 UPM, Serdang, Selangor, Malaysia

ABSTRACT

Gallic acid (GA) is a phenolic compound found in almost all plants and has been reported to possess powerful health benefits such as anti-oxidant, anti-inflammatory, anti-cancer, and anti-diabetic properties. However, GA suffers a short half-life when administered *in vivo*. Recent studies have employed graphene oxide (GO), a biocompatible and cost-effective graphene derivative, as a nanocarrier for GA. However, the toxicity effect of this formulated nano-compound has not been fully studied. Thus, the present study aims to evaluate the toxicity and teratogenicity of GA loaded GO (GAGO) against zebrafish embryogenesis to further advance the development of GA as a therapeutic agent. GAGO was exposed to zebrafish embryos ($n \geq 10$; 24hr post fertilization (hpf)) at different concentrations (0-500

$\mu\text{g/ml}$). The development of zebrafish was observed and recorded twice daily for four days. The toxicity of pure GO and GA was also observed at similar concentrations. Distilled water was used as control throughout the experiment. A significantly high mortality rate, delayed hatching rate and low heartbeat were recorded in embryos exposed to GO at concentrations of $\geq 150 \mu\text{g/ml}$ at 48 hr ($p < 0.01$), 72 hr ($p < 0.001$) and 96 hr ($p < 0.0001$) post-

ARTICLE INFO

Article history:

Received: 29 August 2019

Accepted: 27 November 2019

Published: 13 January 2020

E-mail addresses:

ahmadashrafhadi@gmail.com

(Ahmad Ashrafu Hadi Abdul Ghafor)

nurhudaelias1806@gmail.com (Nurhuda Elias)

sh_suhaili@upm.edu.my (Suhaili Shamsi)

fmy@upm.edu.my (Faizah Md Yasin)

serinarti@upm.edu.my (Seri Narti Edayu Sarchio)

*Corresponding author

exposure. Interestingly, all measured parameters were significantly improved in embryos exposed to the same concentration of GAGO (100-150 µg/ml), which was comparable to control group at all-time points. The present data demonstrated that GAGO is safe to be used at low concentration exposure (0-150 µg/ml), but further study has to be conducted to correlate the toxicity of GAGO with its effective concentration in *in vitro* and *in vivo* model.

Keywords: Gallic acid, graphene oxide, nanoparticles, toxicity, zebrafish embryo

INTRODUCTION

In recent years, the advancement and development of nanotechnology have been used in various kinds of areas such as engineering, biotechnology and also in medicine. Nanomaterial can be defined as a particle or constituent that is produced by nanotechnology at nano-scale dimension. Nanomaterials characteristic which have small properties in size can aid in the study of drug mechanism to increase the therapeutic efficiency. There is a significant advantage of using nanomaterial in medicine for the diagnosis and treatment of diseases, especially in drug delivery. The ability of nanomaterials is mostly based on their physical properties which can carry drug or compound on their surface plane. Thus, it can enhance the drug to transport directly into the targeted site.

Graphite is a carbon compound made up by single or multi-layer sheets of graphene films consist of single lattice-shaped carbon layer with atomic thickness (Sheshmani & Fashapoyeh, 2013). Meanwhile, graphene oxide (GO) consists of a single-atom-thick layer of graphene sheets with hydroxyl, carboxylic acid and epoxide groups on the surface plane (Dikin et al., 2007). It is produced when graphite undergoes oxidation process, in which oxygenated functionalities are introduced in the graphite structure, and thus expand the layer separation. This structure makes the material more hydrophilic on its basal planes and edges which aid GO to produce water stability suspension and is easily exfoliated into monolayer sheets (Sheshmani & Fashapoyeh, 2013).

GO nanoparticle has tremendous properties and application features according to its physical (light), strength, good thermal, and electrical conductivity such as polymer composites, sensors, 'paper'-like materials, field-effect transistors, energy-related materials and biomedical applications (Yang et al., 2013; Geim & Novoselov., 2007). GO can also be applied in energy storage, nanoelectronics devices, biosensors, drug delivery, cell imaging and tissue engineering (Yang et al., 2011). GO is fluorescent, which makes it especially suitable for various medical applications. Previous studies have reported that GO has anti-microbial activity against gram-negative and gram-positive bacteria (Hu et al., 2010; Santos et al., 2012; Shamsi et al., 2018). In addition, due to its low toxicity, GO has also been investigated for targeted drug delivery in cancer therapy (Chang et al., 2011). GO has a

high surface area and this enables a lot more drugs to be loaded onto its surface. This could potentially reduce the side effects of the current cancer treatment (Danovich et al., 2017).

Gallic acid (GA), 3,4,5-trihydroxybenzoic acid, a type of phenolic acid, is commonly found in gallnuts, sumac, oak bark and many other plants (Dorniani et al., 2012). Previous study has reported that GA has anti-cancer properties by suppressing tumor angiogenesis (Lu et al., 2010). GA also dominates various physiological functions like anti-aging, anti-inflammatory, anti-carcinogenic and anti-melanogenic activity (Dorniani et al., 2016). However, GA suffers a short half-life when administered *in vivo*. GA has specific conformation with three adjacent aromatic phenoxy groups involved in intra- and inter-molecular hydrogen bonding, which is exhibited in binding and it also exhibits strong chelating abilities with numerous inorganic ligands and proteins (Masoud et al., 2012; Rawel et al., 2006). These unique characteristics allow GA to be modified and loaded to the drug carrier, such as GO.

Zebrafish has emerged as a powerful *in vivo* model system for small molecule screening which is utilized as the alternative model organism for rodent. It is a good model for its unique characteristics which are small, transparent and fast developing eggs that aid high throughput chemical screening and short generation times (Gerlai et al., 2009). In addition, zebrafish also features 70% of genetic homology to human, robust, phenotypes, high-throughput genetic and it also exhibits similar physiological responses, especially during the development of chronic diseases (Howe et al., 2013). Zebrafish can act as an attractive model for studies that aimed at understanding toxic mechanisms, morphological assessment and environmental risk assessment of chemicals such as oxidative stress indices and anti-oxidant parameters.

In this study, we have selected GO as the nanocarrier to create composite nanoparticles that incorporate GA for active drug delivery, GAGO. This nanocompound is believed to produce beneficial synergistic properties especially in anti-cancer (Dorniani et al., 2016) and anti-microbial (Shamsi et al., 2018) activities. However, the underlining toxic effects of GAGO are still largely unclear, especially at the critical period of embryogenesis. Thus, the present study was intended to evaluate the toxicity and teratogenicity effects of a newly formulated nanocomposite compound, as well as its pure forms, GA and GO, in zebrafish embryogenesis.

MATERIALS AND METHODS

Graphene Oxide (GO) Synthesis

An improved Hummers method was used to synthesize GO using graphite powder (Marcano et al., 2010). A 9:1 mixture of concentrated H_2SO_4/H_3PO_4 (360:40 ml) was added to a mixture containing 3 g graphite powder. While stirring, 18 g of $KMnO_4$ was added gradually and slowly to the above reaction mixture, at temperature of 40°C. Then, the mixture was

heated up to 50°C and continued stirring for 12 hr. The reaction mixture was cooled to room temperature for 2 hr and poured onto ice bath (400 ml) with the addition of 3 ml H₂O₂. A centrifugation technique (Sorvall, USA) at 1073 x g was used to decant the supernatant from the mixture above. The suspension was washed in succession with 1:1:1 ratio of 200 ml of distilled water, HCl and ethanol to remove any impurities by centrifugation (1073 x g, 15 min, room temperature). The suspension obtained was vacuum-filtered using PTFE membrane (50 mm of diameters and 0.45 µm pore size) (Sigma-Aldrich, United States) and left to dry overnight at room temperature.

Preparation of GAGO Nanoformulation

Pure drugs, GA (0.25 g) and GO (0.05 g), were dissolved in 50 ml of distilled water (pH 4.71). The mixture was stirred for 16 hr, centrifuged at 1073 x g for 15 min and washed thoroughly in distilled water to remove any unreacted GA. The suspension was stored overnight in an oven at 40°C. Then, the dry suspension were weighted and stored in glass tube (Dorniani et al., 2016).

Characterization of GO and GAGO

The synthesized GO was characterized by using a UHTS 300 Raman spectroscopy (WITec, Germany) with an excitation wavelength of 532 nm. The morphology of GO nanocarrier and GAGO nano-formulation was observed on a scanning electron microscope (SEM) (FEI, USA). Fourier transform infrared spectra (FTIR) (Shimadzu, Tokyo, Japan) was performed on the synthesized GO, GAGO and pure GA using the KBr disc method (Forato et al., 1998). The percentage yield of GAGO was determined for three different batches. The loading capacity and efficiency of GAGO were measured using UV-Vis spectrophotometer (Biorad, USA).

Zebrafish Embryo Toxicity Assessments

The Danio Assay Kit for toxicity assessment was purchased from the Danio Assay Laboratories (Danio Assay Laboratories Sdn. Bhd, UPM, Malaysia), which was equipped with 300 live zebrafish embryos, 96 well plates, 500 ml of Danio-embryo media containing 0.1% DMSO and manual instruction. The wild-type Zebrafish (AB strain) was maintained by Danio Assay Laboratories according to standard in a recirculation system, and under the permission of the Institutional Animal Care and Use Committee (IACUC), Universiti Putra Malaysia.

The principle of embryonic toxicity assessment on zebrafish embryo was based on the method developed by Schulte and Nagel (Schulte & Nagel, 1994; Nagel, 2002). Briefly, 4 hr post-fertilization (hpf) healthy embryos were transferred into 96-well culture plates (1

embryo in 200 μ l of Danio embryo media per well) and acclimatized for 24 hr in a 12-hr light-12-hr dark (LD) cycle. Any dead or unfertilized embryos were removed, and the old medium was replaced with new embryo media. The viable embryos were then treated with different concentrations of GAGO (0-500 μ g/ml) at 28°C in a semi-static condition for 96 hr (24 hpf to 120 hpf). GA, GO and distilled water were used as controls. All solutions were refreshed every 24 hr. The different toxicological end-points including mortality rate, heart rate and hatching rate, were observed and captured by using an inverted microscope (Olympus IX73, equipped with DinoCapture camera) at 24 hr, 48 hr, 72 hr and 96 hr post-exposure. The mortality of embryo was indicated when it formed coagulation and absence of heartbeat (Nagel, 2002). Survival rate was analysed by counting the number of live embryos or larvae at each time point. The hatching rate was recorded at 24 hr and 48 hr post-exposure. Dead embryos were removed during the observation time to avoid any contamination. Three independent experiments were performed for each treatment group ($n \geq 10$ embryos per exposure group).

Statistical Analysis

Differences between groups were analysed by Log-rank (Mantel-Cox) test, one- or two-way ANOVA with Tukey's and Dunnet post-test comparison where indicated. All experiments were repeated three times independently. Statistical analyses were performed by using GraphPad Prism 7.0d statistical analysis software (GraphPad Software, La Jolla California USA). Data was presented as mean \pm standard error of the mean (SEM). A *p* value of less than 0.05 was considered to be statistically significant.

RESULTS AND DISCUSSION

The Characterization of GO and GAGO

The GO obtained was observed to be black in colour and appeared flaky (Figure 1A) with a relatively large surface area and morphology that resembles thin folded and crumpled paper under SEM (Figure 1D). The Raman spectra of GO showed significant structural changes and broadening of the D band at 1373 cm^{-1} and 1908 cm^{-1} of G band (Figure 1C). Following the successful synthesis of GO, GA was loaded onto GO, to produce GAGO (Figure 1B), which percentage yield (88.4%), loading of GA (0.382 g/g of GAGO) and loading efficiency of 33.79%. The GAGO obtained was in the form of black thin film (Figure 1B) and SEM image showed the thickness of the GAGO structure, as compared to pure GO (Figure 1E), which indicates the loading of GA.

In order to investigate the different types of interactions, the pure GA and GO as well as the new formulated GAGO were further characterized by using FTIR. This analysis has been performed to investigate the structure and presence of functional groups of the

materials. The presence of new peaks (labelled as black spots) as shown in Figure 2 for GAGO at around 3734 cm^{-1} corresponds to the characteristics peak at 3730 cm^{-1} that appears as well in GA (Figure 2A). Then, the peak in the region 2362 cm^{-1} and 2117 cm^{-1} can also be assigned to ascertain the attachment of GA to the GO nanocarrier. The infrared spectrum of GAGO nanoformulation shows the characteristic peaks of both GO nanocarrier and GA, which suggest the successful loading of GA, hence the formation of GAGO nanoformulation.

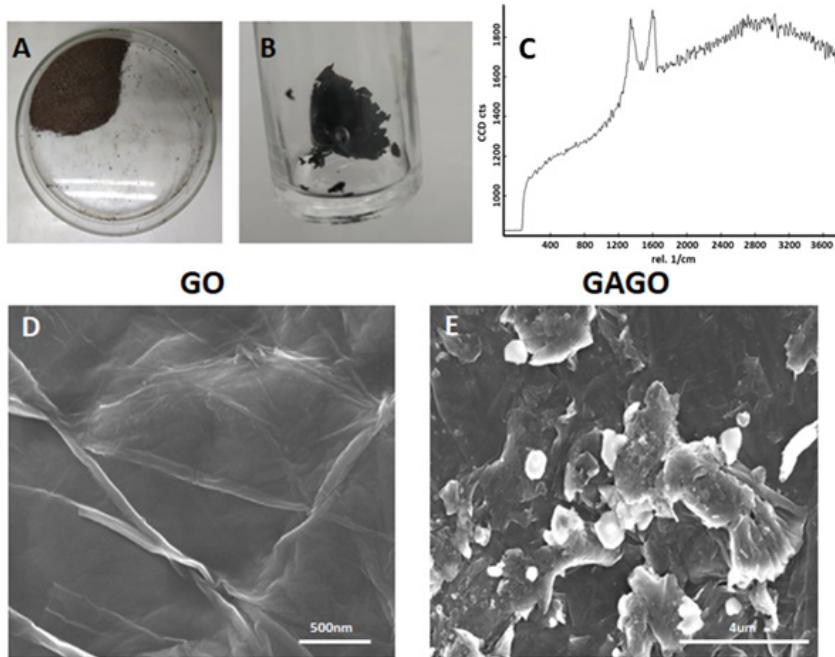


Figure 1. (A) GO flakes synthesized by a modified Hummer’s method (B) Freshly prepared GA loaded GO (GAGO). (C) Raman spectra of GO obtained at 532 nm. FESEM images of (D) GO and (E) GAGO at 100x magnification. Scale bar represents 500 nm for GO and 4 μm for GAGO.

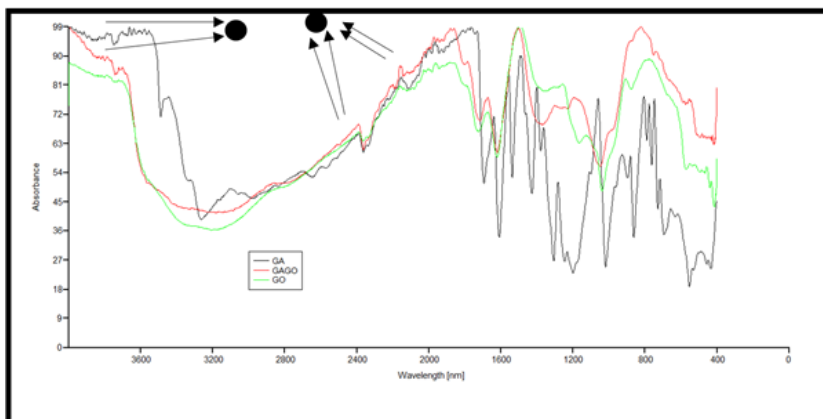


Figure 2. FTIR spectra of (A) pure GA (B) GAGO and (C) GO. The black spots depict new peaks that exist on GAGO spectrum that correspond to the peaks on GA spectrum.

Survival Rate of Zebrafish Embryo Treated with GA, GO and GAGO

In order to assess and compare the possible toxicity effects of GAGO during zebrafish embryogenesis, the survival rate of zebrafish embryos exposed to different concentrations of GAGO (0-500 $\mu\text{g/ml}$) as observed at 24, 48, 72 and 96 hr post-treatment (Figure 3A-C). In this study, pure GA and GO were used as comparisons to GAGO, concentrations of pure GA (0-191 $\mu\text{g/ml}$) were based on the percent of drug loading on GO (0-500 $\mu\text{g/ml}$) obtained during GAGO preparation, and water was used as control. The total percentage of survival rate was represented by dead and unfertilized embryos which exhibited coagulated embryos, lack of somite formations, non-detachment of the tail and absence of heartbeat (Busquet et al., 2013).

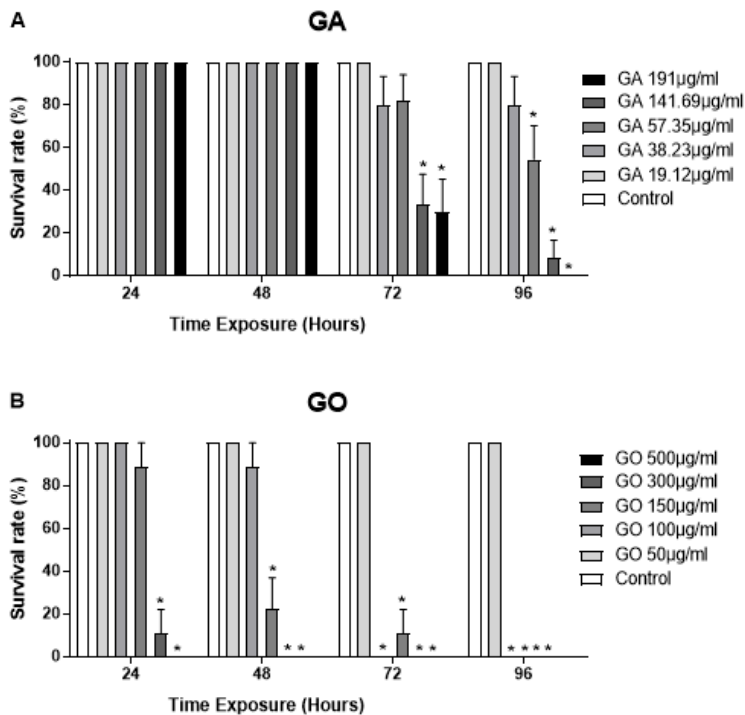
As shown in Figure 3A-B, both pure GA and GO caused significant toxicity to the zebrafish embryos. The two highest concentrations of GA (141.69 and 191 $\mu\text{g/ml}$) increased the mortality rate of treated embryos, with less than 50% and 10% survival recorded at 72 hr and 96 hr post-treatment, respectively. Compared to GA, pure GO shows more potent toxicity to the embryos, with none survival recorded as early as 24 hr post-treatment at 500 $\mu\text{g/ml}$ (Figure 3B). By 96 hr, complete mortality was recorded in ≥ 100 $\mu\text{g/ml}$ of GO. However, all embryos treated with the lowest concentration of both, pure GA (19.12 $\mu\text{g/ml}$) and GO (50 $\mu\text{g/ml}$), survived this study, and were comparable to the control group. The potential toxicity of GA and GO might be due to their structure that contains multiple hydroxyl groups, particularly in B-rings, which significantly increased the production of reactive oxygen species (ROS) and free radicals that lead to the induction of oxidative stress, results in interruption of normal biological function during the developmental period of zebrafish embryo (Lee & Lee, 2006; Li et al., 2016). This is in contradiction with previous study reported that GA (up to 120 $\mu\text{g/ml}$) showed no toxicity when exposed to zebrafish embryo for up to 48 hr (Singulani et al., 2017). Together, these data indicate the potential toxicity of prolong exposure of pure GA and GO at high concentrations during zebrafish embryogenesis.

Interestingly, embryos treated with GAGO shows significant improvement in survival rate compared when they were treated with similar concentration of pure GA or GO (Figure 3C). Unlike toxicity seen in GA and GO, treatment with 50-150 $\mu\text{g/ml}$ of GAGO has no significant effect on the survival rate, with 90% survivability of embryos was recorded, at all measured time points, throughout 96 hr exposure. The only fatal concentrations that caused 100% mortality in GAGO were seen at 300 and 500 $\mu\text{g/ml}$, as early as 24-hour post-treatment. These findings indicate that the toxicity effects of GA and GO, but not GAGO, are based on time- and dose-dependent manners.

The improvement on survival rate observed in GAGO-exposed group might be contributed by the structure of GAGO. Structurally, GO having hydroxyl, epoxy, and carboxyl groups on its surface, which can be covalently bonded with another particle

to functionalize as potential drug treatment (Stankovich et al., 2006). Previous study has reported that the surface charge of graphene has a strong impact on the disruption of red blood cell membranes, which is attributed to the strong electrostatic interactions between negatively charged oxygen groups on the GO surface and positively charged phosphatidylcholine lipids on the cell membranes (Hu & Zhou, 2013). Thus, it is possible that these functional groups may have interacted with the membrane encapsulated the embryos and induces toxicity.

On the other hand, GA naturally works as anti-oxidant, which can inactivate the free radicals reaction hence preventing the building up of oxidative stress. In addition, GA also has phenolic groups that are a source of readily available hydrogen atom, which can delocalize free radicals over its phenolic structure (Nikolic, 2006). Therefore, it is possible that the functionalization of GO, by loading with GA, might has naturalize the negative charges in the GO structure, hence hindering the toxicity effect of pure GO. Moreover, the structure of sharp edge of GO also could potentially disrupt the membrane of embryo that lead and cause death of embryos (Qiu et al., 2018). However, when GO as loaded with GA, the sharp edge surface might be masked and protected from disrupting the membrane of zebrafish embryo, hence increasing the survivability of zebrafish embryo in GAGO treatment group (Sahay et al., 2010).



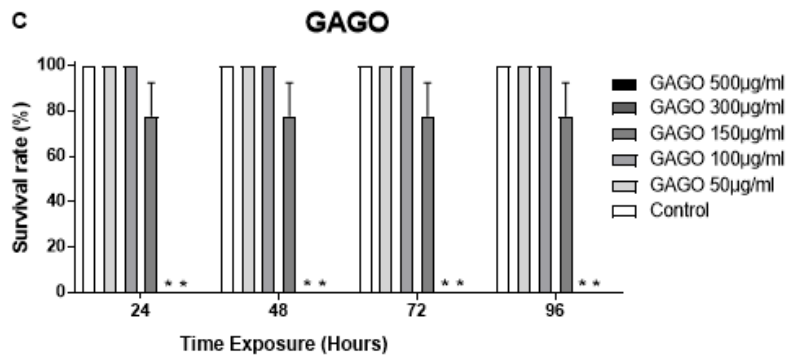


Figure 3. Effects of different treatments on survival of zebrafish (*Danio rerio*) embryos during 96 hr time course. Embryos of zebrafish were exposed at different concentrations of either GA, GO, or GAGO (50, 100, 150, 300, 500 µg/ml). Distilled water was used as control. Data were averaged from three independent experiments and are shown as mean \pm SEM. Significant differences between experimental groups are denoted by “**” (One-way ANOVA, $p < 0.05$).

Hatching Rate of Zebrafish Embryo Treated with GA, GO and GAGO

Hatching rate is one of the important parameters to determine the toxicity status of nanomaterials using zebrafish model. Zebrafish embryo normally hatched between 48 and 72 hpf, in which occur at 24 and 48 hr post-treatment in this study, and it is considered as one of the critical stages during embryogenesis (d’Amora et al., 2017). The hatching rates of zebrafish embryos exposed to five different concentrations of GA, GO and GAGO are shown in Figure 4A-C.

In this study, embryos treated with ≤ 57.35 µg/ml of pure GA showed 100% normal hatching rate (Figure 4A). However, treatment with ≥ 141.69 µg/ml of GA significantly caused embryonic development delayed, with only 50% hatching rate was recorded between 24 hr and 48 hr post-treatment. As for GO-treated group, less than 20% embryos hatched was recorded when they were treated with ≥ 100 µg/ml of GO (Figure 4B). The only concentration that did not affect embryos hatching rate in GO was 50 µg/ml, with all embryos within this group hatched between 24 hr and 48 hr of exposure and were comparable to the control group. In contrast to GA- and GO-treated groups, a remarkable improvement in hatching rate was observed in GAGO when they were treated with similar concentration of pure GA (141.69 µg/ml) and pure GO (300 µg/ml) (Figure 4C). In addition, all concentrations except 500 µg/ml, showed normal hatching rate based on the fertilization period of embryos, and they were comparable to the control group. Although Figure 3C recorded that none of the embryos survived at 24 hr post-exposure to 500 µg/ml of GAGO, 60% of these embryos were found dead in larvae state (Figure 4C). Our findings indicate that GA, but not GO and GAGO, exhibited a time- and concentration-dependent behaviour. On the other hand, GO and GAGO have only affected the embryos hatching activity in a dosage dependent manner.

The ability of pure GA to simply dilute and adhere onto the surface of the chorion of zebrafish embryo might partially contribute to the lower hatching rate observed in GA-treated embryos (Ong et al., 2014). Moreover, another study also reported similar finding, in which, graphene is adhered firmly to chorion and induced hatching delayed during zebrafish embryogenesis (Manjunatha et al., 2018; Liu et al., 2014). Adherence of GA and GO might cause clogging in the chorion pores, resulting in interfering of hatching enzyme and oxygen exchange, thus lead to hypoxia in zebrafish embryo (Liu et al., 2014; Yan et al., 2012).

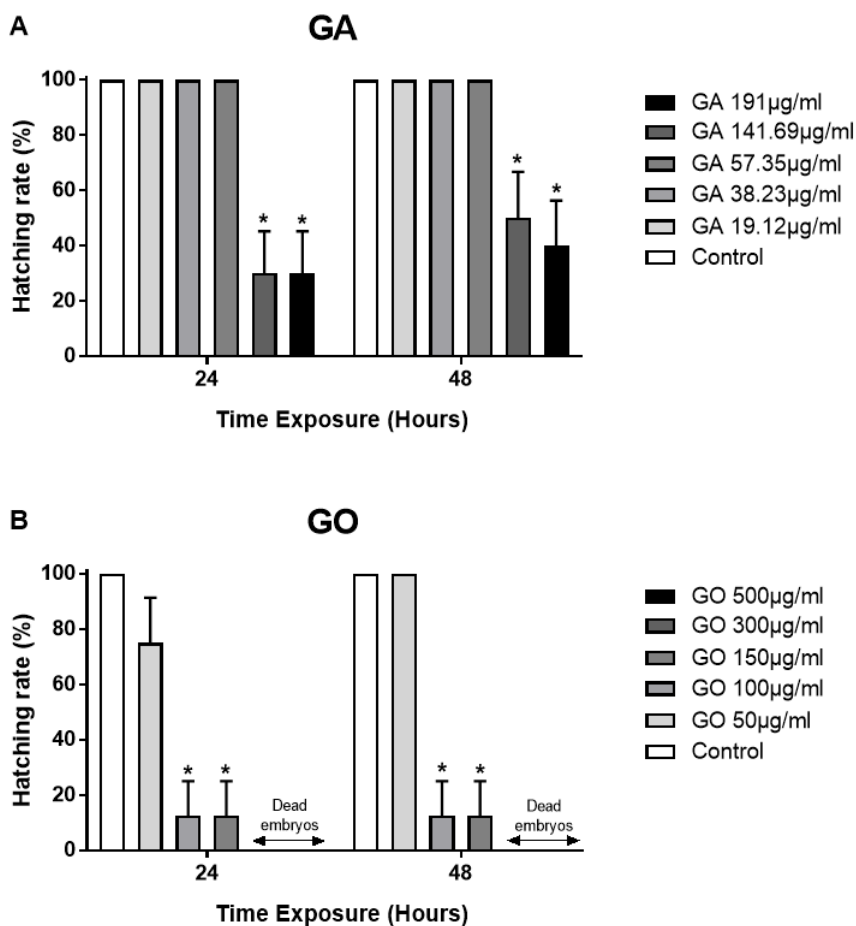


Figure 4. Hatching rate (%) of zebrafish (*Danio rerio*) embryos exposed to different treatments of either GA, GO, or GAGO (50, 100, 150, 300, 500 µg/ml). Distilled water was used as control. Data were expressed as mean ± S.E.M. Significant differences between experimental groups are denoted by “*” (Two-way ANOVA, followed by a post hoc test: Dunnett’s, $p < 0.05$).

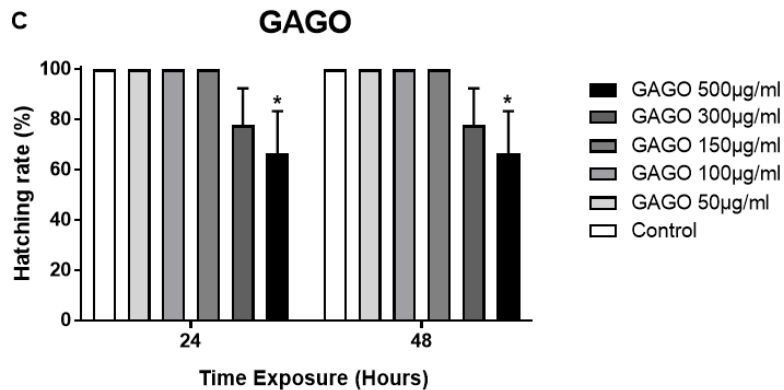


Figure 4. (Continued)

Heart Rate of Zebrafish Embryo Treated with GA, GO and GAGO

Heart is the first organ to develop and function during zebrafish embryonic development (Bakkers, 2011). Heartbeat measurement is important in assessing cardiac function and commonly used to evaluate the toxicity of a toxicant (De Luca et al., 2014). Furthermore, heartbeat induction is also sensitive to nature and can easily be detected due to the embryo characteristic that is transparent and can be visualized at single cell resolution (Verkerk & Remme, 2012). Furthermore, the normal heart rate of zebrafish embryo ranged between 120-180 beats per minute (Baker et al., 1997). The heart rate of embryos exposed to pure GA, GO and GAGO is shown in Figure 5A-L.

As shown in Figure 5, heart rate changes were found in a dose- and time-dependent manner with pure GA and GO exposure, but not GAGO. The heart rate of GA-treated embryos in most concentrations ($\leq 141.69 \mu\text{g/ml}$) was within a normal range for up to 48 hr exposure (Figure 5C-D). However, at 72 hr and 96 hr post-treatment, statistically significant decrease was observed at $\geq 141.69 \mu\text{g/ml}$ and $\geq 57.35 \mu\text{g/ml}$ of GA, respectively. Other GA concentrations show no significant effect on the heart rate and were comparable to the control group. Since all the embryos treated with $\geq 300 \mu\text{g/ml}$ of GO were found dead at 24 hr exposure (Figure 3), a remarkable decrease in the heart rate was in consistent with the data (Figure 5E), and it further decreased in all concentrations, except for $50 \mu\text{g/ml}$, throughout the 96 hr exposure (Figure 5E-H). GAGO treatment has significantly reduced the heart rate when embryos were treated with $\geq 150 \mu\text{g/ml}$ at 24 hr exposure, however, no further decrease was seen and it was maintained throughout 96 hr of exposure. GAGO also posed significant improvement in embryos treated with similar concentrations of GO (Figure 5E-L).

The highly toxicity posed in GO might induce embryonic bradycardia which leads to cardiac arrhythmia (Manjunatha et al., 2018). Bradycardia can be a result of embryonic

distress and/or severe hypoxia. Similarly, this finding was supported by a previous study reported that multi wall carbon nanotube (MWCNT) and GO can alter the heart rate, while reduced graphene oxide (RGO) does not have such effect (Liu et al., 2014). Besides, these results also indicate that combination of GO and GA has promising impact in reducing the toxicity of GO.

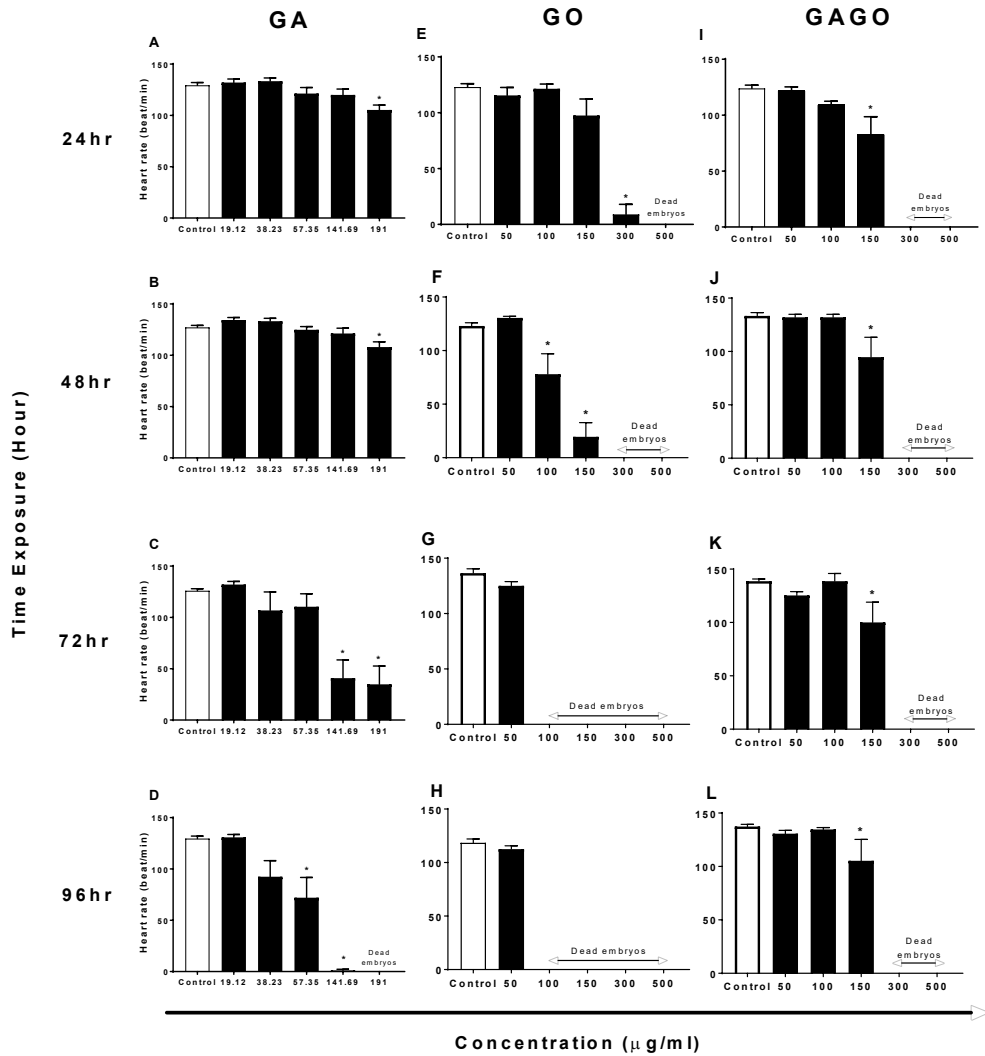


Figure 5. Heart beats of zebrafish embryos in the presence of GA (A-D), GO (E-H) or GAGO (I-L) at different concentrations (50, 100, 150, 300, 500 µg/ml). Embryos treated with GA, GAGO and GO exhibit significant bradycardia at all treated groups. Data were expressed as mean ± S.E.M. Significant differences between experimental groups are denoted by “*” (One-way ANOVA, followed by a post hoc test: Dunnett’s, p < 0.05).

CONCLUSION

In this study, GA, GO and GAGO were found to induce toxicity based on time- and dose-dependent manner. High mortality, delayed hatching rate and reduced in heartbeat were recorded at higher concentrations of all groups. The present finding shows that the newly-formulated GAGO nanoparticle reduced the toxicity of pure GO and GA during zebrafish embryogenesis, by improving the survival rate, hatching rate and heart rate. The safe concentration of GAGO was recorded between 0-150 µg/ml, in which one-fold higher than pure GA and GO. However, further study is still needed to correlate the toxicity of GAGO with its effective concentration through *in vitro* and *in vivo* studies.

ACKNOWLEDGMENT

This research was partially funded by the FRGS (FRGS/1/2017/SKK08/UPM/02/11) and UPM-Geran Putra (UPM/800/2/2/4). We would also like to acknowledge the support and technical assistance of the Animal Biochemistry & Biotechnology Laboratory (ABBTech) facilities in the Faculty of Biotechnology and Biomolecular Science, Universiti Putra Malaysia and Institute of Advanced Technology (ITMA) at Universiti Putra Malaysia.

REFERENCES

- Baker, K., Warren, K. S., Yellen, G., & Fishman, M. C. (1997) Defective “pacemaker” current (I_h) in a zebrafish mutant with a slow heart rate. *Proceedings of the National Academy of Sciences of the United States of America*, 94(9), 4554-4559.
- Bakkers, J. (2011). Zebrafish as a model to study cardiac development and human cardiac disease. *Cardiovasc Research*, 91(2), 279-288.
- Busquet, F., halder, Braunbeck, T., gourmelon, Lillicrap, A., Kleensang, A., ... walter-rohde, S. (2013). OECD guidelines for the testing of chemicals 236 - fish embryo acute toxicity (FET) Test. *The OECD Observer: Organisation for Economic Co-Operation and Development*. Retrieved July 26, 2013, from https://www.oecd-ilibrary.org/environment/test-no-236-fish-embryo-acute-toxicity-fet-test_9789264203709-en
- Chang, Y., Yang, S. T., Liu, J. H., Dong, E., Wang, Y., Cao, A., ... & Wang, H. (2011). *In vitro* toxicity evaluation of graphene oxide on A549 cells. *Toxicology Letters*, 200(3), 201-210.
- d'Amora, M., Camisasca, A., Lettieri, S., Giordani, S., Amora, M., Camisasca, A., & Giordani, S. (2017). Toxicity assessment of carbon nanomaterials in zebrafish during development. *Nanomaterials*, 7(12), 414-425.
- Danovich, M., Aleiner, I. L., Drummond, N. D., & Fal'ko, V. I. (2017). Fast relaxation of photo-excited carriers in 2-D transition metal dichalcogenides. *IEEE Journal of Selected Topics in Quantum Electronics*, 23(1), 168-172.
- De Luca, E., Zaccaria, G. M., Hadhoud, M., Rizzo, G., Ponzini, R., Morbiducci, U., & Santoro, M. M. (2014). ZebraBeat: a flexible platform for the analysis of the cardiac rate in zebrafish embryos. *Scientific Reports*, 4, 1-13.

- Dikin, D. A., Stankovich, S., Zimney, E. J., Piner, R. D., Dommett, G. H. B., Evmenenko, G., ... & Ruoff, R. S. (2007). Preparation and characterization of graphene oxide paper. *Nature*, *448*(7152), 457-460.
- Dorniani, D., Hussein, M. Z., Kura, A. U., Fakurazi, S., Shaari, A. H., & Ahmad, Z. (2012). Preparation of Fe₃O₄ magnetic nanoparticles coated with gallic acid for drug delivery. *International Journal of Nanomedicine*, *7*, 5745-5756.
- Dorniani, D., Saifullah, B., Barahuie, F., Arulselvan, P., Hussein, M. Z., Fakurazi, S., & Twyman, L. J. (2016). Graphene oxide-gallic acid nanodelivery system for cancer therapy. *Nanoscale Research Letters*, *11*(1), 491-499.
- Forato, L. A., Bernardes-filho, R., & Colnago, L. A. (1998). Protein structure in KBr pellets by infrared spectroscopy. *Analytical Biochemistry*, *259*, 136-141.
- Geim, A. K., & Novoselov, K. S. (2007). The rise of graphene. *Nature Materials*, *6*(3), 183-191.
- Gerlai, R., Fernandes, Y., & Pereira, T. (2009). Zebrafish (*Danio rerio*) responds to the animated image of a predator: towards the development of an automated aversive task. *Behavioural Brain Research*, *201*(2), 318-324.
- Howe, K., Clark, M. D., Torroja, C. F., Turrance, J., Berthelot, C., Muffato, M., ... & Stemple, D. L. (2013). The zebrafish reference genome sequence and its relationship to the human genome. *Nature*, *496*(7446), 498-503.
- Hu, X., & Zhou, Q. (2013). Health and ecosystem risks of graphene. *Chemical Reviews*, *113*(5), 3815-3835.
- Hu, W., Peng, C., Luo, W., Lv, M., Li, X., Li, D., ... & Fan, C. (2010). Graphene-based antibacterial paper. *ACS Nano*, *4*(7), 4317-4323.
- Lee, K. W., & Lee, H. J. (2006). Biphasic effects of dietary antioxidants on oxidative stress-mediated carcinogenesis. *Mechanisms of Ageing and Development*, *127*(5), 424-431.
- Li, X., Gao, A., Wang, Y., Chen, M., Peng, J., Yan, H., ... & Chen, D. (2016). Alcohol exposure leads to unrecoverable cardiovascular defects along with edema and motor function changes in developing zebrafish larvae. *Biology Open*, *5*(8), 1128-1133.
- Liu, X. T., Mu, X. Y., Wu, X. L., Meng, L. X., Guan, W. B., Ma, Y. Q., ... & Li, X. F. (2014). Toxicity of multi-walled carbon nanotubes, graphene oxide, and reduced graphene oxide to zebrafish embryos. *Biomedical and Environmental Sciences*, *27*(9), 676-683.
- Lu, Y., Jiang, F., Jiang, H., Wu, K., Zheng, X., Cai, Y., ... & To, S. S. (2010). Gallic acid suppresses cell viability, proliferation, invasion and angiogenesis in human glioma cells. *European Journal of Pharmacology*, *641*(2-3), 102-107.
- Manjunatha, B., Park, S. H., Kim, K., Kundapur, R. R., & Lee, S. J. (2018). *In vivo* toxicity evaluation of pristine graphene in developing zebrafish (*Danio rerio*) embryos. *Environmental Science and Pollution Research*, *25*(13), 12821-12829.
- Marcano, D. C., Kosynkin, D. V., Berlin, J. M., Sinitskii, A., Sun, Z., & Slesarev, A. (2010). Improved synthesis of graphene oxide. *ACS Nano*, *4*(8), 4806-4814.

- Masoud, M., Hagagg, S., Ali, A., & Nasr, N. (2012). Synthesis and spectroscopic characterization of gallic acid and some of its azo complexes. *Journal of Molecular Structure*, 1014, 17-25.
- Nagel, R. V. (2002). DarT: The embryo test with the zebrafish *Danio rerio*--a general model in ecotoxicology and toxicology. *ALTEX*, 19(1), 38-48.
- Nikolic, K. M. (2006). Theoretical study of phenolic antioxidants properties in reaction with oxygen-centered radicals. *Journal of Molecular Structure: THEOCHEM*, 774(1-3), 95-105.
- Ong, K. J., Zhao, X., Thistle, M. E., MacCormack, T. J., Clark, R. J., Ma, G., ... & Goss, G. G. (2014). Mechanistic insights into the effect of nanoparticles on zebrafish hatch. *Nanotoxicology*, 8(3), 295-304.
- Qiu, J., Liu, L., Zhu, H., & Liu, X. (2018). Bioactive materials combination types between graphene oxide and substrate affect the antibacterial activity. *Bioactive Materials*, 3(3), 341-346.
- Rawel, H., Frey, S., Meidtnr, K., Kroll, J., & Schweigert, F. (2006). Determining the binding affinities of phenolic compounds to proteins by quenching of the intrinsic tryptophan fluorescence. *Molecular Nutrition and Food Research*, 50(8), 705-713.
- Sahay, G., Alakhova, D. Y., & Kabanov, A. V. (2010). Endocytosis of nanomedicines. *Journal of Controlled Release: Official Journal of the Controlled Release Society*, 145(3), 182-195.
- Santos, C. M., Mangadlao, J., Ahmed, F., Leon, A., Advincula, R. C., & Rodrigues, D. F. (2012). Graphene nanocomposite for biomedical applications: fabrication, antimicrobial and cytotoxic investigations. *Nanotechnology*, 23(39), 395101-395110.
- Schulte, C., & Nagel, R. (1994). Testing acute toxicity in the embryo of zebrafish, *Brachy danio rerio*, as an alternative to the acute fish test: Preliminary results. *Atla*, 22(1), 12-19.
- Shamsi, S., Elias, N., Sarchio, S., & Yasin, F. M. (2018). Gallic acid loaded graphene oxide based nanoformulation (GAGO) as potential anti-bacterial agent against *Staphylococcus aureus*. *Materials Today: Proceedings*, 5, S160-S165.
- Sheshmani, S., & Fashapoyeh, M. (2013). Suitable chemical methods for preparation of graphene oxide, graphene and surface functionalized graphene nanosheets. *Acta Chimica Slovenica*, 60, 813-825.
- Singulani, J. D. L., Scorzoni, L., Gomes, P. C., Nazaré, A. C., Polaquini, C. R., Regasini, L. O., ... & Mendes-Giannini, M. J. S. (2017). Activity of gallic acid and its ester derivatives in *Caenorhabditis elegans* and zebrafish (*Danio rerio*) models. *Future Medicinal Chemistry*, 9(16), 1863-1872.
- Stankovich, S., Dikin, D. A., Dommett, G. H. B., Kohlhaas, K. M., Zimney, E. J., Stach, E. A., ... & Ruoff, R. S. (2006). Graphene-based composite materials. *Nature*, 442(7100), 282-286.
- Verkerk, A. O., & Remme, C. A. (2012). Zebrafish: a novel research tool for cardiac (patho)electrophysiology and ion channel disorders. *Frontiers in Physiology*, 3, 1-9.
- Yan, L., Wang, Y., Xu, X., Zeng, C., Hou, J., Lin, M., ... & Liu, Y. (2012). Can graphene oxide cause damage to eyesight? *Chemical Research in Toxicology*, 25(6), 1265-1270.
- Yang, K., Feng, L., Shi, X., & Liu, Z. (2013). Nano-graphene in biomedicine: Theranostic applications. *Chemical Society Reviews*, 42(2), 540-547.

Yang, X., Wang, Y., Huang, X., Ma, Y., Huang, Y., Yang, R., ... & Chen, Y. (2011). Multi-functionalized graphene oxide based anticancer drug-carrier with dual-targeting function and pH-sensitivity. *Journal of Material Chemistry*, 21(10), 3448-3454.

Review Article

Light Fishing Fleets Monitoring by GIS-Based Spatiotemporal Analysis in West Sumatera Waters

Nurholis^{1,2*}, Jonson Lumban-Gaol² and Fachrudin Syah Achmad³

¹Graduate School of Marine Technology Program, IPB University, Bogor 16680, Indonesia

²Department of Marine Science and Technology, IPB University, Bogor 16680, Indonesia

³Marine Science Study Program, Faculty of Agriculture, Trunojoyo University, Madura, Indonesia

ABSTRACT

Studies on the spatiotemporal distribution monitoring of light fishing fleets are limited due to extensive study area, data availability, dynamic distributions, limited monitoring technology, and perception of the fishers. This study aims to monitor and estimate the density of light fishing fleets, representing the centre of fishing areas. Using the visible infrared imaging radiometer suite of boat detection data combined with actual fishing data, the pattern of spatiotemporal distribution of light fishing fleets was analysed, displayed with the variations in sea surface temperature and chlorophyll-a concentrations. This study was carried out at west Sumatera waters. The actual fishing data, light fishing fleets data, and environment parameter data were collected in 2014-2018. The calculation of

the geographical distribution was carried out using the geographical information system models with four spatial indicators, i.e., central tendency, spatial dispersion, directional dispersion, and directional trends. The results showed various patterns and behaviours on light fishing fleets spatial distribution. We also revealed the spatiotemporal pattern dynamic of the geographic distribution of light fishing fleets in the west Sumatera waters. The distribution pattern was random compared to the sea surface temperature distribution. On the other hand, it was quite centralized

ARTICLE INFO

Article history:

Received: 28 July 2019

Accepted: 4 November 2019

Published: 13 January 2020

E-mail addresses:

kholiser1@gmail.com (Nurholis)

jonson_lumbangaol@yahoo.com (Jonson Lumban-Gaol)

fachrudinsyah@gmail.com (Fachrudin Syah Achmad)

*Corresponding author

following the chlorophyll-a concentration. The distribution of light fishing fleets was dominant in the area with high chlorophyll-a concentration.

Keywords: CFAs, light fishing fleets, spatial indicators, spatiotemporal analysis

INTRODUCTION

Monitoring and mapping of fishing activities are the critical components in the planning and management of fisheries and marine resources (Booth, 2000). Fishing location data have been used for a long time to identify and delineate fishing areas (Jennings & Lee, 2012), assisting the fisheries resource assessments (Booth 2000; Tidd et al., 2017), estimating the fishing efforts (Parnell et al., 2010) and evaluating the impact of external factor interventions in marine and fisheries resource management (Cabral et al., 2016). However, the monitoring and mapping of the fishing activities still face many problems in Indonesia, such as high cost in fishing data collection, low quality of fishing data, and the perception of fishers about fishing data. Many Southeast Asian countries have high fishing densities (N boat km^{-2}) (Stewart et al., 2010), while the majority of their fishing fleets have not been equipped with a vessel monitoring system (VMS) (Kroodsma et al., 2018)

Night-time satellite imagery provides an alternative source of spatial data in marine and fisheries studies, especially for vessels using lights as fish aggregating devices (FADs) to attract fish (Kroodsma et al., 2018). Elvidge et al. (2015) stated the potential of VBD (VIIRS Boat Detection) as the boat location extracted from visible infrared imaging radiometer suite, day/night band (VIIRS DNB) image data to provide an advance solution of vessel monitoring activities. The light intensity used in this fishing method allows it to be identified through the night-time image (Geronimo et al., 2018).

Various studies can be carried out by utilizing night-time imaging data such as light pollution mapping in marine protected areas (MPA) (Davies et al., 2014; Davies et al., 2016), offshore drilling mapping (Elvidge et al., 2009; Elvidge et al., 2016), vessel detection and monitoring (Elvidge et al., 2015; Straka et al., 2015), the suitability of fish resource habitats mapping (Kiyofuji & Saitoh, 2004), estimation of fishing effort and intensity for single fish species (Saitoh et al., 2010), and mapping predictions of potential fishing zones (PFZs) (Kiyofuji & Saitoh, 2004; Saitoh et al., 2010; Syah et al., 2016; Setiawati & Tanaka, 2017; Zhang et al., 2017; Geronimo et al., 2018).

In some studies, the night-time imagery was compared to the VMS data to understand the relationship between the fishing gears and the light intensity of the image better. The highest light intensity associates with squid lift fishing gear and small purse seine pelagic (Geronimo et al., 2018), which subsequently associates with FADs for hand line fishing, boat lift net and set lift net. It assumes that the VBD data can delineate fishing grounds for specific fishing gears. Indirectly, the fleet distribution always connects with the spatial

distribution of fish. The spatial distribution of fish is a complex phenomenon controlled by the interactions between various oceanographic and environmental parameters, such as sea surface temperature (SST), sea surface height (SSH), and chlorophyll-a concentration, monitored remotely using satellites (Syah et al., 2016; Setiawati & Tanaka, 2017; Zainuddin 2011). Furthermore, dissolved oxygen, upwelling, salinity, and current can also influence fish distribution

Geographic information system (GIS) technology is specifically designed to visualize, manipulate, manage, and analyse various reference data to determine relationships, linkages, patterns, and trends, which may not be directly proven by the existing data sources (Fischer & Getis, 2010). Development devices in GIS, such as spatial statistical analysis methods, make the researcher easier to study and understand the variation and exploration process of marine and fisheries resources in the spatiotemporal domains (Pierce et al., 2002).

Many studies have utilized the GIS in fisheries science and fishing fleets monitoring in the management aspects (Pierce et al., 2002; Palenzuela et al., 2004; Riolo 2006; Jayaraman et al., 2013) including marine area and fisheries planning (Dineshababu et al., 2014), modelling the relationship of environmental parameters and fish distribution (Lan et al., 2013; Lumban-Gaol et al., 2015; Lan et al., 2017; Nurdin et al., 2017). In this study, the GIS-based analysis focused on analysing the light fishing fleets density, the spatiotemporal distribution estimations, and the relationship between environmental parameters and the spatiotemporal distribution of light fishing fleets.

The objectives of this study are: (1) to monitor the light fishing fleets density using VBD and actual fishing data, (2) estimate and observe the pattern of the spatiotemporal distribution of light fishing fleets in the west Sumatera waters (WSW) against SST and chlorophyll-a concentrations. The results are expected to provide information on new approaches for monitoring light fishing fleets and assist the decision makers in managing fisheries resources in WSW.

MATERIAL AND METHODS

Study Area

This research was conducted in the west Sumatera waters (WSW). The WSW is the part of the Republic of Indonesia Fisheries Management Area named WPP RI 572. Characteristically, the WSW is slightly different compared to the South Java Sea (SJS). Upwelling occurs in SJS during the southeast monsoon and also affected by the Indonesian current which flows through Sunda Strait and carries rich nutrients from Java Sea. Our study area is shown in Figure 1.

Fisheries Data

The actual light fishing fleet data were collected from the daily logbook of hand line fishing boats in 2014-2018 within various gross tonnages (GT). The hand line fishing is a simple fishing gear consisting of fishing lines, snap, connectors, and hooks, and generally used for demersal fishery (Mulyadi et al., 2015). The actual fishing fleet data were filtered and selected based on the attributes needed in this study, as shown in Table 1. Furthermore, the data were converted in the GIS software and re-filtered to ensure a clean outliers fishing point. The data were also compiled in GIS software to observe the spatiotemporal distribution. The actual fishing fleet data were overlaid with the VBD density to determine whether VBD data are representative of actual data or not. The aim of overlaying data was to identify the CFAs in the WSW. Flow chart analysis of fishing fleet data can be seen in Figure 2.



Figure 1. Area of Interest (AOI) in West Sumatera Waters (WSW)

Table 1

The actual fishing data used in this study

No	Lon	Lat	(<i>n</i>)	(<i>w</i>)	(<i>t</i>)	day	month	year
1	99.45	-1.26	1	50	38	2	1	2016
2	99.35	-1.32	1	46	49	3	1	2016
3	99.44	-1.42	1	71	49	4	1	2016
4	99.47	-1.46	7	390	49	5	1	2016
No _{<i>i</i>}	Lon _{<i>i</i>}	Lat _{<i>i</i>}	<i>n_i</i>	<i>w_i</i>	<i>t_i</i>	day _{<i>i</i>}	month _{<i>i</i>}	year _{<i>i</i>}

Note: *n* = total fishing catch, *w* = weight of fishing catch, *t* = fishing trip

Source: Daily logbook datasheet of Bungus Fishing Port

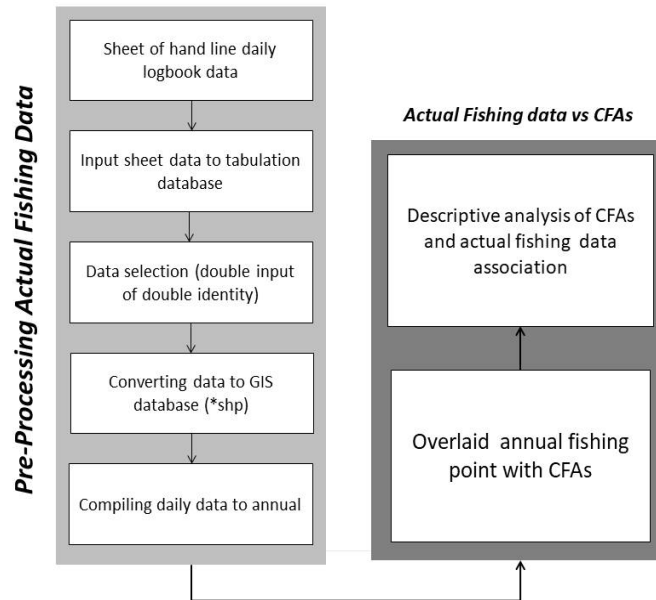


Figure 2. Flowchart of hand line actual fishing data analysis

VIIRS Boat Detection Data

VIIRS is the primary imager on Suomi National Polar Partnership (SNPP) that has been successfully launched in 2011. The VIIRS DNB collects low light imaging data with 45 times smaller pixel footprint than the OLS. One of the initial products of VIIRS DNB is VBD data, known as boat location that detected from present of lights intensity in the ocean (Elvidge et al., 2015). The light fishing fleets data were extracted from the VBD data. Those data were downloaded from the U.S National Oceanic and Atmospheric Administration National Centre for Environmental Information’s Earth Observation Group website (www.ngdc.noaa.gov/eog/viirs/downloadphil.boat.html) from 2014 to 2018. Each VBD datum represents pixels which are suspected to be boat lights in the VIIRS DNB image (Elvidge et al., 2015; Cozzolino & Lasta, 2016; Elvidge et al., 2018).

The VBD data files contained information on the ship’s suspect pixel geolocation, such as radiances value (nanoWatts/cm²/sr), date, image acquisition time, image data processing date, and ship detection quality (quality flag) (Geronimo et al., 2018). Each detection quality information is represented by these symbols, QF_1 (strong boat detection), QF_2 (weak boat detection), QF_3 (blurry boat detection), QF_8 (recurring lights) and QF_10 (weak and blurry lights/gas flares) symbols (Elvidge et al., 2015). In this study, only data with QF_1 criteria were used for further analysis to represent ships with high light intensity, undoubtedly related to the number of FADs (Table 2). The data warehousing process was carried out in GIS platform using several toolboxes.

Generally, the procedures were applied for this study is pre-processing VBD data and pattern identification. Pre-processing activity includes conversion, query, and delineation area of interest. We performed “point to raster” tools in the pattern identification stage to create annual VBD presence raster with 700 x 700 m² resolution. Kernel density was also performed to identify the light fishing fleets spatial pressure. Based on density information we clustered the density by visual interpretation and manual digitation to identified CFAs. The density clustering process also based on field information of dominant traditional PFZs at study area. CFAs location and identity determined by local spatial knowledge, and then we calculated the total area. To obtain information on the dynamics of the geographical distribution of light fishing fleets we also performed the “spatial statistics tool”. Monthly light fishing fleets position data per season then overlaid with spatial analysis results and environmental parameters namely SST and chlorophyll-a concentration. The flow chart for VBD data processing is shown at Figure 3.

Table 2

Dominant fishing gears using light as Fish Aggregating Devices (FADs) in the Western Indian Ocean

No	Fishing Gears	Target Species	Light Description
1	Purse seine	Tuna, Mackerel Tuna, Skipjack, Mackerel	HPIT Spotlights with halogen bulb 1000-5000 watt/ 15-40 bulbs or FADs, depending on the ship size
2	Hand Line	Yellow Fin Tuna, Big Eye Tuna, Demersal Fishes	HPIT Spotlights with halogen bulb 1000-5000 watt/10-20 bulbs or FADs
3	Boat lift net	Skipjack, Mackerel Tuna, Mackerel	HPIT Spotlights with halogen bulb 1000-5000 watt/10-30 bulbs or FADs; sometimes, underwater lights are also used with a capacity of 500-1000 watts/2-8 units or FADs
4	Set lift net	Anchovies, Squid, other little pelagic fish	LED or metal halide bulbs with size 30-100 watt/5-20 bulbs or FADs, sometimes, underwater modified lights are also used.

Source: Statistic report of Bungus Fishing Port (2017) and Geronimo et al. (2018)

Spatiotemporal Analysis of Light Fishing Fleets Distribution Pattern

The calculation of the geographical distribution was carried out using the GIS-based model to determine 4 spatial indicators, namely central tendency, spatial dispersion, directional dispersion, and directional trends (Figure 3) (Fischer & Getis, 2010). GIS based model applied in this study is spatial statistical analysis (Fischer & Getis, 2010; Perzia et al., 2016). It is a well-known spatial modelling because of flexibility in data storage and management, easy to understand both analytical and technical, and applicable. The spatial tendencies

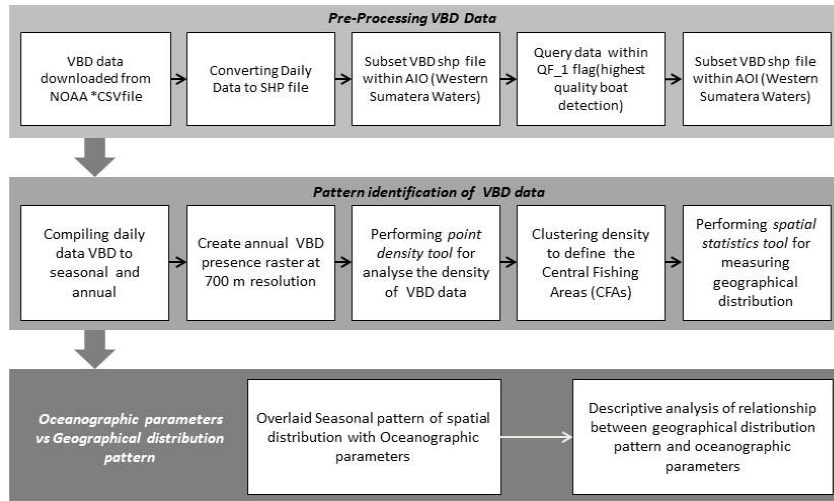


Figure 3. Flowchart of VBD data application to detect spatiotemporal patterns of light fishing fleets distribution in West Sumatera Waters

were calculated using the “mean centre tool” which is the distribution geographical centre calculation of the light fishing fleets, the average x , and y coordinates of the total VBD coordinates in the study area. Changes in the central tendency reflect variations in the distribution of light fishing fleets both spatially and temporally (Perzia et al., 2016).

The spatial dispersion was calculated using a “standard distance tool” representing the degree where the spatial fishing fleets are spatially concentrated or distributed around the central tendency. The spatial dispersion maps is represented by circles with a radius equal to 95% of the total VBD data as input in the study area. The radius value of the circle was assumed as the concentration level of the spatial distribution. The greater of the circle radius value, the more dispersed the light fishing fleet spatial distribution will be or vice versa (Perzia et al., 2016).

Directional dispersion and directional trend were calculated using the “standard deviational ellipses tool.” The directional scattering calculated the standard distance from the direction of the x and y coordinates distributions that were represented by oval visualization containing 95% of the total data input. Thus, the extent of light fishing fleet distribution in an area was determined. On the other hand, directional trends stated the direction degree of the distribution data input. The directional trends are representations of extending clockwise axis rotation starting at mid-day point. Generally, the description and equations of the spatial indicators that performed in this study is shown in Table 3.

Central tendency was average of total x (longitude) and y (latitude) coordinates in the study area. Spatial dispersion was the result of standard deviation of total x and y coordinates over study area, while the directional dispersion was standard deviation over

x coordinates and standard deviation over y coordinates that represent of standard distance over the direction of x and y coordinates. Directional trends were the calculation of degree A, B, and C. Clear brief of this equation explained as follow:

$$A = \left(\sum_{i=1}^n \tilde{x}_i^2 - \sum_{i=1}^n \tilde{y}_i^2 \right) \quad B = \sqrt{\left(\sum_{i=1}^n \tilde{x}_i^2 - \sum_{i=1}^n \tilde{y}_i^2 \right)^2 + 4 \left(\sum_{i=1}^n \tilde{x}_i \tilde{y}_i \right)^2} \quad C = 2 \sum_{i=1}^n \tilde{x}_i \tilde{y}_i$$

\tilde{x}_i and \tilde{y}_i are the deviations for the x - y coordinates from the mean centre calculation.

Table 3

Spatial indicators used in this study

Spatial Indicators	Equations	Spatial Scale	Time Scale	Ecological Explanation
Central Tendency	$\bar{X} = \frac{\sum_{i=1}^n xi}{n} \quad \bar{Y} = \frac{\sum_{i=1}^n yi}{n}$	Global	Daily & Seasonal	Centre of the fishing fleet
Spatial Dispersion	$SD = \sqrt{\frac{\sum_{i=1}^n (xi - \bar{x})^2}{n} + \frac{\sum_{i=1}^n (yi - \bar{y})^2}{n}}$	Global	Daily & Seasonal	Spatial dispersion Coordinates of light fishing fleets
Directional Dispersion	$SDx = \sqrt{\frac{\sum_{i=1}^n (xi - \bar{x})^2}{n}} \quad SDy = \sqrt{\frac{\sum_{i=1}^n (yi - \bar{y})^2}{n}}$	Global	Daily & Seasonal	Directional distribution of axis x and y
Directional Trend	$\tan \theta = \frac{A + B}{C}$	Global	Daily & Seasonal	The directional tendency of light fishing fleets (spatial distribution)

Source: (Perzia et al., 2016)

Effect of Environmental Parameters on Fleet Spatial Distribution

The relationship between spatial fish distribution and oceanographic parameters tends to be non-linear (Bertrand et al., 2004; França et al., 2012). Nevertheless, the prediction of PFZs is still carried out based on signs of biophysical conditions in the aquatic environment. It proves that it has a significant contribution to the influence of the fish distribution and fishing fleets distribution. The SST and chlorophyll-a are known as parameters widely used for PFZs analysis (Zainuddin & Saitoh, 2008; Lanz et al., 2009; Nurdin et al., 2017).

The chlorophyll-a can determine water productivity and fish production even though the relationship is not direct (Bertrand et al., 2002). Lumban-Gaol et al. (2015) explained

that the sea level and eddies current indirectly indicated good habitat for the feeding area. The environment data were overlaid with the VBD's geographical distribution to understand the daily and seasonal distribution patterns of the fishing fleet. The daily sample data were taken at the new moon phase in each month (every season) to ensure that the detected activity points have the best radiance intensities (Elvidge et al., 2015). More explanation on the type of data, unit of data, description, and source of data is shown in Table 4.

Table 4

Materials, data units, descriptions and data sources

Data Type	Data Source	Description
Actual Fishing Data		
Actual fishing data	Daily logbook of the hand line fishing	Bungus fishing port daily logbook datasheets
Environmental Data		
Sea Surface Temperature (SST)	http://marine.copernicus.eu/	Monthly; The Global ARMOR3D L4 dataset; data combination AVHRR, AMSR and in situ observation of NCDC NOAA; spatial resolution 0.25°x0.25°
Chlorophyll-a concentration	http://marine.copernicus.eu/	Monthly; PISCES biogeochemical model data, spatial resolution 0.25°x0.25°;
Light Fishing Data		
VIIRS Boat Detection	https://www.ngdc.noaa.gov/eog/viirs/download_boat.html	Daily; VBD data (VIIRS Boat Detection) level 3; spatial resolution (0.375 km – 1.6 km); scanning width 3000 km

RESULTS AND DISCUSSION

Figure 4 shows the total fleets detected by VIIRS DNB at the pixel area (700 x 700 m). High value of detected fleet (5 to 36 units per pixel) dominantly were at the coast water of west Sumatera, Mentawai strait, and coast water of Bota Island at the southern part of study area. Low value of detected fleet (1 to 5 units per pixel) dispersed within the study area. This information represented fishing pressure at the study area based on light fishing fleets spatial distribution. Figure 5 shows the DNB radiance value that represents the light intensity detected from DNB Image. Both figures relate to the density of the light fishing activity and the dominant fishing gear types operated at that area. Higher radiance value suspected related to the fishing gear that utilized big amount of lights as FADs (Table 2). The light used at the fishing activities linearly correlated with the radiance value that was detected by VIIRS DNB Image.

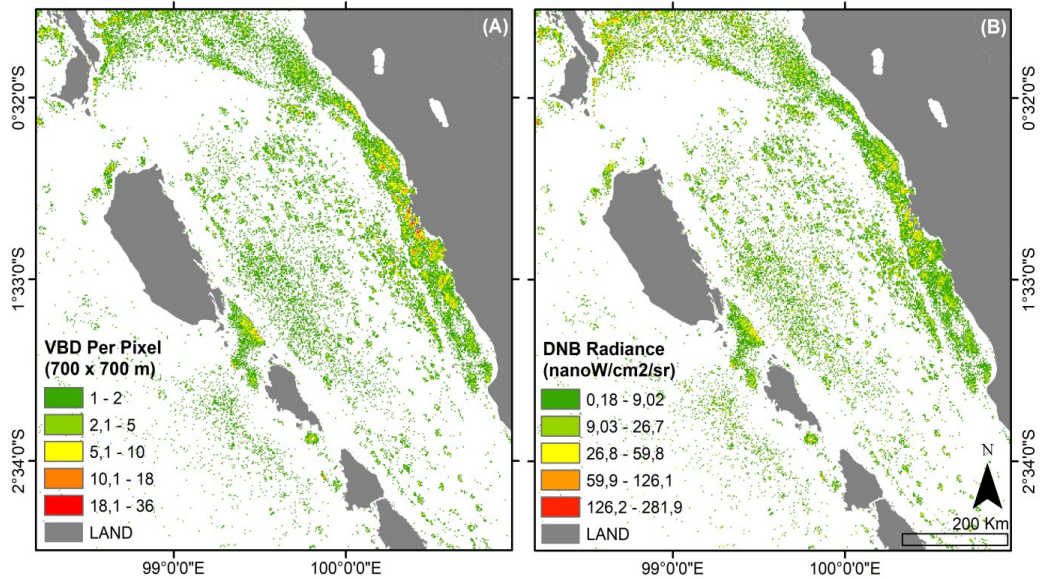


Figure 4. VBD data from 2014 - 2018 were rasterized with a resolution of 700 x 700 m (A) The number of VBD detected per pixel from 1780 nights and (B) Radiance values for each VBD point detected

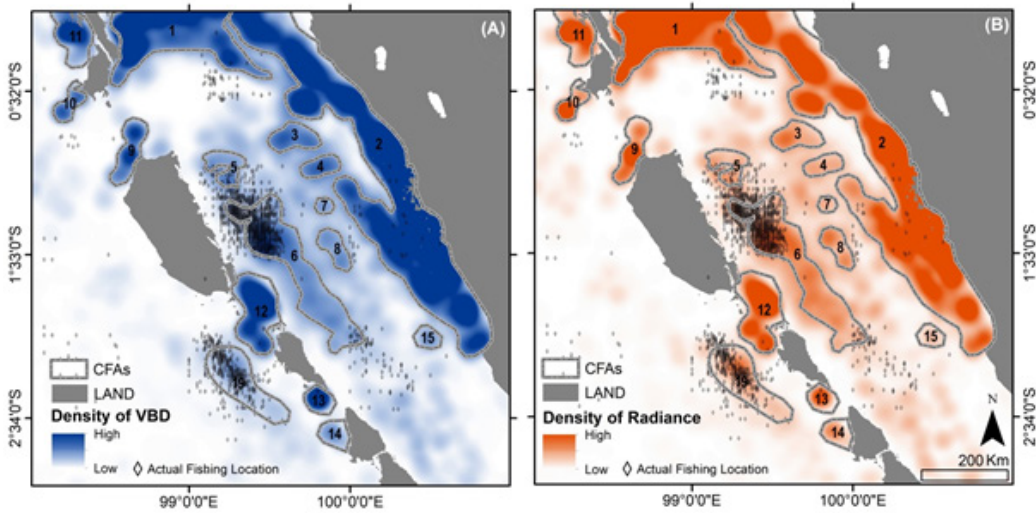


Figure 5. Central Fishing Area (CFA) and actual fishing fleets data in West Sumatra Waters during 2014-2018. (A) CFA and spatial density of the number of VBD/pixel (B) CFA and spatial density of radiance values/pixels

The VBD in WSW indicates a variation in the spatial patterns, i.e., the number of VBD per pixel and radiance value per pixel. The number of VBD per pixel was dominantly seen in classes 1 to 2 VBD, while the class above 2 was dominant at coast waters and Mentawai strait. The dominant radiances have been seen in class that is smaller than 26.71 nW/cm²/sr. The spatial pattern of the high radiances was consistent with the VBD's value per pixel, which tended to be in the coastal water areas (Figure 4).

Figure 4 shows that the spatial pattern of dominant radiance value < 9.03 nW/cm²/sr spread throughout the area, while the spatial pattern of radiance value > 9.03 nW/cm²/sr was dominantly located near the coast and straits of the study area. This due to < 10 GT vessels are generally lift net and mini purse seine that densely distributed in the coastal waters of west Sumatera. They predominantly used 5-40 lights as FADs, causing the value of detected radiances intensity greater and clearer in the coastal area. The difference in detected radiances intensity was highly related to the number of lights used in fishing activities (Hsu et al., 2019).

The radiance intensity was expressed in nW/cm²/sr for the boat detection. Actual radiance intensity data was expressed in W/cm²/sr that had seven to ten zeros after the decimal point before the start of significant digits. For better understanding, the W/cm²/sr was multiplied by billion and became nW/cm²/sr. This idea intended to produce number with one or two digits to the left of decimal point and a string of values to the right of the decimal point (Elvidge et al., 2015). High intensity of radiances represents high intensity light sources at sea. The high radiance distribution at coast water of west Sumatra explained that dominant fishing gear used at that area was boat lift net. Boat lift net is light based fishing gear that catches pelagic fish, operates at night and utilizes 30 – 60 light sources. At the center of Mentawai strait, radiance intensity became smaller due to long line, hand line and purse seine fishing activity.

The ability of VIIRS night imaging is very significant in improving the quality of night-time image results compared to its predecessor, the DMSP satellite in terms of radiometric resolution and spatial resolution; that is very important in the process of extracting information on vessel position through lights in the sea (Miller et al., 2013 & Elvidge et al., 2015). Another advantage of using VIIRS DNB data is VIIRS day/night band (DNB) collects low light imaging data 45 times smaller pixel footprint than the DMSP (Elvidge et al., 2013). Elvidge et al. (2015) explained that VIIRS DNB also had higher level of quantization, rigorous calibration, and additional spectral bands useful for cloud, ocean and combustion source characterization. Further, they stated that VIIRS had high capability of detecting vastly more lit fishing boat features when compared to DMSP.

According to all of the advantages of VIIRS DNB data among DMSP, we assessed some fisheries study based on this datasets. VBD data is a new product that produced from VIIRS DNB data analysis. In this study, we performed VBD data to identify, delineate,

characterize and analyse the CFAs in WSW. The CFAs also compared with actual fishing position data to analyse how the CFAs relates to the actual fishing activities within study area.

CFA from VBD Data

The analysis of the VBD data (2014 - 2018) showed spatially different densities. The high-density radiance was more concentrated in coastal areas while low-density VBD numbers covered a wider area. This spatial density informed that the pressure of fishing activities at WSW tended to occur in the waters of the strait and coast (Figure 5). The pattern of the spatial density was used as an excuse to predict the causes of high fishing activities in these locations.

The pattern of spatial density was used as the basis for determining and identifying CFAs in WSW. Besides, it was also used to compare the spatial patterns of CFAs with the actual fishing data. The spatial interpretation was conducted to delineate the location of the CFAs. A total of 19 CFAs was identified in WSW (Figure 5) with varying areas and shapes (Table 5). The widest CFAs was recognized at CFAs No. 2 which reached 9813.74 km² in the coastal area of the west coast of west Sumatra. The location of the CFAs extends from the south to the north near the strait of the Islands. The smallest CFAs was identified as CFAs No. 16 covering 29.50 km² in the northern coast of North Pagai Island or Pagai waters. It was PFZs for traditional fishers from the north and south Pagai Islands, predominantly using the boat and set lift net. All the extent of CFAs and the identification of each CFAs are shown in Table 5.

The result of CFAs identification and actual data on hand line fishing determined that the actual point of hand line fishing was included in certain CFAs or associated with some CFAs. CFAs No 1, 5, 6, 8, and 19 were the most related CFAs to actual data. The highest intensity of the actual data was at CFAs No 6, which was at range of 99°E - 99.5°E and 1°S - 2°S corresponding to the Mentawai Strait. The intensity of the fishing activities from the actual data was also high at CFAs No. 19, which was west of Sipora Island water. The CFAs data and identification results provided information related to the traditional PFZs at WSW. However, those CFAs intersect with the other conventional PFZs of fishing gear such as lift net, longline and purse seine which were also the dominant fishing gear used by fishers in the WSW (Harahap et al., 2018). Lift net, longline and purse seine PFZs were also used in certain zones around the Mentawai strait in the No.6 CFAs area.

CFAs data also are applied to identify tuna fishing centres, especially hand line fishing. The WPP 572 is also known as traditional PFZs for tuna fishing vessels, coming from Sibolga fishing port at north Sumatra, Bungus fishing port and Nizam Zachman fishing port at Jakarta. WSW is one of strategic traditional PFZs of hand line in west Sumatera in term of accessibility, productivity and connectivity. A traditional PFZs means that the

Table 5

Identification of Core Fishing Area (CFA n = 19) in the West Sumatera Waters

CFAs No	Extensive Estimation (Km ²)	CFAs Description
1	3630.54	Bota Island strait
2	9813.74	West coast waters of West Sumatera
3	507.11	Mentawai strait I
4	307.32	Mentawai strait II
5	433.23	Off the east coast water of Siberut Island I
6	2729.01	Off the east coast water Siberut & Sipora Island
7	118.32	Mentawai strait III
8	380.47	Mentawai strait IV
9	617.64	North coast water of Siberut Island
10	314.89	Southwest coast water of Bota Island
11	921.29	West coast water of Bota Island
12	1276.93	Bunga Laut strait
13	305.86	Sipora strait
14	329.35	South coast water of South Pagai Island
15	226.41	Mentawai strait V
16	129.50	North coast water of North Pagai Island
17	720.20	Off the coast South Pagai Island
18	1082.20	Southern water of Pagai Island
19	1338.26	Western water of Sipora Island

Source: Analysis of VBD and actual fishing data

PFZs is determined by conventional methods, such as fishing habits, natural signs (flying birds, schooling dolphins, ripples on the sea surface) and foreign objects that float in the waters (Nurdin et al., 2010; Nurdin et al., 2015; Nurdin et al., 2017). PFZs is always connected to a fishing base as the pre and post fishing activities base (fishing port) (Hsu et al., 2019). This result is still relevant to explain because fleets detected in the night-time imagery are dominantly catching pelagic fish as well as hand line fishing vessels that catch yellow fin tuna. Yellow fin tuna distributes vertically near to water surface during the night, so it was possible to used lights as FADs for hand line.

Internal and external factors in fishing activities significantly influence the fishing locations base on types of fishing gear in WSW. Thus, the identification results were not representative to describe certain kinds of fishing gear (PFZs). Girardin et al. (2017)

explained similar aspects, where the factors influenced Fisher's decision in choosing fishing locations and also projections of expenditure, estimation of risks, and habits in determining fishing areas. Furthermore, Geronimo et al. (2018) explained that environmental factors had a very high influence on the spatial structure of VBD detection results, especially in locations with high spatial density.

Moreover, the approach used the VBD data which could not distinguish certain types of fishing gear in waters. However, despite these shortcomings, the existence of information regarding the distribution of fishing activities that is openly accessible, made it possible to fill the gaps of data availability that can be used in marine and fisheries management studies (Elvidge et al., 2015; Geronimo et al., 2018).

Geographic Distribution Estimation from VBD Data

Table 6 reveals the results of the estimation of spatial indicators (central tendency, spatial dispersion, directional dispersion, and directional trends) which were estimated from the sample of daily data in 2014-2018. Dataset was selected in the day in the new moon phase to ensure the clearest intensity from ship's lights representing the vessels position (Elvidge et al., 2015). However, there were < 5 units of VBD data detected and causing the estimation of geographical distribution unsuccessful.

The daily VBD unit ranged from 0-200 units during the year. The highest VBD unit was detected in July 23rd, 2017 as many as 174 units (during the day in the southeast monsoon season). The lowest VBD units were 0 units on April 25th, 2017 (during a day in the transition I monsoon). Atmospheric and oceanographic conditions played the main role in determining the VBD unit at sea (Elvidge et al., 2015; Geronimo et al., 2018). The amount of VBD detected daily was very influential on the results of daily geographical distribution estimation per season in 2014-2018. Unsuccessful quantification of geographical distribution was caused by the presence of < 5 unit data at our dataset. The distribution pattern and unsuccessful quantification of geographical distribution are shown at Figure 6.

Generally, the result confirmed that geographic distribution of light fishing fleets was wider during the northwest and southeast monsoon and became more compact at transition I and II monsoon. The variability of SST and chlorophyll-a concentration during different season influenced the geographic distribution of light fishing fleet at west Sumatera waters. Geronimo et al., (2018) reported that environment parameter as the main influence of the light fishing fleet distribution at sea.

Table 6 shows the estimation results of the spatial indicators for the daily data per season in 2014–2018. The highest spatial value of spatial dispersions was identified in the 2016 northwest monsoon with a value of 168.94 km. This value indicates a wider distribution of fishing activities in the study area. The same result was also identified in the spatial

indicator of directional dispersion in the same year for the x value of 204.92 km, but the y value did not necessarily has linear values that increased against the value of x and spatial dispersion. The trend of the direction of distribution monitored from the estimation results showed the geographical orientation in the value range between 97.99° - 171.48° . The value of spatial indicators was determined by fishing points dispersion at sea that influenced by oceanographic parameters, fishers skill, fishing season, and accommodation (Kaschner et al., 2006; Saraux et al., 2014; Perzia et al., 2016; Harahap et al., 2018). Furthermore, it can be seen in Table 6 that the fishing activities were more dispersed in the northwest and southeast monsoon, which was confirmed by the visual appearance in Figure 6.

The central tendency of the VBD distribution or fishing activities of the sample days in each season from 2014 to 2018 is shown in Figure 6. The central tendency on the sample day of the transition I and transition II was more spatially dispersed. It shows that some points located slightly far in the south and west. In the central tendency in the northwest and southeast monsoon, the sample data tended to be centred and shifted less in the study area, which is only concentrated at 99°E - 100°E and 0.5°S - 2°S (Figure 6 of mean centre). This is also clearly confirmed by the results of other spatial indicator estimations shown in Figure 6 and Table 6. The daily sample data showed variations in the distribution of the detected fishing activities based on vessel lights. The spatial pattern and estimation results represented the dynamics of fishing activities of the lighted fishing fleet at the WSW.

The GIS approach has been widely applied in marine and fisheries studies, such as Perzia et al. (2016) in terms of monitoring of sword fishing activities and CPUE (Catch per Unit Effort) analysis; fisheries management planning (Close & Hall, 2006); fish pelagic distribution modelling (Saraux et al., 2014 & Harahap et al., 2018); and the relationship between environmental parameters and fish distribution (Kaschner et al., 2006). The GIS enables more dynamic and efficient management (fisheries and marine spatial) of data with the methods that are flexible regarding storage and processing (Perzia et al., 2016). The GIS-based analysis proved that it could be an alternative approach for marine and fisheries resources management.

Table 6

Spatial indicator values of daily geographical distribution per season 2014-2018

Object ID	Seasons	Spatial Dispersion (km)	Directional Dispersion x (km)	Directional Dispersion y (km)	Directional Trends ($^{\circ}$)
1.14	Northwest Monsoon	147.89	160.69	133.86	156.59
1.15	Northwest Monsoon	124.57	160.34	72.99	150.65

Table 6 (Continued)

Object ID	Seasons	Spatial Dispersion (km)	Directional Dispersion x (km)	Directional Dispersion y (km)	Directional Trends (°)
1.16	Northwest Monsoon	168.94	204.92	122.84	109.95
1.17	Northwest Monsoon	110.21	135.07	77.76	123.47
1.18	Northwest Monsoon	104.57	127.86	74.30	132.85
4.14	Transition I	101.69	132.07	56.92	130.09
4.15	Transition I	0.00	0.00	0.00	0.00
4.16	Transition I	127.61	139.84	114.07	157.46
4.17	Transition I	0.00	0.00	0.00	0.00
4.18	Transition I	0.00	0.00	0.00	0.00
7.14	Southeast Monson	160.61	138.95	179.68	70.04
7.15	Southeast Monson	89.29	95.63	82.46	171.48
7.16	Southeast Monson	172.05	216.65	110.76	97.99
7.17	Southeast Monson	102.37	118.52	83.14	127.70
7.18	Southeast Monson	156.57	213.05	60.32	144.10
10.14	Transition II	112.25	122.45	101.03	124.88
10.15	Transition II	0.00	0.00	0.00	0.00
10.16	Transition II	65.15	91.53	10.61	142.63
10.17	Transition II	123.88	160.21	70.89	154.71

Note: Object ID (Month.Year) → (1.14) → (January 2014)

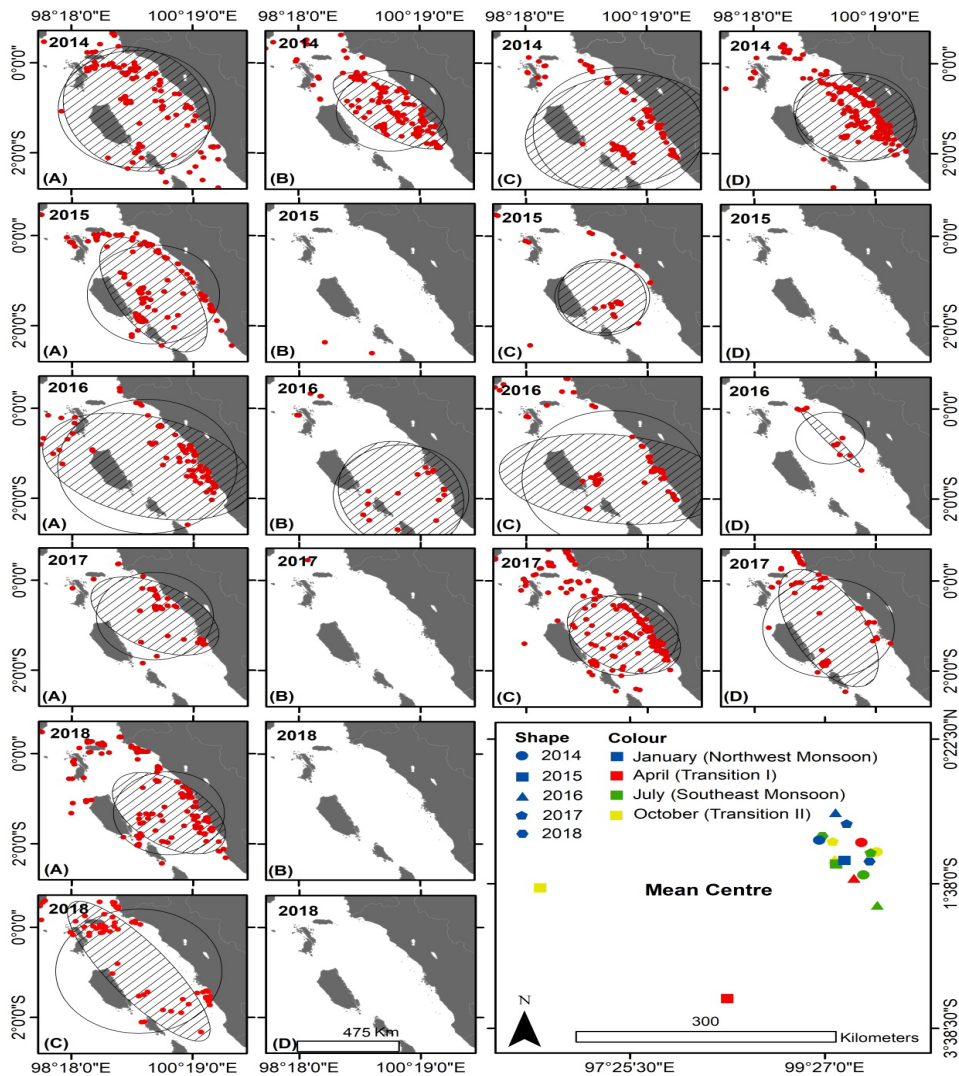


Figure 6. Map of VBD daily distribution per season from 2014 to 2018. Spatial dispersion (circles), directional dispersion, directional trends (ellipses), and mean centre (centre of fleet concentration from daily VBD per season). (A) Northwest monsoon, (B) Transition I, (C) Southeast monsoon, (D) Transition II

Environmental Parameters against Geographical Distribution

According to Siregar et al. (2018), the SST distribution in Indian Ocean is relatively warm with an average 28°C and cooler in southern part during the northwest monsoon so the north and south equatorial currents strengthen westward. SST gets warmer during transition I with value around 29°C and become colder in southeast monsoon because of the surface wind circulation pattern both in the northern hemisphere and southern hemisphere showing

regular patterns. During the transition II season, SST begins to get warmer due to weak wind circulation, the north equatorial current does not move yet causing colder SST at southern hemisphere of Indian Ocean. Chlorophyll-a concentration at western Sumatera waters consistently high at the west coast of Sumatera and at the southern area near Bota Island. Changes in current, wind, and atmospheric event influence the distribution of chlorophyll-a concentration at western Sumatera.

The variability of SST and chlorophyll-a concentration during different season influences the geographic distribution of light fishing fleet at west Sumatera waters. Figure 7 and 8 visually show that the geographical distribution of fishing fleets detected through VBD was very random spatially. In general, the VBD detection spread over a range of SST values between 27°C-32°C and chlorophyll-a concentration between 0.007 mg/m³ to 0.42 mg/m³. The lowest value of SST occurred in the northwest monsoon month in 2014 at a value of 27.96°C, and the highest occurred in the transition II in 2014 at the value of 31.99°C.

Meanwhile, the lowest value of chlorophyll-a concentration occurred in the southeast monsoon months and the first transition in 2014 at a value of 0.007 mg/m³, with the highest value observed in the northwest monsoon in 2017 at 0.42 mg/m³. Those parameters influenced fisheries distribution and determined fish habitat preferences. It is supported by the results of Nurdin et al. (2017) that mackerel preferred habitat at SST between 26.05°C - 31.97°C, with a chlorophyll-a concentration between 0.001 mg/m³-0,1 mg/m³. Siregar et al. (2018) also reported that range of SST preferences around 29°C – 29.5°C for yellow fin tuna species, chlorophyll-a concentration value in range between 0.15 – 0.25 mg m⁻³. Harahap et al. (2018) also reported that variability of SST at range 29 – 31°C and chlorophyll-a concentration varied between 0.10 – 0.40 mg/m³ were the main range related to the pelagic fish distribution at west Sumatera Waters. Chlorophyll-a concentration is a parameter that can indirectly determine water productivity and fish production. Thus, it is widely used in studies related to the determination of fish habitat preferences (Bertrand et al., 2002).

The geographical distribution pattern in the northwest monsoon was consistent with the directional dispersion (ellipse) and the standard dispersion (circles) patterns and had the same model and direction at *x* and *y*. From 2014 to 2017 for all seasons, the lowest distribution occurred in the southeast monsoon 2017 with an SST range between 29.22°C-31.52°C. Widest distribution occurred in the transition II 2015, where the VBD was detected in the Mentawai strait, and extended along the west coast of west Sumatra to the straits of Bota Island.

High SST was monitored at the northwest position of Bota Island and tended to be medium and low on the west coast of west Sumatra (Figure 7), where fishing activity was monitored to be dense from the results of boats detection. This spatial pattern was consistent with the distribution of chlorophyll-a, which was high on the coast (Figure 8). The highest

geographical distribution occurred in the second transitional season in 2015. The VBD points were detected spread and consistent towards the high distribution patterns of the SST in the west of Mentawai waters and on the west coast of West Sumatra. This distribution pattern was inconsistent with the spatial distribution patterns of the chlorophyll-a concentration that was high on the west coast to the south near the Pagai Islands.

Wyrтки (1961) stated that monsoons strongly influenced the circulation of the eastern Indian Ocean. The monsoon winds moving throughout the year affected the speed and direction of the sea surface, not apart from the waters of West Sumatra. Changes in wind direction occurred throughout the year would affect the course of the flow and movement of water masses in the Eastern Indian Ocean (EIO). It also influenced the variability of oceanographic parameters in the WSW, including sea surface temperature and chlorophyll-a concentration.

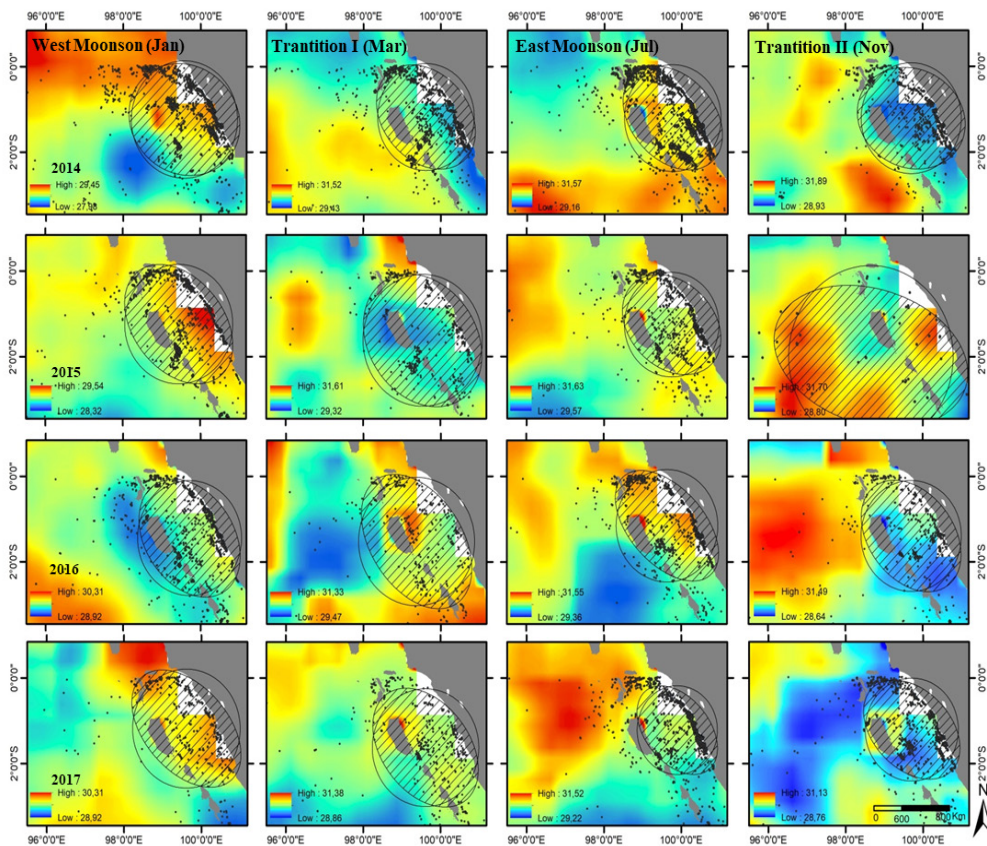


Figure 7. Monthly VBD distribution per season (northwest monsoon = January, transition I = April, southeast = July, transition II = November; consecutive left-to-right rows) in 2014-2017 (consecutive top-down column) on the spatial distribution of sea surface temperature (SST) in the West Sumatera Waters

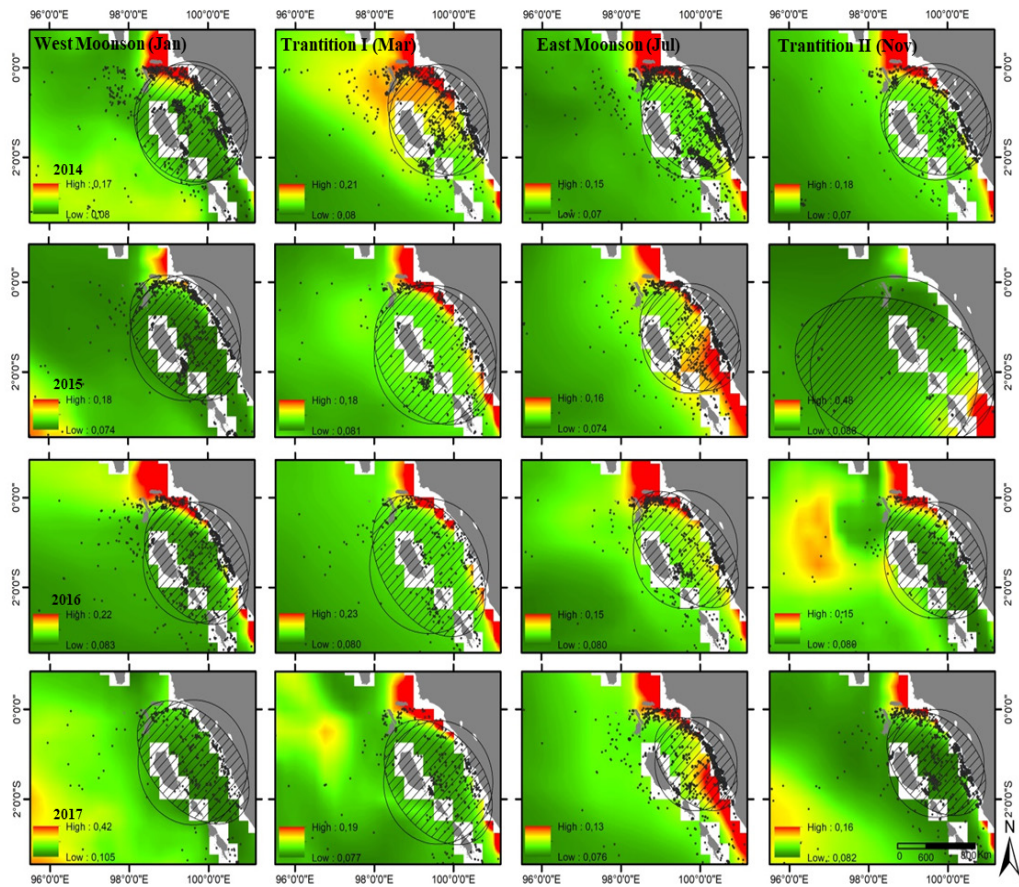


Figure 8. Monthly VBD distribution per season (northwest monsoon = January, transition I = April, southeast = July, transition II = November; consecutive left-to-right rows) in 2014-2017 (consecutive top-down column) on the spatial distribution of chlorophyll-a concentrations in West Sumatra Waters

CONCLUSION

The distribution of the VBD per pixel > 5 VBD/pixel was dominant in coastal waters, including the west coast of West Sumatra, the strait of the Bunga Sea and the coastal waters of Bota Island. The spatial pattern of the radiances showed that the value < 9.03 nW/cm²/sr was dominantly spread out throughout the study area. The spatial models of the radiance values > 9.03 nW/cm²/sr were dominant in waters near the coast and strait. This pattern was consistent with the spatial density, which was high in specific locations identified as CFA in this study. The largest CFA was recognized in CFA 2 with an area reaching 9813.74 km² in the waters of the West Sumatra coast. The CFA location extends from the south to the north near the straits of Bota Island. The smallest CFA was identified as CFA 16 covering

an area of 129.50 km² which was an area of north coast waters of northern Pagai Island or the waters of Pagai Island.

The highest spatial dispersion values were identified in the sample days in the northwest monsoon (2016) with a value of 168.94 km², indicates the wider distribution. The same results were also identified in the directional dispersion in the same year for x values of 204.92 km², but for y values, it did not linearly increase with the value of x and spatial dispersion. The directional trend of the distribution monitored from the estimation results showed the geographical orientation in ranging from 97.99° to 171.48°. The geographic distribution of light fishing fleets were in the SST between 27°C-32°C with chlorophyll- a between 0.007 mg/m³ to 0.42 mg/m³. The tendency of the geographical distribution of the fleet was dominant in coastal and strait waters.

ACKNOWLEDGMENT

The authors would like to express their gratitude to all the Bungus Fishing Port's staff for help in accessing the fishing logbook data. We also thank to Ministry of Research, Technology, and Higher Education of Indonesian Republic for funding this research in the Magister Thesis research scheme. This research was carried out using EU data Copernicus Marine Service Information. The authors also wish to express special thanks to colleagues in Marine Science and Technology Department, Marine GIS Laboratory, Marine Remote Sensing Laboratory, and Spatial Mapping and Modelling Laboratory, IPB University, for their suggestions and inputs in completing this research.

REFERENCES

- Bertrand, A., Josse, E., Bach, P., Gros, P., & Dagorn, L. (2002). Hydrological and trophic characteristics of tuna habitat: consequences on tuna distribution and longline catchability. *Canadian Journal of Fisheries and Aquatic Sciences*, 59(6), 1002-1013.
- Bertrand, A., Segura, M., Gutiérrez, M., & Vásquez, L. (2004). From small-scale habitat loopholes to decadal cycles: a habitat-based hypothesis explaining fluctuation in pelagic fish populations off Peru. *Fish and Fisheries*, 5(4), 296-316.
- Booth, A. J. (2000). Incorporating the spatial component of fisheries data into stock assessment models. *ICES Journal of Marine Science*, 57(4), 858-865.
- Bungus Fishing Port. (2017). *Statistical report of bungus fishing port*. Padang, Indonesia.
- Cabral, R. B., Gaines, S. D., Johnson, B. A., Bell, T. W., & White, C. (2016). Drivers of redistribution of fishing and non-fishing effort after the implementation of a marine protected area network. *Ecological Applications*, 27(2), 416-428.
- Close, C. H., & Hall, G. B. (2006). A GIS-based protocol for the collection and use of local knowledge in fisheries management planning. *Journal of Environmental Management*, 78(4), 341-352.

- Cozzolino, E., & Lasta, C. A. (2016). Use of VIIRS DNB satellite images to detect jigger ships involved in the *Illex argentinus* fishery. *Remote Sensing Applications: Society and Environment*, 4, 167-178.
- Davies, T. W., Duffy, J. P., Bennie, J., & Gaston, K. J. (2014). The nature, extent, and ecological implications of marine light pollution. *Frontiers in Ecology and the Environment*, 12(6), 347-355.
- Davies, T. W., Duffy, J. P., Bennie, J., & Gaston, K. J. (2016). Stemming the tide of light pollution encroaching into marine protected areas. *Conservation Letters*, 9(3), 164-171.
- Dineshbabu, A. P., Thomas, S., & Rohit, P. (2014). GIS-based spatial data analysis for marine fisheries management as a prerequisite for mariculture development. *Fishing Chimes*, 33(10-1), 91-93.
- Elvidge, C. D., Baugh, K. E., Zhizhin, M., & Hsu, F. C. (2013). Why VIIRS data are superior to DMSP for mapping nighttime lights. *Proceedings of the Asia-Pacific Advanced Network*, 35(0), 62-69.
- Elvidge, C. D., Ghosh, T., Baugh, K., Zhizhin, M., Hsu, F. C., Katada, N. S., ... & Hung, B. Q. (2018). Rating the effectiveness of fishery closures with visible infrared imaging radiometer suite boat detection data. *Frontiers in Marine Science*, 5(April), 1-15.
- Elvidge, C. D., Zhizhin, M., Baugh, K., & Hsu, F. C. (2015). Automatic boat identification system for VIIRS low light imaging data. *Remote Sensing*, 7(3), 3020-3036.
- Elvidge, C., Zhizhin, M., Baugh, K., Hsu, F. C., & Ghosh, T. (2016). Methods for global survey of natural gas flaring from visible infrared imaging radiometer suite data. *Energies*, 9(1), 14-28.
- Elvidge, C. D., Ziskin, D., Baugh, K. E., Tuttle, B. T., Ghosh, T., Pack, D. W., ... & Zhizhin, M. (2009). A fifteen year record of global natural gas flaring derived from satellite data. *Energies*, 2(3), 595-622.
- Fischer, M. M., & Getis, A. (2010). *Handbook of Applied Spatial Analysis*. Heidelberg, Germany: Springer-Verlag
- França, S., Vasconcelos, R. P., Fonseca, V. F., Tanner, S. E., Reis-Santos, P., Costa, M. J., & Cabral, H. N. (2012). Predicting fish community properties within estuaries: Influence of habitat type and other environmental features. *Estuarine, Coastal and Shelf Science*, 107, 22-31.
- Geronimo, R., Franklin, E., Brainard, R., Elvidge, C., Santos, M., Venegas, R., & Mora, C. (2018). Mapping fishing activities and suitable fishing grounds using nighttime satellite images and maximum entropy modelling. *Remote Sensing*, 10(10), 1604-1626.
- Girardin, R., Hamon, K. G., Pinnegar, J., Poos, J. J., Thébaud, O., Tidd, A., ... & Marchal, P. (2017). Thirty years of fleet dynamics modelling using discrete-choice models: What have we learned? *Fish and Fisheries*, 18(4), 638-655.
- Harahap, M. A., Siregar, V. P., & Agus, S. A. (2018). *Analisis sebaran spasial dan temporal Ikan Pelagis berdasarkan parameter oseanografi di Perairan Sumatera Barat* [Analisis Spatial and Temporal Pelagic Fish Based on Oceanography Parameters in the Waters of West Sumatera] (Master Thesis). IPB University, Indonesia.
- Hsu, F. C., Elvidge, C. D., Baugh, K., Zhizhin, M., Ghosh, T., Kroodsma, D., ... & Sudarja, Y. (2019). Cross-Matching VIIRS Boat Detections with Vessel Monitoring System Tracks in Indonesia. *Remote Sensing*, 11(9), 995-1020.

- Jayaraman, J., George, G., Ambrose, T. V., & Manjeesh, R. (2013). Marine Geographic Information Systems and their Application in Fisheries Management. In S. K. Soam, P. D. Sreekanth & N. H. Rao (Eds.), *Geospatial technologies for natural resources management* (pp. 437-449). New Delhi, India: New India Publishing Agency.
- Jennings, S., & Lee, J. (2012). Defining fishing grounds with vessel monitoring system data. *ICES Journal of Marine Science*, 69(1), 51-63.
- Kaschner, K., Watson, R., Trites, A. W., & Pauly, D. (2006). Mapping world-wide distributions of marine mammal species using a relative environmental suitability (RES) model. *Marine Ecology Progress Series*, 316, 285-310.
- Kiyofuji, H., & Saitoh, S. I. (2004). Use of nighttime visible images to detect Japanese common squid (*Todarodes pacificus*) fishing areas and potential migration routes in the sea of Japan. *Marine Ecology Progress Series*, 276(1), 173-186.
- Kroodsma, D. A., Mayorga, J., Hochberg, T., Miller, N. A., Boerder, K., Ferretti, F., ... & Woods, P. (2018). Tracking the global footprint of fisheries. *Science*, 359(6378), 904-908.
- Lan, K. W., Evans, K., & Lee, M. A. (2013). Effects of climate variability on the distribution and fishing conditions of yellowfin tuna (*Thunnus albacares*) in the western Indian Ocean. *Climatic Change*, 119(1), 63-77.
- Lan, K. W., Shimada, T., Lee, M. A., Su, N. J., & Chang, Y. (2017). Using remote-sensing environmental and fishery data to map potential yellowfin tuna habitats in the Tropical Pacific Ocean. *Remote Sensing*, 9(5), 1-14.
- Lanz, E., López-Martínez, J., Nevarez-Martínez, M., & Dworak, J. A. (2009). Small pelagic fish catches in the Gulf of California associated with sea surface temperature and chlorophyll. *CalCOFI Reports*, 50, 134-146.
- Lumban-Gaol, J., Leben, R. R., Vignudelli, S., Mahapatra, K., Okada, Y., Nababan, B., ... & Syahdan, M. (2015). Variability of satellite-derived sea surface height anomaly, and its relationship with Bigeye tuna (*Thunnus obesus*) catch in the Eastern Indian Ocean. *European Journal of Remote Sensing*, 48(1), 465-477.
- Miller, S. D., Straka, W., Mills, S. P., Elvidge, C. D., Lee, T. F., Solbrig, J., ... & Weiss, S. C. (2013). Illuminating the capabilities of the suomi national polar-orbiting partnership (NPP) visible infrared imaging radiometer suite (VIIRS) day/night band. *Remote Sensing*, 5(12), 6717-6766.
- Mulyadi, R. A., Brown, A., & Rengi, P. (2015). Study technology hand line fishing in Port Bungus West Sumatra. *Online Journal*, 2, 1-13.
- Nuridin, S., Mustapha, A., Chan, Y., & Lihan, T. (2010, July 26-28). Mapping of potential fishing grounds of *Rastrelliger kanagurta* (Cuvier, 1817) using satellite images. In *Proceedings of Map Asia & ISG* (pp. 1-9). Kuala Lumpur, Malaysia.
- Nuridin, S., Mustapha, A., Lihan, T., & Ghaffar, A. A. (2015). Determination of potential fishing grounds of *Rastrelliger kanagurta* using satellite remote sensing and GIS technique. *Sains Malaysiana*, 44(2), 225-232.
- Nuridin, S., Mustapha, M. A., Lihan, T., & Zainuddin, M. (2017). Applicability of remote sensing oceanographic data in the detection of potential fishing grounds of *Rastrelliger Kanagurta* in The Archipelagic Waters of Spermonde, Indonesia. *Fisheries Research*, 196(July), 1-12.

- Palenzuela, J., Iglesias, G., & Vilas, L. (2004). Pelagic fisheries study using GIS and remote sensing imagery in Galicia (Spain). *ICES CM*, 44, 1-5.
- Parnell, P. E., Dayton, P. K., Fisher, R. A., Loarie, C. C., & Darrow, R. D. (2010). Spatial patterns of fishing effort off San Diego: implications for zonal management and ecosystem function. *Ecological Applications*, 20(8), 2203-2222.
- Perzia, P., Battaglia, P., Consoli, P., Andaloro, F., & Romeo, T. (2016). Swordfish monitoring by a GIS-based spatial and temporal distribution analysis on harpoon fishery data: A case of study in The Central Mediterranean Sea. *Fisheries Research*, 183(2016), 424-434.
- Pierce, G. J., Wang, J., Zheng, X., Bellido, J. M., Boyle, P. R., Denis, V., & Robin, J. (2002). A cephalopod fishery GIS for the Northeast Atlantic: Development and application. *International Journal of Geographical Information Science*, 15(8), 1-22.
- Riolo, F. (2006). A geographic information system for fisheries management in American Samoa. *Environmental Modelling and Software*, 21(7), 1025-1041.
- Saitoh, S., Fukaya, A., Saitoh, K., Semedi, B., & Mugo, R. (2010). Estimation of number of pacific saury fishing vessels using night-time visible images. *International Archives of the Photogrammetry, Remote Sensing and Spatial Information Science*, 38, 1013-1016.
- Saraux, C., Fromentin, J. M., Bigot, J. L., Bourdeix, J. H., Morfin, M., Roos, D., ... & Bez, N. (2014). Spatial structure and distribution of small pelagic fish in the northwestern mediterranean sea. *PLoS ONE*, 9(11), 1-12.
- Setiawati, M., & Tanaka, T. (2017). Utilization of scatterplot smoothers to understand the environmental preference of Bigeye Tuna in the Southern Waters off Java-Bali: Satellite remote sensing approach. *Fishes*, 2(1), 1-16.
- Siregar, E. S., Siregar, V. P., & Agus, S. A. (2018). *Prediksi zona potensi penangkapan Ikan Tuna Sirip Kuning (Thunnus Albacares) menggunakan model gam di Perairan Sumatera Barat* [Prediction of Potential Fishing Zones for Yellowfin Tuna (*Thunnus albacares*) Using GAM Models in West-Sumatera Waters] (Master Thesis). IPB University, Indonesia.
- Stewart, K. R., Lewison, R. L., Dunn, D. C., Bjorkland, R. H., Kelez, S., Halpin, P. N., & Crowder, L. B. (2010). Characterizing fishing effort and spatial extent of coastal fisheries. *PLoS ONE*, 5(12), 1-8.
- Straka, W. C., Seaman, C. J., Baugh, K., Cole, K., Stevens, E., & Miller, S. D. (2015). Utilization of the suomi national polar-orbiting partnership (SNPP) visible infrared imaging radiometer suite (VIIRS) day/night band for arctic ship tracking and fisheries management. *Remote Sensing*, 7(1), 971-989.
- Syah, A. F., Saitoh, S. I., Alabia, I. D., & Hirawake, T. (2016). Predicting potential fishing zones for pacific saury (*Cololabis saira*) with maximum entropy models and remotely sensed data. *Fishery Bulletin*, 114(3), 330-342.
- Tidd, A., Brouwer, S., & Pilling, G. (2017). Shooting fish in a barrel? Assessing fisher-driven changes in catchability within tropical tuna purse seine fleets. *Fish and Fisheries*, 18(5), 808-820.
- Wyrtki, K. (1961). *Physical oceanography of the Southeast Asian waters*. San Diego, California: Scripps Institution of Oceanography.

- Zainuddin, M. (2011). Skipjack tuna in relation to sea surface temperature and chlorophyll-a concentration of bone bay using remotely sensed satellite data. *Jurnal Ilmu Dan Teknologi Kelautan Tropis*, 3(1), 82-90.
- Zainuddin, M., & Saitoh, K. (2008). Albacore (*Thunnus alalunga*) fishing ground in relation to oceanographic conditions in the western North Pacific Ocean using remotely sensed satellite data. *Fisheries Oceanography*, 17(2), 61-73.
- Zhang, X., Saitoh, S. I., & Hirawake, T. (2017). Predicting potential fishing zones of Japanese common squid (*Todarodes pacificus*) using remotely sensed images in coastal waters of south-western Hokkaido, Japan. *International Journal of Remote Sensing*, 38(21), 6129-6146.



Dye Removal by Membrane Technology for Wastewater Treatment using a Cationic Carrier

Huda Adil Sabbar¹, Wasan Omar Noori² and Ahmed Samir Naje^{3*}

¹Department of Biochemical Engineering, Al-khwarizmi College of Engineering, University of Baghdad, Baghdad 10071, Iraq

²Department of Chemical Engineering, College of Engineering, University of Baghdad, Baghdad 10071, Iraq

³Collage of Water Resource Engineering, AL-Qasim Green University, Babylon 51031, Iraq

ABSTRACT

The removal efficiency of malachite green (MG) dye ions by using a bulk liquid membrane was investigated. The transport of MG dye ions was accomplished using a bulk liquid membrane, which contained salicylic acid as carrier, sodium hydroxide as extractant, and acetic acid as acceptor. Different factors were examined for removal efficiency, such as pH of the acceptor phase in the range of pH 3–7, initial dye concentration at 20–60 mg/L, and concentration of carrier in the range of 8–12 mg/L. Box-Wilson method for experimental design was adopted to establish the relationships between these operating variables attributed to affecting the treatment process, and the mechanism of dye transport from feeding to acceptor phase. The results indicated that the optimum conditions for dye extraction were achieved at pH 6, dye concentration of 20 mg/L, and carrier concentration

of 12mg/L. The implementation of these parameters on the prepared dye solution revealed a relatively high removal efficiency of MG dye (98.4%). A Box-Wilson model was modified and found to fit the effect of variable response, with a correlation coefficient (R) = 0.977 and root-mean square error (S) = 1.8%. This work proved that liquid membrane was effectively useful for dye removal from the wastewater.

ARTICLE INFO

Article history:

Received: 18 April 2019

Accepted: 04 October 2019

Published: 13 January 2020

E-mail addresses:

enghudaadil@gmail.com (Huda Adil Sabbar)

wasanmch234@gmail.com (Wasan Omar Noori)

ahmednamesamir@yahoo.com (Ahmed Samir Naje)

* Corresponding author

Keywords: BLM, malachite green, mathematical model, salicylic acid

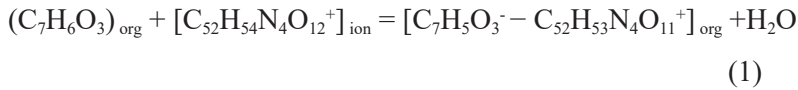
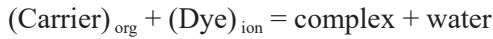
INTRODUCTION

One of the major environmental problems currently highlighted is the removal of dyes within the textile industries and wastewater prior to their discharge into natural water streams (Mohammad et al., 2017; Elumalai et al., 2015). Dyes are very toxic, carcinogenic, and risky towards aquatic living organisms. They can cause irritation to the skin and pose a serious threat to human beings and the environment alike (Soniya & Muthuraman, 2015). However, they are commonly used in many industries in products like paper, rubber, plastic, pharmaceutical items, textiles, and aquaculture (Abou-Gamra & Ahmed, 2015). Malachite green (MG) is a cationic dye (triphenylmethane) used in many fields such as color paper and fabric. It has also been used to treat protozoal and fungal infections in fish and fish eggs, it generally found in the form of crystal powder, revealing a metallic green luster and has high solubility in water and ethanol. The base dye is toxic and associated with harmful effects towards the kidney, gonads, reproductive system, brain and nervous system, the intestines, and pituitary gonadotropic cells. Due to its serious threat towards the aquatic life, MG is not one of the registered substances allowed for use in aquaculture. Therefore, MG should not be found in fish sold for human consumption. According to the latest studies, MG poses a significant threat to human health in concentrations of 0.1 mg/L–10 mg/L (Papinutti et al., 2006). The minimum requirement for performance limit to allow laboratories in carrying out surveillance for the sum of MG and leucomalachite green is 2µg/kg (Gavrilenko et al., 2019). There are many methods to treat dyes found in wastewater, such as sedimentation, crystallization, and gravity separation. Treatment methods like solvent extraction, reverse osmosis, ion exchange, electrodialysis, electrolysis, and adsorption may also be used (Muthuraman et al., 2009a; Muthuraman et al., 2009b).

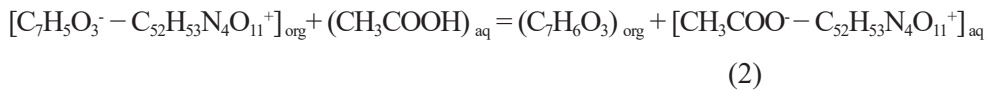
Recently, the liquid membrane (LM) technique has become popular among to researchers in different fields of science, such as chemical engineering, biotechnology, biomedical engineering (Al-Hemiri & Noori, 2009; Rounaghi et al., 2016), and wastewater treatment. LM can be defined as the process of transferring a solution from the aqueous phase to another phase via an immiscible organic phase (Noble & Way, 1987; Zeng et al., 2019).

Extraction and recovery of MG ($C_{52}H_{54}N_4O_{12}$) can be explained by the following mechanism: NaOH reacts with dye in the feed phase, isolating the dye from water and causing it to become an ion (El-Ashtoukhy & Fouad, 2015). Ion dye encompassing transport from the feed phase through the liquid membrane at either feed membrane interface is associated with the presence of salicylic acid as the carrier in membrane, which reacts and forms an ion pair complex $[(R^- \text{ Dye}^+)_{\text{org}} [(C_7H_5O_3^-)-(C_{52}H_{53}N_4O_{11}^+)]$ (Equation 1) (Sathya et al., 2016). This complex dissolves completely in the liquid membrane, following which the (salicylic acid - dye⁺ ion) pair complex reacts with acetic acid complex when it reaches the interface (membrane/acceptor). Then, the salicylic acid receives proton (H⁺) from the

acetic acid in the acceptor phase and diffuses back into the organic membrane as a neutral carrier to repeat the cycle (Elumalai & Muthuraman, 2013; Baylan & Çehreli, 2019). Next, the dye diffuses into the acceptor phase with the acetate (CH_3COO^-) ion, forming the safety solution (Naim et al., 2016). The proposed mechanism is shown in Figure 1.



The 2nd reaction in the inter phase of (membrane/acceptor) can be explained using the following Equation 2:



LM offers many advantages compared to other separation methods, such as high selectivity, efficient high fluxes, high potential of removing cationic and anionic dyes, reusability, and low energy consumption (Marchetti et al., 2014; Han et al., 2017). According to configurative definition, it is very actively utilised in water treatment for the removal of cationic and anionic dyes from industrial water (Joshi et al., 2004). LM can be categorised as bulk liquid membrane (BLM), emulsion liquid membrane (ELM), and supported liquid membrane (SLM) (Bahram & Pourabdollah, 2015; Chang et al., 2011a; Hernandez et al., 1986). The main technological problems of using ELM and SLM are the irreversibility of the operation and their instability in terms of long-term performance (Saeed et al., 2016). Furthermore, BLM is a simple design for liquid membrane processes and associated with many advantages, such as simple equipment, high separation and uses less amounts of organic solvent and carrier (extractant) (Chang et al., 2011b). The BLM technique has been successfully employed in the treatment of metal ions and hydrocarbons (Laki & Kargari, 2016; Candela et al., 2013) and cationic and anionic dyes, such as methylene blue (Soniya & Muthuraman, 2015) and rhodamin B (Elumalai & Muthuraman, 2013). The objective of the present study was to eliminate MG (oxalate) dye by using BLM via hexane utilisation as the membrane. Furthermore, parameters, such as pH, carrier concentration, dye concentration, and the mechanism of dye transport from feed to acceptor phase via LM were investigated. In the recent years, a remarkable increase of LM applications in separation processes has been observed. In the present work, BLM was used as a low cost process with the Box-Wilson rotatable central composite design to maximize dye removal efficiency from waste water. It can also optimize pH acceptor phase, the concentration of dye, and the concentration of carrier.

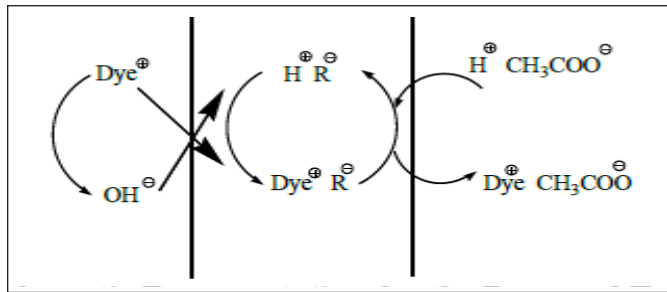


Figure 1. A schematic shows mechanism transport of dye in liquid membrane

MATERIALS AND METHODS

Materials

Hexane (95%, Merck), salicylic acid ($C_7H_6O_3$, 99.8%, Merck), sodium hydroxide (NaOH, Merck, $\geq 97\%$ purity), acetic acid (CH_3COOH , Thomas Baker, $\geq 98\%$ purity), and malachite green oxalate ($C_{52}H_{54}N_4O_{12}$ $\geq 80\%$ purity) were supplied by HiMedia.

Equipment

The feed, acceptor, and membrane phases were stirred using a magnetic stirrer (Fisher Scientific, JENWAY, 1000, UK). The absorbance of dye sample was determined using UV visible spectrophotometer (GBC Cintra 6 series V-3656), while the pH of the feed phase (dye solutions) and acceptor phase were determined by using pH meter (pH7110 WTW, Germany).

Procedure

The experiments of MG removal by implementing BLM were carried out in two beakers that were concentric at the bottom portion. The outer beaker (ID=11.5 mm, V=1000 ml) is bigger than the inner beaker (ID=9 mm, V=500 ml) as shown in Figure 2 (Noori et al., 2018). In this design, the outer beaker contained feed aqueous solution comprised of dye in different quantities, 400 mL distilled water, and drops of NaOH to yield pH of 9. It was placed in a magnetic stirrer set up. Meanwhile, the inner beaker contained the acceptor aqueous solution (CH_3COOH and 200 mL of distilled water) that was fixed by two stands inside the outer beaker. Both aqueous solutions were above the liquid membrane (i.e. 300 ml hexane

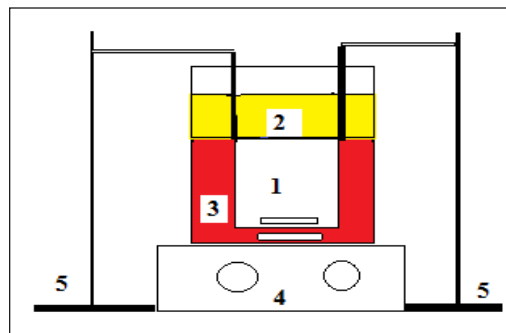


Figure 2. BLM (1-acceptor phase, 2-membrane phase, 3-feed phase, 4-magnetic stirrer, 5-a stand)

and salicylic acid as the carrier in different quantities), whereby the liquid membrane was poured above the two layers of previous aqueous phases using a mechanical pipette for the measurement of dye absorbance and concentration, while reaction time takes (15-20) min. The measurements were obtained using the UV-spectrophotometer at a wavelength of 618 nm. Similarly, the corresponding concentration of MG was calculated from the calibration curve (Sathya et al., 2016). The controlled temperature was also varied from 25°C to 27°C to study its effect on the removal of MG dye.

Most importantly, different densities were maintained to keep the three phases immiscible with each other. The operating parameter used for the Box-Wilson method of experimental design was feed phase containing dye (i.e. 20–60 mg/L, V=250 mL). The same volume of the acceptor solution (pH=3–7, V=250 mL) was adjusted by using NaOH and acetic acid solution, while the organic phase was undertaken using salicylic acid (8–12 mg/L, V=300mL). Experiments were performed by using the magnetic stirrer set up, which was speed-adjusted to ensure the contents did not mix with each other. Then, samples were taken every 30 min from the feed and acceptor solutions (Eljaddi et al., 2017).

Mathematical Model

With the aim of establishing the phenomenon of dye removal, a standard Response Surface Methodology (RSM) design known as the Box-Wilson central composite design was adopted and using the statistical software version 10. This design can reduce the number of experimental trails needed to evaluate multiple parameters and their interactions (Majeed et al., 2017). From the preliminary experiments, independent variables were determined to be pH of the acceptor phase (x_1), concentration of the dye (x_2), and concentration of the carrier (x_3). The response of the experiments was determined according to the Box-Wilson method (Box & Wilson, 1951). It comprised of a linear equation with four parameters (Equation 3), whereby the result was used as an initial approximation for the second model (Equation 4).

Simple linear multi-variable model:

$$y = b_0 + b_1x_1 + b_2x_2 + b_3x_3 \quad (3)$$

Where,

y is the dependent variable or response

x_i is the independent variable

b_0, b_1, b_2 and b_3 are four parameters to be obtained by curve-fitting from the observed results.

Second polynomial model:

$$y = b_0 + b_1x_1 + b_2x_2 + b_3x_3 + b_4x_1x_2 + b_5x_1x_3 + b_6x_2x_3 + b_7x_1^2 + b_8x_2^2 + b_9x_3^2 \quad (4)$$

Thus, for a three-variable process, the number of experiments needed were according to the following Equation 5:

$$N_0 = 2^P + 2P + 1 \tag{5}$$

Where, N is the number of optimization processes(experiments) and P is the number of factor.

There were 15 experiments applied to Equation 5 in finding the optimum operating conditions, whereby the results indicated the following conditions (Alalayah et al., 2010).

- x_1 = pH acceptor phase = 3–7
- x_2 = Concentration of dye = 20–60 mg/L
- x_3 = Concentration of carrier = 8–12 mg/L

More precise model of the following form can be obtained:

$$\sum \frac{x_1}{n} = \sum \frac{x_2}{n} = \sum \frac{x_3}{n} = \sum \frac{x_1x_2}{n} = \sum \frac{x_1x_3}{n} = \sum \frac{x_2x_3}{n} = 0, \text{ and}$$

$$\sum \frac{x_1^2}{n} = \sum \frac{x_2^2}{n} = \sum \frac{x_3^2}{n} = 0.933$$

The model can be used to reach even more precise regression following Equation 6:

$$y = b_0 + b_1x_1 + b_2x_2 + b_3x_3 + b_4x_1x_2 + b_5x_1x_3 + b_6x_2x_3 + b_7(x_1^2 - 0.933) + b_8(x_2^2 - 0.933) + b_9(x_3^2 - 0.933) + b_{10}x_1^3 + b_{11}x_2^3 + b_{12}x_3^3 + b_{13}x_1x_2x_3 \tag{6}$$

Substituting the parameters obtained by minimizing the sum of squared errors, Equation 6 became Equation 7:

$$y = 325.4675 + 9.514032x_1 + 1.77026x_2 - 68.4625x_3 + 0.280709x_1x_2 + 1.590699x_1x_3 + 0.123205x_2x_3 - 4.79326(x_1^2 - 0.933) + 0.018892(x_2^2 - 0.933) + 6.360562(x_3^2 - 0.933) + 0.303146x_1^3 - 0.000155x_2^3 - 0.214358x_3^3 - 0.031284x_1x_2x_3 \tag{7}$$

The above equations were used to obtain a correlation factor nearer to one. Meanwhile, the percentage of dye removal was obtained following Equation 8:

$$\text{Dye removal (\%)} = \frac{\text{Initial concentration of dye} - \text{Final concentration of dye}}{\text{Initial concentration of dye}} \times 100 \quad (8)$$

RESULTS AND DISCUSSION

Effect of Acceptor Phase pH Value on Removal Percentage of Dye

The effect of acceptor phase PH in the percentage of dye removal is shown in Figure 3 and Figure 4.

Feed aqueous solutions prepared using a constant dye concentration of 20 mg/L at different pH values of the acceptor phase varying from 3 to 7 were used and carrier concentration was changed from 8 to 12 mg/L. In Figure 3, the removal of dye changed alongside increasing pH from 3 to 6, then it decreased when pH increased to 7. The results were observed in all carrier concentrations.

The highest dye removal was 100% obtained at the pH of 6 and S of 12 mg/L, which were considered the optimum operating conditions and the lowest dye removal was obtained at pH of 7 (93.28%, S=8 mg/L acetic acid). The weak aliphatic acid was used as an acceptor phase to react with the compound of (dye-salicylic acid) at the interphase of the (membrane/acceptor) to form (dye-acetic acid) ion pair compound (Sathya et al., 2016).

Furthermore, Figure 4 shows the effect of pH on dye removal at different initial dye concentrations and fixed initial carrier concentration of 12 mg/L.

It was observed that the change of pH for the acceptor phases yielded the best results when the pH value was 6. When the concentration of dye increased from 20 mg/L to 50 mg/L, the percentage of dye removal decreased and the compound formed was reverted to the acceptor phase solution. At a high pH value, the ionized group present in the carrier

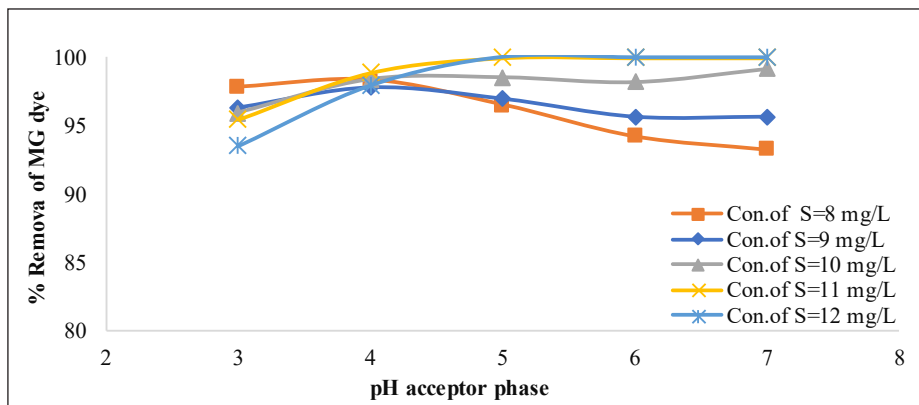


Figure 3. Effect of initial pH of acceptor phase at different initial carrier concentration) and fixed dye concentration =20mg/L, here (S: Initial carrier concentration & d ;dye concentration)

salicylic acid can attract more dye and lead to the formation of compounds capable of enhancing dye transport processes. The maximum removal rate was found to be 99.96% at the pH of 6 and initial dye concentrations of 20 mg/L. Hence these were considered the optimum operating conditions (Patro, 2016).

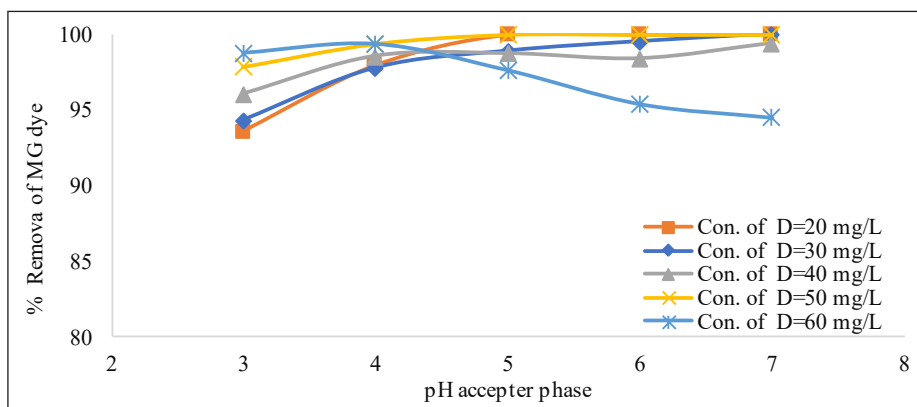


Figure 4. Effect of initial pH of acceptor phase at different dye concentration and fixed initial carrier concentration=12mg/L

Effect of Dye Concentration

The effect of MG concentration in the feed phase towards the percentage of dye removal is presented in Figure 5 and Figure 6. The experimental dye ranging between the concentration of 20 mg/L and 60 mg/L in the feed phase was investigated by fixing the optimum operating conditions. They were utilized per the first study on the previous effects, namely S of 12 mg/L and pH of 6.

Figure 5 shows the effect of dye concentration on the percentage of dye removal at different pH values at a constant initial carrier concentration of 12 mg/L (i.e. optimum operating conditions). It was clearly revealed that the percentage of dye removal decreased with increasing concentration of dye from 20 mg/L to 60 mg/L. The maximum removal of 100% was observed at the pH of 6 and D of 20 mg/L, which were considered the optimum operating conditions. The reasons behind these results were due to the low MG concentration in the feed phase that leads to enough amount of carrier covering all present dye molecules, consequently the area of ionic attraction (electrostatic attraction) leading to increase the ionic strength of the feed solution, as well as molecular geometry in the (feed/liquid membrane) interface. It can also be explained by the fact that at higher dye concentrations and limited carrier in the LM, inability of salicylic acid to react with the excess dye can be seen. Similar results were obtained in BLM for the removal of metals (Elumalai et al., 2014).

Figure 6 depicts the removal percentage of dye studied using four different initial salicylic acid concentration values at a constant initial pH of acceptor phase (pH=6). It can be observed that the increasing values of the salicylic acid concentration will increase the removal percentage. The maximum removal was at 100% for S of 12 mg/L and D of 20 mg/L, which were considered the optimum operating conditions. These results were attributable to the high concentration of salicylic acid that interacted well with the MG dye at the (feed/membrane) interface. Hence, the transport of MG increased. Furthermore, the increase of the salicylic acid concentration resulted in the increase of the MG influx. The first part was due to the enhancement of contact influence between MG and salicylic acid, along with the increasing dye concentration (Othman et al., 2014).

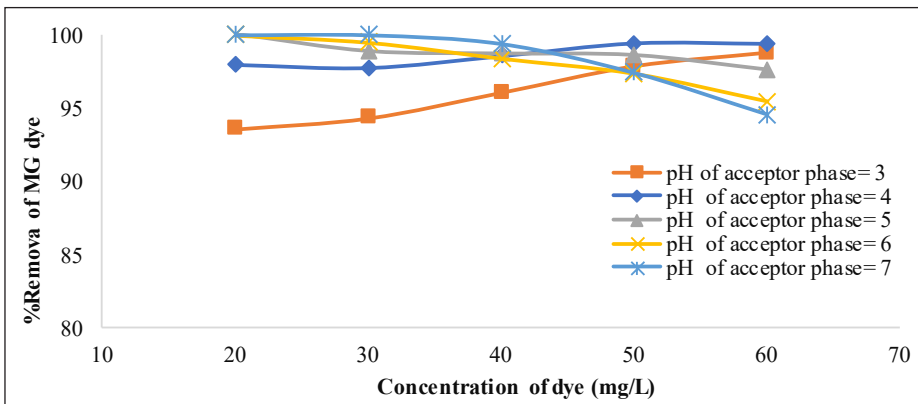


Figure 5. Effect of initial dye concentration at different initial pH of acceptor phase and fixed initial carrier concentration =12mg/L

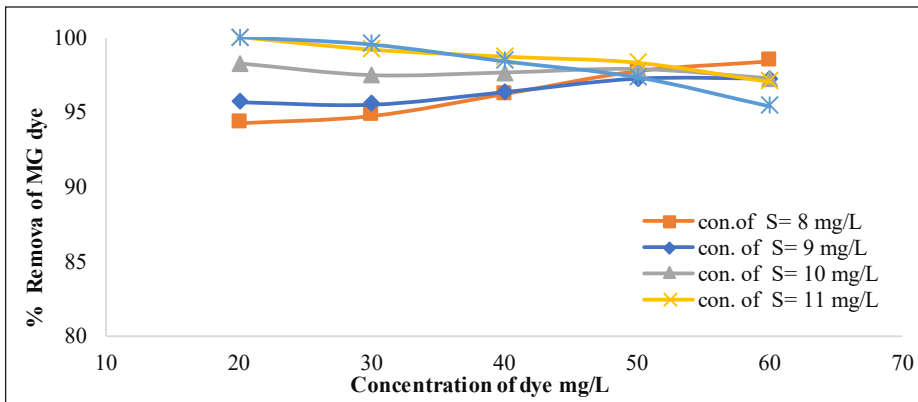


Figure 6. The effect of initial dye concentrations at different initial carrier concentrations s and fixe initial pH of acceptor phase =6

Effect of Carrier Concentration on Removal Percentage of Dye

The amount of carrier (salicylic acid) plays an important role in dye transfer and removal. In this work, the concentration range between 8 mg/L and 12 mg/L was maintained throughout.

Figure 7 shows the effect of increasing the carrier concentration on MG removal percentage. The concentration of the carrier in the membrane showed a clear effect on the compound transfer, which was formed between the dye and carrier through the membrane. It was found that increasing the carrier concentration would increase the MG removal efficiency, whereby the MG dye removal percentages and the variation of carrier concentration were studied using five different initial concentrations of dye. The acceptor pH of 6 was kept constant as shown in Figure 8. The maximum removal was

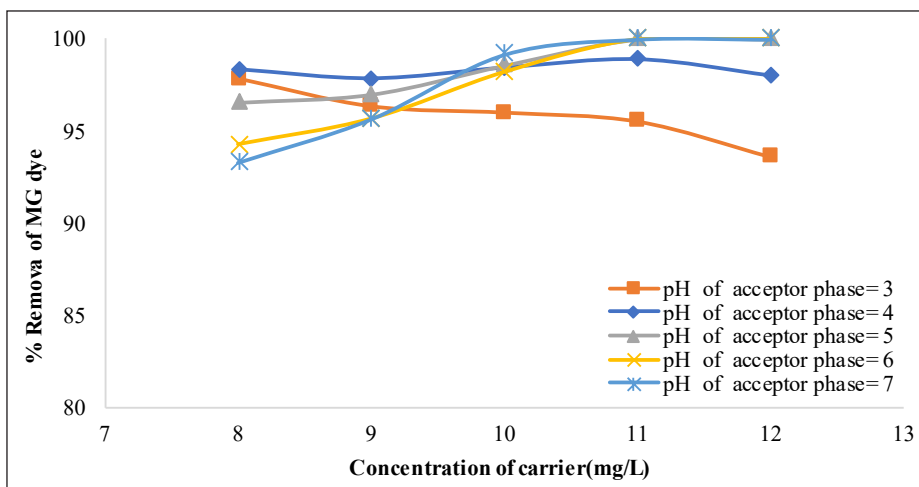


Figure 7. Relations between removal of dye with initial carrier concentration at different initial pH of acceptor phase and fixed initial carrier concentration

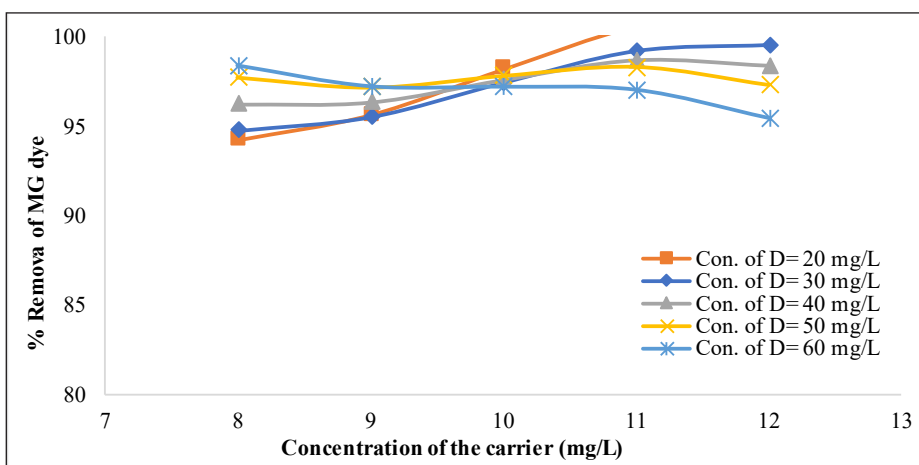


Figure 8. Effect of initial carrier concentration at different initial dye concentration and fixed initial pH of acceptor phase

observed at 98.4% at the perimeters of S (12 mg/L) and D (20 mg/L), thus considered as the optimum operating conditions. The carrier forms a transportable compound diffusing in the membrane, which then releases carrier into the acceptor phase. The carrier enables and provides the opportunity for its movement in the system using two ways, namely chemical reaction with the dye or diffusion. In the selected system, the dye first reacts with the carrier to form a dye-carrier compound that spreads through the liquid membrane and releases the solute in the acceptor phase. In this study, the effect of increasing the concentration of salicylic acid resulted in it being chosen as an appropriate carrier in the liquid membrane for the process of dye removal. Similar results were also reported by Ng et al. (2011).

Mathematical Model Calculations

Table 1 shows the values of the independent variables corresponding to the final form of the dye removal equation. To find the best condition, the variable that achieved maximum dye removal was studied. Table 2 shows the values from each variable, which are dependent on Equation 7. It was found that the optimum operating conditions consisted of the acceptor phase pH between 5 and 7, dye concentration of 20 mg/L, and carrier concentration of 12 mg/L. Further accuracy was ensured using the last process performed using the optimization conditions, whereby all processes became 28 (as show in Table 2) and the optimum pH was 6. The final result obtained yielded the correlation coefficient (R) = 0.977 and root mean square error (S) = 1.8%.

Table 1
The initial guess and values of real variables for the calculations of dye removal using the BLM method

Run No.	Initial values			Final converged values			%Removal (y)	%Real removal (Y)	Residual
	x ₁	x ₂	x ₃	x ₁	x ₂	x ₃			
1	-1	-1	-1	3.845	28.452	8.845	96.728	96.596	0.133
2	1	-1	-1	6.155	28.452	8.845	94.201	94.942	-0.741
3	-1	1	-1	3.845	51.547	8.845	98.623	99.404	-0.780
4	1	1	-1	6.155	51.547	8.845	96.309	96.706	-0.3972
5	-1	-1	1	3.845	28.452	11.155	97.548	96.53	1.019
6	1	-1	1	6.155	28.452	11.155	98.757	97.362	1.395
7	-1	1	1	3.845	51.547	11.155	99.599	98.294	1.305
8	1	1	1	6.155	51.547	11.155	97.168	96.73	0.438
9	-1.732	0	0	3.00	40	10	98.419	99.188	-0.769
10	1.732	0	0	6.99	40	10	99.026	99.423	-0.398
11	0	-1.732	0	5	20.000	10	99.687	100.632	-0.944
12	0	1.732	0	5	59.999	10	99.968	100.209	-0.241
13	0	0	-1.732	5	40	8.000	99.008	97.871	1.137
14	0	0	1.732	5	40	11.999	99.844	102.128	-2.284
15	0	0	0	5	40	10	98.587	98.642	-0.055

Table 2
Studying best variable that achieve maximums dye removal

No.	Constant variable	Best variables in constant certain variable			Maximum dye removal
pH=3					
	pH of acceptor phase	Concentration of the dye (mg/L)	Concentration of the carrier (mg/L)	(%)Maximum dye removal	
1	3	20	8	97.827	
2	3	40	8	97.951	
3	3	60	8	98.309	
4	3	20	10	95.994	
5	3	40	10	97.292	
6	3	60	10	98.824	
7	3	20	12	93.6	
8	3	40	12	96.072	
9	3	60	12	98.778	
pH=5					
	pH of acceptor phase	Concentration of the dye (mg/L)	Concentration of the carrier (mg/L)	(%)Maximum dye removal	
10	5	20	8	96.540	
11	5	40	8	97.881	
12	5	60	8	99.457	
13	5	20	10	98.567	
14	5	40	10	98.580	
15	5	60	10	98.827	
16	5	20	12	99.92	
17	5	40	12	98.717	
18	5	60	12	97.635	
pH=7					
	pH of acceptor phase	Concentration of the dye (mg/L)	Concentration of the carrier (mg/L)	(%)Maximum dye removal	
19	7	20	8	93.285	
20	7	40	8	95.844	
21	7	60	8	98.637	
22	7	20	10	99.172	
23	7	40	10	97.899	
24	7	60	10	96.861	
25	7	20	12	99.97	
26	7	40	12	99.393	
27	7	60	12	94.524	
pH=6					
	pH of acceptor phase	Concentration of the dye (mg/L)	Concentration of the carrier (mg/L)	(%)Maximum dye removal	
28	6	20	12	100	

CONCLUSION

Malachite green (MG) dye was transported by means of a liquid membrane. The efficiency of the system was dependent upon the principal parameters, such as the acceptor phase pH, dye concentration, and carrier concentration. The most suitable conditions were confirmed to be at the pH of 6, dye concentration of 20 mg/L, and carrier concentration of 12mg/L. Using these optimal conditions, the maximum removal efficiency of MG dye was found to be 99.7%. The Box-Wilson model was established accordingly, which further correlated the effect of such variables towards the responses with the correlation coefficient $R = 0.977$ and root mean square error(s)=1.8%.

ACKNOWLEDGEMENTS

The authors would like to thank the University of Baghdad and the Ministry of Higher Education and Scientific Research, Iraq for funding and supporting this research.

REFERENCES

- Abou-Gamra, Z., & Ahmed, M. (2015). TiO₂ nanoparticles for removal of malachite green dye from wastewater. *Advances in Chemical Engineering and Science*, 5(03), 373-388.
- Alalayah, W. M., Kalil, M. S., Kadhum, A. A. H., Jahim, J., Zaharim, A., Alauj, N. M., & El-Shafie, A. (2010). Applications of the box-wilson design model for bio-hydrogen production using *Clostridium saccharoperbutylacetonicum* N1-4 (ATCC 13564). *Pakistan Journal of Biological Sciences*, 13(14), 674-682.
- Al-Hemiri, A., & Noori, W. (2009). Extraction of atropine from *Datura Innoxia* using liquid membrane technique. *Iraqi Journal of Chemical and Petroleum Engineering*, 10(1), 23-27.
- Bahram, M., & Pourabdollah, K. (2015). Emulsion liquid membrane for selective extraction of Bi (III). *Chinese Journal of Chemical Engineering*, 23(4), 641-645.
- Baylan, N., & Çehreli, S. (2019). Removal of acetic acid from aqueous solutions using bulk ionic liquid membranes: A transport and experimental design study. *Separation and Purification Technology*, 224, 51-61.
- Box, G. E., & Wilson, K. B. (1951). On the experimental attainment of optimum conditions. *Journal of the Royal Statistical Society: Series B (Methodological)*, 13(1), 1-38.
- Candela, A., Benatti, V., & Palet, C. (2013). Pre-concentration of Uranium (VI) using bulk and supported liquid membrane systems optimized containing bis (2-ethyl hexyl) phosphoric acid as carrier in low concentrations. *Separation and Purification Technology*, 120, 172-179.
- Chang, S. H., Teng, T. T., & Ismail, N. (2011b). Soybean oil-based bulk liquid membrane for simultaneous extraction and stripping of Cu (II) from aqueous solutions. *International Journal of Environmental Science and Development*, 2(5), 389-393.

- Chang, S. H., Teng, T. T., Ismail, N., & Alkarkhi, A. F. (2011a). Selection of design parameters and optimization of operating parameters of soybean oil-based bulk liquid membrane for Cu (II) removal and recovery from aqueous solutions. *Journal of Hazardous Materials*, 190(1-3), 197-204.
- El-Ashtouky, E., & Fouad, Y. (2015). Liquid-liquid extraction of methylene blue dye from aqueous solutions using sodium dodecylbenzenesulfonate as an extractant. *Alexandria Engineering Journal*, 5(1), 77-81.
- Eljaddi, T., Laurent, L., & Miloudi, H. (2017). Review on Mechanism of Facilitated Transport on Liquid Membranes. *Journal of Membrane Science and Research*, 3(3), 199-208.
- Elumalai, S., & Muthuraman, G. (2013). Comparative study of liquid-liquid extraction and bulk liquid membrane for rhodamine B. *International Journal of Engineering and Innovative Technology (IJEIT)*, 3(2), 387-392.
- Elumalai, S., Muthuraman, G., Sathya, M., Soniya, M., & Teng, T. (2014). Recovery of dye from textile effluents using phenol as an extractant. *Journal of Industrial and Engineering Chemistry*, 20(4), 1958-1964.
- Elumalai, S., Sathya, S., & Muthuraman, G. (2015). Recovery of dye from wastewater using liquid-liquid extraction and bulk liquid membrane techniques. *International Journal of ChemTech Research*, 7(7), 3089-3094.
- Gavrilenko, N., Volgina, T., Pugachev, E., & Gavrilenko, M. (2019). Visual determination of malachite green in sea fish samples. *Food Chemistry*, 274, 242-245.
- Han, A., Zhang, H., Sun, J., Chuah, G. K., & Jaenicke, S. (2017). Investigation into bulk liquid membranes for removal of chromium (VI) from simulated wastewater. *Journal of Water Process Engineering*, 17, 63-69.
- Hernandez, A., Ibañez, J. A., & Tejerina, A. F. (1986). A selective parameter for ionic membrane transport selectivity and porosity of several passive membranes. In E. Drioli & M. Nakagaki (Eds.), *Membranes and membrane processes* (pp. 93-99). Boston, MA: Springer.
- Joshi, M., Bansal, R., & Purwar, R. (2004). Colour removal from textile effluents. *Indian Journal of Fibre Textile Research*, 29, 239-259.
- Laki, S., & Kargari, A. (2016). Extraction of silver ions from aqueous solutions by emulsion liquid membrane. *Journal of Membrane Science and Research*, 2(1), 33-40.
- Majeed, N., Sabbar, H., & Al-Musawi, N., (2017). Preparation activated carbon from scrap tires by microwave assisted KOH activation for removal emulsified oil. *Iraqi Journal of Chemical and Petroleum Engineering*, 18(1), 57-69.
- Marchetti, P., Jimenez-Solomon, M. F., Szekely, G., & Livingston, A. G. (2014). Molecular separation with organic solvent nanofiltration: A critical review. *Chemical Reviews*, 114(21), 10735-10806.
- Mohammad, R., Rajoo, A., & Mohamad, M. (2017). Coconut fronds as adsorbent in the removal of malachite green dye. *ARPJ Journal of Engineering and Applied Sciences*, 12(4), 996-1001.
- Muthuraman, G., Teng, T., Peng, L., & Ismail, N. (2009a). Extraction and recovery of methylene blue from industrial wastewater using benzoic acid as an extractant. *Journal of Hazardous Materials*, 163(1), 363-369.

- Muthuraman, G., Teng, T., Peng, L., & Ismail, N. (2009b). Use of bulk liquid membrane for the removal of chromium (VI) from aqueous acidic solutions with tri-n-butyl phosphate as a carrier. *Desalination*, 249(2), 884-890.
- Naim, M., El-Shafei, A., Moneer, A., Elewa, M., & Kandeel, W. (2016). Bulk liquid pertraction of NaCl from aqueous solution using carrier-mediated transport. *Environmental Technology*, 37(4), 495-504.
- Ng., Y., Natesan, J., & Hashim, M. (2011). Behavior of hydrophobic ionic liquids as liquid membranes on phenol removal: Experimental study and optimization. *Desalination*, 278(1-3), 250-258.
- Noble, R. D., & Way, J. D. (1987). Applications of Liquid Membrane Technology. In R. D. Noble & J. D. Way (Eds.), *Liquid membranes: theory and applications* (pp. 110-122). Washington, DC: American Chemical Society.
- Noori, W., Waisi, B., & Alhassani, M. (2018). Extraction of glycyrrhizin from licorice (*Glycyrrhiza Glabra* L.) by bulk liquid membrane. *Environmental Technology and Innovation*, 12, 180-188.
- Othman, N., Zing-Yi, O., Harruddin, N., Norimie, R., Jusoh, N., & Zailani, S. (2014). Carrier assisted emulsion liquid membrane process for recovery of basic dye from wastewater using continuous extractor. *Jurnal Teknologi*, 67(2), 69-74.
- Papinutti, L., Mouso, N., & Forchiassin, F. (2006) Removal and degradation of the fungicide dye malachite green from aqueous solution using the system wheat bran-Fomes sclerodermeus. *Enzyme and Microbial Technology*, 39(4), 848-853.
- Patro, B. L. (2016). *Application of liquid membrane in removal of dyes* (Doctoral dissertation). National Institute of Technology Rourkela, India. 1
- Rounaghi, G., Ghaemi, A., & Chamsaz, M. (2016). Separation study of some heavy metal cations through a bulk liquid membrane containing 1, 13-bis (8-quinoly)-1, 4, 7, 10, 13-pentaoxatridecane. *Arabian Journal of Chemistry*, 9, 490-496
- Saeed, H., Chaudhry, F., Rehman, S., Rashid, Z., Ijaz, A., Javeed, A., & Awan, J. (2016). Removal of toxic metallic ions Cr(VI), Cu(II), Ni(II), Co(II) and Cd(II) from wastewater effluents of tanneries by using *Punica granatum* (pomegranate) membrane. *Iranica Journal of Energy and Environment*, 7(1), 52-57.
- Sathya, M., Muthuraman, G., & Elumalai, S. (2016). Bulk liquid membrane process for the transport and kinetics study of malachite green from textile wastewater. *Iranica Journal of Energy and Environment*, 7(3), 294-303.
- Soniya, M., & Muthuraman, G. (2015). Comparative study between liquid-liquid extraction and bulk liquid membrane for the removal and recovery of methylene blue from wastewater. *Journal of Industrial and Engineering Chemistry*, 30, 266-273.
- Zeng, L., Liu, Q., Luo, L., Liu, L., & Tang, K. (2019). Enhancement mechanism of an improved liquid membrane using selective permeation retardant for heavy metal ions separation. *Chemical Engineering Science*, 201, 1-14.



Comparative Study on Inhibitors Comprising Aromatic and Non-Aromatic Solvents towards Flow Assurance of Crude Oil

S M Anisuzzaman^{1,2*}, Duduku Krishnaiah² and Sharmini Nair Prathaban²

¹Energy Research Unit (ERU), Universiti Malaysia Sabah, 88400 UMS, Kota Kinabalu, Sabah, Malaysia

²Chemical Engineering Programme, Faculty of Engineering, Universiti Malaysia Sabah, 88400 UMS, Kota Kinabalu, Sabah, Malaysia

ABSTRACT

The petroleum industry is facing a critical issue in transporting crude oil through the pipelines from the seashore where crude oil is being drilled off. The problem arises when crude oil exhibits higher sensitivity to the changes of temperature. This actually causes some alterations occurring in the composition, pour point of the oil and flow of the crude oil itself. Thickening of some components such as wax and asphaltenes causes the deposition to occur in the pipelines due to changes in temperature. Eventually, these depositions cause blockage of the pipelines due to reduction in the diameter of the pipelines and causing disruption in the flow of crude oil. The experiments were carried by mixing different ratio of polymer and solvent such as ethylene-vinyl acetate (EVA40) with 40% vinyl acetate, methylcyclohexane (MCH), toluene and butanol together to form an inhibitor. The response surface methodology (RSM) had been used to identify the best formulation of solvents that could act as inhibitors. The final results show that the most optimum ratio of inhibitor that gives the highest reduction in viscosity of the crude oil is 30% EVA, 30% MCH and finally 40% ratio of solvent which is either toluene or butanol.

Keywords: Asphaltene, crude oil, deposition, inhibitors, response surface methodology, wax

ARTICLE INFO

Article history:

Received: 26 April 2019

Accepted: 22 July 2019

Published: 13 January 2020

E-mail addresses:

anis_zaman@ums.edu.my; dr.anis.ums@gmail.com (S M Anisuzzaman)

krishna@ums.edu.my (Duduku Krishnaiah)

prathabansharmininair@gmail.com (Sharmini Nair Prathaban)

* Corresponding author

INTRODUCTION

Crude oil is one of the components in petroleum that is very important to be commercially sold over the world and which is known as non-renewable energy. Crude oil is an unrefined product that is obtained from the exploration process and it varies from light to heavy crude oils based on molecular weight (Aldahik et al.,

2017). It is composed of hydrogen and carbons. The major petroleum constituents from crude oil that can be used for almost all types of manufacturing industries such as fuel for transporting, rubber industries, and leather industries (Aldahik et al., 2017; Amghizar et al., 2017; Sharma, 2006).

There are many problems arising during the transportation of crude oil and the main concern or issue is that the solid deposition in the pipelines (Kriz & Andersen, 2005). Solid deposition here is known as waxes and asphaltene components. Due to this phenomenon, the production lines can be clogged and the production of oil can be effected. The highest molecular weight of n-paraffin or known as n-alkane with hydrocarbon bonding is one of the main components in the wax formation in crude oil (Kriz & Andersen, 2005). Asphaltenes are found in the crude oil and they are known as high molecular polyaromates or called as resin too sometimes (Adebiyi & Thoss, 2014; Wilt et al., 1998).

Although wax and asphaltenes act as structural stabilizer during formation of crude oil, at a certain temperature along the transportation can cause these to turn into large clumps which lead to the deposition process. High deposition of wax and asphaltene causes the blockage in the pipeline due to reduction of space or diameter. As a result, the cost of maintenance of the industries increases gradually as the cost to improve the pipeline is too high and need to be maintained frequently. Thus, an effective method is devised to prevent any issues found from the deposition along the pipelines by improving the flow properties of crude oil (Anisuzzaman et al., 2017a; Anisuzzaman et al., 2017b; Tinsley et al., 2009).

There are many methods that have been introduced in previous studies to reduce the deposition of the wax. One of the traditional methods that had been practiced in the new research was by using acrylate polymer, acting as pour point depressant (PPD) which was a solid form polymer (Admiral et al., 2016). Although there are many traditional methods to remove wax precipitation, the most frequent method is the wax inhibitor. An inhibitor is being categorized as the modifier of the crystals, depressants of the pour point and inhibitors of paraffin followed by the flow improvers (Kriz & Andersen, 2005). A wax inhibitor can ensure that the growth of the wax stopped and able to prevent any wax blockage occur in the pipeline (Theyab & Diaz, 2016).

Asphaltenes are known as impure compounds as they consist of thousands different species with different molecular weights but similar behaviors chemically (Wei et al., 2016). As mentioned before, the best treatment is by using chemical inhibitors to reduce the blockage in the pipelines due to the asphaltene deposition. Thus, solvent treatment becomes the best treatment to treat this issue and the most common solvents that can be used as inhibitors are toluene, benzene and xylene which they are aromatic compounds. Asphaltenes have higher solubility in the non-polar solvent such as toluene and they are less soluble in the polar solvents such as glycerine, water, n-heptane and n-pentane compounds (Adebiyi & Thoss, 2014; Zhang et al., 2014). They are also insoluble in normal

alkane solvent. Moreover, asphaltenes always exist in suspended solid form or known as colloidal particles and the structures of the asphaltenes being interconnected by bridges that are formed from some aromatic compounds as sulphur or alkyl (Ghloum et al., 2010).

Treatment by using chemical solvent can save the cost as well as acts a preventive method for this critical issue. The treatment that has been frequently used is by direct injection process into asphaltene deposition and it is known as a physical-chemical process and chemical inhibitors. The chemical structures of the asphaltene strongly influence the deposition in the crude oil (Ghloum et al., 2010; Rogel, et al., 2001). Thus, it is very important in choosing the proper chemical inhibitors with accurate structural functional groups to treat asphaltene issues in petroleum pipelines so that this issue can be solved easily with less costing (Ridzuan et al., 2016).

Hence, overall purpose of this study is to differentiate the effect of the inhibitors that were formulated from different types of solvents which consisted of aromatic solvent and non-aromatic solvent towards to the solubility of wax and asphaltene. Moreover, response surface methodology (RSM) has been used to identify the best formulation of solvents that can act as inhibitors.

EXPERIMENTAL SECTION

Materials and Chemicals

The main chemical that was used in this experiment is the crude oil that was obtained from Sabah platform, Malaysia. Thus, the type of crude oil is known as Malaysian crude oil where they contain higher fractions of asphaltene compared to the wax fraction (Anisuzzaman et al., 2017a; Anisuzzaman et al., 2017b). Another chemical was the wax inhibitor which was ethylene vinyl acetate (EVA40) with 40% vinyl acetate. EVA is a type of polymer that can increase adhesion process to the surface of wax molecules. The EVA40 had been obtained from the Sigma Aldrich, USA. Another reagent used was the Methylcyclohexane (MCH) which could act as EVA solvent and this was due to EVA properties that would dissolve easily in MCH which had a higher boiling point, 100.4°C (Almeida et al., 2011). The most appropriate inhibitor for asphaltene is toluene but in this experiment, butanol was used together so that the comparison of the aromatic and non-aromatic compounds could be studied. These types of solvents were used to decrease the formation of crystals of asphaltene and increase the adhesion process to the surface of the asphaltene so that flocculation was prevented on the surface of the crude oil. The viscometer was used to obtain the viscosity of the crude oil samples that were being mixed with the different formulation of inhibitors. The viscometer used was the Brookfield Programmable Viscometer DV-III + Rheometer and the standard settings of viscometer such as spindle size and rotational speed was 63 and 100 rpm respectively. Binder oven was used to heat the crude oil pre-night until they reached 90°C before mixing with the inhibitors the next day. Water Bath

was used to decrease the temperature of the sample gradually. All the experiments were carried out at one atmospheric pressure.

Pre-experimental Preparation of Chemicals and Crude Oil

The pre-step for the experiment was that the crude oil was heated in the Binder oven at the temperature about 90°C for an overnight. This step was to melt any deposition of wax crystals that had been formed earlier and the structure of asphaltene being agglomerated in the crude oil. The preliminary step before this experiment was being conducted so that the precipitation of wax and asphaltene at the point of contact between the hot crude oil and cold apparatus could be avoided and to obtain accurate results. Before mixing of the inhibitor together EVA, MCH and toluene or butanol were heated in a water bath to increase the temperature around 50°C to 60°C (Anisuzzaman et al., 2017a; Anisuzzaman et al., 2017b).

Preparation of Inhibitor

The inhibitors were prepared by conducting them on a hot plate at a temperature of about 90°C. Instead of using the oven, using hot plate can help to save time and space for the experiment to be conducted as the limitation of lab equipment in preparing the chemicals. The individual chemicals, EVA, MCH and Toluene were measured separately of its respective volume and weight in accordance with the manipulated percentage composition. The unit for the EVA is grams of mass while MCH is in mL and toluene and butanol are in mL. The total volume of inhibitor used was 0.4g. Thus, for example, if the percentage composition of the samples prepared are 50% EVA, 10% MCH and 40% Toluene, then 0.2 g EVA was measured using a mass balance, 0.04 mL of MCH was measured using a micropipette and 0.16 mL of Toluene was measured using a micropipette. The ratio of the EVA40 used was 30%, 40% and 50%.

The precaution step here was to replace the tube for the micropipette for each new sample that was taken so that contamination can be avoided and accuracy of the results obtained can be improvised. Care was taken to replace the micropipette tube for both chemicals to avoid contamination. The purpose of the reaction to be in high temperature was around 50°C which is to ensure that the EVA pellets are completely melted in the inhibitors and to develop the influence of inhibitors on formed wax crystals (Theyab & Diaz, 2016). After complete melting of EVA, then the crude oil that was placed in the oven overnight was mixed with the EVA and the inhibitor solutions. If the crude oil managed to be heated overnight, then complete dissolved wax crystal was obtained on the next day. Later, the samples obtained were shaken around 30 seconds by magnetic stirrer. This was to ensure the crude oil and the inhibitors completely mixed. Then, the samples are placed again in the oven for 15 minutes to allow the reaction to take place.

Experimental Procedures

The viscosity of the samples was taken from the temperature range from 5°C and 20°C. The control sample in this experiment was blank crude oil that was free from inhibitors. The viscosity of the blank crude oil was measured at earlier stage. The procedure was repeated for each of the other samples that contain the different formulation of inhibitors with different ratio of the composition of solvents and polymers.

Optimization of Experimental Design of Aromatic Inhibitor by using Response Surface Methodology (RSM)

RSM was used to optimize the ratio of each chemical and to test the optimized ratio of formulation inhibitor on the wax and asphaltene solubility. Table 1 shows the design summary of the model for the formulation of inhibitors consists of toluene.

Table 1
The summary of the design model

File Version				Design Expert 7.0					
Study type				Mixture					
Design type				D-optimal					
Design model				Quadratic					
Subtype				Split-plot					
Runs				36					
Factor	Name	Units	Type	Minimum	Maximum	Coded Values			
A	EVA	%	Mixture	20	60	0.00			
B	MCH	%	Mixture	20	60	0.00			
C	Toluene	%	Mixture	10	40	0.00			
Response	Name	Units	Observed value	Analysis	Minimum	Maximum	Std. Dev.	Ratio	Model
R1	Viscosity	cP	36	Polynomial	72	755	181.99	10.49	Special cubic

Based on the Table 1, the study type that had been used was the mixture as there were three different types of chemicals to form a specific inhibitor. The total ratio of chemicals used was 100%. From the Table 1, it shows that that the total runs or samples that we used were 36 samples at different temperature which was around 5°C to 20°C. The parameter that acted as a response was the viscosity of crude oil.

RESULTS AND DISCUSSION

Characterization of Crude Oil

Fourier transform infrared spectroscopy (FTIR) analysis was used as an analytical method to determine the presence of asphaltene content in crude oils qualitatively. The results FTIR analysis of blank crude oil is shown in the Figure 1.

The results of spectrum obtained from FTIR analysis was evaluated by comparing with the literature review that had done in analyzing the asphaltene contents in crude oil using the FTIR (Table 2) (Wilt et al., 1998). Based on the results, there are some similarities on the characteristic of spectrum retrieved from FTIR spectroscopy analysis between the blank crude oil used for the experiment and blank crude oil used in the literature review. The spectrum of FTIR analysis in Figure 1 had been compared with the result of evaluation of the crude oil obtained from existing research sources and confirmed that there was presence of asphaltenes in the Sabah blank crude oil used in this study (Wilt et al., 1998). The peak at 1607.15 cm^{-1} in the Figure 1 shows that the results of FTIR analysis corresponded to the aromatic C=C stretching vibrations. Besides, the absorbance at 1456.07 cm^{-1} shown predominantly is due to its CH_2 bending modes and a part of CH_3 bending modes. Methyl bending vibrations are the main reason for the peak at 1377 cm^{-1} to be occurred in this analysis. The ester linkages present in the asphaltene molecule as indicated by the peak

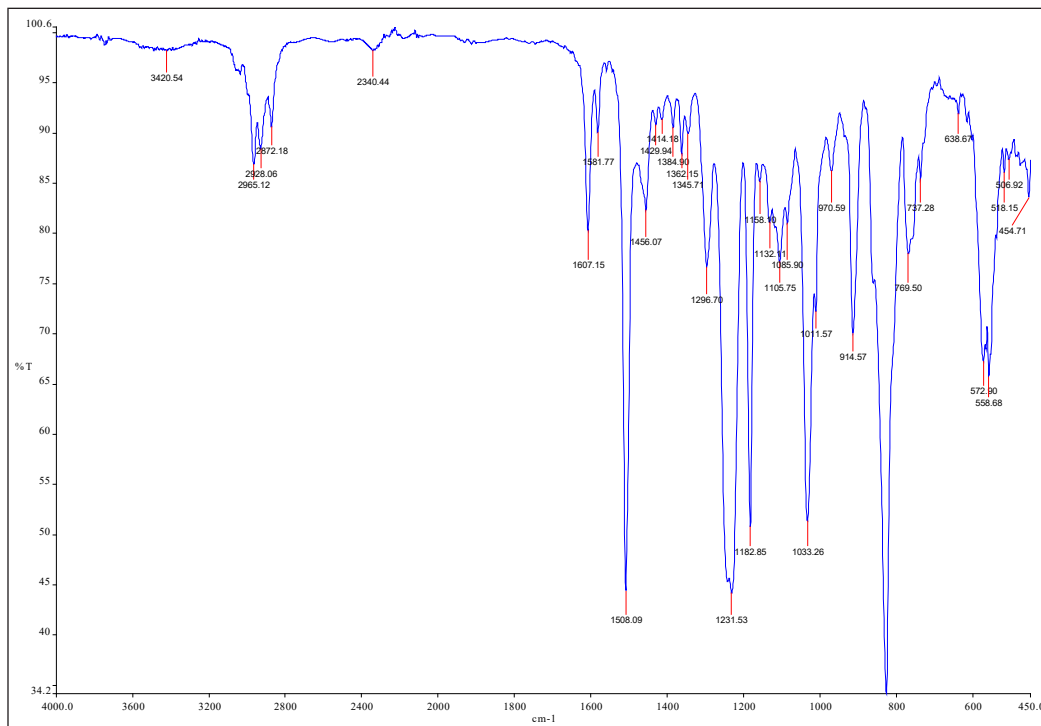


Figure 1. Illustration of blank crude oil FTIR analysis

at 1033.26 cm^{-1} . The three absorbances observed between 870 and 722 cm^{-1} can be the indicator to the aromatic CH out-of-plane bending vibrations.

Table 2
The peaks values of two different sources

Peaks showing presence of asphaltenes, cm^{-1} (Wilt et al., 1998)	Peaks in the FTIR results of Sabah blank crude oil, cm^{-1}	Peak assignment
1602	1607.15	C=O
1032	1033.26	C-O-C
812	819	C-H
752	769	C-H

The spectrum of FTIR analysis also proved that the blank crude oil contained wax as one of the components. Wax paraffin is known as hydrocarbons with the C-H and C-C bonding. Once wax paraffin become saturated hydrocarbons, then their C-H stretching peaks in FTIR will be around 1377 to 1461 cm^{-1} . Thus based on the blank crude oil used in the experiment, the paraffin wax is proven to be saturated (Khan et al., 2017).

Viscosity of Blank Crude Oil

The viscosity of the control sample of the experiment was the blank crude oil as shown as in Figure 2. These samples viscosities were measured at different temperatures in range around 5°C to 20°C .

From the Figure 2, the results show that the viscosity of the crude oil decreases as the temperature of the crude oil increases.

The reduction of the viscosity using aromatic solvent (toluene) is shown in Figure 3.

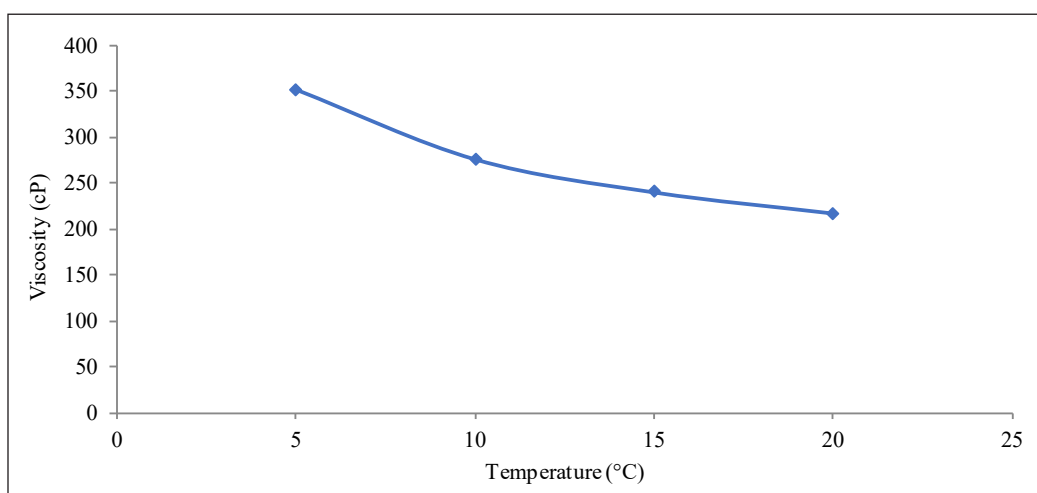


Figure 2. Viscosity of the blank crude oil against temperature

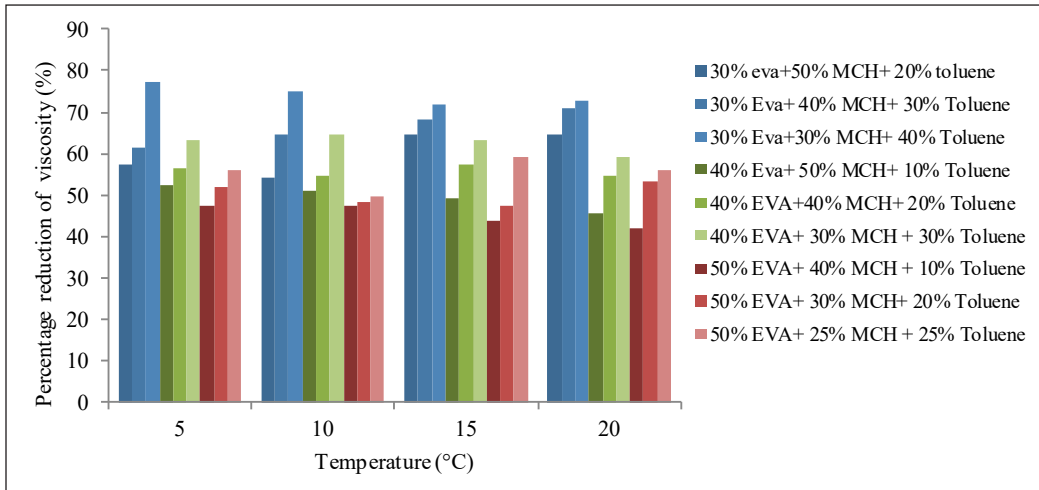


Figure 3. Percentage reduction in viscosity against temperature using aromatic solvent

The results show that higher the percentage of EVA in the solvent used higher the viscosity of the crude oil. In addition to that, it also shows that at higher temperature, the viscosity was too low. Increasing the amount of EVA eventually caused increase in viscosity of crude oil (Anisuzzaman et al., 2017a; Anisuzzaman et al., 2017b; Quan et al., 2016). Thus, an optimum amount of EVA is required to act as an inhibitor for wax. This is because the solubility of asphaltene in the presence of toluene is actually a balance between the π - π stacking of aromatic ring systems from the toluene and the repulsion which comes in steric form that comes from the alkane chains, which tends to increase the solubility. Thus, it helps to delay the deposition or aggregation of asphaltene in the crude oil (Zarkar et al., 2015).

The reduction of the viscosity using non-aromatic (butanol) is illustrated in Figure 4.

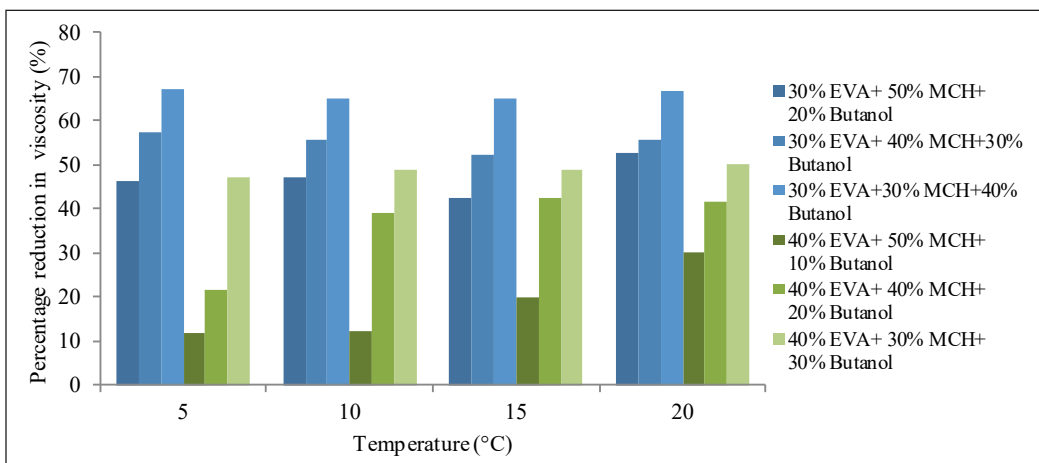


Figure 4. Percentage reduction in viscosity against temperature using non-aromatic solvent

A clear observation was obtained where the viscosity of the crude oil becomes greater than the blank crude oil when the fixed percentage ratio of EVA is the highest which is at 50%. In this situation, there is a significant change where the crude oil was assumed to become thicker and hard to flow with higher percentage of EVA and butanol. As it reaches a saturation point where the level of EVA and butanol in crude oils is maximum, the crude oil becomes thicker and more viscous because there is higher agglomeration of EVA and butanol. Thus, butanol which is the solvent that could not coagulate the EVA sufficiently and it tended to spread over the surface of coagulant causing deposition to occur (Matsumoto et al., 1974). Hence, the usage of non-aromatic compound, butanol is less efficient to aid the wax and asphaltene solubility in the crude oil and to improve the flow assurance of crude oil in pipelines.

Optimization Experimental Design of Aromatic Inhibitor by using RSM

ANOVA analysis was used to determine the regression model equations for this mixture design of these combinations of three chemicals (Bono et al., 2008; Bono et al., 2014). For the ANOVA analysis, the model used for the mix-design model is Scheffe Mix Model as this model is typically used to handle any natural constraints that occur in the mixture design. However, the mix order that we decided to use here was the special cubic as there would be around three different components blend together to form an inhibitor. The equation for the actual responses for the viscosity of the crude oil with a constant of 100 rpm is expressed as shown in equation 1.

$$\begin{aligned} \text{Viscosity (cP)} &= +2.94605A + 1.25404B - 1.09010C - 0.021691AB - 0.02986AC \\ &= +2.94605A + 1.25404B - 1.09010C - 0.021691AB - 0.02986AC \end{aligned} \quad (1)$$

wherein the equation above each term represented as:

A is the ratio of percentage of EVA, B is the ratio of percentage of MCH and C represent the ratio of the toluene.

Statistical Analysis of the Design Model of Aromatic Solvent

Statistical analysis of experiments depends on the ANOVA analysis. The ANOVA analysis can be done by studying the values of probability (p), coefficient of determination (R^2), and adjusted R^2 . The analysis was tabulated as shown in Table 3 based on ANOVA variance analysis.

Table 3 shows that the 'Model F' and value of p are 4.90 and 0.0014 respectively. These values clearly show that the model is significant. Besides, the model terms are significant as the values of "Prob > F" obtained is less than 0.05. From the analysis, predicted R^2 is

actually in a reasonable agreement with the adjusted R^2 . As “Adequate precision” measures the signal to noise ratio, any ratio greater than 4 is desirable. Signal to noise ratio is the interference occurs due any electrical strength as computer signal. Based on the analysis, the obtained ratio is 7.082 which show that it is an adequate signal. R^2 in this model is 0.5037 which indicates that there is about 50% effect that is given to the input variable by the variation output variable.

Table 3
Statistical analysis of variance (ANOVA) for the viscosity using aromatic solvent

Source	Sum of squares	DF	Mean square	F-value	P-value Prob > F	
Model	19004.59	6	3167.43	4.90	0.0014	Significant
Linear mixture	18859.14	2	9429.57	14.60	<0.0001	
AB	3.65	1	3.65	5.659x10 ³	0.9405	
AC	0.70	1	0.70	1.09x10 ³	0.9739	
BC	3.33	1	3.33	5.15x10 ³	0.9432	
ABC	1.06	1	1.06	1.638x10 ³	0.9680	
Residual	18729.05	29	645.83			
Cor Total	37733.64	35				
Std. Deviation = 25.41		Mean = 114.31		Adequate precision = 7.082		
$R^2 = 0.5037$		Adj. $R^2 = 0.4010$				

Interactions between each Component

Each interaction between the three main components was studied. Figure 5 shows the interactions between each component in three-dimensional group based on ANOVA.

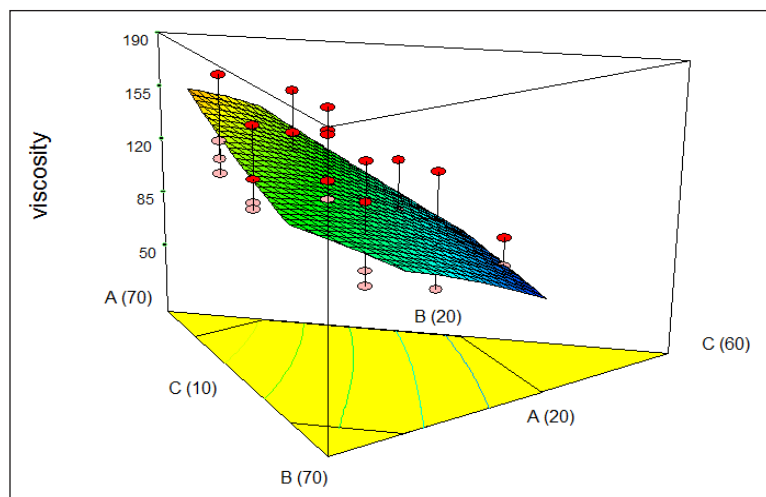


Figure 5. 3D illustration on the interaction between each component using aromatic solvent

Based on Figure 5, each component had been labelled respectively in alphabetical orders such as A represents the percent ratio of EVA, B represents the percent ratio of MCH and last but not least C was the term to describe the toluene ratio in forming an inhibitor. The most effective interaction was between AC where at this region, the lowest viscosity was obtained. This observation clearly proves that the EVA is the wax inhibitor while the toluene acts as asphaltene inhibitor (Wei et al., 2016).

Optimized Results for the Aromatic Compound

The objective of this study is to optimize the ratio of chemicals used and the temperature by using the RSM. Thus, the optimum value for each component is tabulated in Table 4.

Table 4
Optimized result for aromatic solvent

Type of components	Goal to achieve	Optimized value
EVA (%)	In range	30.00
MCH (%)	In range	30.48
Toluene (%)	In range	39.51
Viscosity of crude oil (cP)	Minimize	69.98
Desirability		1.00

Table 4 shows the optimized viscosity of the crude oil obtained is 69.98. In conclusion, addition of the inhibitors can cause reduction in viscosity of the crude oil and caused the flow assurance of crude oil in the pipelines becomes more effective. As the desirability is 1, the optimized ratio for the formulation of inhibitor might give a great effect on the viscosity of the crude oil.

Optimization Experimental Design of Non-Aromatic Inhibitor by using RSM

As mentioned before in aromatic compound design model, the type of model used here was Scheffe Mix model as this model helped to readjust back the natural constraints compared to Slack Model. The mix model used here is special cubic where there are three components used in this design to form the best inhibitors. The equation for the actual responses for the viscosity of the crude oil with a constant of 100 rpm was defined as shown in equation 2.

$$\begin{aligned} \text{Viscosity (cP)} = & 25.71679A + 8.92852B - 60.42534C - 0.449041AB + 1.77294AC \\ & + 1.75675BC - 0.072701ABC \end{aligned} \quad (2)$$

wherein the equation above each term represented as:

A is the ratio of percentage of EVA, B is the ratio of percentage of MCH and C represent the ratio of the toluene.

Statistical Analysis of the Design Model of Non-Aromatic Inhibitor

Table 5 shows results obtained for the inhibitors that consist of non-aromatic compound.

Table 5
Statistical analysis of variance (ANOVA) for the viscosity using non-aromatic solvent

Source	Sum of squares	DF	Mean square	F-value	P-value Prob > F	
Model	9.92×10^5	6	1.665×10^5	25.0	0.0038	Significant
Linear mixture	7.489×10^5	2	3.774×10^5	56.21	<0.0001	
AB	21454.37	1	21454.37	3.22	0.0831	
AC	1038.81	1	1038.81	0.16	0.6958	
BC	2205.68	1	2205.68	0.33	0.5694	
ABC	13904.29	1	13904.29	2.09	0.1592	
Residual	1.932×10^5	29	6661.06	5.54		
Cor Total	1.192×10^6	35				
Std. Deviation = 81.62		Mean = 254.67		Adequate precision = 14.664		
$R^2 = 0.8380$		Adj. $R^2 = 0.8045$				

From the Table 5, the P-value is lower than 0.05, proving that the model is significant. It can be seen that the larger the standard deviation, the accuracy of the results from the mean of the result is low.

Interactions between Components

Interaction between each component in this mixture had been explained with the Figure 6.

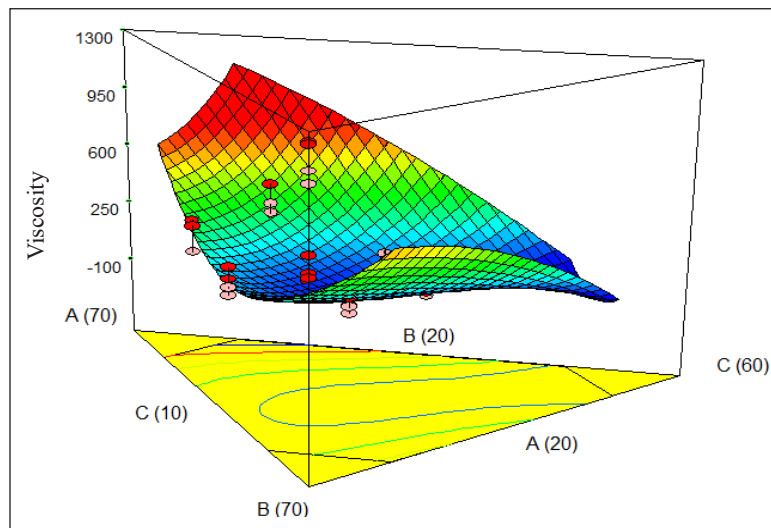


Figure 6. 3D illustration on the interaction between each component using non-aromatic solvent

As shown in Figure 6, the interaction between A which is the EVA and C, butanol (AC) did give significant effect on the viscosity of crude oil. This is due to the higher point of A (EVA) on the plane, the higher the viscosity. However, the higher the point of C (butanol), the viscosity decreases.

Optimized Results for the Non-Aromatic Compound

After analyzing the ANOVA of the design model, the optimized data for each component is shown in Table 6.

Table 6
Optimized result for non-aromatic solvent

Type of components	Goal to achieve	Optimized value
EVA (%)	In range	30.00
MCH (%)	In range	30.00
Butanol (%)	In range	40.00
Viscosity of crude oil (cP)	Minimize	77.00
Desirability		0.993

Based on the Table 6, desirability of the optimized model result is just 0.993 which means that there is lacking of “quality” in the component process data thus this optimized ratio for this formulation of inhibitors might be less efficient in giving great reduction in viscosity. The optimized viscosity obtained for this formulation of inhibitors using butanol is 77 cP.

Comparison between Aromatic Compound and Non-Aromatic Solvent

Comparison between these two solvents was done to identify the effect of two different solvents as inhibitors toward solubility of wax and asphaltene in the crude oil. The comparison was done based on percentage of reduction of viscosity for the optimised ratio of both inhibitors. Figure 7 shows the comparison in percentage reduction for this specified ratio of chemicals:

Figure 7 shows that the toluene which is aromatic solvent is the best inhibitor compared to non-aromatic solvent, butanol. This is due to the percentage reduction of viscosity of crude oil at 10°C with formulation of inhibitor is the highest which is 77% compared to butanol which was just 65%. Thus, it can be proven that aromatic solvent plays the effective role as the best inhibitor in improving the solubility of wax and asphaltene. Indirectly, it helps to increase flow assurance of crude oil in pipelines compared to non-aromatic solvent.

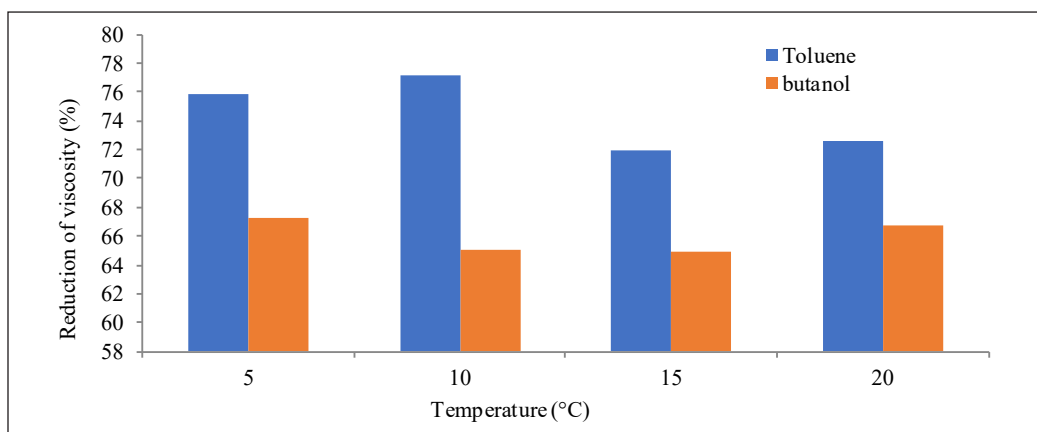


Figure 7. Percentage reduction of viscosity against temperature

CONCLUSION

In conclusion, both inhibitors consisting toluene and butanol showed effect on reduction in viscosity of the crude oil. Thus, it indicates that the aromatic solvent and non-aromatic solvent could act as inhibitors for the deposition of wax and asphaltene and could increase the solubility of wax and asphaltene in the crude oil. However, the level of certainty is that all non-aromatic solvent can reduce the viscosity of the crude oil but still at a very low level as this study was done with a specific type of solvent. From the optimization, the best inhibitor for reduction of viscosity can be formulated in the ratio of 30% EVA, 30% MCH and finally 40% of the solvent either toluene or butanol. The results show that the formulation of inhibitor using butanol as solvent gives higher percentage reduction in viscosity than formulation of inhibitor using toluene.

ACKNOWLEDGEMENTS

The authors would like to express their greatest appreciation to the Centre of Research and Innovation (PPI), Universiti Malaysia Sabah (UMS) for the support to this study (Grant No. SBK0346-2017).

REFERENCES

- Adebiyi, F. M., & Thoss, V. (2014). Organic and elemental elucidation of asphaltene fraction of Nigerian crude oils. *Fuel*, *118*, 426-431.
- Admiral, A., Abdullah, M. K., & Ariffin, A. (2016). Evaluation of emulsified acrylate polymer and its pour point depressant performance. *Procedia Chemistry*, *19*, 319-326.
- Aldahik, A., Schulz, H. M., Horsfield, B., Wilkes, H., Dominik, W., & Nederlof, P. (2017). Crude oil families in the Euphrates Graben (Syria). *Marine and Petroleum Geology*, *86*, 325-342.

- Almeida, A., Possemiers, S., Boone, M. N., De Beer, T., Quinten, T., Van Hoorebeke, L., ... & Vervaeck, C. (2011). Ethylene vinyl acetate as matrix for oral sustained release dosage forms produced via hot-melt extrusion. *European Journal of Pharmaceutics and Biopharmaceutics*, 77(2), 297-305.
- Amghizar, I., Vandewalle, L. A., Van Geem, K. M., & Marin, G. B. (2017). New trends in olefin production. *Engineering*, 3(2), 171-178.
- Anisuzzaman, S. M., Abang, S., Bono, A., Krishnaiah, D., Karali, R., & Safuan, M. K. (2017a). Wax inhibitor based on ethylene vinyl acetate with methyl methacrylate and diethanolamine for crude oil pipeline. *IOP Conference Series: Materials Science and Engineering*, 206(012074), 1-8.
- Anisuzzaman, S. M., Abang, S., Bono, A., Krishnaiah, D., Ismail, N. M., & Sandrison, G. B. (2017b). An evaluation of solubility of wax and asphaltene in crude oil for improved flow properties using a copolymer solubilized in organic solvent with an aromatic hydrocarbon. *International Journal of Chemical and Molecular Engineering*, 11(10), 688-695.
- Bono, A., Anisuzzaman, S. M., & Ding, O. W. (2014). Effect of process conditions on the gel viscosity and gel strength of semi-refined carrageenan (SRC) produced from seaweed (*Kappaphycus alvarezii*). *Journal of King Saud University Engineering Sciences*, 26(1), 3-9.
- Bono, A., Duduku, K., & Rajin, M., (2008). *Products and process optimization using Response Surface Methodology*. Sabah, Malaysia: Penerbit Universiti Malaysia Sabah.
- Ghloum, E. F., Al-Qahtani, M., & Al-Rashid, A. (2010). Effect of inhibitors on asphaltene precipitation for Marrat Kuwaiti reservoirs. *Journal of Petroleum Science and Engineering*, 70(1-2), 99-106.
- Khan, M. K., Kwek, W., Kim, J. J. D., Behbahani, T. J., Miranbeigi, A. A., Sharifi, K., & Diaz, P. (2017). Rheological properties and viscosity reduction of South China Sea crude oil. *Journal of Petroleum Science and Engineering*, 146(1-2), 74-86.
- Kriz, P., & Andersen, S. (2005). Effect of asphaltenes on crude oil wax crystallization. *Energy and Fuels*, 19(3), 948-953.
- Matsumoto, T., Nakamae, K., Ochiuni, T., Tamur, T., & Shioyam, T. (1974). The solubility and the wet spinning of ethylene-vinyl alcohol copolymers. *Bulletin of the Institute for Chemical Research, Kyoto University* 52(2), 403-415.
- Quan, Q., Wang, W., Wang, P., Yang, J., Gao, G., Yang, L., & Gong, J. (2016). Effect of oil temperature on the wax deposition of crude oil with composition analysis. *Brazilian Journal of Chemical Engineering*, 33(4), 1055-1061.
- Ridzuan, N., Adam, F., & Yaacob, Z. (2016). Evaluation of the inhibitor selection on wax deposition for Malaysian crude oil. *Petroleum Science and Technology*, 34(4), 366-371.
- Rogel, E., Leon, O., Espidel, Y., & Gonzalez, Y. (2001). Asphaltene Stability in Crude Oils. *SPE Production and Facilities*, 16(2), 84-88.
- Sharma B. K. (2006). *Industrial chemistry (including chemical engineering)*. Delhi, India: GOEL Publishing House.
- Theyab, M., & Diaz, P. (2016). Experimental study of wax deposition in pipeline – effect of inhibitor and spiral flow. *International Journal of Smart Grid and Clean Energy*, 5(3), 174-181.

- Tinsley, J. F., Jahnke, J. P., Dettman, H. D., & Prud'home, R. K. (2009). Waxy gels with asphaltenes 1: characterization of precipitation, gelation, yield stress, and morphology. *Energy and Fuels*, 23, 2056-2064.
- Wei, D., Simon, S., Barriet, M., & Sjöblom, J. (2016). An ITC study of interaction and complexation of asphaltene model compounds in apolar solvent II: Interactions with asphaltene inhibitors. *Colloids and Surfaces A: Physicochemical and Engineering Aspects*, 495, 87-99.
- Wilt, B., Welch, W., & Rankin, J. (1998). Determination of asphaltenes in petroleum crude oils by fourier transform infrared spectroscopy. *Energy and Fuels*, 12(5), 1008-1012.
- Zarkar, S., Pauchard, V., Farooq, U., Couzis, A., & Banerjee, S. (2015). Interfacial properties of asphaltenes at toluene-water interfaces. *Langmuir*, 31(17), 4878-4886.
- Zhang, L. L., Yang, G. H., Wang, J. Q., Li, Y., Li, L., & Yang, C. H. (2014). Study on the polarity, solubility, and stacking characteristics of asphaltenes. *Fuel*, 128, 366-372.

An Integration Based Optimization Approach (ABC and PSO) for Parameter Estimation in BLRP Model for Disaggregating Daily Rainfall

Zulkarnain Hassan

Civil Engineering Programme, School of Environmental Engineering, Universiti Malaysia Perlis, Kompleks Pusat Pengajian Jejawi 3, 02600 UniMAP, Arau, Perlis, Malaysia

ABSTRACT

Fine resolution (hourly rainfall) of rainfall series for various hydrological systems is widely used. However, observed hourly rainfall records may lack in the quality of data and resulting difficulties to apply it. The utilization of Bartlett-Lewis rectangular pulse (BLRP) is proposed to overcome this limitation. The calibration of this model is regarded as a difficult task due to the existence of intensive estimation of parameters. Global optimization algorithms, named as artificial bee colony (ABC) and particle swarm optimization (PSO) were introduced to overcome this limitation. The issues and ability of each optimization in the calibration procedure were addressed. The results showed that the BLRP model with ABC was able to reproduce well for the rainfall characteristics at hourly and daily rainfall aggregation, similar to PSO. However, the fitted BLRP model with PSO was able to reproduce the rainfall extremes better as compared to ABC.

Keywords: Bartlett-lewis rectangular pulse, disaggregation, optimization, rainfall

ARTICLE INFO

Article history:

Received: 26 June 2019

Accepted: 13 September 2019

Published: 13 January 2020

E-mail address:

zulkarnainh@unimap.edu.my

INTRODUCTION

In many regions, the rainfall data are recorded based on the daily time step. However, many hydrological studies and designs require a fine-scale data, such as hourly rainfall rather than daily rainfall (Debele et al., 2007; Vanhaute et al., 2012a). Therefore, it is necessary to obtain a fine-

scale data (e.g. hourly time step) from the higher time scale (e.g. daily time step) and this transformation is named as disaggregation. Many disaggregation theories were developed for this purpose such as Poisson cluster-based models (Rodriguez-Iturbe et al., 1987), Markov chain models (Hutchinson, 1990; Sansom 1998) and semi-empirical models. The scope of this study is limited to Bartlett–Lewis Rectangular Pulses (BLRP), which utilizes the stochastic models based on the Poisson cluster.

Pui et al. (2009) stated that the BLRP model was developed for the simulation of rainfall and was modified to disaggregate rainfall. Intensive studies were conducted in many regions, which included the United States (Velghe et al., 1994; Rodriguez-Iturbe et al., 1987), United Kingdom (Abdellatif et al., 2013), Australia (Hansen 1982), New Zealand (Cowpertwait et al., 2007) and Africa (Smithers et al., 2002). Based on these studies, it was revealed that the use of the BLRP model in matching the statistical properties including the extremes of the rainfall for a wide range of temporal scales was a success. Recently, the application of the BRLP model was extensively studied in Malaysia. Hanaish et al. (2013) evaluated two types of BLRP, namely the original and modified BLRP models in Peninsular Malaysia. The findings of their study found that the modified BLRP fitted well with Malaysia's rainfall condition as compared to the original BLRP model. Yusop et al. (2014) also studied the use of the BLRP model in the centre of Peninsular Malaysia and found that the BLRP model was able to disaggregate hourly to 48 hours rainfall that closely matched the observed series. However, both studies suggest that the model is not able to disaggregate well the extreme rainfall for the Malaysia region.

Since the BLRP model is complex to calibrate due to the application of the formulation of stochastic approaches, there was no previous studies in Malaysia [including the research by Hanaish et al. (2013) and Yusop et al. (2014)] and only a few studies worldwide, which had been conducted to find and/or to optimize the calibration of the BLRP model. Therefore, an evaluation of the recent optimization algorithm towards the calibration of the BLRP model becomes the main focus to improve the fitness of this model in this study, especially to the humid tropical region like in Malaysia.

Generally, in order to obtain the fitness of the BLRP model to an observed series, the generalized method of moments is applied (Rodriguez-Iturbe et al., 1987; Cowpertwait et al., 1996; Verhoest et al., 1997). This method is implemented by fitting the BLRP model to the observed rainfall characteristics at different aggregation levels. Therefore, function of the model parameters is expressed based on the derivation of the analytical expression of an expected value (Rodriguez-Iturbe et al., 1987). Verhoest et al. (1997) reported that the calibration of BLRP was a burdensome process due to the existence of multiple local minima. The local search techniques in which sub-optimal solution was applied to the optimization problem failed to overcome these local minima. Vanhaute et al. (2012a) stated

that global optimization approaches were expected to be more accurate in searching the BLRP parameters compared to the local search techniques.

In this study, two recent global optimization algorithms, which are artificial bee colony (ABC) and particle swarm optimization (PSO), were adopted. The PSO algorithm was developed by Kennedy and Eberhart (1995) and this algorithm is the population-based stochastic optimization techniques, in which inspired by social behavior of bird flocking. PSO is successfully applied in many applications (Eberhart & Yuhui, 2001). As the concern of the author, only a few studies on the PSO algorithm are applied with the BLRP model. Vanhaute et al. (2012a) presented and tested four global optimizations (Downhill Simplex Method, Simplex-Simulated Annealing, Particle Swarm Optimization and Shuffled Complex Evolution) for their capability to calibrate the BLRP model. Their findings suggested that the global optimizations were providing promising results in calibrating the BLRP model, in which it could disaggregate daily rainfall very well. Vanhaute et al. (2012b) extended their previous study (Vanhaute et al., 2012a) to improve the quality of disaggregation results on the extreme of rainfall using the global optimization methods. Both studies found that the performances of each global optimization were varying to each other and the PSO showed a promising tool for estimation of the BLRP parameters.

The ABC model was proposed by Karaboga (2005) and this algorithm was also the population-based stochastic optimization techniques, similar to PSO. This algorithm adopted the foraging behavior of honey bee swarm. The ABC model does not have any background application in this field (Karaboga et al., 2012), but it shows a very good performance in solving classical benchmark equations and other forms of applications. Therefore, the evaluation of the performance of ABC and PSO with the BLRP model becomes a platform of continuity in future studies.

Therefore, the objective of this study is to propose the use of the ABC algorithm in the estimation of the parameters of BLRP and to compare its performance according to the disaggregation results with the PSO model. The selected stations in Peninsular Malaysia are used to evaluate those methods. In the following sections, the materials and methods are presented and followed with the results and the discussions of this study. Next, the conclusions and recommendations are presented.

MATERIAL AND METHODS

Study Area and Data

Four rainfall stations were selected in Peninsular Malaysia to represent four regions with various climatic conditions. The locations and details of each station are shown in Figure 1 and Table 1, respectively. Generally, the rainfall occurrence of Peninsular Malaysia is influenced mostly by two monsoons, named as the south-west monsoon (from May to August) and the north-east monsoon (from November to February), with the two inter

monsoons. During the south-west monsoon, Regions 1 (Alor Setar) and 3 (Melaka) receives heavy rainfall. Otherwise, those regions are the driest part of the Peninsular during the north-east monsoon period. Both regions are less influenced by the north-east monsoon because the regions are blocked by the Titiwangsa Range.

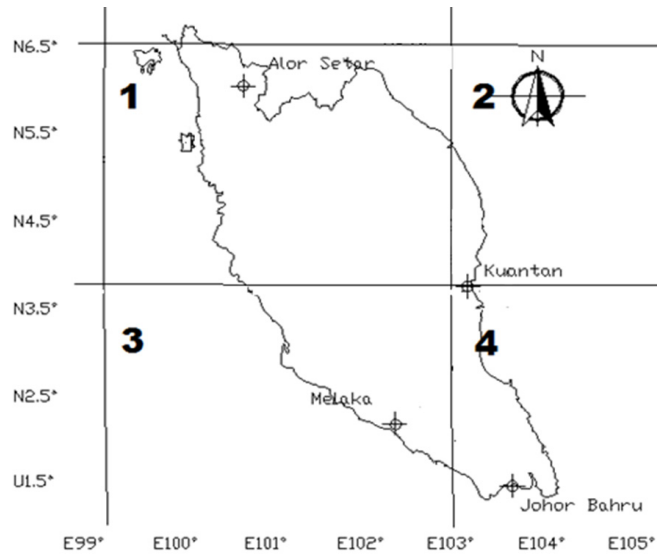


Figure 1. Location of rainfall stations

Table 1

Details and description of rainfall stations

Region	ID	Name of Station	Location		Period
			Lat (°N)	Long (°E)	
1	6108001	Alor Setar	6.11	100.85	2001-2012
2	3833002	Kuantan	3.81	103.33	2001-2012
3	2528012	Melaka	2.29	102.49	1991-2000
4	1437116	Johor Bahru	1.47	103.75	2002-2012

The hourly and daily rainfall data were obtained from the Department of Irrigation and Drainage Malaysia (DID) and their detail periods are illustrated in Table 1. All stations contained smaller missing data (<5%), and the missing data were filled with the expectation-maximization algorithm using PASW software. Before the rainfall data series were applied, the homogeneity of rainfall time series data was tested. In this study, the Pettitt, SNHT, Buishand, and von Neumann tests were applied to the annual rainfall series of each station. Results revealed that the graph produced for each test was almost a straight line and no breakpoints were detected. The p-value for each test was also computed using the Monte

Carlo simulation in order to enhance the reliability of the tests. The p-value was greater than the significance level alpha ($\alpha=0.05$) were obtained. Therefore, the assumption that the rainfall data series are homogenized is accepted.

Bartlett-Lewis Rectangular Pulse

Description of the BLRP Model. The basic structure of the BLRP model assumes the storm arrivals (T) developed in a Poisson process with λ . Every single of T is tailed by the cell origins (t) under the Poisson process with rate β . The new cell origins after the duration of period (s) is generated by exponential distributed with rate γ . Then, the cell origins are paired with the rainfall cell. Duration (W) and depth (X) are randomly extracted from the exponential distributions with parameters η and $1/\mu_x$, respectively. These continuous processes will develop a rainfall series.

In this study, the modified BLRP model was used. This model allows the average cell duration to vary between storm by letting the parameter η following a Gamma distribution of shape and parameters of α and v . This situation leads by the generation of $E[\eta]=\alpha/v$ and $Var[\eta]=\alpha/v^2$, with $\alpha>1$ to show the expected duration to be finite. The model also applied $\kappa=\beta/\eta$ and $\varphi=\gamma/\eta$, which were introduced by Rodriguez-Iturbe et al. (1987).

Two parameters gamma with mean (μ_x) and standard deviation (σ_x) can be distributed with the value of X . Therefore, the number of cells per storm can be expressed as $\mu_c=1+k/\varphi$. In total, the BLRP model contains 7 parameters ($\lambda, K, \varphi, \alpha, v, \mu_x$ and σ_x) that need to be estimated. The details of estimation process are discussed in the following section.

Estimation of BLRP Parameters. The estimation of BLRP parameters in this study is based on generalized method of moments, in which the minimum value between the observed and simulated rainfall properties was identified. The estimation was based on the monthly basis and the objective function $f(x)$ can be expressed as:

$$\text{minimum of } f(x) = \sum_{i=1}^k w_i [M'_i - M_i(x)]^2 \tag{1}$$

where, x is the parameter vector, w_i is the positive weight, M'_i is the vector of observed values, $M_i(x)$ is the vector of expected values, and k is the defined statistical properties of rainfall to the BLRP parameters. w_i is set as 1, following the rules set by Velghe et al. (1994). This study used an alternative $f(x)$ that was introduced by Cowperton et al. (2007) and Eq (1) is revised as follows:

$$\text{minimum of } f(x) = \sum_{i=1}^k \left[\left(\frac{M_i(x)}{M'_i} - 1 \right)^2 + \left(\frac{M'_i}{M_i(x)} - 1 \right)^2 \right] \tag{2}$$

The list of k applied in this study includes the mean ($E[Y_i^{(h)}]$), variance ($var[Y_i^{(h)}]$), autocorrelation for lag-1hour ($cov[Y_i^{(h)}, Y_{i+j}^{(h)}]$) and the probability of rainfall days ($p(h')$).

The list of k can be defined as (Rodriguez-Iturbe et al., 1988):

$$E[Y_i^{(h)}] = \lambda h \mu_x \left(\frac{1+\kappa/\phi}{\alpha-1} \right) \tag{3}$$

$$\begin{aligned} var[Y_i^{(h)}] &= 2A_1[(\alpha-3)hv^{2-\alpha} - v^{3-\alpha} + (v+h)^{3-\alpha}] - \\ &2A_2[\phi(\alpha-3)hv^{2-\alpha} - v^{3-\alpha} + (v+\phi h)^{3-\alpha}] \end{aligned} \tag{4}$$

$$\begin{aligned} cov[Y_i^{(h)}, Y_{i+j}^{(h)}] &= A_1\{[v+(j+1)h]^{3-\alpha} - 2(v+jh)^{3-\alpha} + [v+(j-1)h]^{3-\alpha}\} - A_2\{[v+ \\ &(j+1)\phi h]^{3-\alpha} - 2(v+j\phi h)^{3-\alpha} + [v+(j-1)\phi h]^{3-\alpha}\} \end{aligned} \tag{5}$$

$$p(h)' = exp\left\{-\lambda h - \lambda \mu_T + \lambda G_p^*(0,0) \frac{\phi+\kappa \left[\frac{v}{v+(\kappa+\phi)h}\right]^{\alpha-1}}{\phi+\kappa}\right\} \tag{6}$$

where;

$$A_1 = \frac{\lambda \mu_c v^\alpha}{(\alpha-1)(\alpha-2)(\alpha-3)} \left[E(X^2) + \frac{\kappa \phi \mu_x^2}{\phi^2-1} \right] \tag{7}$$

$$A_2 = \frac{\lambda \mu_c \kappa \mu_x^2 v^\alpha}{\phi^2(\phi^2-1)(\alpha-1)(\alpha-2)(\alpha-3)} \tag{8}$$

In these equations, X is the cell depth, i is the current time, j is the lag-1 time, and T is the data set of selected k of various time scale.

The study performs at aggregation levels of 1 hour and 1 day. As discussed previously, the BLRP parameters were distributed in the different probabilities. The range of values for those parameters are shown in Table 2.

Table 2
Boundary constraints of parameters used at the four sites

Parameter	Lower Limit	Upper Limit
λ (mm/day)	0	0.1
$\kappa = \beta/\eta$	0	20
$\phi = \gamma/\eta$	0	1
α	1	20
v (day)	0	20
μ_x (mm/day)	0	99
σ_x (mm/day)	0	99

Hyetos. The current BLRP model is not able to derive a synthetic disaggregation of hourly rainfall series independently. Therefore, Hyetos developed by Koutsoyiannis and Onof (2001), which utilized the BLRP model for rainfall disaggregation was applied in this study. This model itself was not able to estimate the BLRP parameters. Therefore, global optimization approaches were used to fit the model and it will be discussed in the following section.

Based on the Hyetos model, the first step is to distribute the total daily observed rainfall to hourly rainfall based on the wet days using the BLRP parameters. Each distribution or group of wet days are finalised until its arrangement matches the arrangement of observed daily rainfall with a tolerance distance (d_t) and d_t is defined as;

$$d_t = \left[\sum_{i=1}^L \ln \left(\frac{Z_i + 0.1}{\bar{Z}_i + 0.1} \right)^2 \right]^{0.5} \tag{9}$$

where, Z_i and \bar{Z}_i are the observed and simulated total daily rainfall and L is the length of arrangement wet days.

The next step is to adjust the disaggregated hourly rainfall (X_s) produced from the first step. This adjustment is to ensure that the new disaggregated rainfall (\hat{X}_s) is consistent with the given total daily rainfall (N). The adjustment is written as:

$$X_s = \hat{X}_s \left(\frac{N}{\sum_{s=1}^{24} \hat{X}_s} \right), \quad s=1,2, \dots,24. \tag{10}$$

Optimization of BLRP using ABC and PSO

Estimation of the BLRP parameters (Equations 3-6) is a cumbersome task. Artificial bee colony (ABC) and particle swarm optimization (PSO) are introduced to tackle this task. The description and details of each optimization will be discussed in detail in the following section. To utilize both optimization methods, the possible solution of BLRP parameters are needed to organize for both, ABC and PSO. Size of possible solution need to be similar for both optimizations and this expression can be written as:

$$Solution = \begin{bmatrix} Particle_1 \\ Particles_2 \\ Particles_3 \\ \vdots \\ Particles_{NS \text{ or } N} \end{bmatrix} \tag{11}$$

where, $Particle = [\lambda, \kappa, \phi, \alpha, v, \mu_x]$ is the set of BLRP parameters, $Solution$ is the possible solution and NS or N is the size of $Solution$. For these optimizations, $\mu_x = \sigma_x$

Description of ABC. Artificial bee colony (ABC) algorithm was introduced by Karaboga (2005) and it is applied in many optimization applications (Karaboga et al., 2012). This algorithm was inspired by the honeybee foraging behavior and three types of honeybee are introduced: employed, onlookers and scouts. Inside the ABC algorithm, the food source

collected by honeybee is an analogy to the possible solution to the optimization problem. The fitness of the objective solution is represented by the position of the food source. The number of the employed and onlooker bees is set as equal to the number of solutions in the population.

For the beginning of ABC, population of NP solutions is random initial, where NP is the size of population. The number of food source (NS) is introduced, where $NS = NP/2$. Each solution, x_i ($i=1,2,3, \dots, NS$) is a n -dimensional vector. Then, all honeybees are performing a cyclic search, based on the given rules.

The update solution (v_i^j) is modified by an employed bee that produces a modification on the position of solution based on the local information and tests the fitness value of the new solution. The v_i^j generated from the old solution (x_i^j) can be expressed as:

$$v_i^j = x_i^j + \phi_{ij}(x_i^j - x_k^j) \quad (12)$$

where $k \in \{1, 2, \dots, NS\}$ and $j \in \{1, 2, \dots, n\}$ are random indexes, k is different from i , ϕ_{ij} is a uniformly distributed random number in the range of -1 to 1.

Provided that the update solution of the new solution is better than the previous solution, the old solution is replaced with the new solution. Otherwise, the old solution is applied. The employed bees return to their centre (hive) and share this information with the onlooker bees. In the next step, the onlooker bee selects one of the new solution sources based on the fitness value. The probability of a solution source (p_i) that will be selected by the onlooker bees can be expressed as:

$$p_i = \frac{fit_i}{\sum_{j=1}^{NS} fit_i} \quad (13)$$

where, fit_i is the fitness value of solution source i , which is proportional to the objective function value of the solution (in the BLRP model, please refer to Eq. 2).

After the solution source is selected, each onlooker bee searches a new solution source in the neighborhood of that source by using Eq. 11. The new solution source is identified by the greedy selection to evaluate its fitness. If a position cannot be improved due to limit cycles, that solution source is abandoned. The employed bee becomes a scout bee and the solution sources are replaced with an updated solution found by the scout bee. If the scout bees discover the abandoned solution (x_i^j) and replace it with x_i , it can be expressed as:

$$x_i^j = x_{min}^j + rand(0,1)(x_{max}^j - x_{min}^j) \quad (14)$$

where, x_{max}^j and x_{min}^j are upper and lower bonds (Table 2) of x_i^j , and $rand(0,1)$ is a uniform distribution number in between 0 to 1.

The whole process will be repeated until the maximum iterations or it achieves the objective function.

Description of PSO. Particle swarm optimization (PSO) consists of a variable set named as swarm of the random variables and named as particles. Each particle represents the possible solution to the optimization problem. This algorithm uses the movement and velocity of particles for the search space of global optimum state. In each iteration, PSO collects the local optimum and evaluate it with the global optimum value. Generally, the PSO algorithm can be described into three main stages, which are; 1) position and velocity of swarms are initiated; 2) position of swarms is evaluated; and 3) position and velocity of swarms are updated (Shamsudin et al., 2013; Salami et al., 2018).

In the initial stage, the swarm initial of position (x_0^i) and velocity (v_0^i) stages are created randomly within the search space in a certain particle i , with $i=1, 2, \dots, N$. This stage is written as:

$$x_0^i = x_{min} + rand(x_{max} - x_{min}) \tag{15}$$

$$v_0^i = \frac{x_{min} + rand(x_{max} - x_{min})}{\Delta t} \tag{16}$$

where, x_{min} and x_{max} are the lowest and highest values of x respectively (Table 2) and Δt is the time duration of swarm position.

For the second stage, the position x_i of a particle is improved (x_{k+1}^i) by increasing its speed vector (v_i) to the previous position. It can be defined as:

$$x_{k+1}^i = x_k^i + v_{k+1}^i \Delta t \tag{17}$$

where, $v_{k+1}^i \Delta t$ is the added velocity vector, and k and $k + 1$ represents the previous and subsequent iteration step respectively.

For the final stage (velocity update), the updated swarm velocity (v_{k+1}^i) is revised with the best position (p_i) and the global best (p_g) becomes a reference. This revision can be expressed as:

$$v_{k+1}^i = wv_k^i + c_1 rand\left(\frac{p_i - x_k^i}{\Delta t}\right) + c_2 rand\left(\frac{p_g - x_k^i}{\Delta t}\right) \tag{18}$$

$$w = (w_1 - w_2) \frac{iter_{max} - iter}{iter_{max}} + w_2 \tag{19}$$

where, c_1 and c_2 are the positive acceleration constants, w is the inertia weight and $rand$ is the random component. In this study, the maximum number of iterations ($iter_{max}$) was 1000 and the initial (w_1) and final (w_2) weights were 0.9 and 0.4, respectively.

RESULTS AND DISCUSSION

Parameter Estimation of BLRP using ABC and PSO

Figure 2 shows the list of optimum estimation of BLRP parameters using the ABC and PSO

algorithms for the selected rainfall stations in Peninsular Malaysia. The mean, variance, autocorrelation for lag-1hour (*AC Lag-1h*) and the probability of rainfall days (proportion dry) of the observed hourly and daily rainfalls were calculated as an input parameter for BLRP and optimized using ABC and PSO. The values were derived on a monthly basis. The studied rainfall properties are similar to the properties of rainfall studied by Cowpertwait et al. (2007) and Yusop et al. (2014), but the difference is in the aspect of aggregation levels (in this study the limit is between 1 and 24 hours). This limit is chosen as a way to reduce the extensive calculation. From the figure, all parameters do not show an identical value of estimated parameters between each station and the type of optimization method. The estimated parameters were randomly estimated within the range of the studied boundary constraints (Table 2). For ABC optimization, the study found that the estimated parameters were near to the value of the studied boundary constraints. It is also obviously seen that λ estimate by ABC is 0.1mm/day for almost all of the months for each station. In terms of PSO's estimation, the figure shows that the estimated parameters are well randomly estimated within the range of studied boundary constraints.

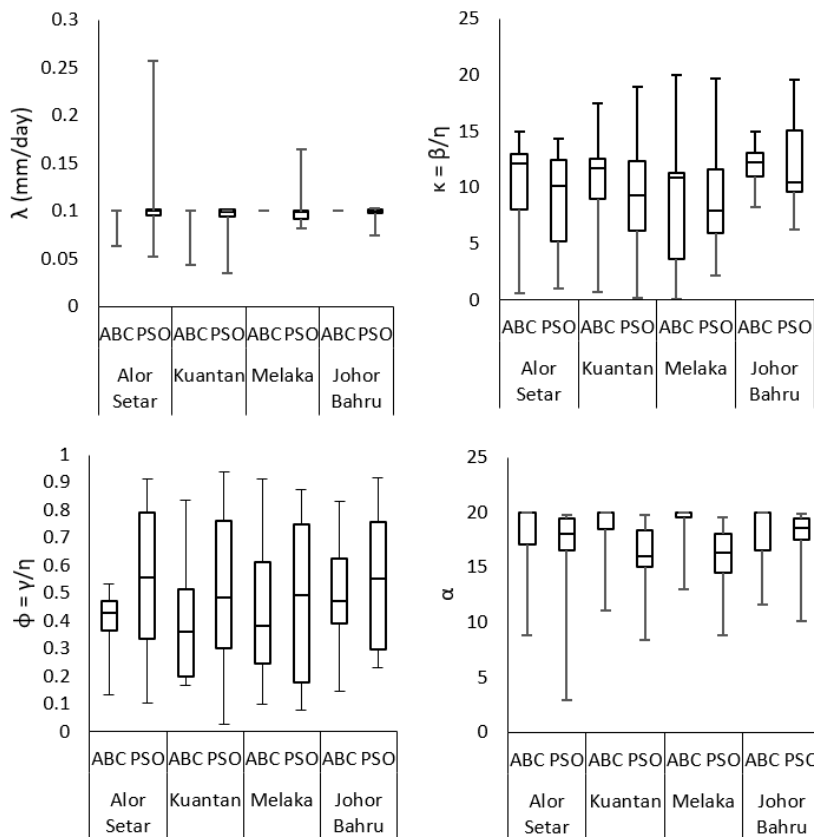


Figure 2. Global estimated BLRP parameters using ABC and PSO for each parameter

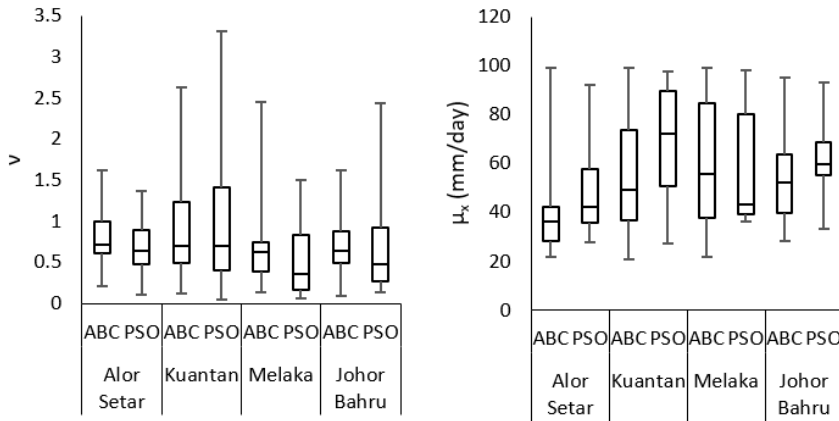


Figure 2. (Continued)

The minimum of the objective function ($f(x)$) for each month can also be referred to as detailed in Figure 3. The closer $f(x)$ value to 0, the fitter the BLRP model. Based on Figure 3, it is clearly seen that the ABC and PSO algorithms give almost similar values. The range of $f(x)$ is between 0.4260 and 13.8882, with the highest recorded $f(x)$ can be obtained from Melaka, with the values of 13.8882 and 13.5263 for ABC and PSO, respectively.

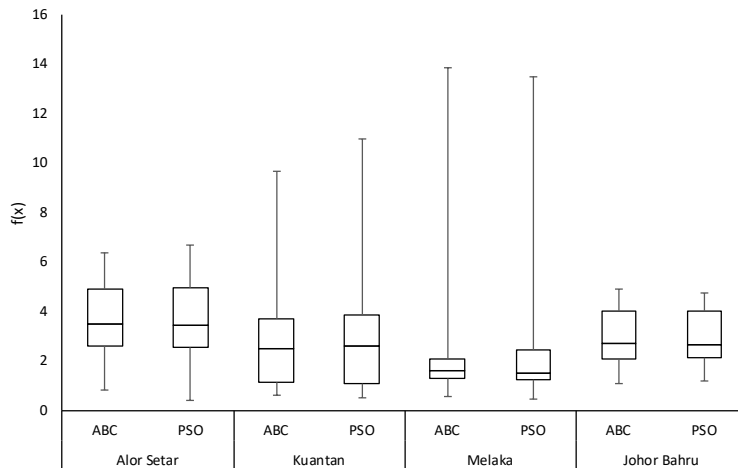


Figure 3. Comparison between the optimum of minimum objective function ($f(x)$) of the ABC and PSO

Generation of Disaggregated Hourly Rainfall Series using Hyetos

Performance of ABC and PSO to Disaggregate Temporal Rainfall Distribution.

Figures 4-7 illustrate the comparison of the performance of Hyetos to simulate hourly rainfall using the optimum parameters generated by the ABC and PSO approaches for the studied stations. Four statistical hourly rainfalls are used, named as mean, standard deviation (SD), autocorrelation lag-1h and proportion of dry days. In general, the Hyetos

model using the parameters from ABC and PSO was able to capture the observed rainfall. In term of SD, both algorithms were slightly able to show a good agreement between the observed and disaggregated rainfall. However, the study found that some stations were unable to perform well in capturing the autocorrelation lag-1h and proportion of dry days. The stations in Kuantan and Melaka were able to capture all rainfall statistical properties very well. However, the studied approaches slightly overestimated the autocorrelation lag-1h and proportion dry for the most months in the Alor Setar and Johor Bahru stations. Nonetheless, the results can still be accepted because the range of differences is not large. Studies by Hanaish et al. (2011), Hanaish et al. (2013), Abdellatif et al. (2013), and Yusop et al. (2014) also provided similar results. Like this study, findings of those studies were also not able to fit the autocorrelation lag-1hour and proportion of dry days perfectly.

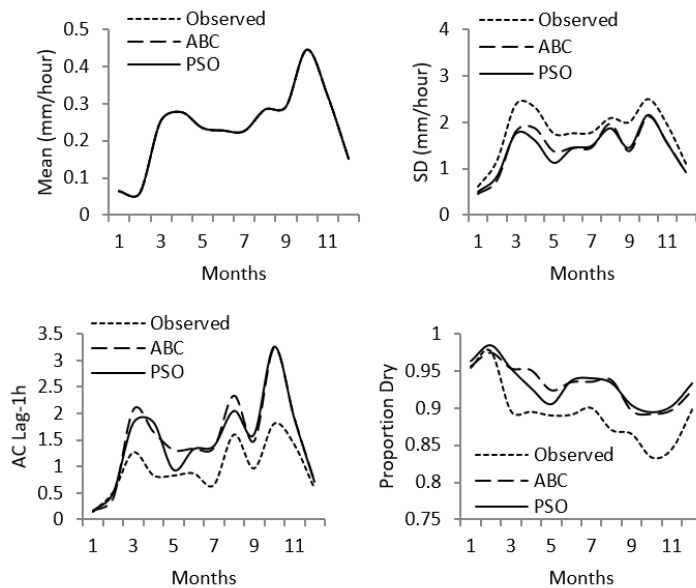


Figure 4. Properties of hourly rainfall for Alor Setar

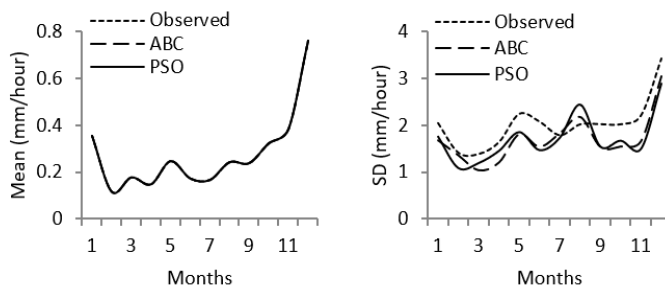


Figure 5. Properties of hourly rainfall for Kuantan

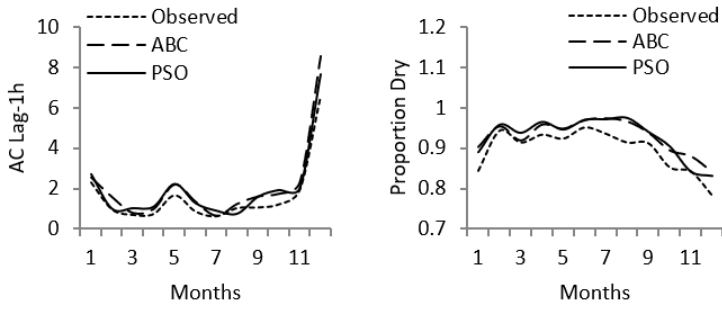


Figure 5. (Continued)

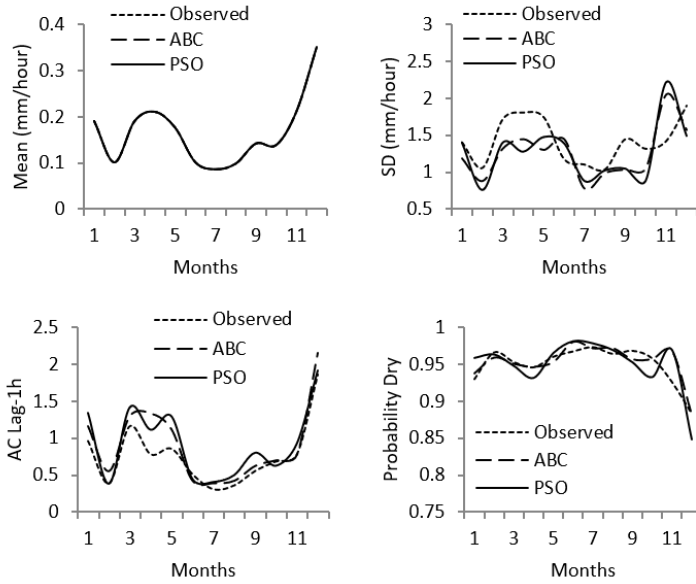


Figure 6. Properties of hourly rainfall for Melaka

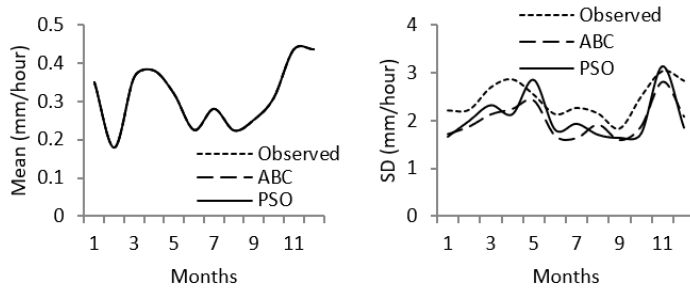


Figure 7. Properties of hourly rainfall for Johor Bahru

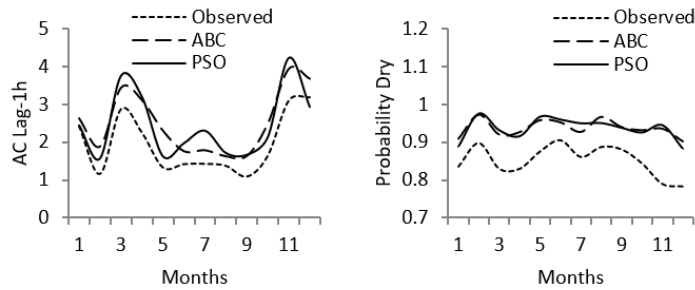


Figure 7. (Continued)

Performance of ABC and PSO to Disaggregate Extreme Rainfall. Figure 8 illustrates the evaluation of the capability of BLRP to replicate the observed extreme values of rainfall. An hourly annual maximum (*AM*) as the extreme rainfall indices is applied and fitted with the Gumbel’s distribution. The relationship between *AM* intensity and return period (*T*) can be defined as:

$$x_T = \bar{x} + K_T s \tag{20}$$

where, x_T is *AM* intensity at *T*, \bar{x} is the average of *AM* data series, K_T is the frequency factor, and s is the standard deviation of *AM* data series. Since this study applied Gumbel’s distribution, K_T values are calculated for different return periods using this distribution. Therefore, K_T can be written as:

$$K_T = -\frac{\sqrt{6}}{\pi} \left\{ 0.5772 + \ln \left[\ln \left(\frac{T}{T-1} \right) \right] \right\} \tag{21}$$

In general, it is suggested that the BLRP model optimized using ABC and PSO is not able to capture well the observed extremes at the hourly scale. However, in Melaka and Johor Bahru, the approaches were able to capture slightly the observed extremes value. For the Alor Setar station (Figure 8a), it showed that both optimization methods were unable to provide fitted parameters to be used by the BLRP model in order to give a satisfactory result in capturing the extreme rainfall. This situation may happen due to the tropical regions of the rainfalls in Malaysia, which is mainly convective and the rains are produced by a sudden burst with high intensities of rainfall and the duration of rainfall is short. In terms of optimization algorithms, the PSO seems to perform slightly well by replicating near to the observed extremes value as compared to the ABC algorithm. Although both models are able to give a similar optimum possible solution, the converged towards it is different. The ABC algorithm is poor in the aspect of exploitation ability to reach the optimum solution as compared to PSO. The study also found that the search for the optimal parameters of the optimization methods requires most efforts for ABC, in which needs a large exploration of the search space (maximum of number of iterations) to find optimum solutions. Those converged results are similar with other research, which applied the ABC

and/or PSO within their own case study such as Zhu and Kwang (2010), Jia et al. (2011), and Hossain and El-shafie (2013).

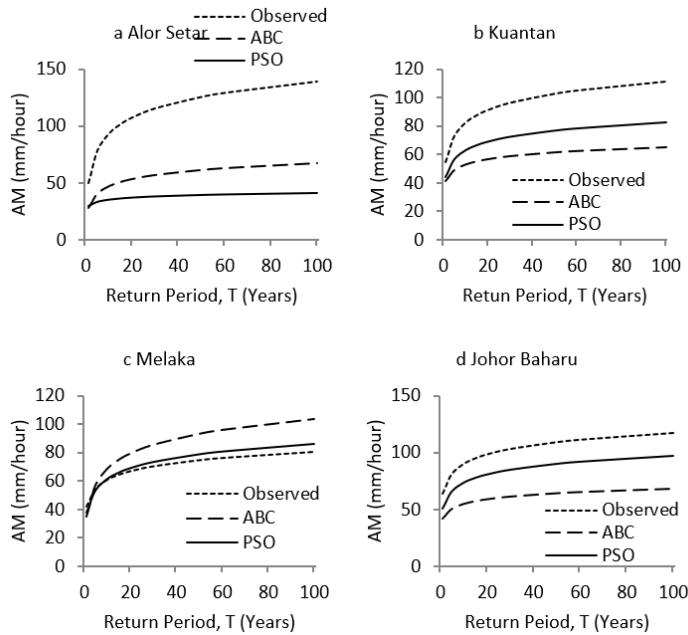


Figure 8. Return level plots of the annual maximum (AM) intensity of hourly rainfall series in a) Alor Setar, b) Kuantan, c) Melaka, and d) Johor Bahru

CONCLUSION

This study proposed a further improvement on the calibration process of the Bartlett-Lewis rectangular pulse (BLRP) with applications of the artificial bee colony (ABC) and particle swarm optimization (PSO). Historical rainfall data from four selected stations in Peninsular Malaysia were used for this study.

In the calibration of the BLRP model, estimation of the BLRP parameters was addressed. Those parameters were obtained by using a combination of different moments generated from four statistical properties of hourly and daily rainfalls. The optimized parameters obtained from the ABC and PSO algorithms were discovered that the different combinations of parameters were directed to identical results. Both models are also able to match the rainfall properties. Although ABC is claimed to much reliable in finding optimal solutions (Karaboga & Akay, 2009; Akay & Karaboga, 2012), the result is different with the application of the BLRP model with the PSO, in which it is able to find the optimal solution much better as compared to the ABC algorithm.

Hyetos was used to regenerate the statistical and extreme properties by utilizing the optimized BLRP parameters. In general, the statistical properties obtained from Hyetos with the parameters optimized by ABC and PSO are able to give a satisfactory agreement

between the simulated and observed hourly data. The model does not have the ability to match the extreme rainfall. However, some stations namely Melaka and Johor Bahru are able to slightly match the extreme rainfall. In terms of optimization algorithm in matching extreme rainfall, the study found that the BLRP parameters optimized by PSO can nearly replicate the extreme rainfall as compared to the ABC algorithm.

Further study is required to improve the quality of the BLRP model especially for rainfall events model, which involves extreme rainfalls. Effect of the alternative function towards the performance of the model in reproducing the rainfall series and its extremes can be applied in the future study.

ACKNOWLEDGEMENTS

This work had been financially supported by the Ministry of Education Malaysia, under Fundamental Research Grant Scheme (FRGS) with the grant number of FRGS/1/2019/TK01/UNIMAP/02/4. I would like to thank the editor and the anonymous reviewers whose remarks helped to improve the quality of this paper. The author would also like to thank the Department of Irrigation and Drainage Malaysia for providing the data and technical support.

REFERENCES

- Abdellatif, M., Atherton, W., & Alkaddar, R. (2013). Application of the stochastic model for temporal rainfall disaggregation for hydrological studies in north western England. *Journal of Hydroinformatics*, 15(2), 555-567.
- Akay, B., & Karaboga, D. (2012). A modified artificial bee colony algorithm for real-parameter optimization. *Information Sciences*, 192, 120-142.
- Cowpertwait, P. S. P., O'Connell, P. E., Metcalfe, A. V., & Mawdsley, J. A. (1996). Stochastic point process modelling of rainfall. I. Single-site fitting and validation. *Journal of Hydrology*, 175(1-4), 17-46.
- Cowpertwait, P. S. P., Isham, V., & Onof, C. (2007). Point process models of rainfall: developments for fine-scale structure. *Proceedings of the Royal Society A: Mathematical, Physical and Engineering Sciences*, 463(2086), 2569-2587.
- Debele, B., Srinivasan, R., & Parlange, J. Y. (2007). Accuracy evaluation of weather data generation and disaggregation methods at finer timescales. *Advances in Water Resources*, 30(5), 1286-1300.
- Eberhart, R. C., & Yuhui, S. (2001). Particle swarm optimization: developments, applications and resources. *Evolutionary Computation*, 1, 81-86.
- Hanaish, I. S., Ibrahim, K., & Jemain, A. A. (2011). Stochastic modeling of rainfall in Peninsular Malaysia using Bartlett Lewis rectangular pulses models. *Modelling and Simulation in Engineering*, 2011, 1-6.
- Hanaish, I. S., Ibrahim, K., & Jemain, A. A. (2013) On the potential of Bartlett Lewis rectangular pulse models for simulating rainfall in Peninsular Malaysia. *Hydrological Sciences Journal*, 58(8), 1690-1703.

- Hansen, L. P. (1982). Large properties of generalized method of moments estimators, *Econometrica*, 50, 1029-1054.
- Hossain, M. S., & El-Shafie, A. (2013). Performance analysis of artificial bee colony (ABC) algorithm in optimizing release policy of Aswan High Dam. *Neural, Computing and Applications*, 24(5), 1199-1206.
- Hutchinson, M. F. (1990). A point rainfall model based on a three-state continuous Markov occurrence process. *Journal of Hydrology*, 114(1-2), 125-148.
- Jia, D., Zheng, G., Qu, B., & Khan, M. K. (2011). A hybrid particle swarm optimization algorithm for high-dimensional problems. *Computers and Industrial Engineering*, 61(4), 1117-1122.
- Karaboga, D., & Akay, B. (2009). A survey: algorithms simulating bee swarm intelligence. *Artificial Intelligence Review*, 31(1), 55-68.
- Karaboga, D. (2005). *An idea based on honey bee swarm for numerical optimization* (Technical Report-TR06). Computer Engineering Department, Engineering Faculty, Erciyes University, Turkey.
- Karaboga, D., Gorkemli, B., & Ozturk, C. (2012). A comprehensive survey: artificial bee colony (ABC) algorithm and applications. *Artificial Intelligence Review*, 2012, 1-37.
- Kennedy, J., & Eberhart, R. (1995). Particle swarm optimization. *Neural Network*, 4, 1942-1948.
- Koutsoyiannis, D., & Onof, C. (2001). Rainfall disaggregation using adjusting procedures on a Poisson cluster model. *Journal of Hydrology*, 246(1-4), 109-122.
- Pui, A., Sharma, A., & Mehrotra, R. (2009, July 13-17). A comparison of alternatives for daily to sub-daily rainfall disaggregation. In *Eighteenth World IMACS / MODSIM Congress* (pp. 3535-3541). Cairns, Australia.
- Rodriguez-Iturbe, I., Cox, D. R., & Isham, V. (1988). A point process model for rainfall: further developments. *Proceedings of the Royal Society of London. A. Mathematical and Physical Sciences*, 417(1853), 283-298.
- Rodriguez-Iturbe, I., De Power, B. F., & Valdes, J. B. (1987). Rectangular pulses point process models for rainfall: analysis of empirical data. *Journal of Geophysical Research: Atmospheres*, 92(D8), 9645-9656.
- Salami, M., Sobhani, F. M., & Ghazizadeh, M. S. (2018). Short-term forecasting of electricity supply and demand by using the Wavelet-PSO-NNs-SO technique for searching in big data of Iran's Electricity Market. *Data*, 3(4), 43-68.
- Sansom, J. (1998). A hidden Markov model for rainfall using breakpoint data. *Journal of Climate*, 11, 42-53.
- Shamsudin, S., Dan'azumi, S., Aris, A., & Yusop, Z. (2013). Optimum combination of pond volume and outlet capacity of a stormwater detention pond using particle swarm optimization. *Urban Water Journal*, 11(2), 127-136.
- Smithers, J. C., Pegram, G. G. S., & Schulze, R. E. (2002). Design rainfall in South Africa using Bartlett-Lewis rectangular pulse rainfall models. *Journal of Hydrology*, 258(1-4), 83-99.
- Vanhaute, W. J., Vandenberghe, S., Scheerlinck, K., De Baets, B., & Verhoest N. E. C. (2012a). Calibration of the modified Bartlett-Lewis model using global optimization techniques and alternative objective functions. *Hydrology and Earth System Sciences*, 16(3), 873-891.

- Vanhaute, W. J., Vandenberghe, S., Scheerlinck, K., De Baets, B., & Verhoest, N. E. C. (2012b, April 22-27). Improving the extreme value behaviour of Bartlett-Lewis rectangular pulse models. In *EGU General Assembly Conference Abstracts* (p. 2692). Vienna, Austria
- Velghe, P. A., Troch, P. A., De Troch, F. P., & Van de Velde, J. (1994). Evaluation of cluster-based rectangular pulses point process models for rainfall. *Water Resources Research*, *30*(10), 2847-2857.
- Verhoest, N. E. C., Troch, P. A., & De Troch, F. P. (1997). On the applicability of Bartlett-Lewis rectangular pulses models in the modeling of design storms at a point. *Journal of Hydrology*, *202*(1-4), 108-120.
- Yusop, Z., Nasir, H., & Yusof, F. (2014). Disaggregation of daily rainfall data using Bartlett Lewis Rectangular Pulse model: a case study in central Peninsular Malaysia. *Environmental Earth Sciences*, *71*(8), 3627-3640.
- Zhu, G., & Kwong, S. (2010). Gbest-guided artificial bee colony algorithm for numerical function optimization. *Applied Mathematics and Computation*, *217*, 3166-3173.

Study on Progressive Wear of Machine Reamer while Reaming Al6061/SiC Composite

Sandeep Nambiar, Raviraja Adhikari*, Nagaraja Upadhy and Rajarama Hande

Department of Mechanical and Manufacturing Engineering, Manipal Institute of Technology, Manipal Academy of Higher Education, Manipal, India

ABSTRACT

The present study deals with reaming of Al6061/SiC metal matrix composite. For the fabrication of the composite, stir casting technique was used. In the castings, 5 and 10 weight percentages of Silicon Carbide (SiC) 23 μ m size was used as the reinforcing material. The tensile and hardness tests carried out on the specimen indicated that it increased with the addition of SiC. The images from scanning electron microscope showed the fair distribution of reinforcement. After drilling 7.8 mm diameter holes, reaming was performed with 8mm diameter straight fluted HSS reamer under dry condition at cutting speeds of 18 and 24 m/min and feed rates of 0.2 and 0.4 mm/rev. Torque required for reaming was measured using 4 component Drill tool Kistler dynamometer 9272A. The estimation of progressive wear of the reamer was undertaken using a profile projector. With the introduction of SiC as reinforcement, the wear rate of the reamer increased as the reinforcement was highly abrasive in nature. The performance of HSS machine reamer was evaluated in terms of reaming torque, tool wear and surface roughness of the hole.

Keywords: Al6061/SiC, flank wear, machine reamer, metal matrix composite (MMC), stir casting

ARTICLE INFO

Article history:

Received: 09 October 2018

Accepted: 23 April 2018

Published: 13 January 2020

E-mail addresses:

sandy4593@gmail.com (Sandeep Nambiar)

ravi.adhikari@manipal.edu (Raviraja Adhikari)

nag.mech@manipal.edu (Nagaraja Upadhy)

rajaram.hande@manipal.edu (Rajarama Hande)

* Corresponding author

INTRODUCTION

The aluminium based matrix composites have emerged as materials for several applications in aerospace, automobile, defense and other sectors due to their high specific strength and stiffness, superior wear resistance as compared to the alloy (Kumar et al., 2011). Stir casting is one of the most widely used technique for processing of aluminium based metal matrix composite. Stir casting involves melting of the matrix

material, followed by introducing reinforcement material into the melt, obtaining a suitable dispersion through stirring (Soltani et al., 2015). The composites are known as difficult to machine materials because of hardness and abrasive nature of reinforcement material (Srinivasan et al., 2012). The presence of harder and well bonded SiC particles in aluminium matrix that impedes the movement of dislocations increases the hardness. (Rahmana & Al Rashed, 2014). Abrasion is the major mechanism causing tool wear when machining metal matrix composite (MMC) reinforced with abrasive particles such as SiC (Chambers & Stephens, 1991). Higher weight percentage of SiC reinforcement needs higher cutting forces during machining and produced a higher surface roughness (Behera et al., 2011). The review of literature has revealed that majority of research work on machining of Al-SiC metal matrix composite has been carried out on turning and drilling. Reaming is one such important machining operation used to enhance the quality of drilled holes. The dimensional stability (diameter, roundness and cylindricity) and surface roughness of reamed holes in aluminum silicon SAE322 alloy using K10 cemented carbide welded blade reamers and found that accuracy of hole diameter can be increased by increasing the feed rate (Bezerra et al., 2001). Melo et al. (2019) concluded that feed rate was the most influential factor affecting the torque and cutting speed was the main factor influencing the quality of the reamed hole after conducting reaming study on AISI P20 hardened steel. While reaming C355 aluminium alloy by Rattanakit et al. (2015), smearing of Al material and BUE was prevalent on the flank faces of the uncoated WC reamers at low (32 m/min) and high (96 m/min) cutting speeds. However, this was not apparent with the brazed PCD or the CVD diamond 229 coated WC reamers, regardless of machining conditions (Rattanakit et al., 2015). While conducting reaming study on Al-Si-Mg alloy (6351) with different copper contents using HSS reamer, it was found that torque and thrust force were influenced more by feed when compared with thrust (Gonçalves et al., 2018). During reaming on ZL102 aluminium cast alloys by PCD reamer, the thrust was found to decrease significantly as a result of the growing cutting speed by fixing the cutting feed, whereas there was an increase in thrust with increasing feed in the same cutting speed (Wang et al., 2013). The experimental results on reaming AlSi12 alloys with PCD reamer are verified as a stable process in terms of the quality of the holes produced and the main surface anomalies are re-deposited work material (chip) onto already machined surface, surface grooves and notch, feed marks, surface shrinkage cavities and porosities, metal debris, and micro-pits (Yan et al., 2013). The study of influence of process errors and multi blade reamer geometry on the hole quality while reaming valve guides made of sintered steel alloys revealed that enlarged contact zone between the secondary cutting edge and the work piece material would lead to improved straightness tolerances (Schutzer et al., 2014). It is essential to create more knowledge about reaming on Al6061/SiC metal matrix composite. The aim of this study is to obtain the influence of varying percentage of SiC present in the matrix, cutting speed and feed on wear of reamer.

MATERIALS AND METHODS

Fabrication of MMC Specimens

The matrix material chosen for the present study was Al6061 alloy and was acquired from HINDALCO Industries Limited, India. The chemical composition of Al6061 compound, as given by the provider is given in Table 1. Silicon carbide particles of average size 23 microns was used as reinforcement material. Silicon carbide has properties such as high hardness and strength, chemical and thermal stability, high melting point, oxidation resistance and high erosion resistance. The schematic diagram of the setup used for fabrication of metal matrix composite is shown in Figure 1. Al6061 rods melted at a temperature of 800°C in an electric furnace. Preheating of silicon carbide particles was done at 400°C for an hour to remove the moisture and gases from the surface of the particulates. To increase the wettability of the silicon carbide particles in the matrix material, 1% by weight magnesium ribbon was added to the molten metal at 750 °C (Hashim et al., 2001). Stirring of molten metal was done for 10 minutes during which SiC particles were added. The molten metal was degassed at a temperature of 750°C using nitrogen gas. Degassing dispenses a variety of impurities which otherwise could act as deterrent in the creation of good castings. The solubility of hydrogen in liquid aluminum increases with temperature. Material must reject the hydrogen during solidification or else the quality of the composite is affected due to porosity.

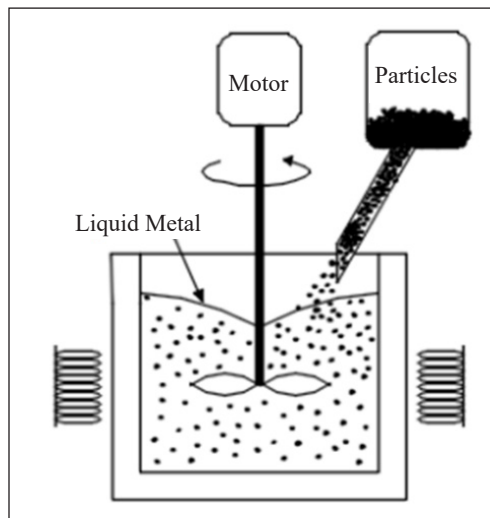


Figure 1. Schematic diagram of stir casting setup

Table 1
Chemical Composition of Al6061

Contents	Al	Si	Fe	Mn	Mg	Cu	Ti	Cr
Weight %	97.54	0.77	0.22	0.06	0.92	0.27	0.02	0.07

Characterization of Material

Vickers Hardness and Tensile Test. Standard specimen for hardness measurement were prepared after polishing with different grades of abrasive paper. Hardness test was carried out using Macro Vickers Hardness Tester (M/s Fuel Instruments, India). Three samples and five readings on each sample were taken for averaging the hardness value. The tensile test specimens were prepared by machining casting obtained in pin molds in CNC turning center, according to ASTM E8/E8M-11 standard, as shown in Figures 2 and 3. The tensile test samples were prepared. The tensile test was performed on an electronic tensometer (M/s Khudal Instruments, India). Three samples were taken for each weight percentage of SiC for averaging the tensile test value.



Figure 2. Casting used for Tensile test specimen

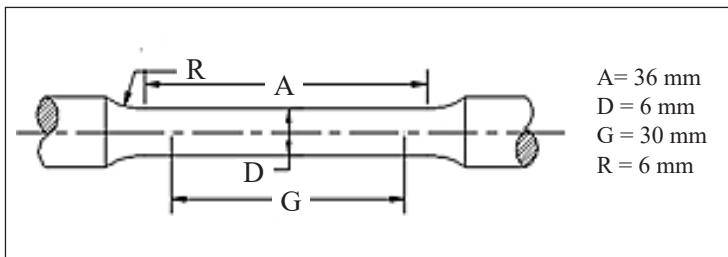


Figure 3. Tensile test specimen

Micro Structure. The microstructure affects the performance of the composite. The microstructure, reinforcement particle size, shape and distribution in the alloy influence the physical properties of the composite. Microstructure study of the composite was done using Zeiss EVO 18 Special Edition Scanning Electron Microscope.

Experimentation

The cast Al6061/SiC specimens were machined to billets of size $120 \times 45 \times 10$ mm. The holes for reaming were prepared using carbide drills of diameter 7.8 mm. These holes were reamed in the specimen by high speed steel (HSS) straight four fluted machine reamer shown in Figure 4. The specification of the reamer used for experimentation is given in Table 2. For measuring torque produced during the reaming operation, 4 component drill tool dynamometer 9272A (Kistler make) was used. Reaming experiments were conducted on Computer Numerical control (CNC) vertical machining centre (M/s Ace Manufacturing Systems, Bangalore, India) at feed rates of 0.2 and 0.4 mm/rev. with speeds 18 and 24



Figure 4. HSS straight, four fluted 8mm diameter machine reamer

m/min. The material behavior of Al6061/SiC composite was expected to be in between aluminium alloy and cast iron (CMTI, 1987). The cutting speed for the reaming operation was selected between the reaming speed for cast iron (14-18 m/min) and aluminium (24-28 m/min). The feed for the reaming operation was selected between the reaming feed rate for cast iron (0.1-0.2 mm/rev.) and aluminium (0.4-0.6 mm/rev.). The actual values of cutting parameters used for reaming is shown in Table 2. One hundred and four holes were reamed on specimens each with 5 and 10 weight percentage of SiC, 18 and 24 m/min cutting speed and 0.2 and 0.4 mm/rev. feed rate. Figure 5 shows the arrangement used for conducting reaming experiment. The torque during reaming was measured at regular intervals. The Dynoware software installed on a computer connected to the Kistler 9272A dynamometer through A/D converter and 5070A10100 charge amplifier provided the variation of torque with respect to time, during reaming. The schematic of data flow in the experimental setup is shown Figure 6. A sample specimen with reamed holes is shown in the Figure 7.

Table 2
Cutting parameters used while reaming

Cutting Parameter	Value
Cutting Speed (m/min)	18, 24
Feed (mm/rev)	0.2, 0.4

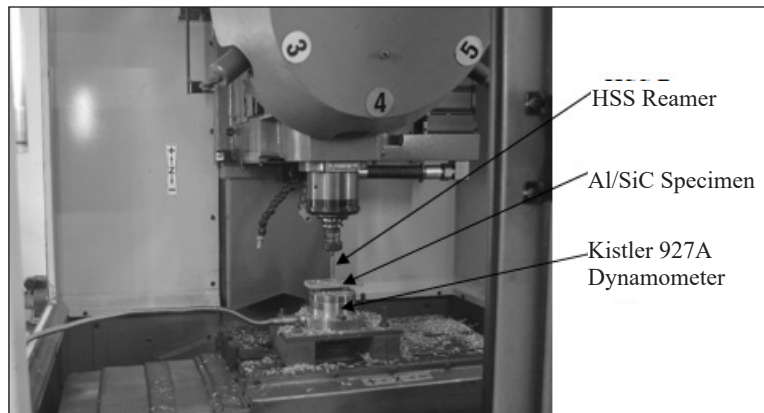


Figure 5. Arrangement used for conducting reaming experiments on composites

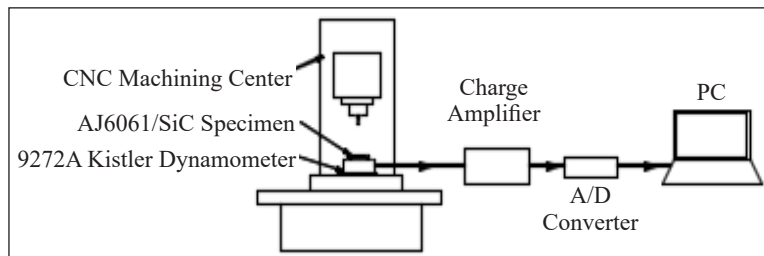


Figure 6. Schematic of data flow in the experimental setup

The specification of reamer used in the experiment is given in the Table 3.

Table 3
Reamer Specification

Material	M42 HSS
No. of flutes	4
Shank	Cylindrical
Helix angle	0°
Chamfer	2×45°
Rake Angle	8°
Primary Clearance Angle	6°
Secondary Clearance Angle	15°
Overall length	92 mm
Flute length	47 mm
Cutting diameter	8 mm

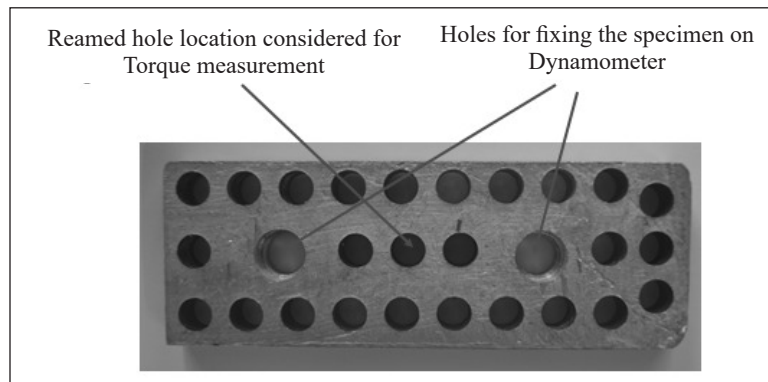


Figure 7. Al6061/SiC specimens with reamed holes

Measurement of Flank Wear

The wear pattern of the machine reamer was measured using a Profile Projector (METZER, India make) with micrometer accuracy of 0.01 mm and magnification of 20× on the display. The display of the reamer was located on the screen by adjusting the micrometer of the projector such that the axis of the tool coincided with the cross hair in the projector screen. The reading in the micrometer in this position indicated the location of the axis of the reamer. The outer contour along the axial direction of the reamer was traced on the projector screen to set the reference for subsequent measurements as shown in Figure 8. The outer contour of the tool in the display after reaming 26 holes was made to coincide with the reference previously set in the projector. The difference between previous and present micrometer readings was calculated as the reduction in height of the tooth (h) as shown in Figure 9. The procedure was repeated to get the progressive reduction in height of the tooth after reaming 52, 78 and 104 holes. The progressive reduction in height of the tooth

was marked as a point on rake face in each case. The horizontal lines were drawn from these points to intersect the flank surface. The progressive flank wear (h_f) was estimated by measuring the length of each line. The procedure adapted is shown in Figure 10.

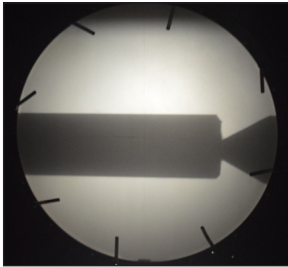


Figure 8. Display of reamer profile in the Profile Projector

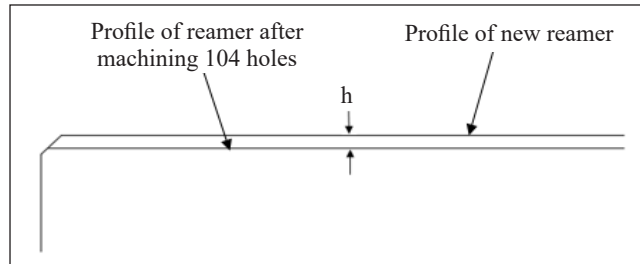


Figure 9. Profile of the reamer tooth

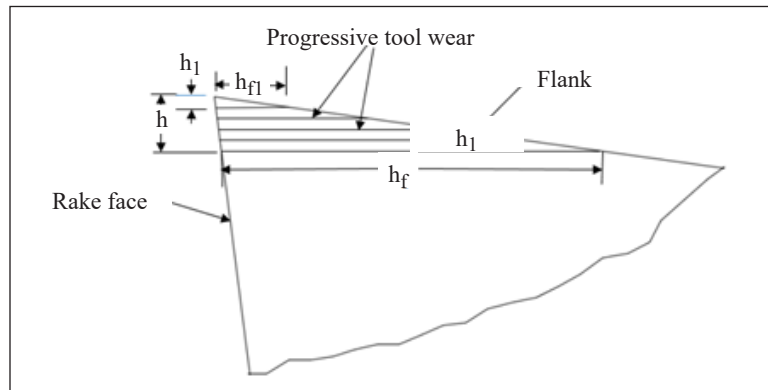


Figure 10. Flank Wear (h_f) derived from reduction in height of the tooth (h)

Measurement of Surface Roughness

Surface roughness of the reamed holes (hole no. 1,26,52,78 and 104) for all composites (5 weight. %, and 10 weight. % of SiC) was measured using Surtronic 3+ surface roughness measuring instrument. The sampling length for each measurement of surface roughness was 0.25mm. The surface roughness of each hole was estimated as the average of three readings.

RESULTS AND DISCUSSIONS

Characterization of Al/SiC Composite

Table 4 shows the hardness values of metal matrix composites at different percentages of SiC. The hardness value increased with increase in weight percentage of SiC. This trend is conforming with the same reported earlier (Su et al., 2010). The increase in hardness could be attributed to the influence of hard SiC particle acting as barriers to the movement of dislocations within the Al6061 matrix (Kannan & Kishawy, 2008).

Table 4
Vickers micro hardness test results

Material	Vickers Hardness Number (VHN)
Al + 5 weight. % SiC	81.4
Al + 10 weight. % SiC	98.5

From Table 5, it is observed that the ultimate tensile strength (UTS) measured using a tensometer increased with the addition of SiC. This increase in UTS may be due to the increased presence of SiC particles acting as barriers to dislocation in microstructure (Kannan & Kishawy, 2008)

Table 5
Tensile test results

Material	Average Ultimate Tensile Strength (MPa)
Al + 5 weight. % SiC	118.27
Al + 10 weight. % SiC	146.4

The literature (Wenner & Holmestad, 2016) available reports recipe for sample preparation for studying distribution of precipitates, inclusions under electron microscopy. An attempt was made to bring out the precipitate details in the samples under investigation. Using energy dispersive spectroscopy (EDS), the composition for the precipitate-like-structures were brought out, showing significant presence of silicon and carbon which could be possible signatures of silicon carbides or other complexes. As in Figure 11, the micro features are possibly SiC.

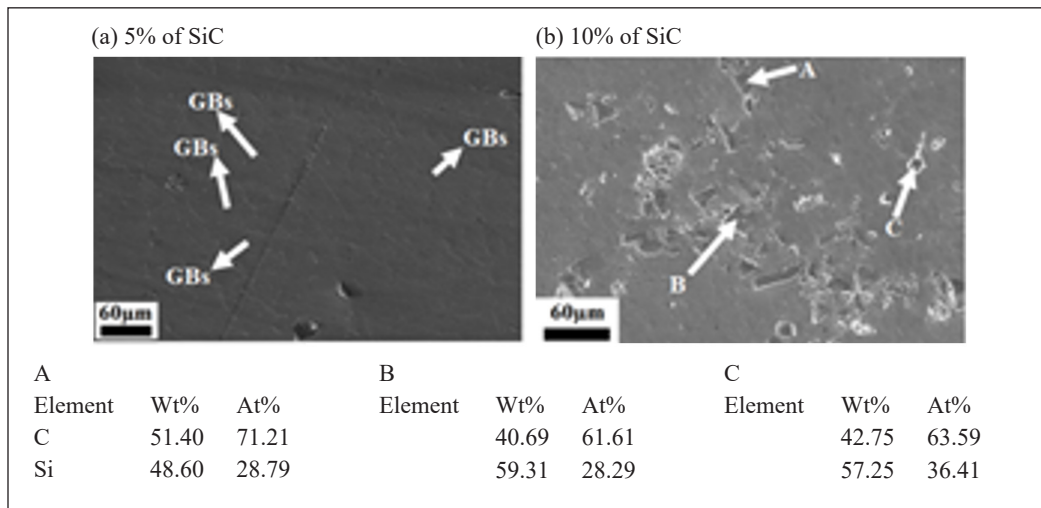


Figure 11. Composition of Al/SiC composite

The addition of silicon carbide introduced subtle differences in microstructures which are brought out in the Figure 12. These differences are largely seen in terms of grain size refinement, nature of grain boundary, formation of dendritic structures etc. With addition of 5% SiC, the grain size is relatively larger with serrated boundaries as apparent in the microstructures. With 10% addition of SiC, fine dendritic structures are seen to be nucleating at multiple sites within the microstructure. Presence of dendritic structures introduced strengthening due to fine grain distribution leading to ‘grain refinement strengthening’.

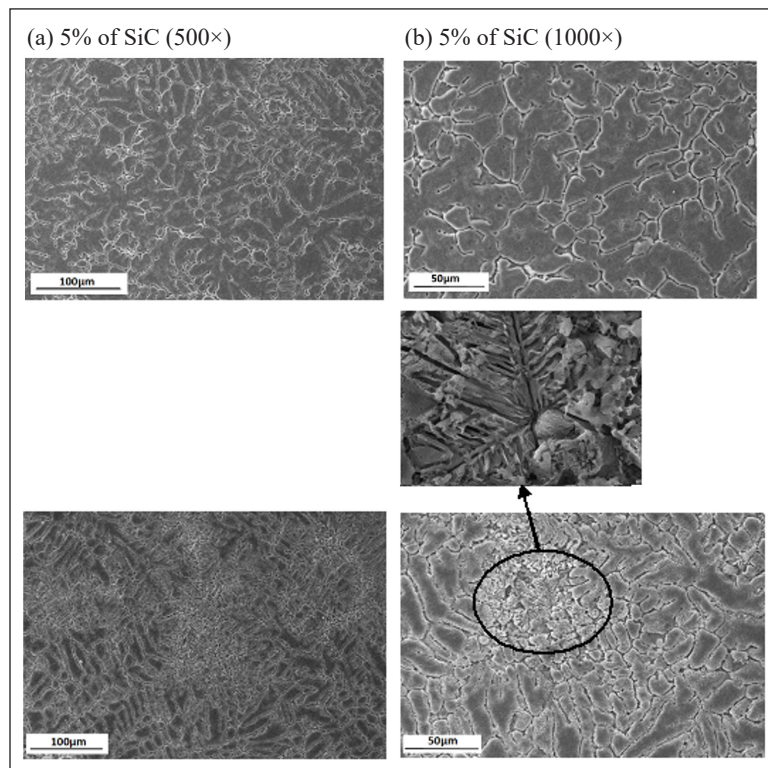


Figure 12. Microstructure of Al/SiC composite

Flank Wear

The torque required for reaming Al/SiC MMC was measured at regular intervals. This was done for indirect assessment of the progressive wear of reaming tool. The typical plot of torque captured in during reaming is shown in Figure 13. It was expected that the torque had to increase gradually from zero to its peak value as the chamfer section of the reaming tool progressively engaged with the hole for finishing. It got stabilized when the chamfer section fully engaged with the hole. The torque decreased gradually from the peak value to become zero when the chamfer section of the tool progressively emerged out and gets disengaged from the hole. The qualitative trend shown in the Figure 13 fully confirms with the expected pattern of variation of torque during reaming.

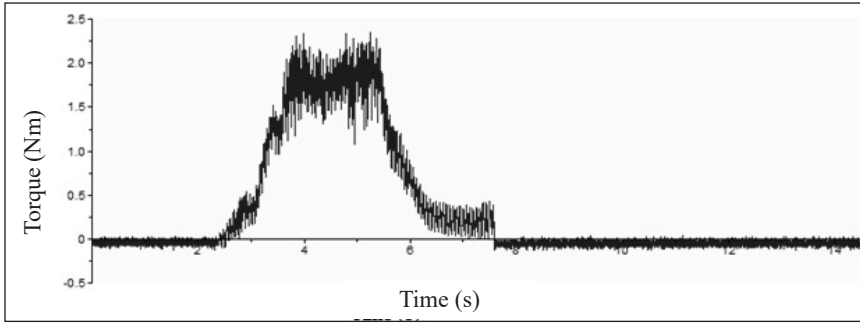


Figure 13. Sample plot for torque variation during reaming

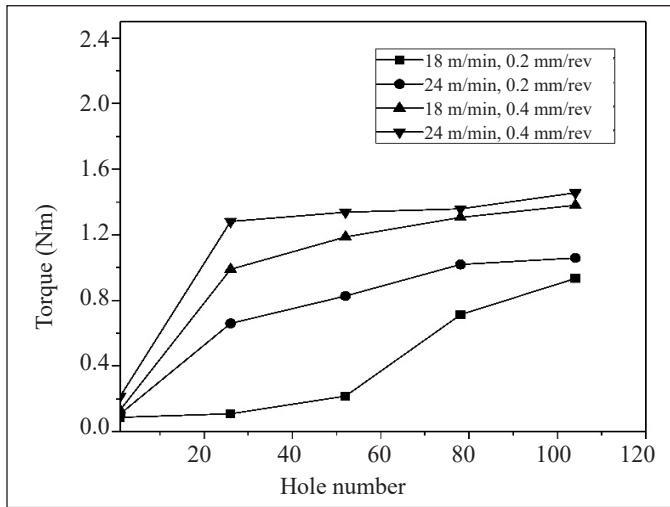


Figure 14. Torque while machining 1, 26, 52 and 78 and 104 holes for 5 weight % SiC at various speeds and feeds

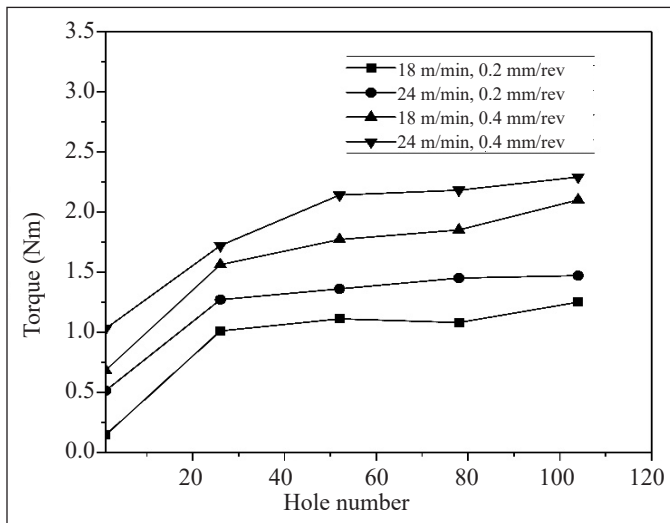


Figure 15. Torque while machining 1, 26, 52 and 78 and 104 holes for 10 weight % SiC at various speeds and feeds

It is observed from Figures 14 and 15 that increase in weight % of SiC, speed and feed rate increased the torque required for reaming. While reaming the first hole in the specimen with 5 weight % SiC at 18 m/min speed and 0.2 mm/rev. feed, the torque required is 0.087 Nm while it increased to 0.108 Nm at the speed of 24m/min and at same feed rate. While reaming the first hole in the same specimen at 24 m/min speed and 0.2 mm/rev. feed, the torque required was 0.108 Nm while it increased to 0.214 Nm at the feed of 0.4mm/rev. and at same speed.

While reaming 104th hole in the specimen with 5 weight % SiC at 18 m/min speed and 0.2 mm/rev. feed, the torque required was 0.934 Nm while it increased to 0.1059 Nm at the speed of 24 m/min at same feed rate. While reaming the 104th hole in the same specimen at 24 m/min speed and 0.2 mm/rev. feed, the torque required was 1.059 Nm while it increased to 1.456 Nm at the feed of 0.4 mm/rev. and at same speed.

During machining, increase in feed rate enhances the chip load while increase in speed reduces the chip load. Influence of feed rate on the torque required for machining is higher as both material removal rate (MRR) and chip load increase with feed rate. However, influence of speed on the torque required for machining is lower as with the speed, MRR increases but the chip load decreases. From the results, it is evident that for a given speed, increase in feed has greater influence on torque required for reaming when compared with the influence of increase of speed for a given feed. It is because while reaming, the increase of feed proportionately increases the chip load on the cutting edges as the chip load on cutting edge is a direct function of feed. Whereas, the increase of cutting speed does not increase the chip load on cutting edges in the same proportion. A similar trend was observed while reaming the holes in the composite with 10 weight % of SiC. The only difference was that the torque levels in 10 weight % of SiC composite were higher when compared with the same in 5 weight % of SiC at all combinations of speed and feed. Further, it was also noticed that for all combinations of speed and feed, there was progressive increase in torque with increase in number of holes reamed. This is possibly because of the damage due to progressive wear undergone by the reaming tool.

It is observed from Figure 16 that increase in weight % of SiC, speed and feed rate increased the progressive wear of the reamer. After reaming the 26th hole in the specimen with 5 weight % SiC at 18 m/min speed and 0.2 mm/rev. feed, the progressive wear was 0.0046 mm while it increased to 0.0067 mm at the speed of 24m/min and at same feed rate. After reaming the 26th hole in the same specimen at 24 m/min speed and 0.2 mm/rev. feed, the progressive wear was 0.0067 mm while it increased to 0.014 mm at the feed of 0.4mm/rev. at same speed. After reaming 104th hole in the specimen with 5 weight % SiC at 18 m/min speed and 0.2mm/rev. feed, the progressive wear was 0.046 mm while it increased to 0.051 mm at the speed of 24 m/min at same feed rate. After reaming the 104th hole in the same specimen at 24 m/min speed and 0.2 mm/rev. feed, the progressive wear

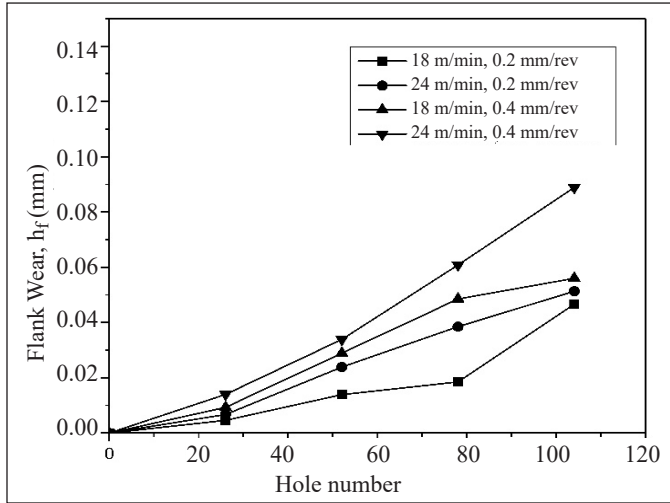


Figure 16. Flank wear after machining 26, 52 and 78 and 104 holes for 5 weight % SiC at various speeds and feeds

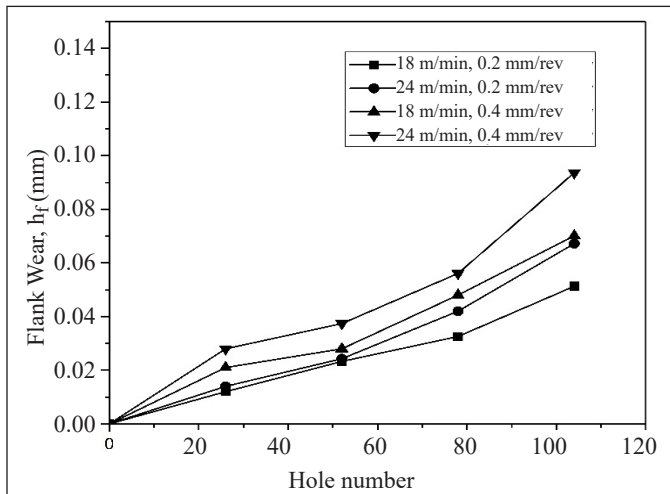


Figure 17. Flank wear after machining 26, 52 and 78 and 104 holes for 10 weight % SiC at various speeds and feeds

was 0.051 mm while it increased to 0.088 mm at the feed of 0.4 mm/rev. at same speed. Increase in chip load on the tool due to increase in feed rate enhanced the torque required for reaming resulting in higher force on the cutting edge and greater rubbing action of the flank of tool with the wall of drilled hole. The increased requirement of torque at higher feed rate enhances the rate of run in wear of the tool.

From the Figure 17, it was found that while reaming the holes in 10 weight % of SiC specimen, the patterns of variation of progressive wear for different combinations of speed and feed were similar to those observed in case of 5 weight % of SiC. For a given speed, the rate of initial run in wear was greater at the feed rate of 0.4 mm/rev. when compared

with the same at 0.2 mm/rev. Increase in speed at a given feed rate also increased the rate of run in wear but to a much lesser extent. This trend is because of dominating influence of feed rate on reaming process when compared with that of cutting speed as discussed already. In addition to this, magnitude of progressive wear on the flank of tool for 10 weight % of SiC was much higher when compared with the same for 5 weight % of SiC. Increase in percentage of SiC in the composite increased the rate of abrasion at the interface of tool flank and hole due to the presence of more particles of SiC.

Further, it is also noticed that for all combinations of speed and feed, there was increase of progressive wear magnitude with increase in number of holes reamed. With the progression of reaming process, the reaming tool lose its sharpness of cutting edge and became dull. Increased flank wear results in progressive reduction of clearance angle on the clearance face of the tool. Reaming of holes further with the same tool continuously increased magnitude of energy required. The increase in torque during reaming with increase in number of holes, as shown in Figures 14 and 15 further strengthened this phenomenon. Reduced clearance at flank increases the frictional resistance. It produces wear land on the flanks of the tool, on account of the rubbing action of the machined surface. In the beginning of reaming process, the tool is sharp with no wear land. However very soon the wear land develops and grows in size on account of abrasion, adhesion and shear (Teti, 2002). The maximum value of flank wear (0.0936 mm) was after reaming 104 holes at the speed of 24 m/min and the feed of 0.4 mm/rev with the composite having 10 weight % of SiC.

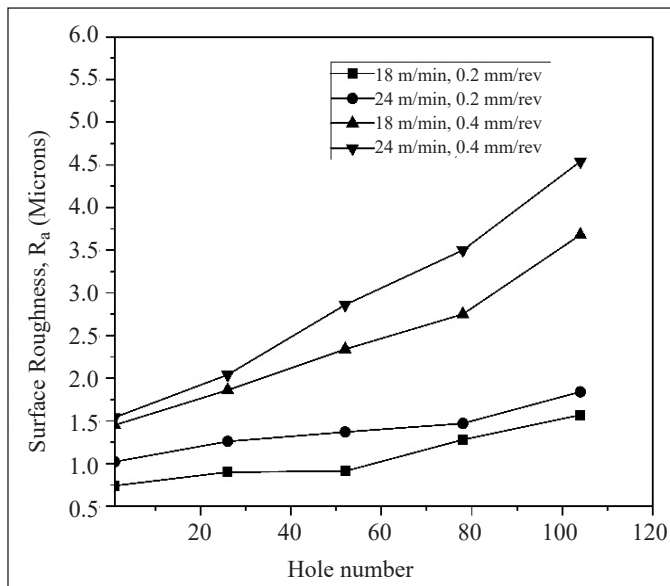


Figure 18. Surface Roughness of reamed holes 1, 26, 52 and 78 and 104 for 5 weight % SiC at various speeds and feeds

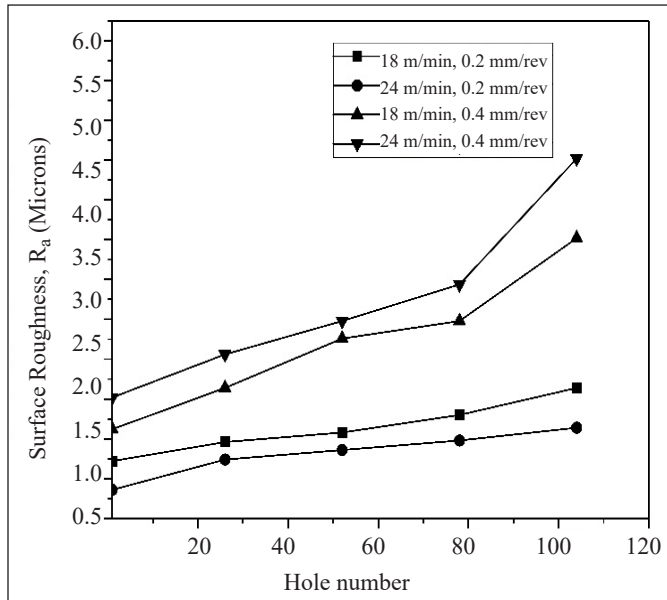


Figure 19. Surface Roughness of reamed holes 1, 26, 52 and 78 and 104 for 10 weight % SiC at various speeds and feeds

It is observed from Figure 18 and 19 that increase in weight % of SiC, speed and feed rate enhanced the surface roughness of the reamed hole surface. After reaming the first hole in the specimen with 5 weight % SiC at 18 m/min speed and 0.2 mm/rev. feed, the surface roughness (R_a) is 0.74 microns while it increased to 1.02 microns at the speed of 24 m/min at same feed rate. After reaming the first hole in the same specimen at 24 m/min speed and 0.2 mm/rev. feed, the surface roughness was 1.02 microns while it increased to 1.54 microns at the feed of 0.4mm/rev. at same speed. After reaming 104th hole in the specimen with 5 weight % SiC at 18 m/min speed and 0.2mm/rev. feed, the surface roughness was 1.57 microns while it increased to 1.84 microns at the speed of 24m/min at same feed rate. After reaming the 104th hole in the same specimen at 24 m/min speed and 0.2 mm/rev. feed, the surface roughness required was 1.84 microns while it increased to 4.54 microns at the feed of 0.4mm/rev. at same speed. For a given speed, the surface roughness value was greater at the feed rate of 0.4mm/rev. when compared with the same at 0.2 mm/rev. A similar trend was observed while reaming the holes in the composite with 10 weight % of SiC. Increase in speed at a given feed rate also increases the surface roughness, but to a much lesser extent. This trend is because of dominating influence of feed rate on reaming process due to increase in chip load when compared with of cutting speed, as discussed already in this paper. Further, it is observed that the surface roughness of the reamed hole increased progressively with the increase in number of holes. This is true with all speeds, feeds and weight percentages of SiC particles. Flank wear affects the geometry of the tool

and its cutting action. This would lead to the poor surface finish of the reamed hole. It is a fact that the hard reinforcing particles in the matrix of composites may not get sheared off when they come across the cutting edge of the tool. Instead, they would either remain embedded to the surface or get dislodged from the surface creating dents on the reamed surface. The progressively damaged (worn out) portions of the cutting edges of machine reamer which interact with surface of the hole affect the surface finish of reamed holes.

The surface morphology images of the reamed hole surfaces were captured using Zeiss EVO 18 Special Edition Scanning Electron Microscope. The morphology study was undertaken to investigate on the possible mode of failure of work material causing the formation of chips, during reaming. It is evident from SEM images shown in Figure 20 to 21 that the mode of failure of work material is due to ductile fracture of matrix material of chips. It also reveals the possible debonding or dislodging, during the process.

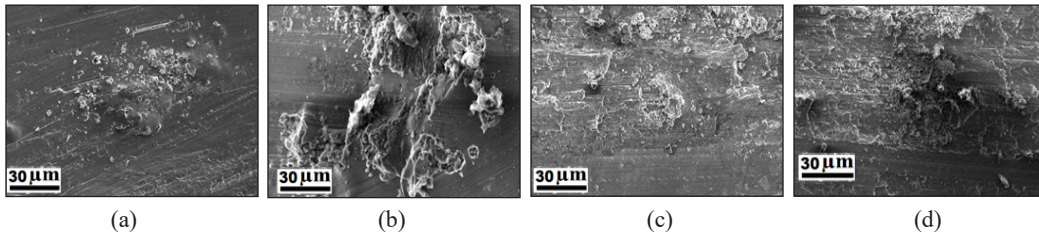


Figure 20. SEM image (2000×) of reamed surface of specimen with 5 weight. % SiC at 18 m/min speed (a) First Hole (b) 104th Hole at 0.2 mm/rev (c) First Hole (d) 104th Hole at 0.4 mm/rev.

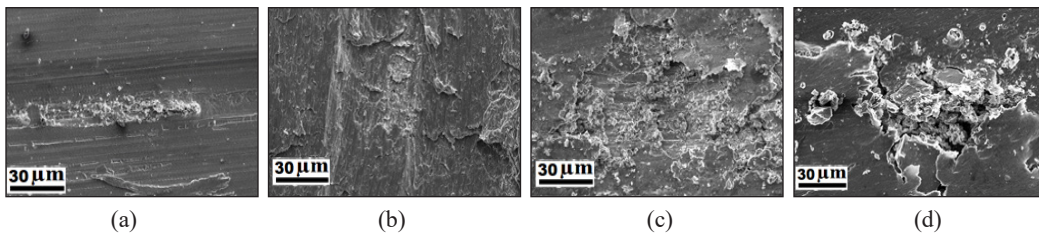


Figure 21. SEM image (2000×) of reamed surface of specimen with 10 weight. % SiC at 18 m/min speed (a) First Hole (b) 104th Hole at 0.2 mm/rev (c) First Hole (d) 104th Hole at 0.4 mm/rev.

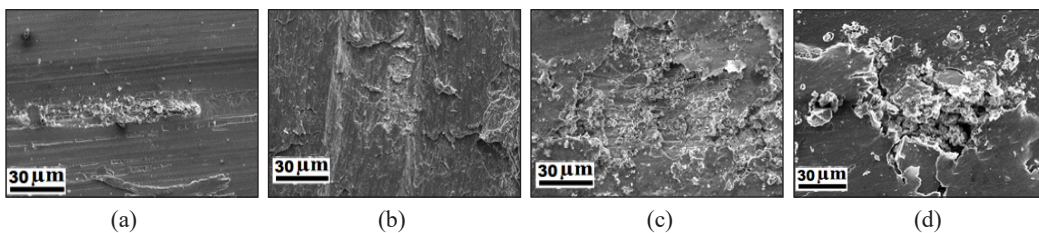


Figure 22. SEM image (2000×) of reamed surface of specimen with 10 weight. % SiC at 24 m/min speed (a) First Hole (b) 104th Hole at 0.2 mm/rev (c) First Hole (d) 104th Hole at 0.4 mm/rev.

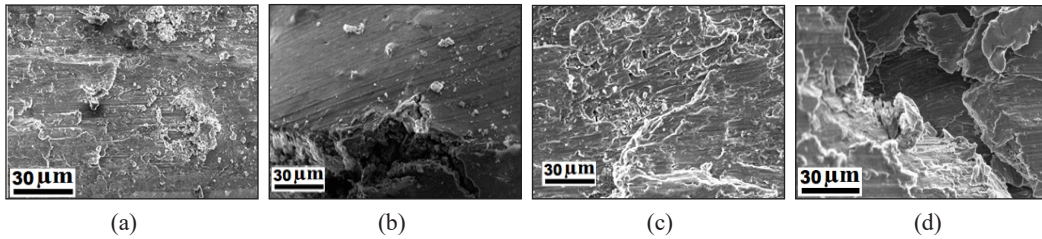


Figure 23. SEM image (2000 \times) of reamed surface of specimen with 10 weight % SiC at 24 m/min speed (a) First Hole (b) 104th Hole at 0.2 mm/rev (c) First Hole (d) 104th Hole at 0.4 mm/rev.

Work hardening of the soft matrix and cracking or debonding of the particles are typical sub surface defects in machining of MMCs. From SEM images shown in Figure 20 to 23, it was evident that increase in speed and weight % of SiC particles from 5 to 10 had resulted in flaky reamed hole surface and poor surface finish. Further, from Figure 23(b) and 23(d), it was evident that tendency for possible dislodging of SiC particles from the hole surface increased with increase in feed. With the increase in number of holes reamed, the flank of the cutting edge of the reamer might get worn out due to rubbing action of dislodged SiC particle from the reamed hole surface, as shown in Figure 22(d) and 23(d). Such debonded particles might get entrapped between the flank of cutting edge of reamer and hole surface during reaming act as abrasive particles and caused damage to the hole surface, resulting in poor surface finish.

CONCLUSIONS

In this experimental investigation, the performance of uncoated four fluted HSS machine reamer is evaluated in the form of tapping torque, progressive flank wear and surface roughness of reamed surfaces. The conclusions derived from the outcome of this study are as follows:

- Increase in the weight percentage of SiC particles results in the increase of hardness and tensile strength of composite influences the rate of flank wear of tool.
- The torque required and flank wear during reaming increase with increase in weight percentage of SiC in Al/SiC composite, cutting speed and feed rate.
- The feed rate has dominating influence on torque required for reaming and progressive flank wear of reaming tool when compared with that of cutting speed.
- The progressive wear out of reaming tool increases the torque required for reaming. Further, at higher feed rates, dislodging of SiC particles from the hole surface deteriorates the surface quality of the reamed holes.

ACKNOWLEDGEMENT

The authors acknowledge the support and facilities extended by Manipal Institute of Technology, Manipal, India for carrying out experimental work.

REFERENCES

- Behera, R., Das, S., Chatterjee, D., & Sutradhar, G. (2011). Characterization of silicon carbide reinforced aluminum matrix composites. *Journal of Minerals and Materials Characterization and Engineering*, 10(10), 923-939.
- Bezerra, A. A., Machado, A. R., Souza, A. M., & Ezugwu, E. O. (2001). Effect of machining parameters when reaming aluminium-silicon (SAE322) alloy. *Journal of Material Processing Technology*, 112, 185-198.
- Chambers, A. R., & Stephens, S. E. (1991). Machining of Al-5 Mg reinforced with 5 vol% Saffil and 15 vol% SiC. *Materials Science and Engineering: A*, 135, 287-290.
- CMTI. (1987). *Machine tool design handbook*. Central Machine Tool Institute. New Delhi, India: Tata McGraw-Hill.
- Gonçalves, R. A., Silva, M. B., & Costa, É. S. (2018). Statistical analysis of cutting forces and hole accuracy in reaming an Al-Si-Mg alloy (6351) with different copper contents. *Journal of the Brazilian Society of Mechanical Sciences and Engineering*, 40, 1-19.
- Hashim, J., Looney, L., & Hashmi, M. S. J. (2001). The wettability of SiC particles by molten aluminium alloy. *Journal of Material Processing Technology*, 119, 324-328.
- Kannan, S., & Kishawy, H. A. (2008). Tribological aspects of machining aluminum metal matrix composites. *Journal of Material Processing Technology*, 198, 399-40.
- Kumar, G. B. V., Rao, C. S. P., & Selvaraj N. (2011). Mechanical and tribological behavior of particulate reinforced aluminum metal matrix composites – a review. *Journal of Minerals and Materials Characterization & Engineering*, 10(1), 59-91.
- Melo, T. F. L., Filho, S. L. M. R., Arruda, É. M., & Brandão L. C. (2019). Analysis of the surface roughness, cutting efforts, and form errors in bore reaming of hardened steel using a statistical approach. *Measurement*, 134, 845-854.
- Rahmana, M. H., Al Rashed, H. M. M. (2014). Characterization of silicon carbide reinforced aluminum matrix composites. *Procedia Engineering*, 90, 103-109.
- Rattanakit, R., Soo, S., Aspinwall, D., Harden, P., Haffner, B., Zhang, Z., & Arnold, D. (2015, March 28-30). The effect of cutting speed and tool material on hole quality when reaming C355 aluminium alloy. In *Proceedings of the 38th International Matador Conference* (pp. 224-230). Huwei, Taiwan, Province of China.
- Schutzer, K., Roth, M., Abele, E., & Hauer, T. (2014). Experimental investigation of hole quality during reaming applications using multi-blade tools. *The Brazilian Society of Mechanical Sciences and Engineering*, 36(4), 797-806.

- Soltani, S., Khosroshahi, R. A., Mousavian, R. T., Jiang, Z. Y., Boostani, A. F., & Brabazon, D. (2015). Stir casting process for manufacture of Al–SiC composites. *Rare Metals*, 36(7), 581-590.
- Srinivasan, A., Arunachalam, R. M., Ramesh, S., & Senthilkumar, J. S. (2012). Machining performance study on metal matrix composites-a response surface methodology approach. *American Journal of Applied Sciences*, 9(4), 478-483.
- Su, H., Gao, W., Zhang, H., Liu, H., Lu, J., & Lu, Z. (2010). Optimization of stirring parameters through numerical simulation for the preparation of aluminum matrix composite by stir casting process. *Journal of Manufacturing Science and Engineering*, 132(6), 0610071-0610077.
- Teti, R. (2002). Machining of composite materials. *CIRP Annals-Mfg. Technology*, 51(2), 611- 634.
- Wang, Y., Cui, X., Xu, H., & Jiang, K. (2013). Cutting force analysis in reaming of ZL102 aluminium cast alloys by PCD reamer. *International Journal of Advanced Manufacturing Technology*, 67, 1509-1516.
- Wenner, S., & Holmestad, R. (2016). Accurately measured precipitate–matrix misfit in an Al– Mg–Si alloy by electron microscopy. *Scripta Materialia*, 118, 5-8.
- Yan, X., Li, B., Li, J., & Yang, L. (2013). Analysis of the machining characteristics in reaming AlSi12 alloy with PCD reamer. *International Journal of Advanced Manufacturing Technology*, 69, 2387-2399.

**REFEREES FOR THE PERTANIKA
JOURNAL OF SCIENCE AND TECHNOLOGY**

VOL. 28 (1) JAN. 2020

The Editorial Board of the Journal of Science and Technology wishes to thank the following:

Abdul Samad Shibghatullah
(UCSI, Malaysia)

Abdullah Hisam Omar
(UTM, Malaysia)

Addie Irawan Hashim
(UMP, Malaysia)

Adil Salhi
(UAE, Morocco)

Ahmad Baharuddin Abdullah
(USM, Malaysia)

Ahmad Ramli Mohd Yahya
(USM, Malaysia)

Aishah Hani Azil
(PPUKM, Malaysia)

Amir Izzwan Zamri
(UMT, Malaysia)

Ariffin Samsuri
(UTM, Malaysia)

Arun Karnwal
(LPU, India)

Aslina Baharum
(UMS, Malaysia)

Aweng Eh Rak
(UMK, Malaysia)

Azizul Azhar Ramli
(UTHM, Malaysia)

Azmah Hanim Mohamed Ariff
(UPM, Malaysia)

Azura Che Soh
(UPM, Malaysia)

Bakhtiar Affendi Rosdi
(USM, Malaysia)

Barakatun Nisak Mohd Yusof
(UPM, Malaysia)

Che Zulzikrami Azner Abidin
(UNIMAP, Malaysia)

Chee Hui Yee
(UPM, Malaysia)

Chua Han Bing
(Curtin University, Malaysia)

Chuah Joon Huang
(UM, Malaysia)

Darius El Pebrian
(UiTM, Malaysia)

Edriyana Abd. Aziz
(UMP, Malaysia)

Faizir Ramlie
(UTM, Malaysia)

Farhan Mohamed
(UTM, Malaysia)

Hasfalina Che Man
(UPM, Malaysia)

Helmi Zulhaidi Mohd Shafri
(UPM, Malaysia)

Issham Ismail
(UTM, Malaysia)

Jumat Sulaiman
(UMS, Malaysia)

Kasturi Dewi Varathan
(UM, Malaysia)

Kek Sie Long
(UTHM, Malaysia)

Khairil Anas Md Rezali
(UPM, Malaysia)

Khalim Amjad Meerja
(VRSEC, India)

Lai Kee Huong
(Sunway University, Malaysia)

Lee Teang Shui
(UPM, Malaysia)

Lem Kong Hoong
(UTAR, Malaysia)

Lim Siew Huah
(UM, Malaysia)

Loh Su Peng
(UPM, Malaysia)

Luis Miguel Contreras-Medina
(UAQ, Mexico)

Maziah Mohamad
(UTM, Malaysia)

Mohamed Hasnain Isa
(UTB, Brunei Darussalam)

Mohammad Effendy Yaacob
(UPM, Malaysia)

Mohammed Saedi Jami
(IIUM, Malaysia)

Mohan Reddy Moola
(Curtin University, Malaysia)

Mohd Asyraf Mansor
(USM, Malaysia)

Mohd Hamzah Mohd Nasir
(IIUM, Malaysia)

Mohd Sapuan Salit
(UPM, Malaysia)

Mohd Shamsul Anuar
(UPM, Malaysia)

Mostafa Abdulghafoor Mohammed
(UPB, Romania)

Muhamad Mat Noor
(UMP, Malaysia)

Muhammad Syafiq Hazwan Ruslan
(UTP, Malaysia)

Muhd Danish Daniel Abdullah
(UMT, Malaysia)

Muzzneena Ahmad Mustapha
(UKM, Malaysia)

Narcisse MS Joseph
(UPM, Malaysia)

Nor Amirah Abu Seman
(UNIMAP, Malaysia)

Nor Azura Husin
(UPM, Malaysia)

Nuramidah Hamidon
(UTHM, Malaysia)

Othman A. Karim
(UKM, Malaysia)

Phang Chang
(UTHM, Malaysia)

Razali Yaakob
(UPM, Malaysia)

Reda Hassanien
(Cairo University, Egypt)

Rohana Abdul Ghani
(UiTM, Malaysia)

Sabariah Julai @ Julaihi
(UM, Malaysia)

Sarinder Kaur Kashmir Singh
(UM, Malaysia)

Sheikh Mohamed Hassan Ibrahim
(UMT, Malaysia)

Syamsul Rizal Abd Shukor
(USM, Malaysia)

Syerina Azlin Md Nasir
(UiTM, Malaysia)

Tay Chia Chay
(UiTM, Malaysia)

Tay Meng Guan
(UNIMAS, Malaysia)

Thaned Rojsiraphisal
(CMU, Thailand)

Tye Ching Thian
(USM, Malaysia)

Umi Kalsom Yusof
(USM, Malaysia)

Viv Djanat Prasita
(Universitas HangTuah, Indonesia)

Wan Ainun Mior Othman
(UM, Malaysia)

Wan Azizun Wan Adnan
(UPM, Malaysia)

Wan Mohd Rauhan Wan Hussin
(UMT, Malaysia)

Wang Seok Mui
(UiTM, Malaysia)

Zainul Amiruddin Zakaria
(UPM, Malaysia)

Zamzuri Hamedon
(UMP, Malaysia)

Zanariah Hashim
(UTM, Malaysia)

Zeinab Abbas Jawad
(Curtin University, Malaysia)

CMU	- Chiangmai University	UPB	- Politehnica University of Bucharest
LPU	- Lovely Professional University	UPM	- Universiti Putra Malaysia
UAE	- Université Abdelmalek Essadi	USM	- Universiti Sains Malaysia
UAQ	- Universidad Autónoma de Querétaro	UTAR	- Universiti Tunku Abdul Rahman
UiTM	- Universiti Teknologi MARA	UTB	- Universiti Teknologi Brunei
UKM	- Universiti Kebangsaan Malaysia	UTHM	- Universiti Tun Hussein Onn Malaysia
UM	- Universiti Malaya	UTM	- Universiti Teknologi Malaysia
UMP	- Universiti Malaysia Pahang	UTP	- Universiti Teknologi Petronas
UMS	- Universiti Malaysia Sabah	VRSEC	- Velagapudi Ramakrishna Siddhartha Engineering College
UMT	- Universiti Malaysia Terengganu		
UNIMAP	- Universiti Malaysia Perlis		
UNIMAS	- Universiti Sarawak Malaysia		

While every effort has been made to include a complete list of referees for the period stated above, however if any name(s) have been omitted unintentionally or spelt incorrectly, please notify the Chief Executive Editor, *Pertanika* Journals at executive_editor.pertanika@upm.edu.my

Any inclusion or exclusion of name(s) on this page does not commit the *Pertanika* Editorial Office, nor the UPM Press or the University to provide any liability for whatsoever reason.



Pertanika Journals

Our goal is to bring high quality research to the widest possible audience

INSTRUCTIONS TO AUTHORS (Manuscript Preparation & Submission Guide)

Revised: June 2019

Please read the Pertanika guidelines and follow these instructions carefully. The Chief Executive Editor reserves the right to return manuscripts that are not prepared in accordance with these guidelines.

MANUSCRIPT PREPARATION

Manuscript Types

Pertanika accepts submission of mainly **four** types of manuscripts for peer-review.

1. REGULAR ARTICLE

Regular articles are full-length original empirical investigations, consisting of introduction, materials and methods, results and discussion, conclusions. Original work must provide an explanation on research results that contain new and significant findings. Analysis and Discussion must be supported with relevant references.

Size: Generally, these are expected to be between **6 and 12 journal pages or not exceeding 6000 words** (excluding the abstract, references, tables and/or figures), a maximum of **80 references**, and **an abstract of 100–200 words**.

2. REVIEW ARTICLE

These report critical evaluation of materials about current research that has already been published by organizing, integrating, and evaluating previously published materials. It summarizes the status of knowledge and outline future directions of research within the journal scope. Review articles should aim to provide systemic overviews, evaluations and interpretations of research in a given field. Re-analyses as meta-analysis and systemic reviews are encouraged. The manuscript title must start with "Review Article:".

Size: Generally, these are expected to be between **8 and 12 journal pages or not exceeding 6000 words** (excluding the abstract, references, tables and/or figures), a maximum of **80 references**, and **an abstract of 100–200 words**.

3. SHORT COMMUNICATIONS

They are timely and brief. These are suitable for the publication of significant technical advances and may be used to:

- (a) report new developments, significant advances and novel aspects of experimental and theoretical methods and techniques which are relevant for scientific investigations within the journal scope;
- (b) report/discuss on significant matters of policy and perspective related to the science of the journal, including 'personal' commentary;
- (c) disseminate information and data on topical events of significant scientific and/or social interest within the scope of the journal.

Size: These are usually between **2 and 4 journal pages** and have a maximum of **3 figures and/or tables, from 8 to 20 references, and an abstract length not exceeding 100 words**. Information must be in short but complete form and it is not intended to publish preliminary results or to be a reduced version of Regular or Rapid Papers.

4. OTHERS

Brief reports, case studies, comments, concept papers, letters to the editor, and replies on previously published articles may be considered.

Language Accuracy

Pertanika **emphasizes** on the linguistic accuracy of every manuscript published. Articles must be in **English** and they must be competently written and argued in clear and concise grammatical English. Contributors are strongly advised to have the manuscript checked by a colleague with ample experience in writing English manuscripts or a competent English language editor.

Author(s) **may be required to provide a certificate** confirming that their manuscripts have been adequately edited. **All editing costs must be borne by the author(s).**

Linguistically hopeless manuscripts will be rejected straightaway (e.g., when the language is so poor that one cannot be sure of what the authors really mean). This process, taken by authors before submission, will greatly facilitate reviewing, and thus publication if the content is acceptable.

MANUSCRIPT FORMAT

The paper should be submitted in one column format with at least 4cm margins and 1.5 line spacing throughout. Authors are advised to use Times New Roman 12-point font and *MS Word* format.

1. Manuscript Structure

Manuscripts in general should be organised in the following order:

- **Page 1: Running title**

This page should **only** contain the running title of your paper. The running title is an abbreviated title used as the running head on every page of the manuscript. The running title **should not exceed 60 characters, counting letters and spaces.**

- **Page 2: Author(s) and Corresponding author information**

General information: This page should contain the **full title** of your paper **not exceeding 25 words**, with name(s) of all the authors, institutions and corresponding author's name, institution and full address (Street address, telephone number (including extension), hand phone number, and e-mail address) for editorial correspondence. **First and corresponding authors must be clearly indicated.**

Authors' name: The names of the authors should be named **in full without academic titles.** For Asian (Chinese, Korean, Japanese, Vietnamese), please write first name and middle name before surname (family name). The last name in the sequence is considered the surname.

Authors' addresses: Multiple authors with different addresses must indicate their respective addresses separately by superscript numbers.

Tables / figures list: A **list** of number of **black and white / colour figures and tables** should also be indicated on this page. See "**6. Figures & Photographs**" for details.

Example (page 2):

In vivo Fecundity Evaluation of Phaleria macrocarpa Extract Supplementation in Male Adult Rats

Sui Sien Leong^{1} and Mohamad Aziz Dollah²*

¹*Department of Animal Sciences and Fishery, Universiti Putra Malaysia, 97008 Bintulu, Sarawak, Malaysia*

²*Department of Biomedical Sciences, Universiti Putra Malaysia, 43400 Serdang, Malaysia*

leongsuisien@upm.edu.my (Sui Sien Leong), Contact number
aziddollah@gmail.com (Mohamad Aziz Dollah), Contact number

**Corresponding author*

List of Table / Figure:

Table 1.

Figure 1.

- **Page 3: Abstract**

This page should **repeat** the **full title** of your paper with only the **Abstract** (the abstract should be less than 250 words for a Regular Paper and up to 100 words for a Short Communication), **and Keywords**.

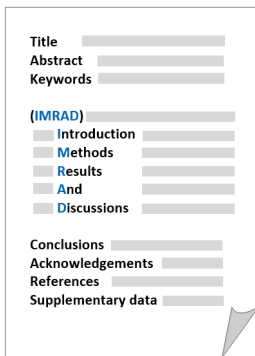
Keywords: Not more than 8 keywords in alphabetical order must be provided to describe the contents of the manuscript.

- **Page 4: Introduction**

This page should begin with the **Introduction** of your article and followed by the rest of your paper.

2. Text

Regular Papers should be prepared with the headings *Introduction, Materials and Methods, Results and Discussion, Conclusions, Acknowledgements, References, and Supplementary data* (if any) in this order. The literature review may be part of or separated from Introduction.



MAKE YOUR ARTICLES AS CONCISE AS POSSIBLE

Most scientific papers are prepared according to a format called IMRAD. The term represents the first letters of the words Introduction, Materials and Methods, Results, And, Discussion. It indicates a pattern or format rather than a complete list of headings or components of research papers; the missing parts of a paper are: Title, Authors, Keywords, Abstract, Conclusions, and References. Additionally, some papers include Acknowledgments and Appendices.

The Introduction explains the scope and objective of the study in the light of current knowledge on the subject; the Materials and Methods describes how the study was conducted; the Results section reports what was found in the study; and the Discussion section explains meaning and significance of the results and provides suggestions for future directions of research. The manuscript must be prepared according to the Journal's instructions to authors.

3. Levels of Heading

Level of heading	Format
1 st	LEFT, BOLD, UPPERCASE
2 nd	Flush left, Bold, Capitalise each word
3 rd	Bold, Capitalise each word, ending with .
4 th	Bold italic, Capitalise each word, ending with .

4. Equations and Formulae

These must be set up clearly and should be typed double spaced. Numbers identifying equations should be in square brackets and placed on the right margin of the text.

5. Tables

- All tables should be prepared in a form consistent with recent issues of Pertanika and should be numbered consecutively with Roman numerals (Table 1, Table 2).
- A brief title should be provided, which should be shown at the top of each table (**APA format**):

Example: Table 1

PVY infected Nicotiana tabacum plants optical density in ELISA

- Explanatory material should be given in the table legends and footnotes.
- Each table should be prepared on a new page, embedded in the manuscript.
- Authors are advised to keep backup files of all tables.

**** Please submit all tables in Microsoft word format only - because tables submitted as image data cannot be edited for publication and are usually in low-resolution.**

6. Figures & Photographs

- Submit an **original** figure or photograph.
- Line drawings must be clear, with high black and white contrast.
- Each figure or photograph should be prepared on a new page, embedded in the manuscript for reviewing to keep the file of the manuscript under 5 MB.
- These should be numbered consecutively with Roman numerals (Figure 1, Figure 2).
- Provide a brief title, which should be shown at the bottom of each table (**APA format**):

Example: Figure 1. PVY-infected in vitro callus of Nicotiana tabacum

- If a Figure has been previously published, acknowledge the original source and submit written permission form the copyright holder to reproduce the material.
- Authors are advised to keep backup files of all figures.

**** Figures or photographs must also be submitted separately as TIFF, JPEG, because figures or photographs submitted in low-resolution embedded in the manuscript cannot be accepted for publication. For electronic figures, create your figures using applications that are capable of preparing high resolution TIFF files.**

7. References

References begin on their own page and are listed in alphabetical order by the first author's last name. Only references cited within the text should be included. All references should be in 12-point font and double-spaced.

NOTE: When formatting your references, please follow the **Pertanika-APA-reference style** (6th Edition) (*refer to examples*). Ensure that the references are strictly in the journal's prescribed style, failing which your article will **not be accepted for peer-review**. You may refer to the *Publication Manual of the American Psychological Association* for further details <https://apastyle.apa.org/>.

Examples of reference style are given below:

Books

Books	Insertion in Text	In Reference List
Book with 1-2 authors	<p>Information prominent' (the author's name is within parentheses):</p> <p>... (Cochrane, 2007) ...</p> <p>Or</p> <p>'Author prominent' (the author's name is outside the parentheses):</p> <p>Cochrane (2007) ...</p>	Cochrane, A. (2007). <i>Understanding urban policy: A critical approach</i> . Malden, MA: Blackwell Publishing.
Book with 3 or more authors (Pertanika's format)	<p><i>For all in-text references, list only the first author's family name and followed by 'et al.'</i></p> <p>Information prominent' (the author's name is within parentheses):</p> <p>... (Seeley et al., 2011) ...</p> <p>Or</p> <p>'Author prominent' (the author's name is outside the parentheses):</p> <p>Seeley et al. (2011) ...</p>	Seeley, R., VanPutte, C., Regan, J., & Russo, A. (2011). <i>Seeley's anatomy & physiology</i> . New York, NY: McGraw-Hill.

Books	Insertion in Text	In Reference List
Book with 6-7 authors	<p><i>For all in-text references, list only the first author's family name and followed by 'et al.'</i></p> <p>Information prominent' (the author's name is within parentheses):</p> <p>... (Bulliet et al., 2011) ...</p> <p>Or</p> <p>'Author prominent' (the author's name is outside the parentheses):</p> <p>Bulliet et al. (2011) ...</p>	<p>Bulliet, R. W., Crossley, P. K., Headrick, D. R., Hirsch, S. W., Johnson, L. L., & Northrup, D. (2011). <i>The earth and its peoples: A global history</i> (5th ed.). Boston, MA: Wadsworth.</p>
Book with more than 8 authors	<p><i>For all in-text references, list only the first author's family name and followed by 'et al.'</i></p> <p>A recent study (Edge et al., 2011) concluded that...</p> <p>Or</p> <p>Edge et al. (2011) concluded that</p>	<p>For books with eight or more authors, please follow the guidelines for journal articles with eight or more authors.</p>
Chapter in edited book	<p>Information prominent' (the author's name is within parentheses):</p> <p>... (Richards, 1997) ...</p> <p>Or</p> <p>'Author prominent' (the author's name is outside the parentheses):</p> <p>Richards (1997) ...</p>	<p>Richards, K. C. (1997). Views on globalization. In H. L. Vivaldi (Ed.), <i>Australia in a global world</i> (pp. 29-43). Sydney, Australia: Century.</p>
e-book/online book	<p>Information prominent' (the author's name is within parentheses):</p> <p>... (Niemann et al., 2004) ...</p> <p>Or</p> <p>'Author prominent' (the author's name is outside the parentheses):</p> <p>Niemann (2004) ...</p>	<p>Niemann, S., Greenstein, D., & David, D. (2004). <i>Helping children who are deaf: Family and community support for children who do not hear well</i>. Retrieved June 1, 2019, from http://www.hesperian.org/publications_download_deaf.php</p> <p>Schiraldi, G. R. (2001). <i>The post-traumatic stress disorder sourcebook: A guide to healing, recovery, and growth</i> [Adobe Digital Editions version]. doi:10.1036/0071393722</p>
Editor	<p>Information prominent' (the author's name is within parentheses):</p> <p>... (Zairi, 1999) ...</p> <p>Or</p> <p>'Author prominent' (the author's name is outside the parentheses):</p> <p>Zairi (1999) ...</p>	<p>Zairi, M. (Ed.). (1999). <i>Best practice: Process innovation management</i>. Oxford, United Kingdom: Butterworth- Heinemann.</p>

Books	Insertion in Text	In Reference List
Several works by same author in the same year	<p>Information prominent' (the author's name is within parentheses):</p> <p>... (Fullan, 1996a, 1997b) ...</p> <p>Or</p> <p>'Author prominent' (the author's name is outside the parentheses):</p> <p>Fullan (1996a, 1996b) ...</p>	<p>Fullan, M. (1996a). Leadership for change. In <i>International handbook for educational leadership and administration</i>. New York, NY: Kluwer Academic .</p> <p>Fullan, M. (1996b). <i>The new meaning of educational change</i>. London, United Kingdom: Casell.</p>
Several authors, different years referred to collectively in your work	<p>List sources alphabetically by family name in the in-text reference in the order in which they appear in the Reference List.</p> <p>The cyclical process (Carr & Kemmis, 1986; Dick, 2000) suggests...</p>	<p>Carr, W., & Kemmis, S. (1986). <i>Becoming critical: Education knowledge and action research</i>. London, United Kingdom: Falmer Press.</p> <p>Dick, B. (2000). <i>A beginner's guide to action research</i>. Retrieved June 1, 2019, from http://www.scu.edu.au/schools/gcm/ar/arp/guide.html</p>

Journals

Journals	Insertion in Text	In Reference List
Journal article with 1-2 authors	<p>Information prominent' (the author's name is within parentheses):</p> <p>... (Kramer & Bloggs, 2002)...</p> <p>Or</p> <p>'Author prominent' (the author's name is outside the parentheses):</p> <p>Kramer and Bloggs (2002) ...</p>	<p>Kramer, E., & Bloggs, T. (2002). On quality in art and art therapy. <i>American Journal of Art Therapy</i>, 40, 218-231.</p>
Journal article with 3 or more authors (Pertanika's format)	<p><i>For all in-text references, list only the first author's family name and followed by 'et al.'</i></p> <p>Information prominent' (the author's name is within parentheses):</p> <p>... (Erlo et al., 2008) ...</p> <p>Or</p> <p>'Author prominent' (the author's name is outside the parentheses):</p> <p>Erlo et al. (2008) ...</p>	<p>Elo, A., Ervasti, J., Kuosma, E., & Mattila, P. (2008). Evaluation of an organizational stress management program in a municipal public works organization. <i>Journal of Occupational Health Psychology</i>, 13(1), 10-23. doi: 10.1037/1076-8998.13.1.10</p>

Journal article with 6 - 7 authors	<p><i>For all in-text references, list only the first author's family name and followed by 'et al.'</i></p> <p>Information prominent' (the author's name is within parentheses):</p> <p>... (Restouin et al., 2009) ...</p> <p>Or</p> <p>'Author prominent' (the author's name is outside the parentheses):</p> <p>Restouin et al. (2008) ...</p>	Restouin, A., Aresta, S., Prébet, T., Borg, J., Badache, A., & Collette, Y. (2009). A simplified, 96-well-adapted, ATP luminescence-based motility assay. <i>BioTechniques</i> , 47, 871–875. doi: 10.2144/000113250
Journal article with more than 8 or more authors	<p>Information prominent' (the author's name is within parentheses):</p> <p>... (Steel et al., 2010)..</p> <p>Or</p> <p>'Author prominent' (the author's name is outside the parentheses):</p> <p>Steel et al. (2010) ...</p>	Steel, J., Youssef, M., Pfeifer, R., Ramirez, J. M., Probst, C., Sellei, R., ... Pape, H. C. (2010). Health-related quality of life in patients with multiple injuries and traumatic brain injury 10+ years postinjury. <i>Journal of Trauma: Injury, Infection, and Critical Care</i> , 69(3), 523-531. doi: 10.1097/TA.0b013e3181e90c24
Journal article with DOI	<p>Information prominent' (the author's name is within parentheses):</p> <p>... (Shaw et al., 2005)..</p> <p>Or</p> <p>'Author prominent' (the author's name is outside the parentheses):</p> <p>Shaw et al. (2005) ...</p>	Shaw, K., O'Rourke, P., Del Mar, C., & Kenardy, J. (2005). Psychological interventions for overweight or obesity. <i>The Cochrane database of systematic reviews</i> (2). doi:10.1002/14651858.CD003818.pub2

Newspapers

Newspapers	Insertion in Text	In Reference List
Newspaper article – with an author	... (Waterford, 2007)...	Waterford, J. (2007, May 30). Bill of rights gets it wrong. <i>The Canberra Times</i> , p. 11.
Newspaper article – without an author	... ("Internet pioneer", 2007) ...	Internet pioneer to oversee network redesign. (2007, May 28). <i>The Canberra Times</i> , p. 15.
Article in an newsletter	... ("Australians and the Western Front", 2009) ...	Australians and the Western Front. (2009, November). <i>Ozculture newsletter</i> . Retrieved from http://www.cultureandrecreation.gov.au/newsletter/

Conference / Seminar Papers

Conference / Seminar Papers	Insertion in Text	In Reference List
<p>Print – If the paper is from a book, use the Book chapter citation format. If it is from regularly published proceedings (e.g. annual), use the Journal article citation format.</p>	<p>... (Edge, 1996) ...</p> <p>Or</p> <p>Edge (1996) ...</p>	<p>Edge, M. (1996). Lifetime prediction: Fact or fancy? In M. S. Koch, T. Padfield, J. S. Johnsen, & U. B. Kejser (Eds.), <i>Proceedings of the Conference on Research Techniques in Photographic Conservation</i> (pp. 97-100). Copenhagen, Denmark: Royal Danish Academy of Fine Arts.</p>
<p>Online</p>	<p>... (Tester, 2008) ...</p> <p>Or</p> <p>Tester (2008) ...</p>	<p>Tester, J. W. (2008). The future of geothermal energy as a major global energy supplier. In H. Gurgenci & A. R. Budd (Eds.), <i>Proceedings of the Sir Mark Oliphant International Frontiers of Science and Technology Australian Geothermal Energy Conference</i>, Canberra, Australia: Geoscience Australia. Retrieved from http://www.ga.gov.au/image_cache/GA11825.pdf</p>

Government Publications

Government Publications	Insertion in Text	In Reference List
Government as author	<p>First in-text reference: Spell out the full name with the abbreviation of the body.</p> <p>... (Department of Finance and Administration [DOFA], 2006) ...</p> <p>Subsequent in-text reference/s: Use the abbreviation of the body.</p> <p>... (DOFA, 2006)...</p>	<p>Department of Finance and Administration. (2006). <i>Delivering Australian Government services: Managing multiple channels</i>. Canberra, Australia: Author.</p>
Government report - online	<p>First in-text reference: Spell out the full name with the abbreviation of the body.</p> <p>... (Department of the Prime Minister and Cabinet [PM&C], 2008) ...</p> <p>Subsequent in-text reference/s: Use the abbreviation of the body.</p> <p>... (PM&C, 2008)...</p>	<p>Department of the Prime Minister and Cabinet. (2008). <i>Families in Australia: 2008</i>. Retrieved June 1, 2019, from http://www.....</p>

8. General Guidelines

Abbreviations: Define alphabetically, other than abbreviations that can be used without definition. Words or phrases that are abbreviated in the introduction and following text should be written out in full the first time that they appear in the text, with each abbreviated form in parenthesis. Include the common name or scientific name, or both, of animal and plant materials.

Acknowledgements: Any individuals and entities who have contributed should be acknowledged appropriately.

Authors' Affiliation: The primary affiliation for each author should be the institution where the majority of their work was done. If an author has subsequently moved to another institution, the current address may also be stated in the footer.

Co-Authors: The commonly accepted guideline for authorship is that one must have substantially contributed to the development of the paper and share accountability for the results. Researchers should decide who will be an author and what order they will be listed depending upon their order of importance to the study. Other contributions should be cited in the manuscript's Acknowledgements.

Copyright Permissions: Authors should seek necessary permissions for quotations, artwork, boxes or tables taken from other publications or from other freely available sources on the Internet before submission to Pertanika. Acknowledgement must be given to the original source in the illustration legend, in a table footnote, or at the end of the quotation.

Footnotes: Current addresses of authors if different from heading may be inserted here.

Page Numbering: Every page of the manuscript, including the title page, references and tables should be numbered.

Spelling: The journal uses American or British spelling and authors may follow the latest edition of the Oxford Advanced Learner's Dictionary for British spellings. Each manuscript should follow one type of spelling only.

SUBMISSION OF MANUSCRIPTS

All submissions must be made electronically using the **online submission system ScholarOne™**, a web-based portal by Clarivate Analytics. For more information, go to our web page and [click "Online Submission"](#).

Submission Checklist

1. MANUSCRIPT:

Ensure your MS has followed the Pertanika style particularly the first four pages as explained earlier. The article should be written in a good academic style and provide an accurate and succinct description of the contents ensuring that grammar and spelling errors have been corrected before submission. It should also not exceed the suggested length.

2. DECLARATION FORM:

- Author has to sign a declaration form. In signing the form, authors declare that the work submitted for publication is original, previously unpublished, and not under consideration for any publication elsewhere.
- Author has to agree to pay the publishing fee once the paper is accepted for publication in Pertanika.

Note:

COPYRIGHT FORM: Author will be asked to sign a copyright form when the paper is accepted. In signing the form, it is assumed that authors have obtained permission to use any copyrighted or previously published material. All authors must read and agree to the conditions outlined in the form, and must sign the form or agree that the corresponding author can sign on their behalf. Articles cannot be published until a signed form (*original pen-to-paper signature*) has been received.

Visit our Journal's website for more details at <http://www.pertanika.upm.edu.my/>

ACCESS TO PUBLISHED MATERIALS

Under the Journal's open access initiative, authors can choose to download free material (via PDF link) from any of the journal issues from Pertanika's website. Under "**Browse Journals**" you will see a link, "*Regular Issue*", "*Special Issue*" or "*Archives*". Here you will get access to all current and back-issues from 1978 onwards. No hard copy of journals or off prints are printed.

Visit our Journal's website at

http://www.pertanika.upm.edu.my/regular_issues.php for "Regular Issue"

http://www.pertanika.upm.edu.my/special_issues.php for "Special Issue"

http://www.pertanika.upm.edu.my/journal_archives.php for "Archives"



PUBLICATION CHARGE

Upon acceptance of manuscript, a processing fee of RM 750 / USD 250 will be imposed on authors; RM 750 for corresponding author affiliated to institution in Malaysia; USD 250 for corresponding author affiliated to institution outside Malaysia. Payment must be made online at <https://paygate.upm.edu.my/action.do?do=>

Any queries may be directed to the **Chief Executive Editor's** office via email to executive_editor.pertanika@upm.edu.my



Toxicity Assessment of Gallic Acid Loaded Graphene Oxide (GAGO) Nano-Formulation in Zebrafish (<i>Danio Rerio</i>) Embryos <i>Ahmad Ashraful Hadi Abdul Ghafar, Nurhuda Elias, Suhaili Shamsi, Faizah Md Yasin and Seri Narti Edayu Sarchio</i>	311
--	-----

Environmental Sciences

Review Article

Light Fishing Fleets Monitoring by GIS-Based Spatiotemporal Analysis in West Sumatera Waters <i>Nurholis, Jonson Lumban-Gaol and Fachrudin Syah Achmad</i>	327
---	-----

Dye Removal by Membrane Technology for Wastewater Treatment using a Cationic Carrier <i>Huda Adil Sabbar, Wasan Omar Noori and Ahmed Samir Naje</i>	353
--	-----

Applied Sciences and Technologies

Comparative Study on Inhibitors Comprising Aromatic and Non-Aromatic Solvents towards Flow Assurance of Crude Oil <i>S M Anisuzzaman, Duduku Krishnaiah and Sharmini Nair Prathaban</i>	369
--	-----

Earth Sciences

An Integration Based Optimization Approach (ABC and PSO) for Parameter Estimation in BLRP Model for Disaggregating Daily Rainfall <i>Zulkarnain Hassan</i>	385
---	-----

Material Sciences

Study on Progressive Wear of Machine Reamer while Reaming Al6061/SiC Composite <i>Sandeep Nambiar, Raviraja Adhikari, Nagaraja Upadhya and Rajarama Hande</i>	403
--	-----

DFRNets: Unsupervised Monocular Depth Estimation Using a Siamese Architecture for Disparity Refinement <i>John Paul Tan Yusiong and Prospero Clara Naval, Jr.</i>	163
Quantitative Assessment of Concept Maps for Conceptualizing Domain Ontologies: A Case of Quran <i>Rizwan Iqbal, Masrah Azrifah Azmi Murad and Adnan Ashraf</i>	179
Mathematical Sciences	
Efficient Model Selection of Collector Efficiency in Solar Dryer using Hybrid of LASSO and Robust Regression <i>Anam Javaid, Mohd. Tahir Ismail and Majid Khan Majahar Ali</i>	193
Logic Mining in League of Legends <i>Liew Ching Kho, Mohd Shareduwan Mohd Kasihmuddin, Mohd. Asyraf Mansor and Saratha Sathasivam</i>	211
Hybrid Discrete Hopfield Neural Network based Modified Clonal Selection Algorithm for VLSI Circuit Verification <i>Saratha Sathasivam, Mustafa Mamat, Mohd. Asyraf Mansor and Mohd Shareduwan Mohd Kasihmuddin</i>	227
Impacts of Asymmetric Biotic Interactions and Environmental Factors on the Presence-Absence of Multispecies <i>James Omaiye Ojonubah and Mohd Hafiz Mohd</i>	245
Medical and Health Sciences	
Aedestech Mosquito Home System Prevents the Hatch of <i>Aedes</i> Mosquito Eggs and Reduces its Population <i>Latifah Saiful Yazan, Kaveinesh Paskaran, Banulata Gopalsamy and Roslaini Abd Majid</i>	263
Acute Moderate and High-Intensity Endurance Exercise Suppresses <i>Ad-libitum</i> Energy Intake in Obese Males <i>Adam Linoby, Muhammad Alif Nazrin Jumat, Ahmad Safwanudin Nordin, Nur Hidayah Asilah Za'don, Jamiaton Kusrin and Sharifah Maimunah Syed Mud Puad</i>	279
Standardised Extracts of <i>Moringa Oleifera</i> and <i>Centella Asiatica</i> Enhanced the Antioxidant Activity, Learning and Memory Effects by Inhibiting Acetylcholinesterase Activity in D-Galactose Induced Ageing Rats <i>Hisyam Jamari, Mohd Salleh Rofiee, Richard James Johari, Mohd Zaki Salleh and Teh Lay Kek</i>	293

Contents

Foreword

Abu Bakar Salleh

Engineering Sciences

Analysis of Velocity Profiles in Rectangular Straight Open Channel Flow 1
Abinash Sahoo, Sandeep Samantaray and Rosysmita Bikram Singh

Physical Characteristics of Structured Lipid Synthesized by Lipase 19
Catalyzed Interesterification of Coconut and Palm Oils
Siti Nurhasanah, S Joni Munarso, Nur Wulandari and Purwiyatno Hariyadi

Effect of DL-Methionine Concentration, Moisture Content and Bulk 33
Density of Animal Feed on the Light-Induced Fluorescence as a Process
Analytical Tool
Mohammad Poozesh, Hamidreza Ghasemzadeh, Shamsollah Ablollahpour and Mitra Amoli Diva

A Novel Approach for Automated Operational Modal Analysis Using 49
Image Clustering
Muhammad Danial Bin Abu Hasan, Zair Asrar Bin Ahmad, Mohd Salman Leong and Lim Meng Hee

The Effect of Javanese Gamelan Music on the Growth of Chinese Broccoli 69
Yusuf Hendrawan, Antonius Rizky, Bambang Susilo, Joko Prasetyo and Retno Damayanti

Information, Computer and Communication Technologies

A Genetic Algorithm Approach for Discovering Fuzzy Hierarchical 91
Censored Classification Rules (FHCCRs)
Renu Bala and Saroj Ratnoo

FLA-SLA Aware Cloud Collation Formation Using Fuzzy Preference 117
Relationship Multi-Decision Approach for Federated Cloud
Pradeep Kumar Vadla, Bhanu Prakash Kolla and Thinakaran Perumal

Clustering with Modified Mutation Strategy in Differential Evolution 141
Seema Patil and Anandhi Rajamani Jayadharmarajan



Pertanika Editorial Office, Journal Division,
Office of Deputy Vice Cahnccellor (R&I),
1st Floor, IDEA Tower II,
UPM-MTDC Technology Centre
Universiti Putra Malaysia
43400 UPM Serdang
Selangor Darul Ehsan
Malaysia
<http://www.pertanika.upm.edu.my>
E-mail: executive_editor.pertanika@upm.edu.my
Tel : +603 9769 1622/1616

PENERBIT
UPM
UNIVERSITI PUTRA MALAYSIA
PRESS

<http://penerbit.upm.my>
E-mail: penerbit@upm.edu.my
Tel : +603 9769 8851

